frontiers
RESEARCH TOPICS

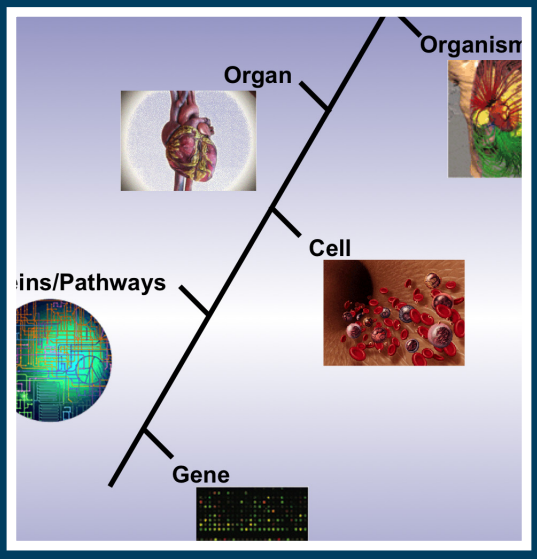

SYSTEMS BIOLOGY APPROACHES TO UNDERSTANDING THE CAUSE AND TREATMENT OF HEART, LUNG, BLOOD, AND SLEEP DISORDERS

Topic Editors
Raimond L. Winslow, Jennie Larkin and Pankaj Qasba

frontiers in PHYSIOLOGY

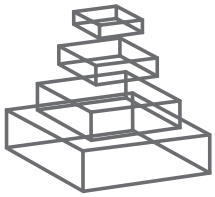

frontiers

ISSN 1664-8714
ISBN 978-2-88919-249-6
DOI 10.3389/978-2-88919-249-6

ABOUT FRONTIERS

Frontiers is more than just an open-access publisher of scholarly articles: it is a pioneering approach to the world of academia, radically improving the way scholarly research is managed. The grand vision of Frontiers is a world where all people have an equal opportunity to seek, share and generate knowledge. Frontiers provides immediate and permanent online open access to all its publications, but this alone is not enough to realize our grand goals.

FRONTIERS JOURNAL SERIES

The Frontiers Journal Series is a multi-tier and interdisciplinary set of open-access, online journals, promising a paradigm shift from the current review, selection and dissemination processes in academic publishing.
All Frontiers journals are driven by researchers for researchers; therefore, they constitute a service to the scholarly community. At the same time, the Frontiers Journal Series operates on a revolutionary invention, the tiered publishing system, initially addressing specific communities of scholars, and gradually climbing up to broader public understanding, thus serving the interests of the lay society, too.

DEDICATION TO QUALITY

Each Frontiers article is a landmark of the highest quality, thanks to genuinely collaborative interactions between authors and review editors, who include some of the world's best academicians. Research must be certified by peers before entering a stream of knowledge that may eventually reach the public - and shape society; therefore, Frontiers only applies the most rigorous and unbiased reviews.
Frontiers revolutionizes research publishing by freely delivering the most outstanding research, evaluated with no bias from both the academic and social point of view.
By applying the most advanced information technologies, Frontiers is catapulting scholarly publishing into a new generation.

WHAT ARE FRONTIERS RESEARCH TOPICS?

Frontiers Research Topics are very popular trademarks of the Frontiers Journals Series: they are collections of at least ten articles, all centered on a particular subject. With their unique mix of varied contributions from Original Research to Review Articles, Frontiers Research Topics unify the most influential researchers, the latest key findings and historical advances in a hot research area!
Find out more on how to host your own Frontiers Research Topic or contribute to one as an author by contacting the Frontiers Editorial Office: researchtopics@frontiersin.org

SYSTEMS BIOLOGY APPROACHES TO UNDERSTANDING THE CAUSE AND TREATMENT OF HEART, LUNG, BLOOD, AND SLEEP DISORDERS

Topic Editors:
Raimond L. Winslow, The Johns Hopkins University, USA
Jennie Larkin, National Heart, Lung, and Blood Institute, USA
Pankaj Qasba, HHS-National Intitutes of Health-Heart Lung and Blood Institute, USA

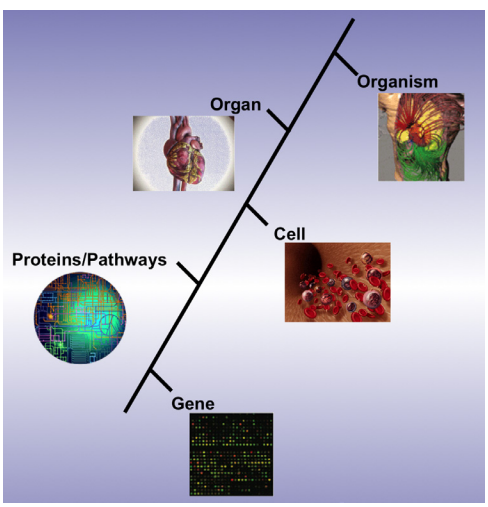

The image was produced by Pankaj Qasba at the National Heart Lung Blood Institute

Development of powerful new high-throughput technologies for probing the transcriptome, proteome and metabolome is driving the rapid acquisition of information on the function of molecular systems. The importance of these achievements cannot be understated – they have transformed the nature of both biology and medicine. Despite this dramatic progress, one of the greatest challenges that continues to confront modern biology is to understand how behavior at the level of genome, proteome and metabolome determines physiological function at the level of cell, tissue and organ in both health and disease. Because of the inherent complexity of biological systems, the development, analysis, and validation of integrative computational models based directly on experimental data is necessary to achieve this understanding. This approach, known as systems biology, integrates computational and experimental approaches through iterative development of mathematical models and experimental validation and testing. The combination of these approaches allows for a mechanistic understanding of the function of complex biological systems in health and their dysfunction in disease.

The National Heart, Lung, and Blood Institute (NHLBI) has recognized the importance of the systems biology approach for understanding normal physiology and perturbations associated with heart, lung, blood, and sleep diseases and disorders. In 2006, NHLBI announced the

Exploratory Program in Systems Biology, followed in 2010 by the NHLBI Systems Biology Collaborations. The goal of these programs is to support collaborative teams of investigators in using experimental and computational strategies to integrate the component parts of biological networks and pathways into computational models that are based firmly on and validated using experimental data. These validated models are then applied to gain insights into the mechanisms of altered system function in disease, to generate novel hypotheses regarding these mechanisms that can be tested experimentally, and to then use the results of experiments to refine the models.

The purpose of this Research Topic is to present the range of innovative, new approaches being developed by investigators working in areas of systems biology that couple experimental and modeling studies to understand the cause and possible treatment of heart, lung, blood and sleep diseases and disorders. This Research Topic will be of great interest to the cardiovascular research community as well as to the general community of systems biologists.

Table of Contents

frontiers in
PHYSIOLOGY

EDITORIAL
published: 28 March 2014
doi: 10.3389/fphys.2014.00107

Systems biology approaches to understanding the cause and treatment of heart, lung, blood, and sleep disorders

Raimond L. Winslow*

Biomedical Engineering, School of Medicine, Institute for Computational Medicine, The Johns Hopkins University, Baltimore, MD, USA
**Correspondence: rwinslow@jhu.edu*

Edited and reviewed by:
George E. Billman, The Ohio State University, USA

Keywords: computational medicine, pulmonary models, cardiac models, immune system models, sepsis models, micro-RNA networks

Development of powerful new high-throughput technologies for probing the transcriptome, proteome, and metabolome is driving the rapid acquisition of information on the function of molecular systems. One of the greatest challenges that we now confront is to understand how behavior at the level of genome, proteome, and metabolome shapes physiological function at the level of cell, tissue and organ in both health and disease. Because of the inherent complexity of biological systems, the development, analysis, and validation of integrative computational models based directly on experimental data is necessary to achieve this understanding. This approach, known as *systems biology*, integrates computational and experimental approaches through iterative development of mathematical models and experimental validation and testing. The combination of these approaches allows for a mechanistic understanding of the function of complex biological systems in health, and their dysfunction in disease.

In 2006, the National Heart, Lung, and Blood Institute (NHLBI) announced the Exploratory Program in Systems Biology, followed in 2010 by the NHLBI Systems Biology Collaborations. The goal of these programs is to support collaborative teams of investigators in using experimental and computational strategies to integrate the component parts of biological networks and pathways into computational models that are based firmly on and validated using experimental data. These validated models are then applied to gain insights into the mechanisms of altered system function in disease, to generate novel hypotheses regarding these mechanisms that can be tested experimentally, and to then use the results of experiments to refine the models. This Research Topic is comprised of articles by researchers funded by this NHLBI program. One set of publications focus on *lung function in health and disease*. Lauzon et al. (2012) present a multi-scale model of lung function spanning molecular (force production by actin-myosin proteins), cellular (regulation of force production by calcium signaling), tissue (smooth muscle contraction coupled with the biomechanics of airway narrowing), and organ scales (mechanical lung impedance). The model provides a new tool for investigating airway hyper responsiveness in the setting of asthma and other lung diseases. O'Connor et al. (2012) present a closed-loop model of neural control of breathing that includes a neural network model of the respiratory pattern generator that drives a systems-level model of lung contraction with feedback to the respiratory pattern generator driven by mechano- and baro-receptor reflexes. The model provides a framework for studying cough disorders. Segers et al. (2012) present results from an experimental study aimed at identifying the role of different neuronal populations in regulating fricative cough. Finally, Fallahi-Sichani et al. (2012) present a multi-scale model of the lung immune response to *Mycobacterium tuberculosis* and use the model to examine the ways in which the NF-kB signaling pathway regulates inflammatory responses. Another set of publications focus on *blood disease*. Dick et al. (2012) develop a multi-scale model of acute inflammatory disease, such as sepsis, that describes baro-, chemo-, and cytokine-reflex control of cardio-pulmonary function mediated by the nucleus *tractus solitarius* (nTS). They present the model-motivated hypothesis that the dis-regulation of cardio-respiratory patterns in the setting of sepsis results from expression of cytokines in the nTS. Goldman et al. (2012) develop models of the erythrocyte signaling pathways that control ATP release as a function of hemoglobin oxygen saturation. These models provide a new framework for studying regulation of microvascular perfusion distribution. Diamond et al. (2013) resent a modeling approach that combines fluid-dynamics simulation of blood flow in the presence of a developing thrombus, which drives formation of a boundary layer of soluble agonists that drives blood platelet motion and binding to the vessel wall. Platelet activation state is driven by the history of intracellular calcium concentration as determined using a neural network model. This work stands out in terms of the different biological scales that are modeled, the different computational approaches employed at each of these scales, and the ability to personalize the model and predict patient-specific responses. Ghonaim et al. (2013) present results from a combined experimental and modeling study of the relationship between hemoglobin oxygen saturation, erythrocyte capillary transit times, and stimulated ATP release. They use a novel experimental approach that uses micropatterned plastic/glass substrates and a flow chamber to measure tissue hemoglobin oxygen saturation level in response to different patterns of tissue oxygen exposure. Experimental and modeling results demonstrate that erythrocyte ATP release is best stimulated by exposing a larger number of capillaries and endothelial cells to the oxygen signal. The paper by Lemons et al. (2013) is focused on the *regulation of protein-protein interaction networks*. They propose, given the large number of protein-protein interactions regulated by micro-RNAs (miRNAs), that miRNA screening may provide key insights into the specific gene-protein networks that are dis-regulated in disease. Using miRNA screening and analytical approaches for identifying miRNA targets, these investigators identified two miRNAs that are up-regulated in human

heart failure, and that inhibit SERCA2. This novel finding is supported by the fact that down-regulation of SERCA2 is a well-known hall-mark of heart failure. Finally, Gauthier et al. (2012) develop a novel, highly *integrative model of the guinea pig ventricular myocyte* describing the key properties of calcium-induced calcium-release that drives cardiac muscle contraction. Using the model, they show that even subtle changes of action potential shape (as is common in many different types of heart disease) can lead to significant changes in the timing and amplitude of intracellular calcium transients and force generation in the heart.

This body of work illustrates the exciting, new, emerging directions that research on heart, lung, blood, and sleep disorders is taking. This work shares common features. Each takes a systems biology approach in which experimental data are used to formulate and refine computational models. Each of the models presented are multi-scale in that they describe function across different levels of biological organization—ranging from molecular interactions to the function of cells, tissue, and in some cases organs. Some models couple different computational methods between scales. In every case, this dove-tailing of experiment and modeling is leading to novel, deep insights into the nature of heart, lung, and blood disease.

ACKNOWLEDGMENTS

NHLBI Exploratory Programs in Systems Biology and Systems Biology Collaborations

REFERENCES

Diamond, S. L., Purvis, J., Chatterjee, M., and Flamm, M. H. (2013). Systems biology of platelet-vessel wall interactions. *Front. Physiol.* 4:229. doi: 10.3389/fphys.2013.00229

Dick, T. E., Molkov, Y. I., Nieman, G., Hsieh, Y.-H., Jacono, F. J., Doyle, J., et al. (2012). Linking inflammation, cardiorespiratory variability, and neural control in acute inflammation via computational modeling. *Front. Physiol.* 3:222. doi: 10.3389/fphys.2012.00222

Fallahi-Sichani, M., Kirschner, D. E., and Linderman, J. J. (2012). NF-κB signaling dynamics play a key role in infection control in tuberculosis. *Front. Physiol.* 3:170. doi: 10.3389/fphys.2012.00170

Gauthier, L. D., Greenstein, J. L., and Winslow, R. L. (2012). Toward an integrative computational model of the guinea pig cardiac myocyte. *Front. Physiol.* 3:244. doi: 10.3389/fphys.2012.00244

Ghonaim, N. W., Fraser, G. M., Ellis, C. G., Yang, J., and Goldman, D. (2013). Modeling steady state SO2-dependent changes in capillary ATP concentration using novel O2 micro-delivery methods. *Front. Physiol.* 4:260. doi: 10.3389/fphys.2013.00260

Goldman, D., Fraser, G. M., Ellis, C. G., Sprague, R. S., Ellsworth, M. L., and Stephenson, A. H. (2012). Toward a multiscale description of microvascular flow regulation: O2-dependent release of ATP from human erythrocytes and the distribution of ATP in capillary networks. *Front. Physiol.* 3:246. doi: 10.3389/fphys.2012.00246

Lauzon, A-M., Bates, J. H. T., Donovan, G., Tawhai, M., Sneyd, J., and Sanderson, M. J. (2012). A multi-scale approach to airway hyperresponsiveness: from molecule to organ. *Front. Physiol.* 3:191. doi: 10.3389/fphys.2012.00191

Lemons, D., Maurya, M. R., Subramaniam, S., and Mercola, M. (2013). Developing microRNA screening as a functional genomics tool for disease research. *Front. Physiol.* 4:223. doi: 10.3389/fphys.2013.00223

O'Connor, R., Segers, L. S., Morris, K. F., Nuding, S. C., Pitts, T., Bolser, D. C., et al. (2012). A joint computational respiratory neural network-biomechanical model for breathing and airway defensive behaviors. *Front. Physiol.* 3:264. doi: 10.3389/fphys.2012.00264

Segers, L. S., Nuding, S. C., Vovk, A., Pitts, T., Baekey, D. M., O'Connor, R., et al. (2012). Discharge identity of medullary inspiratory neurons is altered during repetitive fictive cough. *Front. Physiol.* 3:223. doi: 10.3389/fphys.2012.00223

Received: 29 January 2014; accepted: 03 March 2014; published online: 28 March 2014.
Citation: Winslow RL (2014) Systems biology approaches to understanding the cause and treatment of heart, lung, blood, and sleep disorders. Front. Physiol. ***5****:107. doi: 10.3389/fphys.2014.00107*
This article was submitted to Computational Physiology and Medicine, a section of the journal Frontiers in Physiology.

frontiers in
PHYSIOLOGY

ORIGINAL RESEARCH ARTICLE
published: 06 June 2012
doi: 10.3389/fphys.2012.00170

NF-κB signaling dynamics play a key role in infection control in tuberculosis

Mohammad Fallahi-Sichani*[1†], *Denise E. Kirschner*[2]* and *Jennifer J. Linderman*[1]

[1] *Department of Chemical Engineering, University of Michigan, Ann Arbor, MI, USA*
[2] *Department of Microbiology and Immunology, University of Michigan Medical School, Ann Arbor, MI, USA*

Edited by:
Jennie Larkin, National Heart, Lung, and Blood Institute, USA

Reviewed by:
Sriram Neelamegham, State University of New York at Buffalo, USA
Donald Paul Gaver, Tulane University, USA

***Correspondence:**
Denise E. Kirschner, Department of Microbiology and Immunology, University of Michigan Medical School, Ann Arbor, MI 48109, USA.
e-mail: kirschne@umich.edu;
Jennifer J. Linderman, Department of Chemical Engineering, University of Michigan, Ann Arbor, MI 48109, USA.
e-mail: linderma@umich.edu

[†]***Present address:***
Mohammad Fallahi-Sichani, Department of Systems Biology, Harvard Medical School, Boston, MA 02115, USA.

The NF-κB signaling pathway is central to the body's response to many pathogens. Mathematical models based on cell culture experiments have identified important molecular mechanisms controlling the dynamics of NF-κB signaling, but the dynamics of this pathway have never been studied in the context of an infection in a host. Here, we incorporate these dynamics into a virtual infection setting. We build a multi-scale model of the immune response to the pathogen *Mycobacterium tuberculosis* (Mtb) to explore the impact of NF-κB dynamics occurring across molecular, cellular, and tissue scales in the lung. NF-κB signaling is triggered via tumor necrosis factor-α (TNF) binding to receptors on macrophages; TNF has been shown to play a key role in infection dynamics in humans and multiple animal systems. Using our multi-scale model, we predict the impact of TNF-induced NF-κB-mediated responses on the outcome of infection at the level of a granuloma, an aggregate of immune cells and bacteria that forms in response to infection and is key to containment of infection and clinical latency. We show how the stability of mRNA transcripts corresponding to NF-κB-mediated responses significantly controls bacterial load in a granuloma, inflammation level in tissue, and granuloma size. Because we incorporate intracellular signaling pathways explicitly, our analysis also elucidates NF-κB-associated signaling molecules and processes that may be new targets for infection control.

Keywords: tuberculosis, granuloma, NF-κB signaling pathway, tumor necrosis factor, systems biology, multi-scale modeling

INTRODUCTION

The transcription factor NF-κB is a central inflammatory mediator that is essential for the induction of a variety of inflammatory genes in response to various pathogens and inflammatory cytokines. One such cytokine is tumor necrosis factor-α (TNF), a key regulator of host responses to infection, in particular immune response to *Mycobacterium tuberculosis* (Mtb), the causative agent of tuberculosis (TB). TNF affects the immune response to Mtb through several mechanisms, including induction of macrophage activation to efficiently kill bacteria (Gutierrez et al., 2008; Harris et al., 2008; Mosser and Edwards, 2008), induction of chemokine and cytokine expression (Algood et al., 2004), and apoptosis (Beg and Baltimore, 1996; Van Antwerp et al., 1996; Keane et al., 1997, 2002). These activities, regulated by the NF-κB signaling pathway, have made TNF a key factor for restricting bacterial growth in granulomas, aggregates of bacteria and immune cells within the lung that form as a result of the immune response (Algood et al., 2003; Turner et al., 2003; Ulrichs et al., 2004; Lin et al., 2006; Morel et al., 2006; Tsai et al., 2006; Davis and Ramakrishnan, 2008). Hence, the TNF-induced NF-κB signaling pathway is central to the Mtb immune response, and regulation of intracellular NF-κB signaling dynamics may be key to controlling Mtb infection.

Granulomas are the key pathological feature of TB. If granulomas are capable of containing mycobacteria growth and spread, humans develop a clinically latent infection (Flynn and Klein, 2010; Russell et al., 2010; Flynn et al., 2011). However, if granulomas are impaired in function, infection progresses, granulomas enlarge, and bacteria seed new granulomas; this results in progressive pathology and disease, i.e., active TB. In clinical latency, immunologic perturbation at the level of the granuloma can result in reactivation of infection (Lin et al., 2010). Several experimental (Flynn et al., 1995; Bean et al., 1999; Roach et al., 2002; Chakravarty et al., 2008; Clay et al., 2008; Lin et al., 2010) and theoretical (Marino et al., 2007, 2012; Ray et al., 2009; Fallahi-Sichani et al., 2010, 2011, 2012) studies have confirmed the principal role of TNF in containment of bacteria within TB granulomas.

NF-κB in resting cells is bound to IκB proteins that hold it latent in cytoplasm. Binding of TNF to TNF receptor type 1 (TNFR1) results in activation of IκB kinase (IKK) and IKK-mediated phosphorylation of IκB proteins that ultimately leads to ubiquitination and proteasome-mediated degradation of IκB. Free NF-κB then accumulates in the nucleus and mediates the transcription of target genes (Hayden and Ghosh, 2008; Baltimore, 2011). These genes include extracellular signaling molecules such as TNF and chemokines, intracellular proteins such as macrophage-activating molecules (referred to here as ACT) and inhibitor of apoptosis proteins (IAPs), as well as negative regulators of NF-κB such as IκBα and A20 (Pahl, 1999; Hoffmann and Baltimore, 2006; Gutierrez et al., 2008). The inhibitory impact of A20 on NF-κB results from its roles in attenuating TNFR1 activity and inhibiting IKK activation (Wertz et al., 2004). The regulation of NF-κB via multiple critical intracellular feedback mechanisms

is important for the control of inflammation and immune activation (Hoffmann et al., 2002; Cheong et al., 2006, 2008; Kearns and Hoffmann, 2009). Further, the structural characteristics of the inflammatory genes induced by NF-κB, particularly stability of their corresponding mRNA transcripts, control the dynamics of NF-κB-mediated responses in cells (Hao and Baltimore, 2009). However, the significance of intracellular molecular mechanisms controlling the dynamics of TNF-induced NF-κB signaling in regulating the long-term immune response to Mtb infection is poorly characterized.

One can hypothesize that molecules such as NF-κB that have been shown to be critical to immunity against Mtb may have significant effects at the cell and tissue scale, namely on the formation and function of granulomas (Barry et al., 2009; Kirschner et al., 2010). However, these effects have not been identified. For example, it is unclear how the dynamics of NF-κB-mediated responses (i.e., expression of chemokines, TNF and IAPs, and activation of macrophages) affect formation and function of a granuloma. A critical requirement for such studies is the integration of biological information across multiple biological scales (molecular, cellular, and tissue; **Figure 1**). In this study, we describe a multi-scale computational model that includes: (i) molecular interactions describing the dynamics of the TNF-induced NF-κB signaling pathway, (ii) molecular interactions describing the dynamics of TNFR binding and trafficking, and (iii) cellular/tissue-scale dynamics of the immune response to Mtb. These processes altogether lead to formation of a granuloma. We incorporate a recent model of the NF-κB pathway developed by Tay et al. (2010) based on cell culture data but never explored in the context of an infection in a host. We show that dynamics of TNF-induced NF-κB signaling are critical to controlling bacterial load and inflammation levels at the tissue scale. Further, TNF-mediated activation of resting macrophages, in addition to infected macrophages, is required for a protective immune response, but must be optimally regulated by the immune system to prevent excessive inflammation. We also predict the impact of the dynamics (the extent and the timing) of various NF-κB-mediated responses (i.e., expression of chemokines, TNF, IAPs, and activation of macrophages) on both formation and function of a granuloma. Finally, we ask whether pharmacologically manipulating the NF-κB signaling pathway (for example, by affecting mRNA stability) can improve the outcome of a granuloma that is initially unable to control infection.

MATERIALS AND METHODS

MULTI-SCALE GRANULOMA MODEL

To address questions regarding TNF-regulated host immune responses to Mtb infection in the lung and the impact of NF-κB signaling dynamics on these responses, we developed a multi-scale computational model (**Figure 1**) that describes processes over three biological length scales: tissue, cellular, and molecular. Cellular and tissue-scale dynamics are captured via probabilistic rules for interactions between immune cells and Mtb using a stochastic two-dimensional agent-based model (ABM). Single-cell level molecular scale processes include TNF/TNFR binding and trafficking events (defined here to include synthesis, internalization, recycling, and degradation of ligand and receptors) as well as intracellular NF-κB signaling pathway interactions and reactions that are captured by non-linear ordinary differential equations (ODEs). We briefly describe these models below and then describe our approach for linking them.

Our ABM builds on our previous models that capture cellular scale interactions leading to a tissue-level readout, namely granuloma formation in response to Mtb infection in primates (Segovia-Juarez et al., 2004; Ray et al., 2009; Fallahi-Sichani et al., 2011). The ABM has the following components: *agents* (immune cells, bacteria, chemokines, and cytokines), the *environment* where agents reside (a two-dimensional grid representing a section of lung tissue), probabilistic *rules* that govern the dynamics of agents, including movement, actions, and interactions among agents and between agents and environment, and *time-scales* on which the rules are executed. Briefly, ABM events include: chemotactic movement and recruitment of immune cells from vascular sources to site of infection, intracellular and extracellular growth of Mtb, phagocytosis of bacteria by macrophages, cell death and apoptosis, macrophage/T-cell interactions such as cytolytic functions of cytotoxic T cells (T_c) and IFN-γ-mediated activation of macrophages by pro-inflammatory T cells (T_γ), down-regulation of immune cells by regulatory T cells (T_{reg}), diffusion of chemokines and soluble TNF (sTNF), and caseation (formation of an area of dead tissue with a cheese-like appearance in the center of granuloma). Some of the ABM rules are shown in **Figure 1A** and a detailed description of these aspects of ABM structure and rules can be found in Fallahi-Sichani et al. (2011). ABM parameters that reflect known biological activities are provided in **Table A1** in Appendix. We have now modified our ABM described in Fallahi-Sichani et al. (2011) to facilitate its linking to an NF-κB signaling dynamics model. We now include NF-κB-mediated macrophage activation, NF-κB-mediated chemokine and TNF expression, and NF-κB-mediated inhibition of apoptosis. All of these activities are now controlled as part of the NF-κB signaling dynamics model.

The ODE model describing kinetic processes of TNF/TNFR binding and trafficking occurring in individual cells follows our previous models (Fallahi-Sichani et al., 2010, 2011; **Figure 1B**; **Tables A2** and **A3** in Appendix). We modified the reactions associated with TNF expression in this model to capture the linkage between this process and the NF-κB signaling pathway.

In order to capture the molecular mechanisms that control TNF-mediated responses at the single-cell level, we first need to have a model describing intracellular NF-κB signaling pathway activation that follows TNFR activation due to TNF binding. Then, NF-κB activation must be linked to each of the NF-κB-mediated cell responses that include macrophage activation and expression of chemokines, TNF and IAPs. The single-cell level intracellular NF-κB signaling pathway interactions and reactions are captured by using the deterministic approximation of the two-compartment NF-κB dynamics model presented by Tay et al. (2010). This model combines the two-feedback NF-κB-IκBα-A20 regulatory module with the signal transduction cascade transmitting the signal from sTNF-bound TNFR1 receptors. TNFR1 activation results in an oscillatory NF-κB response that controls the dynamics of gene expression (Nelson et al., 2004). The model includes noise due to different levels of TNFRs and total NF-κB molecules across the cell population. This noise results from

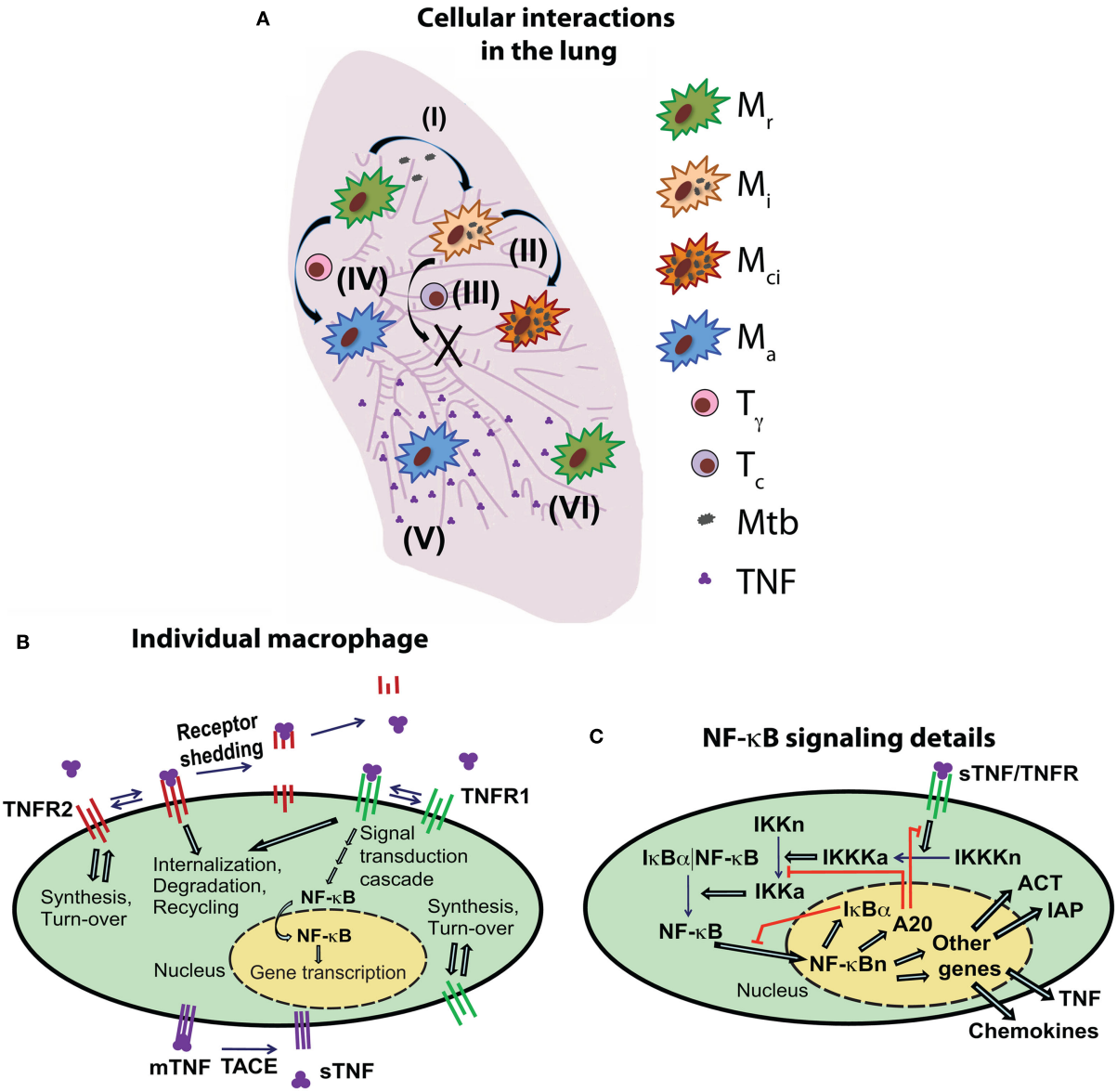

FIGURE 1 | Schematic diagram of the multi-scale model of the immune response to Mtb infection in the lung. (A) An overview of selected cell- and tissue-level ABM rules based on known immunological activities and interactions (M_r, resting macrophage; M_i, infected macrophage; M_{ci}, chronically infected macrophage; M_a, activated macrophage; T_γ, pro-inflammatory IFN-γ producing T cell; T_c, cytotoxic T cell). Example rules are: (I) infection of a resting macrophage after phagocytosis of extracellular Mtb, (II) intracellular growth of Mtb within an infected macrophage, (III) cytotoxic T cell-mediated killing of an infected macrophage, (IV) activation of a macrophage as a result of interaction with IFN-γ producing T cells and TNF, (V) secretion of TNF (and chemokines) from an activated macrophage and diffusion in tissue, (VI) TNF interactions with a macrophage and induction of feedback mechanisms that control TNF-mediated cell responses. For a full description of all ABM rules (see Fallahi-Sichani et al., 2011). **(B)** An overview of TNF/TNFR binding and trafficking interactions and reactions and the NF-κB signal transduction cascade at the level of individual cell. TNF/TNFR-associated processes are modeled in both macrophages and T cells. **(C)** Detailed description of the regulation of the TNF-induced NF-κB signaling pathway and NF-κB-mediated responses [expression of chemokines (CHEM), TNF, inhibitors of apoptosis (IAP), and macrophage-activating molecules (ACT)] for an individual macrophage.

random assignment of initial values for TNFR densities and total NF-κB molecules to each single cell as described in Tay et al. (2010).

In this study, we link the molecular scale NF-κB dynamics model described above to four major NF-κB-mediated cell responses in macrophages (**Figure 1C**). These responses are: TNF expression, chemokine expression, macrophage activation, and inhibition of apoptosis. To do this, we incorporate NF-κB-mediated expression of genes corresponding to TNF, chemokines, a generic IAP, and a generic macrophage-activating molecule (ACT), translation of their mRNA transcripts, and secretion of translated TNF and chemokines into the single-cell level NF-κB dynamics model. The generic IAP represents a family of proteins

that serve as inhibitors of apoptosis (e.g., cellular inhibitors of apoptosis, c-IAPs) via binding and inhibiting caspase activities (Karin and Lin, 2002). The generic ACT represents various molecules (e.g., membrane trafficking molecules or lysosomal enzyme) that are induced by NF-κB and are required for activation of a macrophage to efficiently kill bacteria (Gutierrez et al., 2008). The reactions, parameters, and equations describing intracellular NF-κB signaling pathway processes and NF-κB-mediated responses for an individual cell are listed in **Tables A4–A6** in Appendix. The full range of parameter values explored is given in **Table A5** in Appendix; values in parentheses indicate baseline model values, which are intermediate values in the ranges explored and yield the containment outcome.

LINKING THE SINGLE-CELL MOLECULAR SCALE NF-κB SIGNALING DYNAMICS TO THE TNF/TNFR KINETIC MODEL AND THE CELLULAR/TISSUE-SCALE MODEL

The activation of TNF-induced NF-κB signaling pathway requires sTNF binding to cell surface TNFR1. It is this process that links the TNF/TNFR kinetic model to the intracellular NF-κB signaling dynamics model. The activation of the NF-κB signaling pathway initiates four major cellular responses: induction of chemokine expression, TNF expression, macrophage activation (to efficiently kill bacteria), and inhibition of apoptosis. These responses serve as the link between the single-cell molecular scale NF-κB signaling dynamics model and the cellular/tissue-scale model (**Figure 1**). Secretion of chemokines and TNF by macrophages into extracellular spaces follows NF-κB-mediated expression of their genes and translation of their mRNA transcripts as described in the NF-κB signaling equations (see **Tables A4** and **A6** in Appendix). Recent studies on NF-κB activation and apoptosis have shown that these are processes with discrete nature at the single-cell level, with more cells responding to higher doses of stimuli and longer periods of stimulation (Albeck et al., 2008; Tay et al., 2010). Accordingly, we describe NF-κB-mediated activation of a macrophage as a Poisson process with a probability determined within each time-step (Δt), based on a Poisson rate parameter that is a function of the macrophage activation rate constant (k_{ACT}), intracellular concentration of ACT protein [ACT], and the ACT concentration threshold for macrophage activation (τ_{ACT}):

$$P_{\mathrm{activation}} = \begin{cases} 0 & ;[\mathrm{ACT}] < \tau_{\mathrm{ACT}} \\ 1 - e^{-k_{\mathrm{ACT}}([\mathrm{ACT}]-\tau_{\mathrm{ACT}})\Delta t} & ;[\mathrm{ACT}] \geq \tau_{\mathrm{ACT}} \end{cases} \quad (1)$$

Similarly, we model TNF-induced apoptosis for each individual cell by:

$$P_{\mathrm{apoptosis}} = \begin{cases} 0 & ;[\mathrm{sTNF/TNFR1}_i] < \tau_{\mathrm{apopt}} \\ 1 - e^{-k_{\mathrm{apopt}}([\mathrm{sTNF/TNFR1}_i]-\tau_{\mathrm{apopt}})\Delta t} & ;[\mathrm{sTNF/TNFR1}_i] \geq \tau_{\mathrm{apopt}} \end{cases} \quad (2)$$

We use a Poisson process with a probability computed as a function of the apoptosis rate constant (k_{apopt}), the concentration of internalized sTNF/TNFR1 complexes ($\mathrm{sTNF/TNFR1_i}$), and the concentration threshold for internalized sTNF/TNFR1 (τ_{apopt}). The inhibitory impact of the NF-κB activation on macrophage apoptosis is captured by:

$$k_{\mathrm{apopt}} = \frac{k_{\mathrm{IAP}}}{k_{\mathrm{IAP}} + [\mathrm{IAP}]} k^0_{\mathrm{apopt}} \quad (3)$$

The magnitude of k_{apopt} is a function of the intracellular concentration of IAP, the apoptosis inhibition coefficient (k_{IAP}), and the intrinsic TNF-induced apoptosis rate constant (k^0_{apopt}). Parameters introduced in Eqs 1–3 are listed in **Table A5** in Appendix.

COMPUTER SIMULATIONS AND MODEL OUTPUTS

The multi-scale computational model is used to simulate the immune response to Mtb and granuloma formation in the lung for 200 days post-infection. Simulations are initiated following placement of one infected macrophage with one intracellular bacterium at the center of a grid representing a section of lung tissue (see Fallahi-Sichani et al., 2011 for details). Cell-cell interactions governed by ABM rules are updated within every ABM time-step ($\Delta t = 10$ min). Molecular scale processes, including TNF/TNFR dynamics and NF-κB signaling dynamics at the single-cell level, are updated within shorter time-steps ($dt = 0.5$ s).

We use several model outputs to track formation and function of a granuloma during the immune response to Mtb. Granuloma size and total number of macrophages and T cells in tissue are used as readouts to track granuloma formation. We also track total number of bacteria and total number of activated macrophages as readouts for quantifying granuloma function. These outputs represent the ability of a granuloma to control infection and inflammation, respectively. Other outputs of interest include chemokine and TNF concentrations in tissue, and caseation area.

We previously showed that the efficacy of TNF in controlling Mtb infection is strongly affected by whether or not macrophages stimulated by TNF are infected (Fallahi-Sichani et al., 2011). To analyze how NF-κB signaling affects infected versus uninfected (resting) macrophages in a granuloma, we define *infected/resting cell ratios*, $R_{\mathrm{apoptosis}}$ and $R_{\mathrm{activation}}$, as follows. $R_{\mathrm{apoptosis}}$ is defined as the ratio of the number of infected macrophages that undergo TNF-mediated apoptosis to the number of resting macrophages that undergo TNF-mediated apoptosis during a 200-day period post-infection. $R_{\mathrm{activation}}$ is similarly defined as the number of infected macrophages that become activated (to efficiently kill bacteria) to the number of resting macrophages that become activated during a 200-day period post-infection.

PARAMETER ESTIMATION

We estimate ABM parameter values from literature data or by using uncertainty analysis as described in detail in Marino et al. (2008); Ray et al. (2009); Fallahi-Sichani et al. (2011). Cell-specific TNFR densities and rate constants for TNF/TNFR processes are estimated based on experimental data from our group (Fallahi-Sichani et al., 2010) and other groups as indicated in **Table A3** in Appendix. Intracellular NF-κB signaling parameters are as in Tay et al. (2010; **Table A5** in Appendix). Values of parameters used to describe TNF-induced apoptosis and NF-κB-mediated cell responses, including induction of expression of chemokines

and TNF, macrophage activation and inhibition of apoptosis, are estimated via uncertainty analysis. This is done by varying parameter values in ranges that are consistent with experimental and modeling data on time-scales of events associated with these responses (Fotin-Mleczek et al., 2002; Rangamani and Sirovich, 2007; Albeck et al., 2008; Hao and Baltimore, 2009; Tay et al., 2010). We specify a baseline set of parameter values (containment baseline values as listed in **Tables A1**, **A3**, and **A5** in Appendix) that robustly leads to control of infection in granulomas with organized structures as reported for humans and non-human primates.

MODEL VALIDATION

Immunity to Mtb in humans and animal studies has been attributed to activities of a variety of factors, including specific immune cells (e.g., macrophages and T cells), cytokines (e.g., TNF and IFN-γ), chemokines (e.g., CCL2, CCL5, CXCL9/10/11), immune receptors (e.g., TNFR1), and signaling pathways (e.g., NF-κB). Our new multi-scale computational model [resulting from the incorporation of the single-cell level NF-κB signaling dynamics (Tay et al., 2010), as indicated in **Figure 1**, into our previous generation model (Fallahi-Sichani et al., 2011)] must retain its ability to reproduce experimental findings regarding the importance of these factors in control of infection. Our model is able to recapitulate different types of granuloma with different abilities to control infection and inflammation (**Figure 2**). Using a baseline set of values for model parameters (**Tables A1**, **A3**, and **A5** in Appendix), our model captures a state of equilibrium between the host and Mtb termed *bacterial containment* (**Figure 2A**). This state represents control of infection for more than 200 days within a well-circumscribed granuloma containing stable bacteria numbers ($<10^3$ total bacteria). Simulated containment granulomas closely represent experimentally characterized solid granulomas (Algood et al., 2003; Turner et al., 2003; Ulrichs et al., 2004; Lin et al., 2006; Morel et al., 2006; Tsai et al., 2006; Davis and Ramakrishnan, 2008) that are predominantly composed of uninfected macrophages surrounding a core of bacteria and infected and activated macrophages with T cells localized at the periphery. Varying values of important model parameters lead to other possibilities, including clearance of bacteria, uncontrolled growth of bacteria, or excessive inflammation.

We also perform virtual deletion and depletion experiments that mimic experimental gene knockout or molecule depletion studies. Loss of activity is achieved by setting relevant parameters (e.g., probabilities or rate constants) to zero or raising relevant thresholds to an unattainable level. Virtual deletion refers to the loss of activity from the beginning of simulation (such as a gene knockout) and virtual depletion refers to the loss of activity after establishment of a granuloma. Specifically, we simulate gene knockouts of previously identified essential components of the Mtb immune response (e.g., TNF, TNFR1, IFN-γ, and T cell knockouts). These simulation studies are used for testing the ability of the model to predict different infection outcomes under pathological conditions compatible with both experimental and previous modeling data on granuloma formation. Simulations of TNF or TNFR1 knockout (**Figure 2B**), IFN-γ gene knockout, and deletion of T cells (data not shown), in agreement with experimental data and our previous modeling studies (Flynn, 2004; Segovia-Juarez et al., 2004; Lin et al., 2007; Ray et al., 2009; Lin and Flynn, 2010; Fallahi-Sichani et al., 2011), lead to uncontrolled growth of Mtb and formation of granulomas with irregular structures that include very high numbers of extracellular bacteria, large numbers of infected macrophages, and widespread caseation. In contrast, inhibition of TNFR1 internalization, a process critical to control of TNF concentration and apoptosis (Fallahi-Sichani et al., 2010, 2011), leads to excessive inflammation by which we mean recruitment of a large number of immune cells in tissue, uncontrolled activation of macrophages, and very high concentrations of TNF (**Figure 2C**).

SENSITIVITY ANALYSIS

A second approach to identify important processes that determine infection outcome is to use sensitivity analysis. We use sensitivity analysis to analyze the impact of parameters describing events at different scales (molecular, cellular, or tissue scales) on model outputs describing granuloma outcomes. In particular, we use sensitivity analysis techniques adapted for use in ABMs (Marino et al., 2008) to analyze the impact of NF-κB signaling-associated

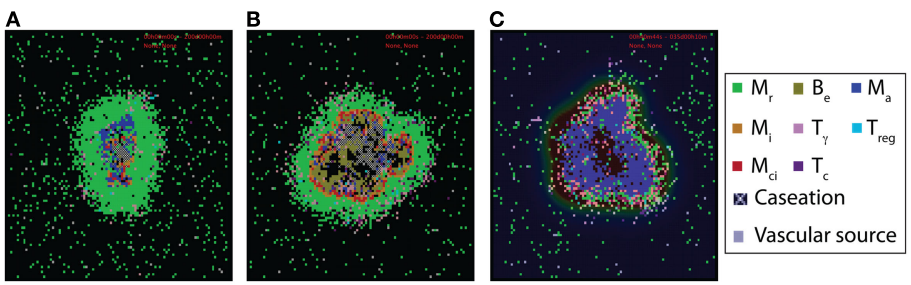

FIGURE 2 | Examples of virtual control experiments for the multi-scale computational model of granuloma formation in response to Mtb infection. (A–C) Granuloma snapshots for **(A)** a scenario of containment (200 days post-infection), **(B)** a TNFR1 knockout ($TNFR1_{mac} = TNFR1_{Tcell} = 0$) scenario resulting in uncontrolled growth of bacteria 200 days post-infection, and **(C)** a scenario of blocking TNFR1 internalization ($k_{int1} = 0$) resulting in excessive inflammation 5 weeks post-infection, respectively. All other model parameter values used for these experiments are listed in **Tables A1**, **A3**, and **A5** in Appendix. Cell types and status are shown by different color squares, as indicated on the right side of the figure (M_r, resting macrophage; M_i, infected macrophage; M_{ci}, chronically infected macrophage; M_a, activated macrophage; B_e, extracellular bacteria; T_γ, pro-inflammatory IFN-γ producing T cell; T_c, cytotoxic T cell; T_{reg}, regulatory T cell). Caseation and vascular sources are also indicated.

parameter values on model outputs such as bacteria numbers, macrophage and T cell numbers, chemokine and TNF concentrations in tissue, granuloma size, and caseation area. Latin hypercube sampling (LHS) is an algorithm that allows multiple parameters to be varied and sampled simultaneously in a computationally efficient manner (Blower and Dowlatabadi, 1994). The correlation of model outputs with each parameter is quantified via calculation of a partial rank correlation coefficient (PRCC). PRCC values vary between −1 (perfect negative correlation) and +1 (perfect positive correlation) and can be differentiated based on p-values derived from Student's t test. Here, we performed 700-sample LHS simulations for each parameter. Each sampled parameter set was run four times (to account for stochasticity) and averages of the outputs were used to calculate PRCC values. The choice of the number of simulations is determined by the desired significance level for the PRCC (Blower and Dowlatabadi, 1994; Marino et al., 2008). Here, 700 runs imply that PRCC values above +0.13 or below −0.13 are significantly different from zero ($p < 0.001$).

PROGRAMMING AND VISUALIZATION

The model was implemented in C++. We use Qt, a C++ framework that runs our simulations on multiple platforms (Linux, Windows, and Mac OS) with a graphical user interface (GUI). Through the GUI, one can visualize and track different aspects of the granuloma, including the structure and molecular concentration gradients, as the granuloma forms and is maintained. Simulations can be run with or without graphical visualization. For more detailed description of the Qt framework applications in studying granuloma characteristics see (Marino et al., 2011).

RESULTS

CONTRIBUTION OF NF-κB SIGNALING FACTORS TO CONTROL OF GRANULOMA OUTCOMES

We know from both experimental data and our previous modeling studies that TNF availability and activities (i.e., macrophage activation, induction of TNF and chemokine expression, regulation of immune cell recruitment, and induction of apoptosis) within a granuloma are essential to control of infection (Keane et al., 2001; Winthrop, 2006; Marino et al., 2007; Chakravarty et al., 2008; Ray et al., 2009; Lin et al., 2010; Fallahi-Sichani et al., 2011). The NF-κB signaling pathway activated as a result of TNF binding to TNFR1 on the membrane of immune cells is critical for regulation of these activities. Having validated that our multi-scale model gives results consistent with experimental data (see Materials and Methods, **Figure 2**), we now predict the role of biochemical factors and interactions associated with the NF-κB signaling pathway on important outcomes at the granuloma level: number of bacteria, granuloma size and amount of caseation, and TNF concentration.

We analyze the impact of TNF-mediated NF-κB signaling-associated parameters in six groups as defined in **Table A5** in Appendix: (1) concentration of intracellular signaling molecules [NF-κB, IκBα kinase (IKK), and IKK kinase (IKKK)], (2) processes associated with activation of the signal transduction cascade, (3) A20 and IκBα synthesis, (4) IκBα interactions, (5) NF-κB and IκBα transport between cytoplasm and nucleus, and (6) NF-κB-mediated cell responses (TNF and chemokine expression, macrophage activation, inhibition of apoptosis). Notably, parameters identified to have strong correlations with bacterial levels within a granuloma, i.e., granuloma function, belong to groups 1–3 and group 6 (see **Table 1** and **Tables A7** and **A8** in Appendix). Processes within groups 4 and 5, although essential for NF-κB activation, have a less significant impact on model outputs as compared to other groups when they are all varied within a 10-fold range around their baseline values. Within group 1, increasing the average number of NF-κB molecules per macrophage significantly enhances macrophage activation and thus reduces bacterial numbers within a granuloma. This is consistent with the published data on the role of NF-κB in activating macrophages to kill mycobacteria (Gutierrez et al., 2008). Similarly, IKKK activation (from group 2), a key process in NF-κB signaling cascade that occurs following TNF binding to TNFR1, strongly and negatively correlates with bacterial load. Among group 3 parameters, the rate of NF-κB binding at A20 and IκBα gene promoters as well as the rates of A20 and IκBα mRNA synthesis and translation positively correlate with bacterial levels. In contrast, increasing A20 and IκBα mRNA and protein degradation rates impairs granuloma's ability to control infection. These results highlight the important role that the NF-κB-IκBα-A20 feedback regulatory module plays in the regulation of the NF-κB-mediated cell responses (Cheong et al., 2008), and thus in the regulation of granuloma function.

Finally, group 6 comprises important parameters with strong effects on most model outcomes. Parameters that control either TNF expression or macrophage activation significantly influence granuloma function and thus bacterial load within a granuloma. In contrast, parameters that only affect chemokine expression or apoptosis do control granuloma size (formation) but without exerting strong effects on bacterial load (see **Table 1** and **Table A8** in Appendix). This is consistent with our previous studies indicating that TNF-induced macrophage activation is a key mechanism for controlling bacterial growth (Ray et al., 2009). The rate of NF-κB-dependent mRNA synthesis for chemokines, TNF, the generic macrophage-activating molecule (ACT), and the inhibitor of apoptosis (IAP) is an important parameter. It strongly and positively correlates with all TNF-induced cellular responses in tissue (i.e., apoptosis, TNF and chemokine expression, and macrophage activation) and negatively correlates with bacterial load, caseation, and granuloma size. The stability of TNF mRNA, as well as TNF translation, degradation, and secretion significantly control granuloma outcomes. Increasing the rates of degradation of TNF mRNA and intracellular TNF or reducing the rates of TNF translation and secretion enhance bacterial numbers, caseation, and granuloma size. In addition, the ACT translation rate (negatively), and the ACT degradation rate as well as the ACT concentration threshold for macrophage activation (positively) correlate with bacterial load within a granuloma. Increasing the chemokine secretion rate or reducing the chemokine mRNA degradation rate elevates chemokine concentration in tissue, enhancing immune cell recruitment, and granuloma growth.

Overall, each of the above parameters identified as critical for formation and function of a granuloma represents a potential target for therapeutic modulation. Hence, we focus our next analysis on the potential effects of manipulation of each of these parameters.

Table 1 | NF-κB-associated model parameters significantly correlated with outputs of interest, i.e., bacterial numbers, granuloma size, caseation area, and TNF concentration at day 200 post-infection.

NF-κB-associated parameter*	Parameter description† (parameter group number‡)	Selected model outputs			
		Total number of bacteria	Granuloma size	Caseation	Average tissue concentration of sTNF
$NF\text{-}\kappa B_{tot}$	Average number of NF-κB molecules per cell (1)	−−		−	
k_a	IKKK activation rate (2)	−−			
k_i	IKKK inactivation rate (2)	+			
q_1	Rate of NF-κB binding at A20 and IκBα gene promoters (3)	+			
c_1	Inducible A20 and IκBα mRNA synthesis rate (3)	++		+	
c_3	A20 and IκBα mRNA degradation rate (3)	−−			
c_4	A20 and IκBα translation rate (3)	++			−−
c_5	A20 degradation rate (3)	−−			++
c_{1r}	Rate of NF-κB-induced mRNA synthesis for chemokines, TNF, ACT, and IAP (6)	−−	−−	−−	++
c_{3rchem}	Chemokine mRNA degradation rate (6)		−−	++	
c_{4chem}	Chemokine translation rate (6)			−−	
e_{3chem}	Chemokine secretion rate (6)		++	−	
c_{3rTNF}	TNF mRNA degradation rate (6)	++	++	++	
c_{4TNF}	TNF translation rate (6)	−−	−−	−−	++
c_{5TNF}	Intracellular TNF degradation rate (6)	++	++	++	
e_{3TNF}	TNF secretion rate (6)	−−	−−	−−	++
c_{4ACT}	ACT translation rate (6)	−−			
c_{5ACT}	ACT degradation rate (6)	++			
τ_{ACT}	ACT concentration threshold for macrophage activation (6)	++			
c_{5IAP}	IAP degradation rate (6)		−−	−−	−

*Detailed sensitivity analysis results are presented in **Tables A7** and **A8** in Appendix.*

**Only parameters with significant PRCC values are indicated. Significant positive and negative correlations are shown using + and − as follows: −/+: 0.001 < p-value < 0.01, −−/++: p-value < 0.001.*

† IKKK, IKK kinase; IKK, IκBα kinase; ACT, generic macrophage-activating molecule; IAP, inhibitor of apoptosis.

*‡ NF-κB signaling-associated parameters are categorized in six groups as defined in **Table A5** in Appendix: (1) concentration of intracellular signaling molecules [NF-κB, IκBα kinase (IKK), and IKK kinase (IKKK)], (2) processes associated with activation of the signal transduction cascade, (3) A20 and IκBα synthesis, (4) IκBα interactions, (5) NF-κB and IκBα transport between cytoplasm and nucleus, and (6) NF-κB-mediated cell responses.*

OPTIMAL REGULATION OF NF-κB SIGNALING DYNAMICS FOR CONTROL OF INFECTION WITHOUT INDUCING EXCESSIVE INFLAMMATION

The analysis above highlights various NF-κB signaling pathway-associated biochemical factors and intracellular interactions that show significant impacts on infection outcomes at all scales (molecular, cellular, and tissue). How do these responses influence granuloma formation? Does manipulation of these mechanisms alter infection outcome at the granuloma level? The effects of manipulation of four important NF-κB-associated factors as identified by sensitivity analysis - (i) average number of NF-κB molecules per cell, $NF\text{-}\kappa B_{tot}$, (ii) IKKK inactivation rate constant, k_i, (iii) A20 and IκBα mRNA degradation rate constant, c_3, and (iv) TNF mRNA degradation rate constant, c_{3rTNF} - on granuloma formation, total number of bacteria, sTNF concentration, and macrophage activation after Mtb infection are shown in **Figure 3**.

The values of these parameters significantly determine the ability of a granuloma to control bacterial load. Small numbers of NF-κB molecules per cell, slow rates of A20 and IκBα mRNA degradation, rapid rates of IKKK inactivation, and rapid rates of TNF mRNA degradation all lead to uncontrolled growth of bacteria within a 200-day period post-infection (**Figure 3B**). These effects result from reduced rates of TNF-induced activation of macrophages, diminishing their ability to kill bacteria. Slowly altering the values of these parameters to intermediate levels reduces bacteria numbers and leads to containment of bacteria within a stable granuloma. Further increasing the values of parameters $NF\text{-}\kappa B_{tot}$ and c_3, or further reducing the values of parameters c_{3rTNF} and k_i from their containment-level values each further reduces bacterial numbers and increases the chance of infection clearance. However, these clearance outcomes are generally accompanied by uncontrolled rates of macrophage activation and cell infiltration as well as very high concentrations of TNF in tissue; markers of excessive inflammation and immunopathology (**Figures 3C,D**). Overall, as depicted in **Figures 3A–D**, intermediate (containment baseline) values of $NF\text{-}\kappa B_{tot}$, k_i, c_3 and c_{3rTNF} (listed in **Table A5** in Appendix) lead to control of infection in stable granulomas with very low bacteria numbers (and sometimes clearance), low levels of TNF, and low levels of macrophage

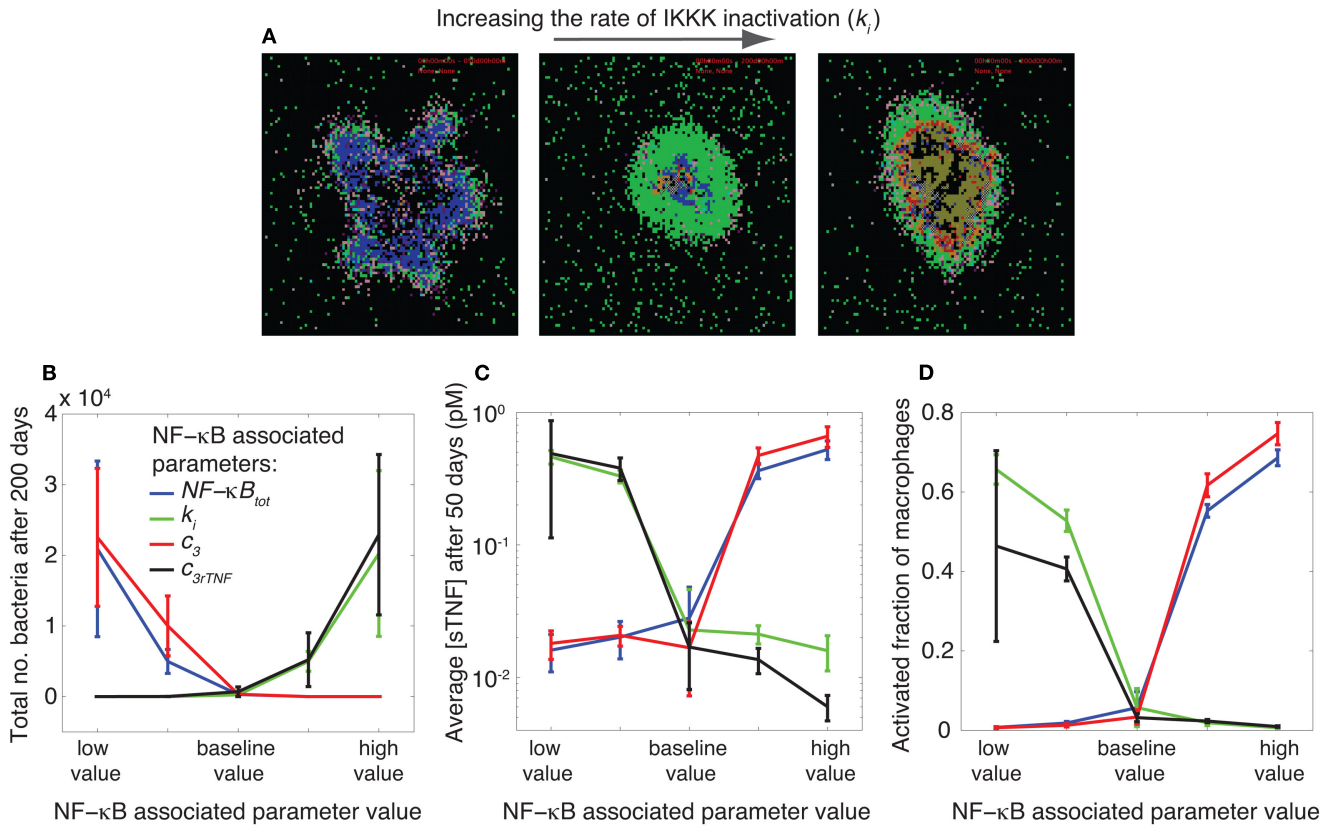

FIGURE 3 | NF-κB signaling dynamics control bacterial growth and inflammation level in tissue. (A) Granuloma snapshots for slow ($k_i = 3.2 \times 10^{-3}$ s^{-1}), intermediate ($k_i = 10^{-2}$ s^{-1}), and rapid ($k_i = 3.2 \times 10^{-2}$ s^{-1}) rates of IKKK inactivation. Slow rates of IKKK inactivation lead to uncontrolled macrophage activation and excessive inflammation. An intermediate value of k_i results in control of infection in a stable granuloma containing small numbers of bacteria. Rapid rates of IKKK inactivation lead to large numbers of bacteria and infected macrophages as well as widespread caseation. The colors representing cells of different type and status in granuloma snapshots are the same as those shown and defined in **Figure 2**. **(B–D)** Simulation results showing the effects of four important parameters, as identified by sensitivity analysis, controlling NF-κB signaling dynamics on granuloma outcomes (total number of bacteria, tissue concentration of TNF, and macrophage activation). The parameters are: the average number of NF-κB molecules per cell ($NF\text{-}κB_{tot}$), IKKK inactivation rate (k_i), A20 and IκBα mRNA degradation rate (c_3), and TNF mRNA degradation rate (c_{3rTNF}). In each simulation, only one of these parameters is varied. The baseline (intermediate) values of these parameters lead to clearance or control of infection in stable granulomas with very low bacterial numbers, low levels of TNF, and low levels of macrophage activation. Perturbing the NF-κB signaling dynamics by varying values of these parameters impair the balance toward either uncontrolled growth of bacteria or excessive inflammation (high TNF concentrations and high levels of macrophage activation) in tissue. The baseline value of each parameter is as reported in **Table A5** in Appendix and is as follows: $NF\text{-}κB_{tot} = 10^5$, $k_i = 10^{-2}$ s^{-1}, $c_3 = 7.5 \times 10^{-4}$ s^{-1}, $c_{3rTNF} = 3.8 \times 10^{-4}$ s^{-1}. The difference between the low value and high value presented in the figure is one order of magnitude.

activation. Perturbing NF-κB signaling dynamics by varying values of these parameters (i.e., rates at which these processes occur) impairs the balance toward either uncontrolled growth of bacteria or excessive inflammation in tissue. Hence, our model predicts that the optimal regulation of the TNF-mediated NF-κB signaling pathway is essential to controlling infection and inflammation in tissue. The balance between the NF-κB-mediated bacterial killing activities and the NF-κB-mediated inflammation results in an equilibrium state, i.e., containment of bacteria within a stable granuloma with minimal inflammation.

HOW DO NF-κB SIGNALING DYNAMICS BALANCE INFLAMMATION AND BACTERIAL KILLING?

How do the NF-κB-associated intracellular processes identified above affect the balance of inflammation and bacterial killing activities within a granuloma? We previously showed that the impact of TNF concentration on granuloma outcomes is strongly correlated with whether or not macrophages stimulated by TNF are infected (Fallahi-Sichani et al., 2011). This motivates us to test whether there is a correlation between the effect of NF-κB signaling dynamics on granuloma function (as described in **Figure 3**) and the infection status of macrophages stimulated by TNF during the immune response. Thus, we analyze the infection status of macrophages that become activated or undergo apoptosis after Mtb infection by computing infected/resting cell ratios, $R_{activation}$ and $R_{apoptosis}$, as defined in Section "Materials and Methods." Our model predicts a very significant effect of important NF-κB-associated parameters on both $R_{activation}$ and $R_{apoptosis}$ (**Figure 4**). At small numbers of NF-κB molecules per cell, slow rates of A20 and IκBα mRNA degradation, rapid rates of IKKK inactivation, or rapid rates of TNF mRNA degradation, infected macrophages are the main cells that become activated or undergo apoptosis as

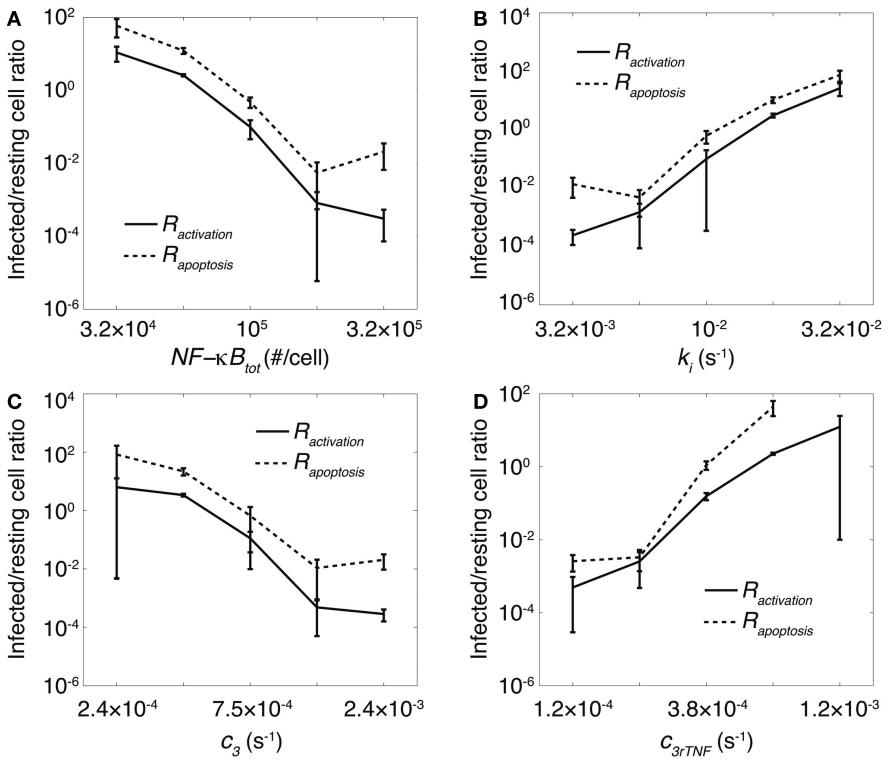

FIGURE 4 | The impact of important processes associated with the NF-κB signaling dynamics on granuloma outcomes is correlated with status of macrophages that undergo apoptosis or become activated by TNF. Simulation results show the effect of **(A)** the average number of NF-κB molecules per cell, $NF\text{-}\kappa B_{tot}$, **(B)** IKKK inactivation rate, k_i, **(C)** A20 and IκBα mRNA degradation rate, c_3, and **(D)** TNF mRNA degradation rate, c_{3rTNF} on infected/resting cell ratios $R_{apoptosis}$ and $R_{activation}$ within a 200 day period after Mtb infection.

a result of TNF activities ($R_{activation}$ and $R_{apoptosis} \gg 1$). However, with one order of magnitude increase in each of these parameters, resting macrophages become the main responders to TNF signaling ($R_{activation}$ and $R_{apoptosis} \ll 1$). Comparing these results with results from the previous section (**Figure 3**), we observe a significant correlation between infected/resting cell ratios, $R_{activation}$ and $R_{apoptosis}$, and the granuloma outcomes (i.e., bacterial load and inflammation). At large values of $R_{activation}$ and $R_{apoptosis}$ (values of 1–10 or greater), we observe uncontrolled growth of Mtb. Small values of these ratios (smaller than ∼0.1) correlate with excessive inflammation in tissue. Intermediate values of infected/resting cell ratios (between 0.1 and 1) are correlated with control of infection without excessive inflammation. The absolute values of these ratios are calculated based on our two-dimensional simulations and might change in three-dimensional settings. These results suggest that a *balance* between the number of resting macrophages and infected macrophages responding to TNF signaling is required for control of infection and inflammation within a stable granuloma, and that such a balance is critically regulated by NF-κB signaling dynamics.

THE STABILITY OF mRNA TRANSCRIPTS CONTROLS BACTERIAL LOAD, INFLAMMATION, AND GRANULOMA SIZE BY AFFECTING THE DYNAMICS OF NF-κB-MEDIATED RESPONSES

A key advantage of incorporating NF-κB signaling dynamics into our granuloma model is the ability to study the impact of the dynamics of NF-κB-mediated responses (i.e., macrophage activation, expression of chemokines, TNF, and inhibitors of apoptosis) on granuloma outcomes. These responses follow NF-κB oscillations (Nelson et al., 2004). The dynamics of these responses depend, to a large extent, on the stability of their corresponding mRNA transcripts (Hao and Baltimore, 2009). Thus, we analyzed the effect of varying the stability of mRNA transcripts corresponding to macrophage activation (ACT), and expression of chemokines (CHEM), TNF, and inhibitors of apoptosis (IAP) on granuloma outcomes, bacterial load, and inflammation level (represented by the activated fraction of macrophages). Varying the stability (half-life; $t_{1/2}$) of mRNA transcripts significantly influences the dynamics of the NF-κB-mediated responses (e.g., chemokine secretion) in an individual cell (**Figure 5A**). Simulations show that the stability of mRNA transcripts for NF-κB-mediated responses, particularly ACT, TNF, and CHEM, significantly control bacteria numbers and inflammation level in tissue (**Figures 5B,C**). The impact of the IAP mRNA stability on these model outcomes is less significant.

Our analysis shows that there are combinations of TNF, ACT, CHEM, and IAP mRNA transcript half-lives that lead to distinct model outcomes such as control of infection within stable granulomas, clearance, uncontrolled growth of bacteria, or excessive inflammation (see **Figure 2**). For example, a containment outcome (as highlighted by yellow stars in **Figures 5B,C**)

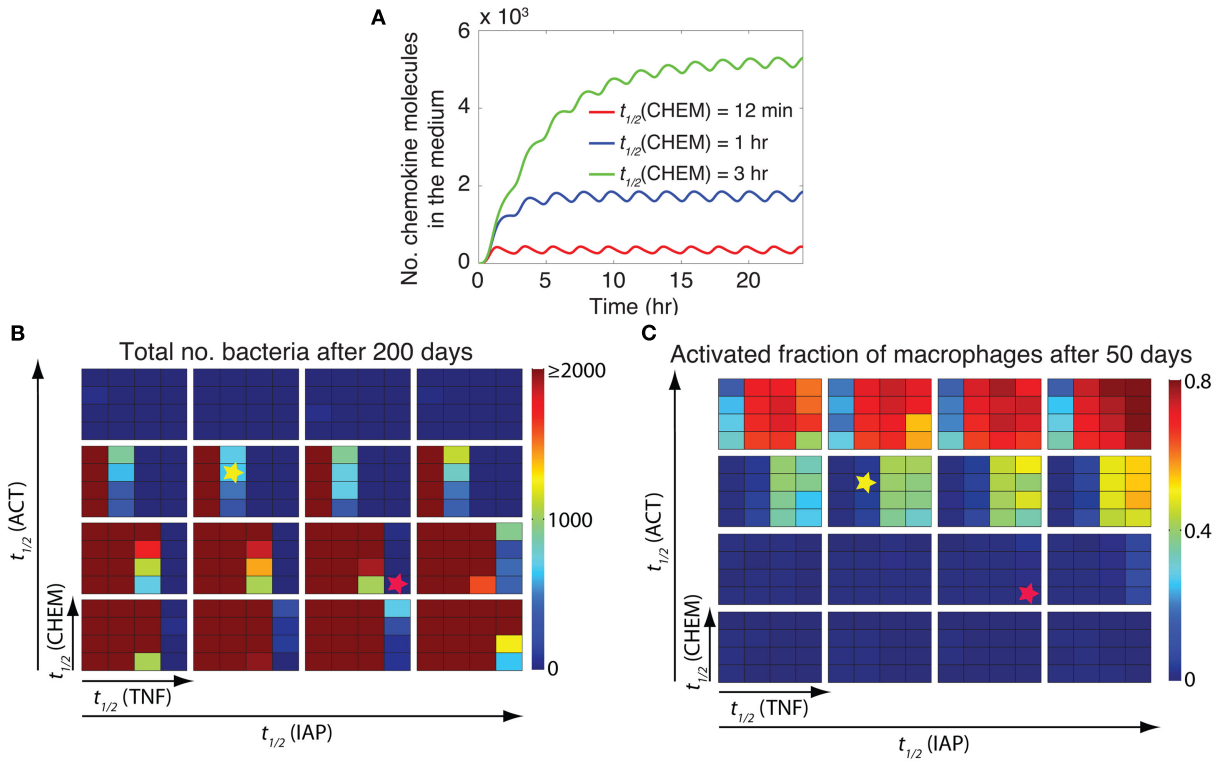

FIGURE 5 | The stability of mRNA transcripts controls bacterial load and inflammation by affecting the dynamics of NF-κB-mediated responses. **(A)** The effect of the stability (half-life) of chemokine mRNA transcripts [$t_{1/2}$(CHEM)] on the dynamics of chemokine secretion by an individual cell. Simulated results are produced using the single-cell level NF-κB signaling dynamics model for continuous stimulation of a cell by 1 ng/ml TNF, with parameters and equations as described in **Tables A3**, **A5**, and **A6** in Appendix. A similar pattern of response can be observed when the effects of mRNA stability on the dynamics of other NF-κB-mediated responses (i.e., expression of ACT, IAP, and TNF) are studied (data not shown). **(B,C)** Simulation results for the effect of the stability of mRNA transcripts corresponding to major NF-κB-mediated responses, including macrophage activation [$t_{1/2}$(ACT)], TNF expression [$t_{1/2}$(TNF)], chemokine expression [$t_{1/2}$(CHEM)], and inhibitor of apoptosis protein expression [$t_{1/2}$(IAP)], on bacteria numbers **(B)** and on the activated fraction of macrophages **(C)** 200 days post-infection. Small squares represent different values of $t_{1/2}$(CHEM) vertically and different values of $t_{1/2}$(TNF) horizontally. Large boxes represent different values of $t_{1/2}$(ACT) vertically and different values of $t_{1/2}$(IAP) horizontally. Four values of mRNA half-life were tested in simulations: 12 min, 30 min, 1 h, and 3 h. Simulation results were averaged over 10 repetitions. Yellow stars represent an example scenario with containment outcome. This state represents control of infection for more than 200 days within a well-circumscribed granuloma containing stable bacteria numbers ($<10^3$ total bacteria). Red stars represent an example scenario that leads to clearance of Mtb (total bacteria = 0) without inducing excessive inflammation (activated fraction of macrophages <0.15).

may result from the following parameter combination: mRNA transcript half-life of 30 min for TNF, mRNA transcript half-life of 1 h for ACT, mRNA transcript half-life of 1 h for CHEM, and mRNA transcript half-life of 30 min for IAP. Increasing mRNA transcript stabilities for TNF and ACT from these values increases the chance of extensive inflammation in tissue, whereas reducing their values significantly enhance bacterial load. Increasing mRNA transcript stabilities for CHEM from the suggested value also slightly enhances bacterial load as well as granuloma size (data not shown). Further, our results suggest that there are combinations of mRNA stabilities for TNF-mediated responses that lead to clearance of Mtb without inducing excessive inflammation (see red stars in **Figures 5B,C** as an example). This set of mRNA stability values significantly enhances the ability of granuloma to kill bacteria while limiting inflammation by controlling macrophage activation and apoptosis. Overall, these results suggest that the differential dynamics of NF-κB-mediated responses resulting from differential stabilities of their corresponding mRNA transcripts are essential to regulate granuloma's ability to control infection and inflammation.

THE TIMING OF NF-κB-INDUCED MACROPHAGE ACTIVATION IS CRITICAL TO CONTROLLING EXCESSIVE INFLAMMATION

In the previous section, we showed that stability of mRNA transcripts associated with NF-κB-mediated inflammatory molecules significantly affects the immune response to Mtb. The stability of mRNA controls both the extent and the timing of NF-κB-mediated responses in individual cells (Tay et al., 2010). However, it is not clear whether it is mostly the extent of response, the timing of response, or both that influence granuloma outcomes. In other words, how important is the speed of each individual macrophage's response to TNF signals in determining the overall function of a granuloma? To address this question, we analyzed the effect on granuloma outcomes of varying the stability of ACT, CHEM, TNF, and IAP mRNA transcripts while maintaining the average extent of these responses at their containment baseline

levels (determined in the previous section). To maintain the average extent of each response as its corresponding mRNA stability is varied, we simultaneously vary another parameter associated with a process downstream of mRNA translation. Parameters varied to adjust the extent of the four NF-κB-mediated responses are: TNF secretion rate ($e_{3\text{TNF}}$), chemokine secretion rate ($e_{3\text{chem}}$), ACT concentration threshold for macrophage activation (τ_{ACT}), macrophage activation rate constant (k_{ACT}), and apoptosis inhibition constant (k_{IAP}). For example, we increase the chemokine mRNA half-life [$t_{1/2}$(CHEM)] and decrease the chemokine secretion rate ($e_{3\text{chem}}$) simultaneously to achieve the same average number of chemokine molecules secreted in tissue by an individual macrophage (**Figure 6A**).

Analysis of granuloma simulations indicates that among the four major NF-κB-mediated responses studied here (TNF, CHEM, ACT, and IAP), only the timing of ACT response, i.e., macrophage activation, is critical to control of inflammation in tissue as well as bacterial load within a granuloma (**Figures 6B,C**). Early NF-κB-mediated activation of macrophages that occurs because of highly unstable ACT mRNA transcripts lead to uncontrolled activation of macrophages and excessive inflammation in tissue. This suggests that both extent and timing of NF-κB-mediated macrophage activation are critical to control of the immune response to Mtb.

CAN MANIPULATING TNF-MEDIATED NF-κB SIGNALING DYNAMICS IMPROVE GRANULOMA FUNCTION?

Above we showed that optimal regulation of NF-κB signaling dynamics is critical to control of infection within a granuloma and control of inflammation in lung tissue. Thus, impairing NF-κB activation leads to uncontrolled growth of bacteria that is in agreement with NF-κB knockout experimental studies (Yamada et al., 2001). The repression of NF-κB signaling in infected macrophages is also a mechanism that pathogenic mycobacteria use to enhance their survival and growth (Gutierrez et al., 2008). An important question is then: can we find a hypothetical treatment strategy that

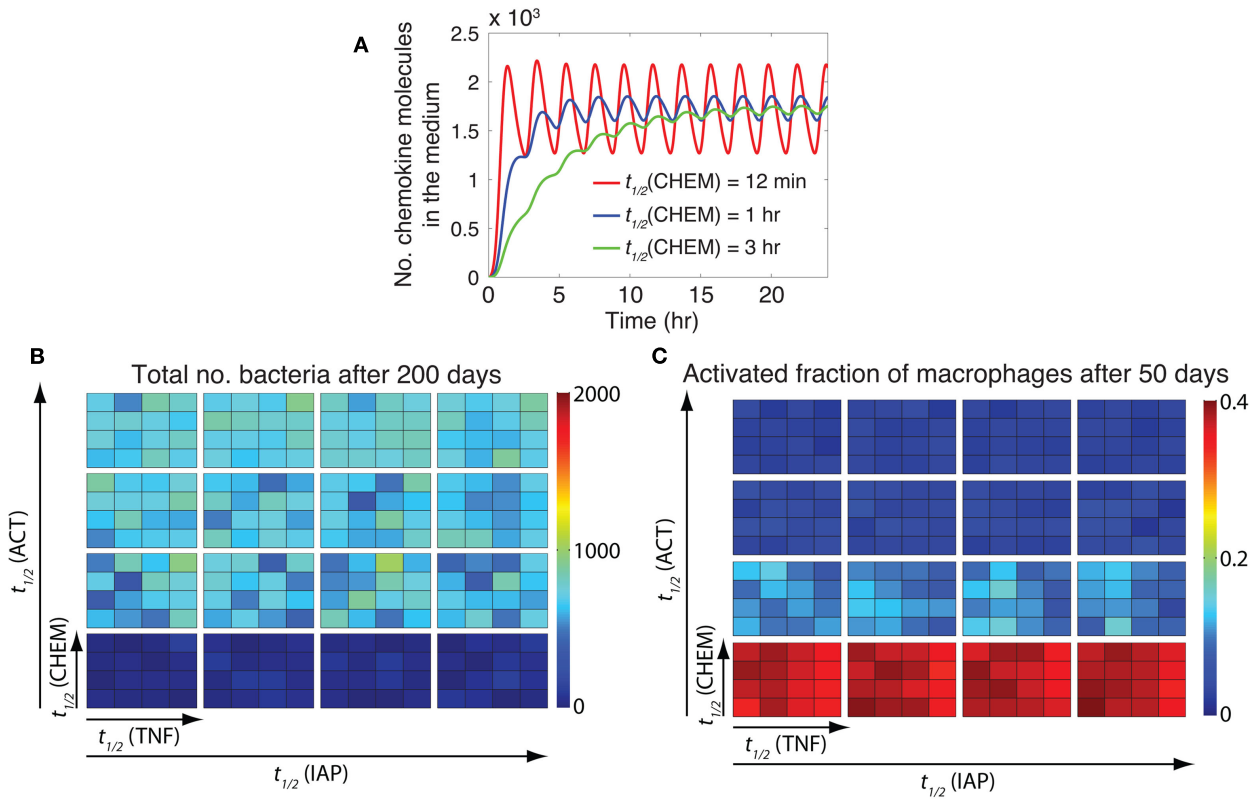

FIGURE 6 | The timing of NF-κB-induced macrophage activation is critical to control of inflammation. (A) Varying the chemokine mRNA half-life [$t_{1/2}$(CHEM): 12 min, 1 h, and 3 h, respectively] and the chemokine secretion rate ($e_{3\text{chem}}$: 7.65×10^{-5} s^{-1}, 1.39×10^{-5} s^{-1}, 4.52×10^{-6} s^{-1}, respectively) by an individual macrophage simultaneously leads to secretion of the same average number of chemokine molecules, but with distinct temporal patterns of chemokine secretion. Simulated results are produced using the single-cell level NF-κB signaling dynamics model for continuous stimulation of a cell by 1 ng/ml TNF, with parameters and equations as described in **Tables A3**, **A5**, and **A6** in Appendix. A similar pattern of response can be observed when the effects of mRNA stability on the timing of other NF-κB-mediated responses (i.e., expression of ACT, IAP, and TNF) are studied (data not shown). **(B,C)** Simulation results for the effect of the timing of NF-κB-mediated responses, including macrophage activation [regulated by $t_{1/2}$(ACT)], TNF expression [regulated by $t_{1/2}$(TNF)], chemokine expression [regulated by $t_{1/2}$(CHEM)], and inhibitor of apoptosis protein expression [regulated by $t_{1/2}$(IAP)], on bacteria numbers **(B)**, and on the activated fraction of macrophages **(C)** at 200 days post-infection. Small squares represent different values of $t_{1/2}$(CHEM) vertically and different values of $t_{1/2}$(TNF) horizontally. Large boxes represent different values of $t_{1/2}$(ACT) vertically and different values of $t_{1/2}$(IAP) horizontally. Four values of mRNA half-life were tested in simulations: 12 min, 30 min, 1 h, and 3 h. Simulation results were averaged over 10 repetitions.

affects TNF-mediated NF-κB signaling in a granuloma to improve ability to control bacteria? We first simulate formation of a granuloma that is unable to control bacterial growth due to impaired NF-κB signaling (e.g., at high rates of IKKK inactivation, k_i) for 100 days. Then, we change one or more of the NF-κB-associated parameters to restore NF-κB activities within the granuloma and resume simulation for another 100 days.

Our analysis, as depicted in **Figure 7**, indicates that reducing k_i (IKKK inactivation rate constant) from high values to intermediate (containment-level) values (Treatment I) enhances the ability of a granuloma to control bacteria. However, average bacteria levels for a 200-day granuloma after changing k_i are generally higher than bacteria levels resulting from simulating a containment scenario. A further decrease in the value of k_i (Treatment II) is more successful in killing bacteria. However, it leads to uncontrolled activation of macrophages and excessive inflammation in tissue. This suggests that targeting the process of IKKK inactivation alone is not sufficient for infection control at the granuloma scale. In another set of simulations (Treatment III), decreasing k_i to intermediate values, together with manipulating stability of mRNA transcripts associated with NF-κB-mediated responses (based on results from **Figure 5**) leads to better outcomes. Increasing the half-life of TNF

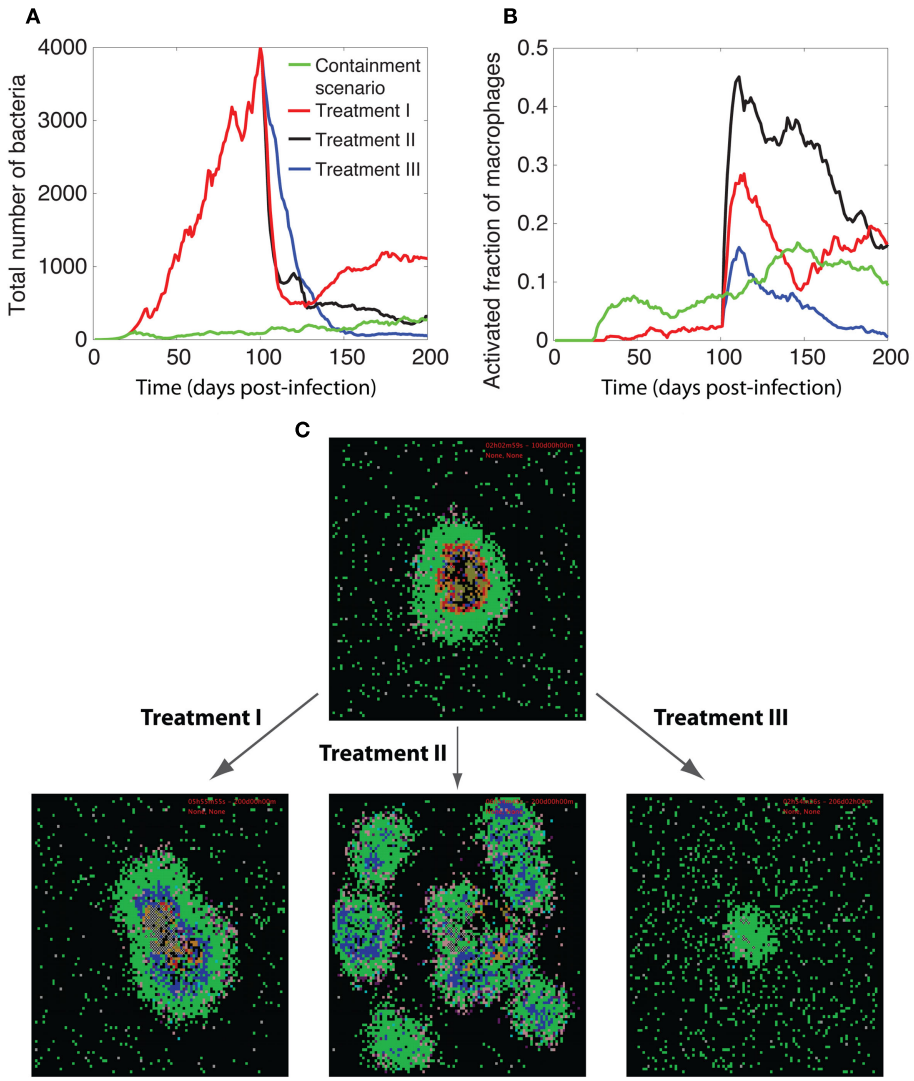

FIGURE 7 | Manipulation of TNF-mediated NF-κB signaling for improving granuloma function. Comparison of the dynamics of **(A)** bacteria growth, **(B)** activated fraction of macrophages, and **(C)** granuloma snapshots among three different treatment methods for enhancing NF-κB activities. In all treatments, we first simulate formation of a granuloma that is unable to control bacteria growth due to impaired NF-κB signaling at high rates of IKKK inactivation ($k_i = 3.16 \times 10^{-2}\ s^{-1}$) for 100 days (all other parameter values are as listed in **Tables A1**, **A3**, and **A5** in Appendix). Then, we change one or more of the NF-κB-associated parameters to restore NF-κB activities within the granuloma and resume simulation for another 100 days. Parameter changes in each treatment are as follows: treatment I: $k_i = 1 \times 10^{-2}\ s^{-1}$, Treatment II: $k_i = 3.16 \times 10^{-3}\ s^{-1}$, Treatment III: $k_i = 1 \times 10^{-2}\ s^{-1}$, $t_{1/2}$(TNF) = 3 h, $t_{1/2}$(ACT) = 30 min, $t_{1/2}$(TNF) = 1 h. Simulation results were averaged over 10 repetitions. The colors representing cells of different type and status in granuloma snapshots are the same as those shown and defined in **Figure 2**.

mRNA transcripts to 3 h, reducing the half-life of ACT mRNA transcripts to 30 min, and setting the IAP mRNA transcripts to 1 h improves the granuloma outcome, inducing efficient killing of bacteria without excessive inflammation. Overall, this suggests that manipulating the dynamics of NF-κB-mediated responses, particularly macrophage activation, TNF and IAP expression, can improve the function of a TB granuloma.

DISCUSSION

Systems biology approaches have been increasingly helpful for studying the interactions between the components of biological systems, and understanding how these interactions give rise to the function of the system. These approaches are particularly essential for studying systems that consist of several components on different spatial and temporal scales, as they are extremely challenging to study using traditional experimental methods. An important example is to study the role that the dynamics of intracellular signaling pathways, with time-scales of seconds to hours, play in the long-term immune response of a host to a pathogen. In this work, we focus on this problem by asking if simulations of the immune response can successfully capture both short and long-term dynamics over length scales that range from molecular to tissue. We build and simulate a multi-scale model to explore the impact of NF-κB dynamics on the long-term immune response to the pathogen Mtb. NF-κB plays an important role in coordinating both innate and adaptive immunity. A recently published study of the pathway uses data from cells in culture to elucidate the kinetics of the pathway and to identify critical intracellular mechanisms controlling the NF-κB response in a single cell (Tay et al., 2010). A recent modeling study has also shown how NF-κB response can control cytokine waves in tissue (Yde et al., 2011). Yet it is unclear how these mechanisms affect the immune response in tissue, where immune cells and bacteria interact with each other and determine the outcome of infection.

Immune responses induced by Mtb infection are myriad and complex, and it remains incompletely understood which responses are required for protection and which contribute to pathology (Cooper, 2009; Lin and Flynn, 2010). Indeed, there is significant overlap among protective and pathological responses. An important example, as dissected in this study, is TNF-induced NF-κB activation. **Figure 8** summarizes our results showing how NF-κB-mediated responses are critical for restricting bacterial growth in a granuloma, but excessive activation of the NF-κB pathway in macrophages leads to pathological inflammation in tissue. Containment of bacteria, particularly at the level of the granuloma, is achieved when a balance exists between the NF-κB-mediated bacterial killing activities and the NF-κB-mediated inflammation. Such a balance is controlled by a combination of molecular scale biochemical processes identified in detail in this study, such as IKKK activity, A20 and IκBα interactions, and stability of mRNA transcripts associated with NF-κB-mediated responses. Optimal regulation of these processes, in the presence of an efficient T cell-meditated response, can lead to clearance of bacteria. Further, we find that processes controlling the dynamics of NF-κB signaling critically regulate whether resting macrophages or infected macrophages are the major targets for TNF signaling within a granuloma. Unless sufficient numbers of resting macrophages relative to infected macrophages become activated by TNF, uncontrolled growth of Mtb occurs. On the other hand, excessive activation of resting macrophages leads to uncontrolled inflammation. These findings highlight the potential importance of NF-κB-associated processes as targets in future studies examining approaches to controlling both TB infection and pathology.

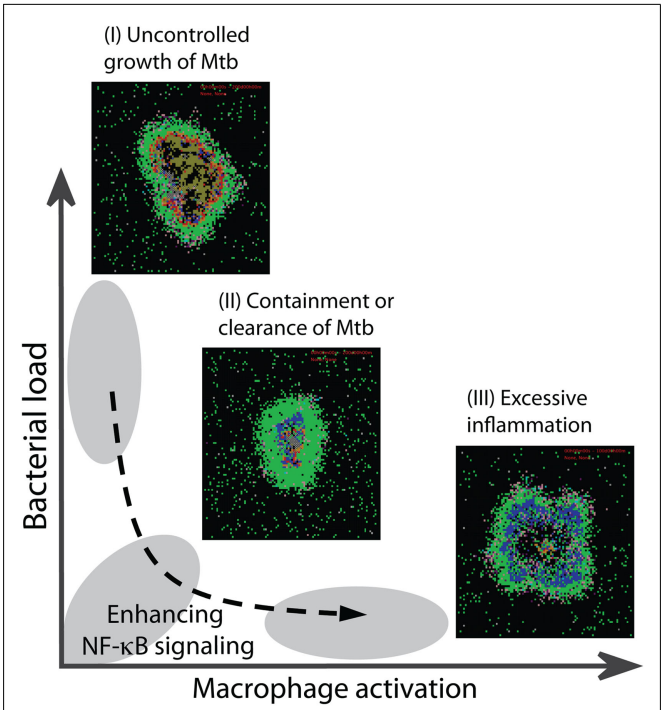

FIGURE 8 | Optimal regulation of the TNF-mediated NF-κB signaling dynamics is essential for optimal granuloma outcomes. Impaired NF-κB activity leads to uncontrolled growth of bacteria within a granuloma (outcome I). Containment or clearance of bacteria (outcome II) is achieved when the NF-κB-mediated responses are regulated such that small, but sufficient numbers of macrophages become activated to kill bacteria. Uncontrolled macrophage activation due to over-activity of NF-κB leads to excessive inflammation in tissue (outcome III).

Another interesting finding from our study is that the stability of mRNA transcripts corresponding to NF-κB-mediated responses, particularly macrophage activation and expression of TNF and chemokines, significantly affects bacterial load in a granuloma, inflammation level in tissue, and granuloma size. This is due to the impact of mRNA stability on the kinetics of these responses (Hao and Baltimore, 2009). Tay et al. (2010) have also described how differences in stability of NF-κB-induced mRNA transcripts and TNF concentration influence the dynamics of expression of different inflammatory genes. We find that both the extent and the timing of NF-κB-mediated macrophage activation are critical to control of the immune response to Mtb. However, the significance of the stability of TNF and chemokine mRNA transcripts is mostly due its effect on the extent of these responses. This is the first study, to our knowledge, that reveals the importance of the dynamics of various NF-κB-mediated responses on immunity to Mtb. Further, we show that manipulating the dynamics of these

responses in a granuloma that is unable to contain infection due to, for example, pathogen-induced inhibition of NF-κB activation can significantly improve granuloma function.

Finally, our approach is an initial step toward understanding the molecular targets at the level of intracellular signaling pathways for control of the tissue-scale outcomes of the immune response to Mtb, particularly granuloma formation. We anticipate that other factors, including crosstalk between signaling mediated by the Mtb bacteria and other cytokines through various types of receptors and different signaling pathways (Basak and Hoffmann, 2008) in various types of cells, or the noise resulting from discrete regulation of TNFR activity and transcription regulation (Lipniacki et al., 2007) will further influence the ability of a granuloma to contain infection. Importantly, our unique multi-scale approach provides a platform for discovering which intracellular interventions may enhance immunity to Mtb, and has implications for testing and optimizing new vaccine and therapeutic strategies that minimize non-specific or off-target side effects.

ACKNOWLEDGMENTS

This work was supported by National Institutes of Health Grants R33 HL092844 (Jennifer J. Linderman), R33 HL092853 and R01 HL106804 (Denise E. Kirschner), and R01 EB012579 (awarded to both Denise E. Kirschner and Jennifer J. Linderman), and by a University of Michigan Rackham Predoctoral Fellowship awarded to Mohammad Fallahi-Sichani. We thank Simeone Marino for helpful discussions, and Paul Wolberg for software engineering and programming.

REFERENCES

Albeck, J. G., Burke, J. M., Spencer, S. L., Lauffenburger, D. A., and Sorger, P. K. (2008). Modeling a snap-action, variable-delay switch controlling extrinsic cell death. *PLoS Biol.* 6, 2831–2852. doi:10.1371/journal.pbio.0060299

Algood, H. M., Chan, J., and Flynn, J. L. (2003). Chemokines and tuberculosis. *Cytokine Growth Factor Rev.* 14, 467–477.

Algood, H. M., Lin, P. L., Yankura, D., Jones, A., Chan, J., and Flynn, J. L. (2004). TNF influences chemokine expression of macrophages *in vitro* and that of CD11b+ cells *in vivo* during Mycobacterium tuberculosis infection. *J. Immunol.* 172, 6846–6857.

Baltimore, D. (2011). NF-kappaB is 25. *Nat. Immunol.* 12, 683–685.

Barry, C. E.,3rd, Boshoff, H. I., Dartois, V., Dick, T., Ehrt, S., Flynn, J., Schnappinger, D., Wilkinson, R. J., and Young, D. (2009). The spectrum of latent tuberculosis: rethinking the biology and intervention strategies. *Nat. Rev. Microbiol.* 7, 845–855.

Basak, S., and Hoffmann, A. (2008). Crosstalk via the NF-kappaB signaling system. *Cytokine Growth Factor Rev.* 19, 187–197.

Bean, A. G., Roach, D. R., Briscoe, H., France, M. P., Korner, H., Sedgwick, J. D., and Britton, W. J. (1999). Structural deficiencies in granuloma formation in TNF gene-targeted mice underlie the heightened susceptibility to aerosol Mycobacterium tuberculosis infection, which is not compensated for by lymphotoxin. *J. Immunol.* 162, 3504–3511.

Beg, A. A., and Baltimore, D. (1996). An essential role for NF-kappaB in preventing TNF-alpha-induced cell death. *Science* 274, 782–784.

Blower, S. M., and Dowlatabadi, H. (1994). Sensitivity and uncertainty analysis of complex models of disease transmission: an HIV model, as an example. *Int. Stat. Rev.* 62, 229–243.

Chakravarty, S. D., Zhu, G., Tsai, M. C., Mohan, V. P., Marino, S., Kirschner, D. E., Huang, L., Flynn, J., and Chan, J. (2008). Tumor necrosis factor blockade in chronic murine tuberculosis enhances granulomatous inflammation and disorganizes granulomas in the lungs. *Infect. Immun.* 76, 916–926.

Cheong, R., Bergmann, A., Werner, S. L., Regal, J., Hoffmann, A., and Levchenko, A. (2006). Transient IkappaB kinase activity mediates temporal NF-kappaB dynamics in response to a wide range of tumor necrosis factor-alpha doses. *J. Biol. Chem.* 281, 2945–2950.

Cheong, R., Hoffmann, A., and Levchenko, A. (2008). Understanding NF-kappaB signaling via mathematical modeling. *Mol. Syst. Biol.* 4, 192.

Clay, H., Volkman, H. E., and Ramakrishnan, L. (2008). Tumor necrosis factor signaling mediates resistance to mycobacteria by inhibiting bacterial growth and macrophage death. *Immunity* 29, 283–294.

Cooper, A. M. (2009). Cell-mediated immune responses in tuberculosis. *Annu. Rev. Immunol.* 27, 393–422.

Davis, J. M., and Ramakrishnan, L. (2008). "The very pulse of the machine": the tuberculous granuloma in motion. *Immunity* 28, 146–148.

Fallahi-Sichani, M., El-Kebir, M., Marino, S., Kirschner, D. E., and Linderman, J. J. (2011). Multiscale computational modeling reveals a critical role for TNF-{alpha} receptor 1 dynamics in tuberculosis granuloma formation. *J. Immunol.* 186, 3472–3483.

Fallahi-Sichani, M., Flynn, J. L., Linderman, J. J., and Kirschner, D. E. (2012). Differential risk of tuberculosis reactivation among anti-TNF therapies is due to drug binding kinetics and permeability. *J. Immunol.* 188, 3169–3178.

Fallahi-Sichani, M., Schaller, M. A., Kirschner, D. E., Kunkel, S. L., and Linderman, J. J. (2010). Identification of key processes that control tumor necrosis factor availability in a tuberculosis granuloma. *PLoS Comput. Biol.* 6, e1000778. doi:10.1371/journal.pcbi.1000778

Flynn, J. L. (2004). Immunology of tuberculosis and implications in vaccine development. *Tuberculosis (Edinb)* 84, 93–101.

Flynn, J. L., Chan, J., and Lin, P. L. (2011). Macrophages and control of granulomatous inflammation in tuberculosis. *Mucosal Immunol.* 4, 271–278.

Flynn, J. L., Goldstein, M. M., Chan, J., Triebold, K. J., Pfeffer, K., Lowenstein, C. J., Schreiber, R., Mak, T. W., and Bloom, B. R. (1995). Tumor necrosis factor-alpha is required in the protective immune response against Mycobacterium tuberculosis in mice. *Immunity* 2, 561–572.

Flynn, J. L., and Klein, E. (2010). "Pulmonary tuberculosis in monkeys," in *A Color Atlas of Comparative Pulmonary Tuberculosis Histopathology*, eds. J. Leong, V. Dartois, and T. Dick (Boca Raton: CRC Press, Taylor & Francis Publishers), 83–106.

Fotin-Mleczek, M., Henkler, F., Samel, D., Reichwein, M., Hausser, A., Parmryd, I., Scheurich, P., Schmid, J. A., and Wajant, H. (2002). Apoptotic crosstalk of TNF receptors: TNF-R2-induces depletion of TRAF2 and IAP proteins and accelerates TNF-R1-dependent activation of caspase-8. *J. Cell. Sci.* 115, 2757–2770.

Gutierrez, M. G., Mishra, B. B., Jordao, L., Elliott, E., Anes, E., and Griffiths, G. (2008). NF-kappa B activation controls phagolysosome fusion-mediated killing of mycobacteria by macrophages. *J. Immunol.* 181, 2651–2663.

Hao, S., and Baltimore, D. (2009). The stability of mRNA influences the temporal order of the induction of genes encoding inflammatory molecules. *Nat. Immunol.* 10, 281–288.

Harris, J., Hope, J. C., and Keane, J. (2008). Tumor necrosis factor blockers influence macrophage responses to Mycobacterium tuberculosis. *J. Infect. Dis.* 198, 1842–1850.

Hayden, M. S., and Ghosh, S. (2008). Shared principles in NF-kappaB signaling. *Cell* 132, 344–362.

Hoffmann, A., and Baltimore, D. (2006). Circuitry of nuclear factor kappaB signaling. *Immunol. Rev.* 210, 171–186.

Hoffmann, A., Levchenko, A., Scott, M. L., and Baltimore, D. (2002). The IkappaB-NF-kappaB signaling module: temporal control and selective gene activation. *Science* 298, 1241–1245.

Karin, M., and Lin, A. (2002). NF-kappaB at the crossroads of life and death. *Nat. Immunol.* 3, 221–227.

Keane, J., Balcewicz-Sablinska, M. K., Remold, H. G., Chupp, G. L., Meek, B. B., Fenton, M. J., and Kornfeld, H. (1997). Infection by Mycobacterium tuberculosis promotes human alveolar macrophage apoptosis. *Infect. Immun.* 65, 298–304.

Keane, J., Gershon, S., Wise, R. P., Mirabile-Levens, E., Kasznica, J., Schwieterman, W. D., Siegel, J. N., and Braun, M. M. (2001). Tuberculosis associated with infliximab, a tumor necrosis factor alpha-neutralizing agent. *N. Engl. J. Med.* 345, 1098–1104.

Keane, J., Shurtleff, B., and Kornfeld, H. (2002). TNF-dependent BALB/c murine macrophage apoptosis following Mycobacterium tuberculosis infection inhibits bacillary growth in an IFN-gamma independent manner. *Tuberculosis (Edinb)* 82, 55–61.

Kearns, J. D., and Hoffmann, A. (2009). Integrating computational and biochemical studies to explore mechanisms in NF-{kappa}B signaling. *J. Biol. Chem.* 284, 5439–5443.

Kirschner, D. E., Young, D., and Flynn, J. L. (2010). Tuberculosis: global approaches to a global disease. *Curr. Opin. Biotechnol.* 21, 524–531.

Lin, P. L., and Flynn, J. L. (2010). Understanding latent tuberculosis: a moving target. *J. Immunol.* 185, 15–22.

Lin, P. L., Myers, A., Smith, L., Bigbee, C., Bigbee, M., Fuhrman, C., Grieser, H., Chiosea, I., Voitenek, N. N., Capuano, S. V., Klein, E., and Flynn, J. L. (2010). Tumor necrosis factor neutralization results in disseminated disease in acute and latent Mycobacterium tuberculosis infection with normal granuloma structure in a cynomolgus macaque model. *Arthritis Rheum.* 62, 340–350.

Lin, P. L., Pawar, S., Myers, A., Pegu, A., Fuhrman, C., Reinhart, T. A., Capuano, S. V., Klein, E., and Flynn, J. L. (2006). Early events in Mycobacterium tuberculosis infection in cynomolgus macaques. *Infect. Immun.* 74, 3790–3803.

Lin, P. L., Plessner, H. L., Voitenok, N. N., and Flynn, J. L. (2007). Tumor necrosis factor and tuberculosis. *J. Investig. Dermatol. Symp. Proc.* 12, 22–25.

Lipniacki, T., Puszynski, K., Paszek, P., Brasier, A. R., and Kimmel, M. (2007). Single TNFalpha trimers mediating NF-kappaB activation: stochastic robustness of NF-kappaB signaling. *BMC Bioinformatics* 8, 376. doi:10.1186/1471-2105-8-376

Marino, S., El-Kebir, M., and Kirschner, D. (2011). A hybrid multi-compartment model of granuloma formation and T cell priming in Tuberculosis. *J. Theor. Biol.* 280, 50–62.

Marino, S., Fallahi-Sichani, M., Linderman, J. J., and Kirschner, D. E. (2012). "Mathematical Models of Anti-TNF Therapies and their Correlation with Tuberculosis," in *Antibody-Mediated Drug Delivery Systems: Concepts, Technology and Applications*, eds. Y. Pathak and S. Benita (Hoboken, NJ: John Wiley & Sons, Inc.), 83–104.

Marino, S., Hogue, I. B., Ray, C. J., and Kirschner, D. E. (2008). A methodology for performing global uncertainty and sensitivity analysis in systems biology. *J. Theor. Biol.* 254, 178–196.

Marino, S., Sud, D., Plessner, H., Lin, P. L., Chan, J., Flynn, J. L., and Kirschner, D. E. (2007). Differences in reactivation of tuberculosis induced from anti-TNF treatments are based on bioavailability in granulomatous tissue. *PLoS Comput. Biol.* 3, 1909–1924. doi:10.1371/journal.pcbi.0030194

Morel, P. A., Ta'asan, S., Morel, B. F., Kirschner, D. E., and Flynn, J. L. (2006). New insights into mathematical modeling of the immune system. *Immunol. Res.* 36, 157–165.

Mosser, D. M., and Edwards, J. P. (2008). Exploring the full spectrum of macrophage activation. *Nat. Rev. Immunol.* 8, 958–969.

Nelson, D. E., Ihekwaba, A. E., Elliott, M., Johnson, J. R., Gibney, C. A., Foreman, B. E., Nelson, G., See, V, Horton, C. A., Spiller, D. G., Edwards, S. W., McDowell, H. P., Unitt, J. F., Sullivan, E., Grimley, R., Benson, N., Broomhead, D., Kell, D. B., and White, M. R. (2004). Oscillations in NF-kappaB signaling control the dynamics of gene expression. *Science* 306, 704–708.

Pahl, H. L. (1999). Activators and target genes of Rel/NF-kappaB transcription factors. *Oncogene* 18, 6853–6866.

Rangamani, P., and Sirovich, L. (2007). Survival and apoptotic pathways initiated by TNF-alpha: modeling and predictions. *Biotechnol. Bioeng.* 97, 1216–1229.

Ray, J. C., Flynn, J. L., and Kirschner, D. E. (2009). Synergy between individual TNF-dependent functions determines granuloma performance for controlling Mycobacterium tuberculosis infection. *J. Immunol.* 182, 3706–3717.

Roach, D. R., Bean, A. G., Demangel, C., France, M. P., Briscoe, H., and Britton, W. J. (2002). TNF regulates chemokine induction essential for cell recruitment, granuloma formation, and clearance of mycobacterial infection. *J. Immunol.* 168, 4620–4627.

Russell, D. G., Barry, C. E. III, and Flynn, J. L. (2010). Tuberculosis: what we don't know can, and does, hurt us. *Science* 328, 852–856.

Segovia-Juarez, J. L., Ganguli, S., and Kirschner, D. (2004). Identifying control mechanisms of granuloma formation during M. tuberculosis infection using an agent-based model. *J. Theor. Biol.* 231, 357–376.

Tay, S., Hughey, J. J., Lee, T. K., Lipniacki, T., Quake, S. R., and Covert, M. W. (2010). Single-cell NF-kappaB dynamics reveal digital activation and analogue information processing. *Nature* 466, 267–271.

Tsai, M. C., Chakravarty, S., Zhu, G., Xu, J., Tanaka, K., Koch, C., Tufariello, J., Flynn, J., and Chan, J. (2006). Characterization of the tuberculous granuloma in murine and human lungs: cellular composition and relative tissue oxygen tension. *Cell. Microbiol.* 8, 218–232.

Turner, O.C., Basaraba, R. J., Frank, A. A., and Orme, I. M. (2003). "Granuloma formation in mouse and guinea pig models of experimental tuberculosis," in *Granulomatous Infections and Inflammations: Cellular and Molecular Mechanisms*, ed. D. L. Boros (Washington, DC: ASM Press), 65–84.

Ulrichs, T., Kosmiadi, G. A., Trusov, V., Jorg, S., Pradl, L., Titukhina, M., Mishenko, V., Gushina, N., and Kaufmann, S. H. (2004). Human tuberculous granulomas induce peripheral lymphoid follicle-like structures to orchestrate local host defence in the lung. *J. Pathol.* 204, 217–228.

Van Antwerp, D. J., Martin, S. J., Kafri, T., Green, D. R., and Verma, I. M. (1996). Suppression of TNF-alpha-induced apoptosis by NF-kappaB. *Science* 274, 787–789.

Wertz, I. E., O'Rourke, K. M., Zhou, H., Eby, M., Aravind, L., Seshagiri, S., Wu, P., Wiesmann, C., Baker, R., Boone, D. L., Ma, A., Koonin, E. V., and Dixit, V. M. (2004). De-ubiquitination and ubiquitin ligase domains of A20 downregulate NF-kappaB signalling. *Nature* 430, 694–699.

Winthrop, K. L. (2006). Risk and prevention of tuberculosis and other serious opportunistic infections associated with the inhibition of tumor necrosis factor. *Nat. Clin. Pract. Rheumatol.* 2, 602–610.

Yamada, H., Mizuno, S., Reza-Gholizadeh, M., and Sugawara, I. (2001). Relative importance of NF-kappaB p50 in mycobacterial infection. *Infect. Immun.* 69, 7100–7105.

Yde, P., Mengel, B., Jensen, M. H., Krishna, S., and Trusina, A. (2011). Modeling the NF-kappaB mediated inflammatory response predicts cytokine waves in tissue. *BMC Syst. Biol.* 5, 115–123.

Conflict of Interest Statement: The authors declare that the research was conducted in the absence of any commercial or financial relationships that could be construed as a potential conflict of interest.

Received: 19 February 2012; paper pending published: 26 March 2012; accepted: 09 May 2012; published online: 06 June 2012.

*Citation: Fallahi-Sichani M, Kirschner DE and Linderman JJ (2012) NF-κ B signaling dynamics play a key role in infection control in tuberculosis. Front. Physio. **3**:170. doi: 10.3389/fphys.2012.00170*

This article was submitted to Frontiers in Computational Physiology and Medicine, a specialty of Frontiers in Physiology.

APPENDIX

Table A1 | TNF-independent and cellular/tissue-scale parameters, definitions, and values estimated from literature or approximated via uncertainty analysis as described in Ray et al. (2009); Fallahi-Sichani et al. (2011).

Parameter	Parameter description	Value*
N_{source}	Number of vascular sources	50
N_{caseum}	Number of qualified cell deaths required for caseation	10
D_{chem} (cm^2/s)	Diffusion coefficient of chemokines	10^{-8}–10^{-7} (5.2×10^{-8})
δ_{chem} (s^{-1})	Chemokine degradation rate constant	10^{-4}–10^{-3} (4.58×10^{-4})
τ_{chem} (molecules)	Minimum chemokine concentration threshold	1–10 (2)
s_{chem} (molecules)	Saturating chemokine concentration threshold	10^3–10^4 (2000)
M_{init}	Initial number of resident macrophages	105
max_{ageMac} (day)	Maximum lifespan of macrophages	100
$max_{ageActive}$ (day)	Maximum lifespan of an activated macrophage	10
t_{regMac} (h)	Macrophage inactivity time after down-regulation by T_{reg}	12
t_{moveMr} (min)	Time interval for M_r movement	20
t_{moveMa} (h)	Time interval for M_a movement	7.8
t_{moveMi} (h)	Time interval for Mi movement	24
ω_{recTNF}	Effect of TNF on cell recruitment	1
$\omega_{recCCL2}$	Effect of CCL2 on cell recruitment	0.0507
$\omega_{recCCL5}$	Effect of CCL5 on cell recruitment	0.0507
$\omega_{recCXCL9/10/11}$	Effect of CXCL9 on cell recruitment	0.0254
N_{rk}	Number of extracellular Mtb engulfed by M_r or M_i	1
P_k	Probability of M_r killing bacteria	0.01–0.1 (0.015)
B_{actM}	Number of extracellular Mtb activating a macrophage	50–150 (110)
N_c	Number of intracellular Mtb for $M_i \rightarrow M_{ci}$ transition	10
N_{burst}	Number of intracellular Mtb that leads to M_{ci} bursting	20–30 (20)
P_{STAT1}	Probability of STAT-1 activation in M_r or M_i	0.001–0.1 (0.085)
N_{ak}	Number of extracellular Mtb killed by M_a at each ABM time-step	10
τ_{recMac}	TNF/chemokine threshold for M_r recruitment	0.01–0.1 (0.023)
M_{recr}	Probability of M_r recruitment	0.01–0.1 (0.04)
$max_{ageTcell}$ (day)	Maximum lifespan of T cells	3
t_{delay} (day)	T cell recruitment delay	20
T_{moveM}	Probability of T cell moving to a mac-containing location	0.001–0.1 (0.014)
T_{moveT}	Probability of T cell moving to a T cell-containing location	0.001–0.1 (0.08)
T_{recr}	Probability of T cell recruitment	0.05–0.5 (0.15)
$t_{regTgam}$ (min)	T_γ inactivity time after down-regulation by T_{reg}	100
$P_{apop/Fas}$	Probability of Fas/FasL apoptosis by T_γ	0.01–0.1 (0.06)
$\tau_{recTgam}$	TNF/chemokine threshold for T_γ recruitment	0.1–1.0 (0.4)
$T_{recTgam}$	Probability of T_γ recruitment	0.54
$t_{regTcyt}$ (min)	T_c inactivity time after down-regulation by T_{reg}	100
$\tau_{recTcyt}$	TNF/chemokine threshold for T_c recruitment	0.1–1.0 (0.4)
$T_{recTcyt}$	Probability of T_c recruitment	0.36
$P_{cytKill}$	Probability of T_c killing M_i or M_{ci}	0.02 0.2 (0.12)
$P_{cytKillClean}$	Probability of T_c killing all intracellular Mtb by killing M_{ci}	0.75
$\tau_{recTreg}$	TNF/chemokine threshold for T_{reg} recruitment	0.01–0.1 (0.05)
$T_{recTreg}$	Probability of T_{reg} recruitment	0.1
α_{Bi} (per 10 min)	Intracellular Mtb growth rate	2×10^{-4}–2×10^{-3} (1.5×10^{-3})
α_{Be} (per 10 min)	Extracellular Mtb growth rate	10^{-4}–10^{-3} (7×10^{-4})
K_{be}	Capacity of a micro-compartment for extracellular Mtb	200

**Parameters used for sensitivity analysis are indicated by their ranges of values. Values in parentheses are used to generate containment baseline.*

Table A2 | Definition of reaction species, reactions describing TNF/TNFR processes and their rates (v_i).

REACTION SPECIES			
mTNF	Membrane-bound TNF	sTNF/TNFR2	sTNF/TNFR2 complex on the membrane
sTNF	Extracellular soluble TNF	$sTNF/TNFR1_i$	Internalized sTNF/TNFR1 complex
TNFR1	Cell surface TNF receptor 1	$sTNF/TNFR2_i$	Internalized sTNF/TNFR2 complex
TNFR2	Cell surface TNF receptor 2	$sTNF/TNFR2_{shed}$	Shed sTNF/TNFR2 complex
sTNF/TNFR1	sTNF/TNFR1 complex on the membrane	TNF_i	Intracellular translated TNF
MODEL REACTIONS			
1	mTNF expression (T cells): $v_1 = k_{synthTcell}$ (Macrophages): $v_1 = e_{3TNF}[TNF_i]$	9	TNFR2 synthesis $v_9 = V_{r2}$
2	mTNF → sTNF $v_2 = k_{TACE}[mTNF]$	10	TNFR1 → $TNFR1_i$ $v_{10} = k_{t1}[TNFR1]$
3	sTNF + TNFR1 ↔ sTNF/TNFR1 $v_3 = k_{on1}[sTNF][TNFR1] - k_{off1}[sTNF/TNFR1]$	11	TNFR2 → $TNFR2_i$ $v_{11} = k_{t2}[TNFR2]$
4	sTNF + TNFR2 ↔ sTNF/TNFR2 $v_4 = k_{on2}[sTNF][TNFR2] - k_{off2}[sTNF/TNFR2]$	12	$sTNF/TNFR1_i$ → degradation $v_{12} = k_{deg1}[sTNF/TNFR1_i]$
5	sTNF/TNFR1 → $sTNF/TNFR1_i$ $v_5 = k_{int1}[sTNF/TNFR1]$	13	$sTNF/TNFR2_i$ → degradation $v_{13} = k_{deg2}[sTNF/TNFR2_i]$
6	sTNF/TNFR2 → $sTNF/TNFR2_i$ $v_6 = k_{int2}[sTNF/TNFR2]$	14	$sTNF/TNFR1_i$ → TNFR1 $v_{14} = k_{rec1}[sTNF/TNFR1_i]$
7	sTNF/TNFR2 → $sTNF/TNFR2_{shed}$ $v_7 = k_{shed}[sTNF/TNFR2]$	15	$sTNF/TNFR2_i$ → TNFR2 $v_{15} = k_{rec2}[sTNF/TNFR2_i]$
8	TNFR1 synthesis $v_8 = V_{r1}$	16	$sTNF/TNFR2_{shed}$ → sTNF + $TNFR2_{shed}$ $v_{16} = k_{off2}[sTNF/TNFR2_{shed}]$

Table A3 | Molecular/single-cell scale TNF/TNFR parameters, definitions and values estimated from literature.

Parameter	Parameter description	Value*	Reference
$k_{synthTcell}$ (#/cell.s)	Full synthesis rate of mTNF for T cells	10^{-2}–10^{-1} (0.021)	Marino et al., 2007)
$TNFR1_{mac}$ (#/cell)	TNFR1 density on the surface of macrophages	500–5000 (1100–1900)†	Fallahi-Sichani et al. (2010); Imamura et al. (1987); Pocsik et al. (1994); van Riemsdijk-Van Overbeeke et al. (2001)
$TNFR1_{Tcell}$ (#/cell)	TNFR1 density on the surface of T cells	500–5000 (400–1200)†	Fallahi-Sichani et al. (2010); Imamura et al. (1987); Pocsik et al. (1994); van Riemsdijk-Van Overbeeke et al. (2001)
$TNFR2_{mac}$ (#/cell)	TNFR2 density on the surface of macrophages	500–5000 (400–800)†	Fallahi-Sichani et al. (2010); Imamura et al. (1987); Pocsik et al. (1994); van Riemsdijk-Van Overbeeke et al. (2001)
$TNFR2_{Tcell}$ (#/cell)	TNFR2 density on the surface of T cells	500–5000 (600–800)†	Fallahi-Sichani et al. (2010); Imamura et al. (1987); Pocsik et al. (1994); van Riemsdijk-Van Overbeeke et al. (2001)
D_1 (cm^2/s)‡	Diffusion coefficient of sTNF	10^{-8}–10^{-7} (5.2×10^{-8})	Nugent and Jain (1984); Pluen et al. (2001)
D_2 (cm^2/s)‡	Diffusion coefficient of shed TNF/TNFR2 complex	10^{-8}–10^{-7} (3.2×10^{-8})	Nugent and Jain (1984); Pluen et al. (2001)
$k_{TACE\ Mac}$ (s^{-1})	Rate constant for TNF release by TACE activity on a macrophage	10^{-4}–10^{-3} (4.4×10^{-4})	Fallahi-Sichani et al. (2010); Newton et al. (2001); Solomon et al. (1997); Crowe et al. (1995)
$k_{TACE\ Tcell}$ (s^{-1})	Rate constant for TNF release by TACE activity on a T cell	10^{-5}–10^{-4} (4.4×10^{-5})	
δ_{TNF} (s^{-1})	sTNF degradation rate constant	10^{-4}–10^{-3} (4.58×10^{-4})	Cheong et al. (2006)
K_{d1} (M)	Equilibrium dissociation constant of sTNF/TNFR1	10^{-12}–10^{-10} (1.9×10^{-11})	Imamura et al. (1987); Grell et al. (1998)
K_{d2} (M)	Equilibrium dissociation constant of sTNF/TNFR2	10^{-10}–10^{-9} (4.2×10^{-10})	Imamura et al. (1987); Grell et al. (1998); Pennica et al. (1992)
k_{on1} ($M^{-1}s^{-1}$)	sTNF/TNFR1 association rate constant	10^7–10^8 (2.8×10^7)	Grell et al. (1998)
k_{on2} ($M^{-1}s^{-1}$)	sTNF/TNFR2 association rate constant	10^7–10^8 (3.5×10^7)	Grell et al. (1998)
k_{off1} (s^{-1})	sTNF/TNFR1 dissociation rate constant	$k_{on1} \times K_{d1}$	
k_{off2} (s^{-1})	sTNF/TNFR2 dissociation rate constant	$k_{on2} \times K_{d2}$	
k_{int1} (s^{-1})	TNFR1 internalization rate constant	1.5×10^{-4}–1.5×10^{-3} (7.7×10^{-4})	Grell et al. (1998); Higuchi and Aggarwal (1994)
k_{int2} (s^{-1})	TNFR2 internalization rate constant	3.9×10^{-4}–5×10^{-4} (4.6×10^{-4})	Pennica et al. (1992)
k_{shed} (s^{-1})	TNFR2 shedding rate constant	3.9×10^{-4}–1.5×10^{-3} (5×10^{-4})	Crowe et al. (1995); Higuchi and Aggarwal (1994)
k_{rec1} (s^{-1})	TNFR1 recycling rate constant	8.8×10^{-5}–5.5×10^{-4} (1.8×10^{-5})	Vuk-Pavlovic and Kovach (1989); Bajzer et al. (1989)
k_{rec2} (s^{-1})	TNFR2 recycling rate constant	8.8×10^{-5}–5.5×10^{-4} (1.8×10^{-5})	Vuk-Pavlovic and Kovach (1989); Bajzer et al. (1989)
k_{t1} (s^{-1})	TNFR1 turn-over rate constant	3×10^{-4}–5×10^{-4} (3.8×10^{-4})	Vuk-Pavlovic and Kovach (1989); Bajzer et al. (1989)
k_{t2} (s^{-1})	TNFR2 turn-over rate constant	3×10^{-4}–5×10^{-4} (3.8×10^{-4})	Vuk-Pavlovic and Kovach (1989); Bajzer et al. (1989)
k_{deg1} (s^{-1})	TNFR1 degradation rate constant	10^{-5}–10^{-4} (5×10^{-5})	Imamura et al. (1987); Vuk-Pavlovic and Kovach (1989); Bajzer et al. (1989); Tsujimoto et al. (1985)
k_{deg2} (s^{-1})	TNFR2 degradation rate constant	10^{-5}–10^{-4} (5×10^{-5})	Imamura et al. (1987); Vuk-Pavlovic and Kovach (1989); Bajzer et al. (1989); Tsujimoto et al. (1985)
$V_{r1\ mac}$ (#/cell.s)	Cell surface TNFR1 synthesis rate constant for macrophages	$k_{t1} \times TNFR1_{mac}$	
$V_{r1\ Tcell}$ (#/cell.s)	Cell surface TNFR1 synthesis rate constant for T cells	$k_{t1} \times TNFR1_{Tcell}$	
$V_{r2\ mac}$ (#/cell.s)	Cell surface TNFR2 synthesis rate constant for macrophages	$k_{t2} \times TNF21_{mac}$	
$V_{r2\ Tcell}$ (#/cell.s)	Cell surface TNFR2 synthesis rate constant for T cells	$k_{t2} \times TNF21_{Tcell}$	

**Ranges of parameter values used for sensitivity analysis are indicated out of parentheses. Values in parentheses are used to generate baseline model results.*

† Baseline model values for TNFR densities on each recruited individual cell was randomly chosen from the range shown in parentheses.

‡ Diffusion coefficients of the soluble species in granuloma were estimated in line with estimates for diffusible factors of similar molecular weight in tumors (Nugent and Jain, 1984; Pluen et al., 2001).

Table A4 | Definition of reaction species, reactions describing NF-κB signaling and response-associated processes in macrophages and their rates (v_i).

REACTION SPECIES			
sTNF/TNFR1	sTNF/TNFR1 complex on the membrane	NFkB	Cytoplasmic NF-κB
IKKn	Neutral form of IKK kinase	$NFkB_n$	Nuclear NF-κB
IKKa	Active form of IKK	A20	Translated A20
IKKi	Inactive form of IKK	$A20_t$	A20 transcript
IKKii	Inactive intermediate form of IKK	G_{A20}	State of A20 gene
K_{NN}	Total number of IKK molecules (assumed constant in time)	G_{IkB}	State of IκBα gene
IKKKa	Active form of IKKK	G_R	State of genes corresponding to NF-κB-mediated responses
IKKKn	Neutral form of IKKK	$chem_i$	Intracellular translated chemokines
K_N	Total number of IKKK molecules (assumed to be constant in time)	$chem_t$	Chemokine transcript
IkB	Cytoplasmic IκBα	TNF_i	Intracellular translated TNF
IkB_n	Nuclear IκBα	TNF_t	TNF transcript
IkB_t	IκBα transcript	ACT	Generic macrophage-activating molecule
IkB_p	Phosphorylated cytoplasmic IκBα	ACT_t	ACT transcript
NFkB|IkB	Cytoplasmic IκBα|NF-κB complex	IAP	Inhibitor of apoptosis protein
$NFkB\|IkB_p$	Phosphorylated cytoplasmic IκBα in complex with NF-κB	IAP_t	IAP transcript
$NFkB\|IkB_n$	Nuclear IκBα|NF-κB complex		
MODEL REACTIONS			
17	IKKK kinase activation and activity attenuation by A20 $v_{17} = k_a[\text{sTNF/TNFR1}].([K_N] - [\text{IKKKa}]).\frac{K_{A20}}{K_{A20}+[A20]}$	42	Transport of NF-κB|IκBα complex out of nucleus $v_{42} = e_{2a}[NFkB\|IkB_n]$
18	Spontaneous inactivation of IKKKa $v_{18} = k_i[\text{IKKKa}]$	43	A20 gene activation due to NF-κB binding $v_{43} = q_1[NFkB_n](2 - [G_{A20}])$
19	IKKii → IKKn $v_{19} = k_4([K_{NN}] - [\text{IKKn}] - [\text{IKKa}] - [\text{IKKi}])$	44	A20 gene inactivation due to removal of NF-κB molecules by IκBα $v_{44} = q_2[IkB_n][G_{A20}]$
20	IKKn → IKKa mediated by IKKKa phosphorylation at two sites $v_{20} = k_1[\text{IKKKa}]^2[\text{IKKn}]$	45	IκBα gene activation due to NF-κB binding $v_{45} = q_1[NFkB_n](2 - [G_{IkB}])$
21	IKKa → IKKi mediated by A20 $v_{21} = k_3[\text{IKKa}].(k_2 + [A20])/k_2$	46	IκBα gene inactivation due to removal of NF-κB molecules by IκBα $v_{46} = q_2[IkB_n][G_{IkB}]$
22	IKKi → IKKii $v_{22} = k_4[\text{IKKi}]$	47	NF-κB-mediated response gene activation due to NF-κB binding $v_{47} = q_{1r}[NFkB_n](2 - [G_R])$
23	IκBα phosphorylation by IKKa $v_{23} = a_2[\text{IKKa}][IkB]$	48	NF-κB-mediated response gene inactivation due to spontaneous removal of NF-κB molecules $v_{48} = q_{2rr}[G_R]$
24	Degradation of phosphorylated IκBα $v_{24} = t_p[IkB_p]$	49	NF-κB-mediated response gene inactivation due to removal of NF-κB molecules by IκBα $v_{49} = q_{2r}[IkB_n][G_R]$
25	Phosphorylation of IκBα in complex with NF-κB by IKKa $v_{25} = a_3[\text{IKKa}][NFkB\|IkB]$	50	Constitutive transcription of TNF and chemokines $v_{50} = c_{1rrchemTNF}$
26	Degradation of phosphorylated IκBα in complex with NF-κB $v_{26} = t_p[NFkB\|IkB_p]$	51	NF-κB-dependent transcription of chemokines and TNF $v_{51} = c_{1r}[G_R]$
27	Liberation of free NF-κB due to degradation of IκBα in their complex $v_{27} = c_{6a}[NFkB\|IkB]$	52	Chemokine mRNA degradation $v_{52} = c_{3rchem}[chem_t]$

(Continued)

Table A4 | Continued

28	Formation of NF-κB and IκBα complex $v_{28} = a_1[\text{NFkB}][\text{IkB}]$	53	Chemokine translation $v_{53} = c_{4\text{chem}}[\text{chem}_t]$
29	Transport of free cytoplasmic NF-κB to nucleus $v_{29} = i_1[\text{NFkB}]$	54	Intracellular chemokine degradation $v_{54} = c_{5\text{chem}}[\text{chem}_i]$
30	Association of nuclear NF-κB with nuclear IκBα $v_{30} = a_1 k_v[\text{IkB}_n][\text{NFkB}_n]$	55	Chemokine secretion $v_{55} = e_{3\text{chem}}[\text{chem}_i]$
31	A20 translation $v_{31} = c_4[\text{A20}_t]$	56	TNF mRNA degradation $v_{56} = c_{3\text{rTNF}}[\text{TNF}_t]$
32	Constitutive degradation of A20 $v_{32} = c_5[\text{A20}]$	57	TNF translation $v_{57} = c_{4\text{TNF}}[\text{TNF}_t]$
33	NF-κB inducible transcription of A20 $v_{33} = c_1[\text{G}_{\text{A20}}]$	58	Intracellular TNF degradation $v_{58} = c_{5\text{TNF}}[\text{TNF}_i]$
34	Degradation of A20 transcript $v_{34} = c_3[\text{A20}_t]$	59	Constitutive transcription of ACT $v_{59} = c_{1\text{rrACT}}$
35	IκBα translation $v_{35} = c_4[\text{IkB}_t]$	60	ACT mRNA degradation $v_{60} = c_{3\text{rACT}}[\text{ACT}_t]$
36	Constitutive degradation of IκBα $v_{36} = c_{5a}[\text{IkB}]$	61	ACT translation $v_{61} = c_{4\text{ACT}}[\text{ACT}_t]$
37	Transport of IκBα into nucleus $v_{37} = i_{1a}[\text{IkB}]$	62	ACT degradation $v_{62} = c_{5\text{ACT}}[\text{ACT}]$
38	Transport of IκBα out of nucleus $v_{38} = e_{1a}[\text{IkB}_n]$	63	Constitutive transcription of IAP $v_{63} = c_{1\text{rrIAP}}$
39	NF-κB inducible transcription of IκBα $v_{39} = c_1[\text{G}_{\text{IkB}}]$	64	IAP mRNA degradation $v_{64} = c_{3\text{rIAP}}[\text{IAP}_t]$
40	Degradation of IκBα transcript $v_{40} = c_3[\text{IkB}_t]$	65	IAP translation $v_{65} = c_{4\text{IAP}}[\text{IAP}_t]$
41	Association of NF-κB with IκBα in cytoplasm $v_{41} = a_1[\text{IkB}][\text{NFkB}]$	66	IAP degradation $v_{66} = c_{5\text{IAP}}[\text{IAP}]$

Table A5 | Molecular/single-cell scale NF-κB signaling-associated parameters, definitions and values from Tay et al. (2010), or approximated via uncertainty analysis.

Parameter	Parameter description	Value*
CONCENTRATION OF INTRACELLULAR SIGNALING MOLECULES		
K_N (#/cell)	Number of IKKK molecules	3.16×10^4–3.16×10^5 (10^5)
K_{NN} (#/cell)	Number of IKK molecules	6.32×10^4–6.32×10^5 (2×10^5)
NF-κB_{tot} (#/cell)	Average number of NF-κB molecules	3.16×10^4–3.16×10^5 (10^5)
ACTIVATION OF THE SIGNAL TRANSDUCTION CASCADE		
k_a (s^{-1})	IKKK activation rate	6.32×10^{-7}–6.32×10^{-6} (2×10^{-6})
k_i (s^{-1})	IKKK inactivation rate	3.16×10^{-3}–3.16×10^{-2} (10^{-2})
k_1 (s^{-1})	IKKn activation rate	1.9×10^{-10}–1.9×10^{-9} (6×10^{-10})
k_{A20} (#/cell)	Michaelis coefficient in TNFR1 activity attenuation	3.16×10^4–3.16×10^5 (10^5)
k_2 (#/cell)	Michaelis coefficient in IKKa inactivation	3.16×10^3–3.16×10^4 (10^4)
k_3 (s^{-1})	IKKn inactivation rate	6.32×10^{-4}–6.32×10^{-3} (2×10^{-3})
k_4 (s^{-1})	IKKi → IKKii and IKKii → IKKn transformation	3.16×10^{-4}–3.16×10^{-3} (10^{-3})
A20 AND IκBα SYNTHESIS		
q_1 (s^{-1})	NF-κB binding at A20 and IκBα gene promoters	1.26×10^{-7}–1.26×10^{-6} (4×10^{-7})
q_2 (s^{-1})	IκBα inducible NF-κB detaching from A20 and IκBα genes	3.16×10^{-7}–3.16×10^{-6} (10^{-6})
c_1 (s^{-1})	Inducible A20 and IκBα mRNA synthesis	3.16×10^{-2}–3.16×10^{-1} (10^{-1})
c_3 (s^{-1})	A20 and IκBα mRNA degradation	2.37×10^{-4}–2.37×10^{-3} (7.5×10^{-4})
c_4 (s^{-1})	A20 and IκBα translation	1.58×10^{-1}–1.58 (5×10^{-1})
c_5 (s^{-1})	A20 degradation rate	1.58×10^{-4}–1.58×10^{-3} (5×10^{-4})
IκBα INTERACTIONS		
a_1 (s^{-1})	IκBα-NF-κB association	1.58×10^{-7}–1.58×10^{-6} (5×10^{-7})
a_2 (s^{-1})	IκBα phosphorylation	3.16×10^{-8}–3.16×10^{-7} (10^{-7})
a_3 (s^{-1})	IκBα phosphorylation in IκBα|NF-κB complexes	1.58×10^{-7}–1.58×10^{-6} (5×10^{-7})
t_p (s^{-1})	Degradation of phosphorylated IκBα	3.16×10^{-3}–3.16×10^{-2} (10^{-2})
c_{5a} (s^{-1})	Spontaneous IκBα degradation	3.16×10^{-5}–3.16×10^{-4} (10^{-4})
c_{6a} (s^{-1})	Spontaneous IκBα degradation in IκBα|NF-κB complexes	6.32×10^{-6}–6.32×10^{-5} (2×10^{-5})
NF-κB AND IκBα TRANSPORT BETWEEN CYTOPLASM AND NUCLEUS		
i_1 (s^{-1})	NF-κB nuclear import	3.16×10^{-3}–3.16×10^{-2} (10^{-2})
e_{2a} (s^{-1})	IκBα|NF-κB nuclear export	1.58×10^{-2}–1.58×10^{-1} (5×10^{-2})
i_{1a} (s^{-1})	IκBα nuclear import	6.32×10^{-4}–6.32×10^{-3} (2×10^{-3})
e_{1a} (s^{-1})	IκBα nuclear export	1.58×10^{-3}–1.58×10^{-2} (5×10^{-3})
k_v	Ratio of cytoplasmic to nuclear volume for a macrophage	5
NF-κB-MEDIATED CELL RESPONSES AND APOPTOSIS		
q_{1r} (s^{-1})	NF-κB binding at response gene promoters	3.16×10^{-8}–3.16×10^{-7} (10^{-7})
q_{2r} (s^{-1})	IκBα inducible NF-κB detaching from response gene promoters	3.16×10^{-8}–3.16×10^{-7} (10^{-7})
q_{2rr} (s^{-1})	Spontaneous NF-κB detaching from response gene promoters	3.16×10^{-4}–3.16×10^{-3} (10^{-3})
c_{1r} (s^{-1})	Inducible response mRNA synthesis	0 (only resting macrophage), 1.58×10^{-2}–1.58×10^{-1} (5×10^{-2})
$c_{1rrchemTNF}$ (s^{-1})	Constitutive transcription rate for chemokines and TNF	0 (resting macrophage), $0.5 \times c_{1r}$ (infected macrophage), c_{1r} (activated or chronically infected macrophage)
c_{3rchem} (s^{-1})	Chemokine mRNA degradation rate	6.1×10^{-5}–6.1×10^{-4} (1.92×10^{-4})
c_{4chem} (s^{-1})	Chemokine translation rate	1.42×10^{-1}–1.42 (4.5×10^{-1})
c_{5chem} (s^{-1})	Intracellular chemokine degradation rate	1.58×10^{-5}–1.58×10^{-4} (5×10^{-4})
e_{3chem} (s^{-1})	Chemokine secretion rate	4.4×10^{-6}–4.4×10^{-5} (1.39×10^{-5})
c_{3rTNF} (s^{-1})	TNF mRNA degradation rate	1.2×10^{-4}–1.2×10^{-3} (3.8×10^{-4})
c_{4TNF} (s^{-1})	TNF translation rate	4.74×10^{-2}–4.74×10^{-1} (1.5×10^{-1})
c_{5TNF} (s^{-1})	Intracellular TNF degradation rate	1.58×10^{-4}–1.58×10^{-3} (5×10^{-4})
e_{3TNF} (s^{-1})	TNF secretion rate	7.87×10^{-7}–7.87×10^{-6} (2.5×10^{-6})
c_{1rrACT} (s^{-1})	ACT mRNA constitutive synthesis rate	3.16×10^{-4}–3.16×10^{-3} (1×10^{-3})
c_{3rACT} (s^{-1})	ACT mRNA degradation rate	6.1×10^{-5}–6.1×10^{-4} (1.92×10^{-4})

(Continued)

Table A5 | Continued

Parameter	Parameter description	Value*
c_{4ACT} (s^{-1})	ACT translation rate	1.58×10^{-1}–1.58 (5×10^{-1})
c_{5ACT} (s^{-1})	ACT degradation rate	1.58×10^{-4}–1.58×10^{-3} (5×10^{-4})
τ_{ACT} (#/cell)	ACT concentration threshold for macrophage activation	8–80 (25)
k_{ACT} [(#/cell)$^{-1}s^{-1}$]	Macrophage activation rate constant	1.46×10^{-6}–1.46×10^{-5} (7.7×10^{-6})
c_{1rrIAP} (s^{-1})	IAP mRNA constitutive synthesis rate	3.16×10^{-4}–3.16×10^{-3} (1×10^{-3})
c_{3rIAP} (s^{-1})	IAP mRNA degradation rate	6.1×10^{-5}–6.1×10^{-4} (1.92×10^{-4})
c_{4IAP} (s^{-1})	IAP translation rate	1.58×10^{-1}–1.58 (5×10^{-1})
c_{5IAP} (s^{-1})	IAP degradation rate	1.58×10^{-4}–1.58×10^{-3} (5×10^{-4})
k_{IAP} (#/cell)	Apoptosis inhibition coefficient	1.22×10^{1}–1.22×10^{2} (3.86×10^{1})
k^0_{apopt}((#cell)$^{-1}s^{-1}$)	Intrinsic TNF-induced apoptosis rate constant	4.2×10^{-10}–4.2×10^{-9} (1.33×10^{-9})
τ_{apopt} (#/cell)	Internalized sTNF/TNFR1 threshold for TNF-induced apoptosis	50–500 (300)

**Parameters used for sensitivity analysis are indicated by their ranges of values. Values in parentheses are used to generate containment baseline.*

† Baseline model values for intracellular NF-κB_{tot} on each recruited individual macrophage was randomly based on a log-normal distribution as described in Tay et al. (2010).

Table A6 | Differential equations describing molecular single-cell scale TNF/TNFR and NF-κB signaling and response-associated processes.

$$\frac{d[\mathrm{mTNF}]}{dt} = v_1 - v_2$$
$$\frac{d[\mathrm{sTNF}]}{dt} = (\frac{\rho}{N_{av}})(v_2 - v_3 - v_4) + v_{16}$$
$$\frac{d[\mathrm{TNFR1}]}{dt} = v_8 - v_3 - v_{10} + v_{14}$$
$$\frac{d[\mathrm{TNFR2}]}{dt} = v_9 - v_4 - v_{11} + v_{15}$$
$$\frac{d[\mathrm{sTNF/TNFR1}]}{dt} = v_3 - v_5$$
$$\frac{d[\mathrm{sTNF/TNFR2}]}{dt} = v_4 - v_6 - v_7$$
$$\frac{d[\mathrm{sTNF/TNFR1_i}]}{dt} = v_5 - v_{12} - v_{14}$$
$$\frac{d[\mathrm{sTNF/TNFR2_i}]}{dt} = v_6 - v_{13} - v_{15}$$
$$\frac{d[\mathrm{sTNF/TNFR2_{shed}}]}{dt} = \left(\frac{\rho}{N_{av}}\right) v_7 - v_{16}$$
$$\frac{d[\mathrm{IKKKa}]}{dt} = v_{17} - v_{18}$$
$$\frac{d[\mathrm{IKKn}]}{dt} = v_{19} - v_{20}$$
$$\frac{d[\mathrm{IKKa}]}{dt} = v_{20} - v_{21}$$
$$\frac{d[\mathrm{IKKi}]}{dt} = v_{21} - v_{22}$$
$$\frac{d[\mathrm{IkB_p}]}{dt} = v_{23} - v_{24}$$
$$\frac{d[\mathrm{NFkB|IkB_p}]}{dt} = v_{25} - v_{26}$$
$$\frac{d[\mathrm{NFkB}]}{dt} = v_{27} - v_{28} + v_{26} - v_{29}$$
$$\frac{d[\mathrm{NFkB_n}]}{dt} = v_{29} - v_{30}$$
$$\frac{d[\mathrm{A20}]}{dt} = v_{31} - v_{32}$$
$$\frac{d[\mathrm{A20_t}]}{dt} = v_{33} - v_{34}$$
$$\frac{d[\mathrm{IkB}]}{dt} = v_{23} - v_{28} + v_{35} - v_{36} - v_{37} + v_{38}$$
$$\frac{d[\mathrm{IkB_n}]}{dt} = -v_{30} + v_{37} - v_{38}$$
$$\frac{d[\mathrm{IkB_t}]}{dt} = v_{39} - v_{40}$$
$$\frac{d[\mathrm{NFkB|IkB}]}{dt} = v_{41} - v_{27} - v_{25} + v_{42}$$
$$\frac{d[\mathrm{NFkB|IkB_n}]}{dt} = v_{30} - v_{42}$$
$$\frac{d[\mathrm{G_{A20}}]}{dt} = v_{43} - v_{44}$$
$$\frac{d[\mathrm{G_{IkB}}]}{dt} = v_{45} - v_{46}$$
$$\frac{d[\mathrm{G_R}]}{dt} = v_{47} - v_{48} - v_{49}$$
$$\frac{d[\mathrm{chem_t}]}{dt} = v_{50} + v_{51} - v_{52}$$
$$\frac{d[\mathrm{chem_i}]}{dt} = v_{53} - v_{54} - v_{55}$$
$$\frac{d[\mathrm{TNF_t}]}{dt} = v_{50} + v_{51} - v_{56}$$
$$\frac{d[\mathrm{TNF_i}]}{dt} = v_{57} - v_{58} - v_1$$
$$\frac{d[\mathrm{ACT_t}]}{dt} = v_{59} + v_{51} - v_{60}$$
$$\frac{d[\mathrm{ACT}]}{dt} = v_{61} - v_{62}$$
$$\frac{d[\mathrm{IAP_t}]}{dt} = v_{63} + v_{51} - v_{64}$$
$$\frac{d[\mathrm{IAP}]}{dt} = v_{65} - v_{66}$$

In equations describing a reaction or interaction between a soluble molecule and a cell membrane-associated molecule, a scaling factor (ρ/N_{av}) is required as indicated above, where ρ is the cell density in the ABM micro-compartment and can be computed as $(dx)^{-3}$ assuming that each micro-compartment is a cube of side $dx = 20\,\mu m$. N_{av} is the Avogadro's number.

Table A7 | LHS sensitivity analysis results for the effect of important NF-κB-associated model parameters (groups 1–3) on model outputs at day 200 post-infection.

	$NF\text{-}\kappa B_{tot}$	k_a	k_i	q_1	c_1	c_3	c_4	c_5
TNF FUNCTION-RELATED OUTPUTS								
$(\text{No. apoptosis})_{Macs}$								
$(\text{No. apoptosis})_{Mr}$								
$(\text{No. apoptosis})_{Mi\ and\ Mci}$						−−		
$(\text{No. apoptosis})_{Ma}$							−	+
$(\text{No. apoptosis})_{T\ cells}$	+						−−	++
$(\text{No. activation})_{Mr}$	++	++				++	−−	++
$(\text{No. activation})_{Mi}$							−	
CELLULAR-LEVEL OUTPUTS								
B_{int} (intracellular Mtb)	−−	−−−	+	+	+	−−−	++	−−
B_{ext} (extracellular Mtb)	−−	−−−		+	++	−−−	++	−−
B_{tot} (total Mtb)	−−	−−−	+	+	++	−−−	++	−−
Total macrophages								
M_r	−−−	−−−	+++	++	+++	−−−	+++	−−−
M_i and M_{ci}	−−	−−−	+	+	+	−−−	++	−−
M_a	+	+				++	−−	++
Total T cells	+	+						+
T_γ		+					−	+
T_c	+	+					−	+
T_{reg}	+	++				+		++
TISSUE-LEVEL OUTPUTS								
Caseation	−				+			
Granuloma size								
TISSUE CONCENTRATIONS								
$[sTNF]_{avg}$							−−	++
$[Chemokines]_{avg}$						−−	−	+

*Parameter definitions are presented in **Table A5** in Appendix.*

Only parameters with significant PRCC values are indicated. Significant positive and negative correlations are shown using ± as follows:

−/+, 0.001 < p-value < 0.01.

−−/++, 0.0001 < p-value < 0.001.

−−−/+++, p-value < 0.0001.

Table A8 | LHS sensitivity analysis results for the effect of important NF-κB-associated model parameters (group 6) on model outputs at day 200 post-infection.

	c_{1r}	c_{3rchem}	c_{4chem}	e_{3chem}	c_{3rTNF}	c_{4TNF}	c_{5TNF}	e_{3TNF}	c_{4ACT}	c_{5ACT}	τ_{ACT}	c_{5IAP}
TNF FUNCTION-RELATED OUTPUTS												
$(\text{No. apoptosis})_{Macs}$	+++				−−	+++	−−−	+++				
$(\text{No. apoptosis})_{Mr}$	+++				−−−	+++	−−−	+++				
$(\text{No. apoptosis})_{Mi\ and\ Mci}$					−−	++	−−−	+++	−−−	+++	+++	
$(\text{No. apoptosis})_{Ma}$	+++					+++		+++	++	−−	−	
$(\text{No. apoptosis})_{T\ cells}$	+++				−−	+++	−−−	+++	+			
$(\text{No. activation})_{Mr}$	+++				+				+++	−−−	−−−	
$(\text{No. activation})_{Mi}$	+++				++		++	−	+++	−−−	−−−	
CELLULAR-LEVEL OUTPUTS												
B_{int} (intracellular Mtb)	−−−				++	−−−	++	−−	−−−	+++	+++	
B_{ext} (extracellular Mtb)	−−−				++	−−	++	−−	−−−	+++	+++	
B_{tot} (total Mtb)	−−−				++	−−−	++	−−	−−−	+++	+++	
Total Macrophages		−−−	++	+++	+++	−−−	+++	−−−				−
M_r	−−−	−−	+	+++	+++	−−−	+++	−−−	−−−	+++	+++	
M_i and M_{ci}	−−−				++	−−−	++	−−	−−−	+++	+++	
M_a	+++				+++	−−	+++	−−−	+++	−−−	−−−	
Total T cells	+++			++	+++	−−	+++	−−−	+++	−−−	−−−	
T_γ	+++			++	+++	−−	+++	−−−	+++	−−−	−−−	
T_c	+++			++	+++	−−	+++	−−−	+++	−−−	−−−	
T_{reg}	+++			+	+++	−−	+++	−−−	+++	−−−	−−−	
TISSUE-LEVEL OUTPUTS												
Caseation	−−−	+++	−−	−	+++	−−−	+++	−−−				−−−
Granuloma size	−−−	−−		+++	+++	−−−	+++	−−−				−−
TISSUE CONCENTRATIONS												
$[\text{sTNF}]_{avg}$	+++					++		++				−
$[\text{Chemokines}]_{avg}$	+++	−−−	+++	+++	+++	−−−	+++	−−−				−−

*Parameter definitions are presented in **Table A5** in Appendix.*

Only parameters with significant PRCC values are indicated. Significant positive and negative correlations are shown using ± as follows:

−/+, 0.001 < p-value < 0.01.

−−/++, 0.0001 < p-value < 0.001.

−−−/+++, p-value < 0.0001.

REFERENCES

Bajzer, Z., Myers, A. C., and Vuk-Pavlovic, S. (1989). Binding, internalization, and intracellular processing of proteins interacting with recycling receptors. A kinetic analysis. *J. Biol. Chem.* 264, 13623–13631.

Crowe, P. D., Walter, B. N., Mohler, K. M., Otten-Evans, C., Black, R. A., and Ware, C. F. (1995). A metalloprotease inhibitor blocks shedding of the 80-kD TNF receptor and TNF processing in T lymphocytes. *J. Exp. Med.* 181, 1205–1210.

Grell, M., Wajant, H., Zimmermann, G., and Scheurich, P. (1998). The type 1 receptor (CD120a) is the high-affinity receptor for soluble tumor necrosis factor. *Proc. Natl. Acad. Sci. U.S.A.* 95, 570–575.

Higuchi, M., and Aggarwal, B. B. (1994). TNF induces internalization of the p60 receptor and shedding of the p80 receptor. *J. Immunol.* 152, 3550–3558.

Imamura, K., Spriggs, D., and Kufe, D. (1987). Expression of tumor necrosis factor receptors on human monocytes and internalization of receptor bound ligand. *J. Immunol.* 139, 2989–2992.

Newton, R. C., Solomon, K. A., Covington, M. B., Decicco, C. P., Haley, P. J., Friedman, S. M., and Vaddi, K. (2001). Biology of TACE inhibition. *Ann. Rheum. Dis.* 60(Suppl. 3), iii25–iii32.

Nugent, L. J., and Jain, R. K. (1984). Extravascular diffusion in normal and neoplastic tissues. *Cancer Res.* 44, 238–244.

Pennica, D., Lam, V. T., Mize, N. K., Weber, R. F., Lewis, M., Fendly, B. M., Lipari, M. T., and Goeddel, D. V. (1992). Biochemical properties of the 75-kDa tumor necrosis factor receptor. Characterization of ligand binding, internalization, and receptor phosphorylation. *J. Biol. Chem.* 267, 21172–21178.

Pluen, A., Boucher, Y., Ramanujan, S., McKee, T. D., Gohongi, T., di Tomaso, E., Brown, E. B., Izumi, Y., Campbell, R. B., Berk, D. A., and Jain, R. K. (2001). Role of tumor-host interactions in interstitial diffusion of macromolecules: cranial vs. subcutaneous tumors. *Proc. Natl. Acad. Sci. U.S.A.* 98, 4628–4633.

Pocsik, E., Mihalik, R., Ali-Osman, F., and Aggarwal, B. B. (1994). Cell density-dependent regulation of cell surface expression of two types of human tumor necrosis factor receptors and its effect on cellular response. *J. Cell. Biochem.* 54, 453–464.

Solomon, K. A., Covington, M. B., DeCicco, C. P., and Newton, R. C. (1997). The fate of pro-TNF-alpha following inhibition of metalloprotease-dependent processing to soluble TNF-alpha in human monocytes. *J. Immunol.* 159, 4524–4531.

Tsujimoto, M., Yip, Y. K., and Vilcek, J. (1985). Tumor necrosis factor: specific binding and internalization in sensitive and resistant cells. *Proc. Natl. Acad. Sci. U.S.A.* 82, 7626–7630.

van Riemsdijk-Van Overbeeke, I. C., Baan, C. C., Knoop, C. J., Loonen, E. H., Zietse, R., and Weimar, W. (2001). Quantitative flow cytometry shows activation of the TNF-alpha system but not of the IL-2 system at the single cell level in renal replacement therapy. *Nephrol. Dial. Transplant.* 16, 1430–1435.

Vuk-Pavlovic, S., and Kovach, J. S. (1989). Recycling of tumor necrosis factor-alpha receptor in MCF-7 cells. *FASEB J.* 3, 2633–2640.

frontiers in
PHYSIOLOGY

REVIEW ARTICLE
published: 11 June 2012
doi: 10.3389/fphys.2012.00191

A multi-scale approach to airway hyperresponsiveness: from molecule to organ

Anne-Marie Lauzon[1], Jason H. T. Bates[2], Graham Donovan[3], Merryn Tawhai[4], James Sneyd[3] and Michael J. Sanderson[5]*

[1] *Meakins-Christie Laboratories, Department of Medicine, McGill University, Montreal, QC, Canada*
[2] *Department of Medicine, University of Vermont, Burlington, VT, USA*
[3] *Department of Mathematics, University of Auckland, Auckland, New Zealand*
[4] *Auckland Bioengineering Institute, University of Auckland, Auckland, New Zealand*
[5] *Department of Microbiology and Physiological Systems, University of Massachusetts Medical School, Worcester, MA, USA*

Edited by:
Raimond L. Winslow, The Johns Hopkins University, USA

Reviewed by:
Nikolaos Tsoukias, Florida International University, USA
Oliver Jensen, University of Nottingham, UK

***Correspondence:**
Michael J. Sanderson, Department of Microbiology and Physiological Systems, University of Massachusetts Medical School, Worcester, MA, USA.
e-mail: michael.sanderson@umassmed.edu

Airway hyperresponsiveness (AHR), a characteristic of asthma that involves an excessive reduction in airway caliber, is a complex mechanism reflecting multiple processes that manifest over a large range of length and time scales. At one extreme, molecular interactions determine the force generated by airway smooth muscle (ASM). At the other, the spatially distributed constriction of the branching airways leads to breathing difficulties. Similarly, asthma therapies act at the molecular scale while clinical outcomes are determined by lung function. These extremes are linked by events operating over intermediate scales of length and time. Thus, AHR is an emergent phenomenon that limits our understanding of asthma and confounds the interpretation of studies that address physiological mechanisms over a limited range of scales. A solution is a modular computational model that integrates experimental and mathematical data from multiple scales. This includes, at the molecular scale, kinetics, and force production of actin-myosin contractile proteins during cross-bridge and latch-state cycling; at the cellular scale, Ca^{2+} signaling mechanisms that regulate ASM force production; at the tissue scale, forces acting between contracting ASM and opposing viscoelastic tissue that determine airway narrowing; at the organ scale, the topographic distribution of ASM contraction dynamics that determine mechanical impedance of the lung. At each scale, models are constructed with iterations between theory and experimentation to identify the parameters that link adjacent scales. This modular model establishes algorithms for modeling over a wide range of scales and provides a framework for the inclusion of other responses such as inflammation or therapeutic regimes. The goal is to develop this lung model so that it can make predictions about bronchoconstriction and identify the pathophysiologic mechanisms having the greatest impact on AHR and its therapy.

Keywords: smooth muscle contraction, latch-bridge, calcium oscillations and waves, asthma, computational modeling, parenchyma tethering

INTRODUCTION

Airway hyperresponsiveness (AHR) is defined as an excessive and inappropriate narrowing of the airways in response to bronchoconstrictive challenge. While AHR and inflammation are hallmarks of asthma and are primarily responsible for patient dyspnea, we still have an incomplete understanding of how airway smooth muscle (ASM) activation leads to airway narrowing and why asthma exacerbates this response.

Nevertheless, it is clear that AHR involves a dynamic balance between the active forces generated by ASM and the opposing passive forces exerted by the airway and surrounding parenchymal tissues. Importantly, these forces manifest at many length and time scales; from molecular interactions within cells to changes in airway morphology at the level of the whole lung. Furthermore, these forces are dynamic and, in particular, are rhythmically modulated by the act of breathing. For practical reasons, traditional experimental approaches tend to focus on specific levels of time and length scale and this has resulted in the accumulation of numerous disparate facts about many of the individual mechanisms pertaining to AHR. However, a clear view of how these mechanisms interact to mediate AHR has remained elusive because of the difficulty of integrating the many different time and length scales involved.

It is our view that computational modeling provides a way forward, therefore our primary goal is to construct a multi-level computational model of the lung that embodies the key mechanisms impinging on the phenomenon of airway responsiveness. Such a model will not only contribute to a more complete understanding of the pathogenesis of AHR, but it will also provide a virtual laboratory for *in silico* investigation of potential new therapies for obstructive lung diseases and their modes of delivery. This is particularly important in the current era of evidence-based

medicine in which advances in medical practice are driven by the outcomes of clinical trials. The expense and effort involved in such trials are considerable and only a very limited number of questions can be addressed. It is therefore crucial that these questions be selected on the basis of their having the greatest likelihood of yielding useful results. This can be greatly facilitated if the questions are first vetted on the basis of predictions made by a computational model of the lung that integrates experimental data relevant to AHR from all relevant length and time scales.

So far, our modeling and experimental studies have focused on the basic mechanisms of ASM contraction in the healthy state. The initial aim was to develop the basic model framework onto which pathological conditions could be imposed. The obvious next step will be to include, in the case of asthma, the complex process of inflammation. Unfortunately, at the current time, we have inadequate information or models reflecting the action of inflammation on ASM. Therefore, we have not attempted to extensively address this complex aspect of asthma in this review. However, experimental work is proposed to examine ASM responses from asthmatic tissues.

MULTI-SCALE COMPUTATIONAL MODELING

An interest in creating multi-scale models of biological systems has developed rapidly in recent years along with the availability of the required computing power. However, models of biological systems should always be motivated by the need to address biological questions rather than a demonstration that a model can be created. Furthermore, the purpose of a multi-scale model must be more than just a representation of the biological system at different scales of length or time. Ideally, the model must provide scientific insight, particularly in terms of how changes in behavior at one level of scale influence behavior at other scales within the system.

Biological systems are hierarchical; organs are composed of tissues, tissues of cells, cells of organelles, and organelles of macromolecules, with each step exhibiting qualitatively different behaviors. Importantly, interactions between these scales often lead to emergent phenomena that cannot be envisaged when considering only a single scale. Thus, a key goal of multi-scale modeling is to understand how integration of system components at one level of scale produces emergent behavior at higher levels of scale. The model should also provide the reverse function to elucidate how high scale behavior can influence lower scale activity. Multi-scale modeling requires the distillation of these scale-dependent behavioral characteristics into their essential elements for inclusion into the model rather than the inclusion of every detailed interaction. This approach is more efficient from a computational viewpoint and facilitates the likelihood of gaining insight and understanding.

PRINCIPAL LENGTH AND TIME SCALES INVOLVED IN AHR

Because ASM is the source of contractile force in the airway, AHR is a manifestation of its activity. This activity has consequences at four major scales: that of the molecular, the cell, the tissue, and the organ scale.

At the molecular scale

Airway smooth muscle cell (ASMC) contraction is produced by the cyclic cross-bridge formation between myosin and actin that generates force and movement; the kinetics of these cross-bridge interactions primarily determines force-velocity output. However, these cross-bridges can take a unique form called latch-bridges that maintain the ASMC at a shortened length to exert prolonged contraction. For the model, characterization, and understanding of these two cross-bridge mechanisms are required in order to predict their force output and how molecular alterations of actin-myosin interactions may be useful for the relaxation of ASMCs.

At the cellular scale

The contractile activity of the actin-myosin filaments is enzymatically regulated by the antagonistic activities of myosin light chain (MLC) kinase (MLCK) and MLC phosphatase (MLCP). The activity of MLCK is in turn regulated by complex spatiotemporal patterns of Ca^{2+} changes within the ASMC, while MLCP is regulated by a phosphorylation signaling cascade primarily involving Rho Kinase. Of equal importance are the signaling pathways that lead to ASMC relaxation; while this can simply involve the cessation of Ca^{2+} signals, the activation of relaxing signals mediated via protein kinase A (PKA; via β_2-adrenergic agonists) or protein kinase G (PKG; via NO production) is frequently involved. The contractile activity of the ASMC thus reflects a balance between opposing signaling cascades. Consequently, characterization of these regulatory mechanisms of ASMCs is required to make the model responsive to external contractile stimuli.

At the tissue scale

Airway constriction is a dynamic event reflecting the opposing influences of the active forces generated by ASMCs, which act to narrow the airway, and the passive mechanical forces of the airway wall and the surrounding parenchyma, which resist airway narrowing. The passive forces are due to numerous structures in and around the airways including the alveolar walls that tether the airway from the outside, the compressive stiffness of airway wall components such as the epithelium and basement membrane, and the intrinsic stiffness of the ASMC itself. All of these factors, including the force-generating capacity of the ASMC, have the potential to become markedly altered in diseases that involve significant degrees of airway remodeling, such as asthma. A particular challenge in modeling AHR at this level of scale is thus to identify those mechanisms that have the most influence on airway narrowing.

At the organ scale

The lung has a complex anatomy comprising of asymmetrically branching airway and vascular trees embedded in viscoelastic parenchymal tissue. In health, this structure brings air and blood in close juxtaposition over the enormous surface area that is required for adequate diffusive fluxes of oxygen and carbon dioxide, with regional variability in ventilation-perfusion matching having a small influence on total lung gas exchange. In a lung suffering from AHR, however, substantial heterogeneities of regional mechanical function may arise that severely alter the ventilation-perfusion ratios, compromising gas exchange. A computational model that is able to recapitulate this type of behavior, therefore, must incorporate accurate anatomical geometry together with local mechanical properties of both airway and tissue. The respiratory tract is in

constant motion as a result of breathing. Consequently, the spatial distribution of local changes in airway constriction will determine the overall airway impedance, which in turn will influence the distribution and ease of ventilation. To understand this complex behavior, it is necessary to model breathing dynamics in addition to the branching geometry, material properties, and interdependence (through parenchymal tethering) of the airways and parenchyma in which they are embedded. This model incorporates the foregoing scales and thereby provides the ability to observe how emergent properties alter ventilation.

APPROACHES TO MODELING

Predictive modeling

It is common for models to be purely constructive, i.e., constructed in great detail and validated by comparison to existing experimental data. Because these models essentially provide a quantitative explanation for what was already known, they are constrained in their usefulness. By contrast, a model based on physiological principles that can predict novel outcomes that are not intuitively obvious, but which can be experimentally tested, is extremely valuable for advancing an understanding of a system. This modeling approach is successful because it inspires further investigation and thereby provides additional evidence with which to evaluate the predictions. This property of predictive models is the key reason for constructing a multi-scale model of the airway, because it is only with such a model that the complicated behavior of AHR can be evaluated. While experimental investigations are forced to accept limitations, predictive modeling is less constrained.

Functional modeling

A major caveat of building a multi-scale model is that, at least in the initial stages, it is undesirable to include all known complexities. From a practical viewpoint, an all-inclusive model is not feasible because such a model would require excessive computing. Importantly, the model should be constructed on fundamental principles of operation. Most researchers agree with this premise, but can quickly lose confidence in a model if specific details central to their work are not included. However, it is common that the significance of such details to the overall system is rarely known and therefore must be initially omitted. With a basic working model, additional complexity can be added, if validated by iterative testing between model and experiment.

Our approach to building an airway lung model initially follows the fundamental concept of force generation by myosin and actin that is primarily controlled by cellular Ca^{2+} and converted into airway narrowing by the mechanical properties of the lung as outlined across the four major scales. The auxiliary control processes and tissue characteristics can then be applied to this framework. In this review the important details of the physiological process will be initially addressed, for each of the four major scales, followed by the relevant modeling approaches to build the sub-models of each scale. It must be emphasized that this is an on-going endeavor and that the parameters currently included in the model only reflect current progress. The ultimate aim for the model is for it to become a predictive tool that can be used for clinical evaluation and insight. This will require substantially more complexity, but the first step is the construction of a robust foundation and a flexible open-source framework for future development.

Our approach to multi-scale modeling

To construct a multi-scale model there are two major problems that must be solved. Firstly, models for each level need to be constructed, validated against existing data, and improved iteratively with additional experimental data. In general, this first step uses traditional modeling methods and is largely based on existing approaches. Secondly, methods must be devised for coupling these scales together into a single unified model. At this stage, new mathematical methods may need to be developed. There are no standard procedures for the construction of such multi-scale models; every multi-scale model, particularly one that spans such a wide range of spatial scales as ours, will likely depend on the invention of new methods. In addition, the entire multi-scale model must be modular in order to avoid the rebuilding of the entire model with each new iteration or error correction at each scale.

Linking the various spatial scales requires connecting partial and ordinary differential equations, together with judicious use of linearization and interpolation methods. Our approach has been to retain, as far as possible, the richness of our cellular and subcellular models (an alternative would have been to parameterize a lumped-parameter model to represent their essential behaviors). This means that we can explore the sensitivity of the large-scale model behavior to perturbations at the smallest scales; for example, in our multi-scale model it is possible to predict how changes at the level of myosin and actin kinetics will affect ventilation or heterogeneity at the level of the entire lung. Without a multi-scale model, such predictions are simply not possible. One drawback is that computations for a whole lung are demanding. We minimize this problem by use of interpolation methods in the coupling of the spatial scales, but each full model simulation may still take many days of computer time.

THE MOLECULAR SCALE

CONTRACTILE MECHANISMS AND PROTEINS

The contraction of ASM cells appears to be mediated by a two-step process; the first or precursor step is proposed to be a dynamic assembly of actin filaments into a cortical cytoskeleton that couples the cell membrane with more central and stable actin filaments to enable effective force transmission. This is followed by the traditional or familiar role of force generation by cyclic myosin interactions with the pre-formed or stable actin filaments.

The formation of the cortical cytoskeleton is reviewed by Gunst and Zhang (2008) and is only briefly summarized here. A key observation is that agonist-induced tension development is largely inhibited, in a manner independent of MLC phosphorylation, by preventing actin polymerization (Adler et al., 1983; Mauss et al., 1989; An et al., 2002; Shaw et al., 2003). This cytoskeletal assembly involves an increase of ∼20% F-actin (and decrease of ∼30% G-actin), occurs quickly (within ∼60 s) and involves the translocation and interaction of numerous actin-binding proteins and nucleation factors to the adhesion junctions that link the cytoskeleton to the extracellular matrix (Gunst and Zhang, 2008; Huang et al., 2010; Zhang et al., 2010b). Gunst and Zhang (2008) propose

that this dynamically polymerizing actin is required to transmit and potentially amplify the forces generated by the more central actomyosin interactions to the cell-surface. However, it is unclear if this cytoskeletal formation is immediately reversed when the ASM relaxes (e.g., upon agonist removal) or if an extended relaxed state is required. At the current time, our modeling approach assumes a fixed anchorage of the actin-myosin filaments but the inclusion of a cortical cytoskeletal sub-model would be a desirable future direction.

The contractile or "functional" sarcomere

Airway smooth muscle cells generate force by the hydrolysis of MgATP (magnesium ion-adenosine trisphosphate) which provides the energy to power a sliding filament mechanism mediated by cyclic interactions between myosin filament heads and actin filament binding sites (Adelstein and Sellers, 1996). The actin filaments are approximately orientated along the length of the ASMCs (Stephens and Kroeger, 1980). Traditionally, it was believed that actin filaments were embedded in dense bodies that served as anchor points at the cell membrane or within the cell (Bond and Somlyo, 1982; Fay et al., 1983). However, more recent studies have observed that dense bodies are actually tubular structures that run parallel to the contractile filaments (Zhang et al., 2010a). Nevertheless, it is likely that actin filaments are anchored in some sort of alpha-actinin based structure, similar to the z-lines of skeletal muscle, so that contraction at the molecular level can be transmitted to the cellular scale (Gunst and Tang, 2000; Gunst and Zhang, 2008).

The myosin filaments are interspersed between the actin filaments and typically appear thicker being composed of multiple myosin dimers with the myosin heads projecting outward toward the actin filaments (Trybus, 1996). Whereas the myosin heads have a bi-polar orientation in striated muscles, in smooth muscle most of the myosin filaments have a side-polar orientation (Xu et al., 1996). The exact nature of the myosin filaments also varies with the contractile state (Ip et al., 2007). From electron microscopy observations, the thickest and longest myosin filaments appear to occur in relaxed ASMCs whereas myosin filaments appear to redistribute and are difficult to observe in contracted ASMCs (Chin and Seow, personal communication). A possible explanation for this is that unconnected myosin dimers may be able to mediate filament sliding.

Regulation of myosin cross-bridge activity

The ability of myosin to perform force-generating cross-bridge cycling is regulated by Ca^{2+}/calmodulin-MLCK dependent phosphorylation of the regulatory MLCs (rMLC). Once phosphorylated, myosin can hydrolyze MgATP into MgADP and Pi and associate with actin filaments to generate force. It is believed that the faster kinetics of rapidly contracting phasic smooth muscle (e.g., in intestines), as compared to slower contracting tonic smooth muscle (e.g., in blood vessels), is caused by a faster regulatory and contractile system (Horiuti et al., 1989). However, it is unclear whether ASMC exhibits a tonic (Horiuti et al., 1989) or phasic (Malmqvist and Arner, 1991) phenotype. Furthermore, ASM may potentially change its behavior in disease (Souhrada and Dickey, 1976; Davis et al., 1982).

Several accessory proteins, including tropomyosin, caldesmon, calponin, and transgelin are all structurally associated with the actin filaments (Morgan and Gangopadhyay, 2001) and are proposed to play a role in contraction regulation. Tropomyosin appears to have similar properties as in skeletal muscle and facilitates cooperativity between cross-bridges (Morgan and Gangopadhyay, 2001) as well as the action of caldesmon (Shirinsky et al., 1992). Caldesmon inhibits actomyosin ATPase activity (Nagai et al., 1989) and decreases the actin sliding velocity (v_{max}) in *in vitro* motility assays (Shirinsky et al., 1992; Horiuchi and Chacko, 1995). The inhibitory action of caldesmon is reversed by its phosphorylation that can be achieved by several agents including Ca^{2+}-calmodulin, Cam Kinase II (Ngai and Walsh, 1984; Shirinsky et al., 1992).

Similarly, calponin inhibits actomyosin ATPase activity (Winder et al., 1998) and decreases v_{max} in *in vitro* motility assays (Shirinsky et al., 1992). Contrary to the effect of calponin, this decrease in v_{max} is more of an "all or none" mechanism. That is, some of the filaments are completely stopped rather than displaying a simple decrease in v_{max} (Shirinsky et al., 1992). This inhibitory action of calponin is reversed by its phosphorylation by PKC or Cam Kinase II, etc. (Winder and Walsh, 1990; Winder et al., 1998).

Taken together, the above data suggest that activation (by phosphorylation) of actin regulatory proteins may be necessary for cross-bridge cycling and contraction (Winder et al., 1993; Gerthoffer et al., 1996; Pohl et al., 1997). However other studies reported the absence of phosphorylation *in vivo* (Gimona et al., 1992; Adam et al., 1995).

Transgelin (SM22α), a ubiquitous protein found in smooth muscle cells (Solway et al., 1995; Fu et al., 2000), is thought to interact with, or bind to, actin (Gimona and Mital, 1998; Fu et al., 2000) and potentially modulate actin cytoskeleton organization by increasing F-actin bundling to enhance contractility (Han et al., 2009). Studies on smooth muscle from SM22α knockout mice have demonstrated that SM22α is necessary for Ca^{2+} independent contraction but not for Ca^{2+} dependent force generation (Je and Sohn, 2007). Interestingly, SM22α appears to be significantly increased in asthmatic ASMCs, at least at the mRNA level (Leguillette et al., 2009).

Enhanced contraction rates in AHR

There are two isoforms of smooth muscle myosin heavy chain (SMMHC) that are generated by alternative mRNA splicing at the amino-terminus (Eddinger and Murphy, 1988; Nagai et al., 1989). These isoforms differ by the absence [(−)insert] or presence [(+)insert] of a seven amino acid sequence near the ATPase site (Kelley et al., 1993; White et al., 1993). The importance of this insert is that it doubles the actin-activated ATPase activity and actin filament movement in *in vitro* motility assays (v_{max}; Kelley et al., 1993; Rovner et al., 1997; Lauzon et al., 1998). Myosin purified from multiple rat tissues shows a rank correlation between the (+)insert protein expression and v_{max} (Leguillette et al., 2005).

Airway smooth muscle cells from asthmatics and animal models of asthma exhibit increased rates and extents of shortening (Jiang et al., 1992; Bramley et al., 1994; Mitchell et al., 1994; Fan et al., 1997; Wang et al., 1997). This increased shortening rate

correlates with the over-expression of the fast SMMHC mRNA in asthmatic human ASMCs (Leguillette et al., 2009). Increased rates of ASM shortening have also been correlated with increased levels of MLCK (Jiang et al., 1992, 1995; Ma et al., 2002), but a direct link between rMLC phosphorylation and shortening velocity remains controversial (Gerthoffer, 1987; Merkel et al., 1990; Mitchell et al., 2001). Thus, the importance of increased activation or altered expression of contractile proteins in AHR is unknown.

The latch-state

The latch-bridge, or latch-state, is a unique form of the myosin cross-bridge and was originally defined as a state of force maintenance that occurs when rMLC is deactivated by dephosphorylation while the myosin head is still attached to actin (Dillon et al., 1981). Despite the wide acceptance of this hypothesis, a verification of the occurrence of latch-bridges at the molecular level is lacking in both animal and human tissues. This latch-bridge hypothesis also assumes that myosin must be initially phosphorylated in order to attach to actin (Hai and Murphy, 1988). However, tonic force can develop with little or no rMLC phosphorylation suggesting that latch-bridges can be formed by dephosphorylated or unphosphorylated myosin (Sato et al., 1992). Indeed, evidence is accumulating to suggest that unphosphorylated myosin can attach to actin (Leguillette et al., 2008) and our preliminary data also indicate that it can occur in the presence of actin regulatory proteins. Furthermore, the (−)insert SMMHC is preferentially expressed in tonic smooth muscle, where the latch-state is prevalent. This suggests that the unphosphorylated isoform might play a role in force maintenance (Leguillette et al., 2008).

In an alternative hypothesis for latch-bridge formation, the rMLC remains phosphorylated but force regulation is modulated by caldesmon and calponin (Hai and Kim, 2005). Because, in asthma, there is a possibility that contractile protein expression and function are altered by airway inflammation, latch-bridge formation may contribute to the force maintenance observed in AHR.

Dynamic relaxation of ASMCs

A striking feature of AHR in asthmatic subjects is an apparent failure of the ASMCs to relax in response to deep inspiration. The putative mechanisms for this clinically important effect (An et al., 2007) include an alteration of the molecular mechanisms of ASMC force production. Force generation in ASMCs normally results from rapidly cycling cross-bridges but may also result from slowly cycling latch-bridges. These latch-bridges have the potential for force maintenance and thereby prevent relaxation of asthmatic airways (Fredberg et al., 1997). Alternatively, sustained contraction may result from a reduced rate of myosin dephosphorylation; a condition consistent with increased Ca^{2+}-sensitivity mediated by Rho activated Rho kinase (ROK; Somlyo and Somlyo, 2003).

EXPERIMENTAL APPROACHES

Multiple studies have addressed and compared the mechanical properties of normal or asthmatic ASMCs, but none of these studies have performed a multi-level investigation of the component proteins in a single animal species. Our approach is to characterize how the basic properties of ASMC proteins (from mice, rats, and humans) influence actin-myosin interactions in terms of sliding velocity and force production. These studies will provide the parameters necessary to build our model of the normal and hyper-responsive lung.

Purification of ASMC proteins

The functional analysis of individual myosin molecules from animal models has only recently been made possible by our development of techniques to purify it from small tissue samples (Sobieszek, 1994; Leguillette et al., 2005). The main challenge in smooth muscle myosin purification is to detach it from actin. This is achieved by extracting myosin in folding conditions, decreasing its access to actin (Sobieszek, 1994) followed by myosin filament formation. Precipitation of myosin is then performed by ammonium sulfate fractionation. Myosin fractions are then dissolved and dialyzed against low-salt buffer to purify the myosin filaments from tropomyosin. The purified myosin is then thiophosphorylated, a stable form of phosphorylation that allows mechanics studies without the confounding effect of dephosphorylation. This purification procedure has made possible, for the first time, the study of ASM myosin from rat models of asthma (Leguillette et al., 2005).

In vitro motility assays

The *in vitro* motility assay (**Figure 1**) consists of observing the sliding velocity of fluorescently labeled actin filaments as they are propelled by myosin molecules randomly adhered to a nitrocellulose-coated coverslip (Warshaw et al., 1990; Leguillette et al., 2008). The role of the actin regulatory proteins can be addressed by adding them individually or in combination to the assay. The sliding velocity (v_{max}) of single actin filaments is determined in presence of MgATP and is calculated by dividing the path length traveled by the elapsed time.

Force measurements with optical tweezers

The laser trap assay is used to measure unitary displacement and force generated by myosin molecules. The assay uses laser light to create potential energy wells which are capable of capturing and manipulating beads in solution (Dupuis et al., 1997). By attaching actin filaments to two such beads, a single fluorescently labeled actin filament can be brought into contact with myosin molecules adhered to a pedestal on a coverslip. The displacement distance and attachment time of a single myosin molecule can be estimated by measuring the movement of one of the beads while myosin undergoes its power-stroke. Alternatively, the force generated by a single myosin molecule can be estimated by using a feedback system to prevent bead movement by generating an equal and opposite force. The laser trap can also be used to measure the behavior of several myosin molecules at a time (Leguillette et al., 2008; **Figure 2A**). In this case, only one bead is required to bring an actin filament in contact with multiple myosin molecules. Displacement and force will again be estimated from the displacement of the bead and normalized by the actin filament length or the estimated number of myosin molecules interacting with the filament. To estimate the force of binding of non-phosphorylated myosin to actin (myosin molecules that do not generate movement) the actin-attached bead is moved away from the pedestal at constant velocity (**Figure 2B**). When the pulling force exerted by the laser trap exceeds the binding

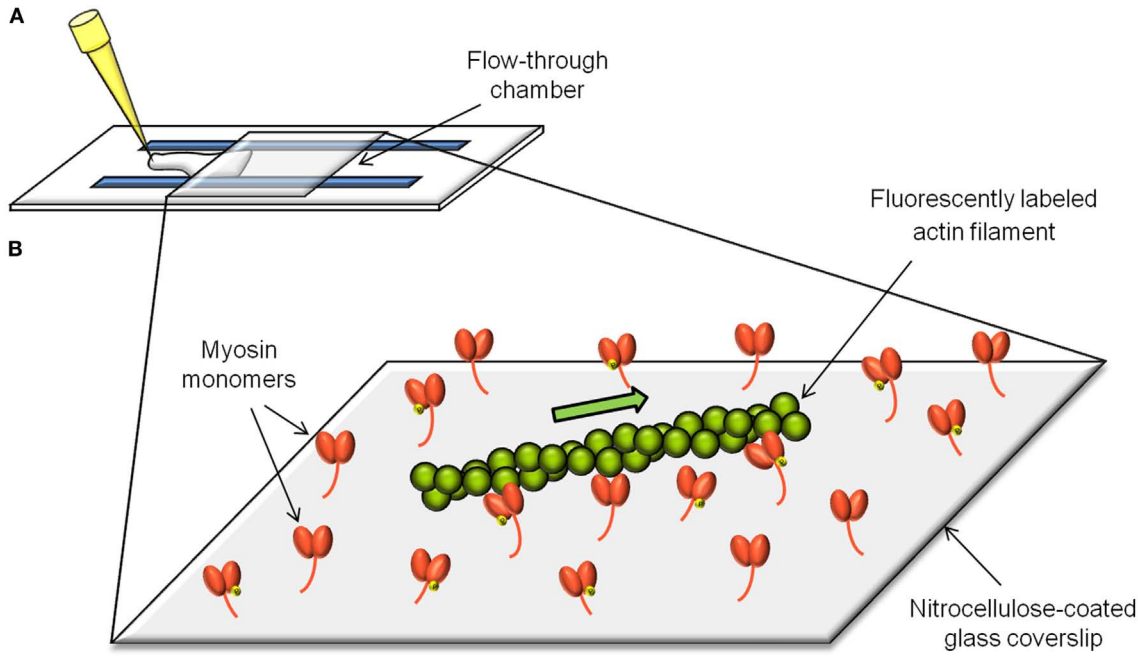

FIGURE 1 | The *in vitro* motility assay. The *in vitro* motility assay consists of measuring the velocity (v_{max}) of actin filaments as they get propelled by myosin molecules randomly adhered to a microscope coverslip **(B)**. The flow-through chamber to setup and perform the assay is constructed from a nitrocellulose-coated coverslip and a microscope slide separated by plastic shims **(A)**.

force of the non-phosphorylated myosin molecules to actin, the trapped bead snaps back to its unloaded position (**Figure 2C**). The product of the laser trap stiffness (Dupuis et al., 1997) and the maximum distance between the bead and the trap center (**Figure 2B**) gives the binding force of the unphosphorylated myosin to actin. This force is then normalized as above.

MODELING APPROACHES AT THE MOLECULAR SCALE

Our initial model of the smooth muscle cross-bridge cycle (Wang et al., 2008) is based on a modified version of the Hai–Murphy model (Hai and Murphy, 1988; Mijailovich et al., 2000; Hai and Kim, 2005; **Figure 3**). Myosin is assumed to exist in one of four states: the base state of myosin (M) that is neither phosphorylated nor attached to actin; a phosphorylated myosin that is not attached to actin (Mp); a phosphorylated myosin that is attached to actin (AMp); and a myosin that is attached to actin but not phosphorylated (AM).

Myosin can only exert a force when it is attached to actin. The transition from Mp to AMp, i.e., the attachment of phosphorylated myosin to actin, is believed to occur upon hydrolysis of ATP. During the cross-bridge cycle, myosin cycles between the Mp and AMp states, continually binding to and unbinding from actin, and hence consuming ATP to generate force. By controlling the rate of myosin phosphorylation, the ASMC can presumably control the velocity of shortening and the amount of force generated. The Ca^{2+}-dependent mechanisms by which myosin phosphorylation is regulated are discussed in Section "The Cellular Scale."

In smooth muscle, myosin is believed to remain attached to actin after dephosphorylation (Dillon et al., 1981). As mentioned above, this state (AM) is called the latch-state. Because the rate of transition from AM to M is typically slow, this allows the smooth muscle to remain in a state where it can no longer relax or contract quickly, but requires less ATP to maintain contraction. The kinetics of the latch-state, as well as that of the cross-bridge cycle are vital for understanding ASMC contraction and relaxation.

This model plays two major roles. Firstly, it is the force-generating mechanism that, ultimately, results in airway narrowing in the full multi-scale model. To accomplish this, the model parameters are determined by comparison with data taken from molecular scale experiments, as well as data collected from muscle strips. Thus, we aim to ensure the model generates physiological levels of force when incorporated into the multi-scale model. Secondly, the model can be used as a predictive tool to understand the consequences of the possible binding of unphosphorylated myosin.

In addition to modeling the cross-bridges with a version of the Hai–Murphy model, our molecular scale model also includes a hypothetical type of binding protein, which we call a cross-linker (Donovan et al., 2010). Cross-linkers are included to give a biophysical basis for the plastic-like properties of unactivated smooth muscle, such as fluidization upon stretching. They are modeled similarly to cross-bridges, except that the attachment functions are symmetrical with respect to the distance variable. A cross-bridge generates active force as a result of the attachment function being asymmetrical, thus biasing the cross-bridge to bind in a position that exerts active force. An identical binding mechanism, but one with a symmetrical binding function, does not generate active force, but exhibits similar dynamic behavior upon stretching. Since

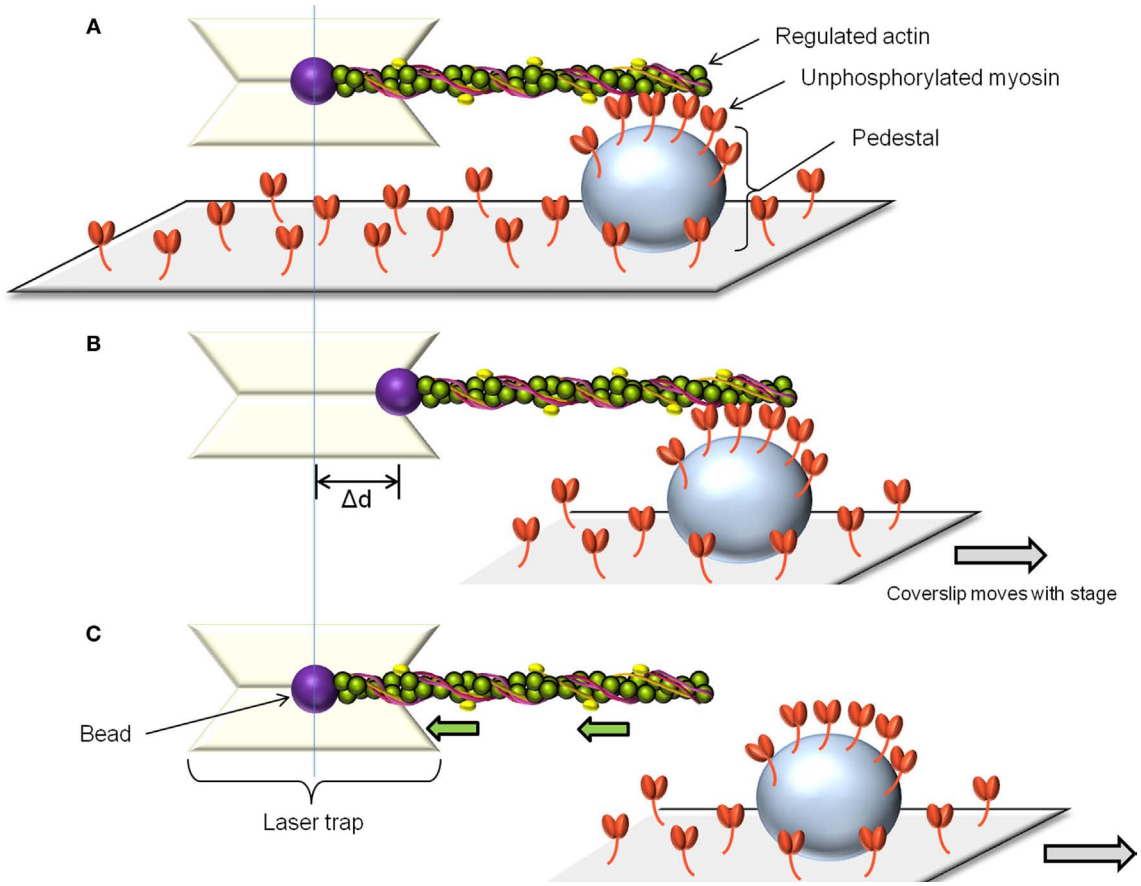

FIGURE 2 | The laser trap assay. To measure the force of binding to actin of unphosphorylated myosin, a single beam laser trap assay is used as follows: The laser trap is used to capture a polystyrene bead coated with *N*-ethylmaleimide modified myosin. Such myosin can attach to actin but does not cycle, so it is used to glue the fluorescently labeled actin filament. The actin is then brought in contact with the randomly adhered unphosphorylated myosin on a pedestal on the coverslip **(A)**. After allowing time for binding, the pedestal is moved away from the laser trap at constant speed **(B)**. Initially, the bead remains offset from the trap center. When the pulling force exerted by the trap exceeds the binding force of the unphosphorylated myosin molecules, the bead springs back into the trap center, its unloaded position. **(C)** The unbinding force is the product of the maximal distance between the bead and the trap center (Δd) by the trap stiffness. This force can be normalized by the number of myosin molecules estimated to interact with the actin filament.

the cross-linker model is validated mostly by comparison to data collected at the tissue scale, and has no known specific associated proteins, it is discussed further in Section "The Tissue Scale."

THE CELLULAR SCALE

PHYSIOLOGICAL SIGNALING MECHANISMS

Ca^{2+} oscillations and waves

A fundamental stimulus for ASMC contraction is an increase in $[Ca^{2+}]_i$. This commonly occurs in ASMCs in response to agonist activation of G-protein coupled receptors (GPCRs; Sanderson et al., 2008; **Figure 4**). We have found that Ca^{2+} oscillations are induced in mouse, rat, and human ASMCs by methacholine, 5HT, histamine, NO, endothelin, and LTD_4 (Perez and Sanderson, 2005; Perez-Zoghbi and Sanderson, 2007, 2010; Bai et al., 2009; Ressmeyer et al., 2010). However, changes in membrane potential (e.g., induced with external KCl) can also lead to Ca^{2+} changes (Perez-Zoghbi et al., 2009; **Figure 4**). The key function of the increased $[Ca^{2+}]_i$ is the activation, via calmodulin, of MLCK to phosphorylate rMLC to initiate cross-bridge formation (**Figure 3**) Consequently, the form and magnitude of the Ca^{2+} signals influence the extent of force generation.

Importantly, these changes in $[Ca^{2+}]_i$ in ASMC from the small airways of a variety of species in near *in situ* conditions occur as sustained Ca^{2+} oscillations rather than static elevations of $[Ca^{2+}]_i$ while the agonist remains present (**Figure 5**; Sanderson et al., 2008; Bai et al., 2009; Delmotte and Sanderson, 2010; Perez-Zoghbi and Sanderson, 2010; Ressmeyer et al., 2010). Each Ca^{2+} oscillation is often initiated at one end of the cell and propagates along the cell as a Ca^{2+} wave. By correlating airway responses with the occurrence of agonist-induced Ca^{2+} oscillations, it has become clear that increased airway contraction correlates with an increased Ca^{2+} oscillation frequency (**Figure 6**; Sanderson et al., 2008; Delmotte et al., 2010; Ressmeyer et al., 2010). Because it appears that the frequency of the Ca^{2+} oscillations is important in force regulation, this relationship is termed frequency-modulated (FM) regulation (Berridge, 1997). However, the outcome of our modeling indicates that this form of control involves more than just the frequency aspect of the Ca^{2+} oscillation and probably relates

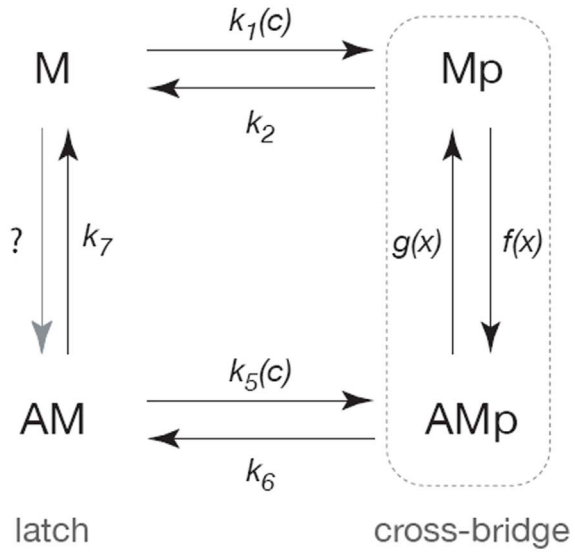

FIGURE 3 | Schematic diagram of the cross-bridge model. Following Hai and Murphy (1988) the myosin is assumed to exist in four forms; unphosphorylated and unattached (M), phosphorylated and unattached (Mp), phosphorylated and attached (AMp), attached and unphosphorylated (AM). Cycling between the Mp and AMp states generates active force, while the AM state can maintain tension but cannot generate force (and is thus called the latch-state). Rates of phosphorylation are assumed to be sigmoidal functions of Ca^{2+} concentration (c). The rates of attachment and detachment are functions of the distance (x) to the actin-binding site, and thus the model is a system of partial differential equations of conservation type.

to frequency-dependent changes in the form of the Ca^{2+} oscillations (Wang et al., 2010). A second interesting finding is that the relationship between contraction and the frequency of the Ca^{2+} oscillations differs between species (**Figure 6**; Bai and Sanderson, 2009). In mouse, Ca^{2+} oscillations of about 20–30 min^{-1} induced a similar extent of airway contraction as 8–10 Ca^{2+} oscillations per minute in human airways (Ressmeyer et al., 2010). While some of this difference may be attributable to the form of the Ca^{2+} oscillation at different rates, it is likely that a second mechanism termed "Ca^{2+} sensitivity" is responsible (see later; Bai and Sanderson, 2009).

Mechanisms of agonist-induced Ca^{2+} signaling

Agonist-induced Ca^{2+} oscillations in ASMCs primarily rely on Ca^{2+} release from the sarcoplasmic/endoplasmic reticulum (S/ER). In general, agonist stimulation of GPCRs results in the production of inositol trisphosphate (IP_3). This, in turn, binds to and releases Ca^{2+} from the S/ER via IP_3 receptors (IP_3Rs). The sensitization of all the IP_3Rs of an ASMC with IP_3 primes the ASMC to display Ca^{2+} oscillations and waves. A Ca^{2+} transient occurring at one group or cluster of IP_3Rs leads to, by the diffusion of Ca^{2+} through the cytosol, the stimulation of other nearby IP_3Rs to release Ca^{2+}, a process called Ca^{2+}-induced Ca^{2+} release (CICR; Berridge et al., 2003; Berridge, 2009). The sequential repeat of this activity propagates a Ca^{2+} wave. Therefore, it appears that Ca^{2+} wave properties are a consequence of Ca^{2+} diffusion rates and IP_3R distribution and sensitivity. The S/ER Ca^{2+} ATPase (SERCA) pumps sequester much of the cytosolic Ca^{2+} back into the S/ER to allow the process to recycle. Although a direct role for Ca^{2+} influx is not required for Ca^{2+} oscillations, the long-term maintenance of Ca^{2+} oscillations does rely on the Ca^{2+} content of the SR (Perez and Sanderson, 2005). Most likely, Ca^{2+} enters the cell via a store-operated channel (SOC) influx mediated by membrane channels, Orai1, activated by STIM1, a Ca^{2+} sensor within the S/ER (Parekh and Putney, 2005; Putney and Bird, 2008). However, when the S/ER Ca^{2+} content is low, Ca^{2+} may also enter via receptor-operated channels, TRP channels, or the reversal of the Na^{+}-Ca^{2+} exchanger (Rahman et al., 2012).

Ca^{2+} oscillations have also been proposed to be mediated by CICR via the ryanodine receptor (RyR) of the S/ER (Dai et al., 2007). These may result by a direct influx action of Ca^{2+} or following sensitization of the RyR by cADP-ribose (cADPR; Prakash et al., 1998; Jude et al., 2008). However, in all our experiments with normal lung slices, on-going Ca^{2+} oscillations or waves are not inhibited in anyway by ryanodine (Bai et al., 2009), an antagonist of the RyR or antagonists of cADP-ribose. While other RyR antagonists such as tetracaine do inhibit Ca^{2+} oscillations (Dai et al., 2007), these appear to result from their non-specific anesthetic effects that decrease IP_3 production or Ca^{2+} sensitivity (Bai et al., 2009).

Ca^{2+} signaling associated changes in membrane potential

Membrane depolarization has commonly been associated with smooth muscle contraction; and is believed to be mediated by the opening of voltage-dependent Ca^{2+} channels and the influx of Ca^{2+} perhaps followed by CICR via the RyR (Janssen, 2002). However, ASMCs in lung slices do not appear to follow this scheme. In response to membrane depolarization, induced by external KCl, ASMCs display Ca^{2+} oscillations with a very slow rate (1–2 min^{-1}) as compared to agonist-induced Ca^{2+} oscillations (**Figure 5**; Perez and Sanderson, 2005; Bai et al., 2009; Ressmeyer et al., 2010). Importantly, these Ca^{2+} oscillations have a significantly different appearance and occur as large prolonged increases in $[Ca^{2+}]_i$ that are preceded by numerous elemental Ca^{2+} responses. In contrast to agonist-induced oscillations, KCl-induced oscillations are inhibited by ryanodine (**Figure 5**) and the removal of extracellular Ca^{2+} (Perez and Sanderson, 2005; Bai et al., 2009). The implication is that KCl-induced oscillations are mediated by a slow Ca^{2+} influx that overfills the S/ER to sensitize the RyR to CICR.

It seems clear from these studies that both IP_3Rs and RyR are present in ASMCs, but they appear to function independently of each other during normal Ca^{2+} signaling. However, since both receptors rely on the same Ca^{2+} resource, they are unavoidably linked by the Ca^{2+} content of the S/ER. Indeed, slow Ca^{2+} oscillations mediated by the RyR can be replaced by fast Ca^{2+} oscillations via the IP_3R. An explanation for this conversion is that the partial emptying of the S/ER Ca^{2+} inactivates the RyR (Wang et al., 2010) and this also explains why the RyR does participate in CICR Ca^{2+} signaling during IP_3-dependent Ca^{2+} oscillations.

Ca^{2+} sensitivity

A complementary mechanism enhancing ASMC that works in parallel to the activation of MLCK by Ca^{2+} is the inactivation

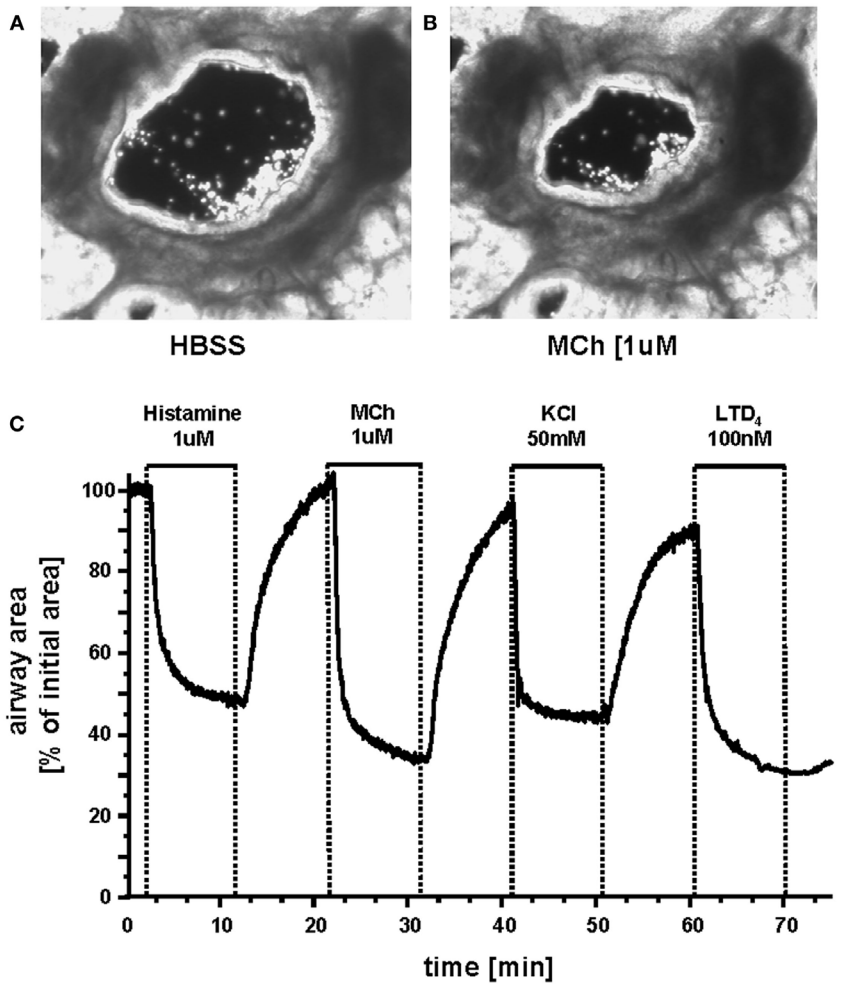

FIGURE 4 | Airways in human lung slices. (A) A human small airway in Hanks' balanced salt solution (HBSS). **(B)** In response to 1 μM MCH, the airway has contracted. **(C)** The change in airway cross section area (as a % of the initial area) in response to a variety of contractile stimuli. Agonists Histamine, Methacholine and leukotriene D4 and membrane depolarization with KCl induce airway contraction.

of the antagonistic enzyme, MLCP that dephosphorylates rMLC to mediate ASMC relaxation (Schaafsma et al., 2008; Chiba et al., 2010; Mbikou et al., 2011). The inhibition of MLCP is commonly achieved by an increased activity of Rho kinase (ROK; by Rho A) in response to the same agonist stimulation that induced increases in Ca^{2+}. Similar changes can be induced by PKC in response to activation by diacylglycerol. Phosphorylation of the regulatory or accessory proteins of MLCP by ROK or PKC prevent its association with rMLC; decreased MLCP activity allows the phosphorylation state of rMLC to persist (Somlyo and Somlyo, 2003; Sanderson et al., 2008).

ASMC relaxation by β_2-adrenergic receptor agonists

A major objective of therapies for AHR is the relaxation of contracted ASMCs and the prominent pharmaceuticals in this strategy are β_2-adrenergic receptor agonists. Although widely used, the mechanism of action of these compounds is not fully understood at the cellular level; a common belief is that increases in cAMP lead to Ca^{2+} decreases and thereby relaxation.

Because it will be important to include β_2-adrenergic receptor signaling in our lung model, we have initially explored this signaling pathway with lung slices (see below). An important finding was that both short-acting (albuterol) and long-acting (formoterol) β_2-adrenergic receptor agonists slowed the Ca^{2+} oscillations induced by methacholine or histamine in mouse or human airways (Delmotte et al., 2010). This appeared to be achieved by a reduced activation-sensitivity to IP_3 and increased inhibition-sensitivity to Ca^{2+} of the IP_3R (Bai and Sanderson, 2006a). The production of IP_3 may have also been reduced in the case of high formoterol concentrations (Delmotte and Sanderson, 2010). These conclusions appear to differ from earlier studies that proposed that increased cAMP reduced internal Ca^{2+} by activating Ca^{2+}-dependent K^+ channels that mediate membrane hyperpolarization to reduce Ca^{2+} influx (Kume et al., 1994). Although the earlier studies implied that this was a direct mechanism to reduce $[Ca^{2+}]_i$, it is not totally incompatible with decreased Ca^{2+} oscillation frequency if the Ca^{2+} influx is directed to refilling the supportive Ca^{2+} store. This hypothesis has similar implications

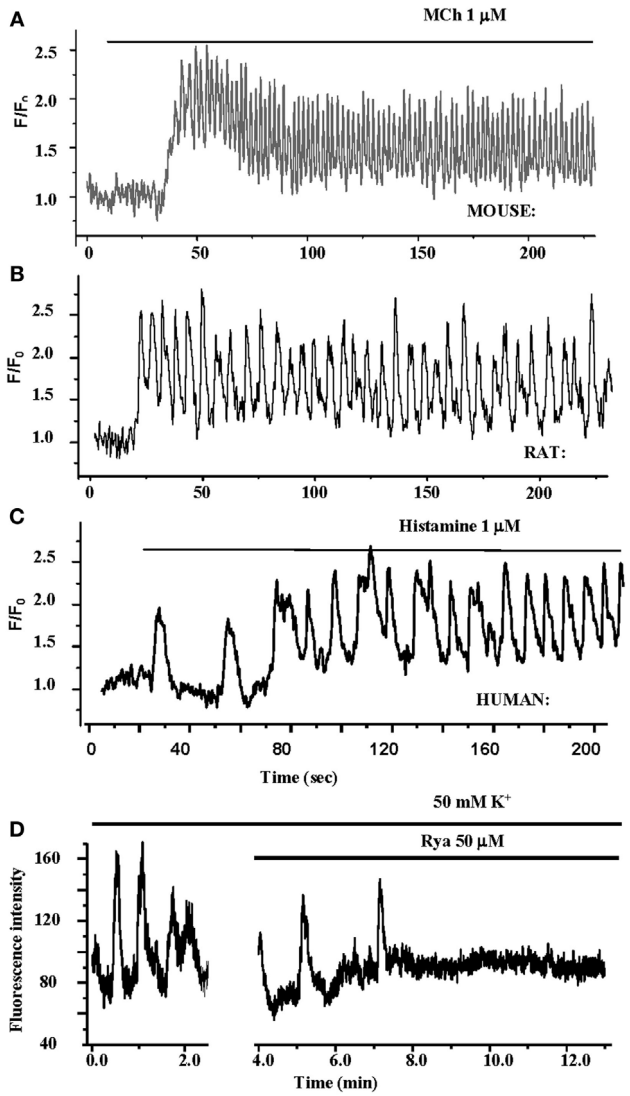

FIGURE 5 | Ca^{2+} oscillations in ASMCs in lung slices. (A–C) The contractile agonists methacholine and histamine induce Ca^{2+} Oscillations in mouse, rat, and human ASMCs in lung slices. The frequency of the Ca^{2+} oscillations varies between species. **(D)** KCl also induces Ca^{2+} oscillations in human ASMCs in lung slices. Theses Ca^{2+} oscillations are slow and are inhibited by RyR.

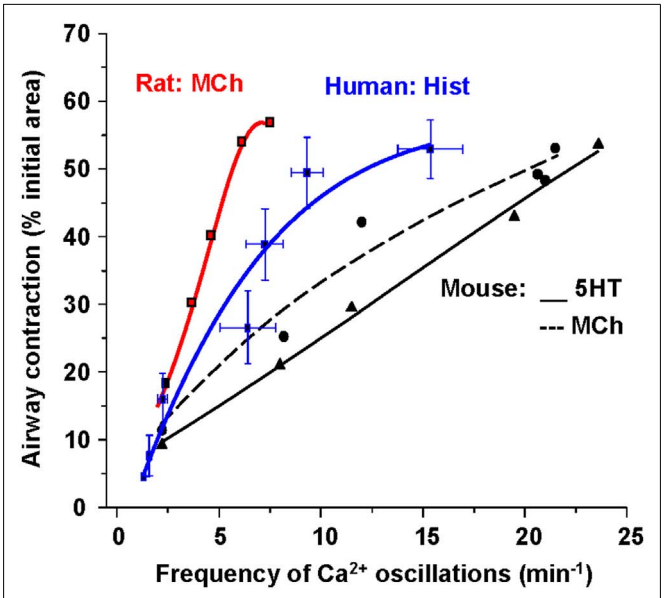

FIGURE 6 | The relationship between Ca^{2+} oscillation frequency of ASMCs and the extent of airway contraction. The gradient of the relationship is different for each species.

for the idea that spontaneous Ca^{2+} sparks, (mediated by RyRs) that also activate Ca^{2+}-dependent K^+ channels and observed in isolated ASMCs (Zhuge et al., 2010), serve as a relaxation mechanism.

In addition to Ca^{2+} reduction, β_2-adrenergic receptor agonists also reduce the Ca^{2+} sensitivity of ASMCs. Importantly, this effect is very potent with formoterol (Delmotte and Sanderson, 2010; Delmotte et al., 2010). At a low concentration (5 nM) that is insufficient to alter the Ca^{2+} oscillation frequency, formoterol induces a substantial relaxation of the ASM. A change in ASMC Ca^{2+} sensitivity may also explain some of the effects of membrane hyperpolarization; with the Ca^{2+} clamped in a lung slice, we have found that KCl (depolarization) also increased contraction. KCl can activate Rho kinase (Janssen et al., 2004) and this suggests that hyperpolarization will decrease Ca^{2+} sensitivity to help relax ASMCs. These mechanisms emphasize that Ca^{2+} sensitivity is an equally relevant signaling mechanism that must be considered when addressing the cause and relief of AHR (Chiba et al., 2010).

EXPERIMENTAL APPROACHES

A major advance that has facilitated our investigation of the cellular regulation of airway contraction is our ability to examine changes in ASMC physiology while simultaneously measuring airway contraction. These correlations are made possible by a unique lung slice preparation that has been used with mouse, rat, guinea pig, horse, monkey (Sanderson, 2011), and most importantly, human airways (Ressmeyer et al., 2010; **Figure 4**).

Briefly, isolated lungs are re-inflated via the trachea to a normal size with a solution of warm agarose (∼2%). After cooling and gelling of the agarose, the lungs are sufficiently stiff to be cut into serial slices, ∼200 μm thick (Perez and Sanderson, 2005). Only lung slices containing airway cross sections that lack agarose within the lumen and have an intact epithelium and ciliary activity are selected for study. Lung slices are robust, being viable for 3 days and highly compatible with experimental imaging. By loading the cells of the lung slice with Ca^{2+} reporter dyes, changes in $[Ca^{2+}]_i$ in ASMCs can be observed with scanning laser microscopy during contraction.

The lung slices can also be used to investigate the mechanism of "Ca^{2+} sensitivity." This requires that the $[Ca^{2+}]_i$ of the ASMCs is "clamped" to a constant level. This is achieved by irreversibly emptying the S/ER of Ca^{2+} by treatment with caffeine and ryanodine to invoke continuous Ca^{2+} influx via SOCs (Bai and Sanderson,

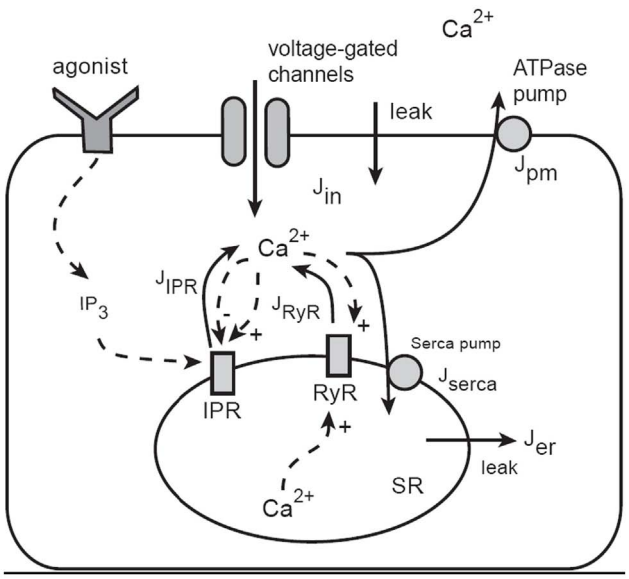

FIGURE 7 | Schematic diagram of the Ca^{2+} model. Calcium can enter the cytosol through IP_3 receptors (IPR), ryanodine receptors (RyR), or generic voltage-gated channels and leaks. Ca^{2+} is removed from the cytoplasm by ATPase pumps on the membrane of the SR and on the plasma cell membrane. IPR are activated by IP_3, which is produced as an end-product of agonist stimulation of cell-surface receptors. Calcium in the cytosol can diffuse, and is heavily buffered. The buffers are not shown explicitly as they are incorporated via an effective diffusion coefficient and effective reaction rates.

2006b; Cahalan, 2009). Increased force production under these conditions implies that an alternative method besides Ca^{2+} is acting.

MODELING APPROACHES

Ca^{2+} oscillations

The model of Ca^{2+} oscillations is based on the dynamics of Ca^{2+} leaving or entering the cytosol (**Figure 7**). Ca^{2+} can enter the cytosol from outside the cell (J_{in}) or from the S/ER (J_{SR}). Conversely, Ca^{2+} can be removed from the cytoplasm by Ca^{2+}ATPase pumps in the SR (J_{serca}) and the plasma membrane (J_{pm}). This model construction is well developed (Falcke, 2004) and has been used extensively to further develop our model and test predictions (Sneyd et al., 2004, 2006).

Although the overall structure is simple, each of the individual fluxes can be modeled in a complex way; J_{SR} includes Ca^{2+} flux through IP_3 receptors (J_{IPR}) as well as ryanodine receptors (J_{RyR}). The J_{IPR} flux also requires that we incorporate sensitivity to IP_3 binding and Ca^{2+} feedback. In the initial version of the model, this was achieved by using a model of the IP_3R developed by De Young and Keizer (1992), although more recent work uses more modern IP_3R models (Gin et al., 2009a,b,c; Siekmann et al., 2011). The RyR is modeled using the model of Keizer and Levine (1996).

J_{in} incorporates Ca^{2+} fluxes through voltage-gated Ca^{2+} channels and this is regulated by the membrane potential. Ca^{2+} influx via a capacitative Ca^{2+} entry mechanism or arachidonic-acid-regulated channels is incorporated in the current model of mouse ASMCs, but only in a simplistic way. More detailed models of Ca^{2+} influx in human ASMCs are being developed by an associated group (Croisier and Brook, unpublished).

Ca^{2+} buffering is modeled by incorporating a fast buffering approximation. Nuclear and mitochondrial Ca^{2+} fluxes, although present, have a secondary effect and are modeled as immobile buffers. The modulation of IP_3 production and degradation is not an important part of the mechanism underlying Ca^{2+} oscillations in ASMC (Sneyd et al., 2006) so these pathways are not included.

Our current model of Ca^{2+} dynamics does not attempt to include a wide variety of membrane ion channels that have been found in ASM, primarily because there are few data directly linking the activity of such channels to agonist-induced Ca^{2+} changes in ASM *in situ*. Although a correlation of ASM contraction and channel activity has been often observed, this is inadequate for Ca^{2+} modeling since the underlying Ca^{2+} changes cannot be assumed. The induction of slow Ca^{2+} oscillations by KCl is a good example of an unexpected form of Ca^{2+} signaling in response to a stimulus that is commonly expected to induce a sustained Ca^{2+} elevation in response to the opening of voltage-dependent Ca^{2+} channels. Ion channel activity may also affect Ca^{2+} sensitivity. From our experience, we emphasize that it is essential to collect information on contraction, Ca^{2+} changes and Ca^{2+} sensitivity, before mechanisms and conclusions can be made with models.

The full model provides a good fit to Ca^{2+} oscillations induced by stimulation with MCh (**Figures 8A,B**) and importantly has made some interesting predictions (Wang et al., 2010). Although experiments and model indicate that the RyR is not a key feature of on-going Ca^{2+} oscillations, the model surprisingly predicts that the first Ca^{2+} transient is dominated by RyR activity (**Figure 8**). This possibility was not original envisaged and resulted in experimental design that only added ryanodine to on-going Ca^{2+} oscillations. However, an initial role for RyR can be experimentally tested by having ryanodine present before the stimulation of Ca^{2+} oscillations with agonist. A second model prediction is that the S/ER Ca^{2+} content rapidly falls with each Ca^{2+} oscillation to reach a new but lower equilibrium. This lower S/ER Ca^{2+}concentration predicts that the RyR will be insensitive to CICR and explains why the RyR cannot contribute to on-going Ca^{2+} oscillations. Importantly, the model also reproduces the experimental response of slow Ca^{2+} oscillations upon depolarization with KCl (**Figures 8B,C**). The prediction of this aspect of the model is that the SR becomes overfilled with Ca^{2+} to sensitize the RyR to CICR. The model further predicts that agonist-induced oscillations would empty the SR so that the KCl-induced Ca^{2+} oscillations operating through the RyR would become inoperative as a result of reduced SR Ca^{2+}. This prediction was upheld in the experimental examination of cytosolic Ca^{2+} oscillations; measurement of SR Ca^{2+} is still required (**Figure 8E**).

Ca^{2+} waves

An important aspect of the Ca^{2+} signaling occurring within the ASMCs is their spatial organization; each Ca^{2+} oscillation propagates as a Ca^{2+} wave. This serves to distribute the stimulus equally across the cell but it also determines the duration of the signal at points within the cell. To model this spatial behavior, it

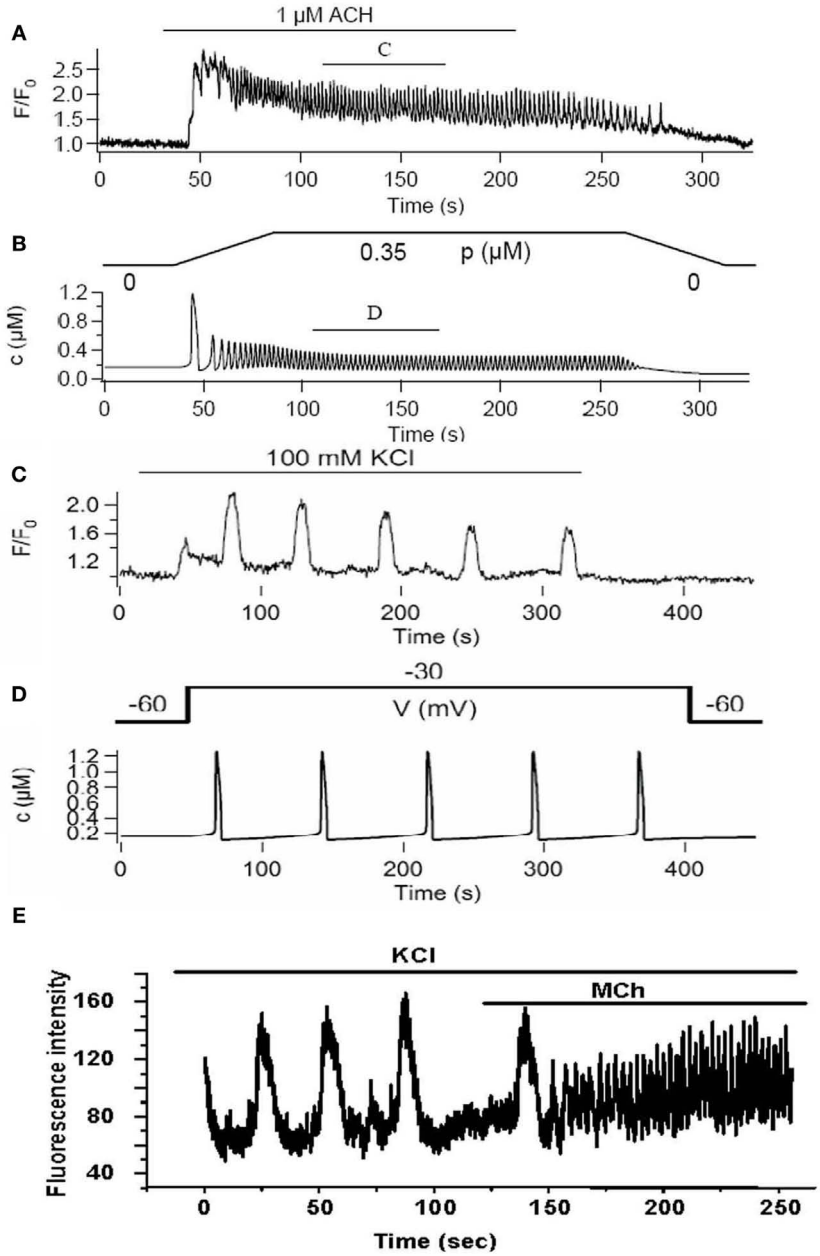

FIGURE 8 | A comparison of experimental and model Ca^{2+} oscillations induced by agonist (A,B) and KCl (C,D). Agonist-induced Ca^{2+} oscillations are fast compared to KCl-induced Ca^{2+} oscillations. **(E)** Experimentally, we observe that slow Ca^{2+} oscillations induced by KCl are converted into fast Ca^{2+} oscillations by the addition of agonist in the presence of KCl.

is necessary to incorporate a spatial distribution for the release channels and to model the diffusion of Ca^{2+}. The Ca^{2+} oscillations can then be visualized as propagating waves (for both agonist and KCl stimulation) that reflect the experimental data (Wang et al., 2010). However, the model predicts that both the IP_3Rs and RyRs need to be asymmetrically distributed; there appears to be a requirement for receptor density to be greater toward one end of the cell in order to reproduce the propensity for Ca^{2+} waves to initiate at one end of the cell, as well as show intermittent wave failure followed by a reversal of the wave propagation direction. It is not clear why this organization is required, or if it occurs biologically, but we intend to test this prediction by examining receptor distribution.

Coupling Ca^{2+} signal to force production

To incorporate the cellular signaling into the larger lung model, it is necessary to couple our Ca^{2+} dynamics model to our model for force generation. We discussed the cross-bridge model in Section "The Molecular Scale." The coupling of Ca^{2+} to force generation requires the activation of MLCK by Ca^{2+}/calmodulin and we use

a Hill function to mimic cooperative binding of four Ca^{2+} ions to calmodulin.

Force generation also requires the consideration of myosin dephosphorylation by MLCP. This is influenced by both agonist and KCl. An additional complication is that in mouse but not human ASMCs, MLCP appears to be activated (on a slower time base relative to MLCK) by Ca^{2+} (Bai and Sanderson, 2006b, 2009; Ressmeyer et al., 2010). To model fast Ca^{2+} activation of MLCK followed by slower Ca^{2+} activation of MLCP, we introduced an additional differential equation for *Q*, the fraction of activated MLCP (Wang et al., 2008). The rate constants were determined by fitting to the airway response to a step increase in Ca^{2+} (**Figure 3**).

With this mouse model, that translates Ca^{2+} oscillations into force production, we were able to explore the hypothesis of FM regulation to identify the key features of the Ca^{2+} oscillations that are the most significant in force generation. Interestingly, whole-cell Ca^{2+} oscillations (a simultaneous uniform increase in Ca^{2+} throughout the whole-cell) induced greater force than propagating Ca^{2+} oscillations (i.e., Ca^{2+} waves), even through the frequency and mean Ca^{2+} concentration of the two processes were similar (Wang et al., 2010). It is important to point out that in this mouse model, a constant increase in $[Ca^{2+}]_i$ induced less force than either type of Ca^{2+} oscillation. This is believed to result, in part, from the slow activation of MLCP that can decrease force. Therefore, what appears to be important for force production is the shape or duration of the Ca^{2+} oscillation. If the Ca^{2+} oscillation becomes more like that of a constant increase in $[Ca^{2+}]_i$, (i.e., it broadens) by becoming lower in magnitude but longer in duration in the case of a whole-cell Ca^{2+} oscillation or spatially broader in the case of the Ca^{2+} wave, it will induce less force even though the mean Ca^{2+} remains little changed. This relationship between oscillatory Ca^{2+} changes and force may be different in human ASM cells, in view of the fact that Ca^{2+} has less effect on Ca^{2+} sensitivity of human ASM cells.

By examining the proportion of cross-bridges in the latch-state, the model is used to determine the importance of the latch-state in controlling the speed of relaxation. Initial results from the model indicate that the gradual movement of cross-bridges into the latch-state causes a gradual decline in the speed of contraction, with a power-law decay profile (see The Tissue Scale). These model results agree qualitatively with experimental data. However, understanding of the relationship between the latch-state, muscle stiffness, and the speed of contraction remains incomplete.

Stochastic modeling of Ca^{2+} oscillations and waves

The current Ca^{2+} signaling models are deterministic. However, the behavior of channels such as the IP_3R, are for the most part, essentially stochastic. Stochastic behavior is observable in long-duration recordings of low frequency Ca^{2+} oscillations, which have an increased variance in the inter-spike interval. Even at higher IP_3 concentrations, i.e., at higher oscillation frequencies, there is clear stochastic variation in the oscillation period. Consequently, a major goal will be to convert our models to include stochastic behavior, in order to see how important stochastic effects are in force generation.

Our initial stochastic models have incorporated the most recent data on the dynamical behavior of IP_3R, collected from single channels in the nuclear membrane (Betzenhauser et al., 2008). By fitting new Markov models to these single channel data, the next generation of IP_3R models has more accurately determined the time scales of Ca^{2+} and IP_3 control of IP_3R open probability (Gin et al., 2009a,b; Siekmann et al., 2011). Initial simulations using a more accurate IP_3R model suggest that a stochastic IP_3R-based model is unable to generate long-period oscillations. How such long-period oscillations occur remains an open question.

Once stochastic effects are incorporated in the model, and their effects on force generation determined, the challenge will be to develop formulations of the stochastic model that allow for coupling to the next higher spatial scale. There is no standard methodology for such coupling, and new methods will have to be developed.

THE TISSUE SCALE

The aim of the tissue scale model is to reproduce the active and passive mechanical properties of ASMCs and the viscoelastic properties of the surrounding tissue against which the ASMC shortens. However, ASMCs are complicated by the fact that their mechanical properties are malleable depending on the physiological circumstances.

ASMC AND TISSUE MECHANICAL PROPERTIES

Inherent ASMC properties

Airway smooth muscle cells exhibit a hyperbolic force-velocity relationship (Hanks and Stephens, 1981) and a characteristic tension transient in response to step length changes (Fredberg et al., 1997; Bates et al., 2009). However, this force-length relationship is not fixed; when stimulated repeatedly, at a given length, ASMCs adapt in order to maintain their current length at the peak of the force-length relationship (Bullimore et al., 2011). This provides the ASMCs with the ability to generate maximal force even after shortening; a response that, if unregulated, would enhance AHR. In addition, and as mentioned earlier, ASMCs are able to form latch-bridges. Such latch-bridges maintain force for long periods with low energy consumption and a decreased ASMC shortening velocity (Dillon et al., 1981; Fredberg et al., 1997). Thus, by entering the latch-state the mechanical properties of ASMCs markedly change to a stiffened state. ASMCs also exhibit force adaptation; total force gradually increases when ASM is stimulated repeatedly in the presence of baseline tone (Gunst and Wu, 2001; Gunst et al., 2003).

Parenchyma tissue properties

The dynamic environment of the *in vivo* airway is determined to a substantial extent by the forces imparted by parenchymal tethering. Parenchymal attachments to the outside of the airway wall are responsible for conveying transpulmonary pressure from the pleural surface to the airway wall, and thus impart an outwardly directed force that opposes airway narrowing. Consequently, when the airways are challenged with a smooth muscle agonist, their contractile response is exquisitely sensitive to transpulmonary pressure.

The mechanical properties of the parenchyma can be described to a first approximation in terms of a linear single-valued stress-strain function such that transpulmonary pressure depends linearly on lung volume. This description accounts for the majority

of the mechanical behavior that influences airways responsiveness over the range of volumes encountered during normal breathing. However, the stress-strain behavior of lung tissue exhibits significant strain stiffening beyond this volume range due to a variety of mechanisms; a key mechanism being the progressive recruitment of collagen fibers that become straight and bear the load as volume increases (Maksym and Bates, 1997; Maksym et al., 1998). Lung tissue is also highly viscoelastic (Bates et al., 1994), so the outward force it exerts on a tethered airway depends on volume history in addition to the current volume itself.

EXPERIMENTAL METHODS

ASM strips

We have made substantial progress toward understanding the mechanical behavior of activated and non-activated ASM by characterizing the dynamic force-length behavior of strips of rat trachealis muscle (Bates et al., 2009; Bullimore et al., 2011). We measured the slowing of contraction velocity during activation (a characteristic of the latch-state) and examined if the isotonic releases influence the degree of velocity slowing. This was done by comparing shortening velocity after 15 min of isometric activation with the shortening velocity of the same ASM strip when velocity was measured once per min for 15 min. Velocity at 15 min was very similar under the two conditions. We also studied velocity slowing over time in ASM from rat and sheep trachea and found that the time course of velocity slowing was similar in both preparations and could be described by a power-law.

Stretching lung slices

To explore if airway stretching associated with breathing relaxes airway ASM, lung slices can be stretched and changes in airway size recorded. To ensure tethering is active, the lung slice periphery must be stabilized and this can be achieved by attaching the lung slice edge to a silicon sheet with glue. By applying oscillating stretches to the preparation the airway appears to simulate the cyclic expansion during breathing. Preliminary data indicate that human airways contracted with MCh respond to rhythmic stretch by relaxing (**Figure 9**). When stretching ceased, the airway re-contracted. These results are consistent with the idea that stretching is a protective mechanism against agonist-induced contraction, which was inspired by studies in isolated strips of ASM (Fredberg et al., 1997; Wang et al., 2000) leading to the hypothesis that fluidization of the ASM causes its contractile state to be determined dynamically (Krishnan et al., 2008). On the other hand, evidence of this effect *in vivo* is scant, being limited to volume changes that are very large (Bates et al., 2007). Recent studies of the contractile response of isolated airways subjected to transmural pressure changes have also failed to show that pressure oscillations reduce airway contractility (LaPrad et al., 2010; Noble et al., 2011). Our working hypothesis is that the protective mechanism we observe in our explant preparation derives from the dynamic properties of the ASM cross-linkers and cross-bridges, which exhibit fluidization when stretched. Nevertheless, it will be interesting to see whether these effects manifest in a measurable way at the level of the whole organ when incorporated into a global model of lung responsiveness.

MODELING APPROACHES

Empirical models of ASM contraction dynamics

To model the dynamic force-length behavior of an ASM strip, we have used two complementary approaches. One uses traditional viscoelastic theory (Bates et al., 2009) based on spring-and-dashpot models and has the advantage that it is based on ordinary differential equations and is therefore relatively straightforward to simulate. Here, we assume that the contractile machinery in the ASMC is presented as a force generator that acts in concert with non-linear passive elements representing the connective tissues that are mechanically arranged both in series and parallel with the force generator. This model mimics the key features of the oscillatory force-length behavior of ASM strips both when they are passive and when the ASMCs are activated by an applied stimulus (**Figure 10**). Of particular note, in order to reproduce the rapid transient decrease in peak oscillatory force observed upon the initiation of activation (**Figure 10**), it is necessary to have the

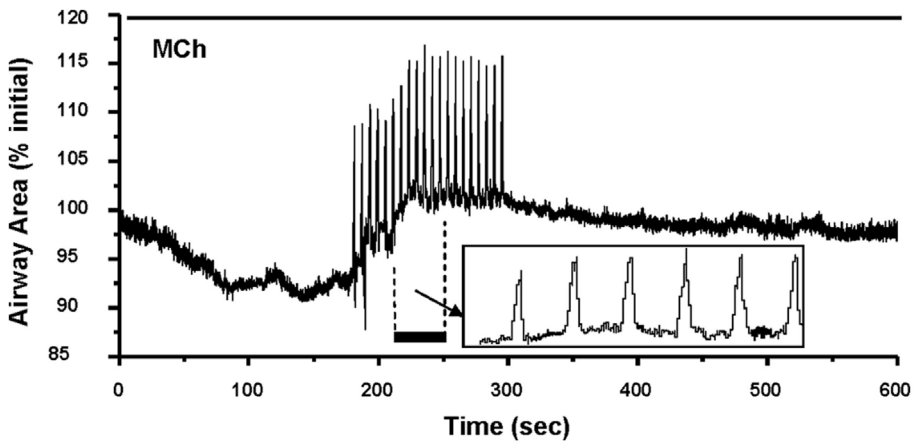

FIGURE 9 | Effect of stretch on airway contraction. A human airway contracted with MCh and exposed to sequential uni-axial stretching to mimic breathing (details of the effect of each stretch is shown in the insert box) responded with an increase in the baseline of airway size (relaxed). When stretching was terminated, the airway began to slowly re-contract in response to the continual presence of MCH.

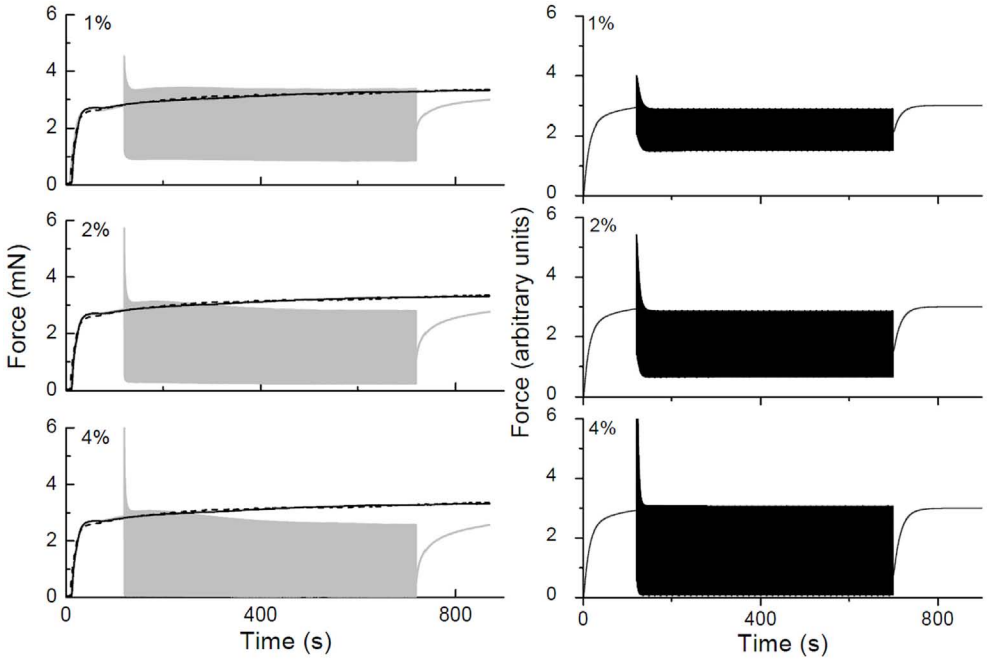

FIGURE 10 | Force-time traces obtained in a strip of rat trachealis muscle. The gray curves show data obtained with 2 Hz length oscillations having amplitudes of ±1, ±2, and ±4% baseline length as indicated. Isometric force-time curves are shown in black (solid lines obtained prior to collecting oscillation data, dashed lines obtained afterward). The black curves in the right-hand panels show corresponding force-time plots simulated by a lumped-parameter model of the ASM strip that includes an empirical mechanism accounting for cross-bridge attachment and detachment kinetics.

force-generating capacity of the ASMCs be reduced in proportion to the rate of change of ASM strip length. This mechanism is still empirical, but is motivated by the notion that cross-bridge attachment is impaired by relative movement of actin and myosin filaments (Fredberg et al., 1999).

We have incorporated a simplified version of the above model into a model of the contraction of ASM around an airway embedded in the lung parenchyma in order to mimic the marked dependence of airway responsiveness on transpulmonary pressure. Here, it is necessary to take into account not only transpulmonary pressure itself, but also the increased translumenal pressure across the airway wall that arises from local distortion of the parenchyma caused by airway narrowing. The latter can be usefully approximated by a relationship derived by Lai-Fook (1979). Using this relationship, together with the classic hyperbolic description of the force-velocity relationship for ASM, the dynamic response of the airways to intravenous methacholine over a range of inflation pressures can be accurately reproduced by a model consisting of a single airway embedded within linearly elastic parenchyma (Bates and Lauzon, 2007; Cojocaru et al., 2008). Importantly, the adequacy of the model fit (**Figure 11**) relies on the inclusion of a finite stiffness to the airway wall, which provides a significant load opposing smooth muscle shortening in addition to that of the parenchyma itself. This approach to balancing the force of smooth muscle contraction against the opposing mechanical loads can be taken with respect to the individual airways in a model of the lung that includes the branching structure of the airway tree, thereby allowing regional differences in responsiveness to be taken into account (Politi et al., 2010).

Mechanistic models of ASM force-length dynamics

The second approach we have used to model the dynamic force-length behavior of the ASM strip takes the underlying cross-bridge mechanism specifically into account (Wang et al., 2008; Donovan et al., 2010). This approach has the advantage of a specific biophysical basis, but it is based on partial differential equations and is therefore more difficult to implement than the spring-and-dashpot model described above. Again, the dynamic mechanical properties of ASM are obtained experimentally from its transient force-length behavior during cyclic stretching, with peak force and stiffness being initially high but rapidly falling to become at or below isometric values. While some of this behavior can be predicted using an adaptation of Huxley's cross-bridge model of skeletal muscle (Mijailovich et al., 2000) we have found that the non-linear viscoelastic properties of ASM tissue must also be taken into account (Bates and Lauzon, 2005). However, this still does not account for all the dynamic force-length behavior of ASM. In particular, when activated ASM is stretched to mimic deep inhalation, there is a protracted decrease in its subsequent ability to generate force that is not predicted by models based solely on cross-bridges. We have proposed that this loss of ASM force generation results from the disruption of the contractile apparatus (Bates et al., 2009), the actin cytoskeleton, or other proteins comprising ASM and its connections to the airway.

Models of passive parenchymal tissue

The modeling of soft tissue mechanics using empirical constructs such as assemblies of springs and dashpots is well-established (Fung, 1981). Such models do not, however, embody any particular

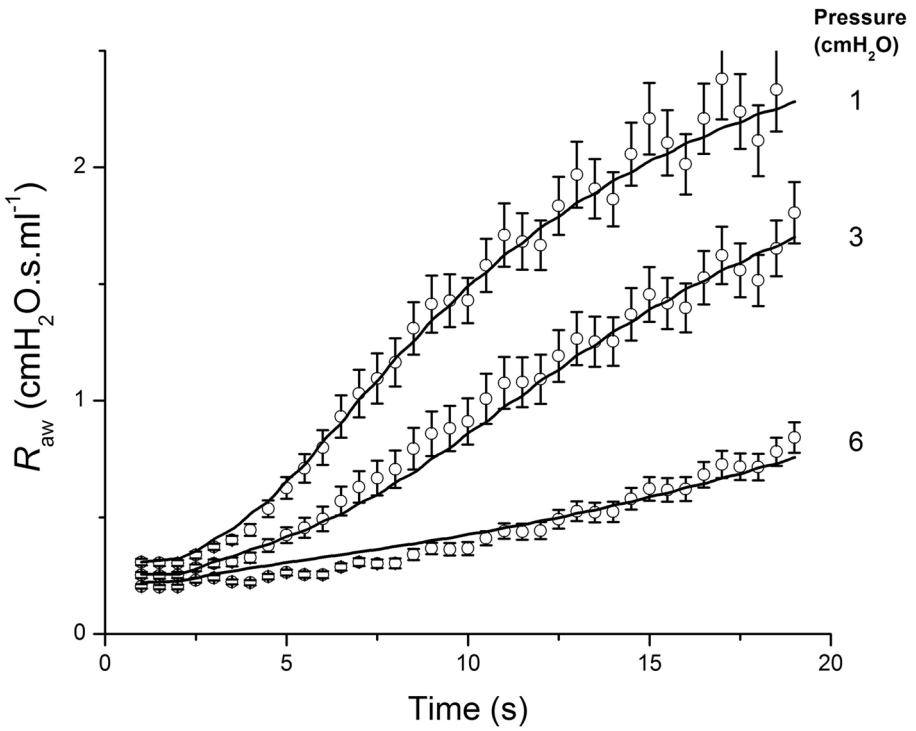

FIGURE 11 | Airway resistance measured in mice (open circles: mean ± SEM) following an intravenous injection of methacholine at time 0, when the lung inflation pressure was set to the three different values indicated at the right of the figure. The solid line shows the fit provided by a computational model of an elastic airway embedded in parenchyma that contracts according to a hyperbolic force-velocity relationship. Adapted from Cojocaru et al. (2008).

underlying biophysical mechanisms for complex tissue rheology; indeed, this remains an active research field that has much attention from both biological and physical scientists (Suki and Bates, 2011). Recently, we have proposed a novel mechanism for the genesis of the rheological behavior that has been observed in lung tissue (Bates et al., 1994). This mechanism is based around the notion that stress is released within stressed tissue through a sequence of micro yield events that occur throughout the tissue (Bates, 2007), as opposed to the smooth relative sliding of multiple components as is implied by spring-and-dashpot models. The appeal of this model is that, although still empirical in terms of specific mechanisms, it exhibits quasi-linear viscoelastic behavior in which the static non-linear stress-strain behavior of the tissue is separable from the dynamic non-linear behavior. Furthermore, the latter is predicted to manifest as a power-law decay of stress with time following a step increase in strain, as is observed experimentally (Bates et al., 1994).

We have recently proposed a specific mechanism for the micro yield events described above that derives from the Huxley-type cross-bridge models of active ASM that are now well-established (Mijailovich et al., 2000). Specifically, we have proposed that the passive stress in ASM tissue is mediated by cross-linking proteins that temporarily bind protein fibers together within the tissue via thermodynamically driven interactions (Donovan et al., 2010). The cross-linkers extend from one filament and bind to attachment sites on an adjacent filament, and can account for many of the passive mechanical behaviors observed in ASMC such as the responses to cyclic stretching and deep inspirations and fluidization upon stretching. The cross-linker model also suggests a compelling unification between the mechanical mechanisms of passive and active tissue; both involve cross-bridges, the only difference being that the binding probabilities in passive tissue are symmetric functions of distance and are driven thermodynamically while the binding probabilities in active tissue are asymmetric and require the energy supplied by ATP (Donovan et al., 2010).

THE ORGAN SCALE

To this point we have described the balance of forces for a single airway. However, the mechanical properties of the lung vary significantly along the airway tree. For example, the amounts of collagen and ASM in the airway wall progressively decrease toward the periphery. In lung disease, it is also common that the properties of the airway wall and the parenchyma are altered, (e.g., airway remodeling associated with AHR). These regional passive (mechanical and structural) and active (force-generating) heterogeneities have a major influence on the overall mechanical behavior of the lungs. For example, when regions of the lung that are connected in parallel become mechanically disparate (so-called "parallel heterogeneities"), the apparent overall resistance of the lung, which normally has an inverse dependence on the frequency of oscillatory flow, decreases with frequency even more precipitously. Conversely, for mechanically disparate regions of the lung

that are connected in series, some of the oscillatory flow can be shunted into the proximal elastic compartment (e.g., the central airways) which causes overall lung elastance to increase dramatically with frequency. Thus, the crucial question is: how does the function of the whole organ arise from the distributed nature of structure and function at the level of the individual airways?

EXPERIMENTAL METHODS

The state-of-the-art method to assess the overall mechanical properties of the lung is based on the measurement of input impedance. A broad-band flow perturbation is applied at the trachea while pressure is measured at the same site. This is achieved with a forced flow oscillation technique. In mice, a computer-controlled mechanical ventilator (Flexivent) can be used to apply and measure a controlled mechanical perturbation to the lungs at frequencies of up to 20 Hz or more (Schuessler and Bates, 1995). Although technically less challenging due to the larger lung volume, the approach is essentially the same for human subjects (Bates et al., 2011). However, flow perturbations in human subjects have to be applied via the mouth rather than the trachea so some shunting of flow into cheeks and pharynx can influence the results related to the lung.

The pressure $[P(t)]$ and flow signals $[V'(t)]$ are related in the frequency domain by the relationship $P(f) = Z(f)V'(f)$, where frequency (f) indicates the Fourier transform of the corresponding function of time (t). The complex function $Z(f)$ is the input impedance and is a model independent function that encapsulates the mechanical properties of the lung. The physiological information inferred from measurements of $Z(f)$ depends on the frequency range of the flow oscillations applied to the lungs (Bates, 2009; Bates et al., 2011). By fitting physiologically motivated mathematical models to $Z(f)$, the model parameters can be determined as measures of the physiological quantities they represent (Bates, 2009).

INCREASED LUNG IMPEDANCE ASSOCIATED WITH AHR

Using these approaches, Hantos et al. (1992) proposed a model known as the constant-phase model. In this model, a uniformly ventilated lung is accessed by single airway that has a Newtonian resistance (R_n). This airway is coupled to a distal alveolar unit composed of viscoelastic tissue that has mechanical impedance with real and imaginary parts that have a constant ratio to each other with frequency (i.e., "constant-phase"). The dissipative component, G, of this tissue impedance reflects the resistive properties of the tissue, while the conservative component, H, is a measure of tissue stiffness.

We have used the constant-phase model in studies of AHR in mice to help identify the underlying mechanisms that are responsible for exaggerated responses to methacholine. For example, in BALB/c mice that were allergically sensitized to challenge with ovalbumin, we found that AHR to a methacholine aerosol resulted from a thickened epithelium and increased airway secretions, but not from increased shortening of ASM (Wagers et al., 2004). By contrast, when mice were treated with intra-tracheal cationic protein, which has the effect of damaging the epithelium, mice exhibited AHR characterized by increased ASM shortening (Bates et al., 2006). When both mechanisms were present simultaneously, mice were extremely hyperresponsive, arguably recapitulating the essential features of a severe asthma attack (Bates et al., 2008). However, when methacholine is administered via the peripheral circulation rather than as an aerosol, the ASM exhibits increased shortening relative to the control. We hypothesize that this exaggerated response to injection reflects an increased leakiness of an inflamed pulmonary endothelium, allowing a greater dose of methacholine to reach the ASM (Cojocaru et al., 2008). These results highlight the important role that inflammation plays in AHR. This role is well known in allergic asthma, which has been shown to lead to alterations in the excitation-contraction coupling behavior of ASM (Bjorck et al., 1992; Mitchell et al., 1994), in addition to the biophysical roles alluded to above.

THE MULTI-SCALE MODEL OF THE LUNG

INTEGRATING ACROSS THE SCALES TO ACHIEVE A FULL LUNG MODEL

To scale up to the level of the lung from a model of a single airway, we embed the conducting airway tree within a parenchymal tissue continuum (**Figure 12** – organ scale). The airway tree geometry is generated using an asymmetrically branching, 3-D tree-generating algorithm that aims to be morphometrically accurate (Tawhai et al., 2004). There are several important reasons for scaling to a full lung topology instead of only studying the behavior of a limited number of airways. First, we can impose physiological boundary conditions that are consistent with the environment and function of the lung. Second, we can exploit medical lung imaging to create subject-specific models in order to test the sensitivity of regional bronchoconstriction to airway geometry. And third, it is only by correctly accounting for the spatial distribution of the airway tree within the lung parenchyma that the appropriate contribution of regional differences in tissue expansion (due to gravity and normal variability in material properties) can be assigned to the balance of forces on the airway wall during its constriction.

To achieve computational feasibility when scaling the model to represent an entire human lung (that contains about 60,000 bronchial airways), we assume each airway is radially symmetric and that changes in airway mechanics during breathing are determined only by changes in radius and not length. At the tissue level, each airway is comprised of an airway wall and a surrounding ASM layer that interacts mechanically with the parenchyma (**Figure 12** – tissue scale). In this way, we calculate the active contractive force generated by the ASM and the opposing passive mechanical forces provided by airway wall stiffness and outward parenchymal tethering. From the resulting balance of all these forces, we can determine the airway radius; this calculation is repeated for each airway with respect to time.

For computational simplification, we initially considered an arbitrary 3-D unit of lung tissue that is representative of the whole lung and its airways (this includes a range of airway sizes). The location of the unit is relatively unimportant for establishing an initial understanding of the system behavior, but it can be scaled to the whole lung and fitted to the anatomically based geometry of the full conducting airway tree – this is a question of computational rather than conceptual complexity. The tissue unit contains all the key elements of the airways embedded in a parenchymal continuum. The alveoli are not represented discretely, but are assumed to operate as a smooth, homogeneous material (as part of

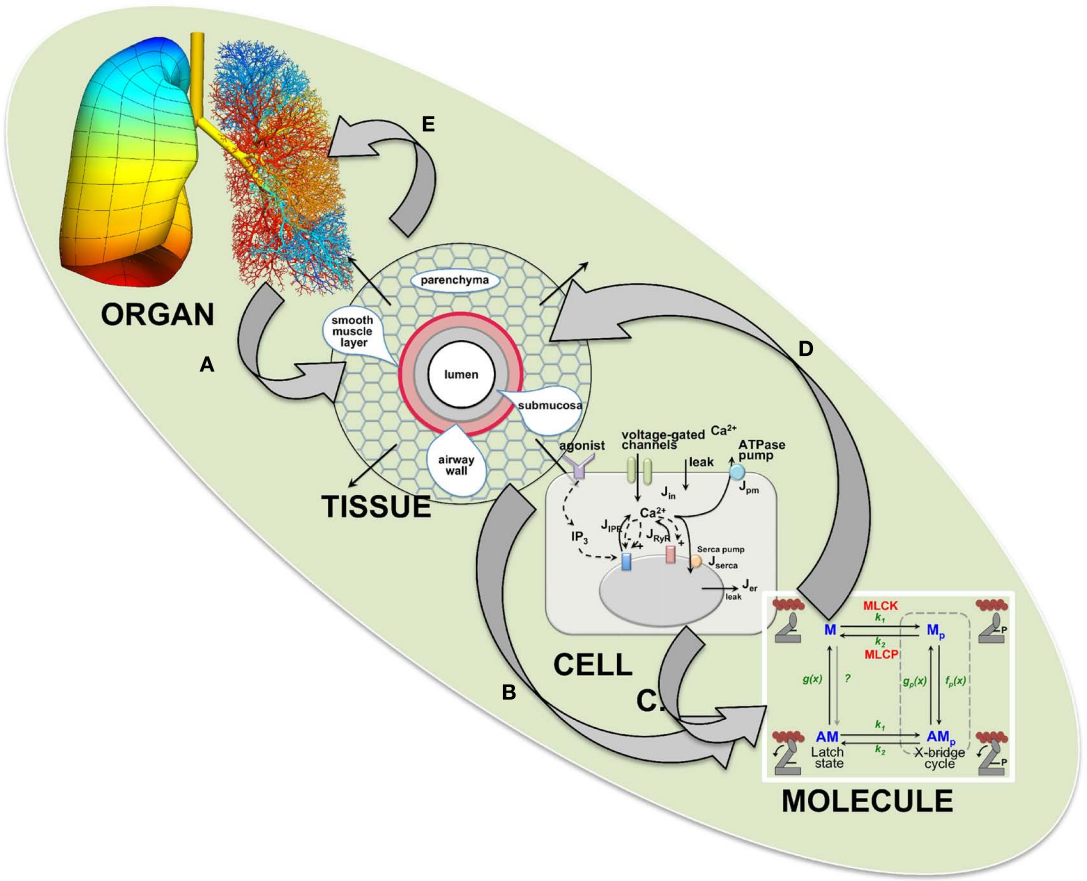

FIGURE 12 | The four spatial scales and their interactions in the multi-scale lung and airway model. The four scales of organ, tissue, cell, and molecule interact as follows: **(A)** anisotropic strain from the parenchymal continuum model (organ scale), linearized to an expression for parenchymal tethering, **(B)** Shortening velocity that is limited by the balance of active and passive forces, **(C)** Coupling of calcium to force generation via activation of MLCK, **(D)** Active and passive force generation from cross-bridges and cross-linkers, **(E)** Airway constriction and redistribution of ventilation.

the organ scale parenchymal continuum) regardless of the airway size or order. The airways included in the unit have eight orders of branching (generated by a space-filling branching algorithm; Tawhai et al., 2004). Again, for simplification and scaling feasibility, each airway segment is assumed to be radially symmetric and longitudinally stiff. Length changes are assumed independent of radial changes.

We use a continuum approach to embed the airway tree within "lung tissue" that is a compressible, hyper-elastic material in 3-D (Tawhai et al., 2006, 2009). This "tissue" is essentially a homogenization of the elastic properties of the parenchyma, air, airways, and blood vessels. We assume material compressibility because the tissue contains air that is free to move into or out of the lung. Stress and strain are related by a strain energy density function, and the response parameters of the tissue are selected such that normal lung inflation pressures give rise to expected expansion volumes for the tissue (Tawhai et al., 2009). By solving the governing equations of finite elasticity (large deformation) mechanics using a finite element method, our model is capable of simulating tissue deformation due to both gravity and the expansion and recoil associated with cyclic changes in pressure on the model surface due to breathing. **Figure 12** (organ level) illustrates a distribution of recoil pressures on a finite element model of the right lung in the upright position under gravitational load. Due to the inaccessibility of the lung tissue to direct measurement and limitation of high resolution imaging of supine or prone postures, data for the validation of the tissue mechanics model are limited (discussed later). However, we have validated the prediction of the distribution of tissue density due to the model's deformation under gravity in the supine posture by comparing this against imaging data of subjects in the same posture (Tawhai et al., 2009). This model provides the boundary pressures and local elastic properties of the parenchyma that are required for interaction with the tissue level model. The airway lumen radii computed at the tissue level depend on their coupling with the organ level model, the non-linear properties of the airway wall, and ASM force generation.

Each airway segment is classified according to its Horsfield order and has three layers with properties that depend on the order: an inner wall layer that contributes passive stiffness, an active ASM layer that generates force, and an outer parenchymal layer, which serves as an interface with the parenchymal continuum that

surrounds the lung segment, and mediates tethering (**Figure 12** – tissue scale). Airway diameter is a function of transmural pressure generated by stress within the ASM layer, external forces acting via the parenchyma, and luminal air pressure (Lambert et al., 1982). To enable coupling across the tissue-organ scales, the model uses two representations of the parenchyma: a local layer and the conditions of the parenchymal continuum at the location of the airway. These layers are connected with the material properties of the local layer determined from a linearization of the anisotropic continuum at the location of the airway (**Figure 12**). That is, the lung tissue will have undergone local volumetric changes that depend on its location in the lung; tissue in the gravitationally dependent regions will generally be under less tension than tissue in the non-dependent regions, and the irregular curvilinear shape of the lung introduces variability in the distribution of strain. Note that this variability occurs independently of any assumptions of heterogeneity in the intrinsic tissue properties.

Airway smooth muscle stress is generated by a cross-bridge model of sliding filaments within the ASMCs (**Figure 12** – molecule scale) under the regulation of Ca^{2+} signaling (**Figure 12** – cell scale). The models defining these processes were addressed in detail earlier and are include in the whole lung model. Thus, overall airway diameter is regulated by ASMC contraction acting against parenchymal tethering which varies with gravity and breathing. We consider breathing that is driven by changes in force or displacement at the (pleural) surface of the model, as opposed to positive pressure ventilation that is driven by increasing the pressure at the mouth. We have therefore assumed that the air pressure remains small relative to the parenchymal and ASMC forces, and so does not make a significant contribution to the transmural pressure. This is in contrast to positive pressure models with fixed tidal volume in which the air pressure can make a significant contribution (Venegas et al., 2005).

Coupling of all of these models and solving simultaneously for each airway with respect to time is a significant computational problem. Not only must all models be solved simultaneously for force balance, but a numerical continuation is also required (Allgower and Georg, 2003) because of the bistability inherent in the Lambert model of the pressure-radius relationship for the small airways (Affonce and Lutchen, 2006). It is this computational complexity (i.e., modulating transitions between the two stable states for each airway) which most limits the computational scope. However, the process is inherently parallel and potentially amenable to parallel computing approaches.

MODEL OUTCOMES

It should be initially emphasized that the major outcome of this multi-scale modeling is the first working, biologically based *in silico* lung and the proof-of concept of the feasibility of this approach (Politi et al., 2010). Although many aspects of lung physiology are not yet included in the current model, their incorporation is now more a function of time and experimentation rather than a major modeling concept.

Reduced airway contraction due to breathing

Our simulations of breathing with contractile agonist exposure demonstrated that, as expected, the extent of airway contraction was a function of pressure changes induced by breathing imposed on pressure changes induced by ASMC stress. Importantly, the organ model also revealed the emergent behavior of increased airway diameter associated with breathing as compared to static conditions. Sensitivity analysis suggested this response was (again, as expected from experimental work) a function of the ASMC cross-bridge kinetics determined by the attachment and detachment rates. However, the model also suggested that the maximal isometric force and the rMLC dephosphorylation rate were also important (Politi et al., 2010).

Although airway radius was increased by breathing, this increase was smaller than that proposed from experimental studies (Politi et al., 2010). This raises interesting questions about the significance of the effect and the conditions under which it is observed. Our model simulates tidal breathing rather than experimental deep inspiration which appears to have a large relaxation effect on ASMCs. More importantly, experimental approaches often examine isolated ASM strips which alter or abolish the organization constraints of the airway and remove the multi-scale interactions. Thus, a small change in airway diameter may be a more realistic response. On the other hand, passive ASMC properties, which exhibit fluidization responses, are not yet included in the multi-scale model and these are expected to enhance the magnitude of airway relaxation.

The importance of spatial heterogeneity at the cellular scale

Simulations at the scale of the individual ASMCs have shown that the amount of force generated by the ASMCs is especially sensitive to the spatial distributions of the Ca^{2+} responses (i.e., the shape of the Ca^{2+} waves; Wang et al., 2008, 2010). Thus, unexpectedly, overall airway contraction can be modified and controlled by relatively minor and subtle changes in Ca^{2+} signaling at the cellular scale.

The interplay between passive and active elements at the molecular scale

At the molecular scale, passive elements such as cross-linkers generate complex dynamic behavior, including fluidization, adaptation, and velocity-dependent force generation (Donovan et al., 2010). Hence, many of the mechanical properties of ASMCs are the emergent result of these molecular scale interactions, and are thus a blend of both active and passive processes. Tissue scale mechanical behavior cannot be understood by considering cross-bridges alone.

Slow transitions between open and closed airway states

A result which has emerged only from the coupling of multiple scales in the model is a slow and steady transition between an open and closed airway state, with the transition being modulated by cross-bridge dynamics (Politi et al., 2010). It s well known that bistability between open and closed states is an inherent characteristic of the Lambert airway wall model (Lambert et al., 1982; Affonce and Lutchen, 2006) but this static model allows for instantaneous transitions between the open and closed state. Only by coupling the tissue scale with the dynamics of the cross-bridge model of ASMCs are these airway transitions modulated into the slow and steady behavior seen experimentally (Latourelle

et al., 2002; Oliver et al., 2007). This result cannot be obtained by considering either scale in isolation.

Heterogeneity and gravitational gradients

Heterogeneity in airway constriction is an important aspect in the manifestation of AHR and changes in ventilation and has been explained by changes in dynamic factors as opposed to structural factors. Some studies suggest the constriction pattern can be altered by deep inspiration while other studies suggest that clustered ventilation occurs preferentially in gravitationally dependent tissue (Venegas et al., 2005; Tgavalekos et al., 2007). The coupling of non-linear sub-scale models in the multi-scale model allows us to consider the degree of heterogeneity attributable to structural factors. A significant gravitational gradient is developed, and airways located in dependent tissue are exposed to parenchymal conditions which differ significantly (Politi et al., 2010). This suggests that some heterogeneity, particularly that found in dependent tissue, may be explained by structural phenomena; however, "resetting" of the constriction pattern still requires a dynamic explanation.

Passive tissue fluidization

One result which has the potential to significantly impact the dynamic equilibration of *in vivo* airways is strain-induced fluidization of passive ASM. When exposed to oscillatory strain, the force exerted by stretched, passive ASM is reduced. This reduction in force is proportional to the strain oscillation amplitude, and persists beyond a 30-s timescale; this occurs in both the experimental and modeling results (Donovan et al., 2010). This has the potential to reduced airway constriction due to tidal breathing and/or deep inspirations (Ijpma and Lauzon, 2012).

FUTURE DIRECTIONS

We emphasize here that the multi-scale model is a work-in-progress. Although there are a huge number of possible additions to the model, we propose a series of questions and modifications we consider to be most important to our current sub-scale models.

AT THE MOLECULAR SCALE

How important is the latch-state in the long-term modulation of force generation?

Can passive elements such as cross-linkers, independent of cross-bridges, reproduce any of the behaviors traditionally thought to be caused by the latch-state? This is question is closely related to the question of how the active and passive elements interact to control force generation in a single ASMC; the latch-state, being in a half-way state between active and passive, will play a central role in these investigations.

What happens if unphosphorylated myosin can bind to actin?

How will this influence AMSC stiffness as a function of time after stimulation or stretching? How should this best be modeled?

Should an ASMC be modeled using a Huxley-style formation for the cross-bridges and cross-linkers, or is a more continuous (a more complicated) approach necessary?

Data indicate that breakage of cross-linkers and cross-bridges after a large stretch plays an important role in decreasing the active force, but such breakage has not yet been included in our models.

AT THE CELLULAR SCALE

How important are stochastic properties of Ca^{2+} release?

We have to develop a stochastic model of Ca^{2+} oscillations and waves and determine whether the measured single channel properties of the IP_3R are sufficient to generate the observed behavior.

How do the patterns of Ca^{2+} waves and oscillations modulate force generation?

Although we know that the shape of the Ca^{2+} oscillation plays a role in modulating force generation, and thus there is a measurable difference between the force generated by Ca^{2+} oscillations and the force generated by Ca^{2+} waves, we need to develop mathematical methods that can take these differences into account without greatly increasing the required computer time for simulations.

How will a human ASMC model differ from a mouse model?

As yet, we have only developed a mouse model. We need to develop a detailed model of Ca^{2+} signaling in human ASMC. This will require additional data from human tissues.

What are the effects of inflammation on force generation?

Inflammatory aspects of the Ca^{2+} signaling pathways and their connection (for example) to Ca^{2+} influx, need to be included in the model so that we can study the effects of inflammation on force generation.

What is the role of mechanotransduction in Ca^{2+} signaling in ASMCs?

Are stretch-activated or compression-activated calcium channels present? If so, how important are they? Can we use a model to predict how important such channels would be expected to be?

AT THE TISSUE SCALE

How important are the interactions between active and passive elements in force generation?

The passive adaptation of stress in lung tissue will change the stress acting on actively cycling cross-bridges and thereby affect their actin-binding probabilities. Conversely, active force generation within the ASM tissue will affect the stress bearing role of the passive connective tissue via the cross-linker mechanism.

How important are regional tissue heterogeneities in airway-parenchymal tethering?

So far, we have modeled the parenchyma as a homogeneous isotropic material, but this is far from reality, particularly in asthma that involves regional tissue remodeling. We have begun to simulate the parenchyma as heterogeneous networks of springs, some of which may be stiffened to represent fibrotic remodeling, in order to determine how parenchymal tethering modulates airway responsiveness.

How important is the complex rheology of lung tissue in determining AHR?

We have also modeled airway-parenchymal interactions under the assumption that the tissue is purely elastic, but we know it is markedly viscoelastic. We would therefore expect that the inflation history of the lung to also affect the extent to which the parenchyma is able to resist ASM contraction.

AT THE ORGAN SCALE

Major assumptions and/or limitations in the model at the organ level are our definition of the material law, neglecting the potential influence of air pressure, weak coupling between the tissue and organ level mechanical models, and limitations on data against which we can validate the model function.

How important is surfactant dynamics to the regional tissue elasticity?

Our continuum model combines the contributions of tissue elasticity and surface forces into a single description of the elastic behavior of the lung parenchyma, parameterized to the expected pressure-volume relationship for an intact lung at only two volumes (functional residual capacity and total lung capacity). This approach has been shown to be satisfactory for simulating static lung deformations in the supine posture in two human subjects, however this single material law parameterization is likely to be inadequate for representing the mechanics of individual subjects, particularly those with chronic lung disease. We have treated the lung tissue mechanics as a sequence of static deformations, but in the dynamic lung the contribution of surfactant dynamics and how this changes with stretch (Majumdar et al., 2011) may be important in the force balances that influence emergent behavior.

Does airway pressure make a significant contribution to the balance of pressures in a breathing lung?

Our initial model has neglected the contribution of air pressure to the balance of forces on the airway. However, other breathing lung models driven by positive pressure inflation with fixed tidal volume have shown that the contribution of the air pressure can be significant (Venegas et al., 2005). We have recently developed a model that couples the tissue deformation model to pressure development and flow distribution in the full airway tree (Swan et al., 2012). This ventilation model is not yet a component of the multi-scale model, however we can control the degree and location of static bronchoconstriction in the model and evaluate the redistribution of alveolar and luminal pressures, which the model predicts are relatively modest. **Figure 12** (organ scale) illustrates a "patchy" flow distribution in this model that results from the interaction of increased airway resistance (**Figure 12E**) and distributed tissue compliance.

How do we introduce bi-directionality in tissue and airway mechanics?

In our multi-scale model, the airways and parenchyma are not tightly coupled. That is, while the balance of forces acting on each airway includes input from the parenchymal mechanics, the deformation of the airway, or its closure does not act in the opposite direction to contribute to the balance of forces in the continuum model. Over long times scales this could exhibit as changes in the surface forces, as we have already described. This limitation in existing models means that we do not yet understand the dependence between local airway constriction and the cyclic pressures of breathing that are transmitted throughout the lung tissue: it is not clear whether airway-parenchymal interdependence will act to further *impede* flow or to *maintain* flow to constricted regions.

Can we define a new protocol for validating multi-scale models?

For single scale models that have been designed to test a hypothesis, the model is considered validated (at least to some degree) if it qualitatively and quantitatively predicts an independent set of experimental data. While the components of these large-scale physiome-type models are data driven, every component is not amenable to independent validation against experiment. This is partly due to limitations on the data that can be acquired for validation, and partly because the intrinsic structural and functional connections across the scales can render meaningless a "validation" that is performed at a single scale or under non-physiological conditions. It is important to emphasize that we have developed the multi-scale model to have a strong biophysical basis: it is grounded in physical conservation laws, and is constrained by physiological and biological parameters. The model's foundation in physical laws means that we only rarely have to revisit our description of the fundamental behavior of its components; rather, our modeling iterations are usually a matter of revisiting the model's parameterization, or our computational methods that allow us to couple different scales. And operating within physiological constraints considerably – and conveniently – reduces the range of parameters that can be chosen for the model. These two considerations provide some assurance that the model does not violate either physical laws or physiological behaviors; this is necessary to demonstrate, but it is not a sufficient "validation." At the level of the integrated model we can say with confidence that the model is predictive of several emergent behaviors that are consistent with pulmonary physiology and asthmatic pathophysiology. This is one important and necessary validation, but it does not guarantee that each model scale is realistic. Understanding uncertainties at each scale in the model is therefore imperative to providing confidence in its integrated predictions.

There are uncertainties in the model parameterization, as well as natural variability in material properties and anatomical geometry in the population. Rather than implementing the multi-scale model in numerous subjects and/or computing a stochastic variant of the model, a more systematic approach can be taken to address uncertainty and to provide confidence in the model predictions. That is, the nature of the model enables us to discover which structural or functional aspects of the integrated system are most critical in the development of bronchoconstriction. Conversely – and just as important – we can identify which model components our predictions are not sensitive to. The most straightforward approach is to perform a sensitivity analysis: simulating whole model bronchoconstriction during systematic variation in the model parameters. This is a standard approach to address uncertainty in model parameterization, but we are not aware of it being used to address the contribution of airway topology to lung function. In terms of addressing population variability, this systematic approach is more useful than repeated analysis of multiple subjects because we can control the nature and extent of the anatomical variation and provide comment on how this contributes to local force balance. For example, a subject-specific definition of the distribution of airway wall thickness and stiffness, and distribution of ASM cell type would be desirable for a truly subject-specific prediction of bronchoconstriction. New insight into how, e.g., localized wall thickening impacts on regional ASM force development could

be gained through pooling simulation data from (many) subject-specific modeling studies, but this introduces similar uncertainty to an experimental study. In contrast, a systematic sensitivity analysis can distinguish between the contribution of airway wall thickening and stiffening (which would not be separable experimentally in the subject-specific analysis), the thresholds at which they become significant, and whether their regional distribution is of importance in the development of localized ventilation defects. Because our model is amenable to implementation in a test unit or in the whole lung, we can test its emergent behavior at the whole organ level against clinical data. Lutchen et al. (Tgavalekos et al., 2003, 2005) have demonstrated the potential of this approach by validating complex global-level model behavior against multiple physiological measurements through their "image-function modeling" approach. In their studies they chose to constrict airways within imaged regions of ventilation defect, and – through trial and error – fit a constriction distribution throughout the conducting airway tree that gave realistic prediction of airway impedance. We now have the opportunity to extend this approach, by *predicting* the spatial distribution of airway closure, and *validating* the integrative behavior of the model against measurements of inert gas washout, oscillation mechanics, and gas exchange.

CONCLUSION

We focus here on developing a whole lung model to address the phenomenon of AHR, a cardinal feature of asthma. This is a challenging task in its entity because the lung is a complex organ within which qualitatively different behaviors manifest over an enormous range of length and time scales. So far, our approach has been to select what we consider to be the most important levels of scale involved in the genesis of AHR, and to model these phenomena at each level of scale separately before combining the resulting sub-models into a global model that links behaviors between scales. We have made considerable progress by establishing the fundamental framework for an *in silico* lung model that based on key experimental observations made at the levels of the molecule, the cell, the tissue, and the whole organ. Furthermore, at each level of scale these representations are, for the most, based on biophysical mechanisms operative at lower levels of scale, allowing us to trace the global response of the lung, following challenge with ASM agonist, to processes operative all the way down to the molecules involved in ASM force generation. In the future, we anticipate that many other aspects of lung physiology will be included and that the model will be developed to the stage where it can be used to gain further insight into the understanding of AHR and potential therapies.

ACKNOWLEDGMENTS

This work was supported by a multi-PI grant from NIH (grant HL 103405) to Anne-Marie Lauzon, Jason H. T. Bates, James Sneyd, Merryn Tawhai, and Michael J. Sanderson.

REFERENCES

Adam, L. P., Haeberle, J. R., and Hathaway, D. R. (1995). Calponin is not phosphorylated during contractions of porcine carotid arteries. *Am. J. Physiol.* 268, C903–C909.

Adelstein, R., and Sellers, J. R. (1996). *Myosin Structure and Function.* Illinois: Academic Press.

Adler, K. B., Krill, J., Alberghini, T. V., and Evans, J. N. (1983). Effect of cytochalasin D on smooth muscle contraction. *Cell Motil.* 3, 545–551.

Affonce, D. A., and Lutchen, K. R. (2006). New perspectives on the mechanical basis for airway hyperreactivity and airway hypersensitivity in asthma. *J. Appl. Physiol.* 101, 1710–1719.

Allgower, E. L., and Georg, K. (2003). Introduction to numerical continuation methods, Vol. xxv. Philadelphia: SIAM, 388.

An, S. S., Bai, T. R., Bates, J. H., Black, J. L., Brown, R. H., Brusasco, V., Chitano, P., Deng, L., Dowell, M., Eidelman, D. H., Fabry, B., Fairbank, N. J., Ford, L. E., Fredberg, J. J., Gerthoffer, W. T., Gilbert, S. H., Gosens, R., Gunst, S. J., Halayko, A. J., Ingram, R. H., Irvin, C. G., James, A. L., Janssen, L. J., King, G. G., Knight, D. A., Lauzon, A. M., Lakser, O. J., Ludwig, M. S., Lutchen, K. R., Maksym, G. N., Martin, J. G., Mauad, T., McParland, B. E., Mijailovich, S. M., Mitchell, H. W., Mitchell, R. W., Mitzner, W., Murphy, T. M., Paré, P. D., Pellegrino, R., Sanderson, M. J., Schellenberg, R. R., Seow, C. Y., Silveira, P. S., Smith, P. G., Solway, J., Stephens, N. L., Sterk, P. J., Stewart, A. G., Tang, D. D., Tepper, R. S., Tran, T., and Wang, L. (2007). Airway smooth muscle dynamics: a common pathway of airway obstruction in asthma. *Eur. Respir. J.* 29, 834–860.

An, S. S., Laudadio, R. E., Lai, J., Rogers, R. A., and Fredberg, J. J. (2002). Stiffness changes in cultured airway smooth muscle cells. *Am. J. Physiol. Cell Physiol.* 283, C792–C801.

Bai, Y., Edelmann, M., and Sanderson, M. J. (2009). The contribution of inositol 1,4,5-trisphosphate and ryanodine receptors to agonist-induced Ca(2+) signaling of airway smooth muscle cells. *Am. J. Physiol. Lung Cell Mol. Physiol.* 297, L347–L361.

Bai, Y., and Sanderson, M. J. (2006a). Airway smooth muscle relaxation results from a reduction in the frequency of Ca^{2+} oscillations induced by a cAMP-mediated inhibition of the IP3 receptor. *Respir. Res.* 7, 34.

Bai, Y., and Sanderson, M. J. (2006b). Modulation of the Ca^{2+} sensitivity of airway smooth muscle cells in murine lung slices. *Am. J. Physiol. Lung Cell Mol. Physiol.* 291, L208–L221.

Bai, Y., and Sanderson, M. J. (2009). The contribution of Ca^{2+} signaling and Ca^{2+} sensitivity to the regulation of airway smooth muscle contraction is different in rats and mice. *Am. J. Physiol. Lung Cell Mol. Physiol.* 296, L947–L958.

Bates, J. H. (2007). A recruitment model of quasi-linear power-law stress adaptation in lung tissue. *Ann. Biomed. Eng.* 35, 1165–1174.

Bates, J. H., Bullimore, S. R., Politi, A. Z., Sneyd, J., Anafi, R. C., and Lauzon, A. M. (2009). Transient oscillatory force-length behavior of activated airway smooth muscle. *Am. J. Physiol.* 297, L362–L372.

Bates, J. H., Cojocaru, A., Haverkamp, H. C., Rinaldi, L. M., and Irvin, C. G. (2008). The synergistic interactions of allergic lung inflammation and intratracheal cationic protein. *Am. J. Respir. Crit. Care Med.* 177, 261–268.

Bates, J. H., Cojocaru, A., and Lundblad, L. K. (2007). Bronchodilatory effect of deep inspiration on the dynamics of bronchoconstriction in mice. *J. Appl. Physiol.* 103, 1696–1705.

Bates, J. H., and Lauzon, A. M. (2005). Modeling the oscillation dynamics of activated airway smooth muscle strips. *Am. J. Physiol. Lung Cell Mol. Physiol.* 289, L849–L855.

Bates, J. H., and Lauzon, A. M. (2007). Parenchymal tethering, airway wall stiffness, and the dynamics of bronchoconstriction. *J. Appl. Physiol.* 102, 1912–1920.

Bates, J. H., Maksym, G. N., Navajas, D., and Suki, B. (1994). Lung tissue rheology and 1/f noise. *Ann. Biomed. Eng.* 22, 674–681.

Bates, J. H., Wagers, S. S., Norton, R. J., Rinaldi, L. M., and Irvin, C. G. (2006). Exaggerated airway narrowing in mice treated with intratracheal cationic protein. *J. Appl. Physiol.* 100, 500–506.

Bates, J. H. T. (2009). *Lung Mechanics. An Inverse Modeling Approach.* Cambridge: Cambridge University Press.

Bates, J. H. T., Irvin, C. G., Farre, R., and Hantos, Z. (2011). *Oscillation Mechanics of the Respiratory System*, Vol. 1, (Bethesda: American Physiological Society), 1233–1272.

Berridge, M. J. (1997). The AM and FM of calcium signalling. *Nature* 386, 759–760.

Berridge, M. J. (2009). Inositol trisphosphate and calcium signalling mechanisms. *Biochim. Biophys. Acta* 1793, 933–940.

Berridge, M. J., Bootman, M. D., and Roderick, H. L. (2003). Calcium signalling: dynamics, homeostasis and remodelling. *Nat. Rev. Mol. Cell Biol.* 4, 517–529.

Betzenhauser, M. J., Wagner, L. E. II, Won, J. H., and Yule, D. I. (2008). Studying isoform-specific inositol 1,4,5-trisphosphate receptor function and regulation. *Methods* 46, 177–182.

Bjorck, T., Gustafsson, L. E., and Dahlen, S. E. (1992). Isolated bronchi from asthmatics are hyperresponsive to adenosine, which apparently acts indirectly by liberation of leukotrienes and histamine. *Am. Rev. Respir. Dis.* 145, 1087–1091.

Bond, M., and Somlyo, A. V. (1982). Dense bodies and actin polarity in vertebrate smooth muscle. *J. Cell Biol.* 95, 403–413.

Bramley, A. M., Thomson, R. J., Roberts, C. R., and Schellenberg, R. R. (1994). Hypothesis: excessive bronchoconstriction in asthma is due to decreased airway elastance. *Eur. Respir. J.* 7, 337–341.

Bullimore, S. R., Siddiqui, S., Donovan, G. M., Martin, J. G., Sneyd, J., Bates, J. H., and Lauzon, A. M. (2011). Could an increase in airway smooth muscle shortening velocity cause airway hyperresponsiveness? *Am. J. Physiol. Lung Cell Mol. Physiol.* 300, L121–L131.

Cahalan, M. D. (2009). STIMulating store-operated $Ca^{(2+)}$ entry. *Nat. Cell Biol.* 11, 669–677.

Chiba, Y., Matsusue, K., and Misawa, M. (2010). RhoA, a possible target for treatment of airway hyperresponsiveness in bronchial asthma. *J. Pharmacol. Sci.* 114, 239–247.

Cojocaru, A., Irvin, C. G., Haverkamp, H. C., and Bates, J. H. (2008). Computational assessment of airway wall stiffness in vivo in allergically inflamed mouse models of asthma. *J. Appl. Physiol.* 104, 1601–1610.

Dai, J. M., Kuo, K. H., Leo, J. M., Pare, P. D., van Breemen, C., and Lee, C. H. (2007). Acetylcholine-induced asynchronous calcium waves in intact human bronchial muscle bundle. *Am. J. Respir. Cell Mol. Biol.* 36, 600–608.

Davis, C., Kannan, M. S., Jones, T. R., and Daniel, E. E. (1982). Control of human airway smooth muscle: in vitro studies. *J. Appl. Physiol.* 53, 1080–1087.

De Young, G. W., and Keizer, J. (1992). A single pool IP3-receptor based model for agonist stimulated Ca^{2+} oscillations. *Proc. Natl. Acad. Sci. U.S.A.* 89, 9895–9899.

Delmotte, P., Ressmeyer, A. R., Bai, Y., and Sanderson, M. J. (2010). Mechanisms of airway smooth muscle relaxation induced by beta2-adrenergic agonists. *Front. Biosci.* 15, 750–764.

Delmotte, P., and Sanderson, M. J. (2010). Effects of formoterol on contraction and Ca^{2+} signaling of mouse airway smooth muscle cells. *Am. J. Respir. Cell Mol. Biol.* 42, 373–381.

Dillon, P. F., Aksoy, M. O., Driska, S. P., and Murphy, R. A. (1981). Myosin phosphorylation and the cross-bridge cycle in arterial smooth muscle. *Science* 211, 495–497.

Donovan, G. M., Bullimore, S. R., Elvin, A. J., Tawhai, M. H., Bates, J. H. T., Lauzon, A. M., and Sneyd, J. (2010). A continuous-binding cross-linker model for passive airway smooth muscle. *Biophys. J.* 99, 3164–3171.

Dupuis, D. E., Guilford, W. H., Wu, J., and Warshaw, D. M. (1997). Actin filament mechanics in the laser trap. *J. Muscle Res. Cell. Motil.* 18, 17–30.

Eddinger, T. J., and Murphy, R. A. (1988). Two smooth muscle myosin heavy chains differ in their light meromyosin fragment. *Biochemistry* 27, 3807–3811.

Falcke, M. (2004). Reading the patterns in living cells – the physics of Ca^{2+} signaling. *Adv. Phys.* 53, 255–440.

Fan, T., Yang, M., Halayko, A., Mohapatra, S. S., and Stephens, N. L. (1997). Airway responsiveness in two inbred strains of mouse disparate in IgE and IL-4 production. *Am. J. Respir. Cell Mol. Biol.* 17, 156–163.

Fay, F. S., Fujiwara, K., Rees, D. D., and Fogarty, K. E. (1983). Distribution of alpha-actinin in single isolated smooth muscle cells. *J. Cell Biol.* 96, 783–795.

Fredberg, J. J., Inouye, D., Miller, B., Nathan, M., Jafari, S., Raboudi, S. H., Butler, J. P., and Shore, S. A. (1997). Airway smooth muscle, tidal stretches, and dynamically determined contractile states. *Am. J. Respir. Crit. Care Med.* 156, 1752–1759.

Fredberg, J. J., Inouye, D. S., Mijailovich, S. M., and Butler, J. P. (1999). Perturbed equilibrium of myosin binding in airway smooth muscle and its implications in bronchospasm. *Am. J. Respir. Crit. Care Med.* 159, 959–967.

Fu, Y., Liu, H. W., Forsythe, S. M., Kogut, P., McConville, J. F., Halayko, A. J., Camoretti-Mercado, B., and Solway, J. (2000). Mutagenesis analysis of human SM22: characterization of actin binding. *J. Appl. Physiol.* 89, 1985–1990.

Fung, Y. C. (1981). *Biomechanics. Mechanical Properties of Living Tissues.* New York: Springer-Verlag.

Gerthoffer, W. T. (1987). Dissociation of myosin phosphorylation and active tension during muscarinic stimulation of tracheal smooth muscle. *J. Pharmacol. Exp. Ther.* 240, 8–15.

Gerthoffer, W. T., Yamboliev, I. A., Shearer, M., Pohl, J., Haynes, R., Dang, S., Sato, K., and Sellers, J. R. (1996). Activation of MAP kinases and phosphorylation of caldesmon in canine colonic smooth muscle. *J. Physiol. (Lond.)* 495, 597–609.

Gimona, M., and Mital, R. (1998). The single CH domain of calponin is neither sufficient nor necessary for F-actin binding. *J. Cell. Sci.* 111, 1813–1821.

Gimona, M., Sparrow, M. P., Strasser, P., Herzog, M., and Small, J. V. (1992). Calponin and SM 22 isoforms in avian and mammalian smooth muscle. Absence of phosphorylation in vivo. *Eur. J. Biochem.* 205, 1067–1075.

Gin, E., Falcke, M., Wagner, L. E. II, Yule, D. I., and Sneyd, J. (2009a). A kinetic model of the inositol trisphosphate receptor based on single-channel data. *Biophys. J.* 96, 4053–4062.

Gin, E., Falcke, M., Wagner, L. E., Yule, D. I., and Sneyd, J. (2009b). Markov chain Monte Carlo fitting of single-channel data from inositol trisphosphate receptors. *J. Theor. Biol.* 257, 460–474.

Gin, E., Wagner, L. E., Yule, D. I., and Sneyd, J. (2009c). Inositol trisphosphate receptor and ion channel models based on single-channel data. *Chaos* 19, 037104.

Gunst, S. J., and Tang, D. D. (2000). The contractile apparatus and mechanical properties of airway smooth muscle. *Eur. Respir. J.* 15, 600–616.

Gunst, S. J., Tang, D. D., and Opazo Saez, A. (2003). Cytoskeletal remodeling of the airway smooth muscle cell: a mechanism for adaptation to mechanical forces in the lung. *Respir. Physiol. Neurobiol.* 137, 151–168.

Gunst, S. J., and Wu, M. F. (2001). Selected contribution: plasticity of airway smooth muscle stiffness and extensibility: role of length-adaptive mechanisms. *J. Appl. Physiol.* 90, 741–749.

Gunst, S. J., and Zhang, W. (2008). Actin cytoskeletal dynamics in smooth muscle: a new paradigm for the regulation of smooth muscle contraction. *Am. J. Physiol. Cell Physiol.* 295, C576–C587.

Hai, C.-M., and Kim, H. R. (2005). An expanded latch-bridge model of protein kinase C-mediated smooth muscle contraction. *J. Appl. Physiol.* 98, 1356–1365.

Hai, C. M., and Murphy, R. A. (1988). Cross-bridge phosphorylation and regulation of latch state in smooth muscle. *Am. J. Physiol.* 254, C99–C106.

Han, M., Dong, L. H., Zheng, B., Shi, J. H., Wen, J. K., and Cheng, Y. (2009). Smooth muscle 22 alpha maintains the differentiated phenotype of vascular smooth muscle cells by inducing filamentous actin bundling. *Life Sci.* 84, 394–401.

Hanks, B. S., and Stephens, N. L. (1981). Mechanics and energetics of lengthening of active airway smooth muscle. *Am. J. Physiol.* 241, C42–C46.

Hantos, Z., Daroczy, B., Suki, B., Nagy, S., and Fredberg, J. J. (1992). Input impedance and peripheral inhomogeneity of dog lungs. *J. Appl. Physiol.* 72, 168–178.

Horiuchi, K. Y., and Chacko, S. (1995). Effect of unphosphorylated smooth muscle myosin on caldesmon-mediated regulation of actin filament velocity. *J. Muscle Res. Cell. Motil.* 16, 11–19.

Horiuti, K., Somlyo, A. V., Goldman, Y. E., and Somlyo, A. P. (1989). Kinetics of contraction initiated by flash photolysis of caged adenosine triphosphate in tonic and phasic smooth muscles. *J. Gen. Physiol.* 94, 769–781.

Huang, Y., Zhang, W., and Gunst, S. J. (2010). Activation of vinculin induced by cholinergic stimulation regulates contraction of tracheal smooth muscle tissue. *J. Biol. Chem.* 286, 3630–3644.

Ijpma, G., and Lauzon, A. M. (2012). The rise of passive airway smooth muscle mechanics. *J. Appl. Physiol.* 112, 335–336.

Ip, K., Sobieszek, A., Solomon, D., Jiao, Y., Pare, P. D., and Seow, C. Y. (2007). Physical integrity of smooth muscle myosin filaments is enhanced by phosphorylation of the regulatory myosin light chain. *Cell. Physiol. Biochem.* 20, 649–658.

Janssen, L. J. (2002). Ionic mechanisms and $Ca^{(2+)}$ regulation in airway smooth muscle contraction: do the data contradict dogma? *Am. J. Physiol. Lung Cell Mol. Physiol.* 282, L1161–L1178.

Janssen, L. J., Tazzeo, T., Zuo, J., Pertens, E., and Keshavjee, S. (2004). KCl evokes contraction of airway smooth muscle via activation of RhoA and Rho-kinase. *Am. J. Physiol. Lung Cell Mol. Physiol.* 287, L852–L858.

Je, H. D., and Sohn, U. D. (2007). SM22alpha is required for agonist-induced regulation of contractility: evidence from SM22alpha knockout mice. *Mol. Cells* 23, 175–181.

Jiang, H., Rao, K., Halayko, A. J., Liu, X., and Stephens, N. L. (1992). Ragweed sensitization-induced increase of myosin light chain kinase content

in canine airway smooth muscle. *Am. J. Respir. Cell Mol. Biol.* 7, 567–573.

Jiang, H., Rao, K., Liu, X., Liu, G., and Stephens, N. L. (1995). Increased Ca^{2+} and myosin phosphorylation, but not calmodulin activity in sensitized airway smooth muscles. *Am. J. Physiol.* 268, L739–L746.

Jude, J. A., Wylam, M. E., Walseth, T. F., and Kannan, M. S. (2008). Calcium signaling in airway smooth muscle. *Proc. Am. Thorac. Soc.* 5, 15–22.

Keizer, J., and Levine, L. (1996). Ryanodine receptor adaptation and Ca^{2+}-induced Ca^{2+} release-dependent Ca^{2+} oscillations. *Biophys. J.* 71, 3477–3487.

Kelley, C. A., Takahashi, M., Yu, J. H., and Adelstein, R. S. (1993). An insert of seven amino acids confers functional differences between smooth muscle myosins from the intestines and vasculature. *J. Biol. Chem.* 268, 12848–12854.

Krishnan, R., Trepat, X., Nguyen, T. T., Lenormand, G., Oliver, M., and Fredberg, J. J. (2008). Airway smooth muscle and bronchospasm: fluctuating, fluidizing, freezing. *Respir. Physiol. Neurobiol.* 163, 17–24.

Kume, H., Hall, I. P., Washabau, R. J., Takagi, K., and Kotlikoff, M. I. (1994). Beta-adrenergic agonists regulate KCa channels in airway smooth muscle by cAMP-dependent and -independent mechanisms. *J. Clin. Invest.* 93, 371–379.

Lai-Fook, S. J. (1979). A continuum mechanics analysis of pulmonary vascular interdependence in isolated dog lobes. *J. Appl. Physiol.* 46, 419–429.

Lambert, R. K., Wilson, T. A., Hyatt, R. E., and Rodarte, J. R. (1982). A Computational model for expiratory flow. *J. Appl. Physiol.* 52, 44–56.

LaPrad, A. S., Szabo, T. L., Suki, B., and Lutchen, K. R. (2010). Tidal stretches do not modulate responsiveness of intact airways in vitro. *J. Appl. Physiol.* 109, 295–304.

Latourelle, J., Fabry, B., and Fredberg, J. J. (2002). Dynamic equilibration of airway smooth muscle contraction during physiological loading. *J. Appl. Physiol.* 92, 771–779.

Lauzon, A. M., Tyska, M. J., Rovner, A. S., Freyzon, Y., Warshaw, D. M., and Trybus, K. M. (1998). A 7-amino-acid insert in the heavy chain nucleotide binding loop alters the kinetics of smooth muscle myosin in the laser trap. *J. Muscle Res. Cell. Motil.* 19, 825–837.

Leguillette, R., Gil, F. R., Zitouni, N., Lajoie-Kadoch, S., Sobieszek, A., and Lauzon, A. M. (2005). (+)Insert smooth muscle myosin heavy chain (SM-B) isoform expression in human tissues. *Am. J. Physiol. Cell Physiol.* 289, C1277–C1285.

Leguillette, R., Laviolette, M., Bergeron, C., Zitouni, N., Kogut, P., Solway, J., Kachmar, L., Hamid, Q., and Lauzon, A. M. (2009). Myosin, transgelin, and myosin light chain kinase: expression and function in asthma. *Am. J. Respir. Crit. Care Med.* 179, 194–204.

Leguillette, R., Zitouni, N. B., Govindaraju, K., Fong, L. M., and Lauzon, A. M. (2008). Affinity for MgADP and force of unbinding from action of myosin purified from tonic and phasic smooth muscle. *Am. J. Physiol. Cell Physiol.* 295, C653–C660.

Ma, X., Cheng, Z., Kong, H., Wang, Y., Unruh, H., Stephens, N. L., and Laviolette, M. (2002). Changes in biophysical and biochemical properties of single bronchial smooth muscle cells from asthmatic subjects. *Am. J. Physiol. Lung Cell Mol. Physiol.* 283, L1181–L1189.

Majumdar, A., Arold, S. P., Bartolak-Suki, E., Parameswaran, H., and Suki, B. (2011). Jamming dynamics of stretch-induced surfactant release by alveolar type II cells. *J. Appl. Physiol.* 112, 824–831.

Maksym, G. N., and Bates, J. H. (1997). A distributed nonlinear model of lung tissue elasticity. *J. Appl. Physiol.* 82, 32–41.

Maksym, G. N., Fredberg, J. J., and Bates, J. H. (1998). Force heterogeneity in a two-dimensional network model of lung tissue elasticity. *J. Appl. Physiol.* 85, 1223–1229.

Malmqvist, U., and Arner, A. (1991). Correlation between isoform composition of the 17 kDa myosin light chain and maximal shortening velocity in smooth muscle. *Pflugers Arch.* 418, 523–530.

Mauss, S., Koch, G., Kreye, V. A., and Aktories, K. (1989). Inhibition of the contraction of the isolated longitudinal muscle of the guinea-pig ileum by botulinum C2 toxin: evidence for a role of G/F-actin transition in smooth muscle contraction. *Naunyn Schmiedebergs Arch. Pharmacol.* 340, 345–351.

Mbikou, P., Fajmut, A., Brumen, M., and Roux, E. (2011). Contribution of Rho kinase to the early phase of the calcium-contraction coupling in airway smooth muscle. *Exp. Physiol.* 96, 240–258.

Merkel, L., Gerthoffer, W. T., and Torphy, T. J. (1990). Dissociation between myosin phosphorylation and shortening velocity in canine trachea. *Am. J. Physiol.* 258, C524–C532.

Mijailovich, S. M., Butler, J. P., and Fredberg, J. J. (2000). Perturbed equilibria of myosin binding in airway smooth muscle: bond-length distributions, mechanics, and ATP metabolism. *Biophys. J.* 79, 2667–2681.

Mitchell, R. W., Ruhlmann, E., Magnussen, H., Leff, A. R., and Rabe, K. F. (1994). Passive sensitization of human bronchi augments smooth muscle shortening velocity and capacity. *Am. J. Physiol.* 267, L218–L222.

Mitchell, R. W., Seow, C. Y., Burdyga, T., Maass-Moreno, R., Pratusevich, V. R., Ragozzino, J., and Ford, L. E. (2001). Relationship between myosin phosphorylation and contractile capability of canine airway smooth muscle. *J. Appl. Physiol.* 90, 2460–2465.

Morgan, K. G., and Gangopadhyay, S. S. (2001). Invited review: cross-bridge regulation by thin filament-associated proteins. *J. Appl. Physiol.* 91, 953–962.

Nagai, R., Kuro-o, M., Babij, P., and Periasamy, M. (1989). Identification of two types of smooth muscle myosin heavy chain isoforms by cDNA cloning and immunoblot analysis. *J. Biol. Chem.* 264, 9734–9737.

Ngai, P. K., and Walsh, M. P. (1984). Inhibition of smooth muscle actin-activated myosin Mg^{2+}-ATPase activity by caldesmon. *J. Biol. Chem.* 259, 13656–13659.

Noble, P. B., Jones, R. L., Needi, E. T., Cairncross, A., Mitchell, H. W., James, A. L., and McFawn, P. K. (2011). Responsiveness of the human airway in vitro during deep inspiration and tidal oscillation. *J. Appl. Physiol.* 110, 1510–1518.

Oliver, M. N., Fabry, B., Marinkovic, A., Mijailovich, S. M., Butler, J. P., and Fredberg, J. J. (2007). Airway hyperresponsiveness, remodeling, and smooth muscle mass: right answer, wrong reason? *Am. J. Respir. Cell Mol. Biol.* 37, 264–272.

Parekh, A. B., and Putney, J. W. Jr. (2005). Store-operated calcium channels. *Physiol. Rev.* 85, 757–810.

Perez, J. F., and Sanderson, M. J. (2005). The frequency of calcium oscillations induced by 5-HT, ACH, and KCl determine the contraction of smooth muscle cells of intrapulmonary bronchioles. *J. Gen. Physiol.* 125, 535–553.

Perez-Zoghbi, J. F., Karner, C., Ito, S., Shepherd, M., Alrashdan, Y., and Sanderson, M. J. (2009). Ion channel regulation of intracellular calcium and airway smooth muscle function. *Pulm. Pharmacol. Ther.* 22, 388–397.

Perez-Zoghbi, J. F., and Sanderson, M. J. (2007). Endothelin-induced contraction of bronchiole and pulmonary arteriole smooth muscle cells is regulated by intracellular Ca^{2+} oscillations and Ca^{2+} sensitization. *Am. J. Physiol. Lung Cell Mol. Physiol.* 293, L1000–L1011.

Perez-Zoghbi, J. F., and Sanderson, M. J. (2010). Nitric oxide induces airway smooth muscle cell relaxation by decreasing the frequency of agonist-induced Ca^{2+} oscillations. *J. Gen. Physiol.* 135, 247–259.

Pohl, J., Winder, S. J., Allen, B. G., Walsh, M. P., Sellers, J. R., and Gerthoffer, W. T. (1997). Phosphorylation of calponin in airway smooth muscle. *Am. J. Physiol.* 272, L115–L123.

Politi, A. Z., Donovan, G. M., Tawhai, M. H., Sanderson, M. J., Lauzon, A. M., Bates, J. H. T., and Sneyd, J. (2010). A multiscale, spatially distributed model of asthmatic airway hyper-responsiveness. *J. Theor. Biol.* 266, 614–624.

Prakash, Y. S., Kannan, M. S., Walseth, T. F., and Sieck, G. C. (1998). Role of cyclic ADP-ribose in the regulation of $[Ca^{2+}]i$ in porcine tracheal smooth muscle. *Am. J. Physiol.* 274, C1653–C1660.

Putney, J. W., and Bird, G. S. (2008). Cytoplasmic calcium oscillations and store-operated calcium influx. *J. Physiol. (Lond.)* 586, 3055–3059.

Rahman, M., Inman, M., Kiss, L., and Janssen, L. J. (2012). Reverse-mode NCX-current in mouse airway smooth muscle: Na(+) and voltage-dependence, contributions to $Ca(2^{+})$ -influx and contraction, and altered expression in a model of allergen-induced hyperresponsiveness. *Acta Physiol. (Oxf.)* 205, 279–291.

Ressmeyer, A. R., Bai, Y., Delmotte, P., Uy, K. F., Thistlethwaite, P., Fraire, A., Sato, O., Ikebe, M., and Sanderson, M. J. (2010). Human airway contraction and formoterol-induced relaxation is determined by Ca^{2+} oscillations and Ca^{2+} sensitivity. *Am. J. Respir. Cell Mol. Biol.* 43, 179–191.

Rovner, A. S., Freyzon, Y., and Trybus, K. M. (1997). An insert in the motor domain determines the functional properties of expressed smooth muscle myosin isoforms. *J. Muscle Res. Cell. Motil.* 18, 103–110.

Sanderson, M. J. (2011). Exploring lung physiology in health and disease

with lung slices. *Pulm. Pharmacol. Ther.* 24, 452–465.

Sanderson, M. J., Delmotte, P., Bai, Y., and Perez-Zogbhi, J. F. (2008). Regulation of airway smooth muscle cell contractility by Ca^{2+} signaling and sensitivity. *Proc. Am. Thorac. Soc.* 5, 23–31.

Sato, K., Hori, M., Ozaki, H., Takano-Ohmuro, H., Tsuchiya, T., Sugi, H., and Karaki, H. (1992). Myosin phosphorylation-independent contraction induced by phorbol ester in vascular smooth muscle. *J. Pharmacol. Exp. Ther.* 261, 497–505.

Schaafsma, D., Gosens, R., Zaagsma, J., Halayko, A. J., and Meurs, H. (2008). Rho kinase inhibitors: a novel therapeutical intervention in asthma? *Eur. J. Pharmacol.* 585, 398–406.

Schuessler, T. F., and Bates, J. H. (1995). A computer-controlled research ventilator for small animals: design and evaluation. *IEEE Trans. Biomed. Eng.* 42, 860–866.

Shaw, L., Ahmed, S., Austin, C., and Taggart, M. J. (2003). Inhibitors of actin filament polymerisation attenuate force but not global intracellular calcium in isolated pressurised resistance arteries. *J. Vasc. Res.* 40, 1–10.

Shirinsky, V. P., Biryukov, K. G., Hettasch, J. M., and Sellers, J. R. (1992). Inhibition of the relative movement of actin and myosin by caldesmon and calponin. *J. Biol. Chem.* 267, 15886–15892.

Siekmann, I., Wagner, L. E. II, Yule, D., Fox, C., Bryant, D., Crampin, E. J., and Sneyd, J. (2011). MCMC estimation of Markov models for ion channels. *Biophys. J.* 100, 1919–1929.

Sneyd, J., Tsaneva-Atanasova, K., Reznikov, V., Bai, Y., Sanderson, M. J., and Yule, D. I. (2006). A method for determining the dependence of calcium oscillations on inositol trisphosphate oscillations. *Proc. Natl. Acad. Sci. U.S.A.* 103, 1675–1680.

Sneyd, J., Tsaneva-Atanasova, K., Yule, D. I., Thompson, J. L., and Shuttleworth, T. J. (2004). Control of calcium oscillations by membrane fluxes. *Proc. Natl. Acad. Sci. U.S.A.* 101, 1392–1396.

Sobieszek, A. (1994). "Smooth muscle myosin. Molecule conformation, filament assembly and association of regulatory enzymes," in *Airways Smooth Muscle: Biochemical Control of Contraction and Relaxation*, eds D. Raeburn and M. A. Giembycz (Bassel: Birkhäuser), 1–29.

Solway, J., Seltzer, J., Samaha, F. F., Kim, S., Alger, L. E., Niu, Q., Morrisey, E. E., Ip, H. S., and Parmacek, M. S. (1995). Structure and expression of a smooth muscle cell-specific gene, SM22 alpha. *J. Biol. Chem.* 270, 13460–13469.

Somlyo, A. P., and Somlyo, A. V. (2003). Ca^{2+} sensitivity of smooth muscle and nonmuscle myosin II: modulated by G proteins, kinases, and myosin phosphatase. *Physiol. Rev.* 83, 1325–1358.

Souhrada, J. F., and Dickey, D. W. (1976). Mechanical activities of trachea as measured in vitro and in vivo. *Respir. Physiol.* 26, 27–40.

Stephens, N. L., and Kroeger, E. A. (1980). *Ultrastructure, Biophysics, and Biochemistry of Airway Smooth Muscle.* New York: Marcel Dekker.

Suki, B., and Bates, J. H. (2011). Lung tissue mechanics as an emergent phenomenon. *J. Appl. Physiol.* 110, 1111–1118.

Swan, A. J., Clark, A. R., and Tawhai, M. H. (2012). A computational model of the topographic distribution of ventilation in healthy human lungs. *J. Theor. Biol.* 300C, 222–231.

Tawhai, M. H., Hunter, P., Tschirren, J., Reinhardt, J., McLennan, G., and Hoffman, E. A. (2004). CT-based geometry analysis and finite element models of the human and ovine bronchial tree. *J. Appl. Physiol.* 97, 2310–2321.

Tawhai, M. H., Nash, M. P., and Hoffman, E. A. (2006). An imaging-based computational approach to model ventilation distribution and soft-tissue deformation in the ovine lung. *Acad. Radiol.* 13, 113–120.

Tawhai, M. H., Nash, M. P., Lin, C. L., and Hoffman, E. A. (2009). Supine and prone differences in regional lung density and pleural pressure gradients in the human lung with constant shape. *J. Appl. Physiol.* 107, 912–920.

Tgavalekos, N. T., Musch, G., Harris, R. S., Vidal Melo, M. F., Winkler, T., Schroeder, T., Callahan, R., Lutchen, K. R., and Venegas, J. G. (2007). Relationship between airway narrowing, patchy ventilation and lung mechanics in asthmatics. *Eur. Respir. J.* 29, 1174–1181.

Tgavalekos, N. T., Tawhai, M., Harris, R. S., Musch, G., Vidal-Melo, M., Venegas, J. G., and Lutchen, K. R. (2005). Identifying airways responsible for heterogeneous ventilation and mechanical dysfunction in asthma: an image functional modeling approach. *J. Appl. Physiol.* 99, 2388–2397.

Tgavalekos, N. T., Venegas, J. G., Suki, B., and Lutchen, K. R. (2003). Relation between structure, function, and imaging in a three-dimensional model of the lung. *Ann. Biomed. Eng.* 31, 363–373.

Trybus, K. M. (1996). "Myosin regulation and assembly," in *Biochemistry of Smooth Muscle Contraction*, ed. M. Barany (Illinois: Academic Press), 37–45.

Venegas, J. G., Winkler, T., Musch, G., Vidal Melo, M. F., Layfield, D., Tgavalekos, N., Fischman, A. J., Callahan, R. J., Bellani, G., and Harris, R. S. (2005). Self-organized patchiness in asthma as a prelude to catastrophic shifts. *Nature* 434, 777–782.

Wagers, S., Lundblad, L. K., Ekman, M., Irvin, C. G., and Bates, J. H. (2004). The allergic mouse model of asthma: normal smooth muscle in an abnormal lung? *J. Appl. Physiol.* 96, 2019–2027.

Wang, C. G., Almirall, J. J., Dolman, C. S., Dandurand, R. J., and Eidelman, D. H. (1997). In vitro bronchial responsiveness in two highly inbred rat strains. *J. Appl. Physiol.* 82, 1445–1452.

Wang, I., Politi, A. Z., Tania, N., Bai, Y., Sanderson, M. J., and Sneyd, J. (2008). A mathematical model of airway and pulmonary arteriole smooth muscle. *Biophys. J.* 94, 2053–2064.

Wang, I. Y., Bai, Y., Sanderson, M. J., and Sneyd, J. (2010). A mathematical analysis of agonist- and KCl-induced $Ca(^{2+})$ oscillations in mouse airway smooth muscle cells. *Biophys. J.* 98, 1170–1181.

Wang, L., Pare, P. D., and Seow, C. Y. (2000). Effects of length oscillation on the subsequent force development in swine tracheal smooth muscle. *J. Appl. Physiol.* 88, 2246–2250.

Warshaw, D. M., Desrosiers, J. M., Work, S. S., and Trybus, K. M. (1990). Smooth muscle myosin cross-bridge interactions modulate actin filament sliding velocity in vitro. *J. Cell Biol.* 111, 453–463.

White, S., Martin, A. F., and Periasamy, M. (1993). Identification of a novel smooth muscle myosin heavy chain cDNA: isoform diversity in the S1 head region. *Am. J. Physiol.* 264, C1252–C1258.

Winder, S. J., Allen, B. G., Clement-Chomienne, O., and Walsh, M. P. (1998). Regulation of smooth muscle actin-myosin interaction and force by calponin. *Acta Physiol. Scand.* 164, 415–426.

Winder, S. J., Allen, B. G., Fraser, E. D., Kang, H. M., Kargacin, G. J., and Walsh, M. P. (1993). Calponin phosphorylation in vitro and in intact muscle. *Biochem. J.* 296, 827–836.

Winder, S. J., and Walsh, M. P. (1990). Smooth muscle calponin. Inhibition of actomyosin MgATPase and regulation by phosphorylation. *J. Biol. Chem.* 265, 10148–10155.

Xu, J. Q., Harder, B. A., Uman, P., and Craig, R. (1996). Myosin filament structure in vertebrate smooth muscle. *J. Cell Biol.* 134, 53–66.

Zhang, J., Herrera, A. M., Pare, P. D., and Seow, C. Y. (2010a). Dense-body aggregates as plastic structures supporting tension in smooth muscle cells. *Am. J. Physiol. Lung Cell Mol. Physiol.* 299, L631–L638.

Zhang, W., Du, L., and Gunst, S. J. (2010b). The effects of the small GTPase RhoA on the muscarinic contraction of airway smooth muscle result from its role in regulating actin polymerization. *Am. J. Physiol. Cell Physiol.* 299, C298–C306.

Zhuge, R., Bao, R., Fogarty, K. E., and Lifshitz, L. M. (2010). Ca^{2+} sparks act as potent regulators of excitation-contraction coupling in airway smooth muscle. *J. Biol. Chem.* 285, 2203–2210.

Conflict of Interest Statement: The authors declare that the research was conducted in the absence of any commercial or financial relationships that could be construed as a potential conflict of interest.

Received: 28 February 2012; accepted: 21 May 2012; published online: 11 June 2012.

Citation: Lauzon A-M, Bates JHT, Donovan G, Tawhai M, Sneyd J and Sanderson MJ (2012) A multi-scale approach to airway hyperresponsiveness: from molecule to organ. Front. Physio. ***3****:191. doi: 10.3389/fphys.2012.00191*

This article was submitted to Frontiers in Computational Physiology and Medicine, a specialty of Frontiers in Physiology.

frontiers in
PHYSIOLOGY

PERSPECTIVE ARTICLE
published: 02 July 2012
doi: 10.3389/fphys.2012.00222

Linking inflammation, cardiorespiratory variability, and neural control in acute inflammation via computational modeling

Thomas E. Dick[1], Yaroslav I. Molkov[2], Gary Nieman[3], Yee-Hsee Hsieh[1], Frank J. Jacono[1,4], John Doyle[5,6], Jeremy D. Scheff[7], Steve E. Calvano[8], Ioannis P. Androulakis[7], Gary An[9] and Yoram Vodovotz[10,11]*

[1] Division of Pulmonary, Critical Care and Sleep Medicine, Department of Medicine, Case Western Reserve University, Cleveland, OH, USA
[2] Department of Mathematical Sciences, Indiana University-Purdue University Indianapolis, Indianapolis, IN, USA
[3] Department of Surgery, Upstate Medical University, Syracuse, NY, USA
[4] Division of Pulmonary, Critical Care and Sleep Medicine, Louis Stokes Cleveland VA Medical Center, Cleveland, OH, USA
[5] Department of Electrical Engineering, California Institute of Technology, Pasadena, CA, USA
[6] Department of Bioengineering, California Institute of Technology, Pasadena, CA, USA
[7] Department of Biomedical Engineering, Rutgers University, Piscataway, NJ, USA
[8] Department of Surgery, University of Medicine and Dentistry of New Jersey-Robert Wood Johnson Medical School, New Brunswick, NJ, USA
[9] Department of Surgery, University of Chicago, Chicago, IL, USA
[10] Department of Surgery, University of Pittsburgh, Pittsburgh, PA, USA
[11] Center for Inflammation and Regenerative Modeling, McGowan Institute for Regenerative Medicine, University of Pittsburgh, Pittsburgh, PA, USA

Edited by:
Raimond L. Winslow, Johns Hopkins University, USA

Reviewed by:
Zhihui Wang, School of Medicine, University of New Mexico, USA
Emilia Entcheva, Stony Brook University, USA

***Correspondence:**
Yoram Vodovotz, Department of Surgery, University of Pittsburgh, W944 Starzl Biomedical Sciences Tower, 200 Lothrop Street, Pittsburgh, PA 15213, USA.
e-mail: vodovotzy@upmc.edu

Acute inflammation leads to organ failure by engaging catastrophic feedback loops in which stressed tissue evokes an inflammatory response and, in turn, inflammation damages tissue. Manifestations of this maladaptive inflammatory response include cardio-respiratory dysfunction that may be reflected in reduced heart rate and ventilatory pattern variabilities. We have developed signal-processing algorithms that quantify non-linear deterministic characteristics of variability in biologic signals. Now, coalescing under the aegis of the NIH Computational Biology Program and the Society for Complexity in Acute Illness, two research teams performed iterative experiments and computational modeling on inflammation and cardio-pulmonary dysfunction in sepsis as well as on neural control of respiration and ventilatory pattern variability. These teams, with additional collaborators, have recently formed a multi-institutional, interdisciplinary consortium, whose goal is to delineate the fundamental interrelationship between the inflammatory response and physiologic variability. Multi-scale mathematical modeling and complementary physiological experiments will provide insight into autonomic neural mechanisms that may modulate the inflammatory response to sepsis and simultaneously reduce heart rate and ventilatory pattern variabilities associated with sepsis. This approach integrates computational models of neural control of breathing and cardio-respiratory coupling with models that combine inflammation, cardiovascular function, and heart rate variability. The resulting integrated model will provide mechanistic explanations for the phenomena of respiratory sinus-arrhythmia and cardio-ventilatory coupling observed under normal conditions, and the loss of these properties during sepsis. This approach holds the potential of modeling cross-scale physiological interactions to improve both basic knowledge and clinical management of acute inflammatory diseases such as sepsis and trauma.

Keywords: mathematical model, inflammation, physiologic variability, heart rate variability, neural control

INTRODUCTION

Sepsis is a significant public health concern, accounting for approximately 10% of total U.S. deaths annually (Angus et al., 2001; Martin et al., 2003; Vincent et al., 2006; Heron et al., 2009). For most infections, despite antibiotic treatments, death occurs primarily through the final common pathway of sepsis-induced multiple organ dysfunction syndrome (MODS).As the population ages, the preponderance of complex medical co-morbidities increases and the impact of sepsis is expected to increase (Anonymous, 1990; Angus et al., 2001; Martin et al., 2003; Weycker et al., 2003).

Despite a large body of scientific literature concerning individual mechanisms involved in sepsis – disordered endothelial activation (Aird, 2003; Ait-Oufella et al., 2010), organ dysfunction due to epithelial cell failure (Protti and Singer, 2006; Balestra et al., 2009), dysregulated inflammation and the associated complement, and coagulation networks (Rittirsch et al., 2008; Levi and van der Poll, 2010) – the primary challenge lies in integrating a large body

of data into a cohesive whole that can guide novel therapies. Effectively modulating, or controlling, the inflammatory response in sepsis, without adverse effects, has proven daunting. Currently no drug is approved by the U.S. Food and Drug Administration (FDA) for MODS. A previously approved drug, recombinant human activated protein C, failed to offer a benefit over standard of care on a FDA-mandated repeat Phase III clinical trial and was removed from the market (Angus, 2011; Mitka, 2011).

We suggest that the rational development of new therapies for sepsis and other acute inflammatory diseases requires characterizing the functional architecture and control points of multi-compartment inflammation. Specifically, we suggest that MODS could be thought of as arising from containment failure (i.e., failure to contain pathogens as well as failure to contain inflammation appropriately) driven by multi-scale "tipping points" that drive a forward feedback loop of inflammation → tissue damage/dysfunction → inflammation (An et al., 2012). We use the term "tipping point" to refer to a functional threshold beyond which a particular compartment/subsystem/system undergoes a phase transition from one range of dynamic behaviors to another. Implicit in this concept is that the internal feedback control processes of a particular compartment/subsystem act to maintain its behavior within a physiological functional range in response to perturbation, but that eventually the persistence and magnitude of the perturbation can lead to control failure. This control feature leads to a shift in the behavioral domain of the subsystem that can in turn lead to disorders in associated compartments/subsystems. This conceptual architecture has the potential to allow: (1) identification of intra-compartment-specific metrics that can be used to determine how close that compartment is to its "tipping point;" (2) identification of inter-compartmental control structures and their associated metrics for efficacy of control; and (3) propose both intra- and inter-compartmental control points that can be targeted for therapeutic intervention.

Studies from our groups, which coalesced under the U.S. National Institute of Health Computational Biology Program[1] and the Society for Complexity in Acute Illness[2], have led us to hypothesize that these multi-scale inflammatory "tipping points," subsequent containment failure, and forward feedback to further propagate inflammation are either centrally controlled by neural circuits, or that neural circuits are activated once inflammation is induced in the brain during sepsis. We hypothesize that the structural/functional (parenchymal) cells of a given organ, once stressed or injured in a process that accompanies the degradation of organ physiology, release damage-associated molecular patterns (DAMPs) that in turn induce resident inflammatory (non-parenchymal) cells to produce classical pro-inflammatory cytokines, which in turn cause further release of DAMPs. Thus, inflammation would be controlled locally until the threshold for local control is exceeded. Co-incident with the peripheral inflammation, the brain "maps" the peripheral inflammation through its own expression of inflammatory cytokines. Brain inflammation would trigger processes aimed at vagal control of inflammation, to maintain physiologic homeostasis (Piepoli et al., 1995; Annane et al., 1999; Korach et al., 2001).This is a key point: parenchymal cells have no way of "sensing" directly that the organ in which they are contained is functioning in- or out-side its optimal operating parameters; only the brain can "sense" this dysfunction. Moreover, parenchymal cells exhibit dysfunction locally through the release of DAMPs that are "sensed" by inflammatory cells. In this scheme, "tipping points" could occur in two distinct locations – a peripheral compartment in which the initial inflammation is manifest, and a "mirrored" representation of that compartment in the neural circuitry and tissue; both of these "tipping points" would affect – and be affected by – the physiologic function of a given organ. The implication of this hypothesis would be that centrally not only is there a loss of control but also dysfunctional control of other compartments, and that this dysfunction arises from the unique role of the brain as sensor and regulator of both organ function and inflammation.

We suggest that the use of data-driven and computational modeling, combined with experiments in relevant animals models of sepsis/MODS, is necessary to define and rationally modulate these "tipping points." Time-domain signal-processing analysis has correlated alterations (primarily decreases) in physiologic variability with morbidity and mortality in critically ill patients (Pomeranz et al., 1985; Anonymous, 1996; Godin et al., 1996; Korach et al., 2001; Barnaby et al., 2002; Pontet et al., 2003; Kleiger et al., 2005; Chen and Kuo, 2007; Ahmad et al., 2009; Fairchild et al., 2009). To unify these diverse observations, we hypothesize that the progress of tissue-level failure toward MODS is accompanied by defined inflammatory networks in different organs, is controlled by inflammation "maps" in the brain, and manifests as decreased physiologic variability (**Figure 1A**).

We have previously suggested a computational modeling approach to the dilemma of MODS that represents a conceptual departure from the current view of acute inflammation and MODS, and offers a new paradigm of MODS pathogenesis based on multifaceted, multi-compartment, and multi-scale inflammatory processes (An et al., 2012). This approach is based on the following premises:

- The recognition – suggested, driven, and linked by computational modeling – that the inflammatory response is both compartmentalized and tightly coupled with physiological processes.
- Given this architecture, that at a certain level of perturbation the reinforcing feedback loop of inflammation → damage/dysfunction → inflammation leads to failure of intra-compartment control. Such failure manifests as the crossing of compartment-specific "tipping points" that have "all-or-none" systemic and physiologic consequences (An et al., 2012).
- That the control structure for integrating inflammation and physiology is based on neural circuits, and thus disordered and failing control of effectively contained inflammation is manifest as altered physiological variability (Namas et al., 2012).
- Finally, that therapies should be targeted based on this structure and dynamic behavior.

Below, we discuss each of these points and suggest how they connect to drive a novel view of MODS.

[1] http://www.nigms.nih.gov/About/Overview/bbcb.htm
[2] www.scai-med.org

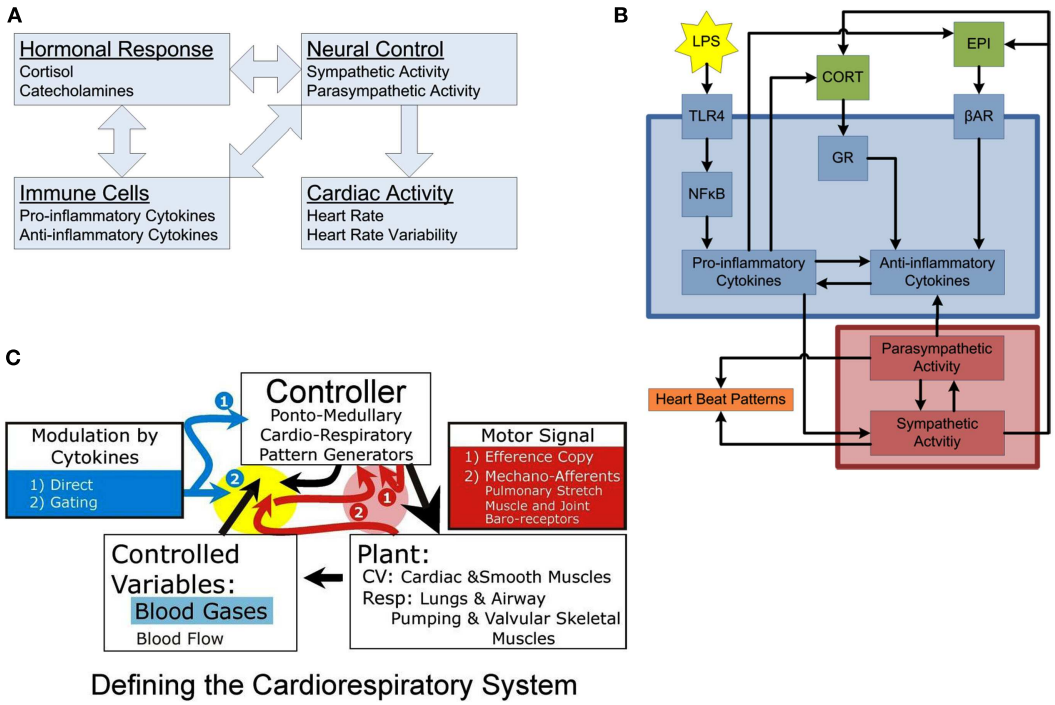

FIGURE 1 | Conceptual models of organization. (A) Inter-compartmental communication. Immune cells provoke activation of hormonal responses and neural controls, systemically manifested in alterations in cardiac activity. The interconnected nature of the regulatory interactions among compartments leads to the emergence of complex systemic responses. **(B)** Intra-compartment dynamics. At the cellular level, LPS is recognized by TLR4, activating the NF-κB signaling, leading to release of pro-inflammatory cytokines which turn on the anti-inflammatory machinery eventually leading to release of hormones driving sympathetic/parasympathetic imbalance altering heart beat patterns leading to diminished heart rate variability. Each individual compartment is characterized by its own, embedded, feedback regulatory structures. **(C)** Basic compartments of a physiologic system: Plant, Controlled Variables, and Controller. The plant is the coupled cardio-respiratory system functioning as single physiologic system serving gas exchange. In this system, blood gases and flow (e.g., vascular resistance, heart rate) are the controlled variables in delivering oxygen to various tissues. The controller generates rhythmic respiratory sympathetic and parasympathetic activities. Pink highlight, these red arrows relate to variables in the red box (1) Efference copy and (2) Mechano-receptors [pulmonary stretch, muscle- and joint-, and baro-receptors] which provide input to controller regarding plant performance on a breath-by-breath or beat-by-beat basis for a given motor signal (large black arrow). Yellow highlight: these arrows relate to how the controlled variables and the mechano-receptor afferents are modulated by the controller and in the presence of cytokines. The yellow and pink highlight areas relate to the nTS and dl pons, respectively. In the dl pons, we hypothesize that mechano-receptor afferent project to the dl pons (via the nTS) and interact with an Efference Copy produced by the controller. Efference Copy is defined as a copy of the motor signal delivered to the plant. Differences between these dl pontine inputs (e.g., the magnitude and strength of the muscle contraction, the lung inflation, etc) are compared to the generated motor signal. Loss of variability in the activity pattern of the plant can result from a failure of the controller to adapt to disparities between sensory input and Efference Copy. In the nTS, cytokines are expressed during ALI and, we expect sepsis, and may affect how afferent input is relayed to the controller. We propose a gating mechanism; one in which afferent inputs are depolarized and neural transmission efficacy is diminished.

THE INFLAMMATORY RESPONSE HAS A COMPARTMENTAL ARCHITECTURE

Inflammation is a prototypical complex system, with multi-feedback interactions among its components, robustness to perturbation coupled with the potential for severe failure at key nodes, and system-level properties difficult to intuit from reductionist analysis (Csete and Doyle, 2002; Vodovotz and An, 2009). We assert that these properties have led to the ineffectiveness of mediator-targeting systemic therapies. As a result, the clinical approach to MODS is focused on providing supportive care of specific points of end-organ failure (e.g., fluids and drugs to alleviate hypotension, ventilation to support failing lungs, etc.). Unfortunately, these interventions often have unintended "ripple effects" that propagate the disordered systemic inflammatory response to the overall detriment of the patient (Ferguson et al., 2005; Sakr et al., 2005; Cotton et al., 2006). Therefore, a disconnect exists between the clinical needs of supporting physiology-level organ function and the need to control the dynamics of the generative cellular-molecular processes that eventually determine that function. This gulf between the cellular-molecular biology of inflammation and organ physiology seen in MODS is precisely the multi-scale barrier that must be traversed to provide a rational basis for potential therapies for MODS.

We view the inflammatory response as compartmentalized both structurally and across multiple scales of organization (Boujoukos et al., 1993; Schein et al., 1996; Molina et al., 2001; Cavaillon and Annane, 2006). Why focus on compartments, when inflammation in sepsis manifests systemically? Despite the attractiveness of purely systemic therapy, the ineffectiveness of such interventions has been demonstrated in multiple studies in animal models of sepsis in which suppressing systemic inflammation resulted in immunosuppression and elevated morbidity and mortality due

to overwhelming infection (Remick et al., 1995; Natanson, 1997). Similarly, an insufficient systemic inflammatory response is associated with elevated morbidity and mortality even in nominally sterile trauma/hemorrhage in both humans and swine (Namas et al., 2009a). Thus, systemic-level interventions may lead to inappropriate damping of a necessary inflammatory response in those tissues and compartments that have not approached their "tipping point." We have begun to refine the dynamic relationships between inflammatory compartments to develop a roadmap toward the translational engineering of therapeutic interventions. We employ progressive use of traditional *in vivo* experiments and platforms, augmented by computational models to explore, explain, and bridge the fundamental aspects of multi-compartment inflammation.

THE ARCHITECTURE OF INFLAMMATION LEADS TO "TIPPING POINTS" OF LOCAL CONTROL FAILURE THAT CAN PROPAGATE TO SYSTEMIC FAILURE

A central aspect of our interdisciplinary approach to deciphering the inflammatory response involves augmenting laboratory studies with computational models that can integrate, suggest, explain, and potentially predict biological knowledge and data. These computational models include both traditional mathematical models based on ordinary differential equations, as well as agent-based and rules-based models (Vodovotz et al., 2004, 2008, 2009; An et al., 2008, 2009; Foteinou et al., 2009b; Vodovotz and An, 2009; Mi et al., 2010; Namas et al., 2012). We initially discerned inflammatory "tipping points" using a multi-scale, multi-tissue, and multi-organ agent-based model (ABM) of the gut-lung axis of systemic inflammation (An, 2008). In this ABM, both organs are represented by spatially distinct, aggregated populations of epithelial and endothelial cells that interact with circulating inflammatory cells and mediators. Simulations of gut ischemia demonstrated a clear gut ischemia threshold, or "tipping point," beyond which MODS could be discerned: first ARDS, then systemic hypoxia, and ultimately *in silico* "death" (An, 2008). Simulation of ventilatory support allowed the system to tolerate more severe gut ischemia, but the "tipping point" persisted. Despite the abstraction of this ABM, it did provide early evidence of the role of compartmental inflammation on the generation of inflammatory "tipping points" and subsequent MODS, and suggested that interventions for sepsis might need to be targeted at the compartment level rather than systemically, or as an adjunct to systemic therapy.

In a similar vein, we created a two-compartment mathematical model of porcine endotoxemia (Nieman et al., 2012), based on an existing mathematical model of mouse endotoxemia (Chow et al., 2005; Lagoa et al., 2006; Prince et al., 2006; Torres et al., 2009). This previous single-compartment mathematical model of inflammation was capable of making qualitative and quantitative predictions with regard to endotoxin-induced inflammation and blood pressure in genetically identical mice (Chow et al., 2005; Lagoa et al., 2006; Prince et al., 2006; Torres et al., 2009). Without compartmentalization, we realized that key meta-behaviors of inflammation were absent, and thus multi-compartment models would be necessary to address the role of inflammatory "tipping." As in the gut/lung ABM described above, this equation-based model was extended to support clinical interventions such as a fluid resuscitation and mechanical ventilation (Nieman et al., 2012). Importantly, this model was capable of addressing individual variations in the porcine inflammatory and pathophysiologic response to endotoxin, including correlation with clinically useful indices such as the Oxygen Index (Nieman et al., 2012).

To define inflammatory networks that drive compartment-specific "tipping points," we have applied Dynamic Network Analysis (DyNA) algorithm (Mi et al., 2011), with a more recently developed Dynamic Bayesian Network (DyBN) algorithm (adapted from; Grzegorczyk and Husmeier, 2011). We utilized the DyBN method to examine the connectivity of inflammation in multiple organs in endotoxemic mice. These studies suggested a high degree of connectivity as well as feed-forward behavior for multiple chemokines, as well as the presence of indirect positive feedback loops, all of which appeared to induce the cytokine IL-6 (a biomarker of dysregulated inflammation in multiple contexts; Abraham and Singer, 2007; Namas et al., 2009b).Based on these studies, we suggest that the compartment-specific response to inflammatory stimuli initially remains within a given compartment, helping to coordinate responses appropriate to a given stimulus. However, when the magnitude or duration of an inflammatory stimulus exceeds certain (likely genetically encoded) thresholds, the response spills over into other compartments. This process could occur via both the systemic and lymphatic circulation, leading to progressive organ dysfunction. We hypothesize that this dysfunction, in turn, further aggravates inflammation.

As noted above, one of our goals is to create multi-scale, multi-compartment computational models of inflammation, and (patho) physiology applicable across species, to transcend the barrier between pre-clinical and clinical studies (An et al., 2010). Accordingly, to facilitate comparison to computational modeling studies calibrated against data in mice (Chow et al., 2005), rats (Daun et al., 2008), and swine (Nieman et al., 2012), we have studied human systemic inflammation in the setting of endotoxemia.Even though species-specific thresholds of responsiveness to microbial product differ, each of the animal models share a common mammalian inflammatory response (Parker and Watkins, 2001). Endotoxemia triggers Toll-like receptor (TLR)4 signaling, and subsequent events propagate through a network of intimately connected and interacting compartments with an end result of either resolution of the inflammatory response, or a self-sustaining imbalance that, we hypothesize, drives inflammatory "tipping points" that manifest in organ dysfunction (**Figure 1B**).

In addition we performed data-driven analyses of high-dimensional leukocyte microarray data taken from human endotoxemia experiments (Calvano et al., 2005), identifying critical transcriptional responses to endotoxemia through a novel clustering approach (Yang et al., 2009). These responses were quantitatively linked through physicochemical modeling, producing an initial computational model of the transcriptional response to human endotoxemia (Foteinou et al., 2009a).

To account for hormonal modulation of the inflammatory response (**Figure 1B**), pharmacokinetic/pharmacodynamic models linking the dynamics of epinephrine, cortisol, and endotoxemia were proposed (Foteinou et al., 2009a). This approach provided fundamental information, so we could explore the impact of hormonal rhythmicity on host fitness, specifically Circadian

rhythms (Coogan and Wyse, 2008). We developed a model to assess the impacts of circadian rhythmicity, as imposed by the suprachiasmatic nucleus (SCN) through circadian hormones, on the response to endotoxemia (Scheff et al., 2010). This model predicted a differential response to identical inflammatory inputs depending on the circadian phase, thus illustrating the importance in circadian rhythmicity in determining the response to endotoxemia.

Hormonal rhythmicity at time scales faster than circadian, called ultradian rhythms, are also increasingly being seen as partaking in important physiological functions (Desvergne and Heligon, 2009; Lightman and Conway-Campbell, 2010). Prominent among the implications of pulsatile secretion of cortisol is the potential role of these ultradian rhythms in regulating the appropriate homeostatic expression of glucocorticoid-responsive genes, including components of the peripheral circadian clock and inflammatory mediators. To investigate the impacts of ultradian rhythms further, we developed a model linking the ultradian production of cortisol in the hypothalamic-pituitary-adrenal (HPA) axis with its downstream effects, which showed the importance of rhythmic hormone patterns in signal transduction (Scheff et al., 2011b). This work was extended to consider the same system in the stress response. One of our key findings was that the homeostatic amplitude of ultradian rhythms was predictive of the responsiveness of the HPA axis to stress (Scheff et al., 2012). This is an example of how characteristics embedded in physiologic rhythms can contain information about the state of a biological system. However, analysis at the level of heart rate variability (HRV) allows for much more significant translational applications through the potential to incorporate hormonal rhythms into single clinically accessible metric.

INFLAMMATION, BREATHING PATTERN VARIABILITY AND BIOLOGICALLY VARIABLE VENTILATION

A central hypothesis underlying our work involves the cross-regulation of inflammation and physiology via neural control mechanisms. The basic elements of a physiologic system defined in engineering terms are the plant, controller, and sensor (**Figure 1C**). Generally, the plant is the end organ whose function is regulated to maintain controlled variables; the controller, a neural network modulating the plant; and the sensor, specialized cells monitoring levels of the controlled variables. Here (**Figure 1C**), the plant is the cardio-pulmonary system; the controller, the coupled cardio-respiratory central pattern generator (CPG; for details see; Baekey et al., 2010; Molkov et al., 2010, 2011); and the controlled variables, blood gases, and flow for gas exchange.

Fundamental questions, which we are beginning to address, are: (1) How does cardio-respiratory control system "sense" peripheral dysfunction? (2) How does central expression of cytokines affect the control of a peripheral compartment and neural function itself? and (3) How are compartments organized in the brainstem? To sense dysfunction, we propose an interaction between efference copy and sensory input [**Figure 1C** (1 and 2, in red highlight)]. Efference copy is the expected effect, specifically, a "copy" of the motor output produced by the controller. This is compared to the sensory input, which is the effective output. Central expression of cytokines could modulate the controller within this functional loop (**Figure 1C**2, in yellow highlight) and by directly affecting the function of neurons in the CPG (**Figure 1C**1, no highlight). Further, the time-dependent properties of the expression of cytokines in this reduced control circuit are unknown; for instance, do cytokines become expressed sequentially or co-incidentally in different control nuclei? Further, cytokines definitely elicit "sickness" behavior, which will affect the output of automatic nuclei. Finally, cytokines evoke various second-messenger systems from glia and neurons and many of these second-messengers, including nitric oxide, act extracellularly. Control of other compartments may be elicited through spread of cytokines themselves, or of their second-order messengers.

As a dynamic controller, the respiratory CPG is capable of producing a wide repertoire of "output patterns" and a particular output pattern depends on peripheral and central inputs but also on prior experience and local internal milieu (Rybak et al., 2008). Without peripheral or central inputs, the respiratory CPG provides an output that is rhythmic and regular, i.e., characterized by low deterministic variability (Dhingra et al., 2011). Under normal conditions the intact cardio-respiratory system exhibits chaotic dynamics with deterministic variability (Sammon and Bruce, 1991). We theorize that alterations in the non-linear properties of cardio-respiratory variability associated with disease depend, at least partially, on cytokine-modulation of sensory feedback, and ponto-sensory interactions. In the presence of elevated levels of cytokines, the efficacy of sensory input is reduced, minimizing the non-linear deterministic properties of pattern variability (**Figure 1C**; Dhingra et al., 2011). Early models of breathing pattern during heart failure have demonstrated that increased gain and delayed feedback lead to sensor over-response and results in a waxing and waning pattern (Cherniack et al., 1966; Cherniack and Longobardo, 2006). In addition, pressure support ventilation (which effectively facilitates a gain of lung stretch receptors feedback) helps to maintain normal breathing pattern variability, which reduces when a patient is separated from ventilation (Wysocki et al., 2006).

We speculate that changes in deterministic variability in the cardio-respiratory patterns associated with systemic inflammation (**Figure 2B3**) are related to expression of cytokines in the nucleus *tractus solitarius* (nTS); which result from vagal input and which "maps" peripheral inflammation. We have preliminary evidence that acute lung injury results in specific expression of IL-1β in the commissural subnucleus in the nTS (Jacono et al., 2011; **Figure 2A**, serology in lower panel and **Figure 2C**, red fluorescent staining). This expression occurred in the absence of significant increases IL-1β, TNFα, and IL-6 in the plasma (Jacono et al., 2011). We have focused on the vagal afferent limb in controlling biologic pattern variability but this neural feedback lies in the context of its own control loop. The respiratory CPG, a major determinant of vagal efferent activity, modulates variability but may also regulate the expression of cytokines. Vagal efferent activity decreases peripheral levels of cytokines, acting as a negative feedback modulating the magnitude of the inflammatory response (Andersson and Tracey, 2012). However, the brainstem connectivity between the CPG network and the immunologic loop is unknown. In particular, it is unknown if the network that mediates biologic variability also modulates the magnitude of the inflammatory response. In

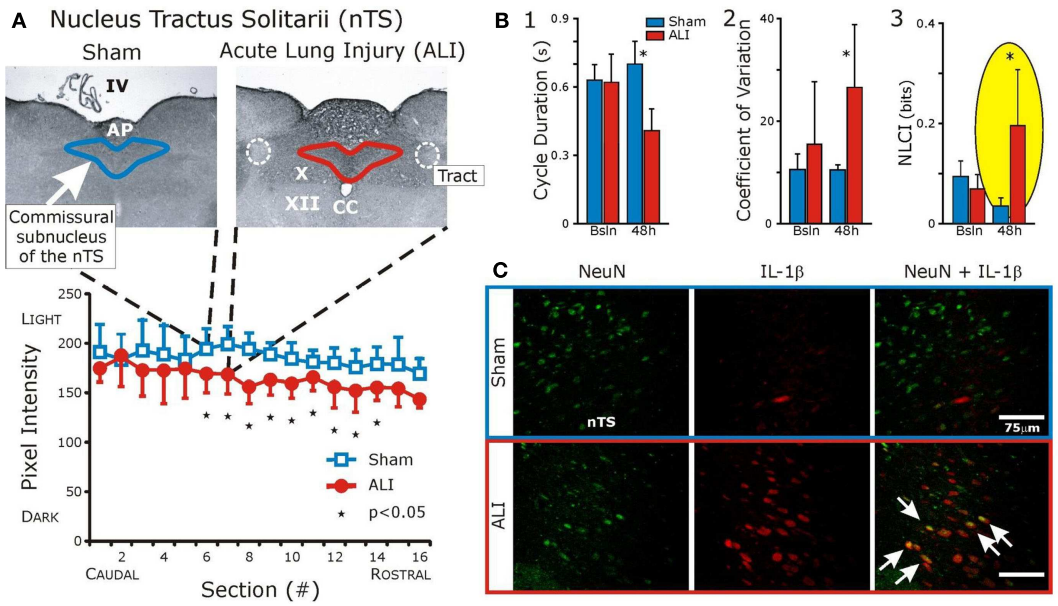

FIGURE 2 | Interleukin-1β expression is increased in the commissural subnucleus of the nTS in the setting of acute lung injury (ALI) and altered ventilatory pattern. Bleomycin (three units) was instilled intratracheally causing ALI. Ventilatory pattern was measured and tissues were obtained 48 h later. **(A)** Histologic examination identified a significant increase in IL-1β in the commissural subnucleus of the nucleus *Tractus Solitarius* (nTS) in the dorsomedial medulla (shown). Abbreviations: AP, area postrema; CC, central canal; IV, fourth ventricle; X, dorsal motor nucleus of the vagus; XII, hypoglossal motor nucleus; white dashed line, solitary tract. **(B)** Compares ventilatory patterns of sham (blue) and ALI (red) rats at baseline and 48 h. After ALI: (1) Increased respiratory rate (significant decrease in cycle duration, TTOT), (2) Increased coefficient of variation (CV) of respiratory cycle length (CV of TTOT), and (3) Increased deterministic non-linear variability of the ventilatory pattern, as measured by a non-linear complexity index (NLCI, yellow highlight) computed using surrogate data analysis. **(C)** Fluorescent staining: IL-1β co-localized with nTS neurons (white arrows) identified using antibodies against the neuronal specific nuclear protein NeuN. (Adapted from; Wysocki et al., 2006).

defining this network, we speculate that this loop is affected by central expression of cytokines and, thus, has a role in determining the "tipping point" and systemic dysfunction.

Further, improved understanding of the feedback loops involved in the neural control of inflammation will serve to identify novel targets for modulation of the immune response. For example, imposing rhythmic vagal afferent activity by mechanical ventilation may impact the neural and peripheral immune responses. Thus, one potential benefit of biologically variable ventilation is that it imposes a sensory input related to lung inflation that artificially replicates a variable "normal" signal. This may predispose the CPG to produce "normal" pattern that, perhaps, reduces inflammation. If biologic variability of rhythmic patterns decreases the cytokine concentration as compared to the "autonomous regime" then cardio-respiratory coupling and the variability in the bursting pattern of its activity, may prevent MODS and the inflammatory response from reaching its "tipping point."

IMPAIRED PHYSIOLOGY MANIFESTS AS ALTERED AND OFTEN REDUCED PHYSIOLOGIC VARIABILITY

Variability is a property of the biological systems we have studied, that in and of itself is neither good nor bad, but may reflect a "state" of the system that is adaptable and responsive (within boundaries). HRV is diminished in various inflammatory conditions, including experimental human endotoxemia. Recent studies have investigated HRV as a predictive metric in trauma patients (Morris et al., 2007; Cancio et al., 2008; Riordan et al., 2009; Batchinsky et al., 2010) and sepsis (Ahmad et al., 2009; Moorman et al., 2011). Although correlations of HRV with disease state have produced many important insights, the physiological processes linking inflammation with systemic changes are not well defined, motivating the development of mathematical models linking inflammation, and HRV (Buchman, 2009; Foteinou et al., 2010; Scheff et al., 2011a; Namas et al., 2012). We linked multi-level dynamics of the molecular and cellular patterns occurring in human endotoxemia to cardiac function through a model that outputs discrete heart beats as modulated by physiological rhythms, which can then be post-processed to assess HR and HRV (Scheff et al., 2011a). Action potentials at the sinoatrial (SA) node of the heart initiate the contraction of cardiac tissue, producing rhythmic heart beats. Sympathetic and parasympathetic nerves converging at the SA node result in fluctuating levels of autonomic neurotransmitters which modulate the firing pattern of SA node cells. Variability in the firing of the SA node, and thus variability in the beating of the heart, is regulated by autonomic output. Thus, we proposed a model of autonomic activity at the SA node, influenced by the inflammatory mediators in our model of human endotoxemia, to modulate the HRV (Scheff et al., 2011a). Our discrete modeling of heart beats allowed the calculation of HRV metrics used in the clinical setting. The diversity of data supporting this modeling work at transcriptional, hormonal, and systemic

levels was matched by appropriate computational modeling techniques to allow for the assessment of autonomic dysfunction, manifested in altered HR rhythmicity, in human endotoxemia. We have demonstrated that stress induces alterations in the homeostatic dynamics of the feedback structures such that some level of perturbation permanently disrupts these regulatory structures; i.e., "tipping points." Progressive crossing of these "tipping points" would lead to cascading systems failure and the clinical syndrome of MODS/sepsis.

CONCLUSIONS, FUTURE DEVELOPMENTS, AND PERSPECTIVES

We suggest that our evolving mathematical models will help identify and predict potential bioactive interventions, and validate those predictions in further experiments in rodents, swine, and, ultimately, in clinical trials based on our *in silico* studies. The multi-compartment/multi-scale computational models could be used to test interventions targeted at effector organs, such as ventilation strategies aimed at manipulating the lung. Importantly, despite their limitations of abstraction of relevant biological interactions, mechanistic mathematical models have the potential to allow us to bridge the gap from rodent studies to large-animal studies and eventually to clinical studies (Vodovotz et al., 2006; An et al., 2010). Trans-species and trans-compartment mechanistic and data-driven modeling will also allow us to integrate those inflammatory networks that help drive "tipping point" behavior.

ACKNOWLEDGMENTS

The authors acknowledge the support of NIH/NHLBI Exploratory Program in Systems Biology. Many of the researchers who are co-authors on this review chapter were supported by this program and specific awards include R33HL087377 (Thomas E. Dick, Yaroslav I. Molkov, Yee-Hsee Hsieh, Frank J. Jacono.) and R33-HL-089082 (Gary Nieman, Yoram Vodovotz). In addition, the authors would like to acknowledge additional grant support from NIH (R01GM67240, P50GM53789, R01HL080926, R01HL76157, UO1DK072146, RO1GM082974, RO1GM34695); National Science Foundation grant 0830-370-V601; Award No. I01BX000873 from the Biomedical Laboratory Research and Development Service of the VA Office of Research and Development; a Shared University Research Award from IBM, Inc.; and grants from the Commonwealth of Pennsylvania, the Pittsburgh Lifesciences Greenhouse, and the Pittsburgh Tissue Engineering Initiative/Department of Defense. The authors would like to acknowledge Dr. IlyaRybak (Drexel University, Department of Neurobiology and Anatomy) for helpful discussion and seminar contributions to the modeling of neural control of breathing patterns.

REFERENCES

Abraham, E., and Singer, M. (2007). Mechanisms of sepsis-induced organ dysfunction. *Crit. Care Med.* 35, 2408.

Ahmad, S., Ramsay, T., Huebsch, L., Flanagan, S., McDiarmid, S., Batkin, I., McIntyre, L., Sundaresan, S. R., Maziak, D. E., Shamji, F. M., Hebert, P., Fergusson, D., Tinmouth, A., and Seely, A. J. (2009). Continuous multi-parameter heart rate variability analysis heralds onset of sepsis in adults. *PLoS ONE* 4, e6642. doi:10.1371/journal.pone.0006642

Aird, W. C. (2003). The role of the endothelium in severe sepsis and multiple organ dysfunction syndrome. *Blood* 101, 3765.

Ait-Oufella, H., Maury, E., Lehoux, S., Guidet, B., and Offenstadt, G. (2010). The endothelium: physiological functions and role in microcirculatory failure during severe sepsis. *Intensive Care Med.* 36, 1286.

An, G. (2008). Introduction of a agent based multi-scale modular architecture for dynamic knowledge representation of acute inflammation. *Theor. Biol. Med. Model.* 5. doi: 10.1186/1742-4682-5-11

An, G., Bartels, J., and Vodovotz, Y. (2010). In silico augmentation of the drug development pipeline: examples from the study of acute inflammation. *Drug Dev. Res.* 72, 1.

An, G., Faeder, J., and Vodovotz, Y. (2008). Translational systems biology: introduction of an engineering approach to the pathophysiology of the burn patient. *J. Burn Care Res.* 29, 277.

An, G., Mi, Q., Dutta-Moscato, J., Solovyev, A., and Vodovotz, Y. (2009). Agent-based models in translational systems biology. *Wiley Interdiscip. Rev. Syst. Biol. Med.* 1, 159.

An, G., Nieman, G., and Vodovotz, Y. (2012). Computational and systems biology in trauma and sepsis: current state and future perspectives. *Int. J. Burns Trauma* 2, 1.

Andersson, U., and Tracey, K. J. (2012). Reflex principles of immunological homeostasis. *Annu. Rev. Immunol.* 30, 313–335.

Angus, D. C. (2011). The search for effective therapy for sepsis: back to the drawing board? *JAMA* 306, 2614.

Angus, D. C., Linde-Zwirble, W. T., Lidicker, J., Clermont, G., Carcillo, J., and Pinsky, M. R. (2001). Epidemiology of severe sepsis in the United States: analysis of incidence, outcome, and associated costs of care. *Crit. Care Med.* 29, 1303.

Annane, D., Trabold, F., Sharshar, T., Jarrin, I., Blanc, A. S., Raphael, J. C., and Gajdos, P. (1999). Inappropriate sympathetic activation at onset of septic shock: a spectral analysis approach. *Am. J. Respir. Crit Care Med.* 160, 458.

Anonymous. (1990). Increase in National Hospital Discharge Survey rates for septicemia – United States, 1979–1987. *MMWR Morb. Mortal. Wkly. Rep.* 39, 31.

Anonymous. (1996). Heart rate variability. Standards of measurement, physiological interpretation, and clinical use. Task Force of the European Society of Cardiology, and the North American Society of Pacing, and Electrophysiology. *Eur. Heart J.* 17, 354.

Baekey, D. M., Molkov, Y. I., Paton, J. F., Rybak, I. A., and Dick, T. E. (2010). Effect of baroreceptor stimulation on the respiratory pattern: insights into respiratory-sympathetic interactions. *Respir. Physiol. Neurobiol.* 174, 135.

Balestra, G. M., Legrand, M., and Ince, C. (2009). Microcirculation and mitochondria in sepsis: getting out of breath. *Curr. Opin. Anaesthesiol.* 22, 184.

Barnaby, D., Ferrick, K., Kaplan, D. T., Shah, S., Bijur, P., and Gallagher, E. J. (2002). Heart rate variability in emergency department patients with sepsis. *Acad. Emerg. Med.* 9, 661.

Batchinsky, A. I., Skinner, J. E., Necsoiu, C., Jordan, B. S., Weiss, D., and Cancio, L. C. (2010). New measures of heart-rate complexity: effect of chest trauma and hemorrhage. *J. Trauma* 68, 1178.

Boujoukos, A. J., Martich, G. D., Supinski, E., and Suffredini, A. F. (1993). Compartmentalization of the acute cytokine response in humans after intravenous endotoxin administration. *J. Appl. Physiol.* 74, 3027.

Buchman, T. G. (2009). The digital patient: predicting physiologic dynamics with mathematical models. *Crit. Care Med.* 37, 1167.

Calvano, S. E., Xiao, W., Richards, D. R., Felciano, R. M., Baker, H. V., Cho, R. J., Chen, R. O., Brownstein, B. H., Cobb, J. P., Tschoeke, S. K., Miller-Graziano, C., Moldawer, L. L., Mindrinos, M. N., Davis, R. W., Tompkins, R. G., Lowry, S. F., and Large Scale Collab. Res. Program. (2005). A network-based analysis of systemic inflammation in humans. *Nature* 437, 1032.

Cancio, L. C., Batchinsky, A. I., Salinas, J., Kuusela, T., Convertino, V. A., Wade, C. E., and Holcomb, J. B. (2008). Heart-rate complexity for prediction of prehospital lifesaving interventions in trauma patients. *J. Trauma* 65, 813.

Cavaillon, J. M., and Annane, D. (2006). Compartmentalization of the inflammatory response in sepsis and SIRS. *J. Endotoxin Res.* 12, 151.

Chen, W. L., and Kuo, C. D. (2007). Characteristics of heart rate variability can predict impending septic shock in emergency department patients with sepsis. *Acad. Emerg. Med.* 14, 392.

Cherniack, N. S., and Longobardo, G. S. (2006). Mathematical models of periodic breathing and their usefulness in understanding cardiovascular and respiratory disorders. *Exp. Physiol.* 91, 295.

Cherniack, N. S., Longobardo, G. S., Levine, O. R., Mellins, R., and Fishman, A. P. (1966). Periodic breathing in dogs. *J. Appl. Physiol.* 21, 1847.

Chow, C. C., Clermont, G., Kumar, R., Lagoa, C., Tawadrous, Z., Gallo, D., Betten, B., Bartels, J., Constantine, G., Fink, M. P., Billiar, T. R., and Vodovotz, Y. (2005). The acute inflammatory response in diverse shock states. *Shock* 24, 74.

Coogan, A. N., and Wyse, C. A. (2008). Neuroimmunology of the circadian clock. *Brain Res.* 1232, 104.

Cotton, B. A., Guy, J. S., Morris, J. A. Jr., and Abumrad, N. N. (2006). The cellular, metabolic, and systemic consequences of aggressive fluid resuscitation strategies. *Shock* 26, 115.

Csete, M. E., and Doyle, J. C. (2002). Reverse engineering of biological complexity. *Science* 295, 1664.

Daun, S., Rubin, J., Vodovotz, Y., Roy, A., Parker, R., and Clermont, G. (2008). An ensemble of models of the acute inflammatory response to bacterial lipopolysaccharide in rats: results from parameter space reduction. *J. Theor. Biol.* 253, 843.

Desvergne, B., and Heligon, C. (2009). Steroid hormone pulsing drives cyclic gene expression. *Nat. Cell Biol.* 11, 1051.

Dhingra, R. R., Jacono, F. J., Fishman, M., Loparo, K. A., Rybak, I. A., and Dick, T. E. (2011). Vagal-dependent nonlinear variability in the respiratory pattern of anesthetized, spontaneously breathing rats. *J. Appl. Physiol.* 111, 272.

Fairchild, K. D., Saucerman, J. J., Raynor, L. L., Sivak, J. A., Xiao, Y., Lake, D. E., and Moorman, J. R. (2009). Endotoxin depresses heart rate variability in mice: cytokine and steroid effects. *Am. J. Physiol. Regul. Integr. Comp. Physiol.* 297, R1019.

Ferguson, N. D., Frutos-Vivar, F., Esteban, A., Anzueto, A., Alia, I., Brower, R. G., Stewart, T. E., Apezteguia, C., Gonzalez, M., Soto, L., Abroug, F., and Brochard, L. (2005). Airway pressures, tidal volumes, and mortality in patients with acute respiratory distress syndrome. *Crit. Care Med.* 33, 21.

Foteinou, P. T., Calvano, S. E., Lowry, S. F., and Androulakis, I. P. (2009a). Modeling endotoxin-induced systemic inflammation using an indirect response approach. *Math. Biosci.* 217, 27.

Foteinou, P., Calvano, S., Lowry, S., and Androulakis, I. P. (2009b). Translational potential of systems-based models of inflammation. *Clinical and Translational Science* 2, 85–89.

Foteinou, P. T., Calvano, S. E., Lowry, S. F., and Androulakis, I. P. (2010). Multiscale model for the assessment of autonomic dysfunction in human endotoxemia. *Physiol. Genomics* 42, 5.

Godin, P. J., Fleisher, L. A., Eidsath, A., Vandivier, R. W., Preas, H. L., Banks, S. M., Buchman, T. G., and Suffredini, A. F. (1996). Experimental human endotoxemia increases cardiac regularity: results from a prospective, randomized, crossover trial. *Crit. Care Med.* 24, 1117.

Grzegorczyk, M., and Husmeier, D. (2011). Improvements in the reconstruction of time-varying gene regulatory networks: dynamic programming and regularization by information sharing among genes. *Bioinformatics* 27, 693–699.

Heron, M., Hoyert, D. L., Murphy, S. L., Xu, J., Kochanek, K. D., and Tejada-Vera, B. (2009). Deaths: final data for 2006. *Natl. Vital Stat. Rep.* 57, 1.

Jacono, F. J., Mayer, C. A., Hsieh, Y. H., Wilson, C. G., and Dick, T. E. (2011). Lung and brainstem cytokine levels are associated with breathing pattern changes in a rodent model of acute lung injury. *Respir. Physiol. Neurobiol.* 178, 429.

Kleiger, R. E., Stein, P. K., and Bigger, J. T. Jr. (2005). Heart rate variability: measurement and clinical utility. *Ann. Noninvasive Electrocardiol.* 10, 88.

Korach, M., Sharshar, T., Jarrin, I., Fouillot, J. P., Raphael, J. C., Gajdos, P., and Annane, D. (2001). Cardiac variability in critically ill adults: influence of sepsis. *Crit. Care Med.* 29, 1380.

Lagoa, C. E., Bartels, J., Baratt, A., Tseng, G., Clermont, G., Fink, M. P., Billiar, T. R., and Vodovotz, Y. (2006). The role of initial trauma in the host's response to injury and hemorrhage: insights from a comparison of mathematical simulations and hepatic transcriptomic analysis. *Shock* 26, 592.

Levi, M., and van der Poll, T. (2010). Inflammation and coagulation. *Crit. Care Med.* 38, S26.

Lightman, S. L., and Conway-Campbell, B. L. (2010). The crucial role of pulsatile activity of the HPA axis for continuous dynamic equilibration. *Nat. Rev. Neurosci.* 11, 710.

Martin, G. S., Mannino, D. M., Eaton, S., and Moss, M. (2003). The epidemiology of sepsis in the United States from 1979 through 2000. *N. Engl. J. Med.* 348, 1546.

Mi, Q., Constantine, G., Ziraldo, C., Solovyev, A., Torres, A., Namas, R., Bentley, T., Billiar, T. R., Zamora, R., Puyana, J. C., and Vodovotz, Y. (2011). A dynamic view of trauma/hemorrhage-induced inflammation in mice: principal drivers and networks. *PLoS ONE* 6, e19424. doi:10.1371/journal.pone.0019424

Mi, Q., Li, N. Y. K., Ziraldo, C., Ghuma, A., Mikheev, M., Squires, R., Okonkwo, D. O., Verdolini Abbott, K., Constantine, G., An, G., and Vodovotz, Y. (2010). Translational systems biology of inflammation: potential applications to personalized medicine. *Per. Med.* 7, 549.

Mitka, M. (2011). Drug for severe sepsis is withdrawn from market, fails to reduce mortality. *JAMA* 306, 2439.

Molina, P. E., Bagby, G. J., and Stahls, P. (2001). Hemorrhage alters neuroendocrine, hemodynamic, and compartment-specific TNF responses to LPS. *Shock* 16, 459.

Molkov, Y. I., Abdala, A. P., Bacak, B. J., Smith, J. C., Paton, J. F., and Rybak, I. A. (2010). Late-expiratory activity: emergence and interactions with the respiratory CpG. *J. Neurophysiol.* 104, 2713.

Molkov, Y. I., Zoccal, D. B., Moraes, D. J., Paton, J. F., MacHado, B. H., and Rybak, I. A. (2011). Intermittent hypoxia-induced sensitization of central chemoreceptors contributes to sympathetic nerve activity during late expiration in rats. *J. Neurophysiol.* 105, 3080.

Moorman, J. R., Carlo, W. A., Kattwinkel, J., Schelonka, R. L., Porcelli, P. J., Navarrete, C. T., Bancalari, E., Aschner, J. L., Whit, W. M., Perez, J. A., Palmer, C., Stukenborg, G. J., Lake, D. E., and Michael, O. T. (2011). Mortality reduction by heart rate characteristic monitoring in very low birth weight neonates: a randomized trial. *J. Pediatr.* 159, 900.

Morris, J. A. Jr., Norris, P. R., Waitman, L. R., Ozdas, A., Guillamondegui, O. D., and Jenkins, J. M. (2007). Adrenal insufficiency, heart rate variability, and complex biologic systems: a study of 1,871 critically ill trauma patients. *J. Am. Coll. Surg.* 204, 885.

Namas, R., Ghuma, A., Torres, A., Polanco, P., Gomez, H., Barclay, D., Gordon, L., Zenker, S., Kim, H. K., Hermus, L., Zamora, R., Rosengart, M. R., Clermont, G., Peitzman, A., Billiar, T. R., Ochoa, J., Pinsky, M. R., Puyana, J. C., and Vodovotz, Y. (2009a). An adequately robust early TNF-α response is a hallmark of survival following trauma/hemorrhage. *PLoS ONE* 4, e8406. doi:10.1371/journal.pone.0008406

Namas, R., Ghuma, A., Hermus, L., Zamora, R., Okonkwo, D. O., Billiar, T. R., and Vodovotz, Y. (2009b). The acute inflammatory response in trauma/hemorrhage and traumatic brain injury: current state and emerging prospects. *Libyan J. Med.* 4, 136.

Namas, R., Zamora, R., Namas, R., An, G., Doyle, J., Dick, T. E., Jacono, F. J., Androulakis, I. P., Chang, S., Billiar, T. R., Kellum, J. A., Angus, D. C., and Vodovotz, Y. (2012). Sepsis: something old, something new, and a systems view. *J. Crit. Care* 27, 314e1–314e11.

Natanson, C. (1997). "Re-evaluation of anti-inflammatory trials in sepsis: a meta-analysis," in *Cytokines and Pulmonary Infection. Part II: The Role of Cytokines in Systemic and Pulmonary Medicine*, ed. M. R. Pratter (Chicago: American Thoracic Society), 7–18.

Nieman, G., Brown, D., Sarkar, J., Kubiak, B., Ziraldo, C., Vieau, C., Barclay, D., Gatto, L., Maier, K., Zamora, R., Mi, Q., Chang, S., and Vodovotz, Y. (2012). A two-compartment mathematical model of endotoxin-induced inflammatory and physiologic alterations in swine. *Crit. Care Med.* 40, 1052–1063.

Parker, S. J., and Watkins, P. E. (2001). Experimental models of gram-negative sepsis. *Br. J. Surg.* 88, 22.

Piepoli, M., Garrard, C. S., Kontoyannis, D. A., and Bernardi, L. (1995). Autonomic control of the heart and peripheral vessels in human septic shock. *Intensive Care Med.* 21, 112.

Pomeranz, B., MacAulay, R. J., Caudill, M. A., Kutz, I., Adam, D., Gordon, D., Kilborn, K. M., Barger, A. C., Shannon, D. C., and Cohen, R. J. (1985). Assessment of autonomic function in humans by heart rate spectral analysis. *Am. J. Physiol.* 248, H151.

Pontet, J., Contreras, P., Curbelo, A., Medina, J., Noveri, S., Bentancourt, S., and Migliaro, E. R. (2003). Heart rate variability as early marker of multiple organ dysfunction syndrome in septic patients. *J. Crit. Care* 18, 156.

Prince, J. M., Levy, R. M., Bartels, J., Baratt, A., Kane, J. M. III, Lagoa, C., Rubin, J., Day, J., Wei, J., Fink, M. P., Goyert, S. M., Clermont, G., Billiar, T. R., and Vodovotz, Y. (2006). In silico and in vivo approach to elucidate the inflammatory complexity of CD14-deficient mice. *Mol. Med.* 12, 88.

Protti, A., and Singer, M. (2006). Bench-to-bedside review: potential strategies to protect or reverse mitochondrial dysfunction in sepsis-

induced organ failure. *Crit. Care* 10, 228.

Remick, D., Manohar, P., Bolgos, G., Rodriguez, J., Moldawer, L., and Wollenberg, G. (1995). Blockade of tumor necrosis factor reduces lipopolysaccharide lethality, but not the lethality of cecal ligation and puncture. *Shock* 4, 89.

Riordan, W. P. Jr., Norris, P. R., Jenkins, J. M., and Morris, J. A. Jr. (2009). Early loss of heart rate complexity predicts mortality regardless of mechanism, anatomic location, or severity of injury in 2178 trauma patients. *J. Surg. Res.* 156, 283.

Rittirsch, D., Flierl, M. A., and Ward, P. A. (2008). Harmful molecular mechanisms in sepsis. *Nat. Rev. Immunol.* 8, 776.

Rybak, I. A., O'Connor, R., Ross, A., Shevtsova, N. A., Nuding, S. C., Segers, L. S., Shannon, R., Dick, T. E., Dunin-Barkowski, W. L., Orem, J. M., Solomon, I. C., Morris, K. F., and Lindsey, B. G. (2008). Reconfiguration of the pontomedullary respiratory network: a computational modeling study with coordinated in vivo experiments. *J. Neurophysiol.* 100, 1770.

Sakr, Y., Vincent, J. L., Reinhart, K., Groeneveld, J., Michalopoulos, A., Sprung, C. L., Artigas, A., and Ranieri, V. M. (2005). High tidal volume and positive fluid balance are associated with worse outcome in acute lung injury. *Chest* 128, 3098.

Sammon, M. P., and Bruce, E. N. (1991). Vagal afferent activity increases dynamical dimension of respiration in rats. *J. Appl. Physiol.* 70, 1748.

Scheff, J. D., Calvano, S. E., Lowry, S. F., and Androulakis, I. P. (2010). Modeling the influence of circadian rhythms on the acute inflammatory response. *J. Theor. Biol.* 264, 1068.

Scheff, J. D., Calvano, S. E., Lowry, S. F., and Androulakis, I. P. (2012). Transcriptional implications of ultradian glucocorticoid secretion in homeostasis and in the acute stress response. *Physiol. Genomics* 44, 121.

Scheff, J. D., Mavroudis, P. D., Calvano, S. E., Lowry, S. F., and Androulakis, I. P. (2011a). Modeling autonomic regulation of cardiac function and heart rate variability in human endotoxemia. *Physiol. Genomics* 43, 951.

Scheff, J. D., Kosmides, A. K., Calvano, S. E., Lowry, S. F., and Androulakis, I. P. (2011b). Pulsatile glucocorticoid secretion: origins and downstream effects. *IEEE Trans. Biomed. Eng.* 58, 3504.

Schein, M., Wittmann, D. H., Holzheimer, R., and Condon, R. E. (1996). Hypothesis: compartmentalization of cytokines in intraabdominal infection [review]. *Surgery* 119, 694.

Torres, A., Bentley, T., Bartels, J., Sarkar, J., Barclay, D., Namas, R., Constantine, G., Zamora, R., Puyana, J. C., and Vodovotz, Y. (2009). Mathematical modeling of post-hemorrhage inflammation in mice: studies using a novel, computer-controlled, closed-loop hemorrhage apparatus. *Shock* 32, 172.

Vincent, J. L., Sakr, Y., Sprung, C. L., Ranieri, V. M., Reinhart, K., Gerlach, H., Moreno, R., Carlet, J., Le Gall, J. R., and Payen, D. (2006). Sepsis in European intensive care units: results of the SOAP study. *Crit. Care Med.* 34, 344.

Vodovotz, Y., and An, G. (2009). "Systems biology and inflammation," in *Systems Biology in Drug Discovery and Development: Methods and Protocols*, ed. Q. Yan (Totowa, NJ: Springer Science and Business Media), 181–201.

Vodovotz, Y., Chow, C. C., Bartels, J., Lagoa, C., Prince, J., Levy, R., Kumar, R., Day, J., Rubin, J., Constantine, G., Billiar, T. R., Fink, M. P., and Clermont, G. (2006). In silico models of acute inflammation in animals. *Shock* 26, 235.

Vodovotz, Y., Clermont, G., Chow, C., and An, G. (2004). Mathematical models of the acute inflammatory response. *Curr.Opin.Crit. Care* 10, 383.

Vodovotz, Y., Constantine, G., Rubin, J., Csete, M., Voit, E. O., and An, G. (2009). Mechanistic simulations of inflammation: current state and future prospects. *Math. Biosci.* 217, 1.

Vodovotz, Y., Csete, M., Bartels, J., Chang, S., and An, G. (2008). Translational systems biology of inflammation. *PLoS. Comput. Biol.* 4, e1000014. doi:10.1371/journal.pcbi.10000141

Weycker, D., Akhras, K. S., Edelsberg, J., Angus, D. C., and Oster, G. (2003). Long-term mortality and medical care charges in patients with severe sepsis. *Crit. Care Med.* 31, 2316.

Wysocki, M., Cracco, C., Teixeira, A., Mercat, A., Diehl, J. L., Lefort, Y., Derenne, J. P., and Similowski, T. (2006). Reduced breathing variability as a predictor of unsuccessful patient separation from mechanical ventilation. *Crit. Care Med.* 34, 2076.

Yang, E. H., Almon, R. R., Dubois, D. C., Jusko, W. J., and Androulakis, I. P. (2009). Identification of global transcriptional dynamics. *PLoS ONE* 4, e5992. doi:10.1371/journal.pone.0005992

Conflict of Interest Statement: The authors declare that the research was conducted in the absence of any commercial or financial relationships that could be construed as a potential conflict of interest.

Received: 29 February 2012; accepted: 03 June 2012; published online: 02 July 2012.

Citation: Dick TE, Molkov YI, Nieman G, Hsieh Y-H, Jacono FJ, Doyle J, Scheff JD, Calvano SE, Androulakis IP, An G and Vodovotz Y (2012) Linking inflammation, cardiorespiratory variability, and neural control in acute inflammation via computational modeling. Front. Physio. ***3****:222. doi: 10.3389/fphys.2012.00222*

This article was submitted to Frontiers in Computational Physiology and Medicine, a specialty of Frontiers in Physiology.

frontiers in
PHYSIOLOGY

ORIGINAL RESEARCH ARTICLE
published: 16 July 2012
doi: 10.3389/fphys.2012.00246

Toward a multiscale description of microvascular flow regulation: O_2-dependent release of ATP from human erythrocytes and the distribution of ATP in capillary networks

Daniel Goldman[1]*, Graham M. Fraser[1], Christopher G. Ellis[1], Randy S. Sprague[2], Mary L. Ellsworth[2] and Alan H. Stephenson[2]

[1] *Department of Medical Biophysics, University of Western Ontario, London, ON, Canada*
[2] *Department of Pharmacological and Physiological Science, Saint Louis University School of Medicine, St. Louis, MO, USA*

Edited by:
Pankaj Qasba, National Intitutes of Health–Heart Lung and Blood Institute, USA

Reviewed by:
William Andrew Pruett, University of Mississippi Medical Center, USA
Jens Christian Brings Jacobsen, University of Copenhagen, Denmark

****Correspondence:***
Daniel Goldman, Department of Medical Biophysics, University of Western Ontario, 407 Medical Sciences Building, London, ON, Canada N6A 5C1.
e-mail: dgoldma2@uwo.ca

Integration of the numerous mechanisms that have been suggested to contribute to optimization of O_2 supply to meet O_2 need in skeletal muscle requires a systems biology approach which permits quantification of these physiological processes over a wide range of length scales. Here we describe two individual computational models based on *in vivo* and *in vitro* studies which, when incorporated into a single robust multiscale model, will provide information on the role of erythrocyte-released ATP in perfusion distribution in skeletal muscle under both physiological and pathophysiological conditions. Healthy human erythrocytes exposed to low O_2 tension release ATP via a well characterized signaling pathway requiring activation of the G-protein, Gi, and adenylyl cyclase leading to increases in cAMP. This cAMP then activates PKA and subsequently CFTR culminating in ATP release via pannexin 1. A critical control point in this pathway is the level of cAMP which is regulated by pathway-specific phosphodiesterases. Using time constants (∼100 ms) that are consistent with measured erythrocyte ATP release, we have constructed a dynamic model of this pathway. The model predicts levels of ATP release consistent with measurements obtained over a wide range of hemoglobin O_2 saturations (sO_2). The model further predicts how insulin, at concentrations found in pre-diabetes, enhances the activity of PDE3 and reduces intracellular cAMP levels leading to decreased low O_2-induced ATP release from erythrocytes. The second model, which couples O_2 and ATP transport in capillary networks, shows how intravascular ATP and the resulting conducted vasodilation are affected by local sO_2, convection and ATP degradation. This model also predicts network-level effects of decreased ATP release resulting from elevated insulin levels. Taken together, these models lay the groundwork for investigating the systems biology of the regulation of microvascular perfusion distribution by erythrocyte-derived ATP.

Keywords: oxygen supply regulation, signal pathway modeling, ATP transport model, O_2 transport model

INTRODUCTION

The regulation of blood flow involves interplay among numerous mechanisms including the tissue specific microvascular architecture, wall shear stress and pressure (myogenic tone), and the activity of the sympathetic nervous system. Although each of these clearly contributes to total microvascular perfusion, these factors alone are insufficient to regulate dynamically the precise distribution of perfusion to meet local tissue oxygen (O_2) need. Such a system requires a mechanism by which the need is detected, quantified, and coupled to a mechanism for the alteration of O_2 delivery. A number of theories have been proposed by which blood flow can be increased in response to decreases in tissue oxygen tension including the arterioles themselves being sensitive to low O_2 levels (Pittman and Duling, 1973; Duling, 1974; Jackson, 1987) the release of vasodilatory metabolites within the tissues or vessels (Hester, 1993), and more recently the release of nitric oxide (Jia et al., 1996) and/or nitrite (Gladwin et al., 2004) from erythrocytes. Although each may play a role, none provides the sensitivity and rapid time course necessary for the precise matching of oxygen supply with need.

One mechanism which has been the subject of significant interest in recent years involves the regulated release of ATP (adenosine triphosphate) from erythrocytes in response to a decrease in hemoglobin oxygen saturation (sO_2; Ellsworth et al., 1995, 2009; Jagger et al., 2001) as would result from their exposure to a reduced oxygen tension environment. The ATP released would bind to endothelial purinergic receptors inducing vasodilation via the synthesis and release of endothelium-derived relaxing factors. Experimentally, studies have established that infusion of ATP into hamster skeletal muscle arterioles and venules, at concentrations observed *in vivo* (Gonzalez-Alonso et al., 2002), induces a vasodilation that is conducted upstream to feed arterioles resulting in

increased perfusion (McCullough et al., 1997; Collins et al., 1998). Such a mechanism would permit the erythrocyte, via a local release of ATP, to evoke an increase in O_2 supply to discrete regions of the microvasculature enabling the dynamic changes in O_2 delivery needed to meet changing local tissue oxygen needs. For this mechanism to be effective, the amount of ATP released from erythrocytes needs to be directly related to the extent of hemoglobin O_2 desaturation (or decrease in sO_2) that occurs when erythrocytes are exposed to low O_2 tension (or partial pressure, PO_2; Jagger et al., 2001).

Several recent reviews (Ellsworth, 2000, 2004; Gonzalez-Alonso, 2008; Ellsworth et al., 2009; Sprague et al., 2011) and previous theoretical models (Arciero et al., 2008; Sprague et al., 2010) have evaluated the impact of erythrocyte-released ATP on microvascular flow regulation. However, a full understanding of the effect of erythrocyte-derived ATP on the regulation of O_2 delivery requires quantification of the interacting physiological processes over a wide range of physical length scales. To accomplish this necessitates the incorporation of several individual experiment-based computational models into a novel multiscale model. Two critical components of such a dynamic model are delineated here.

Significant progress has been made in defining the components of a signaling pathway for ATP release from erythrocytes under conditions of low O_2 tension (Ellsworth et al., 2009). Important elements of this pathway (see **Figure 1**) include activation of the heterotrimeric G-protein Gi (Sprague et al., 2002; Olearczyk et al., 2004a,b) and, subsequently, the activation of adenylyl cyclase (AC) resulting in increases in intracellular cyclic adenosine monophosphate (cAMP; Sprague et al., 2002, 2005, 2006). This results in activation of protein kinase A (PKA; Sprague et al., 2001) and the cystic fibrosis transmembrane conductance regulator (CFTR; Sprague et al., 1998). The final conduit for ATP release in response to this stimulus has been determined to be pannexin 1 (Locovei et al., 2006; Sridharan et al., 2010).

Recent experimental studies demonstrate that insulin, at concentrations observed in humans with pre-diabetes and used to treat individuals with diabetes mellitus type 2 (type 2 diabetes), inhibits low O_2 tension-induced ATP release from human erythrocytes (Hanson et al., 2009). Importantly, animal studies suggest that this defect contributes to the impaired tissue oxygenation in pre-diabetes (Ellis et al., 2010). A critical control point in the low O_2 signaling pathway for regulated ATP release is the concentration of cAMP which is determined by a balance between cAMP synthesis by adenylyl cyclase and its hydrolysis by phosphodiesterases (PDEs). Insulin has been shown to increase hydrolysis of cAMP via the enhancement of PDE3 activity (Hanson et al., 2010).

Although signaling pathways similar to the one responsible for ATP release from erythrocytes have been described previously in other cells (Cazzaniga et al., 2008; Williamson et al., 2009), no quantitative approach has integrated the signaling components of low O_2 tension-induced ATP release from erythrocytes into a unified mathematical framework that would permit the comprehensive study of its regulation. Here we present a single compartment kinetic model of the low O_2 tension-induced ATP release pathway in human erythrocytes that incorporates parameters consistent with experimentally measured ATP release in response to this stimulus in the absence (Sprague and Ellsworth, 2012) and presence (Hanson et al., 2009) of insulin. This model, based on a previously described deterministic model of a G-protein coupled cAMP pathway (Williamson et al., 2009), incorporates interactions among individual cellular components based on our current understanding of the signaling pathway for low O_2 tension-induced ATP release. Our approach involves the use of data obtained from experimental studies including those defining PDE3-mediated cAMP hydrolysis as a critical control point for the regulation of low O_2-induced ATP release from human erythrocytes (Hanson et al., 2010).

In addition to our model of the intracellular ATP release pathway, we utilized *in vivo* data obtained from rat skeletal muscle to construct a realistic model of blood flow, O_2 transport, and ATP transport at the capillary network level to investigate the impact of low O_2-induced ATP release from erythrocytes on

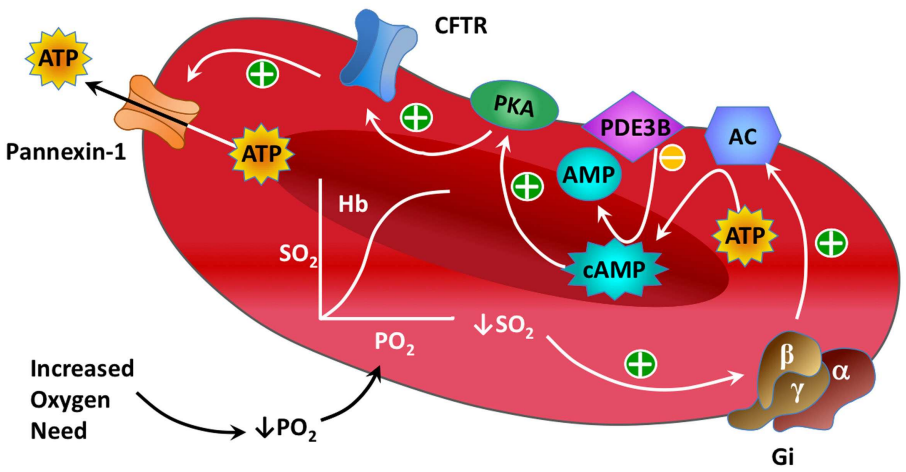

FIGURE 1 | Illustration showing known components of the oxygen-dependent erythrocyte ATP release pathway.

the regulation of perfusion distribution in skeletal muscle under physiological conditions and when plasma insulin is increased. Our model of capillary network ATP transport, although used to obtain steady-state results in the present work, is novel in that it is time-dependent and hence permits simulation of the dynamics of this process. This model will be crucial in future studies of microvascular flow regulation, which is an inherently dynamic physiological process (e.g., due to temporal variations in both local blood flow and O_2 consumption rate), and will allow us to include the ATP release dynamics from our pathway model into a larger-scale model of flow regulation in complete networks containing capillaries, arterioles, and venules.

Our underlying hypothesis is that the O_2-dependent release of ATP from erythrocytes is a key mechanism for the dynamic regulation of the distribution of microvascular perfusion to meet local tissue O_2 needs in skeletal muscle. The long-term goal is to utilize a combination of computational models and experimental studies to ascertain how and under what conditions ATP release from erythrocytes contributes to appropriate O_2 delivery. Furthermore, the use of computational models provides a mechanism by which predictions of impaired ATP release based on known defects associated with certain disease states, and the potential effectiveness of pharmacological interventions to rescue the defect, can be evaluated. Experimental data supporting the stated hypothesis have been reported previously (Collins et al., 1998; Dietrich et al., 2000; Sprague et al., 2009) and were used as a basis for constructing the models. The two components described here complement models of 3D blood-tissue O_2 transport and two-phase blood flow presented previously and will become an important part of a multiscale simulation required to characterize flow regulation based on ATP release from erythrocytes.

MATERIALS AND METHODS

SIMPLIFIED MODEL OF O_2-DEPENDENT Gi-ACTIVATED cAMP PATHWAY

As described above, the basic components of heterotrimeric G-protein (GP)-activated signaling pathways involving cAMP are well-known in many cell types including the erythrocyte. To begin modeling the key components of the O_2-dependent erythrocyte ATP release pathway (**Figure 1**), we modified a simple model of a GP-activated cAMP pathway from the literature (Williamson et al., 2009). Although the exact mechanism that couples a decrease in hemoglobin saturation with GP activation has not been fully elucidated, several studies have linked mechanical force with activation of Gi (Li and Xu, 2000; Wan et al., 2008; Forsyth et al., 2011). Our model requires that the desaturation of oxyhemoglobin induces activation of Gi, identified here as the activated form of GP (GPa). When erythrocyte Gi dissociates, the βγ subunit stimulates production of cAMP (via adenylyl cyclase, AC; Sprague et al., 2002, 2005, 2006) leading to activation of protein kinase A (PKAi → PKAa; Sprague et al., 2001, 2006). The kinetic equations adapted for the activation of PKA in the present model are:

$$\frac{d\,[\mathrm{GPa}]}{dt} = k_{\mathrm{GPf}}\,[\mathrm{GPi}]\,[\mathrm{tHb}]^{\alpha} - k_{\mathrm{GPr}}\,[\mathrm{GPa}] \tag{1}$$

$$\frac{d\,[\mathrm{cAMP}]}{dt} = \frac{\mathrm{AC_{base}} + k_{\mathrm{cAMPf}}\,[\mathrm{GPa}]}{1 + k_{\mathrm{cAMPi}}\,[\mathrm{PKAa}]} - \frac{v_{\mathrm{PDE3}}\,[\mathrm{PKAa}]\,[\mathrm{cAMP}]}{K_{\mathrm{PDE3}} + [\mathrm{cAMP}]} \tag{2}$$

$$\frac{d\,[\mathrm{PKAa}]}{dt} = k_{\mathrm{PKAf}}\,[\mathrm{PKAi}]\,[\mathrm{cAMP}] - k_{\mathrm{PKAr}}\,[\mathrm{PKAa}] \tag{3}$$

Equation 1 above describes GP activation resulting from changes in oxyhemoglobin saturation where [tHb] is the fraction of desaturated Hb (in the tense or "t" state; $[\mathrm{tHb}] = 1 - \mathrm{sO_2}$) and the exponent α is used to modulate the relationship between [tHb] and GPa. Equation 2 describes cAMP production and degradation, where $\mathrm{AC_{base}}$ represents the baseline rate of cAMP production (in the absence of GP activation) and the v_{PDE3} term represents degradation of cAMP by the phosphodiesterase PDE3, a PDE shown to regulate cAMP concentrations in the erythrocyte O_2-dependent ATP release pathway (Adderley et al., 2010). Here, $v_{\mathrm{PDE3}} = v_0 * \mathrm{PDE3}_{rel}$ where v_0 is a baseline rate of cAMP degradation and $\mathrm{PDE3}_{rel}$ is the relative amount of PDE3 activity (assumed to be one under normal baseline conditions). The PKAa terms on the right-hand side represent negative feedback to either inhibit cAMP production (Sobolewski et al., 2004) or enhance cAMP degradation (Murthy et al., 2002). Eq.3 represents direct activation of PKA by cAMP. In all our kinetic equations, the subscript "f" indicates the forward rate constant (e.g., k_{PKAf}) governing production of the species of interest, while the subscript "r" indicates the reverse rate constant (e.g., k_{PKAr}) governing degradation.

PKA/CFTR-ACTIVATED ATP RELEASE

To link the PKA activation as described in Eq. 3 to the release of ATP, two kinetic equations are employed that describe the other known regulatory steps in the process:

$$\frac{d\,[\mathrm{CFTRa}]}{dt} = k_{\mathrm{CFTRf}}\,[\mathrm{CFTRi}]\,[\mathrm{PKAa}]^{\beta} - k_{\mathrm{CFTRr}}\,[\mathrm{CFTRa}] \tag{4}$$

$$F_{\mathrm{ATP}} = k_{\mathrm{ATPflux}}\,[\mathrm{CFTRa}] \tag{5}$$

where the exponent β is used to modulate the relationship between PKA activation and CFTR activation. For simplicity it is assumed that F_{ATP}, the release rate or flux of ATP (via pannexin 1, Sridharan et al., 2010), is proportional to activation of CFTR. In addition to Eqs 1–5, our model assumes conservation of GP, PKA, and CFTR:

$$\begin{aligned} [\mathrm{GPtotal}] &= [\mathrm{GPi}] + [\mathrm{GPa}] \\ [\mathrm{PKAtotal}] &= [\mathrm{PKAi}] + [\mathrm{PKAa}] \\ [\mathrm{CFTRtotal}] &= [\mathrm{CFTRi}] + [\mathrm{CFTRa}] \end{aligned} \tag{6}$$

Figure 2 shows the ATP release pathway model that was originally created using the free software package Cell Designer (http://celldesigner.org). Solution of Eqs 1–6 was implemented in Matlab (Mathworks, Natick, MA, USA) to allow more flexibility in exploring the model (e.g., specifying time-dependent saturation functions and automatically integrating and averaging results over time). A version of our Matlab simulation code is included online as Supplementary Material.

Parameters used in Eqs 2–3 were initially those used by Williamson et al. (2009) with modifications to reflect the much

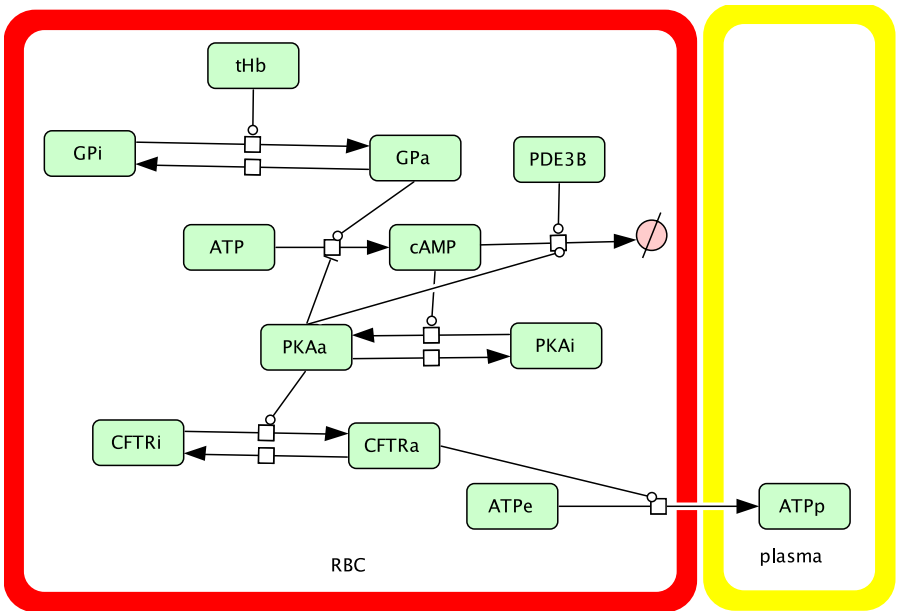

FIGURE 2 | Schematic showing the components and interactions included in our dynamic model of the oxygen-dependent erythrocyte ATP release pathway.

faster time-scale of erythrocyte ATP release (∼100 ms vs. ∼10 s in, Williamson et al., 2009) as reported for shear-induced ATP release in microfluidic experiments (Wan et al., 2008). It is important to recognize that available evidence suggests that shear stress applied to human erythrocytes activates the same pathway as does exposure to reduced O_2 (Sprague and Ellsworth, 2012). Parameters for Eqs 1, 4, and 5 (in particular, the exponents α and β) were then set to represent those required for a similar time-scale, and were varied to match *in vitro* measurements of ATP release as a function of hemoglobin saturation (Sprague and Ellsworth, 2012) where erythrocytes were rapidly desaturated to various sO_2 values starting from ∼100% sO_2. Although the dynamics of O_2-dependent erythrocyte ATP release are important *in vivo*, no dynamic measurements are currently available (Sprague and Ellsworth, 2012). Therefore, we chose to use brief desaturation steps of fixed duration (40 ms) and varying magnitude (38–84%) to investigate the sO_2 dependence of our dynamic ATP release model. The stimulation time of 40 ms was motivated by the experiments by Wan et al. (2008) in which changes in shear needed to be longer than ∼6 ms (activation time) to produce changes in erythrocyte ATP release while the delay time between changes in shear and changes in ATP release was ∼29 ms.

An underlying assumption in our model is that the O_2-dependent pathway does not release ATP when hemoglobin is fully saturated with oxygen (i.e., $AC_{base} = 0$). Therefore, the sO_2 dependence of the model was based on the results reported by Sprague and Ellsworth (2012) with the measured ATP release for 98% sO_2 (5.4 nmol ATP per 4×10^8 erythrocytes) taken to represent full saturation which was subtracted from the ATP release values for lower saturations. This yielded target ATP release values of 3.1, 7.1, and 13.1 nmol ATP/4×10^8 erythrocytes for 61.8, 41.3, and 21.6% sO_2, respectively. To enable the model to predict the inhibitory effect of insulin on O_2-induced ATP release, as reported experimentally (Hanson et al., 2009, 2010), the value of $PDE3_{rel}$ was adjusted to model erythrocyte ATP release upon exposure to reduced O_2 tension in the presence of levels of insulin seen in prediabetes or required for the treatment of type 2 diabetes (Kanauchi et al., 2007; Ellis et al., 2010). Again, the ATP release values were adjusted for zero ATP release at full saturation, yielding a target value for ATP release of 11.8 nmol ATP/4×10^8 erythrocytes at 15.7% sO_2 without insulin and a target value of 2.77 at 20.9% sO_2 with insulin, both determined experimentally (Hanson et al., 2009).

COMPUTATIONAL MODEL OF O_2 AND ATP TRANSPORT IN CAPILLARY NETWORKS

Numerical simulations of steady-state O_2 transport were performed using an established time-dependent, finite-difference computational model (Goldman and Popel, 1999, 2000; Ellis et al., 2010; Sprague et al., 2010) that couples the continuum partial differential equations describing convective transport by flowing blood in the capillaries with equations describing O_2 diffusion and consumption in the tissue. This model incorporates both dissolved and hemoglobin-bound O_2 in the capillaries. Transport of O_2 between the blood and tissue is described using a flux boundary condition with mass transfer coefficients calculated previously using a discrete erythrocyte model (Eggleton et al., 2000). In the model presented here, for all O_2 transport simulations, a capillary network reconstructed from experimental data was used (Fraser et al., 2012) in conjunction with hemodynamic parameters (erythrocyte velocity and hematocrit) determined from *in vivo* measurements in the rat extensor digitorum longus (EDL) muscle. The capillary network was discretized into 208 cylindrical segments and the tissue domain surrounding the capillaries,

which had dimensions of $84 \times 169 \times 342\ \mu m$, was discretized into 632,315 computational nodes. Average capillary entrance saturations (63%) and the tissue O_2 consumption rate (1.5×10^{-4} ml O_2/ml/s) were set based on previous experimental data (Ellis et al., 2002). The geometric and hemodynamic data used in the blood-tissue oxygen transport calculations, as well as the resulting steady-state values for capillary sO_2, are included online as Supplementary Material.

Numerical simulations of steady-state ATP transport within the capillary network were performed using a modified form of our time-dependent finite-difference computational model for intravascular O_2 transport (Goldman and Popel, 2000). Based on a previously described ATP transport model (Arciero et al., 2008), the following continuum partial differential equation was solved for plasma ATP concentration [ATP] using the geometric, hemodynamic, and sO_2 data described above and an initial ATP concentration of zero:

$$(1 - H_T)\frac{\partial}{\partial t}[\mathrm{ATP}] = -u(1 - H_D)\frac{\partial}{\partial z}[\mathrm{ATP}] + H_T C_0 (1 - C_1 S) - \frac{2}{R}k_d[\mathrm{ATP}] \quad (7)$$

where u is the averaged cross-sectional blood velocity at any axial location z, H_D is the discharge hematocrit, H_T is the tube hematocrit, and R is capillary radius. As previously defined (Arciero et al., 2008), the constants C_0 and C_1 are used to produce a linear approximation to the (steady-state) ATP release rate as a function of oxyhemoglobin saturation S, while the constant k_d approximates steady-state degradation of ATP by the endothelium (see **Table 1** for parameter values). To model the effect of elevated plasma insulin on ATP release, we decreased C_0 by 50% based on experimental measurements.

In a previously reported model for microvascular regulation (Arciero et al., 2008), seven representative unbranched vessel segments (artery, large arteriole, small arteriole, capillary, small venule, large venule, vein) were included in the simulation and the inlet [ATP] in the farthest upstream vessel (artery) was set at 0.5 μM. This led to an inlet [ATP] in the capillary of approximately 0.25 μM. Therefore, we used this value for inlet [ATP] in our capillary network simulations. However, since this value depends on other modeling assumptions in the work of Arciero et al. (2008), we also considered the case where [ATP] is zero at the entrance of our capillary network to more clearly illustrate the contribution of erythrocyte-derived ATP in the capillary bed to plasma [ATP].

The spatial distribution of steady-state sO_2 values was computed for the 3D capillary network based on experimental measurements of entrance sO_2 and total erythrocyte supply rate in the network. The same steady-state sO_2 distribution was used for both normal and impaired ATP release. To solve Eq. 7 for steady-state [ATP] once steady-state sO_2 values had been calculated, an arbitrary initial condition ([ATP] = 0) was chosen and simulations were run until [ATP] became constant in all capillary segments. Although the present work focuses on steady-state capillary [ATP] distributions, our computational model is capable of simulating changes in intravascular [ATP] for time-varying blood flow, O_2 consumption rate, or erythrocyte ATP release.

Table 1 | Parameters for ATP release pathway and ATP transport.

Parameter	Value
AC_{base}	0
k_{cAMPf}	49.5
k_{cAMPi}	2.47
v_0	101
K_{PDE3}	1
k_{PKAf}	60.5
k_{PKAr}	10.0
k_{GPf}	25.0
α	1.2
k_{GPr}	3.36
k_{CFTRf}	181
β	6.3
k_{CFTRr}	11.3
$k_{ATPflux}$	2
GP_{total}	1
PKA_{total}	1
$CFTR_{total}$	1
C_0	1.4×10^{-9} mol/s·cm^3
C_1	0.891
k_d	2.0×10^{-4} cm/s

As noted above, to have a major impact on oxygen delivery to meet increased demand, the endothelial signal produced by ATP released in capillaries or venules must be conducted upstream and stimulate arteriolar dilation. Therefore, we integrated [ATP] obtained from Eq. 7 to estimate the total dilatory signal $\sigma_{dilation}$ produced by ATP released from erythrocytes in the capillary network:

$$\sigma_{dilation} = \sum_{i=1}^{208} [\mathrm{ATP}]_i \exp\left(-\frac{L - z_i}{\lambda}\right) \quad (8)$$

where L is the arterio-venous length of the capillary network, and z_i is the axial location of the segment with ATP concentration $[ATP]_i$. The parameter λ determines the length scale of attenuation of the conducted signal and is set to 1 cm based on the work of Arciero et al. (2008) who obtained this approximate value from highly variable (0.15–1.6 cm) experimental data (Xia and Duling, 1995). Note that in the present work, $\sigma_{dilation}$ is simply used as a measure of the dilatation signal originating in the capillaries. Since arterioles are not included in this model, we cannot use $\sigma_{dilation}$ to change vascular diameters.

RESULTS

O_2-DEPENDENT ATP RELEASE PATHWAY

Using Eqs 1–6 and parameters listed in **Table 1**, we simulated the response of the O_2-dependent ATP release pathway in human erythrocytes to a 40 ms period of oxyhemoglobin desaturation starting from an initial condition with all variables equal to zero. **Figure 3** shows the predicted dynamic response of this pathway to a step change in sO_2 from 100 to 15.7% (i.e., increase in [tHb] from 0 to 0.843) with a duration of 40 ms. **Figure 3** describes a temporal

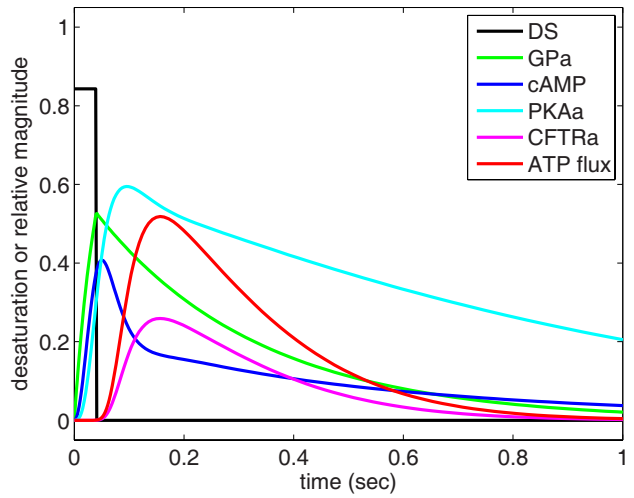

FIGURE 3 | Dynamic behavior of our model of oxygen-dependent erythrocyte ATP release. Hemoglobin oxygen saturation is decreased from 100 to 15.7% for 40 ms, resulting in activation of the ATP release pathway with an initial delay in ATP release followed by a peak in ATP flux at approximately 150 ms. The pulse of hemoglobin desaturation results in a total release of ATP (area under ATP flux curve) that can be compared to experimental measurements. The ATP release delay and peak times are consistent with shear-dependent release dynamics measured by Wan et al. (2008), and the GP activation time-scale is consistent with the measurements of Hein et al. (2005).

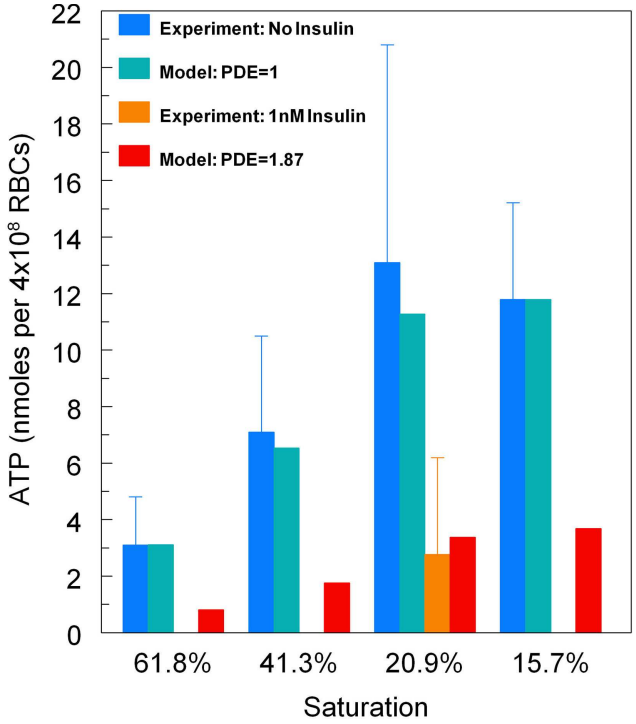

FIGURE 4 | Model predictions for total ATP release vs. hemoglobin saturation. For baseline levels of PDE3 activity, predicted ATP release matches experimental measurements (Sprague and Ellsworth, 2012). For an 87% increase in PDE3 activity, ATP release decreases as seen for erythrocytes incubated in insulin (Hanson et al., 2009). Here ATP release has been normalized so that at 15.7% sO_2 the model matches the ATP release measurements without insulin.

relationship among the components of the signaling pathway in which GP is activated first by hemoglobin desaturation with cAMP peaking at ∼51 ms and the ATP release rate (or flux) peaking at ∼157 ms after this physiological stimulus. Following the return to full hemoglobin saturation, ATP flux returns to zero in less than 1 s. Time-dependent results using this ATP release model will be useful when integrated into future dynamic models of microvascular flow regulation based on O_2-dependent ATP release from erythrocytes.

To relate the results shown in **Figure 3** to experimental measurements, cAMP and ATP flux are integrated over the time required for the desaturation step to turn on and off and for the release of ATP to stop. It is important to recognize that our model computes relative activation and ATP flux values for an average pathway without considering the number of these GP-coupled pathways present in an individual erythrocyte. Therefore, to compare our results directly to measurements of ATP release, we normalized our findings to agree with experimental measurements (Hanson et al., 2009) at 15.7% sO_2 ($[tHb] = 0.843$).

To demonstrate that predictions from our model of the erythrocyte ATP release pathway agree with experimental data, in **Figure 4** we plotted total ATP release vs. sO_2 where the desaturation magnitude $[tHb] = 1 - sO_2$. This comparison confirms that our model captures the dependence of ATP release on sO_2 under conditions in which $PDE3_{rel} = 1$. Importantly, when PDE3 activity is increased by 87% ($PDE3_{rel} = 1.87$) our model predictions of amounts of ATP released when erythrocytes are exposed to reduce O_2 closely match ATP levels measured in the presence of 1 nM insulin (Hanson et al., 2009). The 87% increase in PDE3 activity is based on effects of insulin on the activity of this PDE in adipocytes (Kitamura et al., 1999). Thus, this model allows us to predict the inhibitory effect of insulin-induced increases in PDE3 activity on cAMP levels and ATP release from erythrocytes in which hemoglobin saturation is reduced to 15.7% (**Figure 5A**). As depicted in **Figure 5B**, the model also allows prediction of the level of PDE3 activity required to replicate experimental measurements of erythrocyte cAMP initiated by direct activation of Gi with mastoparin 7 (Mas-7) in the absence and presence of PDE3-stimulating concentrations of insulin (Hanson, 2009; Hanson et al., 2010).

COUPLED O_2-ATP TRANSPORT IN CAPILLARY NETWORKS

The simulated O_2 distribution in our reconstructed capillary network is shown in **Figure 6A**, and the 3D ATP distributions calculated for O_2-dependent erythrocyte ATP release in the absence and presence of insulin are shown in **Figures 6C,E**, respectively. The O_2 transport model shows a nearly linear decrease in sO_2 (**Figure 6B**) with little variation among capillaries, except for one capillary with counter-current flow.

If the capillary inlet [ATP] (ATP_{in}) is set to zero, all capillaries for normal ATP release (blue symbols in **Figure 6D**) show an increase in [ATP] although the variation among vessels is much

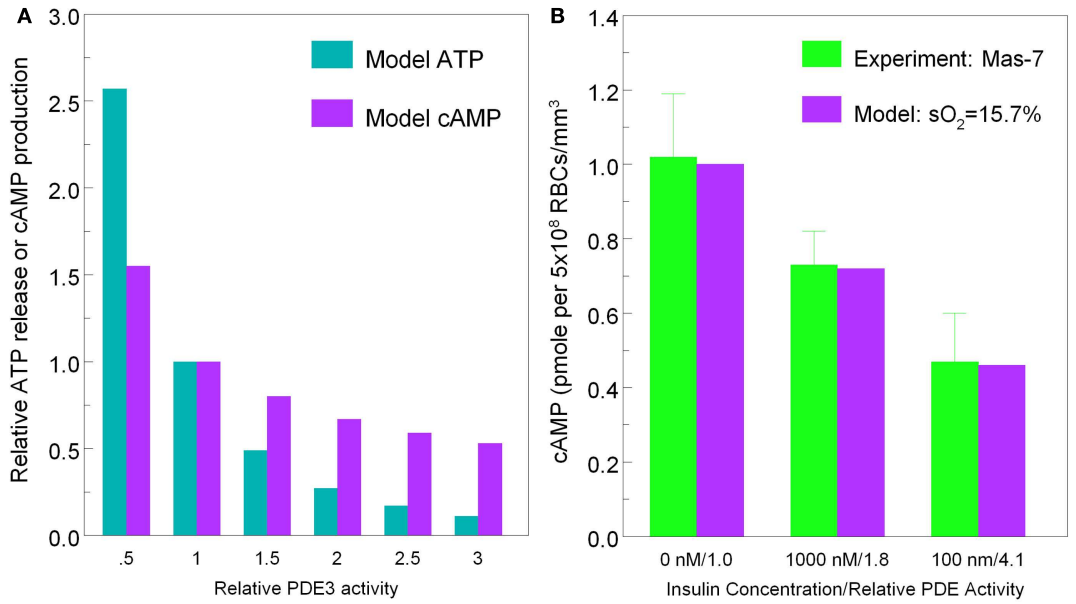

FIGURE 5 | [**(A)**, left] Model predictions for ATP release (cyan bars) and cAMP production (purple bars) at 15.7% hemoglobin saturation vs. PDE3 activity. [**(B)**, right] Measured erythrocyte cAMP production (green bars) in response to Mas-7 stimulation vs. insulin concentration (0, 1 mM, 100 nM) and model predictions of cAMP production (purple bars) at 15.7% sO_2 vs. PDE3 activity ($PDE3_{rel} = 1$, 1.8, 4.1).

greater than the variation in capillary sO_2. The variation in [ATP] is due to the capillary network geometry and convective transport of ATP combined with the degradation of ATP by ecto-ATPases. When ATP release from erythrocytes is impaired (blue symbols in **Figure 6F**), the rate of increase in [ATP] with distance down the network is much less. The mean capillary ATP concentrations in the absence and presence of insulin are 0.076 and 0.038 μM, respectively, implying a 50% decrease when plasma insulin is increased to values found in pre-diabetes.

If $ATP_{in} = 0.25\,\mu M$ (Arciero et al., 2008), degradation of ATP results in a decrease in capillary [ATP] until approximately half way down the network for normal release (red symbols in **Figure 6D**), and slightly further for impaired release (red symbols in **Figure 6F**). In the case in which ATP release is impaired, [ATP] nearly plateaus suggesting that the rate of release is approximately equal to the rate of degradation. When ATP release is unimpaired, [ATP] either plateaus or increases substantially toward the venular end of the network. The mean ATP concentrations in the absence and presence of insulin are 0.115 and 0.077 μM, respectively, a 33% decrease in the presence of insulin. Thus, for either value of ATP_{in}, there is a substantial decrease in capillary ATP when low O_2-induced ATP release from erythrocytes is impaired.

Calculated values of $\sigma_{dilation}$ show behavior similar to that of mean ATP, since the length scale of signal attenuation ($\lambda = 1$ cm) is much greater than the arterio-venous length (~350 μm) of the capillary network. For $ATP_{in} = 0$, $\sigma_{dilation}$ is 1.6×10^{-8} and 0.8×10^{-8} for normal and impaired ATP release, respectively (i.e., a 50% decrease), while for $ATP_{in} = 0.25\,\mu M$ $\sigma_{dilation}$ is 2.4×10^{-8} for normal vs. 1.6×10^{-8} for impaired release (i.e., a 33% decrease).

DISCUSSION

ATP release from erythrocytes in response to both physiological and pharmacological stimuli has been suggested to contribute to the regulation of perfusion distribution in skeletal muscle (Ellis et al., 2010; Sprague et al., 2010). Mechanical deformation (Wan et al., 2008) and exposure to reduced O_2 tension (Ellsworth et al., 2009), both of which occur in small skeletal muscle microvessels, stimulate erythrocyte ATP release. Such a mechanism provides a means by which the distribution of perfusion can be regulated dynamically (Ellsworth, 2000, 2004; Ellsworth et al., 2009; Pittman, 2010). Extensive experimental evidence has established that ATP release from erythrocytes varies in response to changes in the levels of O_2 tension to which these cells are exposed (Ellsworth et al., 1995; Jagger et al., 2001) and that increases in microvascular ATP concentrations result in vasodilation that is conducted to the feed arterioles, promoting an increase in oxygen supply to downstream tissues (McCullough et al., 1997; Collins et al., 1998; Ellsworth, 2000). Importantly, it has been reported that low O_2-induced ATP release and subsequent vascular responses occur at a sufficiently fast time-scale (between 100 and 500 ms) to allow physiologically relevant dynamic regulation of O_2 supply (Dietrich et al., 2000; Wan et al., 2008; Ellis et al., 2010). In addition, defects in O_2-dependent ATP release by erythrocytes are present in both type 2 diabetes and pre-diabetes (Sprague et al., 2006, 2010, 2011) two disorders which are associated with peripheral vascular disease. Taken together, these results support a role for low O_2-induced ATP release from erythrocytes in the microcirculation of skeletal muscle as a means by which the distribution of microvascular perfusion can be dynamically regulated (Ellsworth, 2000, 2004; Ellsworth et al., 2009; Pittman, 2010).

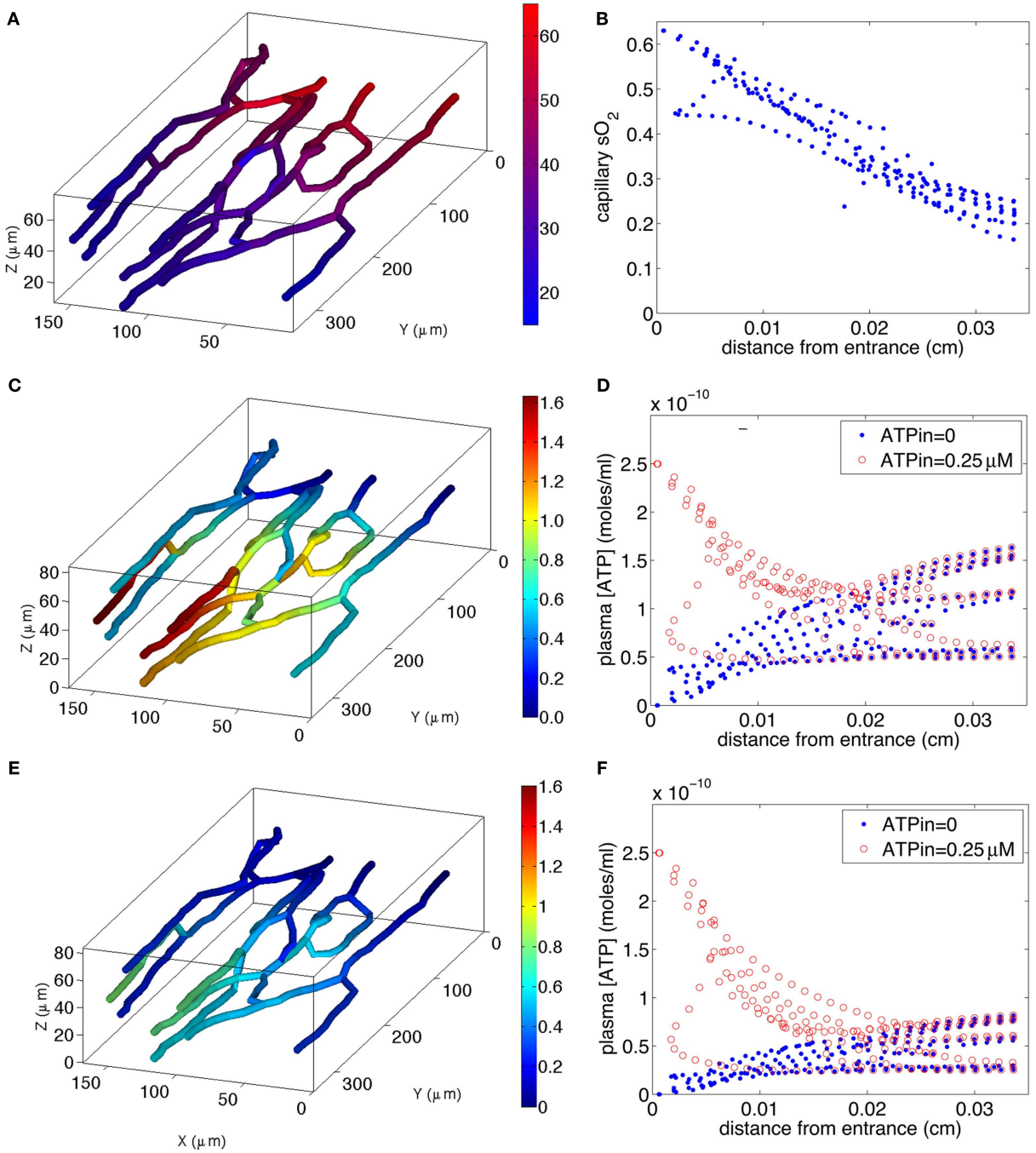

FIGURE 6 | Model of steady-state oxygen-dependent ATP distribution in capillary networks. Top two panels: calculated capillary sO_2 distribution [**(A)**, left] in 3D network and [**(B)**, right] as a function of distance *z* from capillary entrance. Middle two panels: calculated ATP distribution for normal ATP release [**(C)**, left) in 3D network with $ATP_{in} = 0$ and [**(D)**, right) as a function of *z* for $ATP_{in} = 0$ and $ATP_{in} = 0.25\,\mu M$. Bottom two panels: calculated ATP distribution for impaired ATP release due to increased plasma insulin [**(E)**, left] in 3D network with $ATP_{in} = 0$ and [**(F)**, right) as a function of *z* for $ATP_{in} = 0$ and $ATP_{in} = 0.25\,\mu M$. The color bar in (A) indicates the variations in sO_2 (17–63%) in the 3D capillary network, while the color bars in **(C,E)** indicate the variations in [ATP] [0–1.6 μM in **(C)** and 0–0.8 μM in **(E)**] in the network.

Under normal physiological conditions, ATP release would provide an effective mechanism by which perfusion could be dynamically regulated to meet tissue O_2 needs. However, under conditions in which systemic or local microvascular hematocrit is significantly reduced, other mechanisms would be required to increase flow to the tissue to minimize tissue hypoxia (Roy et al., 2012). Such protective mechanisms would likely be the same as those which would become important under conditions in which low O_2-induced

ATP release from erythrocytes is defective as occurs in humans with pre-diabetes (high insulin levels) or type 2 diabetes.

In recent years, a detailed description of microvascular O_2 transport has been developed based on a number of multiscale experimental and theoretical studies (Popel, 1989; Ellsworth et al., 1994;Pittman, 1995, 2005, 2011; Goldman, 2008). A number of studies have described convective and diffusive transport of O_2 inside individual erythrocytes, in single capillary and arteriolar segments, and in arrays or networks of multiple interacting capillaries, arterioles, and venules. A full understanding of the contribution of erythrocyte-derived ATP to the regulation of blood flow distribution in the skeletal muscle microcirculation requires similar theoretical and experimental assessment of the release of ATP from erythrocytes, the diffusion and binding of ATP to the purinergic receptors on the vascular endothelium, and the impact of conducted vasodilation initiated in the microcirculation on flow in both individual vessels and complex vascular networks.

Here we present two experiment-based modeling components of our evolving multiscale approach to the characterization of the regulation of microvascular perfusion in response to low O_2-induced ATP released form erythrocytes. Most importantly, we have a developed a novel dynamic model of the signaling pathway within the erythrocyte that is responsible for this ATP release. The ATP release model is based on previous experimental work describing the components of this pathway. The predictions of the model are consistent with reported time-scales for ATP release (Dietrich et al., 2000; Wan et al., 2008) and agree with measured ATP release from erythrocytes as a function of hemoglobin sO_2 and hydrolysis of cAMP by PDE3. The model also predicts the time course of ATP release, which is a vital determinant of the effectiveness of microvascular flow regulation, and allows us to investigate how defects in that release would compromise optimal O_2 delivery. Finally, the model can be used to predict whether corrections of defects in this pathway may be important therapeutic targets in the treatment of vascular dysfunction associated with diseases such as pre-diabetes and type 2 diabetes in humans.

Little is known about the mechanism linking reduced hemoglobin saturation and G-protein activation in the erythrocyte. However, the time course used in our model for erythrocyte ATP release is similar to the time course reported for other G-protein activated signaling pathways. For example, dopamine activation of a G-protein coupled potassium current ($\sim$250 ms from activation to increased potassium current) in the mouse midbrain (Ford et al., 2009) and $\alpha 2_A$ adrenergic receptor activation of Gi ($<$100 ms) in HEK293 cells stimulated with norepinephrine (Hein et al., 2005) are within the time-scale modeled here for erythrocyte ATP release.

In addition to developing a model for low O_2-induced ATP release from erythrocytes, we present a model of ATP transport in skeletal muscle capillary networks. This model incorporates a reconstructed 3D network and is based on *in vivo* measurements of rat skeletal muscle. This new approach permits the simulation of realistic capillary ATP transport and the consequences for the vasodilatory signal that is conducted from sites of increased O_2 demand (i.e., the capillary bed) to augment blood flow. In addition, we have employed the model to enhance our understanding of the consequences of insulin-induced decreases in erythrocyte ATP release (measured *in vitro*) on conducted signaling and, consequently, on the regulation of local O_2 delivery in a realistic skeletal muscle capillary network. The computational model suggests that details of capillary network geometry and hemodynamics are important in determining the manner in which ATP signaling from erythrocytes is conducted upstream to regulate microvascular O_2 delivery. Importantly, the information obtained from this capillary network model will be important for the further development of a full multiscale description of the regulation of microvascular O_2 delivery in skeletal muscle, allowing us to connect local tissue function (oxygen tension and consumption; Fraser et al., 2012) with mechanisms involved in the regulation of O_2 supply.

MODEL ASSUMPTIONS AND LIMITATIONS

We modeled the O_2-dependent ATP release pathway of the erythrocyte with a series of five biochemical steps described by four time-dependent ordinary differential equations. Although this model can be solved very rapidly using Matlab on a personal computer, it did require inclusion of a number of parameters ($\sim$15 rate constants and half-maximum concentrations) that have not been directly measured. This model also requires assumptions about how oxyhemoglobin desaturation activates Gi and how CFTR activation opens the pannexin 1 channel leading to ATP release. Although most of the biochemical steps used are understood qualitatively and most of the constants can be estimated from measurements of ATP release and cAMP production, one could question the need for such a complex model. If the objective had been only to describe existing data, then a phenomenological model might have been adequate. However, since we were seeking a model that could predict the detailed dynamics of ATP release and the impact of specific changes in the pathway (e.g., increased PDE3 activity), the complexity of the present model was necessary.

A primary assumption made in constructing our model of intravascular ATP transport was that ATP released from erythrocytes into the surrounding plasma becomes well-mixed across the vessel lumen, such that the mean plasma ATP concentration determines ATP binding to endothelial P_{2Y} receptors. Although this may be correct, an alternative possibility is that ATP released near the vessel wall is more important than the mean ATP concentration. If so, this might alter ATP action within the microvasculature as well as other characteristics of the flow regulation system. Presently, it is not known how ATP is radially distributed within the vascular lumen.

There are several limitations to the present model in terms of predicting ATP release by erythrocytes under conditions other than those described here. First, since most parameters have not been directly measured, their values are approximate and may need to be revised once more detailed time-dependent data becomes available. Second, since the relevant details of Gi activation and pannexin 1 opening are not currently known, these were treated phenomenologically. Third, our model has ignored other known mechanisms inducing erythrocyte ATP release including both shear-dependent release, which appears to occur through the same pathway, and receptor-mediated release which utilizes a distinct signaling pathway (Ellsworth and Sprague, 2012). Expansion of this model to include these components would enhance the robustness and utility of the current model and should enable one

to predict the total time-dependent release of ATP by an erythrocyte that would occur *in vivo* under a wide range of physiological or pathophysiological conditions.

MODEL TESTING

As described previously (Ellsworth et al., 2009), testing our full multiscale model of blood-tissue oxygen transport and its regulation based on ATP release by erythrocytes requires *in vivo* experiments. However, a large amount of development and testing of individual model components will be required prior to performing direct comparisons of model predictions to *in vivo* behavior. Currently available microfluidic devices, similar to those of Wan et al. (2008), will allow measurements of the dynamics of O_2-dependent erythrocyte ATP release enabling us to experimentally test the ATP release model's predictions under a wide range of conditions (e.g., increased insulin). These results will provide important dynamic information for the refinement of the model setting the stage for further experimental testing.

MODEL PREDICTIONS AND NOVEL EXPERIMENTS

The ATP pathway model we have developed allows us to make predictions about how the various parameters in Eqs 1–6 interact to determine ATP release, and these predictions can be used as the basis for novel experiments. For example, in humans with type 2 diabetes it is known that there is an approximate 40% decrease in expression of Gi protein in the erythrocyte membrane (Sprague et al., 2006). If we implement this in our model by decreasing GP total accordingly in Eq. 6, we would predict a decrease in ATP release of approximately 60% when sO_2 is decreased briefly from 100 to 15.7%. This prediction links a decrease in a known component of the erythrocyte ATP release pathway with a known measured outcome, i.e., reduced low O_2-dependent ATP release from erythrocytes of humans with type 2 diabetes. An attempt to remedy this defect could be simulated in the model by decreasing PDE3 activity as done experimentally with the selective PDE3 inhibitor cilostazol. Under these conditions, a 60% decrease in PDE3 activity (PDE3rel = 0.6) would return O_2-dependent ATP release back to its normal level. Thus, the model presented here enables us to predict the effect of a known defect in the release pathway on ATP release, and then provides us with a mechanism to evaluate how this defect could be most effectively remedied. This in turn motivates new *in vitro* and *in vivo* experiments to test these predictions in erythrocytes and in intact muscle, to determine if this approach has potential for treating humans with type 2 diabetes.

CONCLUSION

The architectural, biophysical, and temporal complexity of microvascular O_2 transport makes complete understanding of its regulation difficult. However, it is clear that a full understanding of the regulation of microvascular O_2 delivery requires a detailed multiscale approach. The novel theoretical models described here for low O_2-induced ATP release from erythrocytes at the intra-erythrocyte and capillary network levels form the basis for our dynamic systems biology model of microvascular blood flow regulation.

ACKNOWLEDGMENTS

This work is supported by NIH grants HL-089094 and HL-089125. The authors thank J. L. Sprague for inspiration.

SUPPLEMENTARY MATERIAL

The Supplementary Material for this article can be found online at http://www.frontiersin.org/Computational_Physiology_and_Medicine/10.3389/fphys.2012.00246/abstract

REFERENCES

Adderley, S. P., Sprague, R. S., Stephenson, A. H., and Hanson, M. S. (2010). Regulation of cAMP by phosphodiesterases in erythrocytes. *Pharmacol. Rep.* 62, 475–482.

Arciero, J. C., Carlson, B. E., and Secomb, T. W. (2008). Theoretical model of metabolic blood flow regulation: roles of ATP release by red blood cells and conducted responses. *Am. J. Physiol. Heart Circ. Physiol.* 295, H1562–H1571.

Cazzaniga, P., Pescini, D., Besozzi, D., Mauri, G., Colombo, S., and Martegani, E. (2008). Modeling and stochastic simulation of the Ras/cAMP/PKA pathway in the yeast *Saccharomyces cerevisiae* evidences a key regulatory function for intracellular guanine nucleotides pools. *J. Biotechnol.* 133, 377–385.

Collins, D. M., Mccullough, W. T., and Ellsworth, M. L. (1998). Conducted vascular responses: communication across the capillary bed. *Microvasc. Res.* 56, 43–53.

Dietrich, H. H., Ellsworth, M. L., Sprague, R. S., and Dacey, R. G. Jr. (2000). Red blood cell regulation of microvascular tone through adenosine triphosphate. *Am. J. Physiol. Heart Circ. Physiol.* 278, H1294–H1298.

Duling, B. R. (1974). Oxygen sensitivity of vascular smooth muscle. II. In vivo studies. *Am. J. Physiol.* 227, 42–49.

Eggleton, C. D., Vadapalli, A., Roy, T. K., and Popel, A. S. (2000). Calculations of intracapillary oxygen tension distributions in muscle. *Math. Biosci.* 167, 123–143.

Ellis, C. G., Bateman, R. M., Sharpe, M. D., Sibbald, W. J., and Gill, R. (2002). Effect of a maldistribution of microvascular blood flow on capillary O_2 extraction in sepsis. *Am. J. Physiol. Heart Circ. Physiol.* 282, H156–H164.

Ellis, C. G., Goldman, D., Hanson, M., Stephenson, A. H., Milkovich, S., Benlamri, A., Ellsworth, M. L., and Sprague, R. S. (2010). Defects in oxygen supply to skeletal muscle of prediabetic ZDF rats. *Am. J. Physiol. Heart Circ. Physiol.* 298, H1661–H1670.

Ellsworth, M. L. (2000). The red blood cell as an oxygen sensor: what is the evidence? *Acta Physiol. Scand.* 168, 551–559.

Ellsworth, M. L. (2004). Red blood cell-derived ATP as a regulator of skeletal muscle perfusion. *Med. Sci. Sports Exerc.* 36, 35–41.

Ellsworth, M. L., Ellis, C. G., Goldman, D., Stephenson, A. H., Dietrich, H. H., and Sprague, R. S. (2009). Erythrocytes: oxygen sensors and modulators of vascular tone. *Physiology (Bethesda)* 24, 107–116.

Ellsworth, M. L., Ellis, C. G., Popel, A. S., and Pittman, R. N. (1994). Role of microvessels in oxygen-supply to tissue. *News Physiol. Sci.* 9, 119–123.

Ellsworth, M. L., Forrester, T., Ellis, C. G., and Dietrich, H. H. (1995). The erythrocyte as a regulator of vascular tone. *Am. J. Physiol.* 269, H2155–H2161.

Ellsworth, M. L., and Sprague, R. S. (2012). Regulation of blood flow distribution in skeletal muscle: role of erythrocyte-released ATP. *J. Physiol.* doi: 10.1113/jphysiol.2012.233106.

Ford, C. P., Phillips, P. E., and Williams, J. T. (2009). The time course of dopamine transmission in the ventral tegmental area. *J. Neurosci.* 29, 13344–13352.

Forsyth, A. M., Wan, J., Owrutsky, P. D., Abkarian, M., and Stone, H. A. (2011). Multiscale approach to link red blood cell dynamics, shear viscosity, and ATP release. *Proc. Natl. Acad. Sci. U.S.A.* 108, 10986–10991.

Fraser, G. M., Milkovich, S., Goldman, D., and Ellis, C. G. (2012). Mapping 3-D functional capillary geometry in rat skeletal muscle in vivo. *Am. J. Physiol. Heart Circ. Physiol.* 302, H654–H664.

Gladwin, M. T., Crawford, J. H., and Patel, R. P. (2004). The biochemistry of nitric oxide, nitrite, and hemoglobin: role in blood flow regulation. *Free Radic. Biol. Med.* 36, 707–717.

Goldman, D. (2008). Theoretical models of microvascular oxygen transport to tissue. *Microcirculation* 15, 795–811.

Goldman, D., and Popel, A. S. (1999). Computational modeling of oxygen transport from complex capillary

networks. Relation to the microcirculation physiome. *Adv. Exp. Med. Biol.* 471, 555–563.

Goldman, D., and Popel, A. S. (2000). A computational study of the effect of capillary network anastomoses and tortuosity on oxygen transport. *J. Theor. Biol.* 206, 181–194.

Gonzalez-Alonso, J. (2008). ATP: a double-edged signalling molecule regulating the flow of oxygen. *J. Physiol. (Lond.)* 586, 4033–4034.

Gonzalez-Alonso, J., Olsen, D. B., and Saltin, B. (2002). Erythrocyte and the regulation of human skeletal muscle blood flow and oxygen delivery: role of circulating ATP. *Circ. Res.* 91, 1046–1055.

Hanson, M. S. (2009). *Insulin Inhibits Erythrocyte cAMP Accumulation and ATP Release.* Ph.D. Dissertation, Saint Louis University, Saint Louis.

Hanson, M. S., Ellsworth, M. L., Achilleus, D., Stephenson, A. H., Bowles, E. A., Sridharan, M., Adderley, S., and Sprague, R. S. (2009). Insulin inhibits low oxygen-induced ATP release from human erythrocytes: implication for vascular control. *Microcirculation* 16, 424–433.

Hanson, M. S., Stephenson, A. H., Bowles, E. A., and Sprague, R. S. (2010). Insulin inhibits human erythrocyte cAMP accumulation and ATP release: role of phosphodiesterase 3 and phosphoinositide 3-kinase. *Exp. Biol. Med.* 235, 256–262.

Hein, P., Frank, M., Hoffmann, C., Lohse, M. J., and Bunemann, M. (2005). Dynamics of receptor/G protein coupling in living cells. *EMBO J.* 24, 4106–4114.

Hester, R. L. (1993). Uptake of metabolites by postcapillary venules: mechanism for the control of arteriolar diameter. *Microvasc. Res.* 46, 254–261.

Jackson, W. F. (1987). Arteriolar oxygen reactivity: where is the sensor? *Am. J. Physiol.* 253, H1120–H1126.

Jagger, J. E., Bateman, R. M., Ellsworth, M. L., and Ellis, C. G. (2001). Role of erythrocyte in regulating local O2 delivery mediated by hemoglobin oxygenation. *Am. J. Physiol. Heart Circ. Physiol.* 280, H2833–H2839.

Jia, L., Bonaventura, C., Bonaventura, J., and Stamler, J. S. (1996). S-nitrosohaemoglobin: a dynamic activity of blood involved in vascular control. *Nature* 380, 221–226.

Kanauchi, M., Kanauchi, K., Inoue, T., Kimura, K., and Saito, Y. (2007). Surrogate markers of insulin resistance in assessing individuals with new categories "prehypertension" and "prediabetes." *Clin. Chem. Lab. Med.* 45, 35–39.

Kitamura, T., Kitamura, Y., Kuroda, S., Hino, Y., Ando, M., Kotani, K., Konishi, H., Matsuzaki, H., Kikkawa, U., Ogawa, W., and Kasuga, M. (1999). Insulin-induced phosphorylation and activation of cyclic nucleotide phosphodiesterase 3B by the serine-threonine kinase Akt. *Mol. Cell. Biol.* 19, 6286–6296.

Li, C., and Xu, Q. (2000). Mechanical stress-initiated signal transductions in vascular smooth muscle cells. *Cell. Signal.* 12, 435–445.

Locovei, S., Bao, L., and Dahl, G. (2006). Pannexin 1 in erythrocytes: function without a gap. *Proc. Natl. Acad. Sci. U.S.A.* 103, 7655–7659.

McCullough, W. T., Collins, D. M., and Ellsworth, M. L. (1997). Arteriolar responses to extracellular ATP in striated muscle. *Am. J. Physiol.* 272, H1886–H1891.

Murthy, K. S., Zhou, H., and Makhlouf, G. M. (2002). PKA-dependent activation of PDE3A and PDE4 and inhibition of adenylyl cyclase V/VI in smooth muscle. *Am. J. Physiol. Cell Physiol.* 282, C508–C517.

Olearczyk, J. J., Stephenson, A. H., Lonigro, A. J., and Sprague, R. S. (2004a). Heterotrimeric G protein Gi is involved in a signal transduction pathway for ATP release from erythrocytes. *Am. J. Physiol. Heart Circ. Physiol.* 286, H940–H945.

Olearczyk, J. J., Stephenson, A. H., Lonigro, A. J., and Sprague, R. S. (2004b). NO inhibits signal transduction pathway for ATP release from erythrocytes via its action on heterotrimeric G protein Gi. *Am. J. Physiol. Heart Circ. Physiol.* 287, H748–H754.

Pittman, R. N. (1995). Influence of microvascular architecture on oxygen exchange in skeletal muscle. *Microcirculation* 2, 1–18.

Pittman, R. N. (2005). Oxygen transport and exchange in the microcirculation. *Microcirculation* 12, 59–70.

Pittman, R. N. (2010). Erythrocytes: surveyors as well as purveyors of oxygen? *Am. J. Physiol. Heart Circ. Physiol.* 298, H1637–1638.

Pittman, R. N. (2011). Oxygen gradients in the microcirculation. *Acta Physiol. (Oxf.)* 202, 311–322.

Pittman, R. N., and Duling, B. R. (1973). Oxygen sensitivity of vascular smooth muscle. I. In vitro studies. *Microvasc. Res.* 6, 202–211.

Popel, A. S. (1989). Theory of oxygen transport to tissue. *Crit. Rev. Biomed. Eng.* 17, 257–321.

Roy, T. K., Pries, A. R., and Secomb, T. W. (2012). Theoretical comparison of wall-derived and erythrocyte-derived mechanisms for metabolic flow regulation in heterogeneous microvascular networks. *Am. J. Physiol. Heart Circ. Physiol.* 302, H1945–H1952.

Sobolewski, A., Jourdan, K. B., Upton, P. D., Long, L., and Morrell, N. W. (2004). Mechanism of cicaprost-induced desensitization in rat pulmonary artery smooth muscle cells involves a PKA-mediated inhibition of adenylyl cyclase. *Am. J. Physiol. Lung Cell Mol. Physiol.* 287, L352–L359.

Sprague, R., Bowles, E., Stumpf, M., Ricketts, G., Freidman, A., Hou, W. H., Stephenson, A., and Lonigro, A. (2005). Rabbit erythrocytes possess adenylyl cyclase type II that is activated by the heterotrimeric G proteins Gs and Gi. *Pharmacol. Rep.* 57(Suppl.), 222–228.

Sprague, R. S., Bowles, E. A., Achilleus, D., and Ellsworth, M. L. (2011). Erythrocytes as controllers of perfusion distribution in the microvasculature of skeletal muscle. *Acta Physiol. (Oxf.)* 202, 285–292.

Sprague, R. S., Bowles, E. A., Olearczyk, J. J., Stephenson, A. H., and Lonigro, A. J. (2002). The role of G protein beta subunits in the release of ATP from human erythrocytes. *J. Physiol. Pharmacol.* 53, 667–674.

Sprague, R. S., and Ellsworth, M. L. (2012). Erythrocyte-derived ATP and perfusion distribution: role of intracellular and intercellular communication. *Microcirculation.* doi: 10.1111/j.1549-8719.2012.00158.x.

Sprague, R. S., Ellsworth, M. L., Stephenson, A. H., Kleinhenz, M. E., and Lonigro, A. J. (1998). Deformation-induced ATP release from red blood cells requires CFTR activity. *Am. J. Physiol.* 275, H1726–H1732.

Sprague, R. S., Ellsworth, M. L., Stephenson, A. H., and Lonigro, A. J. (2001). Participation of cAMP in a signal-transduction pathway relating erythrocyte deformation to ATP release. *Am. J. Physiol. Cell Physiol.* 281, C1158–C1164.

Sprague, R. S., Goldman, D., Bowles, E. A., Achilleus, D., Stephenson, A. H., Ellis, C. G., and Ellsworth, M. L. (2010). Divergent effects of low-O(2) tension and iloprost on ATP release from erythrocytes of humans with type 2 diabetes: implications for O(2) supply to skeletal muscle. *Am. J. Physiol. Heart Circ. Physiol.* 299, H566–H573.

Sprague, R. S., Hanson, M. S., Achilleus, D., Bowles, E. A., Stephenson, A. H., Sridharan, M., Adderley, S., Procknow, J., and Ellsworth, M. L. (2009). Rabbit erythrocytes release ATP and dilate skeletal muscle arterioles in the presence of reduced oxygen tension. *Pharmacol. Rep.* 61, 183–190.

Sprague, R. S., Stephenson, A. H., Bowles, E. A., Stumpf, M. S., and Lonigro, A. J. (2006). Reduced expression of G(i) in erythrocytes of humans with type 2 diabetes is associated with impairment of both cAMP generation and ATP release. *Diabetes* 55, 3588–3593.

Sridharan, M., Adderley, S. P., Bowles, E. A., Egan, T. M., Stephenson, A. H., Ellsworth, M. L., and Sprague, R. S. (2010). Pannexin 1 is the conduit for low oxygen tension-induced ATP release from human erythrocytes. *Am. J. Physiol. Heart Circ. Physiol.* 299, H1146–H1152.

Wan, J., Ristenpart, W. D., and Stone, H. A. (2008). Dynamics of shear-induced ATP release from red blood cells. *Proc. Natl. Acad. Sci. U.S.A.* 105, 16432–16437.

Williamson, T., Schwartz, J. M., Kell, D. B., and Stateva, L. (2009). Deterministic mathematical models of the cAMP pathway in *Saccharomyces cerevisiae*. *BMC Syst. Biol.* 3, 70. doi:10.1186/1752-0509-3-70

Xia, J., and Duling, B. R. (1995). Electromechanical coupling and the conducted vasomotor response. *Am. J. Physiol.* 269, H2022–H2030.

Conflict of Interest Statement: The authors declare that the research was conducted in the absence of any commercial or financial relationships that could be construed as a potential conflict of interest.

Received: 01 March 2012; paper pending published: 26 March 2012; accepted: 15 June 2012; published online: 16 July 2012. Citation: Goldman D, Fraser GM, Ellis CG, Sprague RS, Ellsworth ML and Stephenson AH (2012) Toward a multiscale description of microvascular flow regulation: O_2-dependent release of ATP from human erythrocytes and the distribution of ATP in capillary networks. Front. Physio. ***3****:246. doi: 10.3389/fphys.2012.00246*

This article was submitted to Frontiers in Computational Physiology and Medicine, a specialty of Frontiers in Physiology.

frontiers in
PHYSIOLOGY

ORIGINAL RESEARCH ARTICLE
published: 23 July 2012
doi: 10.3389/fphys.2012.00264

A joint computational respiratory neural network-biomechanical model for breathing and airway defensive behaviors

Russell O'Connor[1], Lauren S. Segers[1], Kendall F. Morris[1], Sarah C. Nuding[1], Teresa Pitts[2], Donald C. Bolser[2], Paul W. Davenport[2] and Bruce G. Lindsey[1]*

[1] *Department of Molecular Pharmacology and Physiology, Morsani College of Medicine, University of South Florida, Tampa, FL, USA*
[2] *Department of Physiological Sciences, College of Veterinary Medicine, University of Florida, Gainesville, FL, USA*

Edited by:
Raimond L. Winslow, The Johns Hopkins University, USA

Reviewed by:
Raimond L. Winslow, The Johns Hopkins University, USA
Silvina Ponce Dawson, Universidad de Buenos Aires, Argentina

Correspondence:
Bruce G. Lindsey, Department of Molecular Pharmacology and Physiology, Morsani College of Medicine, University of South Florida, 12901 Bruce B. Downs Blvd., Tampa, FL 33612-4799, USA.
e-mail: blindsey@health.usf.edu

Data-driven computational neural network models have been used to study mechanisms for generating the motor patterns for breathing and breathing related behaviors such as coughing. These models have commonly been evaluated in open loop conditions or with feedback of lung volume simply represented as a filtered version of phrenic motor output. Limitations of these approaches preclude assessment of the influence of mechanical properties of the musculoskeletal system and motivated development of a biomechanical model of the respiratory muscles, airway, and lungs using published measures from human subjects. Here we describe the model and some aspects of its behavior when linked to a computational brainstem respiratory network model for breathing and airway defensive behavior composed of discrete "integrate and fire" populations. The network incorporated multiple circuit paths and operations for tuning inspiratory drive suggested by prior work. Results from neuromechanical system simulations included generation of a eupneic-like breathing pattern and the observation that increased respiratory drive and operating volume result in higher peak flow rates during cough, even when the expiratory drive is unchanged, or when the expiratory abdominal pressure is unchanged. Sequential elimination of the model's sources of inspiratory drive during cough also suggested a role for disinhibitory regulation via tonic expiratory neurons, a result that was subsequently supported by an analysis of *in vivo* data. Comparisons with antecedent models, discrepancies with experimental results, and some model limitations are noted.

Keywords: biomechanical model, brainstem, breathing, chest wall dynamics, computational neural network model, cough, inspiratory drive, neuromechanical model simulation

INTRODUCTION

The neural mechanisms that regulate and coordinate breathing and respiratory-related behaviors such as coughing are not well understood. This lack of knowledge hampers elucidation of pathophysiological deficits in airway protection and impedes development of new therapeutic approaches for dystussia that occur with neurological disorders (Suárez et al., 2002; McCool, 2006). Computational neural network models for breathing and the neurogenesis of cough inferred from *in vivo* experiments have iteratively aided prediction and refinement of hypotheses for further *in vivo* testing (Shannon et al., 1998, 2000; Baekey et al., 2001; Rybak et al., 2008; Poliaček et al., 2011). Such data-driven models, based in part on elements and connectivity inferred from simultaneous extracellular recordings of many brainstem neurons (e.g., Segers et al., 2008; Ott et al., 2012), have largely been evaluated in either open loop conditions or with feedback of lung volume simply represented as a filtered version of the motor output (Lindsey et al., 2012). While useful, these approaches have precluded model-based assessment of the potential influence of mechanical properties of the musculoskeletal system on respiratory motor pattern generation and cough effectiveness (Smith et al., 2012). More generally, neuromechanical models can provide a framework for estimating and predicting the extent to which motor patterns are constrained and influenced by mechanical properties and muscle synergies (Chiel et al., 2009).

A model that relates a respiratory neural output to mechanical outputs has been available for some time (Riddle and Younes, 1981; Younes and Riddle, 1981; Younes et al., 1981) and remains an important element in contemporary models of the respiratory system (Cheng et al., 2010; Cheng and Khoo, 2012). However, the Younes–Riddle model with its single inspiratory neural output and single state variable (lung volume) lacks features essential for model-based assessment of the respective contributions and interactions of neural and biomechanical mechanisms during cough. We have developed a respiratory neural network model with inspiratory (phrenic), expiratory (lumbar), and laryngeal neural outputs and required a mechanical model with corresponding inputs to control the abdominal, diaphragm, and laryngeal muscles. Moreover, it is well known that a given lung volume can be achieved with different configurations of the rib cage and abdomen (Konno and Mead, 1967; Younes and Riddle, 1981), and with separate neural control of the diaphragm and abdominal wall muscles

as in our network model, all of these configurations can potentially be achieved. Thus, the first aim of the work reported here was to develop a model of the mechanical respiratory system that includes separate muscle models for the diaphragm, abdominal wall, and larynx, and two state variables to represent the thoracoabdominal configuration.

Our second aim was to link the resulting mechanical subsystem to an enhanced integrate and fire (IF) neural network model of the brainstem network for respiratory motor pattern generation and to assess the integrated system's behavior with muscle activation parameters for eupneic conditions. A third related objective was to extend the simulations to include evoked coughs in order to evaluate the model's performance in response to defined perturbations that enhance or reduce inspiratory drive. This latter goal was motivated in part by evidence that changes in the inspiratory or "operating" volume can influence airflow during the expulsive phase of the cough (Smith et al., 2012).

An additional impetus for the third aim came from results of recent model simulations, which suggested that elevated systemic arterial blood pressure – such as may occur during coughing (Sharpey-Schafer, 1953) – attenuates cough inspiratory drive, a result supported by coordinated *in vivo* experiments (Poliaček et al., 2011). The network model used in the present work builds upon that and other recent prior efforts (Rybak et al., 2008). The network incorporates multiple circuit paths and operations for tuning inspiratory drive that have been inferred from spike train cross-correlation feature sets (Lindsey et al., 1998; Shannon et al., 2000; Segers et al., 2008; Ott et al., 2012). These circuits include parallel channels for modulation of inspiratory phase activity in "tonic" expiratory neurons that inhibit premotor inspiratory bulbospinal neurons and drive.

In the course of sequentially eliminating sources of inspiratory drive for cough in the neuromechanical model, we also noted a contribution of tonic expiratory neuron activity to modulation of inspiratory phase drive during cough. This disinhibitory regulation predicted from the modeling results was subsequently supported by an analysis of *in vivo* data as described in a companion report (Segers et al., 2012).

MATERIALS AND METHODS

Neural circuit components were derived from previously described respiratory network models of discrete "IF" populations after MacGregor (1987) and a "hybrid IF burster" population with Hodgkin–Huxley style equations after Breen et al. (2003). These models were developed iteratively with *in vivo* experiments that both guided model development and tested model predictions, as detailed in Rybak et al. (2008) and Poliaček et al. (2011). The enhanced network model used herein is described further in the Results.

Biomechanical model elements were developed using parameters derived from published work as described in Results. Of particular importance was the work of Grassino et al. (1978), who measured transdiaphragmatic pressure and diaphragm activation while controlling the thoracoabdominal configuration, making it possible to estimate the effect of rib cage motion on the abdominal volume. Our abdominal wall model is based on measurements of the curvature of the abdomen by Song et al. (2006) taken during insufflation for laparoscopic surgery. The rib cage, lung, and diaphragm volumes are derived from the measurements of Cluzel et al. (2000), who measured them from MRI's. The thoracoabdominal configuration at extreme and resting supine lung volumes are from Konno and Mead (1967).

Models were implemented using a program package written in the C language for the UNIX environment. Simulations were run on 64-bit Intel multiprocessor-based computers under the Linux operating system. The GNU Scientific Library was used to solve the differential equations of the biomechanical model, to find the roots of the implicit model equations, to do the abdominal volume integration, and for a spline approximation of the abdominal volume function.

For each condition of the linked neural network and biomechanical model, four trials were run with different random number seeds for the stochastic network model. A pairwise two-sided t-test with non-pooled SD was used for each variable, and the p-values were adjusted for multiple testing (Holm, 1979). A difference was considered significant if the adjusted p-value was less than 0.05.

RESULTS

The results are presented in two main parts. Section "Mechanical Model Implementation: Respiratory Muscles, Chest Wall, and Lungs" details the biomechanical model. Section "Brainstem Network Model Architecture and System Performance When Linked to the Biomechanical Model" describes the linkage between the biomechanical and neural network models and neuromechanical system behavior during various perturbations of the network.

MECHANICAL MODEL IMPLEMENTATION: RESPIRATORY MUSCLES, CHEST WALL, AND LUNGS

The biomechanical model described below converts respiratory neural outputs in the form of spike trains representing lumbar, phrenic, expiratory laryngeal, and inspiratory laryngeal motor neuron activity generated by a stochastic model of the brainstem respiratory network deterministically into mechanical outputs such as lung volume, tracheal flow, and alveolar pressure for a supine male human. Lung volume is fed back to the network model to simulate pulmonary stretch receptors. The mechanical model components include (i) three-element Hill muscle models of the diaphragm and abdominal muscles (Hill, 1938), (ii) a model of the larynx based on the results of Tully et al. (1990, 1991) and Rohrer's (1915) equation, and (iii) lung/diaphragm/ribcage/abdomen volume relationships modeled on the data of Grassino et al. (1978) and the analysis of Mead and Loring (1982).

The first two equations represent the entire mechanical model. Each term is a function of the motor outputs of the network model (u_{di}, u_{ab}, and u_{lm}), and the diaphragm and abdominal wall volumes (V_{di} and V_{ab}) and their time derivatives ($\dot{V}_{di}$ and $\dot{V}_{ab}$), and is defined by the subsequent equations. The parameters referenced in the model equations are listed in **Table 1**.

Pressure balance on the rib cage

In Eq. 1, P_{pl} is the pleural pressure seen by the interior surface of the rib cage, P_{ab-pl} corrects for the fact that the rib cage sees abdominal pressure in the zone of apposition, $F_{di}\sigma_{di}$ is the equivalent pressure due to the insertional forces of the diaphragm on

Table 1 | Parameters used in the biomechanical model.

Parameter	Definition	Value	Units	Source
FREE PARAMETERS USED IN THE MODEL				
C_1	Rib cage contribution to abdominal volume	0.369	Dimensionless	Derived from Grassino et al. (1978)
C_{ab}	Compliance of the abdominal wall	0.108	L/cmH_2O	Derived from Estenne et al. (1985)
C_L	Compliance of the lung	0.201	L/cmH_2O	Derived from Permutt and Martin (1960)
c_t	Transverse chord of the abdominal wall	0.32	m	Derived from Song et al. (2006)
D	Diameter of the trachea	18	mm	Derived from Baier et al. (1977) and Kamel et al. (2009)
f_a^{TLC}	Obligatory ring fraction	0.15	Dimensionless	Mead and Loring (1982)
F_{CEmax}	Maximal force capacity of the external oblique	33	N	Ratnovsky et al. (2003)
F_{di}	Fraction of the diaphragm pressure expanding the rib cage via insertional forces	0.15	Dimensionless	Derived from Loring and Mead (1982)
k	Conversion factor from force to surface tension in abdominal muscle	0.68	m cmH_2O/N	Derived from De Troyer et al. (1990) and Ratnovsky et al. (2003)
L_{CEO}	Length of human transversus abdominis	19.1	cm	Gaumann et al. (1999)
P_{ica}^{abTLC}	Maximal expiratory pressure due to intercostal and accessory muscles at total lung capacity (TLC)	−135	cmH_2O	Derived from Ratnovsky et al. (2008)
R_{ab}	Passive resistance of the abdominal wall	1.5	cmH_2O/(L/s)	Derived from Barnas et al. (1989)
R_{di}	Passive resistance of the diaphragm	6	cmH_2O/(L/s)	Derived from Barnas et al. (1989)
R_{rc}	Passive resistance of the rib cage	2.7	cmH_2O/(L/s)	Derived from Barnas et al. (1989)
V_c	Mediastinal plus lung blood and tissue volume	1.756	L	Derived from Cluzel et al. (2000)
V_{CEmax}	Maximal contractile velocity of the external oblique	34.7	cm/s	Ratnovsky et al. (2003)
V_{di}^{FRC}	Volume under diaphragm at functional residual capacity (FRC)	2.967	L	Derived from Cluzel et al. (2000)
$\dot{V}_{di}^{max}$	Maximal rate of change of volume under diaphragm	2.449	L/s	Derived from Goldman et al. (1978) and Chow and Darling (1999)
FREE PARAMETERS USED IN CALCULATED PARAMETERS				
V_L^{FRC}	Volume of the lung at FRC	2.29	L	Cluzel et al. (2000)
V_{rc}^{kmFRC}	Volume of the rib cage at FRC as a fraction of VC relative to residual volume (RV)	0.1282	Dimensionless	Konno and Mead (1967), Figure 14
V_{ab}^{kmFRC}	Volume of the abdominal wall at FRC as a fraction of VC relative to RV	0.0400	Dimensionless	Konno and Mead (1967), Figure 14
V_{ab}^{kmTLC}	Volume of the abdominal wall at TLC as a fraction of VC relative to RV	0.3391	Dimensionless	Konno and Mead (1967), Figure 14
VC	Vital capacity	5.370	L	Roca et al. (1998)
σ_{di}^{RV}	Passive recoil pressure of the diaphragm at RV	20	cmH_2O	Derived from Agostoni et al. (1966), Grassino et al. (1978) and Siafakas et al. (1979)
V_{rc}^{FRC}	Volume of the rib cage at FRC	7.013	L	Derived from Cluzel et al. (2000)
V_{rc}^{kmTLC}	Volume of the rib cage at TLC as a fraction of VC relative to RV	0.6609	Dimensionless	Konno and Mead (1967), Figure 14
f_{di}	Ratio of diaphragm length at TLC to RV	0.65	Dimensionless	Smith and Bellemare (1987)
C_{rc}	Compliance of the rib cage	0.110	L/cmH_2O	Derived from Gilroy et al. (1985)

(Continued)

Table 1 | Continued

Parameter	Definition	Value	Units	Source
CALCULATED PARAMETERS USED IN CALCULATED PARAMETERS				
V_{ab}^{RV}	Volume behind abdominal wall at RV		L	Eqs 32 and 33
V_{L}^{RV}	Volume of the lung at RV		L	Eq. 34
σ_{L}^{RV}	Passive recoil pressure of the lung at RV		cmH_2O	Eq. 35
σ_{ab}^{RV}	Passive recoil pressure of the abdominal wall at RV		cmH_2O	Eq. 36
V_{ab}^{FRC}	Volume behind abdominal wall at FRC		L	Eq. 37
V_{di}^{RV}	Volume under diaphragm at RV		L	Eq. 38
V_{ab}^{TLC}	Volume behind abdominal wall at TLC		L	Eq. 39
V_{L}^{TLC}	Volume of the lung at TLC		L	Eq. 40
σ_{L}^{TLC}	Passive recoil pressure of the lung at TLC		cmH_2O	Eq. 41
σ_{ab}^{TLC}	Passive recoil pressure of the abdominal wall at TLC		cmH_2O	Eq. 42
σ_{di}^{TLC}	Passive recoil pressure of the diaphragm at TLC		cmH_2O	Eq. 43
σ_{rc}^{TLC}	Passive recoil pressure of the rib cage at TLC		cmH_2O	Eq. 44
σ_{rc}^{RV}	Passive recoil pressure of the rib cage at RV		cmH_2O	Eq. 45
f_{a}^{RV}	Fraction of the rib cage exposed to abdominal pressure at RV		Dimensionless	Eq. 46
CALCULATED PARAMETERS USED IN THE MODEL				
V_{sum}	Sum of diaphragm, rib cage, and abdominal wall volume contributions		L	Eq. 47
V_{ab0}	Volume behind abdominal wall at zero passive tension		L	Eqs 32 and 33
V_{L0}	Volume of the lung at zero passive tension		L	Eq. 48
K_{di}^{psv}	Coefficient of passive diaphragm recoil pressure		cmH_2O/L^2	Eq. 49
L_{di}^{min}	Ratio of diaphragm length at zero volume to resting length		Dimensionless	Eq. 50
P_{ica}^{abRV}	Maximal expiratory pressure due to intercostal and accessory muscles at TLC		cmH_2O	Eq. 51
P_{ica}^{diTLC}	Maximal inspiratory pressure due to intercostal and accessory muscles at TLC		cmH_2O	Eq. 52
σ_{di}^{max}	Maximum active recoil pressure of the diaphragm		cmH_2O	Eq. 53
σ_{rc}^{add}	Passive rib cage recoil pressure midway between volume limits		cmH_2O	Eq. 54
σ_{rc}^{mul}	Rib cage sigmoid compliance coefficient		cmH_2O	Eq. 55
V_{di0}	Volume under diaphragm at zero tension		L	Eq. 56
V_{di}^{TLC}	Volume under diaphragm at TLC		L	Eq. 57
V_{rc}^{max}	Upper limit of rib cage volume		L	Eq. 58
V_{rc}^{min}	Lower limit of rib cage volume		L	Eq. 59
V_{rc}^{RV}	Volume of the rib cage at RV		L	Eq. 60
V_{rc}^{TLC}	Volume of the rib cage at TLC		L	Eq. 61
V_{rc0}	Volume of the rib cage at zero tension		L	Eq. 62

the lower ribs, P_{ica} is the equivalent pressure due to the intercostal and accessory muscles, and σ_{rc} is the recoil pressure of the rib cage that balances the sum of the other pressures.

$$P_{pl} + P_{ab-pl} + F_{di}\sigma_{di} + P_{ica} = \sigma_{rc} \quad (1)$$

Pressure balance on the diaphragm

In Eq. 2, σ_{ab} is the abdominal pressure, the excess of which over the pleural pressure must be balanced by σ_{di}, the recoil pressure of the diaphragm.

$$\sigma_{ab} - P_{pl} = \sigma_{di} \quad (2)$$

Pleural pressure

In Eq. 3, tracheal flow ($\dot{V}_L$) is the derivative of lung volume. R_{rs} is the resistance of the airway, which when multiplied by $\dot{V}_L$ gives the pressure drop, by the hydraulic analog of Ohm's law. σ_L is the recoil pressure of the lung.

$$P_{pl} = -R_{rs}\dot{V}_L - \sigma_L \tag{3}$$

Lung volume

Lung volume is a function of V_{di} and V_{ab}. Diaphragm volume, V_{di}, is the volume above the level of the diaphragm insertions on the rib cage and below the dome of the diaphragm. Abdominal wall volume, V_{ab}, is the volume between the abdominal wall and a frontal plane that coincides with the contracted position of the abdominal wall.

It has been commonly assumed that the abdominal contents are incompressible and that the abdominal cavity has only two movable walls – the diaphragm and the abdominal wall – and that therefore a displacement in one must be met by an equal and opposite displacement of the other (Grimby et al., 1976; Grassino et al., 1978; Macklem et al., 1978; Loring and Mead, 1982; Lichtenstein et al., 1992; Fitz-Clarke, 2007); in other words, that $V_{di} + V_{ab} = V_{sum}$ (V_{sum} constant). Under this assumption, the abdominal volume completely determines the volume under the diaphragm, V_{di}. Following Lichtenstein et al. (1992), V_{di} determines the static contractile pressure generated by the diaphragm at a given activation. However, experimental data (Grassino et al., 1978, Figure 4) show that both rib cage volume and abdominal volume affect this pressure. Therefore, in our model, we added a term, $C_1 V_{rc}$, to the equation, allowing the rib cage and the abdominal wall to independently alter the volume under the diaphragm, effectively adding a third movable wall to the abdominal container, as discussed by Mead and Loring (1982).

The value of C_1 was determined by fitting our model to published data (Grassino et al., 1978, Figure 4) giving diaphragm pressure as a function of rib cage and abdominal volume at a fixed diaphragm activation. Given a value of C_1, our model equations will calculate the diaphragm pressure from the volumes. We then found the value of C_1 that was the best fit of the calculated pressure values to the measured values. The resulting equation is $V_{di} + C_1 V_{rc} + V_{ab} = V_{sum}$, which together with Eq. 20, gives us Eq. 4 for lung volume (V_L).

$$V_L = \frac{V_{sum} - (1 + C_1)\, V_{di} - V_{ab} - C_1 V_c}{C_1} \tag{4}$$

Airway resistance

Rohrer's equation was used to calculate airway resistance (Rohrer, 1915; Hey and Price, 1982). The equation Pressure $= K_1 \cdot \text{Flow} + K_2 \cdot \text{Flow}^2$ or, dividing through by flow, Resistance $= K_1 + K_2\,|\text{Flow}|$ was applied twice, once for laryngeal resistance ($k_1 + k_2|\dot{V}_L|$) and once for the resistance of the oropharynx and lower airway ($0.72 + 0.44|\dot{V}_L|$), to give Eq. 5. We used a value of $K_2 = 0.44$ for the oropharynx and lower airway based on the assumption that K_2 is 0 for the oropharynx (Renotte et al., 1998; Eq. 8), and 0.44 for the lower airway (Renotte et al., 1998, Table 2). Assuming K_1 for the larynx is negligible during quiet breathing (see below), we used 0.34 for the lower airway and 0.38 for the oropharynx (Renotte et al., 1998, Table 2), for a total of 0.72.

The values of k_1 and k_2 for the larynx depend on the diameter of the glottis, as shown in Eqs 6–8. The parameter D is the diameter of the human trachea. The variable u_{lm} is the net laryngeal muscle activation, ranging from −1 (closed glottis) to 1 (open glottis). The variable d is the diameter of the glottis, or more precisely, the diameter of a circle with the same area as the opening of the glottis. The resting diameter (when $u_{lm} = 0$) is taken to be 10.9 mm (Baier et al., 1977; Brancatisano et al., 1983; D'Urzo et al., 1988), and is assumed (see Eq. 8) to change in proportion to u_{lm} (Tully et al., 1990, 1991).

The coefficient k_2 given by Eq. 7 is calculated using the equation for flow through an orifice (Simpson, 1968, Table II). The value of k_2 for the upper airway is different for inspiration and expiration (Renotte et al., 1998, Table 2), which we assume is due to changes in d. Assuming equal excursions from the resting diameter, we solved for the coefficient that would give us the reported values of k_2, and got 0.167. This approach resulted in a resting value for k_2 of 0.681.

We calculated the ratio of the mean resting value of k_1 to the mean resting value of k_2 (Tully et al., 1990, Table 2), and multiplied the ratio by 0.681 to get a resting value of k_1 of 0.0035 for the larynx, which is small relative to K_1 for the rest of the airway, justifying our assumption above that K_1 for the larynx is negligible during quiet breathing.

The Darcy–Weisbach equation for pressure loss in a pipe and the Darcy friction factor for laminar flow tell us that the resistance is proportional to $1/d^4$ (Kreith et al., 2004), which we use in Eq. 6 for k_1. Plugging in the resting value of k_1 determined above and the resting value of d, we solved for the coefficient, which gives us 49.6.

$$R_{rs} = k_1 + 0.72 + (k_2 + 0.44)\,\dot{V}_L \tag{5}$$

$$k_1 = \frac{49.6}{d^4} \tag{6}$$

$$k_2 = 0.167\left(\frac{D^2}{d^4} + \frac{d^2}{D^2} - 1\right) \tag{7}$$

$$d = \begin{cases} D, & u_{lm} > \frac{71}{109} \\ 10.9\,(1 + u_{lm}), & -1 \le u_{lm} \le \frac{71}{109} \\ 0, & u_{lm} < -1 \end{cases} \tag{8}$$

Abdominal pressure on the rib cage

A fraction f_a of the rib cage is exposed to abdominal pressure rather than pleural pressure. The recoil pressure of the diaphragm, σ_{di}, is the difference between abdominal pressure and pleural pressure, so P_{ab-pl} adjusts the pressure seen by the rib cage for this difference.

$$P_{ab-pl} = f_a \sigma_{di} \tag{9}$$

Abdominal fraction of the rib cage

At total lung capacity (TLC), none of the diaphragm is apposed to the rib cage (Mead and Loring, 1982), so we assumed that at all

lung volumes, a portion of V_{di} equal to V_{di} at TLC (V_{di}^{TLC}) does not contribute to the zone of apposition. The remainder ($V_{di} - V_{di}^{TLC}$) is divided by the remainder plus the lung volume ($V_{di} - V_{di}^{TLC} + V_L$) to give an estimate of the fraction of the rib cage surface above the diaphragm insertions that is exposed to abdominal pressure.

The "obligatory ring" below the diaphragm insertions, which is about 15% of the rib cage surface (Mead and Loring, 1982), is always exposed to abdominal pressure, and is represented by f_a^{TLC} in Eq. 10. Our rib cage volume, V_{rc}, is the volume above a plane through the diaphragm attachments (Cluzel et al., 2000, Figure 3).The estimate of 15% of the rib cage surface was in the context of a different definition of rib cage volume in which a change in rib cage volume is equal to the change in lung volume with the abdominal wall held still (Konno and Mead, 1967). This alternative definition implies a larger volume for the rib cage because it includes parts below the diaphragm insertions. From our volume equations, this means that rib cage volume is larger than ours by a factor of $(1 + C_1)$, so we divided the previously calculated fraction of the smaller rib cage by $(1 + C_1)$ to turn it into a fraction of the larger rib cage before adding it to f_a^{TLC}.

$$f_a = \frac{1}{1 + C_1}\left(\frac{V_{di} - V_{di}^{TLC}}{V_{di} - V_{di}^{TLC} + V_L}\right) + f_a^{TLC} \tag{10}$$

Recoil pressure of the lung

Equation 11 assumes a linear relationship between lung volume and recoil pressure. C_L is lung compliance. V_{L0} is the lung volume at zero recoil pressure, which we took to be equal to the residual volume (RV) after a maximal exhalation, the small recoil pressure remaining at RV being close enough to zero for our purposes (Permutt and Martin, 1960; Harris, 2005).

$$\sigma_L = \frac{V_L - V_{L0}}{C_L} \tag{11}$$

Recoil pressure of the diaphragm

In Eq. 12, the term $u_{di}\sigma_{di}^{max}F_{fl}^{di}F_{fv}^{di}$ corresponds to the Hill muscle model (Ratnovsky et al., 2003, Eq. A6), except that σ_{di}^{max} is a pressure rather than a force and F_{fl}^{di} and F_{fv}^{di} are functions of volume and its derivative (flow), respectively, rather than length and velocity.

We substituted pressure for force because, by Laplace's (1808) Law, the pressure is proportional to the force when the curvature is constant, and the curvature of the human diaphragm dome does not change significantly with volume (Braun et al., 1982). Moreover, there is a constant ratio between diaphragm force and pressure in the dog (Kim et al., 1976).

Our substitution of volume for length (with an offset) is supported by the observation that the relationship between diaphragm pressure and length is not clearly different from linear when measured at RV, functional residual capacity (FRC), and TLC (Cluzel et al., 2000). To the extent that the action of the diaphragm resembles that of a piston (Kim et al., 1976), this linearity is expected. There is precedent for a Hill-style model in terms of pressure and flow for the respiratory system (Younes and Riddle, 1981).

In Eq. 12, u_{di} is phrenic activation of the diaphragm; σ_{di}^{max} is static diaphragm recoil pressure at optimum length and maximum activation; $R_{di}\dot{V}_{di}$ is the pressure due to the passive resistance of the diaphragm.

$$\sigma_{di} = u_{di}\sigma_{di}^{max}F_{fl}^{di}F_{fv}^{di} + \sigma_{di}^{psv} + R_{di}\dot{V}_{di} \tag{12}$$

Passive recoil pressure of the diaphragm

In Eq. 13, σ_{di}^{psv} is the passive transdiaphragmatic pressure as a function of diaphragm volume. This pressure is taken to be zero at resting diaphragm volume V_{di}^{FRC} (Agostoni and Rahn, 1960) and below, and quadratic above (Reid et al., 1987).

$$\sigma_{di}^{psv} = \begin{cases} K_{di}^{psv}.\left(V_{di} - V_{di}^{FRC}\right)^2, & V_{di} > V_{di}^{FRC} \\ 0, & V_{di} \le V_{di}^{FRC} \end{cases} \tag{13}$$

Volume-pressure relationship of the diaphragm

In Eq. 14, F_{fl}^{di} is the static pressure-volume relationship of the diaphragm (corresponding to Ratnovsky et al., 2003, Eq. A7 with the relative length replaced by a linear function of volume as described above). The parameter V_{di0} is the volume under the diaphragm at the resting length. This is taken to be equal to the diaphragm volume at RV, based on the observation that the "highest Pdi twitch amplitude was recorded at RV" (Smith and Bellemare, 1987). The parameter L_{di}^{min} is the length of the diaphragm at zero volume (i.e., when the diaphragm is flat) divided by the resting length, and is calculated by assuming that the length of the diaphragm at TLC is 65% of that at RV (Smith and Bellemare, 1987).

$$F_{fl}^{di} = \exp\left(-0.5\left(\frac{\frac{1-L_{di}^{min}}{V_{di0}}V_{di} + L_{di}^{min} - 1.05}{0.19}\right)^2\right) \tag{14}$$

Pressure-flow relationship of the diaphragm

In Eq. 15, F_{fv}^{di} is the pressure-flow relationship of the diaphragm, with the velocity replaced by flow as discussed above (Hatze, 1981; Rosen et al., 1999; Artemiadis and Kyriakopoulos, 2005). The variable $\dot{V}_{di}$ is the time derivative of the volume under the diaphragm. The maximum rate of change of diaphragm volume, $\dot{V}_{di}^{max}$, was derived from data which gives transdiaphragmatic pressure as a function of flow at several levels of diaphragm activation up to 45% (Goldman et al., 1978, Figure 6). Because the rib cage was held still, the flow represents the rate of change of diaphragm volume. Fitting the curves to a Hill-style relation between pressure and flow (Younes and Riddle, 1981), there is a maximum flow (where the pressure goes to zero) for each level of diaphragm activation. Experimental results suggest that the maximum flow increases somewhat linearly to 80% activation and then levels off (Chow and Darling, 1999). We used that assumption together with the results for the maximum flow at lower activations to compute a maximum flow at 100% activation, which we use for $\dot{V}_{di}^{max}$.

$$F_{fv}^{di} = \frac{0.1433}{0.1074 + \exp\left(-1.409\sinh\left(3.2\frac{\dot{V}_{di}}{\dot{V}_{di}^{max}} + 1.6\right)\right)} \tag{15}$$

Pressure of the intercostal and accessory muscles

In Eq. 16, P_{ica} is the effective pressure generated by the intercostal and accessory muscles; positive values act to expand the rib cage.

In Eq. 17, P_{ica}^{di} is the pressure due to the action of the inspiratory intercostals, which are assumed to be inactive when the diaphragm volume is above V_{di}^{FRC} (low lung volumes). Below V_{di}^{FRC}, the pressure exerted by the inspiratory intercostals is assumed to be proportional to the activation of the diaphragm (u_{di}), and the proportionality constant itself is assumed to scale linearly from 0 at V_{di}^{FRC} to its maximum value of P_{ica}^{diTLC} at V_{di}^{TLC}. The parameter P_{ica}^{diTLC} was calculated as the pressure necessary to complete the pressure balance on the rib cage at TLC.

In Eq. 18, P_{ica}^{ab} is the pressure due to the action of the expiratory intercostals, which is assumed to be proportional to the abdominal muscle activation (u_{ab}); the proportionality constant itself is assumed to scale linearly with the rib cage volume, changing from P_{ica}^{abRV} at RV to P_{ica}^{abTLC} at TLC. In Eq. 18, P_{ica}^{abTLC} is the pressure due to the expiratory intercostals at TLC and maximal abdominal activation. This parameter's value was calculated by taking the mean male maximal mouth pressure at TLC (from Ratnovsky et al., 2008, Table 1) and subtracting it from the rib cage recoil pressure at TLC. P_{ica}^{abRV} is the pressure due to the expiratory intercostals at RV and maximal abdominal activation. We calculated this parameter by solving the model equations for P_{ica} while assuming RV conditions. This gives us the intercostal pressure necessary to reach RV.

$$P_{ica} = P_{ica}^{di} + P_{ica}^{ab} \tag{16}$$

$$P_{ica}^{di} = \begin{cases} u_{di} P_{ica}^{diTLC} \frac{V_{di} - V_{di}^{FRC}}{V_{di}^{TLC} - V_{di}^{FRC}}, & V_{di} < V_{di}^{FRC} \\ 0, & V_{di} \geq V_{di}^{FRC} \end{cases} \tag{17}$$

$$P_{ica}^{ab} = u_{ab} \left(P_{ica}^{abRV} + \frac{V_{rc} - V_{rc}^{RV}}{V_{rc}^{TLC} - V_{rc}^{RV}} \left(P_{ica}^{abTLC} - P_{ica}^{abRV} \right) \right) \tag{18}$$

Recoil pressure of the rib cage

The volume of the rib cage is assumed to be a sigmoid function of the recoil pressure of the rib cage, σ_{rc}. With increasing pressure the volume asymptotically approaches a maximum (V_{rc}^{max}), and with decreasing pressure it asymptotically approaches a minimum (V_{rc}^{min}). A generalized logistic function is used for the sigmoid, giving V_{rc} as a function of σ_{rc}; that equation is solved for σ_{rc} to give the first part of Eq. 19. The final term of Eq. 19 is the pressure due to the passive resistance of the rib cage (R_{rc}) and the rate of change of its volume ($\dot{V}_{rc}$) The parameter σ_{rc}^{mul} controls the maximum slope of the sigmoid; the slope is the compliance of the rib cage. It is calculated to make the compliance equal to $C_{rc}/(1 + C_1)$. The factor of $(1 + C_1)$ appears because C_{rc} is for a rib cage volume defined differently than V_{rc}. C_{rc} is the compliance of the rib cage, an average of values for three sitting subjects (Gilroy et al., 1985, Table 1).

$$\sigma_{rc} = \sigma_{rc}^{mul} \log \left(\frac{V_{rc}^{max} - V_{rc}}{V_{rc} - V_{rc}^{min}} \right) + \sigma_{rc}^{add} + R_{rc} \dot{V}_{rc} \tag{19}$$

Volume of the rib cage

The rib cage volume (V_{rc}) is the sum of the lung volume (V_L), the volume under the diaphragm (V_{di}), and the volume of the mediastinum and the lung blood and tissue (V_c).

$$V_{rc} = V_L + V_{di} + V_c \tag{20}$$

Recoil pressure of the abdominal wall

The abdominal wall is modeled as a surface with a circular segment cross-section in each transverse plane, all with the same radius, and a circular segment cross-section in each sagittal plane, all with another radius. The volume behind the abdominal wall, V_{ab}, is bounded by this surface and by a frontal plane. The values for the sagittal (r_s) and transverse (r_t) radii were derived from measurements taken during insufflation for laparoscopic surgery in humans (see Figure 3, Song et al., 2006). We fit exponential curves to the data points and the resulting relationship between the fitted sagittal and transverse radii was found to be well approximated by a linear function: $r_s = 8.00\ r_t - 1.10$. The length of the longest transverse chord in the bounding frontal plane (c_t) was found which gave the volume change stated in the paper.

In Eq. 21, $u_{ab} F_{CEmax} F_{fl}^{ab} F_{fv}^{ab}$ is the Hill muscle model equation (Ratnovsky et al., 2003, Eq. A6); u_{ab} is the activation of the diaphragm by the lumbar motor neurons; F_{CEmax} is the maximal force capacity of the contractile element for a 1.5 cm^2 cross-section of canine external oblique muscle (Ratnovsky et al., 2003, Table 1). The constant k converts from a force to a surface tension, and $(1/r_s + 1/r_t)$ converts the surface tension to a pressure, using the Law of Laplace (Laplace, 1808). The second term on the right, $(V_{ab} - V_{ab0})/C_{ab}$, is the passive recoil pressure of the abdominal wall. V_{ab0} is the volume behind the abdominal wall at which the recoil pressure is 0. This was taken to be equal to V_{ab}^{FRC}, since we assume a supine position. C_{ab} is the compliance of the abdominal wall. The final term is the pressure due to the passive resistance of the abdominal wall (R_{ab}) and the rate of change of abdominal volume ($\dot{V}_{ab}$).

$$\sigma_{ab} = u_{ab} F_{CEmax} F_{fl}^{ab} F_{fv}^{ab} \cdot \left(\frac{k}{r_t} + \frac{k}{r_s} \right) + \frac{V_{ab} - V_{ab0}}{C_{ab}} + R_{ab} \dot{V}_{ab} \tag{21}$$

In Eq. 22, F_{fl}^{ab} is the static force-length relationship of the abdominal wall (Ratnovsky et al., 2003, Eq. A7); L_{CE} is the length of the transversus abdominis; L_{CE0} is its resting length.

$$F_{fl}^{ab} = \exp \left(-0.5 \left(\frac{\frac{L_{CE}}{L_{CE0}} - 1.05}{0.19} \right)^2 \right) \tag{22}$$

In Eq. 23, F_{fv}^{ab} is the force-velocity relationship of the abdominal wall muscles (Hatze, 1981; Rosen et al., 1999; Artemiadis and Kyriakopoulos, 2005). The variable $\dot{L}_{CE}$ is the velocity of the contractile element (the time derivative of L_{CE}) and the parameter V_{CEmax} is the maximal contractile velocity of canine external oblique muscle (Ratnovsky et al., 2003, Table 1).

$$F_{fv}^{ab} = \frac{0.1433}{0.1074 + \exp \left(-1.409 \sinh \left(3.2 \frac{\dot{L}_{CE}}{V_{CEmax}} + 1.6 \right) \right)} \tag{23}$$

Length-volume relationship of the abdominal wall

Equations 24 through 31 calculate the length of the abdominal muscle (L_{CE}) from the volume behind the abdominal wall (V_{ab}). Eqs 26 through 31 calculate V_{ab} as a function of r_t (the transverse radius); Eq. 25 uses the inverse of the resulting function to calculate r_t from V_{ab}; Eq. 24 calculates L_{CE} from r_t. In practice, the function $V_{ab}(r_t)$ is pre-calculated, and approximated and inverted with a spline, and the spline is used to evaluate $r_t(V_{ab})$ during simulation.

$$L_{CE} = 100 r_t \sin^{-1}\left(\frac{c_t}{2r_t}\right) \tag{24}$$

$$r_t\left(V_{ab}\right) = \begin{cases} V^{-1}\left(V_{ab}\right), & V_{ab} > 0 \\ 0.5c_t, & V_{ab} \le 0 \end{cases} \tag{25}$$

$$V\left(r_t\right) = \int_{-c_s/2}^{c_s/2} A\left(r_t, y\right) dy \tag{26}$$

In Eq. 27, the Pythagorean Theorem is applied in the midsagittal plane to get c_s, the length of the chord that connects the ends of the abdominal wall in the frontal plane that serves as a boundary of the abdominal wall volume.

$$c_s = 2\sqrt{{r_s}^2 - \left(h_0 - r_s\right)^2} \tag{27}$$

In Eq. 28, the Pythagorean Theorem is applied in a transverse plane to get h_0, the distance from the peak of the abdominal wall to the frontal plane that serves as a boundary of the abdominal wall volume.

$$h_0 = r_t - \sqrt{r_t^2 - \left(\frac{c_t}{2}\right)^2} \tag{28}$$

In Eq. 29, the formula for the area of a circular segment is applied in the transverse plane at a distance y from the peak of the abdominal wall to get the area between the abdominal wall and the boundary frontal plane.

$$A = \frac{r_t^2}{2}\left(2\cos^{-1}\left(1 - \frac{h}{r_t}\right) + \sin\left(2\cos^{-1}\left(\frac{h}{r_t} - 1\right)\right)\right) \tag{29}$$

In Eq. 30, the Pythagorean theorem is applied in the midsagittal plane to get h, the distance from the abdominal wall to the boundary frontal plane at a distance y in the craniocaudal direction from the peak of the abdominal wall.

$$h = \sqrt{r_s^2 - y^2} - \sqrt{r_s^2 - \left(\frac{c_s}{2}\right)^2} \tag{30}$$

Equation 31 is the relation between the sagittal radius (r_s) and the transverse radius (r_t) derived from the results in Song et al. (2006).

$$r_s = 8.00479 r_t - 1.10158 \tag{31}$$

Equations for calculated parameters

$$\sigma_{ab}\left(u_{ab} = 1,\ V_{ab}^{RV},\ \dot{V}_{ab} = 0,\ V_{ab0}\right) = \sigma_{ab}^{RV} \tag{32}$$

$$V_{ab0} = V_{ab}^{RV} + V_{ab}^{kmFRC} \cdot VC \tag{33}$$

$$V_L^{RV} = V_L^{FRC} - \left(V_{rc}^{kmFRC} + V_{ab}^{kmFRC}\right) \cdot VC \tag{34}$$

$$\sigma_L^{RV} = \frac{V_L^{RV} - V_{L0}}{C_L} \tag{35}$$

$$\sigma_{ab}^{RV} = \sigma_{di}^{RV} - \sigma_L^{RV} \tag{36}$$

$$V_{ab}^{FRC} = V_{ab}^{RV} + V_{ab}^{kmFRC} \cdot VC \tag{37}$$

$$V_{sum} = V_{di}^{FRC} + C_l V_{rc}^{FRC} + V_{ab}^{FRC} \tag{38}$$

$$V_{di}^{RV} = V_{sum} - V_{ab}^{RV} - C_l V_{rc}^{RV} \tag{39}$$

$$V_{ab}^{TLC} = V_{ab}^{FRC} + \left(V_{ab}^{kmTLC} - V_{ab}^{kmFRC}\right) \cdot VC \tag{40}$$

$$V_L^{TLC} = V_{rc}^{TLC} - V_{di}^{TLC} - V_c \tag{41}$$

$$\sigma_L^{TLC} = \frac{V_L^{TLC} - V_{L0}}{C_L} \tag{42}$$

$$\sigma_{ab}^{TLC} = \frac{V_{ab}^{TLC} - V_{ab0}}{C_{ab}} \tag{43}$$

$$\sigma_{di}^{TLC} = \sigma_L^{TLC} - \sigma_{ab}^{TLC} \tag{44}$$

$$\sigma_{rc}^{TLC} = \sigma_{rc}^{mul} \log\left(\frac{V_{rc}^{max} - V_{rc}^{TLC}}{V_{rc}^{TLC} - V_{rc}^{min}}\right) + \sigma_{rc}^{add} \tag{45}$$

$$\sigma_{rc}^{RV} = \sigma_{rc}^{mul} \log\left(\frac{V_{rc}^{max} - V_{rc}^{RV}}{V_{rc}^{RV} - V_{rc}^{min}}\right) + \sigma_{rc}^{add} \tag{46}$$

$$f_a^{RV} = \frac{1}{1 + C_l}\left(\frac{V_{di}^{RV} - V_{di}^{TLC}}{V_{di}^{RV} - V_{di}^{TLC} + V_L^{RV}}\right) + f_a^{TLC} \tag{47}$$

$$V_{L0} = V_L^{RV} \tag{48}$$

$$K_{di}^{psv} = \frac{\sigma_{di}^{RV}}{\left(V_{di}^{RV} - V_{di}^{FRC}\right)^2} \tag{49}$$

$$L_{di}^{min} = \frac{V_{di}^{TLC} - f_{di} V_{di}^{RV}}{V_{di}^{TLC} - V_{di}^{RV}/1.05} \tag{50}$$

$$P_{ica}^{abRV} = \sigma_L^{RV} + \sigma_{rc}^{RV} - \left(f_a^{RV} + F_{di}\right)\sigma_{di}^{RV} \tag{51}$$

$$P_{ica}^{diTLC} = \sigma_L^{TLC} + \sigma_{rc}^{TLC} - \left(f_a^{TLC} + F_{di}\right)\sigma_{di}^{TLC} \tag{52}$$

$$\sigma_{di}\left(u_{di} = 1,\ V_{di}^{TLC},\ \dot{V}_{di} = 0,\ \sigma_{di}^{max}\right) = \sigma_{di}^{TLC} \tag{53}$$

$$\sigma_{rc}^{add} = \sigma_{rc}^{mul} \log\left(\frac{V_{rc0} - V_{rc}^{min}}{V_{rc}^{max} - V_{rc0}}\right) \quad (54)$$

$$\sigma_{rc}^{mul} = \frac{\left(V_{rc}^{max} - V_{rc}^{min}\right)(1 + C_1)}{4C_{rc}} \quad (55)$$

$$V_{di0} = V_{di}^{RV} \quad (56)$$

$$V_{di}^{TLC} = V_{sum} - V_{ab}^{TLC} - C_1 V_{rc}^{TLC} \quad (57)$$

$$V_{rc}^{max} = V_{rc}^{TLC} + 0.05\left(V_{rc}^{TLC} - V_{rc}^{RV}\right) \quad (58)$$

$$V_{rc}^{min} = V_{rc}^{RV} - 0.99\left(V_{rc}^{TLC} - V_{rc}^{RV}\right) \quad (59)$$

$$V_{rc}^{RV} = V_{rc}^{FRC} - \frac{V_{rc}^{kmFRC} \cdot VC}{1 + C_1} \quad (60)$$

$$V_{rc}^{TLC} = V_{rc}^{FRC} + \frac{\left(V_{rc}^{kmTLC} - V_{rc}^{kmFRC}\right) \cdot VC}{1 + C_1} \quad (61)$$

$$V_{rc0} = V_{rc}^{FRC} \quad (62)$$

BRAINSTEM NETWORK MODEL ARCHITECTURE AND SYSTEM PERFORMANCE WHEN LINKED TO THE BIOMECHANICAL MODEL

The computational model of the pontomedullary respiratory network (**Figure 1**) instantiated the hypothesis (Shannon et al., 1998; Rybak et al., 2008) that airway cough receptors affect several neuron populations in the ventral respiratory column (VRC) and pontine respiratory group (PRG) via cough 2nd order neurons. Evoked changes reconfigured the respiratory network to produce the cough motor pattern through the same VRC neurons involved in providing drive to respiratory muscles during normal breathing. The model incorporated recent enhancements (Poliaček et al., 2011) and additional neuron populations and other changes as detailed in **Tables 2–4**.

Linking the neural network and biomechanical models

The diaphragm received input from two phrenic motor neuron populations (PHR, PHR-HT) with different threshold ranges to generate motor unit diversity and facilitate an ordered recruitment during increased inspiratory drive. Diaphragm activation was based on the mean instantaneous firing rates (P, P_1), of the two populations by the expression $(0.3P + 0.7P_1)/X$ where X is the firing rate for maximum diaphragm activation; values of 50–200 spikes/s were used (Nail et al., 1972) to approximate the plot for diaphragm activation in Figure 1 of Mantilla and Sieck (2011). Similarly, two lumbar motor neuron populations (LUM, LUM-HT) activated the abdominal muscle with X set to 80. Inspiratory laryngeal motor (ILM) and expiratory laryngeal motor (ELM) neuron populations regulated laryngeal resistance over a range between fully open (+1) and fully closed (−1), inclusively.

Lung afferent populations were regulated by injected currents defined at each simulation step by evaluation of expressions that included model lung volume. Pulmonary stretch receptors (PSRs) became more active with increasing lung volume V (membrane bias = $0.5V$ mV/%VC) and mediated the Hering–Breuer reflex. Deflation-sensitive lung receptors were also implemented (Paintal, 1955; Luck, 1970; Wei and Shen, 1985; Iscoe and Gordon, 1992; Bergren and Peterson, 1993; Matsumoto et al., 2002; Yu et al., 2003). A low threshold population (Def_1, membrane bias = $-0.225(V - 70)$ mV/%VC) and its afferent pathway introduced in Poliaček et al. (2011) was used to represent a class of possible network mechanisms for generating an inhibitory bias on E-Dec neurons. Simulated "vagotomy" (elimination of the effects of lung afferents) in the present model removed this inhibition, contributing to the observed prolongation of the expiratory phase (Te increased from 2.76 s to 3.15 s (p-value = 0.0004, two-sided t-test). Vagotomy also removed the influence of the PSRs and increased inspiratory phase duration (Ti) from 1.94 s to 2.61 s, (p-value = 4×10^{-7}; see references and discussion in Dick et al., 2008). A higher threshold "distortion" (Dis_1) receptor population (cf. Iscoe and Gordon, 1992) excited the ELM population when lung volume was below FRC (membrane bias = $-1.75(V - 10)$ mV/%VC if $V < 10$, 0 otherwise). We note that the synaptic strength and firing rates of this speculative Dis_1 population, added for development purposes in other work (Hutchison and Lindsey, 2009), resulted in negligible modulation of ELM population activity under the conditions of the present study (see "Influence of Some Added Network Connections").

Additional enhancements to the current network model

The "I-Dec_2" population was added to provide a second inhibitory VRC inspiratory neuron population for tuning inspiratory drive as proposed in Ott et al. (2012) for central chemoreceptor modulation of breathing. In some previous models (Rybak et al., 2008; Poliaček et al., 2011), the "E-Aug-late" population inhibited numerous target populations, but also served to excite the VRG bulbospinal E-Aug-BS (+) population that drives expiratory lumbar motor neurons. A new "E-Aug (+)" population was added to facilitate differential regulation of the lumbar motor neurons and expiratory drive modulation as proposed in the literature (Iscoe, 1998; Shannon et al., 2004; Molkov et al., 2010). Other parameters were adjusted and populations added in anticipation of linking the network model to the biomechanical model derived from data from human subjects. In the antecedent model (Poliaček et al., 2011), the I-Aug-BS population output served both a premotor function and represented the "phrenic" output. The inhibitory connections from the VRC-IE population to the I-Aug-BS population were eliminated in the new model; E-Dec-P inhibition of the I-Aug-BS population was retained. The resulting eupneic respiratory cycle frequency (12.7 cycles/min) was within the range for resting breathing in the human adult (A.D.A.M. Medical Encyclopedia, 2012).

Eupneic motor pattern and "baseline" cough

The joint neuromechanical model generated a eupneic motor pattern and an evoked cough. **Figure 2** shows membrane potential records from simulated neurons in representative PRG, raphé, and VRC neuron populations and the six types of motor neurons. The "IF" neuron populations do not generate action potential-like spikes; instances of threshold crossings are indicated graphically by corresponding vertical spike-like lines. Additional traces include integrated population activity of the three lung afferent populations and biomechanical system metrics,

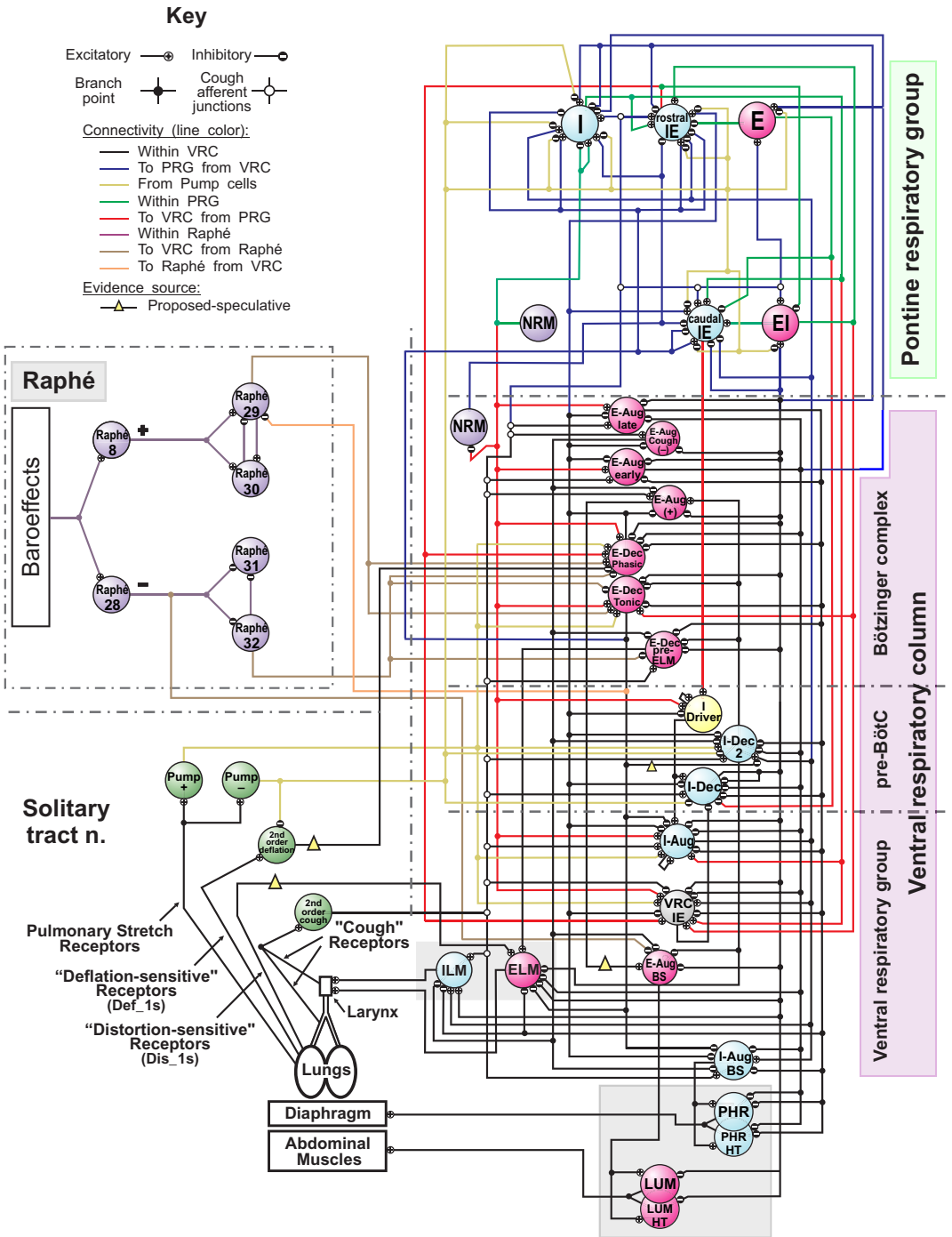

FIGURE 1 | Schematic of the raphé-pontomedullary respiratory network model used in this study. The model extends that used in Poliaček et al. (2011) and Rybak et al. (2008) and follows labeling conventions enumerated therein. Parameters for the represented cell populations (large colored circles) and connections (see Key) are listed in **Tables 2** and **4**. Parameters for the I-Driver population with conditional bursting pacemaker properties were as described previously (Rybak et al., 2008; Poliaček et al., 2011). Abbreviations of brainstem regions or "compartments": pre-BötC, pre-Bötzinger complex; VRC or VRG, ventral respiratory column or group; PRG, pontine respiratory group. Abbreviations of most populations were as enumerated in Table 1 of Rybak et al. (2008): Aug and Dec: neurons with augmenting or decrementing activity patterns, respectively, during the indicated phase (I-inspiratory; E-expiratory) of maximum firing rate. BS, bulbo-spinal; ELM, expiratory laryngeal motoneurons; EI, neurons with a peak firing rate during the E-to-I phase transition; IE, neurons with a peak firing rate during the I-to-E phase transition; ILM, inspiratory laryngeal motoneurons; NRM, non-respiratory-modulated neurons. Two phrenic motor neuron populations with different threshold ranges innervated the diaphragm (PHR, PHR-HT: high threshold); two lumbar motor neuron populations activated the abdominal muscle (LUM, LUM-HT: high threshold). I-Dec_2, second inhibitory I population in the VRC (e.g., see Ott et al., 2012); Lung Def_1s, Lung Dis_1s, Deflation 2nd order: lung deflation-sensing neuronal circuit elements. See text for further discussion.

Table 2 | Population parameters for network model with adjusted (Δ) and additional (+) neuronal populations modified from Poliaček et al. (2011).

Population name	Size	Resting threshold (mV)	THO variability (mV)	Membrane time constant	Post-spike increase in G_{K+}	Post-spike G_{K+} time constant (ms)	Adaptation threshold increase	Adaptation (ms)	Noise amplitude	DC (mV)
	N	*THO*		*TMEM*	*B*	*TGK*	*C*	*TTH*		
I-pons	100	10.0	1.0	9.0	20.0	7.0	0.0	500.0	0.03	2.0
rostral IE-pons	100	10.0	1.0	9.0	20.0	7.0	0.0	500.0	0.3	5.0
caudal IE-pons	100	10.0	1.0	9.0	20.0	7.0	0.0	500.0	0.3	5.0
E-pons	100	10.0	1.0	9.0	20.0	7.0	0.0	500.0	0.3	13.0
EI-pons	100	10.0	1.0	9.0	20.0	7.0	0.0	500.0	0.3	20.0
NRM-pons	100	10.0	1.0	9.0	20.0	7.0	0.0	500.0	0.03	25.0
NRM-BötC	300	10.0	1.0	9.0	20.0	7.0	0.0	500.0	0.03	25.0
ΔI-DRIVER	300	See Table A2 in Rybak et al. (2008) for I-Driver neuron properties								
ΔI-Dec	300	10.0	1.0	6.0	75.0	8.5	0.9	1500.0	0.2	20.0
+I-Dec_2	300	10.0	1.0	6.0	75.0	8.5	0.8	1200.0	0.2	5.0
ΔI-Aug	300	12.0	3.0	6.0	75.0	5.0	0.0	5000.0	0.6	18.0
ΔVRC IE	99	18.0	2.0	9.0	50.0	5.0	0.0	1000.0	0.075	0.0
ΔE-Dec-Phasic	300	9.0	1.0	6.0	75.0	8.5	0.9	1500.0	0.1	4.0
ΔE-Dec-Tonic	300	8.0	1.0	9.0	50.0	3.8	0.8	2000.0	0.3	0.0
E-Aug-early	300	10.0	1.0	6.0	27.0	2.5	0.0	500.0	0.3	30.0
E-Aug-late	300	10.0	1.0	9.0	27.0	2.5	0.0	500.0	0.1	27.0
ΔE-Aug-Cough	300	12.0	2.0	9.0	75.0	7.5	0.0	500.0	0.2	0.0
+E-Aug (+)	300	10.0	2.0	6.0	75.0	7.5	0.1	1000.0	0.5	20.0
ΔE-Aug-BS (+)	300	12.0	3.0	6.0	100.0	6.0	0.1	1000.0	0.5	0.0
ΔPump (+)	300	5.0	0.5	6.0	25.0	3.8	0.08	500.0	0.1	0.0
ΔPump (-)	300	5.0	0.0	6.0	25.0	3.8	0.08	500.0	0.1	0.0
ΔI-Aug-BS	300	12.0	3.0	6.0	75.0	5.0	0.0	5000.0	0.5	0.0
+Phrenic	210	10.0	2.0	5.0	200.0	6.0	0.08	500.0	0.5	0.0
+Phrenic-HT	70	16.0	2.0	60.0	200.0	5.0	0.08	500.0	0.5	0.0
ΔLumbar	210	15.0	2.0	6.0	75.0	7.5	0.08	500.0	0.5	0.0
+Lumbar-HT	70	18.0	2.0	30.0	200.0	7.5	0.1	500.0	0.5	0.0
ΔILM	300	20.0	1.0	6.0	25.0	3.8	0.08	500.0	0.1	2.0
ΔE-Dec-pre-ELM	300	11.0	0.0	6.0	100.0	6.0	0.8	500.0	0.5	1.0
ΔELM	300	18.0	2.0	6.0	100.0	6.0	0.9	100.0	0.5	0.0
ΔLUNG PSRs	300	11.0	1.0	9.0	20.0	7.0	0.0	500.0	0.5	0.0
+Lung deflation receptors (Def_1)	300	10.0	1.0	9.0	20.0	7.0	0.0	500.0	0.5	0.0
+Lung distortion receptors (Dis_1)	300	10.0	1.0	9.0	20.0	7.0	0.0	500.0	0.5	0.0
>Cough 2nd order	100	10.0	1.0	9.0	20.0	7.0	0.3	500.0	0.1	0.0
ΔDeflation 2nd order	300	8.0	1.0	9.0	27.0	2.5	0.5	1000.0	0.3	0.0
Raphé 8	100	10.0	1.0	9.0	20.0	7.0	0.0	500.0	0.01	0.0

(Continued)

Table 2 | Continued

Population name	Size	Resting threshold (mV)	THO variability (mV)	Membrane time constant	Post-spike increase in G_{K+}	Post-spike G_{K+} time constant (ms)	Adaptation threshold increase	Adaptation (ms)	Noise amplitude	DC (mV)
	N	*THO*		*TMEM*	*B*	*TGK*	*C*	*TTH*		
Raphé 28	100	10.0	1.0	9.0	20.0	7.0	0.0	500.0	0.1	0.0
Raphé 29	100	10.0	1.0	9.0	20.0	7.0	0.0	500.0	0.5	0.0
Raphé 30	100	10.0	1.0	9.0	20.0	7.0	0.0	500.0	0.5	0.0
Raphé 31	100	10.0	1.0	9.0	20.0	7.0	0.0	500.0	0.1	10.0
Raphé 32	100	10.0	1.0	9.0	20.0	7.0	0.0	500.0	0.1	10.0

Variable names used by MacGregor (1987) are in italics. All values representing voltages are relative to the resting potential, which is considered equal to zero. N is the number of neurons simulated in each population. THO, the resting threshold, is normally distributed in the population around the value of THO with a standard deviation equal to the "THO variability" value. TMEM is the membrane time constant. B is the amplitude of the post-spike increase in potassium conductance. TGK is the time constant of the potassium conductance decay following an action potential. C and TTH define the change in threshold associated with spike adaptation. C is the ratio of the threshold increase to the membrane potential increase; its value is between 0 and 1. TTH is the time constant of the rise in threshold with spike adaptation. Noise Amplitude: each cell has an internal noise generator that acts like two synapses, one with an equilibrium potential of 70 mV above resting and the other with −70 mV. Each acts like it has an incoming firing probability of 0.05 per time step, and a synapse time constant of 1.5 ms. This parameter is the conductance that gets added to the synapse conductance on each (virtual) spike. DC: an injected current will raise the membrane potential by an amount that is inversely proportional to the membrane conductance. Instead of being specified directly as a current, this parameter is specified in mV, and it is interpreted as the current that is required to raise the membrane potential by the specified number of mV when the membrane conductance has its resting value. The effect on the membrane potential at other membrane conductances will be inversely proportional to the conductance. Note also that as in other types of IF neuron models, our neuron models do not actually generate action potential-like spikes but only identified moments of spikes, so "spiking" shown in all neuron simulations are represented graphically by assigning vertical spike-like lines at computed times of threshold crossing. The population "E-Aug-Late-HT" in Rybak et al. (2008) has been renamed to "E-Aug-Cough" in the base model for this simulation. >, neuron populations that relay perturbations of the network model. A fiber population composed of 100 fibers, each with a firing probability of 0.05 at each simulation time step and 100 type Ex_1 excitatory synaptic terminals (synaptic strength 0.03), represented cough receptor excitation. These fibers excited the Cough 2nd order neuron population. For abbreviations, see list of abbreviations and legend of ***Figure 1*** *in the main text.*

Table 3 | Synaptic parameters for the network model.

Synapse name	Synapse type	Synapse equilibrium potential (mV)	Synapse time constant (ms)
Ex_1	Excitatory	115.0	1.5
Inh_4	Inhibitory	−25.0	1.5
Inh_7	Inhibitory	−25.0	2.0
Inh_10	Inhibitory	−25.0	1.5
Ex_13	Excitatory	115.0	1.5
Pre-ex_13	Inhibitory (pre-synaptic to Ex_13)	0.0	1.5
Ex_19	Excitatory	115.0	5.0
Inh_22	Inhibitory	−25.0	5.0
Inh_25	Inhibitory	−25.0	4.5
Ex_28	Excitatory	115.0	1.5
Pre-ex_28	Inhibitory (pre-synaptic to Ex_28)	−25.0	3.5

including lung volume, tracheal flow, and alveolar pressure. The three phases of the cough cycle (Bolser et al., 2003) are highlighted.

The inspiratory phase of the cough was characterized by increased activation of the diaphragm and enlargement of upper airway via activation of the ILM (abductor) motor neuron population, resulting in an increased lung volume (43% VC), inspiratory flow, and transdiaphragmatic and transpulmonary pressures. The subsequent compressive phase included activation of the ELM (adductor) motor neurons with transient laryngeal closure, together with activation of lumbar motor neurons and abdominal expiratory muscles. During this phase, tracheal airflow stopped and there was an increase in alveolar and abdominal pressure. In the following expulsive phase, high air flow velocity (72.2% VC/s) resulted from the opening of the larynx during continued abdominal muscle activation.

Cough behavior with changes in inspiratory drive

Two series of simulations with complementary perturbations of cough inspiratory drive were made to assess model behavior during the phases of cough. Different sets of random number seeds were used for each simulation to generate variability in model output by altering the thresholds of individual neurons in each population and the convergent and divergent connectivity patterns among populations within ranges defined by the initial baseline parameter settings.

In the first series, the activation strengths for the connections between phrenic motor neuron populations and the diaphragm were increased by factors of 2 and 4. **Figure 3** shows the integrated

Table 4 | Connectivity for the network model modified from Poliaček et al. (2011).

Source population	Target population	Synaptic type	Conduction times		No. of terminals	Synaptic strength	Source pop. N	Target pop. N	Divergence	Mean no. of terminals	Convergence
			Min	Max							
I-Driver	I-Dec	ex_1	2	6	100	0.006	300	300	84.99 ± 3.14	1.18	84.99 ± 7.54
I-Driver	I-Aug	ex_1	2	6	100	0.01	300	300	84.93 ± 3.00	1.18	84.93 ± 7.73
I-Driver	I-Driver	ex_1	0	4	50	0.003	300	300	46.34 ± 1.76	1.08	46.34 ± 5.84
E-Dec-Phasic	I-Driver	inh_22	2	6	50	0.03	300	300	46.16 ± 1.77	1.08	46.16 ± 9.24
E-Dec-Phasic	E-Aug-early	inh_4	0	2	150	0.012	300	300	118.24 ± 4.01	1.27	118.24 ± 8.86
E-Dec-Phasic	E-Aug-late	inh_4	2	4	150	0.04	300	300	118.10 ± 3.94	1.27	118.10 ± 9.61
E-Dec-Phasic	VRC-IE	inh_4	0	2	50	0.1	300	99	39.33 ± 2.31	1.27	119.18 ± 7.22
E-Dec-Phasic	I-Dec	inh_4	0	2	200	0.2	300	300	146.07 ± 4.42	1.37	146.07 ± 8.71
+E-Dec-Phasic	I-Aug-BS	inh_4	2	6	100	0.15	300	300	85.21 ± 3.08	1.17	85.21 ± 7.27
E-Dec-Phasic	I-Aug	inh_4	2	6	50	0.1	300	300	46.19 ± 1.72	1.08	46.19 ± 5.43
E-Dec-Phasic	rostral IE-pons	ex_13	2	4	100	0.001	300	100	63.13 ± 2.98	1.58	189.39 ± 6.74
E-Dec-Phasic	caudal IE-pons	ex_13	2	4	100	0.001	300	100	63.23 ± 3.19	1.58	189.70 ± 9.56
+E-Dec-Phasic	I-Dec_2	inh_4	2	6	150	0.1	300	300	118.39 ± 4.42	1.27	118.39 ± 8.69
+E-Dec-Phasic	E-Aug (+)	inh_4	2	6	100	0.03	300	300	85.18 ± 2.99	1.17	85.18 ± 10.46
+E-Dec-Phasic	E-Aug-Cough (−)	inh_22	2	6	100	0.025	300	300	85.20 ± 3.05	1.17	85.20 ± 9.59
I-Dec	E-Aug-early	inh_7	2	6	115	0.5	300	300	95.67 ± 3.39	1.20	95.67 ± 7.14
I-Dec	E-Dec-Phasic	inh_25	2	6	200	0.2	300	300	145.80 ± 5.20	1.37	145.80 ± 9.31
I-Dec	I-Aug	inh_25	2	6	120	0.025	300	300	99.27 ± 3.48	1.21	99.27 ± 8.70
I-Dec	E-Aug-late	inh_7	2	6	115	0.5	300	300	95.71 ± 3.51	1.20	95.71 ± 7.84
I-Dec	VRC-IE	inh_25	0	4	33	0.025	300	99	28.15 ± 1.85	1.17	85.29 ± 6.01
I-Dec	E-Dec-Tonic	inh_25	2	6	100	0.001	300	300	84.90 ± 2.96	1.18	84.90 ± 9.43
I-Dec	ILM	ex_1	0	3	50	0.002	300	300	46.35 ± 1.71	1.08	46.35 ± 6.00
I-Dec	E-Aug-BS (+)	inh_7	0	4	100	0.05	300	300	85.44 ± 3.02	1.17	85.44 ± 9.96
I-Dec	EI-pons	ex_13	2	4	100	0.001	300	100	63.33 ± 3.16	1.58	190.00 ± 8.78
I-Dec	I-pons	ex_13	2	4	100	0.0005	300	100	63.50 ± 3.23	1.57	190.51 ± 8.03
I-Dec	I-pons	inh_7	2	4	100	0.0005	300	100	63.66 ± 3.21	1.57	190.98 ± 8.42
I-Dec	rostral IE-pons	inh_4	2	4	100	0.0001	300	100	63.55 ± 3.04	1.57	190.65 ± 8.05
I-Dec	caudal IE-pons	inh_7	2	4	100	0.0001	300	100	63.27 ± 3.06	1.58	189.80 ± 8.43
I-Dec	Lumbar	inh_7	0	4	100	0.1	300	210	79.70 ± 3.14	1.25	113.86 ± 8.97
I-Dec	E-Dec-pre-ELM	inh_4	2	6	200	0.06	300	300	146.12 ± 4.70	1.37	146.12 ± 8.41
+I-Dec	E-Aug (+)	inh_4	0	2	130	1.0	300	300	105.84 ± 3.65	1.23	105.84 ± 7.43
+I-Dec	ELM	inh_4	0	5	200	0.06	300	300	146.22 ± 4.96	1.37	146.22 ± 9.62
+I-Dec	Lumbar-HT	inh_7	2	6	100	0.1	300	70	53.32 ± 2.84	1.88	228.53 ± 6.63
+I-Dec	I-Dec	inh_25	2	6	140	0.0125	300	300	112.11 ± 3.97	1.25	112.11 ± 9.09
+I-Dec	E-Aug-Cough (−)	inh_7	2	6	115	0.16	300	300	95.71 ± 3.51	1.20	95.71 ± 7.84
I-Aug	I-Aug	ex_1	0	5	50	0.025	300	300	45.99 ± 1.77	1.09	45.99 ± 5.31
I-Aug	caudal IE-pons	inh_7	2	4	100	0.0001	300	100	63.43 ± 3.19	1.58	190.28 ± 9.05
I-Aug	I-Aug-BS	ex_1	2	6	100	0.06	300	300	85.20 ± 3.01	1.17	85.20 ± 7.27

(Continued)

Table 4 | Continued

Source population	Target population	Synaptic type	Conduction times		No. of terminals	Synaptic strength	Source pop. N	Target pop. N	Divergence	Mean no. of terminals	Convergence
			Min	Max							
I-Aug	ILM	ex_1	2	6	70	0.035	300	300	62.72 ± 2.32	1.12	62.72 ± 6.93
I-Aug	VRC-IE	ex_1	2	6	16	0.0015	300	99	14.82 ± 0.97	1.08	44.92 ± 6.80
I-Aug	I-pons	ex_13	2	4	100	0.0025	300	100	63.59 ± 2.94	1.57	190.76 ± 7.71
I-Aug	rostral IE-pons	inh_4	2	4	100	0.0001	300	100	63.43 ± 2.95	1.58	190.29 ± 8.57
+I-Aug	I-Dec_2	ex_28	2	6	200	0.01	300	300	146.05 ± 4.72	1.37	146.05 ± 9.65
E-Aug-early	E-Dec-Phasic	inh_4	2	6	110	0.007	300	300	92.32 ± 3.45	1.19	92.32 ± 7.95
E-Aug-early	I-Dec	inh_4	0	5	100	0.06	300	300	85.13 ± 2.98	1.17	85.13 ± 7.70
E-Aug-early	I-Aug	inh_4	2	6	100	0.135	300	300	85.44 ± 3.23	1.17	85.44 ± 7.76
E-Aug-early	VRC-IE	inh_4	0	2	24	0.05	300	99	21.46 ± 1.29	1.12	65.02 ± 6.96
E-Aug-early	I-Aug-BS	inh_4	0	2	150	0.001	300	300	118.31 ± 4.21	1.27	118.31 ± 7.57
E-Aug-early	E-Aug-late	inh_10	0	2	50	0.001	300	300	46.01 ± 1.81	1.09	46.01 ± 6.57
E-Aug-early	E-pons	ex_13	2	4	100	0.002	300	100	63.08 ± 2.85	1.59	189.25 ± 7.68
E-Aug-early	I-pons	inh_7	2	4	100	0.0005	300	100	63.08 ± 2.85	1.59	189.25 ± 7.68
+E-Aug-early	I-Dec_2	inh_4	2	6	150	0.08	300	300	118.31 ± 4.21	1.27	118.31 ± 7.57
+E-Aug-early	Phrenic	inh_4	0	2	150	0.001	300	210	107.57 ± 4.12	1.39	153.68 ± 8.34
+E-Aug-early	Phrenic-HT	inh_4	0	2	150	0.001	300	70	61.97 ± 2.40	2.42	265.57 ± 5.37
+E-Aug-early	ELM	inh_4	2	6	175	0.007	300	300	132.52 ± 4.21	1.32	132.52 ± 9.21
E-Aug-late	E-Aug-early	inh_10	0	2	200	0.04	300	300	145.91 ± 4.71	1.37	145.91 ± 9.07
E-Aug-late	I-Dec	inh_4	2	6	55	0.2	300	300	50.33 ± 1.87	1.09	50.33 ± 6.68
E-Aug-late	I-Aug	inh_4	2	6	100	0.1	300	300	85.27 ± 3.04	1.17	85.27 ± 7.41
E-Aug-late	E-Dec-Phasic	inh_4	2	6	120	0.015	300	300	98.86 ± 3.48	1.21	98.86 ± 9.67
E-Aug-late	I-Aug-BS	inh_4	2	6	150	0.06	300	300	118.14 ± 4.18	1.27	118.14 ± 8.44
E-Aug-late	VRC-IE	inh_4	0	2	24	0.02	300	99	21.32 ± 1.39	1.13	64.62 ± 7.03
E-Aug-late	E-Dec-Tonic	inh_4	0	2	100	0.05	300	300	85.18 ± 3.01	1.17	85.18 ± 6.53
E-Aug-late	E-Dec-pre-ELM	inh_22	2	6	115	0.05	300	300	95.69 ± 3.35	1.20	95.69 ± 7.07
E-Aug-late	ELM	inh_7	2	6	200	0.1	300	300	145.91 ± 4.71	1.37	145.91 ± 9.07
+E-Aug-late	I-Dec_2	inh_4	2	6	150	0.075	300	300	118.14 ± 4.18	1.27	118.14 ± 8.44
+E-Aug-late	Phrenic	inh_4	4	8	150	0.06	300	210	107.09 ± 3.99	1.40	152.98 ± 7.22
+E-Aug-late	Phrenic-HT	inh_4	0	2	150	0.06	300	70	61.83 ± 2.37	2.43	265.00 ± 5.23
+E-Aug-late	ILM	inh_4	0	2	115	0.04	300	300	95.59 ± 3.32	1.20	95.59 ± 8.06
VRC-IE	I-Dec	inh_7	0	4	200	0.035	99	300	146.65 ± 4.99	1.36	48.39 ± 5.40
Raphé 8	Raphé 29	ex_1	0	3	50	0.0125	100	100	39.73 ± 2.28	1.26	39.73 ± 5.01
Raphé 28	Raphé 30	ex_1	0	3	50	0.0125	100	100	39.51 ± 2.47	1.27	39.51 ± 4.93
+I-Aug-BS	Phrenic-HT	ex_1	3	6	18	0.05	300	70	15.99 ± 1.24	1.13	68.51 ± 7.54
+I-Aug-BS	Phrenic	ex_1	3	6	50	0.05	300	210	44.95 ± 2.01	1.11	64.21 ± 6.33
NRM-BötC	rostral IE-pons	inh_7	0	1	100	0.002	300	100	63.41 ± 3.22	1.58	190.23 ± 7.92
NRM-BötC	caudal IE-pons	inh_7	0	1	100	0.002	300	100	63.37 ± 3.02	1.58	190.12 ± 7.75
NRM-BötC	I-pons	ex_13	0	1	100	0.002	300	100	63.25 ± 3.00	1.58	189.74 ± 8.31

(Continued)

Table 4 | Continued

Source population	Target population	Synaptic type	Conduction times		No. of terminals	Synaptic strength	Source pop. N	Target pop. N	Divergence	Mean no. of terminals	Convergence
			Min	Max							
+E-Aug-Cough (–)	E-Aug (+)	inh_22	2	6	100	0.05	300	300	85.39 ± 3.06	1.17	85.39 ± 7.75
E-Aug-Cough (–)	E-Aug-BS (+)	inh_22	2	6	100	0.5	300	300	85.34 ± 3.04	1.17	85.34 ± 7.22
+E-Aug-Cough (–)	I-Dec_2	inh_22	0	3	200	0.05	300	300	145.65 ± 4.67	1.37	145.65 ± 8.84
E-Aug-Cough (–)	E-Dec-pre-ELM	inh_4	2	6	100	0.1	300	300	85.22 ± 3.02	1.17	85.22 ± 7.02
+E-Aug-Cough (–)	I-Aug-BS	inh_4	0	3	200	0.025	300	300	145.65 ± 4.67	1.37	145.65 ± 8.84
+E-Aug-Cough (–)	ILM	inh_4	0	3	200	0.025	300	300	146.45 ± 4.63	1.37	146.45 ± 8.96
Lung PSRs	Pump (+)	ex_1	0	3	75	0.015	300	300	66.50 ± 2.43	1.13	66.50 ± 6.72
Lung PSRs	Pump (–)	ex_1	0	3	50	0.015	300	300	46.23 ± 1.78	1.08	46.23 ± 9.43
caudal IE-pons	I-Driver	ex_1	0	5	100	0.001	100	300	85.68 ± 2.78	1.17	28.56 ± 4.45
Pump (–)	E-pons	pre-ex_13	0	4	100	0.99	300	100	63.19 ± 2.88	1.58	189.58 ± 7.28
+Pump (–)	I-Dec_2	inh_4	0	2	25	0.0035	300	300	24.04 ± 0.88	1.04	24.04 ± 5.11
Pump (–)	I-Dec	inh_4	0	2	25	0.0035	300	300	23.98 ± 0.90	1.04	23.98 ± 5.97
Pump (–)	I-pons	pre-ex_13	0	4	100	0.99	300	100	63.53 ± 2.94	1.57	190.58 ± 7.02
Pump (–)	EI-pons	pre-ex_13	2	4	100	0.99	300	100	63.55 ± 2.95	1.57	190.64 ± 7.44
Pump (–)	Lung Def_1s	inh_4	0	4	100	0.02	300	300	85.22 ± 3.09	1.17	85.22 ± 7.46
Pump (–)	rostral IE-pons	pre-ex_13	0	4	100	0.99	300	100	63.63 ± 3.02	1.57	190.88 ± 9.09
Pump (–)	caudal IE-pons	pre-ex_13	0	4	100	0.99	300	100	63.63 ± 3.02	1.57	190.88 ± 9.09
Pump (+)	E-Dec-Phasic	ex_1	0	2	100	0.01	300	300	85.47 ± 2.95	1.17	85.47 ± 8.14
Pump (+)	VRC-IE	ex_1	2	6	100	0.01	300	99	63.10 ± 2.99	1.58	191.20 ± 11.20
Pump (+)	I-Aug	ex_1	0	2	25	0.0	300	300	24.07 ± 0.91	1.04	24.07 ± 4.15
Pump (+)	E-Dec-T	ex_1	0	2	100	0.002	300	300	85.12 ± 3.16	1.17	85.12 ± 6.94
+Pump (+)	I-Dec_2	ex_1	2	6	100	0.005	300	300	85.20 ± 3.05	1.17	85.20 ± 9.59
E-Dec-T	Raphé 29	inh_4	0	3	100	0.001	300	100	63.59 ± 3.05	1.57	190.76 ± 7.20
E-Dec-T	I-Aug-BS	inh_4	2	6	100	0.03	300	300	84.99 ± 3.14	1.18	84.99 ± 7.54
E-Dec-T	rostral IE-pons	ex_13	2	4	100	0.001	300	100	63.26 ± 3.11	1.58	189.77 ± 11.78
E-Dec-T	I-pons	ex_13	2	4	100	0.0005	300	100	63.33 ± 3.02	1.58	189.98 ± 9.72
E-Dec-T	I-pons	inh_7	2	4	100	0.0005	300	100	63.20 ± 3.13	1.58	189.60 ± 7.79
E-Dec-T	rostral IE-pons	inh_4	2	4	100	0.0005	300	100	63.57 ± 3.16	1.57	190.70 ± 7.57
E-Dec-T	caudal IE-pons	ex_13	2	4	100	0.001	300	100	63.20 ± 3.18	1.58	189.61 ± 7.72
E-Dec-T	caudal IE-pons	inh_7	2	4	100	0.0005	300	100	63.40 ± 3.17	1.58	190.20 ± 9.74
E-Dec-T	ELM	inh_4	0	4	100	0.04	300	300	85.04 ± 3.30	1.18	85.04 ± 8.24
E-Dec-T	I-Aug	inh_4	2	6	100	0.0075	300	300	85.12 ± 3.35	1.17	85.12 ± 8.17
+E-Dec-T	I-Dec_2	pre-ex_28	2	6	100	0.2	300	300	84.99 ± 3.14	1.18	84.99 ± 7.54

(Continued)

Table 4 | Continued

Source population	Target population	Synaptic type	Conduction times		No. of terminals	Synaptic strength	Source pop. N	Target pop. N	Divergence	Mean no. of terminals	Convergence
			Min	Max							
rostral IE-pons	EI-pons	inh_4	2	4	100	0.03	100	100	63.79 ± 3.24	1.57	63.79 ± 4.98
rostral IE-pons	VRC-IE	ex_1	0	1	100	0.001	100	99	62.90 ± 3.28	1.59	63.54 ± 4.65
rostral IE-pons	E-Dec-Phasic	ex_1	0	5	100	0.02	100	300	85.06 ± 2.76	1.18	28.35 ± 4.15
EI-pons	rostral IE-pons	ex_1	2	4	100	0.002	100	100	63.47 ± 3.20	1.58	63.47 ± 4.78
EI-pons	caudal IE-pons	ex_1	2	4	100	0.002	100	100	63.36 ± 3.47	1.58	63.36 ± 4.41
EI-pons	VRC-IE	ex_1	0	4	50	0.0003	100	99	39.46 ± 2.35	1.27	39.86 ± 5.11
EI-pons	E-Dec-T	ex_1	0	4	100	0.01	100	300	85.16 ± 3.33	1.17	28.39 ± 5.10
E-Dec-pre-ELM	ELM	ex_19	2	6	250	0.0125	300	300	169.56 ± 5.08	1.47	169.56 ± 7.81
Def 2nd (–)	E-Dec-Phasic	inh_4	2	6	100	0.04	300	300	85.17 ± 3.11	1.17	85.17 ± 9.16
+E-Aug (+)	E-Aug-BS (+)	ex_19	2	6	100	0.02	300	300	85.16 ± 2.97	1.17	85.16 ± 7.43
Raphé 8	Raphé 31	inh_4	0	3	50	0.005	100	100	39.38 ± 2.09	1.27	39.38 ± 6.21
Raphé 8	Raphé 32	inh_4	0	3	50	0.005	100	100	39.51 ± 2.47	1.27	39.51 ± 4.93
Raphé 8	E-Aug-BS (+)	inh_22	0	3	400	0.0	100	300	221.45 ± 4.77	1.81	73.82 ± 4.47
Raphé 29	Raphé 30	ex_1	0	3	50	0.01	100	100	39.51 ± 2.47	1.27	39.51 ± 4.93
Raphé 29	E-Dec-T	ex_19	0	3	100	0.15	100	300	84.74 ± 3.12	1.18	28.25 ± 4.23
Raphé 29	E-Dec-Phasic	ex_19	0	3	100	0.2	100	300	84.74 ± 3.12	1.18	28.25 ± 4.23
Raphé 30	Raphé 29	inh_4	0	3	50	0.01	100	100	39.51 ± 2.47	1.27	39.51 ± 4.93
Raphé 32	Raphé 31	inh_4	0	3	50	0.005	100	100	39.51 ± 2.47	1.27	39.51 ± 4.93
Raphé 32	E-Dec-Tonic	inh_22	0	3	100	0.01	100	300	85.28 ± 3.13	1.17	28.43 ± 4.65
Raphé 32	E-Dec-Phasic	inh_22	0	3	100	0.01	100	300	84.74 ± 3.12	1.18	28.25 ± 4.23
Raphé 32	E-Dec-pre-ELM	inh_22	0	3	100	0.01	100	300	84.74 ± 2.97	1.18	28.25 ± 4.67
>+Cough 2nd order (+)	I-Aug-BS	ex_1	2	6	100	0.02	100	300	85.25 ± 2.83	1.17	28.42 ± 5.15
>Cough 2nd order (+)	I-Aug	ex_1	2	6	100	0.0045	100	300	85.25 ± 2.83	1.17	28.42 ± 5.15
>Cough 2nd order (+)	I-Dec	ex_1	2	6	100	0.0045	100	300	85.27 ± 2.89	1.17	28.42 ± 4.68
>+Cough 2nd order (+)	I-Dec_2	ex_1	2	6	100	0.05	100	300	85.54 ± 3.07	1.17	28.51 ± 4.72
>Cough 2nd order (+)	E-Aug-late	ex_1	2	6	100	0.005	100	300	85.25 ± 2.83	1.17	28.42 ± 5.15
>Cough 2nd order (+)	E-Aug-early	ex_1	0	3	100	0.01	100	300	85.07 ± 3.05	1.18	28.36 ± 4.19
>Cough 2nd order (+)	VRC-IE	inh_4	0	3	100	0.2	100	99	63.13 ± 3.05	1.58	63.77 ± 5.20
>Cough 2nd order (+)	caudal IE-pons	ex_1	0	3	100	0.001	100	100	63.59 ± 3.21	1.57	63.59 ± 5.84
>Cough 2nd order (+)	rostral IE-pons	ex_1	0	3	100	0.001	100	100	63.59 ± 3.21	1.57	63.59 ± 5.84

(Continued)

Table 4 | Continued

Source population	Target population	Synaptic type	Conduction times		No. of terminals	Synaptic strength	Source pop. N	Target pop. N	Divergence	Mean no. of terminals	Convergence
			Min	Max							
>Cough 2nd order (+)	I-pons	ex_1	0	3	100	0.001	100	100	63.59 ± 3.21	1.57	63.59 ± 5.84
>Cough 2nd order (+)	E-pons	ex_1	2	6	100	0.001	100	100	63.59 ± 3.21	1.57	63.59 ± 5.84
>Cough 2nd order (+)	EI-pons	ex_1	0	3	100	0.001	100	100	63.59 ± 3.21	1.57	63.59 ± 5.84
>Cough 2nd order (+)	E-Dec-pre-ELM	ex_19	2	6	100	0.004	100	300	85.14 ± 3.06	1.17	28.38 ± 3.97
>+Cough 2nd order (+)	E-Aug (+)	ex_1	2	6	100	0.05	100	300	85.25 ± 2.83	1.17	28.42 ± 5.15
>+Cough 2nd order (+)	E-Aug-Cough (−)	ex_1	2	6	100	0.04	100	300	85.25 ± 2.83	1.17	28.42 ± 5.15
>+Cough 2nd order (+)	ILM	ex_1	2	6	100	0.001	100	300	84.92 ± 3.23	1.18	28.31 ± 4.63
E-pons	rostral IE-pons	inh_4	2	4	100	0.0001	100	100	63.17 ± 3.15	1.58	63.17 ± 5.22
E-pons	caudal IE-pons	inh_4	2	4	100	0.0001	100	100	63.47 ± 3.13	1.58	63.47 ± 5.60
E-pons	I-Dec	inh_4	0	1	100	0.008	100	300	85.14 ± 3.03	1.17	28.38 ± 4.11
NRM-pons	I-pons	ex_1	0	4	100	0.015	100	100	63.26 ± 3.28	1.58	63.26 ± 4.40
NRM-pons	I-pons	inh_4	0	4	100	0.05	100	100	63.62 ± 3.11	1.57	63.62 ± 4.61
NRM-pons	I-Driver	ex_1	2	6	100	0.11	100	300	85.10 ± 3.00	1.18	28.37 ± 4.51
NRM-pons	VRC-IE	ex_1	0	1	100	0.01	100	99	63.02 ± 2.53	1.59	63.66 ± 4.67
NRM-pons	I-Aug	ex_1	0	1	100	0.01	100	300	85.21 ± 2.94	1.17	28.40 ± 4.81
NRM-pons	E-Aug-early	ex_1	0	4	100	0.025	100	300	85.82 ± 3.10	1.17	28.61 ± 4.20
NRM-pons	E-Aug-late	ex_1	0	4	50	0.003	100	300	45.82 ± 1.89	1.09	15.27 ± 3.67
NRM-pons	E-Dec-Phasic	ex_1	0	1	100	0.01	100	300	84.87 ± 3.22	1.18	28.29 ± 4.18
NRM-pons	E-Dec-Tonic	ex_1	0	1	100	0.1	100	300	85.35 ± 3.04	1.17	28.45 ± 4.06
NRM-pons	NRM-BötC	inh_4	0	1	100	0.001	100	300	85.11 ± 2.96	1.17	28.37 ± 5.07
E-Aug-BS (+)	Lumbar	ex_1	6	10	25	0.03	300	210	23.59 ± 1.14	1.06	33.70 ± 5.45
+E-Aug-BS (+)	Lumbar-HT	ex_1	3	6	10	0.05	300	70	9.34 ± 0.75	1.07	40.03 ± 3.18
I-pons	rostral IE-pons	ex_1	0	4	100	0.005	100	100	62.93 ± 2.89	1.59	62.93 ± 5.56
I-pons	VRC-IE	ex_1	0	5	100	0.005	100	99	63.61 ± 3.41	1.57	64.25 ± 4.84
I-pons	I-Aug	ex_1	0	4	50	0.005	100	300	46.17 ± 1.67	1.08	15.39 ± 3.39
I-pons	caudal IE-pons	ex_1	0	4	100	0.005	100	100	63.67 ± 2.85	1.57	63.67 ± 4.57
+I-Dec_2	E-Dec-Tonic	inh_4	2	6	125	0.1	300	300	102.25 ± 3.60	1.22	102.25 ± 7.81
+I-Dec_2	E-Dec-pre-ELM	inh_4	2	6	100	0.01	300	300	85.11 ± 3.10	1.17	85.11 ± 7.52
+I-Dec_2	E-Aug-BS (+)	inh_4	2	6	50	0.00005	300	300	46.04 ± 1.73	1.09	46.04 ± 8.13
+I-Dec_2	ELM	inh_4	2	6	100	0.02	300	300	85.61 ± 3.37	1.17	85.61 ± 7.12
+I-Dec_2	E-Aug (+)	inh_4	2	6	100	0.02	300	300	85.19 ± 3.09	1.17	85.19 ± 8.08

(Continued)

Table 4 | Continued

Source population	Target population	Synaptic type	Conduction times		No. of terminals	Synaptic strength	Source pop. N	Target pop. N	Divergence	Mean no. of terminals	Convergence
			Min	Max							
+Lung Def_1s	Def 2nd (−)	ex_1	0	3	35	0.03	300	300	33.04 ± 1.38	1.06	33.04 ± 6.68
+Lung DIS_1s	ELM	ex_1	0	3	100	0.09	300	300	84.97 ± 2.93	1.18	84.97 ± 7.40

*+, Connection added to the network in Poliaček et al. (2011). >, Connection relaying a perturbation to the network model. Connections between individual neurons were made according to a sequence of pseudorandom numbers calculated from a unique seed number for each source-to-target connection. Targets were chosen with replacement. This table includes the means ± SD of the number of neurons in each target population innervated by each source neuron in each population. Corresponding values are also shown for source neurons that innervated each target neuron in each population. These data indicate the extent of divergence and convergence, respectively. Most neurons in each source population made a single terminal connection with each target neuron. Mean No. of Terminals, the mean number of terminals from each source neuron innervating each target neuron. The efficacy of connections between populations of neurons was influenced by the change in conductance associated with each action potential at a synapse (Synaptic Strength) and the number of terminals for each axon. Synaptic types were distinguished by their equilibrium potentials and time constants. The time constant of some synapses was slightly longer than others because troughs in cross-correlograms from which the particular synaptic connections were inferred tended to have longer durations. 11 types of synapses were used in the simulation (see **Table 3**). If the value of the presynaptic modulatory strength parameter (Synaptic Strength) was < 1.0, the strength of the connection it modulated was reduced to the product of the presynaptic Synaptic Strength parameter and target synapse conductance. If the presynaptic Synaptic Strength parameter was > 1.0, the amount by which it was greater than 1 was added to its target synapse's conductance. Minimum and maximum conduction times are expressed in 0.5 ms simulation clock ticks for each source-to-target axon population. No. of Terminals, number of terminals from source neuron.*

activity of each motor neuron population together with lung volume, tracheal flow, alveolar pressure, and abdominal pressure for baseline conditions (left) and a trial with four times the baseline activation strength (right).

Outputs from four trials for each amplified condition were compared with each other and with the baseline results. **Figure 4** shows the means (±95% confidence limits) of selected biomechanical outputs measured during baseline cough (1×) and the two conditions of increased activation gain (2×, 4×). Pairs of symbols connected by a line indicate no significant difference. Successively larger peak expiratory flow rates and abdominal pressures were respectively associated with greater lung volumes during preceding inspiratory phases of the evoked coughs, even though abdominal drive did not change. This result established that differences in flow with the generated changes in inspiratory (operating) volumes were the consequence of the modeled biomechanical system.

Mean respiratory cycle frequencies measured during pre-cough eupneic intervals for each condition were also evaluated. The respiratory frequency increased with the highest (4×) inspiratory drive, a change associated with changes in feedback from lung afferents under the "closed loop" conditions evaluated.

In the second series of simulations, inspiratory drive was altered only during the cough cycle by changing synaptic strengths of Cough 2nd order neuron inputs to selected model populations. The top panels in **Figures $5A_1$–C_1** show schematics of a subset of the model network and sites where synaptic strengths were changed relative to the baseline conditions represented in and described for **Figure 3A**. Corresponding panels in **Figures $5A_2$–C_2** show integrated traces of motor neuron population activities and biomechanical model outputs for the respective perturbations; arrows highlight significant changes in the indicated metrics (further enumerated in **Figure 6**).

First (**Figure 5A**), synaptic strengths from the Cough 2nd order population to the I-Aug and I-Aug-BS populations were doubled. The highlighted segment of the inset (**Figure $5A_1$**) shows integrated traces for the I-Aug-BS, I-Dec_2, and E-Dec-Tonic populations during a eupneic cycle and the subsequent evoked cough. I-Aug-BS activity increased under this condition (asterisk).

Next (**Figure 5B**), cough inspiratory drive was decreased relative to baseline by deletion (synaptic strength = 0.0) of the excitatory connections between the Cough 2nd order population and both the I-Aug and I-Aug-BS populations. The excitation of the I-Dec_2 population by 2nd order cough neurons remained, partially suppressing the recurrent inhibition of the I-Dec_2 and two I-Aug populations. The highlighted segment of the inset (**Figure $5B_1$**) shows reduced I-Aug-BS activity during the evoked cough under this condition (asterisk).

The third perturbation further reduced cough inspiratory drive by also transiently blocking I-Dec_2 neuron inhibition of the E-Dec-Tonic population during the cough cycle. The elimination of this influence resulted in increased E-Dec-Tonic inhibition of the I-Aug and I-Aug-BS populations during the cough (asterisk in highlighted segment of **Figure $5C_1$**).

Figure 6 plots (from the top) the means of peak values (±95% confidence limits) for lung volume, expiratory tracheal flow, alveolar pressure, abdominal drive, and abdominal pressure measured under conditions of pre-cough eupnea (Eupnea), baseline cough (Base), and the three conditions represented in **Figure 5**. The differences in peak lung volumes during cough under the three conditions (A–C) confirm functional roles for both the excitatory and disinhibitory influences on inspiratory drive in the model. Deletion of the excitatory component of cough inspiratory drive

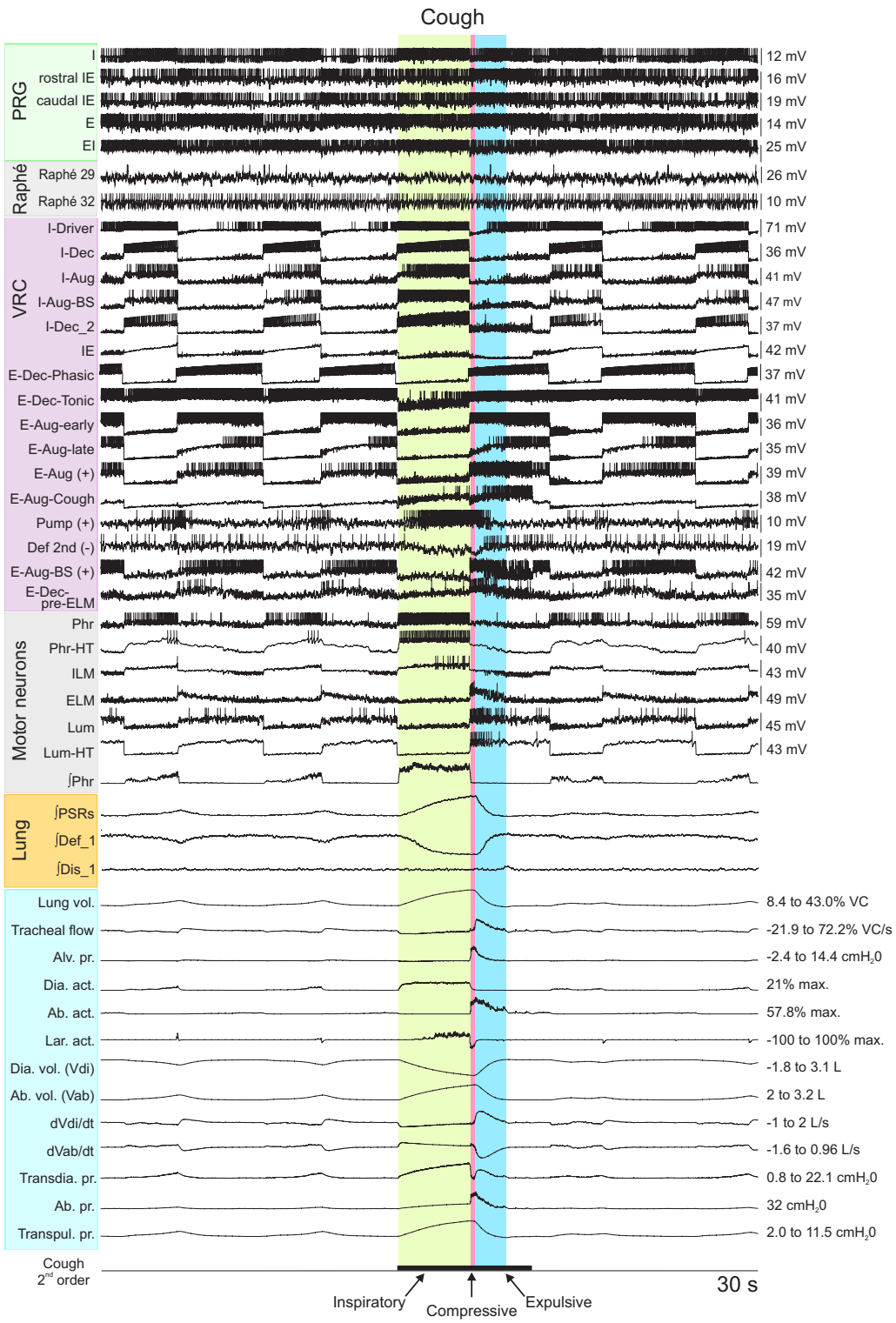

FIGURE 2 | Simulated eupneic respiratory cycles and an evoked cough motor pattern (inspiratory, compressive, and expulsive phases respectively labeled and highlighted by colored columns). The top 29 traces show membrane potentials and discharge patterns of individual respiratory neurons from a subset of the simulated populations as indicated by the labels on the left, arranged by region (PRG, raphé, VRC) or type (Motor neuron populations). The "integrated" phrenic trace represents the threshold crossing activity of the "PHR" population summed over 60 ms windows and indicates the inspiratory and expiratory phases of the respiratory cycle.

(Continued)

FIGURE 2 | Continued
Similarly, integrated traces from three lung afferent populations are plotted below the motor neuron records. (PSR, pulmonary stretch receptors) The 13 traces below those from the afferents show, in order from top to bottom: 1: lung volume (%VC, relative to RV); 2: tracheal flow (%VC/s, expiration positive (up)); 3: alveolar pressure (cmH_2O); 4–6: diaphragm activation, abdominal muscle activation, and net laryngeal muscle activation (dimensionless ratios to maximums); 7: diaphragm volume (L); 8: abdominal volume (L); 9: derivative of diaphragm volume (L/s); 10: derivative of abdominal volume (L/s); 11–13: transdiaphragmatic, abdominal, and transpulmonary pressures (cmH_2O). The bottom trace indicates the duration of a simulated cough stimulus. A fiber population composed of 100 fibers, each with a firing probability of 0.05 at each simulation time step and 100 type Ex_1 excitatory synaptic terminals (synaptic strength 0.03), represented cough receptor excitation. These fibers excited the Cough 2nd order neuron population (**Figure 1**); see **Table 2** for properties of this population and **Table 4** for details of connections with other populations. See text for further discussion.

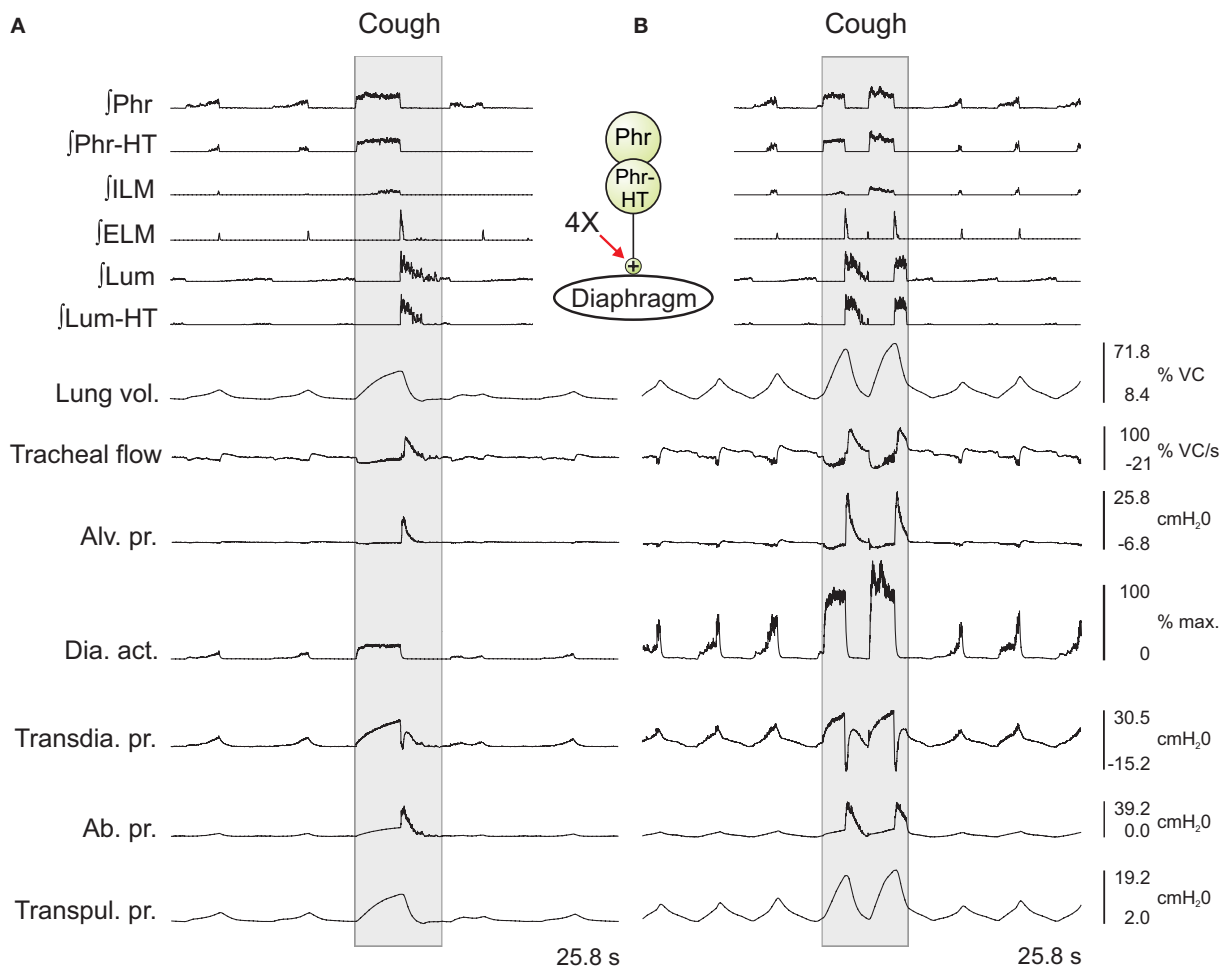

FIGURE 3 | Integrated traces of motor neuron population activities (top 6 traces, population labels on left) and biomechanical model outputs (labels on left; see legends of Figures 1 and 2 for definitions) during eupneic and "baseline" cough motor patterns before (A) and after (B) increasing the gain of diaphragm activation by a factor of 4 (see center schematic inset); otherwise, cough stimulus parameters as in Figure 2. Scales on right are for **(A,B)**. See text for further details.

(B) caused peak expiratory tracheal flow to decrease relative to the previous baseline and enhanced coughs (Base, A). However, peak abdominal drive and abdominal pressure did not change. A further reduction in peak lung volume to levels below eupneic control due to transiently increased E-Dec-Tonic inhibition of inspiratory drive (C) during cough resulted in no further change in expiratory flow, although peak abdominal pressure was reduced relative to baseline cough values.

A third series of simulations was done with the isolated biomechanical model. **Figure 7** plots the peak expiratory flow in four coughs simulated at different operating volumes but equal peak abdominal pressure of 26.5 cmH_2O. In each cough, the diaphragm and abdominal activations were first controlled to produce the desired operating volume, then the laryngeal muscles were controlled to close the airway, then the abdominal activation was controlled to produce an abdominal pressure of 26.5 cmH_2O, and

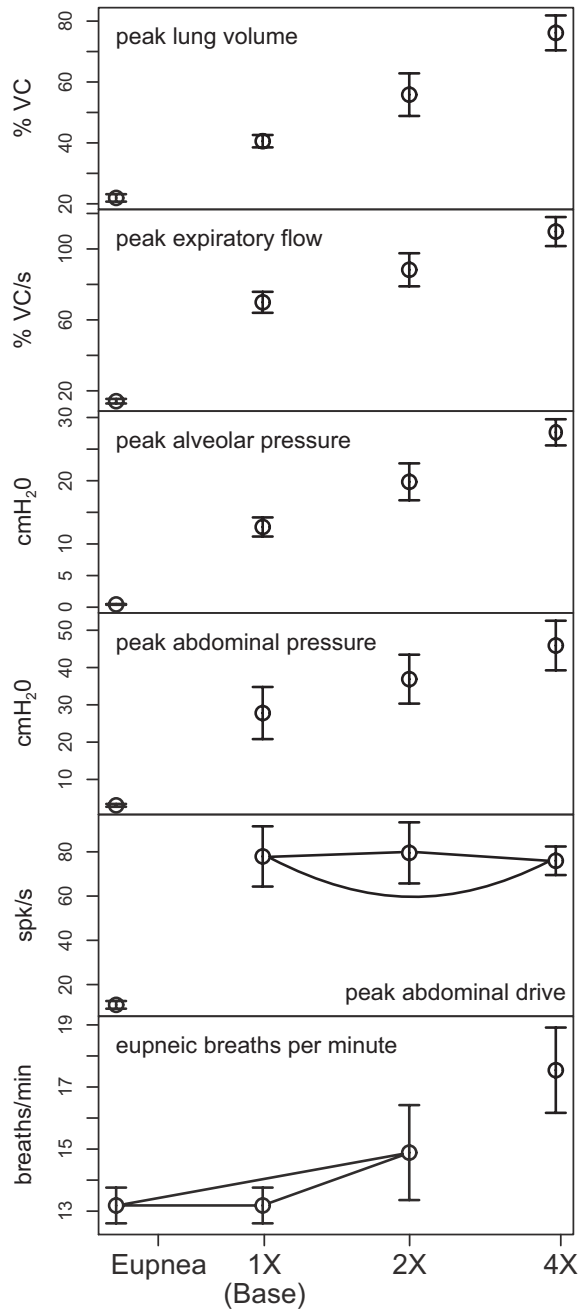

FIGURE 4 | Means of peak values (±95% confidence limits) of (from top) lung volume, expiratory tracheal flow, alveolar pressure, abdominal pressure, and abdominal drive together with respiratory cycle frequencies during pre-cough eupneic intervals (bottom) measured during model simulations of baseline cough (1×) and two conditions of increased phrenic-to-diaphragm activation gain (2×, 4×). Pairs of symbols connected by a line indicate no significant difference.

finally the laryngeal muscles were controlled to open the airway. Note that no statistics were done on these runs because the biomechanical model is deterministic. As in the first series of simulations, successively larger peak expiratory flow rates were associated with greater lung volumes during preceding inspiratory phases of the simulated cough, but unlike the first series, the peak abdominal pressure was the same in each cough. This result established that differences in flow with the generated changes in inspiratory (operating) volumes were not entirely due to the differences in pressure seen in the first series.

Comparisons with behaviors of antecedent models

Table 5 shows means of inspiratory and expiratory phase durations during eupnea and cough and peak firing rates of motor neuron populations common to the present model and those described in Rybak et al. (2008) and Poliaček et al. (2011). The current model has lower firing rates, similar to those observed *in vivo* (Iscoe, 1998; Mantilla and Sieck, 2011), and longer respiratory phase durations; inspiratory phase durations are also more variable (see coefficients of variation, **Table 5**).

These antecedent variants of the present neuronal network model were designed without a linked biomechanical system. The new joint neuromechanical model aids tuning of phase-timing relationships and the scaling of model motor outputs. To illustrate this model feature, we linked the earlier network models to the new biomechanical model. We note that the phrenic and lumbar motor neuron activities from the Rybak and Poliaček models are not strictly comparable because the current model has a second population of each type of motor neuron to model recruitment with increased drive. Lung stretch receptor inputs to the previous network models remained filtered versions of the phrenic motor output (i.e., there was no feedback from the mechanical models to the network). **Figure 8** shows records of lung volume, alveolar pressure, tracheal flow, and laryngeal muscle activation from the current neuromechanical model (**Figure 8A**) and for the two earlier models when connected to the biomechanical system (**Figures 8B,C**). The scaling and activation of the laryngeal muscles caused airway closure prior to each eupneic expiration when using the older models' outputs (lma = −1, flow flattens at 0). During cough in the previous models, the next inspiration started before the previous expiration was complete, resulting in a progressive increase in lung volume from cough to cough.

Influence of some added network connections

As noted in Sections "Linking the Neural Network and Biomechanical Models" and "Additional Enhancements to the Current Network Model," the current network model includes lung afferents responsive to lung deflation and presynaptic inhibition by E-Dec-Tonic neurons of excitatory inputs from the I-Aug population to I-Dec_2 neurons. The latter feature was added to prolong I-Dec_2 neuron activity when E-Dec-Tonic neuron I-phase activity is reduced. Removal of these three speculative model elements resulted in shorter inspiratory phase durations (**Table 5**, "No speculative" and "Current" columns).

DISCUSSION

The new biomechanical model system detailed in the Results incorporates several features developed using measures from human subjects. These include a model of the abdominal volume that captures the interaction of the diaphragm, rib cage, and abdominal wall based on Grassino et al. (1978), an abdominal wall model

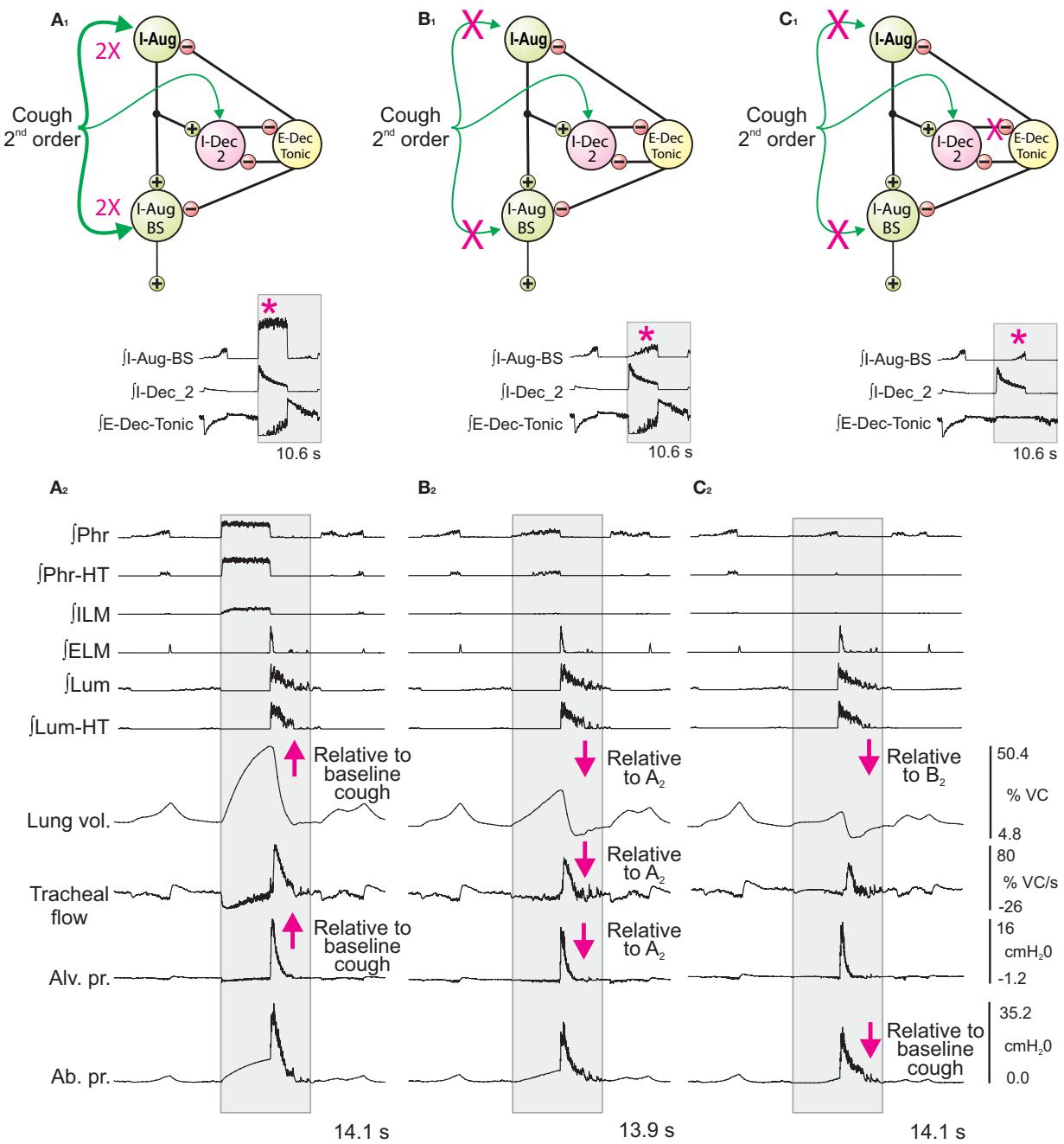

FIGURE 5 | Network perturbations that selectively alter cough inspiratory drive change lung volume and also influence tracheal flow and abdominal pressure during the subsequent expiratory phase of cough. Each panel (**A_1–C_1**) shows a schematic of a subset of the model network and changes in synaptic strengths during simulated cough stimulation relative to the baseline conditions represented in and described for **Figure 3A**. Corresponding panels (**A_2–C_2**) show integrated traces of motor neuron population activities and biomechanical model outputs (left labels) for the respective perturbations of inspiratory drive. Arrows mark changes. See text for further details.

based on measurements of the curvature of the abdomen by Song et al. (2006) taken during insufflation for laparoscopic surgery, and a model of the larynx using results from Tully et al. (1990, 1991). The mechanical model was linked to an enhanced version of a previously described computational network model (Rybak et al., 2008; Poliaček et al., 2011) with IF neuron populations, connections, and other properties measured or inferred from *in vivo* and *in vitro* studies of mammalian brainstem circuits for breathing and cough (Shannon et al., 2000; Segers et al., 2008; Lindsey et al., 2012).

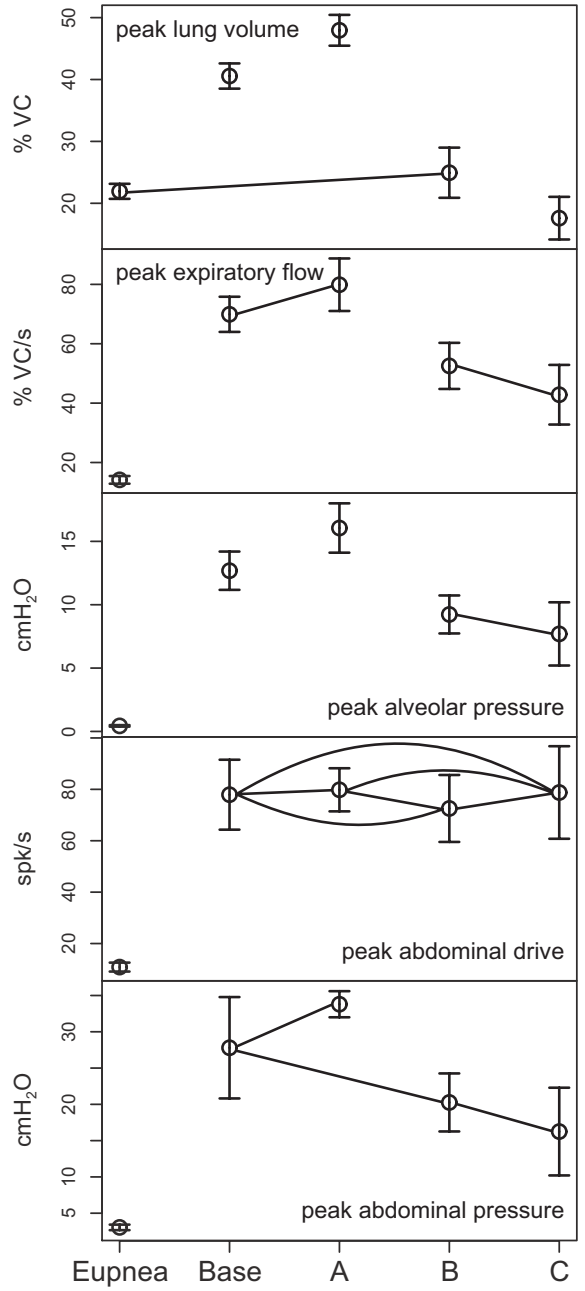

FIGURE 6 | Means of peak values (±95% confidence limits) of (from top) lung volume, expiratory tracheal flow, alveolar pressure, abdominal drive, and abdominal pressure measured under conditions of pre-cough eupnea (Eupnea), baseline cough (Base), doubling of the synaptic strength between Cough 2nd order and the I-Aug and I-Aug-BS populations (A), elimination of Cough 2nd order excitation of the I-Aug and I-Aug-BS populations (B), and additionally, the subsequent elimination of I-Dec_2 neuron inhibition of E-Dec-Tonic neurons *during* the inspiratory phase of the evoked cough cycle (C). Pairs of symbols connected by a line indicate no significant difference.

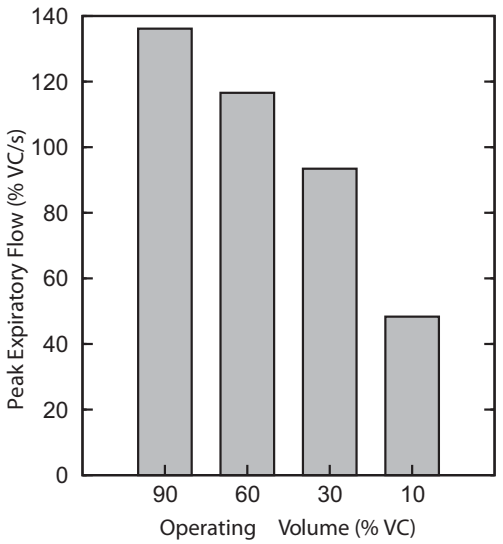

FIGURE 7 | Peak expiratory flow in four coughs simulated with the isolated biomechanical model at different operating volumes but equal peak abdominal pressure of 26.5 cmH_2O. There are no error bars because these are runs of the deterministic model.

The joint neuromechanical system is a prototype for study of the neural control of breathing and airway defensive behaviors. To our knowledge, computational neural network models of cough generation have been evaluated previously using measures of motor neuron burst sequences, phase durations, and the time varying firing rates of neuron populations that only indirectly reflect possible muscle activation patterns and their attendant biomechanical consequences. The new model generated eupneic breathing and cough motor patterns together with corresponding alterations in lung volume, tracheal air flow, and other relevant metrics of cough mechanics. The present results also show the utility of the model as an aid for tuning the motor pattern and as a tool to evaluate the efficacy of phase-timing relationships.

A specific goal of this project was to assess model output during cough under conditions of altered inspiratory drive. We were motivated in part by the recent observation that lung operating volume at the onset of the compressive phase of cough influences subsequent air flow velocities during the expulsive phase (Smith et al., 2012). Inspiratory drive was altered by two distinct approaches: (i) increased gain of phrenic motor neuron activation of the diaphragm, and (ii) sequential modulation or deletion of synaptic inputs to inspiratory premotor populations. Both perturbations altered cough inspiratory volume. We also found changes in expulsive phase air flow associated with corresponding changes in peak abdominal pressure attributable to cough mechanics, results that could not have been achieved by measures of the motor pattern output alone. In the first protocol, higher end inspiratory volumes resulted in greater tracheal air flow during the subsequent expulsive phase under the same abdominal expiratory motor drives. Under the second protocol, the difference in operating volumes between the enhanced drive and reduced excitatory drive states was associated with corresponding reductions in expiratory flow and peak abdominal pressure.

Table 5 | Comparison with previous models.

Variable	Unit	Rybak				Poliaček				No speculative				Current	
		Mean	*p*	CV	*p*	Mean	*p*	CV	*p*	Mean	*p*	CV	*p*	Mean	CV
EUPNEA															
ELM	spk/s	170	0.00*	0.10	0.00*	231	0.00*	0.08	0.00*	19	1.00	0.23	1.00	19	0.23
ILM	spk/s	83	0.00*	0.06	0.00*	49	0.00*	0.07	0.00*	26	0.62	0.29	1.00	19	0.47
LUMBAR	spk/s	24	0.00*	0.05	0.07	135	0.00*	0.08	1.00	10	1.00	0.08	1.00	11	0.08
PHRENIC	spk/s	109	0.00*	0.10	1.00	129	0.00*	0.11	1.00	62	0.33	0.08	1.00	56	0.13
Ti	s	0.663	0.00*	0.04	0.00*	1.506	0.00*	0.07	1.00	1.744	0.03*	0.07	1.00	1.939	0.10
Te	s	1.053	0.00*	0.12	1.00	1.396	0.00*	0.10	1.00	2.905	1.00	0.12	1.00	2.760	0.11
COUGH															
ELM	spk/s	302	0.00*	0.33	0.04*	521	0.00*	0.22	0.86	55	1.00	0.07	1.00	55	0.09
ILM	spk/s	238	0.00*	0.11	1.00	154	0.00*	0.14	1.00	37	1.00	0.10	1.00	36	0.10
LUMBAR	spk/s	235	0.00*	0.07	1.00	536	0.00*	0.10	1.00	76	1.00	0.11	1.00	76	0.06
PHRENIC	spk/s	348	0.00*	0.14	0.16	705	0.00*	0.16	0.07	98	1.00	0.04	1.00	97	0.05
Ti	s	0.494	0.00*	0.20	1.00	0.503	0.00*	0.23	1.00	2.471	1.00	0.09	1.00	2.302	0.12
Te	s	0.564	0.00*	0.24	1.00	0.476	0.00*	0.19	1.00	3.490	1.00	0.19	1.00	3.242	0.15

The behaviors of the networks in Rybak et al. (2008) and Poliaček et al. (2011) and a model without recently added speculative connections are compared with the model in this paper. The mean of the peak (in each respiratory cycle) firing rates for four motor populations and the mean inspiratory (Ti) and expiratory (Te) phase durations are shown. Each mean for each previous model is followed by the p-value from a two-sided t-test with non-pooled SD for the difference in means between the previous model and the current model. The cycle counts for Rybak, Poliaček, No speculative, and Current, respectively, were 67, 40, 24, and 24 for eupnea and 56, 60, 10, and 10 for cough. The table also shows the coefficient of variation (CV) for each firing rate or phase duration for assessment of differences in variability between the models. Each CV is followed by the p-value from an F-test for the ratio of variances of the observations divided by their mean between the previous model and the current model. p-Values have been adjusted for multiple testing (Holm, 1979); significant values (at the 0.05 level) are marked with an asterisk.

DISCREPANCIES WITH EXPERIMENTAL RESULTS AND MODEL LIMITATIONS

The discrepancy between the present results and those of Smith et al. (2012) is noteworthy. The latter study found changes in expulsive flow rates during voluntary coughs from different operating volumes in the absence of significant alterations in thoracic or abdominal pressures, whereas we found changes in flow associated with changes in abdominal pressure, despite no change in abdominal drive. The change in expiratory pressure in the model is due to the action of the intercostal and accessory muscles; the expiratory pressure increases because the pressure from those muscles in the model increases with rib cage volume at constant activation. Our model calculates the expiratory pressure generated by the intercostal and accessory muscles at TLC and full abdominal activation necessary to produce maximal expiratory pressure, and at RV to complete the pressure balance on the rib cage (a much smaller number; see "Additional Enhancements to the Current Network Model"). The model assumes that the expiratory pressure generated by the intercostal and accessory muscles scales linearly with rib cage volume between RV and TLC, and linearly with abdominal activation, leading to higher pressures at higher rib cage volumes with equal activation. The experimentally observed increase in maximal expiratory pressure with rib cage volume could be due to increased activation of the intercostals or improved mechanical advantage at larger volumes or a combination of the two. If improved mechanical advantage is a factor, the brainstem would have to reduce drive at higher volumes during cough to avoid higher pressures, suggesting that it may be sensing the generated pressures and adjusting drive accordingly (see e.g., discussion in "Tonic Expiratory Neurons: Model Results and Predictions"). A refined configuration to accommodate separate intercostal muscles, intercostal motor neuron populations, and muscle afferents (Shannon, 1986) and their control of the chest wall would be useful in this regard.

When we ran the biomechanical model in isolation with reduced abdominal drive at higher volumes in order to maintain an equal peak pressure (see **Figure 7**), we saw peak flow rate changes comparable in magnitude to those seen by Smith et al. (2012, Figure 3B), due to the increasing recoil pressure of the lung at higher volumes. The peak flow rates were comparable despite the fact that the peak abdominal pressure in our simulation was less than half that observed by Smith et al. This lower resistance is likely due to the fact that we did not model airway collapse, which is known to limit peak flow rates (Knudson et al., 1974).

We found that increased flow during cough at higher lung volume is primarily due to increased lung recoil pressure. The lung recoil pressure certainly increases with lung volume, but the accuracy of the resulting flow in the model may be affected by certain known limitations of the model: (i) airway collapse during cough is not modeled, resulting in an underestimate of airway resistance; (ii) the lung compliance is assumed to be constant in the model, whereas it is thought to vary with lung volume *in vivo*; (iii) the model does not take into account hysteresis in the lung flow-volume curve; (iv) volume changes due to blood shift out of the trunk during cough are not modeled; and (v) volume changes due to gas compression are not modeled (see Smith et al., 2012 for data on volume changes due to blood shift and gas compression). Nevertheless, our model suggests the hypothesis that the

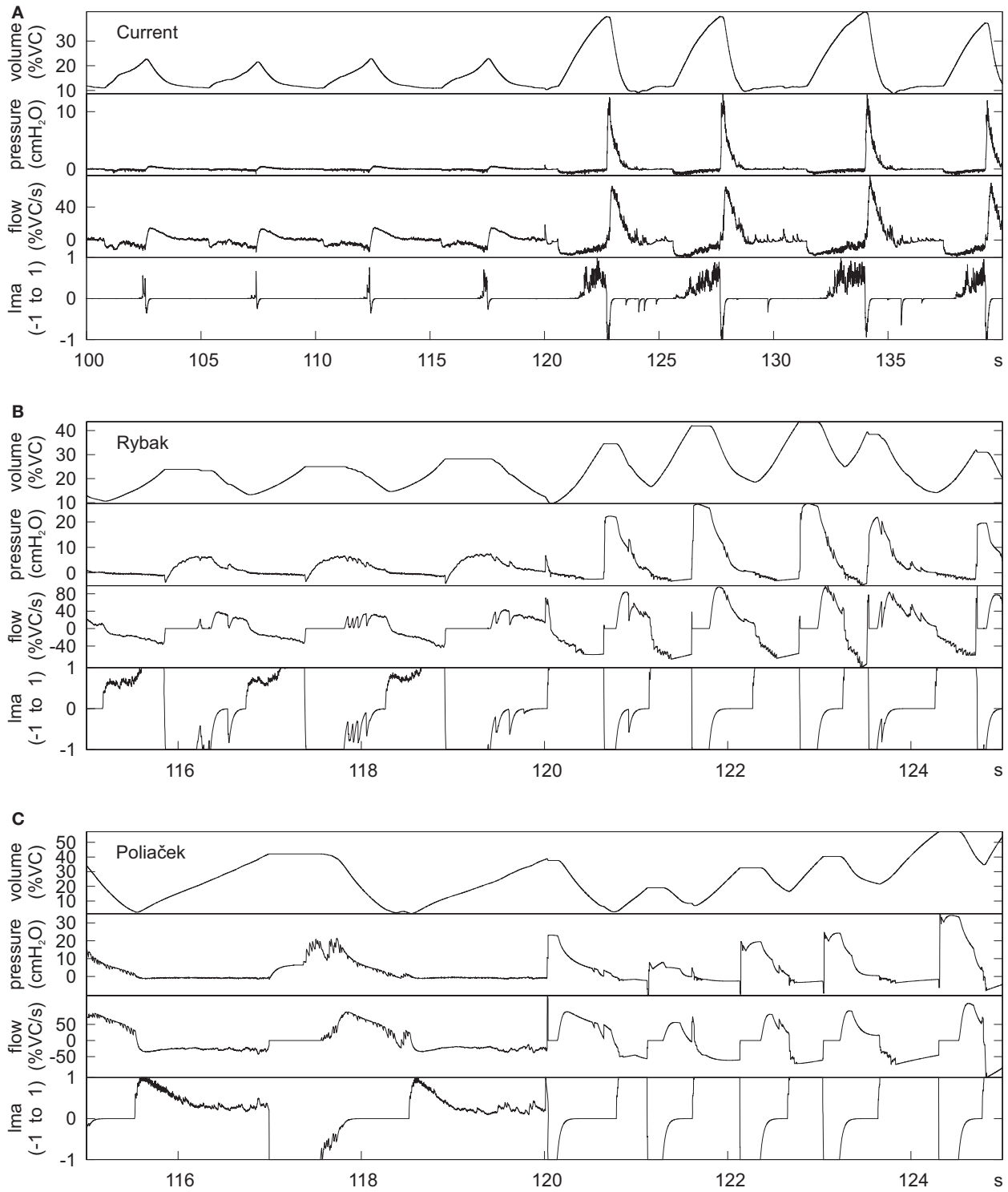

FIGURE 8 | Outputs of the mechanical model when linked to the current network model (A) and the networks in (B) (Rybak et al., 2008) and (C) (Poliaček et al., 2011). The earlier networks were designed without a mechanical model, but were connected to the current mechanical model to generate these plots. The plots are lung volume, alveolar pressure, tracheal flow, and laryngeal muscle activation (lma). The value of lma is 1 for a maximally open glottis, 0 for the resting diameter, and −1 for a closed glottis. The first few cycles are eupneic cycles, and the rest are coughs. The time scale is different for the current model because it was designed with slower cycles to match human respiration.

increased flow during cough is primarily due to increased lung recoil pressure.

TONIC EXPIRATORY NEURONS: MODEL RESULTS AND PREDICTIONS

The model incorporated multiple target sites for cough drive modulation, a feature of the network architecture based on correlational linkage maps of functional connectivity and associated neuronal responses to stimuli that either enhance or suppress inspiratory drive *in vivo* (Lindsey et al., 1998; Shannon et al., 2000; Poliaček et al., 2011; Ott et al., 2012). Deletion of excitatory mechanisms for cough inspiratory drive resulted in reductions in peak lung volume and a subsequently diminished peak air flow relative to baseline during the expulsive phase (**Figure 6B**). Although removal of the disinhibitory component of the drive enhancement mechanism mediated by the E-Dec-Tonic population did not further reduce expulsive phase air flow velocity, it did lead to both an additional decrease in inspiratory phase lung operating volume and a reduced expulsive phase peak abdominal pressure relative to baseline values, even though peak abdominal drive did not change.

We have previously proposed the hypothesis that tonic expiratory neurons provide a reservoir for inspiratory drive modulation. Suppression of their inspiratory phase activity during central chemoreceptor-mediated drive and spike train cross-correlation analyses both suggest that VRC tonic E neuron inhibition of premotor inspiratory neurons is reduced in high drive states, at least in part, by increased I-Dec neuron inhibition (Ott et al., 2012).

The present model included a network "module" previously introduced (Poliaček et al., 2011) for baroreceptor modulation of breathing. That circuit, inferred from spike train correlational linkages and neuron responses to baroreceptor stimulation (Lindsey et al., 1998), operated via excitatory and disinhibitory raphé neuron influences acting upon VRC E-Dec-Phasic and E-Dec-Tonic neuron populations. Simulations of baroreceptor activation using prior models (Poliaček et al., 2011; Lindsey et al., 2012) with circuits inferred from *in vivo* observations (see references in Lindsey et al., 1998; Poliaček et al., 2011; Ott et al., 2012) generated prolongation of expiration and reduced inspiratory drive during both eupneic respiratory cycles and evoked cough.

Collectively, these data support the hypothesis that inhibition of the E-Dec-Tonic population in the cough network amplifies inspiratory drive via disinhibition. Experimental data consistent with this hypothesis is presented in a companion paper (Segers et al., 2012). Modulation of tonic expiratory neuron activity could also operate in a push-pull mechanism in which cough drive is balanced against the potentially suppressive influences of blood pressure changes caused by cough mechanics.

FUTURE DIRECTIONS

The present model provides a framework for integrating respiratory network model development with respiratory mechanics and will guide and facilitate scaling and timing of motor neuron activity patterns and functionally antecedent connectivity for the generation of breathing, cough, and swallow. The simulations of cough and breathing suggest that an important area of focus for future modeling efforts will be reconciliation of known differential effects of pulmonary volume-related feedback on breathing and airway defensive behaviors such as coughing and the expiratory reflex. Specific components of the model that are proposed to have the greatest effect on its potential for prediction are the gain of pulmonary volume-related feedback and the interaction of this feedback with cough-related sensory information. Future models should also guide experiments targeting the control of behavior that must be tightly coordinated with breathing, such as sniffing, swallowing, and vocalization.

ACKNOWLEDGMENTS

This work was supported by NIH grants HL89104, HL89071, and HL103415 from NHLBI, and grant NS19814 from NINDS.

REFERENCES

A.D.A.M. Medical Encyclopedia. (2012). *Rapid Shallow Breathing.* Available at: http://www.nlm.nih.gov/medlineplus/ency/article/007198.htm [accessed May 9, 2012].

Agostoni, E., Gurtner, G., Torri, G., and Rahn, H. (1966). Respiratory mechanics during submersion and negative-pressure breathing. *J. Appl. Physiol.* 21, 251–258.

Agostoni, E., and Rahn, H. (1960). Abdominal and thoracic pressures at different lung volumes. *J. Appl. Physiol.* 15, 1087–1092.

Artemiadis, P. K., and Kyriakopoulos, K. J. (2005). "Teleoperation of a robot manipulator using EMG signals and a position tracker," in *IEEE/RSJ International Conference on Intelligent Robots and Systems, Edmonton, 2005.*

Baekey, D. M., Morris, K. F., Nuding, S. C., Segers, L. S., Li, Z., Lindsey, B. G., and Shannon, R. (2001). Involvement of ventral respiratory group neurons in the fictive expiration reflex. *FASEB J.* abstr. 15, A798.

Baier, H., Wanner, A., Zarzecki, S., and Sackner, M. A. (1977). Relationships among glottis opening, respiratory flow, and upper airway resistance in humans. *J. Appl. Physiol.* 43, 603–611.

Barnas, G. M., Yoshino, K., Stamenovic, D., Kikuchi, Y., Loring, S. H., and Mead, J. (1989). Chest wall impedance partitioned into rib cage and diaphragm-abdominal pathways. *J. Appl. Physiol.* 66, 350–359.

Bergren, D. R., and Peterson, D. F. (1993). Identification of vagal sensory receptors in the rat lung: are there subtypes of slowly adapting receptors? *J. Physiol.* 464, 681–698.

Bolser, D. C., Davenport, P. W., Golder, F. J., Baekey, D. M., Morris, K. F., Lindsey, B. G., and Shannon, R. (2003). "Neurogenesis of cough," in *Cough: Causes, Mechanisms and Therapy*, 1st Edn, eds H. Boushey, K. Chung, and J. G. Widdicombe (Malden: Blackwell Publishing Ltd.), 173–180.

Brancatisano, T., Collett, P. W., and Engel, L. A. (1983). Respiratory movements of the vocal cords. *J. Appl. Physiol.* 54, 1269–1276.

Braun, N. M., Arora, N. S., and Rochester, D. F. (1982). Force-length relationship of the normal human diaphragm. *J. Appl. Physiol.* 53, 405–412.

Breen, B. J., Gerken, W. C., and Butera, R. J. (2003). Hybrid integrate-and-fire model of a bursting neuron. *Neural Comput.* 15, 2843–2862.

Cheng, L., Ivanova, O., Fan, H.-H., and Khoo, M. C. K. (2010). An integrative model of respiratory and cardiovascular control in sleep-disordered breathing. *Respir. Physiol. Neurobiol.* 174, 4–28.

Cheng, L., and Khoo, M. C. (2012). Modeling the autonomic and metabolic effects of obstructive sleep apnea: a simulation study. *Front. Physiol.* 2:111. doi:10.3389/fphys.2011.00111

Chiel, H. J., Ting, L. H., Ekeberg, Ö., and Hartmann, M. J. Z. (2009). The brain in its body: motor control and sensing in a biomechanical context. *J. Neurosci.* 29, 12807–12814.

Chow, J. W., and Darling, W. G. (1999). The maximum shortening velocity of muscle should be scaled with activation. *J. Appl. Physiol.* 86, 1025–1031.

Cluzel, P., Similowski, T., Chartrand-Lefebvre, C., Zelter, M., Derenne, J.-P., and Grenier, P. A. (2000). Diaphragm and chest wall: assessment of the inspiratory pump with MR imaging – preliminary observations. *Radiology* 215, 574–583.

De Troyer, A., Estenne, M., Ninane, V., Van Gansbeke, D., and Gorini, M. (1990). Transversus abdominis muscle function in humans. *J. Appl. Physiol.* 68, 1010–1016.

Dick, T. E., Shannon, R., Lindsey, B. G., Nuding, S. C., Segers, L. S., Baekey, D. M., and Morris, K. F. (2008). Pontine respiratory-modulated activity before and after vagotomy in decerebrate cats. *J. Physiol.* 586, 4265–4282.

D'Urzo, A. D., Rubinstein, I., Lawson, V. G., Vassal, K. P., Rebuck, A. S., Slutsky, A. S., and Hoffstein, V. (1988). Comparison of glottic areas measured by acoustic reflections vs. computerized tomography. *J. Appl. Physiol.* 64, 367–370.

Estenne, M., Yernault, J. C., and De Troyer, A. (1985). Rib cage and diaphragm-abdomen compliance in humans: effects of age and posture. *J. Appl. Physiol.* 59, 1842–1848.

Fitz-Clarke, J. R. (2007). Computer simulation of human breath-hold diving: cardiovascular adjustments. *Eur. J. Appl. Physiol. Occup. Physiol.* 100, 207–224.

Gaumann, A., Hoeckel, M., and Konerding, M. (1999). The anatomic basis of the transversus and rectus abdominis musculoperitoneal (TRAMP) composite flap. *Hernia* 3, 39–41.

Gilroy, R. J., Lavietes, M. H., Loring, S. H., Mangura, B. T., and Mead, J. (1985). Respiratory mechanical effects of abdominal distension. *J. Appl. Physiol.* 58, 1997–2003.

Goldman, M. D., Grassino, A., Mead, J., and Sears, T. A. (1978). Mechanics of the human diaphragm during voluntary contraction: dynamics. *J. Appl. Physiol.* 44, 840–848.

Grassino, A., Goldman, M. D., Mead, J., and Sears, T. A. (1978). Mechanics of the human diaphragm during voluntary contraction: statics. *J. Appl. Physiol.* 44, 829–839.

Grimby, G., Goldman, M., and Mead, J. (1976). Respiratory muscle action inferred from rib cage and abdominal V-P partitioning. *J. Appl. Physiol.* 41, 739–751.

Harris, R. S. (2005). Pressure-volume curves of the respiratory system. *Respir. Care* 50, 78–98.

Hatze, H. (1981). *Myocybernetic Control Models of Skeletal Muscle: Characteristics and Applications*. Pretoria: University of South Africa.

Hey, E. N., and Price, J. F. (1982). Nasal conductance and effective airway diameter. *J. Physiol. (Lond.)* 330, 429–437.

Hill, A. V. (1938). The heat of shortening and the dynamic constants of muscle. *Proc. R. Soc. Lond. B Biol. Sci.* 126, 136–195.

Holm, S. (1979). A simple sequentially rejective multiple test procedure. *Scand. J. Statist.* 6, 65–70.

Hutchison, A. A., and Lindsey, B. G. (2009). "Modeling central brainstem mechanisms in eupnea, grunting, incremental breathing and vagotomy," in *American Journal of Respiratory and Critical Care Medicine (Abstract) from American Thoracic Society International Conference*, San Diego, CA.

Iscoe, S. D. (1998). Control of abdominal muscles. *Prog. Neurobiol.* 56, 433–506.

Iscoe, S. D., and Gordon, S. P. (1992). Chest wall distortion and discharge of pulmonary slowly adapting receptors. *J. Appl. Physiol.* 73, 1619–1625.

Kamel, K. S., Lau, G., and Stringer, M. D. (2009). *In vivo* and *in vitro* morphometry of the human trachea. *Clin. Anat.* 22, 571–579.

Kim, M. J., Druz, W. S., Danon, J., Machnach, W., and Sharp, J. T. (1976). Mechanics of the canine diaphragm. *J. Appl. Physiol.* 41, 369–382.

Knudson, R. J., Mead, J., and Knudson, D. E. (1974). Contribution of airway collapse to supramaximal expiratory flows. *J. Appl. Physiol.* 36, 653–667.

Konno, K., and Mead, J. (1967). Measurement of the separate volume changes of rib cage and abdomen during breathing. *J. Appl. Physiol.* 22, 407–422.

Kreith, F., Berger, S., Churchill, S., Tullis, J. P., Tullis, B., White, F., Kumar, A., Todd, J., Chen, J., Irvine, T., Capobianchi, M., Kennedy, F., Booser, E. R., Wilcock, D., Boehm, R., Reitz, R., Kim, J., McDonald, A., Sherif, S., and Bhushan, B. (2004). "Fluid mechanics," in *The CRC Handbook of Mechanical Engineering*, 2nd Edn, eds F. Kreith and D. Y. Goswami (Boca Raton: CRC Press), 3.1–3.232.

Laplace, P. S. (1808). *Traité de mécanique céleste: supplément au dixième livre du traité de méchanique céleste sur l'action capillaire*. Paris: Duprat.

Lichtenstein, O., Ben-Haim, S. A., Saidel, G. M., and Dinnar, U. (1992). Role of the diaphragm in chest wall mechanics. *J. Appl. Physiol.* 72, 568–574.

Lindsey, B. G., Arata, A., Morris, K. F., Hernandez, Y. M., and Shannon, R. (1998). Medullary raphé neurones and baroreceptor modulation of the respiratory motor pattern in the cat. *J. Physiol.* 512, 863–882.

Lindsey, B. G., Rybak, I. A., and Smith, J. C. (2012). Computational models and emergent properties of respiratory neural networks. *Compr. Physiol.* 2, 1619–1670.

Loring, S. H., and Mead, J. (1982). Action of the diaphragm on the rib cage inferred from a force-balance analysis. *J. Appl. Physiol.* 53, 756–760.

Luck, J. C. (1970). Afferent vagal fibres with an expiratory discharge in the rabbit. *J. Physiol. (Lond.)* 211, 63–71.

MacGregor, R. J. (1987). *Neural and Brain Modeling*. New York: Academic Press.

Macklem, P. T., Gross, D., Grassino, G. A., and Roussos, C. (1978). Partitioning of inspiratory pressure swings between diaphragm and intercostal/accessory muscles. *J. Appl. Physiol.* 44, 200–208.

Mantilla, C. B., and Sieck, G. C. (2011). Phrenic motor unit recruitment during ventilatory and non-ventilatory behaviors. *Respir. Physiol. Neurobiol.* 179, 57–63.

Matsumoto, S., Ikeda, M., Nishikawa, T., Yoshida, S., Tanimoto, T., Ito, M., Saiki, C., and Takeda, M. (2002). Excitatory mechanism of deflationary slowly adapting pulmonary stretch receptors in the rat lung. *J. Pharmacol. Exp. Ther.* 300, 597–604.

McCool, F. D. (2006). Global physiology and pathophysiology of cough. *Chest* 129, 48S–53S.

Mead, J., and Loring, S. H. (1982). Analysis of volume displacement and length changes of the diaphragm during breathing. *J. Appl. Physiol.* 53, 750–755.

Molkov, Y. I., Abdala, A. P. L., Bacak, B. J., Smith, J. C., Paton, J. F. R., and Rybak, I. A. (2010). Late-expiratory activity: emergence and interactions with the respiratory CPG. *J. Neurophysiol.* 104, 2713–2729.

Nail, B. S., Sterling, G. M., and Widdicombe, J. G. (1972). Patterns of spontaneous and reflexly-induced activity in phrenic and intercostal motoneurons. *Exp. Brain Res.* 15, 318–332.

Ott, M. M., Nuding, S. C., Segers, L. S., O'Connor, R., Morris, K. F., and Lindsey, B. G. (2012). Central chemoreceptor modulation of breathing via multipath tuning in medullary ventrolateral respiratory column circuits. *J. Neurophysiol.* 107, 603–617.

Paintal, A. S. (1955). Impulses in vagal afferent fibres from specific pulmonary deflation receptors: the response of these receptors to phenyl diguanide, potato starch, 5-hydroxytryptamine and nicotine, and their rôle in respiratory and cardiovascular reflexes. *Exp. Physiol.* 40, 89–111.

Permutt, S., and Martin, H. B. (1960). Static pressure-volume characteristics of lungs in normal males. *J. Appl. Physiol.* 15, 819–825.

Poliaček, I., Morris, K. F., Lindsey, B. G., Segers, L. S., Rose, M. J., Corrie, L. W.-C., Wang, C., Pitts, T. E., Davenport, P. W., and Bolser, D. C. (2011). Blood pressure changes alter tracheobronchial cough: computational model of the respiratory-cough network and in vivo experiments in anesthetized cats. *J. Appl. Physiol.* 111, 861–873.

Ratnovsky, A., Elad, D., and Halpern, P. (2008). Mechanics of respiratory muscles. *Respir. Physiol. Neurobiol.* 163, 82–89.

Ratnovsky, A., Zaretsky, U., Shiner, R. J., and Elad, D. (2003). Integrated approach for in vivo evaluation of respiratory muscles mechanics. *J. Biomech.* 36, 1771–1784.

Reid, M. B., Feldman, H. A., and Miller, M. J. (1987). Isometric contractile properties of diaphragm strips from alcoholic rats. *J. Appl. Physiol.* 63, 1156–1164.

Renotte, C., Remy, M., and Saucez, P. (1998). Dynamic model of airway pressure drop. *Med. Biol. Eng. Comput.* 36, 101–106.

Riddle, W., and Younes, M. (1981). A model for the relation between respiratory neural and mechanical outputs. II. Methods. *J. Appl. Physiol.* 51, 979–989.

Roca, J., Burgos, F., Sunyer, J., Saez, M., Chinn, S., Anto, J. M., Rodriguez-Roisin, R., Quanjer, P. H., Nowak, D., and Burney, P. (1998). References values for forced spirometry. Group of the European community respiratory health survey. *Eur. Respir. J.* 11, 1354–1362.

Rohrer, F. (1915). Der stromungswiderstand in den menschlichen atemwegen und der einfluss der unregelmassigen verzweigung des bronchialsystems auf den atmungsverlauf in verschiedenen lungenbezirken. *Archiv fur die Gesamte Physiologie des Menschen und der Tiere* 162, 225–299.

Rosen, J., Fuchs, M. B., and Arcan, M. (1999). Performances of Hill-type and neural network muscle models: toward a myosignal-based exoskeleton. *Comput. Biomed. Res.* 32, 415–439.

Rybak, I. A., O'Connor, R., Ross, A., Shevtsova, N. A., Nuding, S. C., Segers, L. S., Shannon, R., Dick, T. E., Dunin-Barkowski, W. L., Orem, J. M., Solomon, I. C., Morris, K. F., and Lindsey, B. G. (2008). Reconfiguration of the pontomedullary respiratory network: a computational modeling study with coordinated in vivo experiments. *J. Neurophysiol.* 100, 1770–1799.

Segers, L. S., Nuding, S. C., Dick, T. E., Shannon, R., Baekey, D. M.,

Solomon, I. C., Morris, K. F., and Lindsey, B. G. (2008). Functional connectivity in the pontomedullary respiratory network. *J. Neurophysiol.* 100, 1749–1769.

Segers, L. S., Nuding, S. C., Vovk, A., Baekey, D. M., O'Connor, R., Morris, K. F., Lindsey, B. G., Shannon, R., and Bolser, D. C. (2012). Discharge identity of medullary inspiratory neurons is altered during repetitive fictive cough. *Front. Physiol.* 3:223. doi:10.3389/fphys.2012.00223

Shannon, R. (1986). "Reflexes from the respiratory muscles and controvertebral joints," in *Handbook of Physiology. The Respiratory System. Control of Breathing*, Sect. 3, Part 1, eds N. S. Cherniack and J. G. Widdicombe (Washington, DC: American Physiological Society), 431–447.

Shannon, R., Baekey, D. M., Morris, K. F., Li, Z., and Lindsey, B. G. (2000). Functional connectivity among ventrolateral medullary respiratory neurones and responses during fictive cough in the cat. *J. Physiol.* 525, 207–224.

Shannon, R., Baekey, D. M., Morris, K. F., and Lindsey, B. G. (1998). Ventrolateral medullary respiratory network and a model of cough motor pattern generation. *J. Appl. Physiol.* 84, 2020–2035.

Shannon, R., Baekey, D. M., Morris, K. F., Nuding, S. C., Segers, L. S., and Lindsey, B. G. (2004). Production of reflex cough by brainstem respiratory networks. *Pulm. Pharmacol. Ther.* 17, 369–376.

Sharpey-Schafer, E. P. (1953). Effects of coughing on intra-thoracic pressure, arterial pressure and peripheral blood flow. *J. Physiol. (Lond.)* 122, 351–357.

Siafakas, N. M., Morris, A. J., and Green, M. (1979). Thoracoabdominal mechanics during relaxed and forced vital capacity. *J. Appl. Physiol.* 47, 38–42.

Simpson, L. L. (1968). Sizing piping for process plants. *Chem. Eng.* 75, 192–214.

Smith, J., and Bellemare, F. (1987). Effect of lung volume on *in vivo* contraction characteristics of human diaphragm. *J. Appl. Physiol.* 62, 1893–1900.

Smith, J. A., Aliverti, A., Quaranta, M., McGuinness, K., Kelsall, A., Earis, J., and Calverley, P. M. (2012). Chest wall dynamics during voluntary and induced cough in healthy volunteers. *J. Physiol. (Lond.)* 590, 563–574.

Song, C., Alijani, A., Frank, T., Hanna, G. B., and Cuschieri, A. (2006). Mechanical properties of the human abdominal wall measured in vivo during insufflation for laparoscopic surgery. *Surg. Endosc.* 20, 987–990.

Suárez, A. A., Pessolano, F. A., Monteiro, S. G., Ferreyra, G., Capria, M. E., Mesa, L., Dubrovsky, A., and De Vito, E. L. (2002). Peak flow and peak cough flow in the evaluation of expiratory muscle weakness and bulbar impairment in patients with neuromuscular disease. *Am. J. Phys. Med. Rehabil.* 81, 506–511.

Tully, A., Brancatisano, A., Loring, S. H., and Engel, L. A. (1990). Relationship between thyroarytenoid activity and laryngeal resistance. *J. Appl. Physiol.* 68, 1988–1996.

Tully, A., Brancatisano, A., Loring, S. H., and Engel, L. A. (1991). Influence of posterior cricoarytenoid muscle activity on pressure-flow relationship of the larynx. *J. Appl. Physiol.* 70, 2252–2258.

Wei, J. Y., and Shen, E. (1985). Vagal expiratory afferent discharges during spontaneous breathing. *Brain Res.* 335, 213–219.

Younes, M., and Riddle, W. (1981). A model for the relation between respiratory neural and mechanical outputs. I. Theory. *J. Appl. Physiol.* 51, 963–978.

Younes, M., Riddle, W., and Polacheck, J. (1981). A model for the relation between respiratory neural and mechanical outputs. III Validation. *J. Appl. Physiol.* 51, 990–1001.

Yu, J., Wang, Y. F., and Zhang, J. W. (2003). Structure of slowly adapting pulmonary stretch receptors in the lung periphery. *J. Appl. Physiol.* 95, 385–393.

Conflict of Interest Statement: The authors declare that the research was conducted in the absence of any commercial or financial relationships that could be construed as a potential conflict of interest.

Received: 14 March 2012; paper pending published: 20 April 2012; accepted: 24 June 2012; published online: 23 July 2012. Citation: O'Connor R, Segers LS, Morris KF, Nuding SC, Pitts T, Bolser DC, Davenport PW and Lindsey BG (2012) A joint computational respiratory neural network-biomechanical model for breathing and airway defensive behaviors. Front. Physio. ***3****:264. doi: 10.3389/fphys.2012.00264*

This article was submitted to Frontiers in Computational Physiology and Medicine, a specialty of Frontiers in Physiology.

frontiers in
PHYSIOLOGY

ORIGINAL RESEARCH ARTICLE
published: 05 July 2012
doi: 10.3389/fphys.2012.00244

Toward an integrative computational model of the guinea pig cardiac myocyte

Laura Doyle Gauthier*, Joseph L. Greenstein and Raimond L. Winslow

Department of Biomedical Engineering, Institute for Computational Medicine, The Johns Hopkins University School of Medicine and Whiting School of Engineering, Baltimore, MD, USA

Edited by:
Jennie Larkin, National Heart, Lung, and Blood Institute, USA

Reviewed by:
Olga Solovyova, Institute Immunology and Physiology, Russia
Johan Elon Hake, Simula Research Laboratory, Norway

****Correspondence:***
Laura Doyle Gauthier, Department of Biomedical Engineering, Institute for Computational Medicine, Johns Hopkins University School of Medicine and Whiting School of Engineering, 3400 North Charles Street, Hackerman Hall 316A, Baltimore, MD 21218, USA.
e-mail: laura.doyle@jhu.edu

The local control theory of excitation-contraction (EC) coupling asserts that regulation of calcium (Ca^{2+}) release occurs at the nanodomain level, where openings of single L-type Ca^{2+} channels (LCCs) trigger openings of small clusters of ryanodine receptors (RyRs) co-localized within the dyad. A consequence of local control is that the whole-cell Ca^{2+} transient is a smooth continuous function of influx of Ca^{2+} through LCCs. While this so-called graded release property has been known for some time, its functional importance to the integrated behavior of the cardiac ventricular myocyte has not been fully appreciated. We previously formulated a biophysically based model, in which LCCs and RyRs interact via a coarse-grained representation of the dyadic space. The model captures key features of local control using a low-dimensional system of ordinary differential equations. Voltage-dependent gain and graded Ca^{2+} release are emergent properties of this model by virtue of the fact that model formulation is closely based on the sub-cellular basis of local control. In this current work, we have incorporated this graded release model into a prior model of guinea pig ventricular myocyte electrophysiology, metabolism, and isometric force production. The resulting integrative model predicts the experimentally observed causal relationship between action potential (AP) shape and timing of Ca^{2+} and force transients, a relationship that is not explained by models lacking the graded release property. Model results suggest that even relatively subtle changes in AP morphology that may result, for example, from remodeling of membrane transporter expression in disease or spatial variation in cell properties, may have major impact on the temporal waveform of Ca^{2+} transients, thus influencing tissue level electromechanical function.

Keywords: calcium cycling, calcium-induced calcium-release, cardiac myocyte, computational model, excitation-contraction coupling, mitochondrial energetics

INTRODUCTION

Since publication of the first computational model of the cardiac myocyte action potential (AP) in 1960 (Noble, 1960), the range of biological processes described in models of the cardiac myocyte has grown continuously. While the integrative nature of today's most commonly used models differ, the sub-cellular processes for which there are quantitative, experimentally based models include: (a) voltage-gated ion channels and currents; (b) intracellular calcium (Ca^{2+}) dynamics and Ca^{2+}-induced Ca^{2+}-release (CICR); (c) electrogenic and ATP-dependent membrane transporters; (d) regulation of intracellular Ca^{2+}, sodium (Na^{+}), potassium (K^{+}), and hydrogen ion (H^{+}) concentrations; (e) mitochondrial ATP production and its regulation; (f) coupling of ATP production to energy requiring membrane transporters and myofilaments; and (g) ligand gated membrane receptors and intracellular signaling pathways. However few models combine electrophysiology with contraction mechanics, mitochondrial energetics, or intracellular signaling due to the computational difficulty of combining disparate time and/or spatial scales. While the incorporation of more cellular component models increases the descriptive power of the combined model, the complexity of whole-cell model behavior and computational cost increase almost exponentially with the number of constitutive mechanisms represented.

The close interplay between modeling and experiments has enabled a remarkably deep understanding of the function of cardiac myocytes. In some cases, myocyte models not only reconstruct the experimental data on which they are based, they predict new emergent behaviors that have been validated subsequently by experiments. As a result, models now play a central role in understanding the relationships between molecular function and the integrated behavior of the cardiac myocyte in health and disease.

The most fundamental property of cardiac myocytes is that they are electrically excitable cells (they generate APs). The rapid increase in membrane depolarization during the early phase of the AP increases the open probability of sarcolemmal L-Type Ca^{2+} channels (LCCs). LCCs are preferentially located in the t-tubules (see **Figure 1A**), which are invaginations of the sarcolemma extending deep into the cell. Further, LCCs within the t-tubules are preferentially localized in structures known as dyads. Dyads are regions where t-tubule membrane is in close opposition to the sarcoplasmic reticulum (SR) membrane. The SR is a luminal organelle located throughout the interior of the cell. It is involved

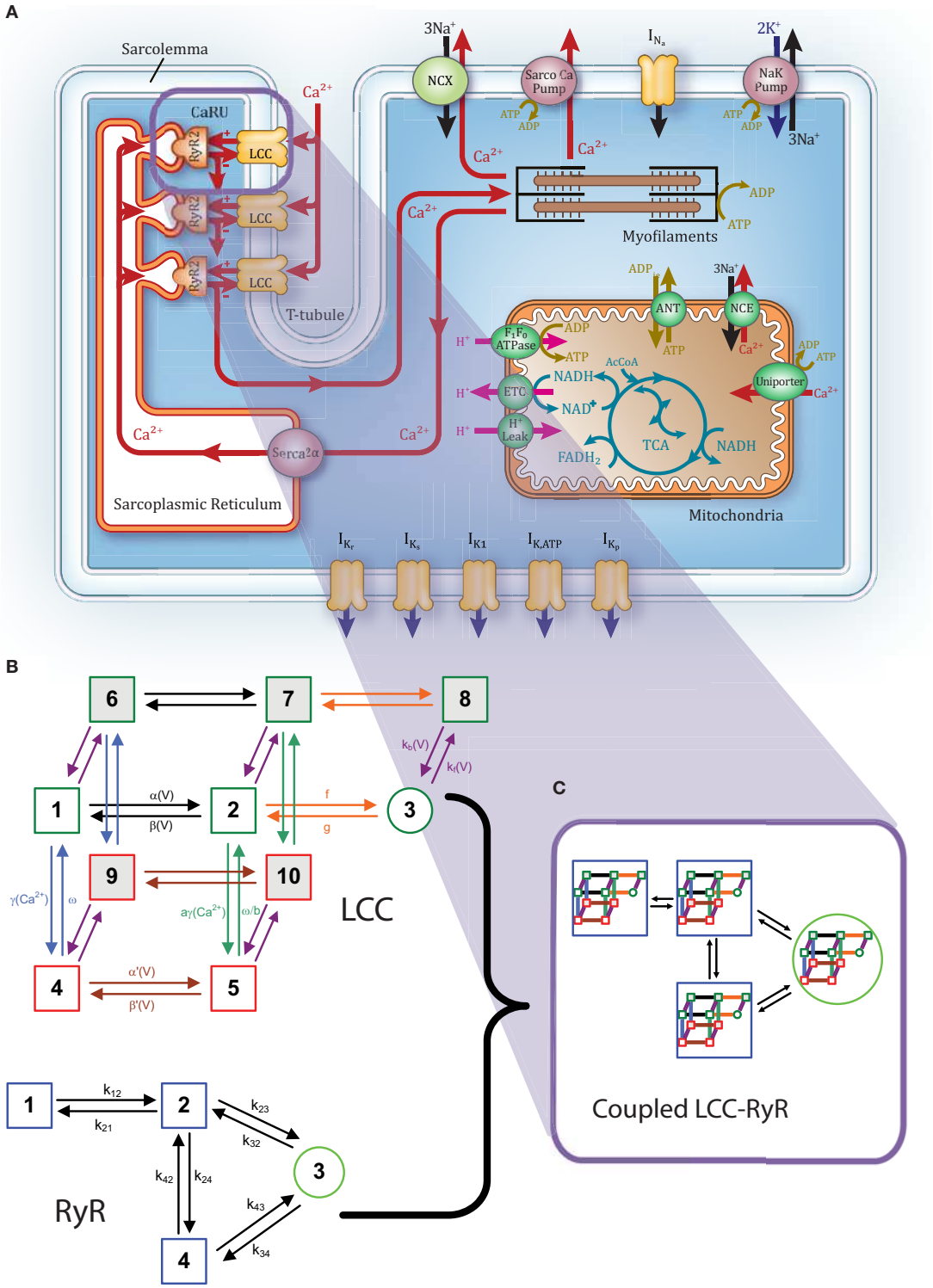

FIGURE 1 | Overview of guinea pig coupled model. (A) Schematic illustration of the model structure. **(B)** LCC (top) and RyR (bottom) Markov model structures. **(C)** The 40-state LCC:RyR model representing each possible pairing of LCC and RyR states.

in uptake, sequestration, and release of Ca^{2+} in a process known as intracellular Ca^{2+} cycling. The junctional SR (JSR) is the portion of the SR most closely approximating the t-tubules. Ryanodine receptors (RyRs) are channels located in the JSR membrane in close opposition to LCCs in the dyad. During the initial phase of the AP, sarcolemmal membrane depolarization increases LCC

open probability. The resulting flux of Ca^{2+} into the dyadic space (trigger flux) leads to Ca^{2+} binding to the RyRs. This increases RyR open probability, and when open, the resulting Ca^{2+} flux through RyRs (release flux) is directed into the dyadic space. There are thousands of dyads within the cardiac myocyte, and the net flux of Ca^{2+} from dyads into the cytosol triggers muscle contraction in a process known as excitation-contraction coupling (ECC). The ratio of release to trigger flux is typically large, and is referred to as ECC gain.

Graded release refers to the phenomenon, originally observed by Fabiato (1985), whereby Ca^{2+} release from JSR is a graded, smooth, continuous function of the amount of trigger Ca^{2+} entering the cell via LCCs. The majority of cardiac myocyte models lump all dyadic spaces together into a common pool known as the subspace, and net trigger flux through LCCs and net release flux through RyRs is directed into this common pool. In a landmark 1992 paper (Stern, 1992), Stern showed that the strong positive feedback effect on RyR open probability due to the fact that release flux is directed into the same pool of Ca^{2+} that serves as the trigger for RyRs (i.e., the common pool) results in all-or-none rather than graded release. More specifically, he showed that common pool models cannot reproduce both high gain and graded release. Despite this fact, early common pool models were able to reproduce a broad range of cardiac myocyte behaviors. However, Greenstein and Winslow (2002) showed that incorporation of new experimental data, demonstrating that Ca^{2+}-dependent inactivation (CDI) of LCCs is stronger than voltage-dependent inactivation (VDI), into common pool models de-stabilized repolarization of the AP due to abnormal Ca^{2+} handling (here, destabilization means that at normal physiological pacing rates, APs could exhibit an oscillatory plateau phase, and large, irregular variation in AP duration, APD). Thus, common pool models not only fail to capture the graded release property, they cannot capture one of the most fundamental properties of normal cardiac myocytes at physiological pacing rates – stable APs.

Stern (1992) showed that graded release is achieved when it is assumed that LCCs can only trigger Ca^{2+} release from their adjacent RyRs in the dyad. Under this assumption, graded release arises as the result of statistical recruitment of release clusters, a process known as local control of Ca^{2+} release. Guided by this insight, Greenstein and Winslow (2002) showed that when local control is incorporated into ventricular myocyte models by simulating the stochastic gating of LCCs and RyRs in each dyad, AP properties are stabilized. However, one drawback of models based on systems of stochastic ordinary differential equations is that solution of these equations is computationally demanding. Hinch et al. (2004) resolved this problem by using the fact that the time rate of change of dyadic Ca^{2+} concentration is so fast relative to the time evolution of any other biological process in the models that it can be assumed to immediately reach its steady-state value. This simple, reasonable assumption enabled the graded release property to be modeled using a low-dimensional system of ordinary differential equations in which LCCs and RyRs behave as a strongly coupled system. Incorporation of this "coupled LCC-RyR model" into cardiac ventricular myocyte models enabled these models to achieve graded release with high gain and stable APs (Greenstein et al., 2006) in a more computationally efficient manner. The advantage of such models, as compared to models with phenomenological formulations of the release mechanism, is that they can be used to study the functional consequences of altered molecular function on ECC gain since this property emerges as a result of capturing fundamental biological detail. This is not true of phenomenological models formulated using ECC gain functions that are explicitly built into the models.

In 2003, Cortassa et al. (2003) formulated a computational model of cardiac mitochondria including descriptions of the tricarboxylic acid (TCA) cycle and its regulation by Ca^{2+}, oxidative phosphorylation, the F_1-F_0 ATPase, the adenine nucleotide translocator, the Ca^{2+} uniporter, the Na^+-Ca^{2+} exchanger, and mitochondrial Ca^{2+} dynamics. In 2006, this model was integrated into a version of the Jafri–Rice–Winslow model of the guinea pig ventricular myocyte (Jafri et al., 1998) that had been extended to include a description of isometric force generation (Rice et al., 2000). This integrative ECC/mitochondrial energetics (ECME) model (Cortassa et al., 2006) also described coupling between mitochondrial ATP production and energy requiring membrane transporters, as well as control of mitochondrial energetics by cytosolic Ca^{2+}. This model was able to reconstruct steady-state relationships between force generation and oxygen consumption at different stimulus frequencies, as well as rapid temporal changes in mitochondrial NADH and Ca^{2+} in response to abrupt changes in workload. Nonetheless, this model is a common pool model exhibiting non-physiological all-or-none Ca^{2+} release. Incorporating the graded release property into this model is important because mitochondria are bounded at each end by the JSR Ca^{2+} release sites, a close association that is supported by the observation that there are electron dense structures linking the mitochondrial outer membrane to t-tubules (Hayashi et al., 2009). This possible colocalization of mitochondria and the Ca^{2+} release sites implies that mitochondria may sense the local dyadic Ca^{2+} signal rather than the bulk cytosolic Ca^{2+} signal exclusively. In addition, mitochondria are "buffers" of Ca^{2+} by virtue of the presence of the Ca^{2+} uniporter in the inner mitochondrial membrane. Therefore, mitochondria may not only sense and be regulated by the large, fast, local dyadic Ca^{2+} signal, they may also act to buffer this signal, thereby influencing ECC (Maack et al., 2006).

As a first step toward investigating these important questions, we present an extension to the ECME model incorporating the coupled LCC-RyR formulation of graded release and description of the local Ca^{2+} signal. We demonstrate that this model of the guinea pig ventricular myocyte is able to reconstruct a broad range of experimental data. The model predicts that interactions between voltage-dependent properties of ECC gain and AP shape during the plateau phase have an important role in the timing of the Ca^{2+} transient and thus force generation. This prediction, which emerges from the underlying graded release model, is validated by experimental data. Further, we show that factors influencing AP plateau shape such as magnitude of the fast transient outward K^+ current (in species other than guinea pig) can significantly affect timing of Ca^{2+} release. This model prediction is also validated by experimental data. These behaviors are specific to the graded release model, and cannot be revealed when using common pool models with all-or-none release. Finally, we show preliminary results indicating that the model predicts experimentally measured

effects of mitochondrial Ca^{2+} uniporter block on amplitude of the cytosolic and mitochondrial Ca^{2+} transients, demonstrating the important role of beat-to-beat Ca^{2+} buffering by mitochondria.

MATERIALS AND METHODS

THE COUPLED LCC-RyR Ca^{2+} RELEASE UNIT

We have incorporated a coupled LCC-RyR model of CICR into the ECME guinea pig myocyte model of Cortassa et al. (2006; **Figure 1A**). The coupled LCC-RyR model of the Ca^{2+} release unit (CaRU) is based on that presented previously for canine myocytes by Greenstein et al. (2006; see **Figures 1B,C**). The CaRU is represented by a single LCC in the t-tubule membrane, a single RyR located in the closely opposed JSR membrane, and a dyadic volume in the space between them, which functions as a separate Ca^{2+} compartment (**Figure 1A**). The rate of Ca^{2+} diffusion from the dyadic space to the cytosol is sufficiently rapid allowing for the assumption that subspace Ca^{2+} levels equilibrate instantaneously and can therefore be expressed algebraically in terms of the fluxes through the LCC and RyR. Another simplification arises from the assumption that refilling of the JSR occurs quickly enough that the Ca^{2+} levels in the JSR can be assumed to be approximately equal to network SR (NSR) Ca^{2+} levels. In this minimal model, the single model RyR represents the estimated number of release channels per LCC measured in guinea pig (Bers and Stiffel, 1993), and thus corresponds to a cluster of five simultaneously gating RyRs. Therefore, unitary flux is increased to five times that of a single-channel. The CaRU model is made up of 40 states (**Figure 1C**), which represent all possible pairings of the 10 state LCC model and the four state RyR model. Further details on the coupled LCC-RyR formulation may be found in Greenstein et al. (2006).

Figure 2 demonstrates kinetic and steady-state properties of the LCC model. Parameters of the LCC model were constrained using voltage-clamp data obtained from isolated guinea pig ventricular myocytes measured at 34–37°C. **Figure 2A** shows the L-type Ca^{2+} current peak I–V relationship. $I_{Ca,L}$ is non-zero for test potentials between approximately −40 and +60 mV with a maximal peak of −32 μA/μF at +10 mV. The membrane potential at which the I–V curve peaks is in good agreement with data from four different guinea pig studies (Rose et al., 1992; Allen, 1996; Grantham and Cannell, 1996; Linz and Meyer, 1998). Peak current

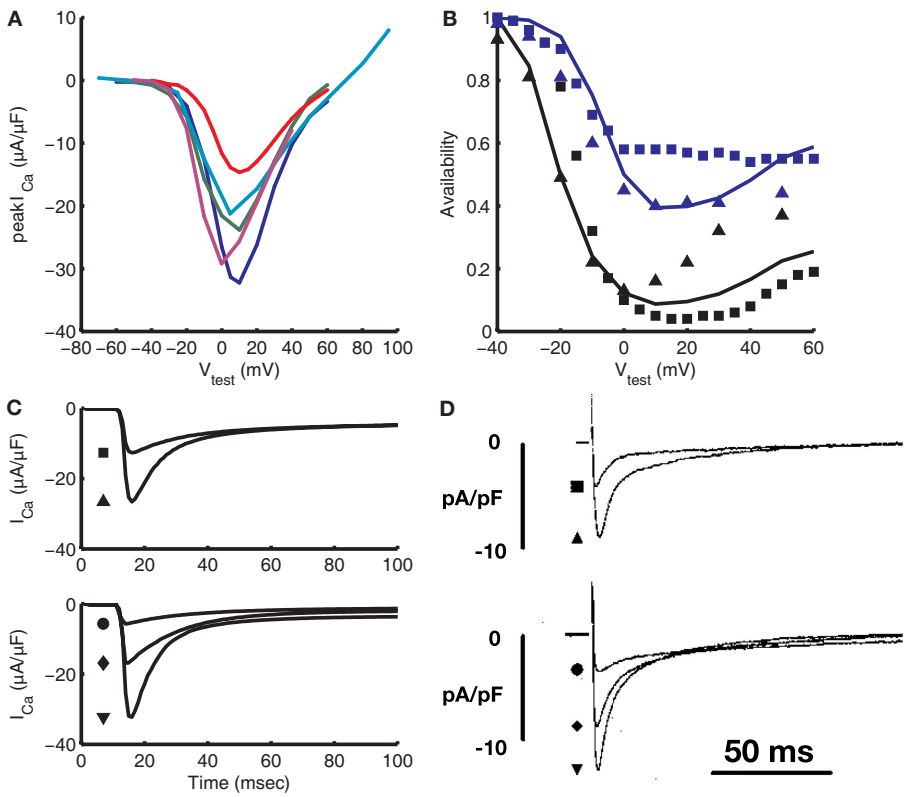

FIGURE 2 | Validation of the L-type Ca^{2+} current. (A) Current-voltage relation for the model (blue) compared with experimental data from Rose et al. (1992; green), Linz and Meyer (1998; red), Grantham and Cannell (1996; teal), and Allen (1996; purple). Recordings from Rose et al. (1992), Linz and Meyer (1998), and Allen (1996) were adjusted to 37°C using the Q_{10} value from Cavalié et al. (1985). **(B)** Steady-state availability in the presence of CDI and VDI (black) and with VDI only (blue) from the model (lines) is compared to experimental data from Linz and Meyer (1998; squares) and Hadley and Lederer (1991; triangles). **(C)** Model traces of $I_{Ca,L}$ vs. time for 400 ms test pulses from a pre-clamp of −40 mV. **(D)** Experimental $I_{Ca,L}$ traces from Linz and Meyer (1998), also from a pre-clamp of −40 mV. For the top set of traces in **(C,D)**, the square represents a test potential of −10 mV and the triangle a test potential of 0 mV. For the bottom set, test potentials are 10, 30, and 50 mV for the circle, diamond, and triangle, respectively. **(D)** Was reproduced with copyright permission of John Wiley and Sons.

is −32 μA/μF at +10 mV, at the high end of measured values. For comparison, experiments show −21 μA/μF at 37°C (Grantham and Cannell, 1996), −25.68 μA/μF temperature-adjusted from 34 (Allen, 1996) to 37°C, and −24 μA/μF temperature-adjusted from 22 (Rose et al., 1992; Allen, 1996; Grantham and Cannell, 1996; Linz and Meyer, 1998) to 37°C, where adjustments are made using a Q_{10} value of 2.96 from Cavalié et al. (1985) Steady-state CDI (**Figure 2B**), was constrained using data from double-pulse voltage-clamp protocols (Hadley and Lederer, 1991; Linz and Meyer, 1998), with CDI being greater than VDI at all potentials. VDI properties were constrained using data from Linz and Meyer (1998), who measured a non-specific current through LCCs in a Ca^{2+}-free solution, and from Hadley and Lederer (1991), who determined VDI from measurements of LCC gating current charge immobilization. Rate of recovery from VDI was constrained using double-pulse voltage-clamp data from isolated rabbit ventricular myocytes (Mahajan et al., 2008). **Figure 2C** shows the time course of $I_{Ca,L}$ at various test potentials. The current peaks 3 ms after stimulus before decaying over approximately 100 ms to a value near zero. The time course of $I_{Ca,L}$ recordings, including time to peak $I_{Ca,L}$, are in good agreement with data from Linz and Meyer (1998; **Figure 2D**). Different peak magnitudes between model and experimental results suggest differing channel density, which is also reflected in **Figure 2A**. The number of LCCs (and thus release units) in the model was set to 339,000 in order to match experimental data on fractional release, as discussed in Section "CICR During the Action Potential" below. This number of LCCs is between the estimate of ≈276,000 predicted by binding experiments (Bers and Stiffel, 1993) and the estimate of ≈500,000 from LCC gating current studies (Hadley and Lederer, 1991).

Ryanodine receptor properties are those from our previous model (Greenstein et al., 2006). Briefly, the RyR model comes from a formulation by Rice et al. (1999), which was modified from a model by Keizer and Smith (1998; **Figure 1B**). Upon elevation of subspace Ca^{2+} levels, RyRs rapidly transition from state 1 through state 2 into state 3, the open state. Termination of release occurs as the channel transitions from state 3 to state 4, the inactive state, where it remains until subspace Ca^{2+} levels drop and the RyR returns to state 1. Within the context of the whole-cell model, this RyR model produces an increasing load-dependent fractional release relationship. **Figure 3** shows the fraction of total SR Ca^{2+} released by an AP at varying SR loads. The model relationship is qualitatively similar to experimental data from rabbit (Shannon et al., 2000) and ferret (Bassani et al., 1995), two species which have strong Na^+-Ca^{2+} exchanger (NCX) contribution to relaxation, resulting in Ca^{2+}-cycling that is more similar to guinea pig than rat or mouse.

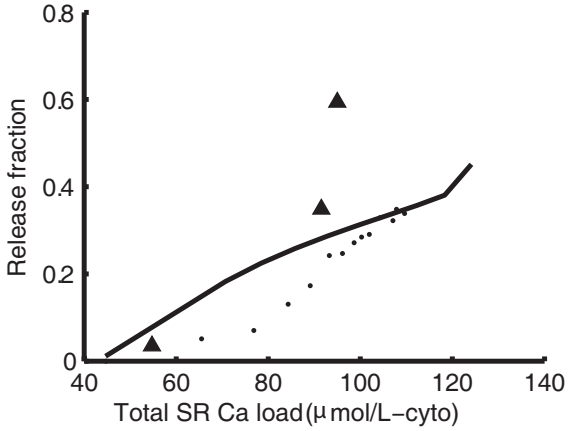

FIGURE 3 | Sarcoplasmic reticulum load-dependence of fractional release. Model SR load vs. fractional release (solid line) compared to experimental data from Shannon et al. (2000) in rabbit (dots) and Bassani et al. (1995) in ferret (triangles).

ION CHANNELS AND Ca^{2+} CYCLING

Models for the remaining (non-dyadic) channels, pumps, and exchangers are based on those of the 2006 ECME model (Cortassa et al., 2006) with the following changes. The previous formulation of the delayed rectifier potassium current I_K is replaced with the formulation of Zeng et al. (1995) that separates this current into two components, the rapid and slow (I_{Kr} and I_{Ks}) delayed outward rectifier currents. I_{Kr} and I_{Ks} current amplitudes were adjusted to match model APD to experimental data (see Results). The equation for I_{Kp} was modified to better fit experimental data (Yue and Marban, 1988). The NCX model was updated with the model of Weber et al. (2001), which incorporates allosteric regulation by cytosolic Ca^{2+}. NCX affinity constants for allosteric Ca^{2+} regulation and for intracellular Na^+ were modified slightly to fit guinea pig NCX voltage dependant behavior (Maack et al., 2005) and diastolic Ca^{2+} levels under voltage-clamp (Han et al., 1994; Isenberg and Han, 1994). This allowed the model to maintain appropriate diastolic Ca^{2+} levels while still achieving a time constant of SR load rest decay of approximately 80 s (not shown), in qualitative agreement when compared with experimental data exhibiting a tau of 36 s (Terracciano et al., 1995). A mitochondrial Na^+-H^+ exchanger (Wei et al., 2011) was also added, which helps to ensure conservation of Na^+ between the cytosolic and mitochondrial compartments. Ca^{2+} cycling was modified by adjusting NCX magnitude to achieve the approximately 60:40 balance of Ca^{2+} resequestration vs. Ca^{2+} export fluxes during diastole at a pacing frequency of 1 Hz (Bers, 2001). The ATP-dependent K^+ current ($I_{K(ATP)}$) was also added using a model by Ferrero et al. (1996) to incorporate the effects of ATP on APD. The conductance of $I_{K(ATP)}$ was modified to take into account the range of experimental data (Nichols and Lederer, 1990; Weiss et al., 1992). Minor changes were made to rate-limiting mitochondrial parameters in the TCA cycle, respiratory chain, and adenine nucleotide transporter to increase ATP supply at higher pacing frequencies. Ca^{2+}-regulation of the mitochondria remains unchanged. Ca^{2+} uptake fluxes during 1 Hz pacing were numerically integrated at 1 ms resolution from the peak of the Ca^{2+} transient to the end of diastole (see **Figure 4A**) to simulate experimental relaxation protocols (Bers, 2001). Comparing the total moles of Ca^{2+} removed from the cytosol, the SR Ca^{2+}-ATPase (SERCa) takes up 65.9% of the transported cytosolic Ca^{2+}, NCX removes 28.9%, and the sarcolemmal (SL) Ca-pump removes 5.1%, close to estimates of 67% SERCa, 30% NCX, and 3% slow processes (Bers, 2001). The mitochondrial uniporter removes Ca^{2+} from the cytosol most effectively during the upstroke of the Ca^{2+} transient, while Ca^{2+}

extrusion by the mitochondrial Na^+/Ca^{2+} exchanger dominates during relaxation (see **Figure 4B**). The result is that a bolus of Ca^{2+} 12.7% of the size of the net integrated Ca^{2+} flux is directed back into the cytosol during relaxation. This illustrates the buffering role that mitochondria in this model play during Ca^{2+} cycling. Recirculation fraction, calculated as the amount of Ca^{2+} contributing to the Ca^{2+} transient that is derived from the SR stores at steady-state, is 69%. This is close to estimates between 63 and 67% (Bers, 2001). At steady-state, the amount of Ca^{2+} released from the SR must equal the amount resequestered during a given beat (see **Figure 4B**). Analogously the amount of Ca^{2+} entering the cell across the cell membrane must be extruded during relaxation. Thus the ratio of cytosolic Ca^{2+} extruded during relaxation to the amount resequestered into the SR is a good approximation of the ratio of Ca^{2+} flux into the cell across the sarcolemma to SR Ca^{2+} release. Here we have approximately 31% of cytosolic Ca^{2+} due to transsarcolemmal influx and 69% due to SR release. As expected at steady-state, total and mitochondrial integrated fluxes start and end at zero (see **Figure 4B**). Due to conservation of Ca^{2+}, at steady-state the integrals of inbound and outbound fluxes across the sarcolemma also sum to zero.

COMPUTATIONAL METHODS

Model code was written in C++ using the SUNDIALS CVODE integration library and run using an IBM PC workstation with a 2.80-GHz processor and 2.5 GB of RAM. On such a workstation, this 75-state model takes approximately 15 s to compute 10 1 Hz APs with no output written to files. This is comparable to the performance of current models for which code is available (Shannon et al., 2004; Faber et al., 2007). Code and additional information are available online (http://www.icm.jhu.edu/models/). Equations and parameters for the model are also available in the online supplement.

RESULTS

CICR DURING THE ACTION POTENTIAL

Figure 5A shows the model AP, which has a steady-state duration of 189 ms at 1 Hz pacing. This is consistent with experimental recordings obtained near the physiological temperature of 37°C with a 1-Hz APD range of approximately 130–180 ms (Arreola et al., 1991; Sicouri et al., 1996; Chen et al., 2000). AP shape, including resting membrane potential, peak voltage, and phase 2 and 3 AP slope, are in good correspondence with these experimental data.

The model Ca^{2+} transient begins to increase as soon as $I_{Ca,L}$ is triggered, but the peak is delayed 119 ms with respect to the peak voltage of the AP (**Figures 5A,D**). A delay of 144–190 ms is supported by experimental recordings (Sipido et al., 1995b; Grantham and Cannell, 1996; see also **Figures 5B,E**) and by the prediction of local control theory that local fidelity of ECC decreases at highly depolarized potentials, such as those that occur early in the guinea pig AP. At highly depolarized potentials, the driving force for Ca^{2+} current through LCCs is reduced, even though whole-cell LCC flux may be large (**Figure 5C**). The resulting smaller unitary currents are less likely to trigger release via RyRs, and hence ECC gain is reduced. This counteracts the increase in gain resulting from increased LCC open probability at more depolarized potentials.

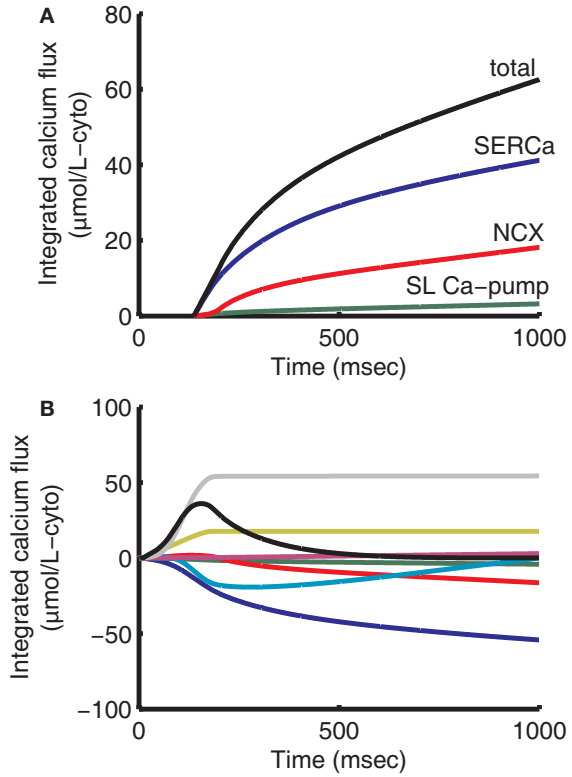

FIGURE 4 | Integrated cytosolic Ca^{2+} fluxes. Cytosolic Ca^{2+} uptake is given as the sum of SERCa, NCX, and sarcolemmal Ca^{2+}-pump fluxes **(A)**. SERCa contributes 65.9% of uptake, NCX 28.9%, and SL Ca-pump 5.1%. In this model mitochondria contribute significant beat-to-beat buffering. The mitochondrial uniporter predominates during the first 300 ms of the cycle, resulting in a net uptake of Ca^{2+} from the cytosol **(B)**. For the remainder of the cycle, mitochondrial Na^+-Ca^{2+} exchanger predominates, resulting in Ca^{2+} being transferred back out of the mitochondria to the cytosol. The mitochondria release an amount of Ca^{2+} equal to 12.7% of the net integrated Ca^{2+} uptake flux into the cytosol during relaxation. Integrating over the entire 1000 ms period **(B)**, fluxes into the cytosol are given as positive and fluxes removing Ca^{2+} from the cytosol are negative. Fluxes shown represent SERCa (blue), NCX (red), SL Ca-pump (green), mitochondria (teal), background Ca^{2+} current (magenta), L-type Ca^{2+} current (yellow), SR release (gray), and total (black).

The model predicts that triggering of SR Ca^{2+} release is lowest during the early phases of the AP, and increases slowly as the AP evolves (**Figure 5F**) because of this initial low gain. This leads to a relative delay in the peak of the Ca^{2+} transient waveform as compared to other species. In contrast, the Greenstein et al. (2006) canine model, which also features the coupled LCC-RyR formulation of CICR, exhibits a cytosolic Ca^{2+} transient that peaks approximately 80 ms earlier. The difference can be attributed to the presence of an early repolarization phase in the canine AP, which quickly hyperpolarizes the membrane potential into the range where ECC gain is maximal. The guinea pig models of Faber et al. (2007) and Gaur and Rudy (2011), which represent the same species as the present model, but use different release formulations, also demonstrate earlier cytosolic Ca^{2+} peaks than shown in this model (see Discussion for a full analysis).

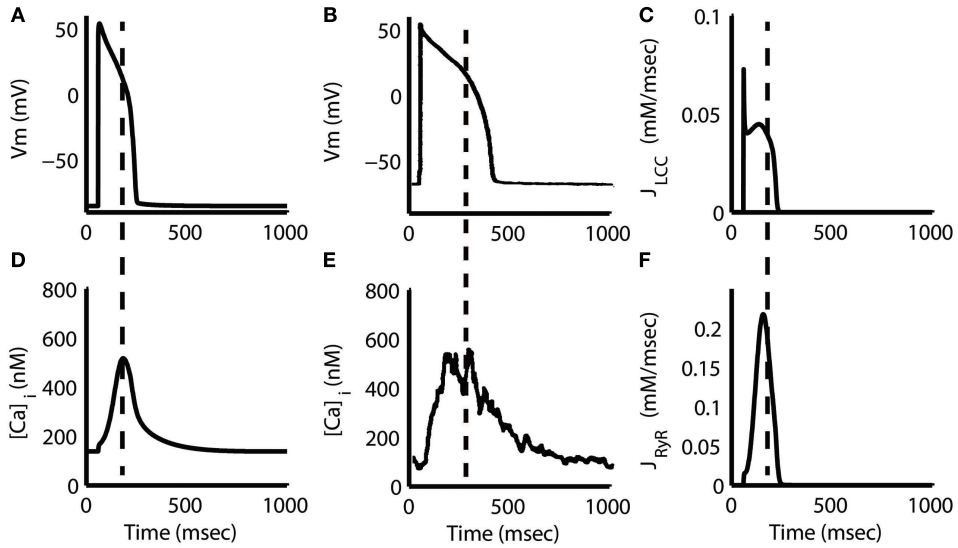

FIGURE 5 | Action potential and Ca^{2+} transient. Steady-state AP at 1 Hz pacing from the model **(A)** and experiment (Sipido et al., 1995b) **(B)** along with the corresponding Ca^{2+} transients **(D,E)**. Note that the peak of the model transient is aligned with the middle of the AP plateau phase (dashed line), approximately 127 ms after stimulus. Experimental data in **(E)** show a similar delay in the Ca^{2+} transient peak of approximately 190 ms. L-type Ca^{2+} flux (J_{LCC}) **(C)** shows a large, but brief peak aligned with the initial AP depolarization followed by a slow peak during the AP plateau. RyR flux **(F)** increases slowly and reaches its maximum in parallel with the J_{LCC} slow peak and AP plateau. Dashed lines in **(C,F)** correspond to the time of Ca^{2+} transient peak from **(D)**. Flux measurements are given with respect to subspace volume. **(B,E)** Were reproduced with copyright permission from The Physiological Society.

Figure 6 shows the characteristic fast peak, early decay, and late peak shape of the guinea pig model $I_{Ca,L}$, which is in good correspondence with experimental recordings (Arreola et al., 1991; Grantham and Cannell, 1996). Following the early decay, the current magnitude recovers partially in response to the increased driving force as the AP voltage drops, but the extent of this recovery is limited by increased Ca^{2+} release from the SR causing CDI. As the membrane potential repolarizes, the L-type current undergoes both VDI, as well as CDI resulting from SR Ca^{2+} release (see **Figure 2B**). LCC availability during the AP is shown in **Figure 7**. This quantity represents the occupancy of non-inactivated states in the channel model. The relation of LCC availability calculated from the model to membrane potential follows closely that of Linz and Meyer (1998). The kinetics vary between model and experiment due to the long APD in the experimental data. The APD_{90} from the experimental data is 380 ms, which more closely resembles the APD of a midmyocardial cell (Szigligeti et al., 1996), while the model is more representative of an epicardial cell. Simulations were also performed using the AP recording from the Linz and Meyer (1998) data as a voltage-clamp (**Figures 7C,F**). These simulations also show a rapid loss of availability, decreasing to a minimum of approximately 5% during the AP and a slow recovery of availability during the end of the repolarization phase.

The purpose of introducing the local control CaRU model is to incorporate a biophysically realistic representation of graded release in the myocyte model. As shown in **Figure 8A**, the RyR release and LCC trigger fluxes are smooth, continuous functions of membrane potential. The RyR release flux exhibits a peak that is displaced in the hyperpolarizing direction from that of the LCC trigger flux, a key feature of experimental measurements of Ca^{2+} release. This is again seen in the normalized RyR release flux (**Figure 8B**), better illustrating the representative leftward shift with relation to the LCC flux, as seen in the experimental data from Wier et al. (1994). Here, the LCC flux peaks at +10 mV while the RyR flux peaks at +5 mV. It is this shift that results in the characteristic monotonically decreasing gain function (**Figure 8C**). Voltage-dependent gain has not been measured in guinea pig, but the gain at 0 mV is close to experimental estimates in guinea pig (Sipido and Wier, 1991; Rocchetti et al., 2005).

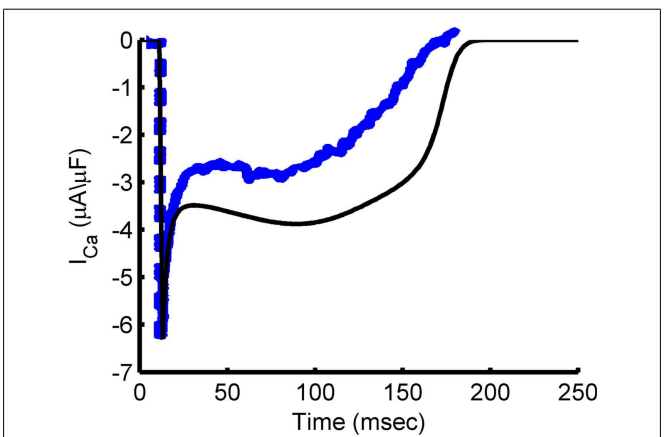

FIGURE 6 | $I_{Ca,L}$ during the AP. Simulated $I_{Ca,L}$ trace during steady-state AP at 1 Hz pacing (black) and experimental $I_{Ca,L}$ trace from a guinea pig ventricular myocyte undergoing 1 Hz pacing at 35–37°C (blue). Blue trace is reproduced from Grantham and Cannell (1996) by copyright permission of the American Heart Association.

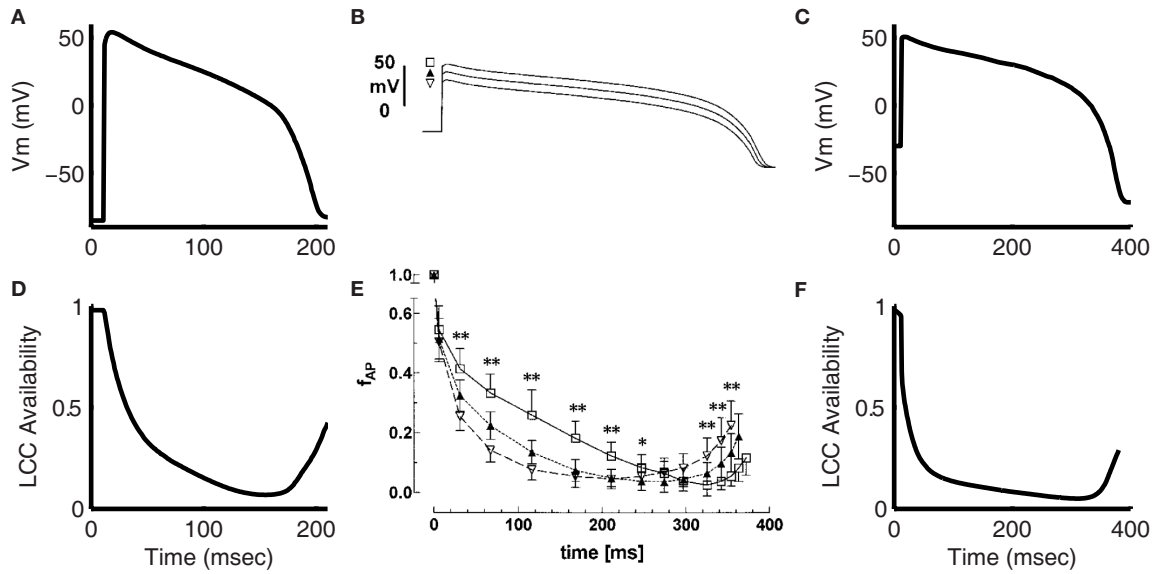

FIGURE 7 | Inactivation of the L-type Ca^{2+} current during the AP. **(A)** Model 1 Hz AP. **(D)** Simulated LCC availability during the AP shown in **(A)**. Experimental data from Linz and Meyer (1998) showing the AP clamp waveform **(B)** and LCC availability during the AP clamp **(E)** for guinea pig myocytes at 35˚C. **(C)** Shows model membrane potential output using the trace from **(B)** as an AP clamp. The LCC availability during the AP clamp is given in **(F)**. **(B,E)** Were reproduced by copyright permission of John Wiley and Sons.

At 1 Hz pacing, the fractional release of total Ca^{2+} from the SR is approximately 33% (not shown). This quantity was calculated as unity minus the ratio of total systolic SR Ca^{2+} to total diastolic SR Ca^{2+}. The 33% measurement given by the model agrees with 35% estimated in ferret (Bassani et al., 1995), a species with a similar recirculation fractional as the guinea pig (Bers, 2001). The peak RyR open probability is 2.9% at 1 Hz. As described by Bers (2001), given an experimentally measured peak release flux of 3 mM/s (Wier et al., 1994) and a unitary RyR flux near 0.4 pA (Mejía-Alvarez et al., 1999), only 40,000 RyRs need to be open at the time of maximal release. This is only 2% of the number of total RyRs calculated by Bers and Stiffel (1993).

Incorporation of the local control model of the CaRU into the myocyte model allows for the prediction of localized subspace Ca^{2+} levels (**Figure 9**). The model calculates subspace Ca^{2+} for four different dyad macrostates: with LCC and RyRs closed, with only the LCC open, with only the RyRs open, and with both the LCC and RyRs open. Average subspace Ca^{2+} can be estimated by summing over the predicted Ca^{2+} concentrations for these four scenarios, weighted by their respective probability of occurrence. During 1 Hz pacing, the predicted average subspace Ca^{2+} level peaks near 2 μM, four times higher than the peak of the cytosolic transient. Subspace Ca^{2+} for dyads with open LCCs and RyRs reaches a maximum of 45 μM during the AP plateau.

APD RESTITUTION

Action potential duration restitution describes the electrical response of the myocyte to a premature stimulus. When a myocyte is paced to steady-state at a constant basic cycle length (BCL), APD becomes constant from beat to beat. The time between the end of the AP and the onset of the next stimulus is the diastolic interval (DI). Immediately following an AP the cell will be in an inexcitable refractory state. As the DI increases beyond this refractory period toward the steady-state DI, an AP can be triggered, but its duration is less than that of the steady-state AP due to incomplete recovery from inactivation of $I_{Ca,L}$ and I_{Na}. At the tissue level, slow APD restitution and high pacing frequency can lead to the formation of a functional conduction block as the wave of depolarization catches up with refractory tissue from the previous beat. This block fails to excite and changes the direction of wavefront propagation. Additionally, the relationship between DI and APD has been shown to influence whether such aberrant conduction patterns damp out or devolve into arrhythmias (Qu et al., 1999; Garfinkel et al., 2000).

An electrical restitution curve was generated for the model by pacing to steady-state at 2000 ms BCL and then saving the state of the model at the end of an AP. Using the state values from this time as initial conditions, premature stimuli at increasing DIs were applied and the resulting APD_{90} was measured. The results are compared to recordings under the same protocol from (mid-myocardial) strips of guinea pig ventricle at 37˚C (**Figure 10A**). A single exponential fit to the model results (yellow curve in **Figure 10A**) yields a time constant of 165 ms. This differs from measurements by Sicouri et al. (1996) and Davey et al. (2001) which are 26.7 and 78.4 ± 12.1 ms respectively for single guinea pig myocytes at 32˚C. Possible causes of this discrepancy are presented in Section "Critique of the Model" below.

FREQUENCY-DEPENDENCE OF APD AND ECC

To determine the frequency-dependence of APD and accumulated force, the pacing protocol of Szigligeti et al. (1996) was followed. Briefly, the model was first paced to steady-state at 3000 ms BCL. Pacing frequency was then increased in a stepwise manner. APD,

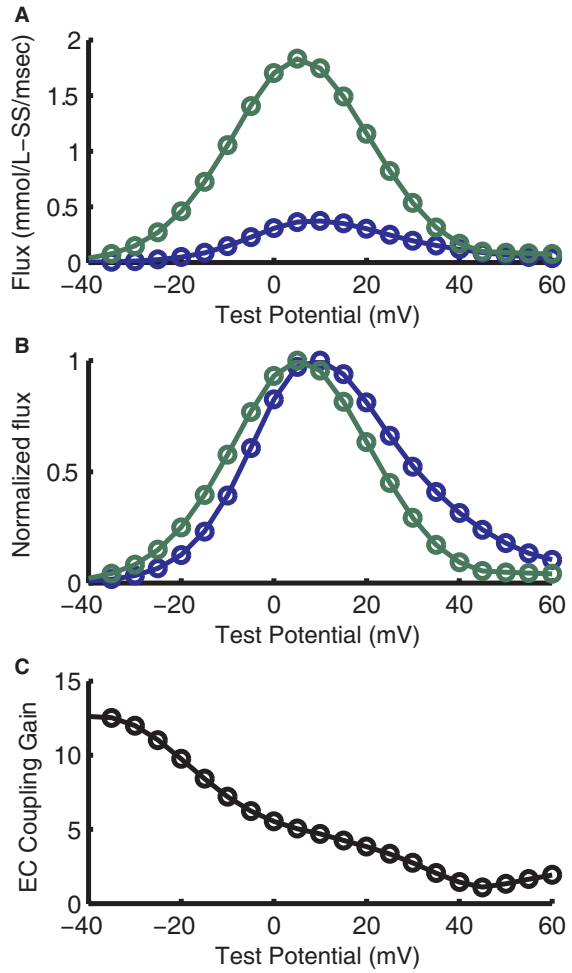

FIGURE 8 | Voltage-dependence of flux through LCCs and RyRs and ECC gain. (A) Voltage-dependence of maximal Ca^{2+} flux through LCCs (blue) and RyRs (green). **(B)** Normalized fluxes from **(A)**. **(C)** ECC gain, as formulated by the ratio of maximal LCC flux to maximal RyR flux.

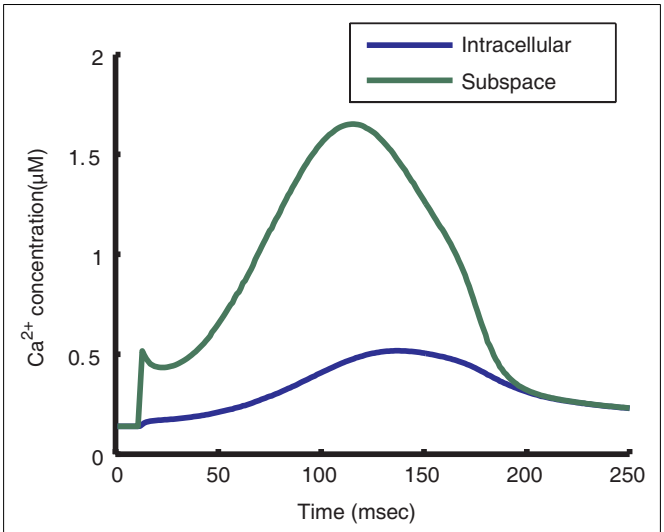

FIGURE 9 | Predicted subspace Ca^{2+} levels. Model cytosolic Ca^{2+} transient during a steady-state 1 Hz AP (blue) and subspace Ca^{2+} transient averaged across all dyads (green). While the average subspace Ca^{2+} is approximately four times higher than that of the cytosol, the maximum subspace Ca^{2+} for a single dyad may reach 45 μM, measured as the maximum subspace Ca^{2+} for the open-open LCC-RyR configuration during a release event.

peak cytosolic Ca^{2+} and accumulated force were recorded after 3 min at 3000, 2000, 1500, 1000, 700, 500, and 300 ms BCL.

The model results presented in **Figure 11A** (blue line) show a decrease in APD with increasing pacing frequency, from an APD_{90} of 261 ms at 3000 ms BCL to an APD_{90} of 114 ms at 300 ms BCL. The rate of decrease of APD with increasing frequency follows closely the data of Szigligeti et al. (1996; **Figure 11A**; green line). Experimental studies have shown that intracellular sodium ($[Na^+]_i$) varies as a function of pacing frequency (Cohen et al., 1982; Wang et al., 1988; Maier et al., 1997). The model exhibits similar frequency-dependence of Na^+ levels with average $[Na^+]_i$ near 5.5 mM at 3000 ms BCL increasing to 8 mM by the end of the Szigligeti protocol. This Na^+ accumulation is mediated through a frequency-dependent change in the balance of the Na^+ entry via the fast sodium current (I_{Na}) that initiates the AP and the export of Na^+ by the Na^+-K^+ pump during diastole. In this model, NCX plays a large role in early repolarization of the plateau at slow frequencies. As $[Na^+]_i$ continues to decrease with an increase in BCL, outward NCX current is reduced, allowing prolongation of the AP plateau phase.

The force model used here is the same as that implemented previously in the ECME model (Cortassa et al., 2006). The frequency-dependence of peak force follows closely the data from Szigligeti et al. (1996) in guinea pig papillary muscle (**Figure 11B**). As BCL decreases, isometric force increases exponentially as a result of the underlying increase in peak cytosolic Ca^{2+} concentration associated with increased SR load and gain. To compare the normalized force output of the model with those data the cross-sectional area used is 0.013 mm^2, which is equivalent to a fiber with an elliptical profile of width 0.24 mm and thickness 0.069 mm, the minimum of the range of measurements for the Cortassa et al. (2006) right ventricular trabecula samples. The frequency-dependence of both cytosolic Ca^{2+} and isometric force play an important part in the ability of the model to reproduce experimental results on energy supply during work transitions (see below). Both cytosolic Ca^{2+} and force transients show faster peaks at higher pacing frequencies, as has been shown experimentally (Layland and Kentish, 1999; Bluhm et al., 2000; Davey et al., 2001; Raman et al., 2006; not shown). Cytosolic Ca^{2+} transients also show frequency-dependent acceleration of relaxation (not shown), such that the time of decay to half peak amplitude is decreased with increasing frequency. Force transients have been shown to have a similar property (Bers, 2001; Davey et al., 2001), but the rate of force transient relaxation in the model does not vary significantly across pacing frequencies.

MITOCHONDRIAL ENERGETICS

Control of mitochondrial energy production is mediated via the Ca^{2+} sensitivity of key enzymes in the tri-carboxylic acid (TCA)

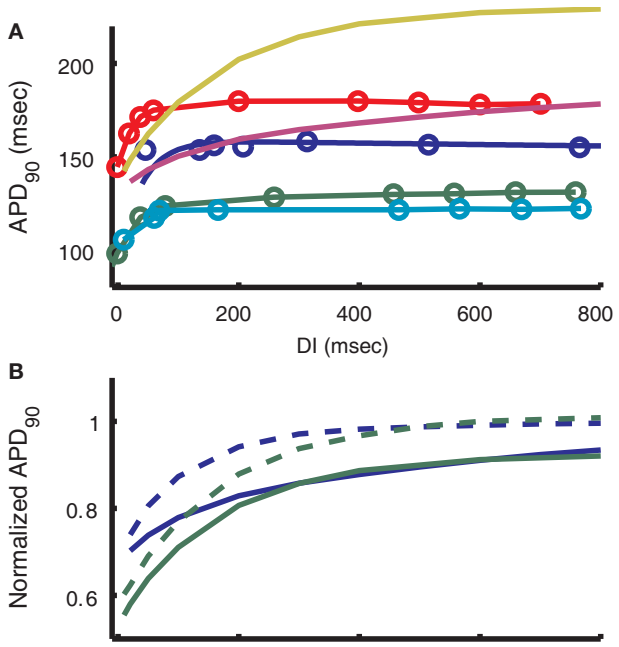

FIGURE 10 | Restitution of APD. (A) APD restitution curves from guinea pig experimental data and models. Blue dots show 2000 ms BCL data from Bjornstad et al. (1993) connected by the biexponential fit reported by those authors. Green, red, and teal respectively show epicardial, midmyocardial, and endocardial experimental data from Sicouri et al. (1996). The purple line depicts output from the LRd07 model (Faber et al., 2007) and yellow is from the present model. A standard S1–S2 protocol was used to simulate APD restitution, starting from 0.5 Hz steady-state as in the protocol used by Sicouri et al. (1996). The single exponential time constant for restitution of the present model is 165 ms, compared with approximately 40 ms for Bjornstad et al. (1993) and approximately 46, 27, and 31 ms for Sicouri et al. (1996) epicardial, midmyocardial, and endocardial, respectively. **(B)** Alteration of the model restitution curve by reverting to the unmodified IKs formulation from Zeng et al. (1995). Blue is LRd07 model, green is the present model. Solid lines are simulations using the latest IKs formulation (one fast gate, one slow), dashed lines are for simulations with 1995 IKs formulation (two fast gates). Curves are normalized to the 2000-ms steady-state APD_{90} for each model, respectively.

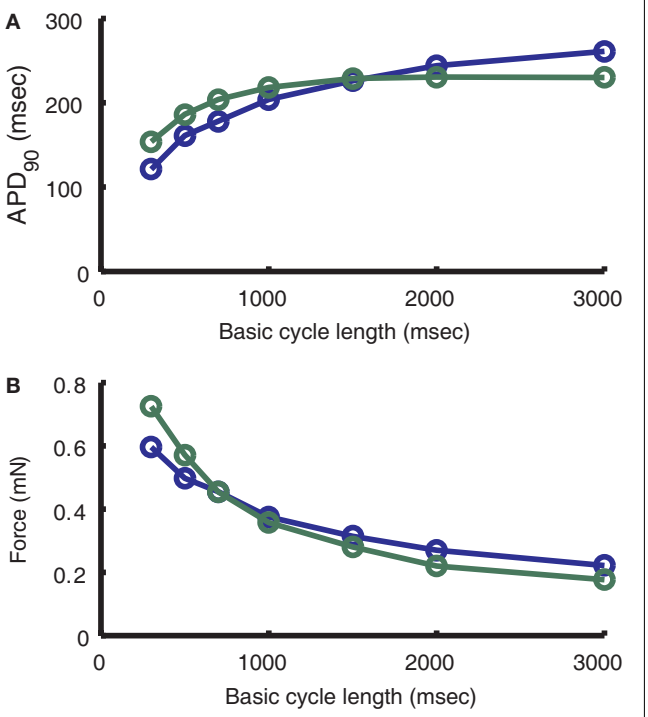

FIGURE 11 | Frequency-dependence of APD and Force. (A) Comparison of model (blue) dependence of APD on frequency to that of Szigligeti et al. (1996; green). **(B)** Comparison of model (blue) dependence of force on frequency to that of Szigligeti et al. (1996; green). See Section "Frequency-Dependence of APD and ECC" of the text for conversion of normalized model output to force units.

cycle, and through regulation of the F_1-F_0 ATPase by ADP. As pacing frequency increases, a higher ADP:ATP ratio results from the increased ATP consumption at rapid contraction rates. Increased mitochondrial ADP levels stimulate the F_1-F_0 ATPase to generate ATP by utilizing the proton-motive force as an energy source. Flux of electrons through the electron transport chain would in and of itself deplete the NADH pool. However, the amplitude of the cytosolic Ca^{2+} transient also increases with pacing frequency, and this Ca^{2+} signal is communicated to the mitochondria via Ca^{2+} uptake by the mitochondrial Ca^{2+} uniporter. Elevated mitochondrial Ca^{2+} levels stimulate the TCA cycle to increase production of NADH to sustain a higher rate of respiration. As in the original ECME model (Cortassa et al., 2006), the rate of respiration for the model presented here increases with increasing pacing frequency. Respiration rate increases 3.3× between 4000 ms BCL pacing and 300 ms pacing, similar to Cortassa et al. (2006; their **Figure 4A**).

During abrupt changes in pacing frequency, the mechanism described above results in NADH transients with complex kinetics. While increased mitochondrial Ca^{2+} levels stimulate NADH supply, this occurs with slower kinetics than the increase in demand. The result is an abrupt decrease in NADH before restoration to a new steady-state at the higher pacing frequency. For decreases in pacing frequency, ATP demand drops causing an overshoot in NADH levels, since production is still stimulated by high mitochondrial Ca^{2+}. Cytosolic Ca^{2+} transient amplitudes drop and mitochondrial Ca^{2+} levels eventually follow as Ca^{2+} is pumped out of the mitochondria by the mitochondrial Na^{+}-Ca^{2+} exchanger. After tens or hundreds of seconds NADH levels reach a steady-state corresponding to the slower pacing frequency.

Figures 12A–C shows the response of the model to changes in workload. To simulate changes in heart rate, the model is paced at 0.25 Hz for 100 s, then pacing frequency is increased to a high workload frequency for 200 s before being allowed to recover at 0.25 Hz for another 200 s. This protocol is repeated for high workload frequencies of 0.5, 1, 1.5, and 2 Hz. Simulated NADH levels (**Figure 12A**) show an undershoot upon initiation of the high frequency stimulation, followed by a recovery to higher levels. Upon return to 0.25 Hz pacing, NADH levels exhibit an overshoot before beginning recovery to the steady-state 0.25 Hz level. In the model, NADH recovery to a steady-state is slow, taking approximately

600 s. The simulation results in **Figure 12A** were performed using the same experimental protocol. As a result, model NADH levels do not reach a steady-state within 200 s. While the kinetics and waveform of the NADH transients in the model are qualitatively similar to experimental data (**Figure 12D**), the lack of quantitative correspondence between the magnitudes of under- and over-shoots in our model, and the data of Brandes and Bers (1999), also seen in the original ECME model (Cortassa et al., 2006), may arise from the effects of ADP compartmentation. The smaller transient effects seen in the model indicate that the changes in workload in the cytosol are not inducing sufficiently large changes in the mitochondrial ADP pool. Averaged force (**Figure 12B**) shows an increase during high workload frequencies, up to 16.4 mN/mm^2 at the end of 2 Hz pacing. These increases are indicative of larger cytosolic Ca^{2+} transients (not shown) and are followed by a recovery to rest levels at approximately 0.9 mN/mm^2 during 0.25 Hz pacing. Mitochondrial Ca^{2+} levels (**Figure 12C**) show minimal beat-to-beat variation with significant increases in Ca^{2+} occurring gradually during periods of high pacing frequency. This property of mitochondrial Ca^{2+} loading is analogous to mitochondria acting as a low-pass filter of cytosolic Ca^{2+} changes. While the amplitude of cytosolic Ca^{2+} transients increases gradually after an increase in pacing frequency, Ca^{2+} levels always return to a diastolic value between beats. In contrast, mitochondrial Ca^{2+} accumulates almost monotonically during periods of high pacing frequency with only minor beat-to-beat variation.

To further illustrate the role of the Ca^{2+} uniporter in conveying cytosolic Ca^{2+} signals to the mitochondria, **Figure 13** shows a comparison of model results with experimental data for uniporter block at 1 Hz pacing. After 75% of mitochondrial Ca^{2+} uniporters are blocked in the model, the cytosolic Ca^{2+} transient peak increases 51%, similar to the data shown from Maack et al. (2006). Conversely, uniporter block results in a decrease of the mitochondrial Ca^{2+} transient of about 60%. These effects also demonstrate the significance of beat-to-beat buffering of cytosolic Ca^{2+} by the mitochondria, since enough Ca^{2+} is taken up to reduce the amplitude of the cytosolic Ca^{2+} transient by approximately one-third. This also supports the results shown earlier (**Figure 4**) of Ca^{2+} fluxes during Ca^{2+} transient relaxation, where mitochondria exported an amount of Ca^{2+} into the cytosol 12.7% the size of the net cytosolic Ca^{2+} export flux. However, it is important to note that while the model mitochondria exchange large quantities of Ca^{2+} with the cytosol, strong buffering of Ca^{2+} in the mitochondrial matrix limits beat-to-beat variation of mitochondria Ca^{2+} transients to approximately 2% of peak mitochondrial Ca^{2+} at 1 Hz.

In this model, the influence of the mitochondria on force production and vice versa is mediated largely through changes in the concentrations of cytosolic species. As described above, the Ca^{2+} buffering properties of the mitochondria affect the amplitude of the cytosolic Ca^{2+} transient. This in turn modulates the amplitude of the force transient. The myofibrils influence the mitochondria via their influence on ADP levels. Isometric contraction is linked to ADP:ATP levels via the acto-myosin ATPase, which is responsible for the bulk of ATP hydrolysis in the contracting myocyte. Increases in workload lead to a greater consumption of ATP, which results in a rise in ADP levels. This signal is conveyed from the cytosol to the mitochondria via creatine kinase acting on the diffusible creatine phosphate pool. It is the time delay imposed by this lengthy signaling cascade that leads to the disconnect between NADH supply and subsequent complex NADH transients.

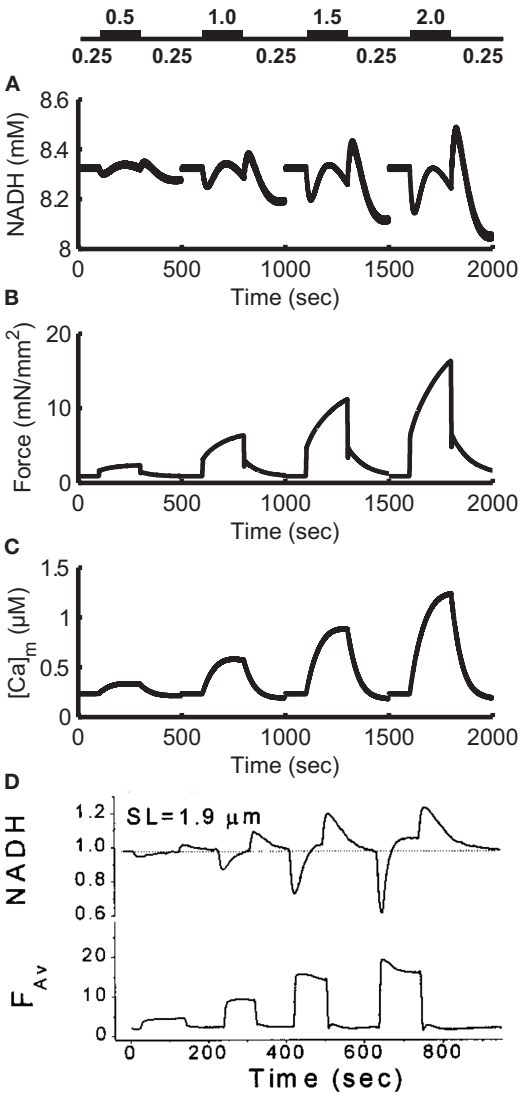

FIGURE 12 | Frequency-dependence of NADH levels. (A) Simulation of NADH concentration for a pacing protocol consisting of 100 s at 0.25 Hz [see labels above **(A)**], 200 s at higher pacing frequencies of 0.5, 1.0, 1.5, and 2.0 Hz then 200 s recovery at 0.25 Hz. Each 500 s protocol is started from 0.25 Hz steady-state initial conditions. **(B)** Moving average of model force output using a 4000-ms window. Force ranges from approximately 0.9 mN/mm^2 at 0.25 Hz to 16.4 mN/mm^2 at the end of the 2-Hz pacing period. **(C)** Model mitochondrial Ca^{2+} concentration. **(D)** Experimental data from Brandes and Bers (1999) follow a similar protocol. NADH signal is normalized to 0.25 Hz level. **(D)** Was reproduced from Brandes and Bers (1999) by copyright permission of the Biophysical Society.

DISCUSSION

The work presented here describes a mathematical model which represents the electrophysiology, Ca^{2+} cycling, isometric force

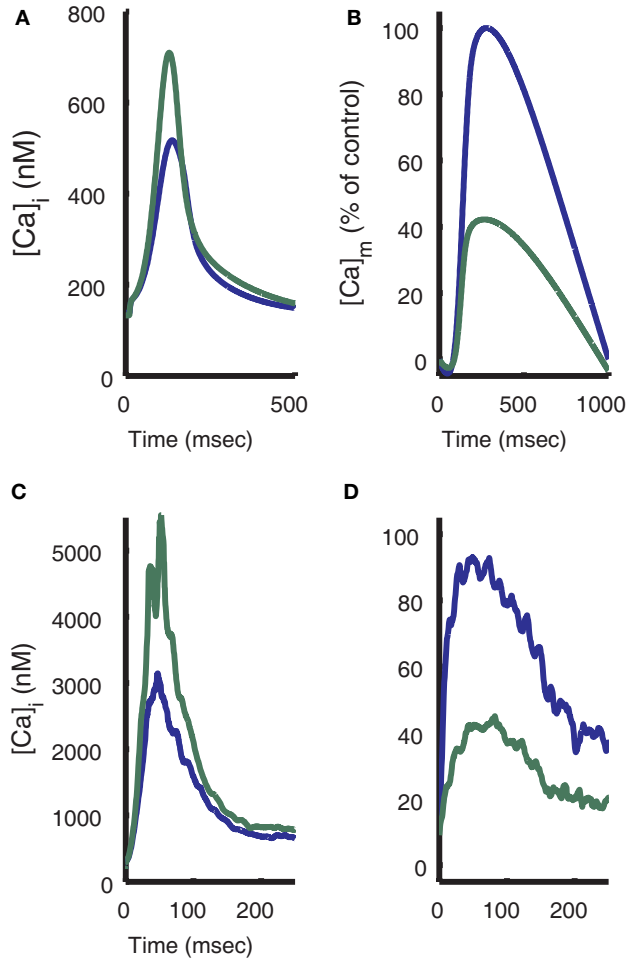

FIGURE 13 | Effect of mitochondrial uniporter block. (A) Model results show the effect of 75% block of the mitochondrial uniporter (simulated by reducing the parameter Vmuni to 25% of its control value). Cytosolic Ca^{2+} transient magnitude is increased and **(B)** mitochondrial Ca^{2+} transient magnitude is decreased. Experimental data (Maack et al., 2006) for cytosolic Ca^{2+} levels **(C)** and mitochondrial Ca^{2+} levels **(D)** with addition of 10 nM Ru, a blocker of the mitochondrial uniporter.

development and mitochondrial energetics of the guinea pig cardiac myocyte. The novel feature of this model is the incorporation of a previously developed (Hinch et al., 2004; Greenstein et al., 2006) biophysically based model of local control of SR Ca^{2+} release. An advantage of this model is that it captures the key features of CICR (gradedness of Ca^{2+} release, voltage-dependent ECC gain) and does not require computationally expensive stochastic simulations of large numbers of individual ion channels (Greenstein and Winslow, 2002; Gaur and Rudy, 2011). We have previously shown that the inclusion of such a local control mechanism, which exhibits graded SR Ca^{2+} release, is crucial for the stability of the AP (Greenstein and Winslow, 2002), given that CDI of the LCC is much stronger than VDI (Hadley and Hume, 1987; Hadley and Lederer, 1991; Sipido et al., 1995a; Linz and Meyer, 1998;Peterson et al., 1999, 2000). Without a mechanistic description of this mechanism, common pool models are unstable because the strong negative feedback on $I_{Ca,L}$ via CDI resulting from regenerative RyR Ca^{2+} release into the common pool essentially switches LCC trigger flux off prematurely. While other models (Viswanathan et al., 1999; Faber and Rudy, 2000; ten Tusscher et al., 2004; Mahajan et al., 2008) have been able to reproduce experimental features of ECC by incorporating phenomenological descriptions of graded release, use of phenomenological models always presents the risk that model predictions may be less reliable. Therefore the key question is: what do we gain from the formulation of a model that incorporates a biophysically based description of local control of Ca^{2+} release? This and other issues are discussed in the following sections.

LOCAL CONTROL MODEL PREDICTS EFFECTS OF AP SHAPE ON CALCIUM-RELEASE

The results of this study demonstrate an important functional relationship between early phase AP morphology and the kinetic properties of the cytosolic Ca^{2+} and force transients. The guinea pig ventricular myocyte model presented here, which includes an implementation of the new local control CaRU model (Greenstein et al., 2006), predicts that as a consequence of the shape of the guinea pig ventricular myocyte AP during the plateau phase, the Ca^{2+} transient peaks during the late phase of the AP (127 ms after the stimulus current; see **Figure 14**). This correlation of delayed Ca^{2+} transient peak with slowly repolarizing AP plateau voltage is seen in the experimental data (Arreola et al., 1991; Sah et al., 2003; Nishizawa et al., 2009). Consequently, the force transient is also delayed, having a peak that occurs after the AP is repolarized (**Figure 14**). This crucially important feature of the relative timing of the Ca^{2+} transient cannot be reconstructed using a common pool model, such as the prior version of the guinea pig ECME model (Cortassa et al., 2006). The delay in release timing exhibited by the present model is caused by a relatively low driving force for $I_{Ca,L}$ early in the AP. While many LCCs open in the first few millisecond following the upstroke of the AP, unitary currents are small and the amount of Ca^{2+} entering any particular dyad via an open LCC is usually insufficient to trigger regenerative RyR opening. As the AP repolarizes, the driving force for $I_{Ca,L}$ increases, LCC openings provide larger unitary currents, and hence are more effective at promoting the opening of RyRs, and release is more effectively triggered. This behavior, which was not built into the model, emerges as a result of incorporating the deterministic local control model which captures graded release and variable ECC gain. This model result emphasizes the role of the plateau potential in the nature of SR release triggering.

As a consequence, it is important to note that differences in AP morphology (**Figure 15A**) can result in very different trigger L-Type Ca^{2+} currents (**Figure 15B**), and therefore Ca^{2+} transients with very different timing (**Figure 15C**). For example, the previously published canine myocyte model incorporating this same CaRU formulation (Greenstein et al., 2006) produced a cytosolic Ca^{2+} transient that peaked in the early phase of the AP (44 ms after the stimulus current; see **Figures 15A,C**). While the canine AP has a strong phase 1 repolarization due to the presence of the I_{to} current, guinea pig ventricular myocytes lack I_{to} (Findlay, 2003; Zhabyeyev et al., 2004) and their APs repolarize more

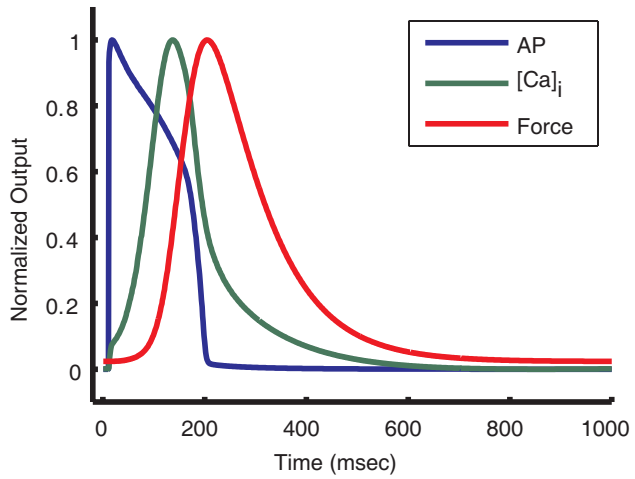

FIGURE 14 | Action potential shape causes delayed Ca^{2+} transient and force. Normalized output from the guinea pig model is used to compare the kinetics of the AP, $[Ca]_i$ transient, and force transient. As seen above, the $[Ca]_i$ transient peaks near the end of the AP plateau. The force transient peak is further delayed and occurs after almost full repolarization of the cell.

slowly during the time period following the upstroke. When the guinea pig AP is at voltages near +40 mV, the canine AP has already repolarized to approximately +10 mV. As evident from the ECC gain curve (see **Figure 8C**), the canine AP will repolarize to a voltage at which gain is large very rapidly and trigger a relatively strong and synchronized release forming the early Ca^{2+} transient. In contrast, the slow repolarization of the guinea pig AP leads to a very slow increase in gain such that Ca^{2+} release is triggered in a more gradual manner, leading to a delay in the peak of the Ca^{2+} transient.

Many aspects of the canine and guinea pig local control models differ, including resting SR load, Ca^{2+} cycling parameters, and L-type Ca^{2+} channel parameters. To further test the hypothesis that AP shape is responsible for release timing, the control version of the guinea pig model was compared to a version with an AP which more closely resembles that of the canine model. The comparison version of the model incorporates a model of the $I_{to,fast}$ current developed in the Shannon–Bers rabbit model (Shannon et al., 2004) representing the Ca^{2+}-independent component of I_{to} ($I_{to,1}$) and consisting of one Hodgkin and Huxley (1952) activation gate and a second, slower Hodgkin–Huxley inactivation gate (**Figures 15D–F**). Both versions of the model were started from the control model's 1 Hz initial conditions. The added $I_{to,fast}$ model introduces a brief outward current upon depolarization to positive potentials. With this current included, the AP features rapid phase 1 repolarization and a Ca^{2+} transient that triggers with much less of a delay, similar to that of the canine model (**Figures 15D–F**). Addition of $I_{to,fast}$ hyperpolarizes the initial membrane potential of the plateau to a voltage associated with high ECC gain. After LCCs open in response to the AP upstroke to approximately +50 mV, the I_{to}-induced repolarization reduces membrane potential and increases the driving force for $I_{Ca,L}$. This larger single-channel influx of Ca^{2+} triggers a larger Ca^{2+} flux from the RyRs by way of triggering release at a larger population of release sites than for the control AP at the same time. The result is that a larger release occurs earlier in the AP with $I_{to,fast}$, yielding a Ca^{2+} transient peak that occurs earlier in the AP than in control. Results were similar using an AP clamp recorded from the canine model, which yielded a Ca^{2+} transient peak of 1.05 μM occurring approximately 10 ms after the peak of the AP (not shown).

Use of a local control model such as this one featuring AP shape-dependent release will have important implications regarding behavior of tissue level model electro-mechanics. For example, in many species there are significant transmural differences in the expression levels of many key ion channels. The result is that APs from different tissue sites take on different morphologies (Nerbonne and Kass, 2005). This model predicts that these changes in AP shape will lead to changes in the timing of Ca^{2+} release, shape of the Ca^{2+} transient, and timing of force generation. AP clamp waveforms from guinea pig epicardial, midmyocardial, and endocardial cells as recorded by Sicouri et al. (1996) were input to the model to simulate the corresponding SR Ca^{2+} release and Ca^{2+} transient in each cell type (not shown). A 36% gradient of SERCa expression, measured with high resolution and accuracy by Anderson et al. (2011) was also applied. Epicardial cells were taken to have the control level of SERCa while SERCa expression was decreased by 18 and 36% in midmyocardial and endocardial cells, respectively. The resulting simulations show that release occurs earliest in midmyocardial cells due to the relatively hyperpolarized potential at the start of the AP plateau. Times to peak change by less than 10% without the application of a SERCa expression gradient, and rankings of times to peak remain the same between tissue types.

Given that this model predicts changes in release timing with AP morphology, the AP shape of the experimental species used may impact the strength of the conclusions that can be inferred about human electrophysiology. Among rabbit, canine, and human, all of which express I_{to}, the AP notch is more prominent in recordings from epicardial than endocardial myocytes (Fedida and Giles, 1991; Liu et al., 1993; Liu and Antzelevitch, 1995; Nabauer et al., 1996). For epicardial cells, canine APs exhibit a more pronounced notch than human, while rabbit APs have a noticeable early repolarization characteristic of I_{to}, but no strict spike-notch-dome morphology. Following phase 1 early repolarization, human AP plateau values peak below 25 mV for epicardial cells (Drouin et al., 1998; Piacentino et al., 2003). In comparison, canine plateau values for epicardial recordings at 1 Hz peak in the range of 10–15 mV (Liu et al., 1993; Liu and Antzelevitch, 1995) and rabbit plateau maxima take on values from 25 to 40 mV (Fedida and Giles, 1991; Puglisi et al., 1999). Guinea pig epicardial APs do not have a phase 1 repolarization and may take 50 ms for the plateau to decrease to 25 mV from the peak value near 50 mV (Sicouri et al., 1996). The current model predicts that these differences in notch depth and initial plateau height may significantly influence the timing of Ca^{2+} release and force generation in these different species. These results emphasize the importance of the inclusion of graded release in electromechanical models. Common pool electromechanical models without graded release are limited in their predictive scope. The all-or-none release produced by such common pool models fails to capture the sensitivity

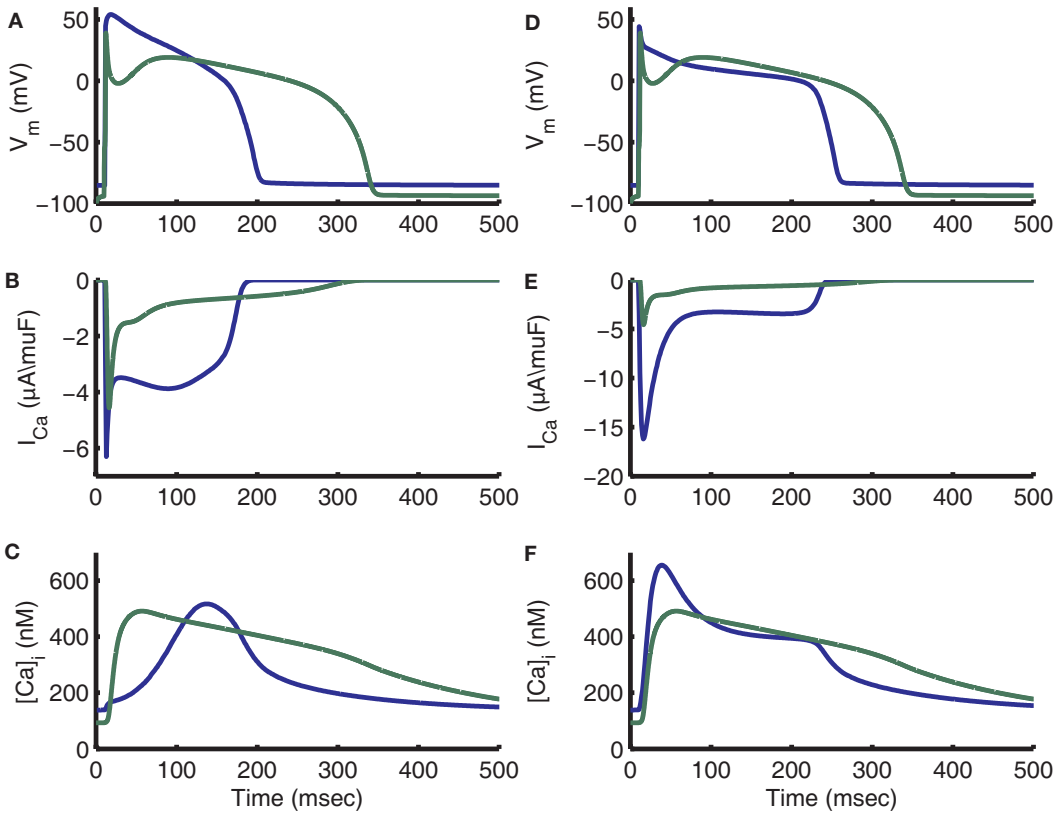

FIGURE 15 | Impact of guinea pig and canine AP morphology on $I_{Ca,L}$ and $[Ca]_i$ transients. In all panels blue traces are guinea pig model output and green traces are canine model output. **(A)** Comparison of APs from guinea pig and canine models (Greenstein et al., 2006). The canine AP has a significant early repolarization notch and a significantly longer APD. **(B)** L-type current traces peak near the same value, but guinea pig shows a much larger amount of late current. **(C)** Canine $[Ca]_i$ transient peak is approximately aligned with the AP notch, while the guinea pig $[Ca]_i$ transient peak occurs during the late plateau phase. **(D)** On the first beat after adding $I_{to,fast}$ as in the Shannon et al. (2004) model with conductance of 0.2 mS/μF, the guinea pig AP exhibits a rapid initial repolarization and APD approaches that of canine. **(E)** With addition of $I_{to,fast}$, the guinea pig $I_{Ca,L}$ trace exhibits a relation between fast peak and late current more similar to canine. The fast peak amplitude also increases substantially. **(F)** The peak of the guinea pig $[Ca]_i$ transient is now aligned with that of the canine model.

of the intracellular Ca^{2+} transient, and thus force transient, to changes in AP shape, as may occur with the reduction in $I_{to,1}$ in heart failure (Greenstein et al., 2006). Some of the earliest models incorporating electrophysiology with mechanical components were limited in their predictive scope because they modeled electrophysiology without any description SR release (Li et al., 2004) or with a description resulting in all-or-none release (Li et al., 2006). However as newer release descriptions succeeded in representing graded release (Chudin et al., 1999; Shannon et al., 2004; Mahajan et al., 2008), electromechanical models incorporating those advances gained the ability to predict mechanoelectrical feedback in arrhythmia (Jie et al., 2010; Keldermann et al., 2010) and patient-specific changes in electrical activation during heart failure (Aguado-Sierra et al., 2011).

In addition to AP morphology differences between species, diseases such as heart failure can produce significant alteration of AP morphology. In human heart failure I_{to} density has been shown to be downregulated (Beuckelmann et al., 1993; Nabauer et al., 1996). This is the major factor in the reduction of the AP notch in recordings from isolated failing cardiac myocytes. Another consequence to AP morphology is that the initial value of the plateau is elevated in heart failure. As discussed above, the membrane potential immediately following the AP peak plays a large role in the timing and magnitude of the Ca^{2+} transient. These findings corroborate those from Greenstein and Winslow (2002), which show that different I_{to} current densities have a significant impact on the efficacy of ECC, making AP morphology an important factor in predicting ECC properties during heart failure.

CRITIQUE OF THE MODEL

As with any computational model, compromises must be made in order to fit the range of experimental data for different protocols. The model restitution curves for 0.5 Hz pacing shown in **Figure 10A** gradually reach a plateau at which APD_{90} is approximately 219 ms. The time constant for this restitution (165 ms) is much slower than that observed in experiments (Bjornstad et al., 1993; Sicouri et al., 1996). This feature of the restitution curve in the model can be attributed to the time constant of I_{Ks} near the resting potential. Due to the slow deactivation time constants of I_{Ks}, there is a significant accumulation of active channels at DIs

less than 1000 ms. The amount of current remains small because voltage is near the K^+ reversal potential. If a premature stimulus shortens the DI, an even larger fraction of channels remain active, leading to larger I_{Ks} during the prematurely triggered AP. This results in a larger outward current that shortens the AP. Shorter DIs provide less time for I_{Ks} to deactivate, resulting in a larger I_{Ks} and shorter AP following the next stimulus. Thus the time constant of AP restitution is closely related to the time constant of I_{Ks} deactivation at negative potentials.

The model of I_{Ks} used here was formulated in the LRd99 model (Viswanathan et al., 1999) and was well fit to the two time constants of deactivation shown in experimental data (Matsuura et al., 1987). However, the Rudy group's previous I_{Ks} model (Zeng et al., 1995), which shows a faster overall rate of deactivation, leads to faster restitution behavior that is a closer match to experimental data (**Figures 10A,B**), though still not as fast. Due to the dependence of I_{Ks} on the duration of diastole, this current's kinetics affect both AP restitution and frequency-dependence behavior. The frequency-dependence of cytosolic Ca^{2+}, force, and energy supply by mitochondria exhibited by the model is a good match to the experimental data (Szigligeti et al., 1996; Brandes and Bers, 1999). This model is unable to simultaneously achieve this frequency-dependent behavior and match the experimentally measured rate of AP restitution. Incorporation of a more detailed Markov model of I_{Ks} behavior (Silva and Rudy, 2005) may help reconcile these two cellular properties.

In addition, this model is not able to reproduce the Ca^{2+} restitution and related short-term interval-force relationships as described by Wier and Yue (1986). In other models (Rice et al., 2000; Faber et al., 2007) this behavior is mediated by a slow recovery of RyRs from inactivation. For short DIs, many RyRs remain inactivated so the maximal open probability is reduced, leading to smaller release and smaller Ca^{2+} transients. However, consistent with estimates by Bers (2001), this model has a much lower peak RyR open probability of 2.9% at 1 Hz pacing (compare to 100% for Faber et al., 2007 and 60% for Rice et al., 2000) and the proportion of channels that are closed and not inactivated does not drop below 70% at 1 Hz. The majority of RyRs are still available for activation in the event of a premature stimulus. As a result, the maximal RyR open probability triggered by a premature stimulus is not significantly reduced from control. This, coupled with the residual cytosolic Ca^{2+} stemming from the delayed Ca^{2+} transient exhibited by this model, limits the degree of Ca^{2+} restitution. A stimulus following a 1-Hz steady-state AP by a DI of 50 ms results in a premature AP with 26.5% shorter APD, but only a 7.7% smaller Ca^{2+} transient (not shown). In the coupled LCC-RyR formulation of Ca^{2+} release used in this model, JSR depletion cannot be tracked locally at individual release sites because the JSR and NSR are assumed to be in rapid equilibrium. Recent evidence suggests that the primary determinant of SR release termination and restitution of Ca^{2+} of sparks is the dynamics of local JSR refilling (Terentyev et al., 2002; Sobie et al., 2005; Zima et al., 2008b). Incorporation of a mechanistic formulation of this feature in future versions of this model should provide the ability to better reconstruct properties of Ca^{2+} restitution.

Computational models must weigh the advantages of physiological and mechanistic detail with computational efficiency in order to make useful predictions while still remaining tractable. Due to diffusion and compartmentation effects, the cardiac myocyte is subject to dynamic spatial gradients of a wide variety of ions and second messengers. In order to avoid the complexity of partial differential equations, the majority of models define compartments of uniform concentration. However the simple scenario of cytosolic, SR, mitochondrial, and dyadic compartments may not be sufficient to reproduce some experimental results. Experimental evidence (Weber et al., 2002, 2003) suggests that the concentrations of ions in close proximity to the sarcolemma may vary from those of the bulk cytosol. To account for this, several models feature a subsarcolemmal compartment (Shannon et al., 2004; Mahajan et al., 2008; Gaur and Rudy, 2011). While the model presented here was able to reproduce many critical ECC experiments without a submembrane volume, the addition of such a compartment may better account for the activity of sarcolemmal proteins that sense Na^+ and Ca^{2+}, such as NCX.

Greenstein and Winslow (2002) and Gaur and Rudy (2011) have previously published canine and guinea pig myocyte models, respectively, featuring a stochastic description of local control of SR Ca^{2+} release, a property that strongly motivated the work presented here. The ECC gain function of the low-dimensional ordinary differential equation model presented here is similar to that of the stochastic canine model. However, the ECC gain function of the Gaur and Rudy (2011) guinea pig model differs significantly from that shown here. Specifically, the gain in the model presented here decreases monotonically as membrane potential increases (**Figure 8C**) while the ECC gain of Gaur and Rudy (2011) decreases rapidly at hyperpolarized potentials and plateaus at a relatively high value at positive voltages. The gain for their model at +40 mV, which is the approximate peak of the AP, is roughly 10 times higher than that of the present model. As a result, Ca^{2+} release in their model (their **Figure 3**) is triggered fully at the start of the AP and terminates within 30 ms. In contrast, the lower gain in the present model at membrane potentials near the peak of the AP leads to incomplete, but persistent release that inactivates gradually during phase 3 repolarization. While, to the authors' knowledge, voltage-dependent ECC gain has not been measured in guinea pig, the relative displacement of voltage-dependent LCC and RyR fluxes in this model closely resemble the shifted bell-shaped curves that give rise to the monotonic decreasing voltage-dependent ECC gain function measured in rat (Wier et al., 1994; Santana et al., 1996; Song et al., 2001).

An alternative approach to modeling graded release in deterministic myocyte models is to utilize more abstracted release descriptions. For example, the Rudy group (Faber et al., 2007; Gaur and Rudy, 2011) modeled the rate of Ca^{2+} flux through open RyRs as a function of the voltage-dependent Ca^{2+} trigger flux. Mahajan et al. (2008) utilized a simpler formulation lacking any description of RyR gating. Instead, the rate of Ca^{2+} release events was modeled as being proportional to the product of LCC open probability and a voltage-dependent gain function. One advantage of such models formulations is that they "break" the strong positive feedback loop that is well known to lead to all-or-none Ca^{2+} release in common pool models (Stern, 1992). These formulations can also reduce the number of model state variables, facilitating large-scale simulations at the tissue and whole-heart levels. In fact

the Mahajan model (2008) is able to reproduce the late peak of the Ca^{2+} transient observed in this work through its phenomenological incorporation of voltage-dependent gain. However, a disadvantage of these more abstract models is that they cannot be used to predict the effects of events such as fundamental changes in RyR gating on ECC gain properties (Hashambhoy et al., 2010) without additional assumptions, because the gain function itself is built directly into the models.

The approach of approximating cellular function using more abstract (i.e., less mechanistic) descriptions to reduce the number of state variables could also be applied to the mitochondria. In a scenario where abnormal ATP supply does not need to be addressed, the Ca^{2+} buffering role of the mitochondria could be approximated by a slow buffer. Such an approximation would continue to influence the cytosolic Ca^{2+} transients on a beat-to-beat basis and over longer periods of stimulation by accumulating or releasing Ca^{2+} slowly as cytosolic Ca^{2+} peaks change. However, the slow buffer approximation would begin to break down under conditions where a large mitochondrial to cytosolic Ca^{2+} gradient is present, such as upon commencement of beta adrenergic stimulation.

The model presented here lacks a JSR compartment, which was combined with the network SR in developing the deterministic formulation of the CaRU model (Hinch et al., 2004). As a result, the model does not reproduce local SR depletion during release. Instead, this CaRU model relies on RyR inactivation for termination of release. While some experimental data supports inactivation as a possible mechanism of release termination (Sham et al., 1998), more recent work suggest that local JSR Ca^{2+} depletion may be the major mechanism for release termination (Terentyev et al., 2002; Zima et al., 2008a,b; Domeier et al., 2009; Stevens et al., 2009). The RyR model presented here precludes the possibility of incorporating local JSR depletion. In addition, other groups (Shannon et al., 2004; Mahajan et al., 2008; Gaur and Rudy, 2011) have incorporated SR load-dependence into RyR behavior, a feature not included in this model. Its inclusion may help reconstruct the steep SR load-dependent increase in fractional release seen in some datasets (Shannon et al., 2000).

Other models that incorporate both ECC and mitochondrial energetics exist. Magnus and Keizer (1998) developed one of the first comprehensive models of cytosolic and mitochondrial Ca^{2+} handling in pancreatic β-cells. Their Ca^{2+}-regulation of the TCA cycle was the basis on which the energetics model used here was developed (Cortassa et al., 2003, 2006). Subsequently, Matsuoka et al. (2004) formulated a cardiac myocyte model describing electrophysiology and Ca^{2+} handling between mitochondria and cytosol. However, this model is not able to capture the biphasic response of NADH levels to changes in pacing frequency. Another recent model (Hatano et al., 2011) is novel in that it describes electrophysiology, mitochondrial energetics, and spatiotemporal changes in Ca^{2+} and many metabolites. While this model supports the existence of subsarcolemmal Ca^{2+} gradients as predicted by NCX calculations (Weber et al., 2002), and predicts the cellular distribution of ADP, the coarse resolution of the 3D mesh required for computational tractability precludes the ability to make predictions regarding subspace Ca^{2+} levels. The advantage of the model presented here is that its mechanistic description of ECC and Ca^{2+} cycling in the cell will provide a platform for future investigations in Ca^{2+}-regulation of mitochondrial energy production.

CONCLUSION

We have developed a mechanistically detailed description of ECC in the guinea pig cardiac myocyte combined with modules describing energetics and isometric force. This model successfully reproduces key ECC properties of graded SR Ca^{2+} release and voltage-dependent gain. Additionally, the incorporation of mitochondrial energetics allows the model to qualitatively reproduce changes in NADH in response to changes in cardiac workload. Using this model we can improve our understanding of how changes in AP shape and Ca^{2+} transients affect energy supply and developed force in normal and failing myocytes.

ACKNOWLEDGMENTS

This work was supported by the National Heart, Lung and Blood Institute (HL105216, HL105239) to R. L. Winslow and NSF and NDSEG graduate fellowships to L. D. Gauthier. R. L. Winslow is the Raj and Neera Singh Professor of Biomedical Engineering.

SUPPLEMENTARY MATERIAL

The Supplementary Material for this article can be found online at http://www.frontiersin.org/Computational_Physiology_and_Medicine/10.3389/fphys.2012.00244/abstract

REFERENCES

Aguado-Sierra, J., Krishnamurthy, A., Villongco, C., Chuang, J., Howard, E., Gonzales, M. J., Omens, J., Krummen, D. E., Narayan, S., Kerckhoffs, R. C. P., and Mcculloch, A. D. (2011). Patient-specific modeling of dyssynchronous heart failure: a case study. *Prog. Biophys. Mol. Biol.* 107, 147–155.

Allen, T. J. A. (1996). Temperature dependence of macroscopic L-type calcium channel currents in single guinea pig ventricular myocytes. *J. Cardiovasc. Electrophysiol.* 7, 307–321.

Anderson, T., Wulfkuhle, J., Petricoin, E., and Winslow, R. L. (2011). High resolution mapping of the cardiac transmural proteome using reverse phase protein microarrays. *Mol. Cell. Proteomics* 10, M111.008037.

Arreola, J., Dirksen, R. T., Shieh, R. C., Williford, D. J., and Sheu, S. S. (1991). Ca2+ current and Ca2+ transients under action potential clamp in guinea pig ventricular myocytes. *Am. J. Physiol. Cell Physiol.* 261, C393–C397.

Bassani, J. W., Yuan, W., and Bers, D. M. (1995). Fractional SR Ca release is regulated by trigger Ca and SR Ca content in cardiac myocytes. *Am. J. Physiol. Cell Physiol.* 268, C1313–C1319.

Bers, D. M. (2001). *Excitation-Contraction Coupling and Cardiac Contractile Force.* Boston: Kluwer Academic Publishers.

Bers, D. M., and Stiffel, V. M. (1993). Ratio of ryanodine to dihydropyridine receptors in cardiac and skeletal muscle and implications for E-C coupling. *Am. J. Physiol. Cell Physiol.* 264, C1587–C1593.

Beuckelmann, D. J., Nabauer, M., and Erdmann, E. (1993). Alterations of K+ currents in isolated human ventricular myocytes from patients with terminal heart failure. *Circ. Res.* 73, 379–385.

Bjornstad, H., Tande, P. L. M., Lathrop, D. A., and Refsum, H. (1993). Effects of temperature on cycle length dependent changes and restitution of action potential duration in guinea pig ventricular muscle. *Cardiovasc. Res.* 27, 946–950.

Bluhm, W. F., Kranias, E. G., Dillmann, W. H., and Meyer, M. (2000). Phospholamban: a major determinant of the cardiac force-frequency relationship. *Am. J. Physiol. Heart Circ. Physiol.* 278, H249–H255.

Brandes, R., and Bers, D. M. (1999). Analysis of the mechanisms of mitochondrial NADH regulation in cardiac trabeculae. *Biophys. J.* 77, 1666–1682.

Cavalié, A., Mcdonald, T. F., Pelzer, D., and Trautwein, W. (1985). Temperature-induced transitory and steady-state changes in the calcium current of guinea pig ventricular myocytes. *Pflugers Arch.* 405, 294–296.

Chen, C. C., Lin, Y. C., Chen, S. A., Luk, H. N., Ding, P. Y. A., Chang, M. S., and Chiang, C. E. (2000). Shortening of cardiac action potentials in endotoxic shock in guinea pigs is caused by an increase in nitric oxide activity and activation of the adenosine triphosphate-sensitive potassium channel. *Crit. Care Med.* 28, 1713.

Chudin, E., Goldhaber, J., Garfinkel, A., Weiss, J., and Kogan, B. (1999). Intracellular Ca2+ dynamics and the stability of ventricular tachycardia. *Biophys. J.* 77, 2930–2941.

Cohen, C. J., Fozzard, H. A., and Sheu, S. S. (1982). Increase in intracellular sodium ion activity during stimulation in mammalian cardiac muscle. *Circ. Res.* 50, 651–662.

Cortassa, S., Aon, M. A., Marbán, E., Winslow, R. L., and O'Rourke, B. (2003). An integrated model of cardiac mitochondrial energy metabolism and calcium dynamics. *Biophys. J.* 84, 2734–2755.

Cortassa, S., Aon, M. A., O'Rourke, B., Jacques, R., Tseng, H.-J., Marbán, E., and Winslow, R. L. (2006). A computational model integrating electrophysiology, contraction, and mitochondrial bioenergetics in the ventricular myocyte. *Biophys. J.* 91, 1564–1589.

Davey, P., Bryant, S., and Hart, G. (2001). Rate-dependent electrical, contractile and restitution properties of isolated left ventricular myocytes in guinea-pig hypertrophy. *Acta Physiol. Scand.* 171, 17–28.

Domeier, T. L., Blatter, L. A., and Zima, A. V. (2009). Alteration of sarcoplasmic reticulum Ca2+ release termination by ryanodine receptor sensitization and in heart failure. *J. Physiol. (Lond.)* 587, 5197–5209.

Drouin, E., Lande, G., and Charpentier, F. (1998). Amiodarone reduces transmural heterogeneity of repolarization in the human heart. *J. Am. Coll. Cardiol.* 32, 1063–1067.

Faber, G. M., and Rudy, Y. (2000). Action potential and contractility changes in [Na+]i overloaded cardiac myocytes: a simulation study. *Biophys. J.* 78, 2392–2404.

Faber, G. M., Silva, J., Livshitz, L., and Rudy, Y. (2007). Kinetic properties of the cardiac L-type Ca2+ channel and its role in myocyte electrophysiology: a theoretical investigation. *Biophys. J.* 92, 1522–1543.

Fabiato, A. (1985). Time and calcium dependence of activation and inactivation of calcium-induced release of calcium from the sarcoplasmic reticulum of a skinned canine cardiac Purkinje cell. *J. Gen. Physiol.* 85, 247–289.

Fedida, D., and Giles, W. R. (1991). Regional variations in action potentials and transient outward current in myocytes isolated from rabbit left ventricle. *J. Physiol. (Lond.)* 442, 191–209.

Ferrero, J. M., Saiz, J., Ferrero, J. M., and Thakor, N. V. (1996). Simulation of action potentials from metabolically impaired cardiac myocytes: role of ATP-sensitive K+ current. *Circ. Res.* 79, 208–221.

Findlay, I. (2003). Is there an A-type K+ current in guinea pig ventricular myocytes? *Am. J. Physiol. Heart Circ. Physiol.* 284, H598–H604.

Garfinkel, A., Kim, Y.-H., Voroshilovsky, O., Qu, Z., Kil, J. R., Lee, M.-H., Karagueuzian, H. S., Weiss, J. N., and Chen, P.-S. (2000). Preventing ventricular fibrillation by flattening cardiac restitution. *Proc. Natl. Acad. Sci. U.S.A.* 97, 6061–6066.

Gaur, N., and Rudy, Y. (2011). Multiscale modeling of calcium cycling in cardiac ventricular myocyte: macroscopic consequences of microscopic dyadic function. *Biophys. J.* 100, 2904–2912.

Grantham, C. J., and Cannell, M. B. (1996). Ca2+ influx during the cardiac action potential in guinea pig ventricular myocytes. *Circ. Res.* 79, 194–200.

Greenstein, J. L., Hinch, R., and Winslow, R. L. (2006). Mechanisms of excitation-contraction coupling in an integrative model of the cardiac ventricular myocyte. *Biophys. J.* 90, 77–91.

Greenstein, J. L., and Winslow, R. L. (2002). An integrative model of the cardiac ventricular myocyte incorporating local control of Ca2+ release. *Biophys. J.* 83, 2918–2945.

Hadley, R. W., and Hume, J. R. (1987). An intrinsic potential-dependent inactivation mechanism associated with calcium channels in guinea-pig myocytes. *J. Physiol. (Lond.)* 389, 205–222.

Hadley, R. W., and Lederer, W. J. (1991). Properties of L-type calcium channel gating current in isolated guinea pig ventricular myocytes. *J. Gen. Physiol.* 98, 265–285.

Han, S., Schiefer, A., and Isenberg, G. (1994). Ca2+ load of guinea-pig ventricular myocytes determines efficacy of brief Ca2+ currents as trigger for Ca2+ release. *J. Physiol. (Lond.)* 480, 411–421.

Hashambhoy, Y. L., Greenstein, J. L., and Winslow, R. L. (2010). Role of CaMKII in RyR leak, ECC and action potential duration: a computational model. *J. Mol. Cell. Cardiol.* 49, 617–624.

Hatano, A., Okada, J.-I., Washio, T., Hisada, T., and Sugiura, S. (2011). A three-dimensional simulation model of cardiomyocyte integrating excitation-contraction coupling and metabolism. *Biophys. J.* 101, 2601–2610.

Hayashi, T., Martone, M., Yu, Z., Thor, A., Doi, M., Holst, M., Ellisman, M., and Hoshijima, M. (2009). Three-dimensional electron microscopy reveals new details of membrane systems for Ca2+ signaling in the heart. *J. Cell. Sci.* 122, 1005–1013.

Hinch, R., Greenstein, J. L., Tanskanen, A. J., Xu, L., and Winslow, R. L. (2004). A simplified local control model of calcium-induced calcium release in cardiac ventricular myocytes. *Biophys. J.* 87, 3723–3736.

Hodgkin, A. L., and Huxley, A. F. (1952). A quantitative description of membrane current and its application to conduction and excitation in nerve. *J. Physiol. (Lond.)* 117, 500–544.

Isenberg, G., and Han, S. (1994). Gradation of Ca2+-induced Ca2+ release by voltage-clamp pulse duration in potentiated guinea-pig ventricular myocytes. *J. Physiol. (Lond.)* 480, 483.

Jafri, M. S., Rice, J. J., and Winslow, R. L. (1998). Cardiac Ca2+ dynamics: the roles of ryanodine receptor adaptation and sarcoplasmic reticulum load. *Biophys. J.* 74, 1149–1168.

Jie, X., Gurev, V., and Trayanova, N. (2010). Mechanisms of mechanically induced spontaneous arrhythmias in acute regional ischemia. *Circ. Res.* 106, 185–192.

Keizer, J., and Smith, G. D. (1998). Spark-to-wave transition: saltatory transmission of calcium waves in cardiac myocytes. *Biophys. Chem.* 72, 87–100.

Keldermann, R. H., Nash, M. P., Gelderblom, H., Wang, V. Y., and Panfilov, A. V. (2010). Electromechanical wavebreak in a model of the human left ventricle. *J. Physiol. (Lond.)* 273, H1246–H1254.

Layland, J., and Kentish, J. C. (1999). Positive force- and [Ca2+]i-frequency relationships in rat ventricular trabeculae at physiological frequencies. *Am. J. Physiol.* 276, H9–H18.

Li, W., Kohl, P., and Trayanova, N. (2004). Induction of ventricular arrhythmias following mechanical impact: a simulation study in 3D. *J. Mol. Histol.* 35, 679–686.

Li, W., Kohl, P., and Trayanova, N. (2006). Myocardial ischemia lowers precordial thump efficacy: an inquiry into mechanisms using three-dimensional simulations. *Heart Rhythm* 3, 179–186.

Linz, K. W., and Meyer, R. (1998). Control of L-type calcium current during the action potential of guinea-pig ventricular myocytes. *J. Physiol. (Lond.)* 513, 425–442.

Liu, D.-W., and Antzelevitch, C. (1995). Characteristics of the delayed rectifier current (IKr and IKs) in canine ventricular epicardial, midmyocardial, and endocardial myocytes: a weaker IKs contributes to the longer action potential of the M cell. *Circ. Res.* 76, 351–365.

Liu, D. W., Gintant, G. A., and Antzelevitch, C. (1993). Ionic bases for electrophysiological distinctions among epicardial, midmyocardial, and endocardial myocytes from the free wall of the canine left ventricle. *Circ. Res.* 72, 671–687.

Maack, C., Ganesan, A., Sidor, A., and O'Rourke, B. (2005). Cardiac sodium-calcium exchanger is regulated by allosteric calcium and exchanger inhibitory peptide at distinct sites. *Circ. Res.* 96, 91–99.

Maack, C., Cortassa, S., Aon, M. A., Ganesan, A. N., Liu, T., and O'Rourke, B. (2006). Elevated cytosolic Na^+ decreases mitochondrial Ca^{2+} uptake during excitation-contraction coupling and impairs energetic adaptation in cardiac myocytes. *Circ. Res.* 99, 172–182.

Magnus, G., and Keizer, J. (1998). Model of β-cell mitochondrial calcium handling and electrical activity. I. Cytoplasmic variables. *Am. J. Physiol. Cell Physiol.* 274, C1158–C1173.

Mahajan, A., Shiferaw, Y., Sato, D., Baher, A., Olcese, R., Xie, L.-H., Yang, M.-J., Chen, P.-S., Restrepo, J. G., Karma, A., Garfinkel, A., Qu, Z., and Weiss, J. N. (2008). A rabbit ventricular action potential model replicating cardiac dynamics at rapid heart rates. *Biophys. J.* 94, 392–410.

Maier, L. S., Pieske, B., and Allen, D. G. (1997). Influence of stimulation frequency on [Na+]i and

contractile function in Langendorff-perfused rat heart. *Am. J. Physiol.* 273, H1246–H1254.

Matsuoka, S., Sarai, N., Jo, H., and Noma, A. (2004). Simulation of ATP metabolism in cardiac excitation-contraction coupling. *Prog. Biophys. Mol. Biol.* 85, 279–299.

Matsuura, H., Ehara, T., and Imoto, Y. (1987). An analysis of the delayed outward current in single ventricular cells of the guinea-pig. *Pflugers Arch.* 410, 596–603.

Mejía-Alvarez, R., Kettlun, C., Ríos, E., Stern, M., and Fill, M. (1999). Unitary Ca2+ current through cardiac ryanodine receptor channels under quasi-physiological ionic conditions. *J. Gen. Physiol.* 113, 177–186.

Nabauer, M., Beuckelmann, D. J., Âœberfuhr, P., and Steinbeck, G. (1996). Regional differences in current density and rate-dependent properties of the transient outward current in subepicardial and subendocardial myocytes of human left ventricle. *Circulation* 93, 168–177.

Nerbonne, J. M., and Kass, R. S. (2005). Molecular physiology of cardiac repolarization. *Physiol. Rev.* 85, 1205–1253.

Nichols, C. G., and Lederer, W. J. (1990). The regulation of ATP-sensitive K+ channel activity in intact and permeabilized rat ventricular myocytes. *J. Physiol. (Lond.)* 423, 91–110.

Nishizawa, H., Suzuki, T., Shioya, T., Nakazato, Y., Daida, H., and Kurebayashi, N. (2009). Causes of abnormal Ca2+ transients in Guinea pig pathophysiological ventricular muscle revealed by Ca2+ and action potential imaging at cellular level. *PLoS ONE* 4, e7069. doi:10.1371/journal.pone.0007069

Noble, D. (1960). Cardiac action and pacemaker potentials based on the Hodgkin-Huxley equations. *Nature* 188, 495–497.

Peterson, B. Z., Demaria, C. D., and Yue, D. T. (1999). Calmodulin is the Ca2+ sensor for Ca2+-dependent inactivation of L-type calcium channels. *Neuron* 22, 549–558.

Peterson, B. Z., Lee, J. S., Mulle, J. G., Wang, Y., De Leon, M., and Yue, D. T. (2000). Critical determinants of Ca2+-dependent inactivation within an EF-hand motif of L-type Ca2+ channels. *Biophys. J.* 78, 1906–1920.

Piacentino, V., Weber, C. R., Chen, X., Weisser-Thomas, J., Margulies, K. B., Bers, D. M., and Houser, S. R. (2003). Cellular basis of abnormal calcium transients of failing human ventricular myocytes. *Circ. Res.* 92, 651–658.

Puglisi, J. L., Yuan, W., Bassani, J. W. M., and Bers, D. M. (1999). Ca2+ influx through Ca2+ channels in rabbit ventricular myocytes during action potential clamp: influence of temperature. *Circ. Res.* 85, e7–e16.

Qu, Z., Weiss, J. N., and Garfinkel, A. (1999). Cardiac electrical restitution properties and stability of reentrant spiral waves: a simulation study. *Am. J. Physiol.* 276, H269–H283.

Raman, S., Kelley, M., and Janssen, P. (2006). Effect of muscle dimensions on trabecular contractile performance under physiological conditions. *Pflugers Arch.* 451, 625–630.

Rice, J., Jafri, M., and Winslow, R. (2000). Modeling short-term interval-force relations in cardiac muscle. *Am. J. Physiol. Heart Circ. Physiol.* 278, H913–H931.

Rice, J. J., Saleet Jafri, M., and Winslow, R. L. (1999). Modeling gain and gradedness of Ca2+ release in the functional unit of the cardiac diadic space. *Biophys. J.* 77, 1871–1884.

Rocchetti, M., Besana, A., Mostacciuolo, G., Micheletti, R., Ferrari, P., Sarkozi, S., Szegedi, C., Jona, I., and Zaza, A. (2005). Modulation of sarcoplasmic reticulum function by Na+/K+ pump inhibitors with different toxicity: digoxin and PST2744 [(E,Z)-3-((2-Aminoethoxy)imino)androstane-6,17-dione hydrochloride]. *J. Pharmacol. Exp. Ther.* 313, 207–215.

Rose, W. C., Balke, C. W., Wier, W. G., and Marban, E. (1992). Macroscopic and unitary properties of physiological ion flux through L-type Ca2+ channels in guinea-pig heart cells. *J. Physiol. (Lond.)* 456, 267–284.

Sah, R., Ramirez, R. J., Oudit, G. Y., Gidrewicz, D., Trivieri, M. G., Zobel, C., and Backx, P. H. (2003). Regulation of cardiac excitation–contraction coupling by action potential repolarization: role of the transient outward potassium current (Ito). *J. Physiol. (Lond.)* 546, 5–18.

Santana, L. F., Cheng, H., Gómez, A. M., Cannell, M. B., and Lederer, W. J. (1996). Relation between the sarcolemmal Ca2+ current and Ca2+ sparks and local control theories for cardiac excitation-contraction coupling. *Circ. Res.* 78, 166–171.

Sham, J. S. K., Song, L.-S., Chen, Y., Deng, L.-H., Stern, M. D., Lakatta, E. G., and Cheng, H. (1998). Termination of Ca2+ release by a local inactivation of ryanodine receptors in cardiac myocytes. *Proc. Natl. Acad. Sci. U.S.A.* 95, 15096–15101.

Shannon, T. R., Ginsburg, K. S., and Bers, D. M. (2000). Potentiation of fractional sarcoplasmic reticulum calcium release by total and free intra-sarcoplasmic reticulum calcium concentration. *Biophys. J.* 78, 334–343.

Shannon, T. R., Wang, F., Puglisi, J., Weber, C., and Bers, D. M. (2004). A mathematical treatment of integrated Ca dynamics within the ventricular myocyte. *Biophys. J.* 87, 3351–3371.

Sicouri, S., Quist, M., and Antzelevitch, C. (1996). Evidence for the presence of M cells in the Guinea pig ventricle. *J. Cardiovasc. Electrophysiol.* 7, 503–511.

Silva, J., and Rudy, Y. (2005). Subunit interaction determines IKs participation in cardiac repolarization and repolarization reserve. *Circulation* 112, 1384–1391.

Sipido, K. R., Callewaert, G., and Carmeliet, E. (1995a). Inhibition and rapid recovery of Ca2+ current during Ca2+ release from sarcoplasmic reticulum in Guinea pig ventricular myocytes. *Circ. Res.* 76, 102–109.

Sipido, K. R., Carmeliet, E., and Pappano, A. (1995b). Na+ current and Ca2+ release from the sarcoplasmic reticulum during action potentials in guinea-pig ventricular myocytes. *J. Physiol. (Lond.)* 489, 1.

Sipido, K. R., and Wier, W. G. (1991). Flux of Ca2+ across the sarcoplasmic reticulum of guinea-pig cardiac cells during excitation-contraction coupling. *J. Physiol. (Lond.)* 435, 605–630.

Sobie, E. A., Song, L.-S., and Lederer, W. J. (2005). Local recovery of Ca2+ release in rat ventricular myocytes. *J. Physiol. (Lond.)* 565, 441–447.

Song, L.-S., Wang, S.-Q., Xiao, R.-P., Spurgeon, H., Lakatta, E. G., and Cheng, H. (2001). β-Adrenergic stimulation synchronizes intracellular Ca^{2+} release during excitation-contraction coupling in cardiac myocytes. *Circ. Res.* 88, 794–801.

Stern, M. D. (1992). Theory of excitation-contraction coupling in cardiac muscle. *Biophys. J.* 63, 497–517.

Stevens, S. C. W., Terentyev, D., Kalyanasundaram, A., Periasamy, M., and Györke, S. (2009). Intra-sarcoplasmic reticulum Ca2+ oscillations are driven by dynamic regulation of ryanodine receptor function by luminal Ca2+ in cardiomyocytes. *J. Physiol. (Lond.)* 587, 4863–4872.

Szigligeti, P., Pankucsi, C., Bányász, T., Varró, A., and Nánási, P. P. (1996). Action potential duration and force-frequency relationship in isolated rabbit, guinea pig and rat cardiac muscle. *J. Comp. Physiol. B Biochem. Syst. Environ. Physiol.* 166, 150–155.

ten Tusscher, K. H. W. J., Noble, D., Noble, P. J., and Panfilov, A. V. (2004). A model for human ventricular tissue. *Phys. Med. Biol.* 286, H1573–H1589.

Terentyev, D., Viatchenko-Karpinski, S., Valdivia, H. H., Escobar, A. L., and Gyorke, S. (2002). Luminal Ca2+ controls termination and refractory behavior of Ca2+-induced Ca2+ release in cardiac myocytes. *Circ. Res.* 91, 414–420.

Terracciano, C. M. N., Naqvi, R. U., and Macleod, K. T. (1995). Effects of rest interval on the release of calcium from the sarcoplasmic reticulum in isolated Guinea pig ventricular myocytes. *Circ. Res.* 77, 354–360.

Viswanathan, P. C., Shaw, R. M., and Rudy, Y. (1999). Effects of IKr and IKs heterogeneity on action potential duration and its rate dependence: a simulation study. *Circulation* 99, 2466–2474.

Wang, D. Y., Chae, S. W., Gong, Q. Y., and Lee, C. O. (1988). Role of aiNa in positive force-frequency staircase in guinea pig papillary muscle. *J. Physiol. (Lond.)* 255, C798–C807.

Weber, C. R., Ginsburg, K. S., and Bers, D. M. (2003). Cardiac submembrane [Na+] transients sensed by Na+-Ca2+ exchange current. *Circ. Res.* 92, 950–952.

Weber, C. R., Ginsburg, K. S., Philipson, K. D., Shannon, T. R., and Bers, D. M. (2001). Allosteric regulation of Na/Ca exchange current by cytosolic Ca in intact cardiac myocytes. *J. Gen. Physiol.* 117, 119–132.

Weber, C. R., Piacentino, V., Ginsburg, K. S., Houser, S. R., and Bers, D. M. (2002). Na+-Ca2+ exchange current and submembrane [Ca2+] during the cardiac action potential. *Circ. Res.* 90, 182–189.

Wei, A.-C., Aon, M. A., O'Rourke, B., Winslow, R. L., and Cortassa, S. (2011). Mitochondrial energetics, pH regulation, and ion dynamics: a computational-experimental approach. *Biophys. J.* 100, 2894–2903.

Weiss, J. N., Venkatesh, N., and Lamp, S. T. (1992). ATP-sensitive K+ channels and cellular K+ loss in hypoxic and ischaemic mammalian ventricle. *J. Physiol. (Lond.)* 447, 649–673.

Wier, W. G., Egan, T. M., López-López, J. R., and Balke, C. W. (1994). Local control of excitation-contraction

coupling in rat heart cells. *J. Physiol. (Lond.)* 474, 463–471.

Wier, W. G., and Yue, D. T. (1986). Intracellular calcium transients underlying the short-term force-interval relationship in ferret ventricular myocardium. *J. Physiol. (Lond.)* 376, 507–530.

Yue, D. T., and Marban, E. (1988). A novel cardiac potassium channel that is active and conductive at depolarized potentials. *Pflugers Arch.* 413, 127–133.

Zeng, J., Laurita, K. R., Rosenbaum, D. S., and Rudy, Y. (1995). Two components of the delayed rectifier K+ current in ventricular myocytes of the Guinea pig type: theoretical formulation and their role in repolarization. *Circ. Res.* 77, 140–152.

Zhabyeyev, P., Asai, T., Missan, S., and Mcdonald, T. F. (2004). Transient outward current carried by inwardly rectifying K+ channels in guinea pig ventricular myocytes dialyzed with low-K+ solution. *Am. J. Physiol. Cell Physiol.* 287, C1396–C1403.

Zima, A. V., Picht, E., Bers, D. M., and Blatter, L. A. (2008a). Partial Inhibition of sarcoplasmic reticulum Ca release evokes long-lasting Ca release events in ventricular myocytes: role of luminal Ca in termination of Ca release. *Biophys. J.* 94, 1867–1879.

Zima, A. V., Picht, E., Bers, D. M., and Blatter, L. A. (2008b). Termination of cardiac Ca2+ sparks: role of intra-SR [Ca2+], release flux, and intra-SR Ca2+ diffusion. *Circ. Res.* 103, e105–e115.

Conflict of Interest Statement: The authors declare that the research was conducted in the absence of any commercial or financial relationships that could be construed as a potential conflict of interest.

Received: 15 March 2012; paper pending published: 19 April 2012; accepted: 14 June 2012; published online: 05 July 2012.

Citation: Gauthier LD, Greenstein JL and Winslow RL (2012) Toward an integrative computational model of the guinea pig cardiac myocyte. Front. Physio. ***3****:244. doi: 10.3389/fphys.2012.00244*

This article was submitted to Frontiers in Computational Physiology and Medicine, a specialty of Frontiers in Physiology.

frontiers in
PHYSIOLOGY

ORIGINAL RESEARCH ARTICLE
published: 29 June 2012
doi: 10.3389/fphys.2012.00223

Discharge identity of medullary inspiratory neurons is altered during repetitive fictive cough

L. S. Segers[1], S. C. Nuding[1], A. Vovk[2], T. Pitts[2], D. M. Baekey[2], R. O'Connor[1], K. F. Morris[1], B. G. Lindsey[1], R. Shannon[1] and Donald C. Bolser[2]*

[1] Department of Molecular Pharmacology and Physiology, Morsani College of Medicine, University of South Florida, Tampa, FL, USA
[2] Department of Physiological Sciences, College of Veterinary Medicine, University of Florida, Gainesville, FL, USA

Edited by:
Raimond L. Winslow, The Johns Hopkins University, USA

Reviewed by:
Daniel Goldman, The University of Western Ontario, Canada
Ravi Radhakrishnan, University of Pennsylvania, USA

***Correspondence:**
Donald C. Bolser, Department of Physiological Sciences, University of Florida, P.O. Box 100144, Gainesville, FL 32610-0144, USA.
e-mail: bolser@ufl.edu

This study investigated the stability of the discharge identity of inspiratory decrementing (I-Dec) and augmenting (I-Aug) neurons in the caudal (cVRC) and rostral (rVRC) ventral respiratory column during repetitive fictive cough in the cat. Inspiratory neurons in the cVRC ($n = 23$) and rVRC ($n = 17$) were recorded with microelectrodes. Fictive cough was elicited by mechanical stimulation of the intrathoracic trachea. Approximately 43% (10 of 23) of I-Dec neurons shifted to an augmenting discharge pattern during the first cough cycle (C1). By the second cough cycle (C2), half of these returned to a decrementing pattern. Approximately 94% (16 of 17) of I-Aug neurons retained an augmenting pattern during C1 of a multi-cough response episode. Phrenic burst amplitude and inspiratory duration increased during C1, but decreased with each subsequent cough in a series of repetitive coughs. As a step in evaluating the model-driven hypothesis that VRC I-Dec neurons contribute to the augmentation of inspiratory drive during cough via inhibition of VRC tonic expiratory neurons that inhibit premotor inspiratory neurons, cross-correlation analysis was used to assess relationships of tonic expiratory cells with simultaneously recorded inspiratory neurons. Our results suggest that reconfiguration of inspiratory-related sub-networks of the respiratory pattern generator occurs on a cycle-by-cycle basis during repetitive coughing.

Keywords: respiratory pattern generator, cough, breathing, inspiratory, expiratory, medulla

INTRODUCTION

Airway stimulation can elicit repetitive coughs which may outlast the duration of the stimulus in animal models (Bongianni et al., 1998; Shannon et al., 1998, 2000; Bolser and Davenport, 2000). In humans, bouts of repetitive coughing, called paroxysms, can induce significant morbidity due to ballistic motor activation of respiratory muscles and large intrathoracic and abdominal pressure changes (Morice et al., 2004). The specific physiological mechanisms that are responsible for the production of paroxysmal coughing are unknown. The lack of this knowledge is an impediment to the development of more effective cough suppressant therapies. Significant advancements have been made in understanding specific central mechanisms in the neurogenesis of single coughs from animal models (Shannon et al., 1998, 2000; Baekey et al., 2001, 2003). Preliminary evidence from this laboratory has suggested the presence of unique behavior of previously identified central elements during repetitive coughing. Elucidation of these mechanisms, and their role in governing the pattern of coughing, may lead to new avenues for the pharmacological suppression of cough.

In recent models for cough motor pattern generation, brainstem neurons that generate and shape breathing patterns are reconfigured to produce a cough; their responses and interactions during cough have been previously described (Shannon et al., 1996, 1998; Baekey et al., 2001, 2003; Bolser et al., 2003, 2006). Briefly, respiratory neurons that exhibit an augmenting or decrementing discharge pattern during the inspiratory phase of eupnea (I-Aug and I-Dec, respectively) are excited by peripheral sensory airway afferents via second order neurons in the nucleus tractus solitarius, resulting in inhibition of expiratory neuronal activity and an increase in the ramp, duration, and amplitude of phrenic activity. A decrease in inspiratory (I-Aug and I-Dec) and an increase in expiratory augmenting and decrementing (E-Aug and E-Dec, respectively) neural activity terminate the inspiratory phase and initiate the compressive and expulsive phases of cough.

Most inspiratory neurons in defined regions within the medulla are proposed to have specific roles in cough motor pattern generation. Premotor I-Aug neurons in the caudal ventrolateral respiratory column (cVRC) excite inspiratory motoneurons, such as those in the phrenic motor nucleus, that innervate inspiratory pump muscles, including the diaphragm. Propriobulbar I-Dec neurons shape the discharge pattern of I-Aug neurons (via inhibition), inhibit E-Aug and E-Dec neurons and help regulate inspiratory duration along with I-Driver neurons (for review refer to Shannon et al., 1996). Previous studies have shown that a group of I-Dec neurons in the cVRC and E-Aug neurons in the rostral ventrolateral respiratory column (rVRC) change their pattern of discharge, or discharge identity, during single fictive coughs: 82% of the caudal I-Dec neurons switched to an augmenting discharge identity (Shannon et al., 1998) and 50% of the rostral E-Aug neurons switched to a decrementing discharge identity (Oku et al., 1994; Shannon et al., 1998, 2000). In the current model, alterations of discharge identity of the rostral E-Aug population during fictive cough have been represented by separating the E-Aug neurons

into two functional subpopulations: E-Aug early (decrementing during cough) and E-Aug late (augmenting or continuous during cough). This process highlighted heterogeneity within this population of neurons and allowed specific modeling of the unique synaptic effects that each subpopulation had on the rest of the respiratory network. For inspiratory neurons during single fictive coughs, Shannon et al. (1998) reported little change in discharge identity for both rostral and caudal I-Aug neurons, but heterogeneity among rostral I-Dec neurons, approximately half of which converted to an augmenting discharge pattern during single fictive coughs.

The results described above were from measurements of single-cough episodes and the first coughs of repetitive series. During repetitive cough episodes, phrenic amplitude can decrease with each subsequent cough (Bongianni et al., 1998), suggesting a decrease in inspiratory motor drive. Given that I-Dec neurons help shape phrenic nerve activity and hence inspiratory motor drive, it is unknown whether the shift in I-Dec discharge pattern observed during single fictive coughs is preserved during repetitive coughing. The purpose of this study was to examine the discharge pattern of I-Dec neurons in the cVRC and rVRC during eupnea, single and repetitive coughs, and recovery breaths. We speculated that the discharge identity of the I-Dec population would be labile during repetitive coughing. Furthermore, we investigated whether the stable discharge identity of I-Aug neurons during single coughs would be preserved throughout repetitive cough episodes.

Simulations of a new computational neuromechanical model (see companion manuscript in this issue – O'Connor et al., 2012) suggest that inhibitory VRC I-Dec neurons contribute to the augmentation of cough inspiratory drive, which can – via operating volume-dependent cough mechanics – increase tracheal air flow during the subsequent expulsive phase (Smith et al., 2012). The proposed circuit mechanism includes I-Dec neuron inhibition of the inspiratory phase activity of VRC tonic E-Dec neurons that, in turn, inhibit premotor inspiratory neurons. As a step in evaluating this model-driven hypothesis, we also assessed responses and short-time scale correlations of tonic expiratory neuron spike trains that were recorded simultaneously with the inspiratory neurons.

MATERIALS AND METHODS

SURGICAL PROCEDURE AND INSTRUMENTATION

All experimental protocols were approved by the Institutional Animal Care and Use Committee at the University of South Florida and were conducted in accordance with the American Physiological Society's *Guiding Principles in the Care and Use of Vertebrate Animals in Research and Training*. Other results from some of these experiments were included in a previous report of single-cough responses to tracheal stimulation (Shannon et al., 1998). Ten cats (2.4–5.7 kg) were initially anesthetized with 22 mg/kg (iv) thiopental sodium. To reduce mucous secretion from the airways during the cough trials, 0.5 mg/kg (im) of atropine was administered. To help prevent hypotension and minimize brain stem swelling during the craniotomy, 2.0 mg/kg (iv) of dexamethasone was given. The femoral artery and vein were catheterized to monitor blood pressure, acquire blood samples and administer fluids. Animals were placed in a stereotaxic frame and decerebrated at the midcollicular level. Anesthesia with thiopental sodium was maintained throughout the decerebration process and discontinued when this surgery was complete. After decerebration, animals were paralyzed by continuous intravenous infusion of gallamine triethiodide (4 mg/kg/h) and artificially ventilated through a tracheal cannula with a phrenic-driven ventilator. A bilateral thoracotomy was performed to minimize brainstem movement.

Throughout the surgery and cough protocol, end-tidal CO_2 was maintained at 4–5% and the fraction of inspired O_2 was increased when necessary to prevent hypoxemia. Arterial blood samples were periodically analyzed for arterial PCO_2, PO_2, pH, and HCO_3^- and maintained within normal parameters. Blood pressure was maintained $\geq$100 mmHg by intravenously administering solutions of 5% dextrose in 0.45% NaCl, 5% dextran, or lactated Ringer's solution when needed. Body temperature was maintained at 38 ± 0.5°C using a rectal temperature probe and a servo-controlled heating pad.

PERIPHERAL NERVE PREPARATION AND RECORDING

The right cranial iliohypogastric (or lumbar; L_1) and left phrenic (C_5) nerves were desheathed and cut. Efferent activity was recorded with bipolar silver electrodes that were immersed in pools of mineral oil. The right recurrent laryngeal nerve close to the larynx was desheathed and cut. Efferent activity was recorded with bipolar silver electrodes covered with cotton saturated with mineral oil. Nerve signals were amplified and bandpass filtered (10 Hz – 10 kHz). Nerve activity at rest and during the cough protocol were recorded and monitored on a polygraph.

BRAINSTEM NEURON PREPARATION AND CHARACTERIZATION

Microelectrode neural recording and analysis has been previously described (Shannon et al., 1998, 2000; Baekey et al., 2001, 2004). Following occipital craniotomy, portions of the caudal cerebellum were suctioned to expose the medulla. The surface of the medulla was covered with warm mineral oil. Inspiratory neurons in the rostral and caudal VRC were monitored simultaneously with two independently controlled planar arrays of tungsten microelectrodes (10–12 MΩ). Each array consisted of six to eight microelectrodes 150–200 μm apart to allow for recording from separate single neurons. The depth of each electrode was adjusted using micromotor controllers. Signals were amplified and bandpass filtered (0.1–5 kHz).

Positive collision tests were used to identify bulbospinal neurons. Briefly, 0.1 ms single pulses (1–10 V) were delivered through bipolar stainless steel electrodes in the ventral spinal cord at the T1 level contralateral to the medullary recording sites. Spike-triggered averaging of contralateral phrenic and ipsilateral recurrent laryngeal nerve efferent activities was also used to aid in the identification of phrenic premotoneurons and laryngeal pre- and motoneurons (for details of feature interpretations, see **Figure 3**, Shannon et al., 1998).

DATA ACQUISITION AND PREPROCESSING

Neuron signals from the microelectrodes, nerve data from the bipolar electrodes, and arterial blood and tracheal pressures were monitored during the experiment using oscilloscopes, audio

monitors, and a polygraph and recorded on magnetic tape for subsequent offline analysis. Activities of phrenic, lumbar, and recurrent laryngeal nerves were integrated (full-wave-rectified signal to a resistor-capacitor integrator, $\tau = 0.2$ s) to obtain moving time averages. Analog signals of the moving time averages, arterial blood and tracheal pressures, cough stimulus timing marks, and signals from each microelectrode were digitized via a 16-channel analog-to-digital converter and stored on a computer for preprocessing and analysis.

Action potentials from individual respiratory neurons were converted to times of occurrence using spike-sorting software (Datawave Technology). These spike times and the analog signals described above were viewed and analyzed using the program Scope and other methods (Shannon et al., 2000).

FICTIVE COUGH PROTOCOL

Fictive cough was elicited by mechanically stimulating the midcervical to carinal regions of the intrathoracic trachea with a device constructed of two 1 cm loops of polyethylene tubing attached to a thin wire inserted through a port in the tracheal cannula. In eight animals, this device was deployed manually. In the remaining two animals, the device was advanced into the trachea using a custom-built controller and rotated with a frequency of 1.0 Hz; in these cases, stimulus durations ranged from 1.5 to 4 s. Cough was defined as an increase in the maximum amplitude of integrated phrenic nerve activity ($\geq$2 SD above the mean maximum phrenic amplitude for the five eupneic breaths preceding the cough stimulus) that was coincident with or immediately followed by an increase in integrated lumbar nerve activity ($\geq$2 SD above the mean of the maximum eupneic lumbar amplitude). Between trials, the polyethylene tubing was retracted into the tracheal cannula to prevent further stimulation of the trachea. The protocol consisted of at least five cough stimuli separated by $\geq$40 s to allow for eupneic breathing to return to baseline levels. Cough response episodes consisting of two or more consecutive cough cycles were considered for analysis; single coughs were also included if the recording contained at least one instance of a multiple-cough response.

DATA ANALYSIS

Cough responses were grouped according to the number of consecutive cough cycles produced in reaction to the intra-tracheal stimulus. Individual cough cycles within a response were numbered; for example, a triple-cough response consisted of three cough cycles labeled C1, C2, and C3.

A neuron's discharge ratio during one cycle was calculated by dividing the number of spikes occurring in the first half of inspiration by the spike count in the second half; one was added to the total number of spikes in each half of the phase to avoid the presence of zero in the numerator or denominator. In some recordings, a cough response type was elicited more than once (e.g., recording four in animal D contained two instances of a double-cough response; **Table 1**). To insure that the neurons in these recordings were not over-represented within the data set, average neuronal discharge ratios were calculated for each cough cycle of the response by dividing the sum of the spikes (plus one) in the first halves by the sum of the spikes (plus one) in the second halves of the inspiratory phases of, for example, the C1 cycles of all the double-cough responses in that recording. In addition, average discharge ratios for all C1 and C2 cycles of multiple-cough responses were calculated for each cell. Average discharge ratios were obtained for each cell during a control period of at least 5 min before any stimulus protocols were presented and during the five eupneic breaths preceding and the five recovery breaths following the cough cycles.

All discharge ratios were normalized by calculating the log of the ratio. Neurons with log ratios >0 or ≤ 0 were defined as having decrementing or augmenting discharge identities, respectively, during the time period for which the ratio was calculated. A neuron's control discharge identity was characterized by its average ratio during the control period.

Inspiratory neurons in the rostral and caudal areas of the ventral respiratory column were grouped based on stereotaxic coordinates; Fisher exact tests were used to investigate regional differences in discharge identity changes in response to cough stimuli.

Paired *t*-tests were used to identify differences among neuronal log discharge ratios, phrenic amplitudes, and inspiratory durations during eupneic, cough, and recovery breaths. Two-sample *t*-tests assuming unequal variances were used to assess differences among specific cough cycles in single-, double-, and triple-cough episodes. Results were corrected for multiple testing by controlling the false discovery rate to 0.05 (Benjamini and Hochberg, 1995); $p \leq 0.02$ indicate significant differences.

Cross-correlation histograms (CCHs) were calculated for pairs of simultaneously recorded neurons using the entire recording; peak or trough features were identified as departures $\geq$3 SD from the either the mean of the shift-predictor control correlogram calculated using 20 respiratory cycles at a time with all possible shifts of these cycles or the mean of a range of CCH bins that did not include the feature.

RESULTS

DETERMINATION OF DISCHARGE IDENTITY

The top portion of **Figure 1A** shows sorted neuron spike times coincident with and adjacent to the first cough (C1) in a cough response episode and the eupneic breath immediately preceding it (E5) for an I-Dec (more spikes in the first half of the inspiratory phase) and an I-Aug neuron (more spikes in the second half). The inspiratory phases of the E5 and C1 cycles are indicated by a vertical gray bar; the difference in shade delineates the first half of inspiration from the second. Integrated phrenic and lumbar nerve activities are also shown in this inset; note the increases in amplitude of nerve activities and duration of inspiration during C1. The bottom panel of **Figure 1A** expands the time frame of the inset, depicting firing rate histograms of spike events (such plots of firing rate vs. time allow better visualization of neuronal discharge identity) for the same two neurons during a triple-cough response episode; the five breaths preceding (eupneic period) and following (recovery period) the cough response are also shown. The discharge patterns of these cells did not change during the cough episode. **Figure 1B** shows firing rate

Table 1 | Detailed recording and response information.

Animal	Recording	Location: rVRC (R) cVRC (C)	Results of AA and STA analysis	Control discharge identity	Averaged		Number of times neuron was evaluated during these cough response instances			
					C1	C2	Single cough	Double-cough	Triple-cough	≥4 coughs
A	2	R	–	DEC			1*	–	1	–
		R	–	DEC		‡	1*	–	1*	–
B	1	C	BS	AUG			–	–	–	1
C	1	C	–	DEC	‡	‡	1*	1*	1*	–
		C	–	AUG			1	1	1	–
		C	BS	AUG			1	1	1	–
D	4	C	PILM	DEC			1	2	–	1
		C	PPHR/PILM	DEC	‡	‡	1*	2*	–	1*
		R	ILM	DEC	‡	‡	1*	2*	–	1*
E	1	C	ILM	AUG			–	–	–	3
		R	–	DEC			–	–	–	3
		R	PPHR	DEC			–	–	–	3
F	4	C	BS	AUG			1	–	2	1
		C	BS	AUG			1	–	2	1
G	1	R	PPHR	DEC			1	1	3	1
		C	BS	AUG			1	1	3	1
		C	PILM	DEC			1	1	3	1*
		C	–	AUG			1	1	3	1
		C	PILM/BS	DEC	‡	‡	1*	1*	3*	1*
	2	R	–	DEC	‡		–	1	3*	1*
		C	–	DEC	‡		–	1	3*	1*
H	1	C	–	DEC	‡		1*	–	–	1*
	2	R	PPHR	DEC	‡		1*	1*	1*	3*
		C	PILM/BS	DEC	‡		1*	1*	1*	3*
		C	BS	AUG			1	1*	1	3*
		C	PPHR/PILM	AUG			1	1*	1	3*
	3	R	–	DEC			1	4	–	1
		R	–	DEC			1*	4	–	1
		C	BS	DEC	‡	‡	1*	4*	–	1*
I	1	R	–	DEC			1	3	–	–
		R	–	DEC			1	3	–	–
	2	R	–	DEC			1*	–	2	–
		R	–	AUG	‡	‡	1*	–	2*	–
		C	BS	AUG		‡	1	–	2*	–
		C	–	AUG			1	–	2	–
		R	–	DEC			1	–	2	–
		C	–	AUG			1	–	2	–
J	2	C	BS	AUG			1	7	1	1
		R	PPHR	AUG			1	7	1	1
		R	–	AUG			1	7	1	1

**Response episodes during which, on average, the neuron changed its discharge identity during at least one cough cycle; ‡= neurons that changed their discharge identity during C1 and/or C2 when log ratios for those cough cycles were averaged across multiple-cough response types. Twenty-one cells were identified as motor or premotor neurons based upon the results of STA of nerve activity and AA from the spinal cord. Test results for four caudal VRC cells suggested multiple projections. PPHR – STA suggests premotor phrenic; BS – Bulbospinal, antidromically activated from T1 spinal cord stimulation; PILM – STA suggests inspiratory premotor to recurrent laryngeal nerve; ILM – unrectified STA suggests inspiratory recurrent laryngeal nerve motoneuron.*

histograms for two I-Dec cells whose discharge identities changed from decrementing to augmenting during C1 (i.e., their log discharge ratios changed from ≤ 0 to >0). By the second cough cycle, I-Dec^a returned to a decrementing pattern, whereas I-Dec^b maintained an augmenting discharge throughout the repetitive cough episode.

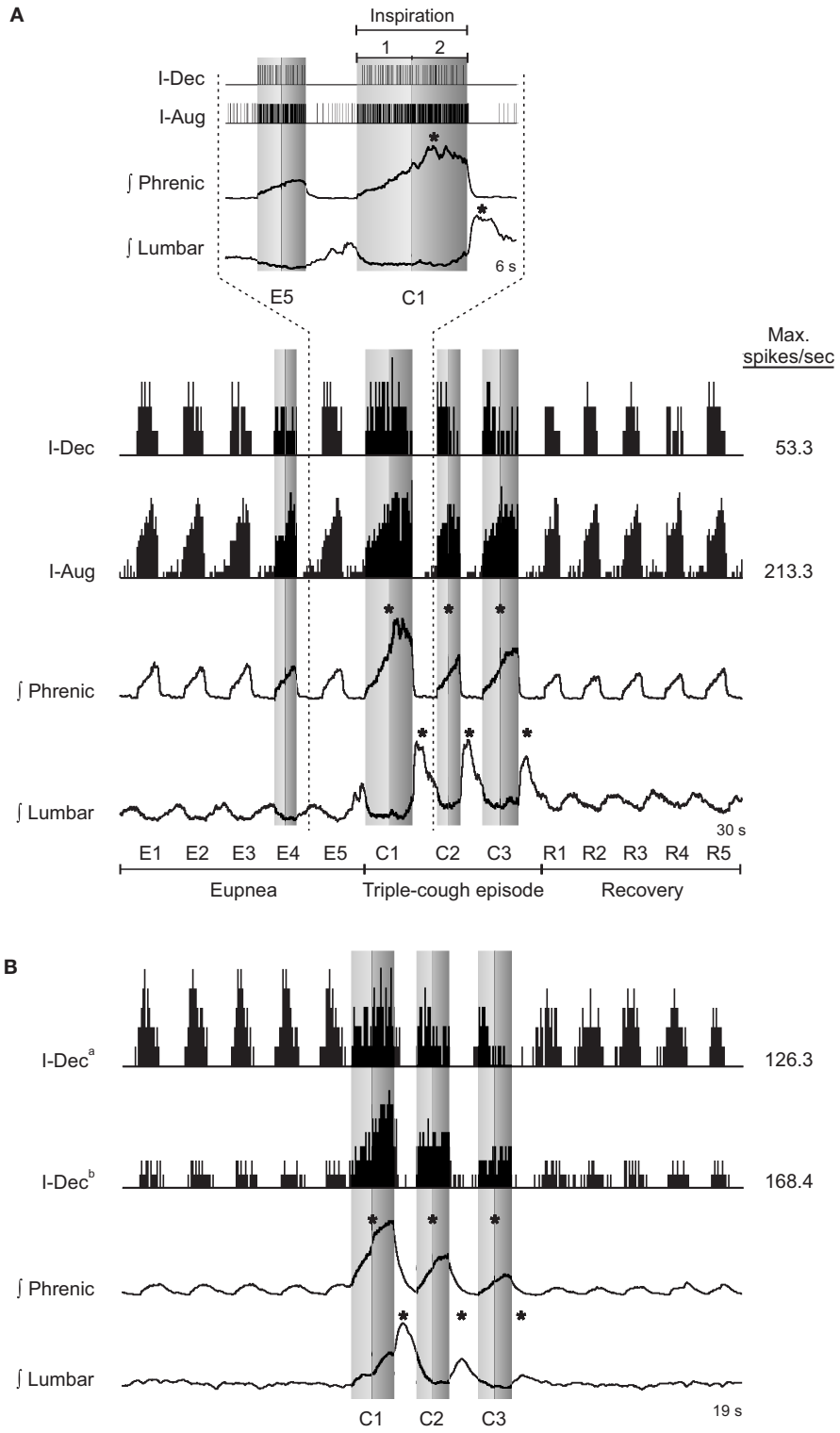

FIGURE 1 | (A) Neuronal spike times (top) and firing rate histograms (firing rate vs. time; binwidth = 75.0 ms; bottom) of two VRC cells recorded during a triple-cough response episode; the discharge identities of these cells did not change during this cough episode. **(B)** Firing rate histograms (binwidth = 47.5 ms) of two I-Dec neurons illustrating their change to an augmenting discharge pattern during C1 of the cough response; cell I-Dec[a] returned to a decrementing pattern by cycle C2, but cell I-Dec[b] maintained an augmenting pattern throughout the cough episode before returning to a decrementing discharge during the recovery period. Gray vertical bars indicate inspiratory phases; the difference in shade delineates the first half of inspiration from the second. E, eupneic respiratory cycles; C, cough cycles; R, recovery cycles; *, amplitude of integrated phrenic (lumbar) nerve activity is ≥2 SD above the mean maximum amplitude during eupneic period.

RECORDING LOCATIONS AND AXONAL PROJECTIONS OF NEURONS

The stereotaxic coordinates of the recording locations of cells within the rostral VRC ($n = 17$) ranged from 2.4 to 5.0 mm rostral to the obex, 2.7–3.6 mm lateral to the midline, and 3.4–5.2 mm below the dorsal surface of the medulla. Caudal VRC neurons ($n = 23$) were located 2.0 mm caudal to 0.9 mm rostral to the obex, 3.3–3.9 mm lateral to the midline, and 2.5–4.2 mm below the dorsal surface.

Ten I-Dec neurons were identified as motoneurons or premotor neurons based on STA and/or antidromic activation (AA) from the T1 level of the ventral spinal cord (**Table 1**). The discharge identities of four of the six I-Dec cells identified as inspiratory recurrent laryngeal pre- or motoneurons changed with cough (i.e., became I-Aug) when all C1 and C2 cycles of multiple-cough episodes were averaged (see ‡marking the third cell in animal D, recording 1 in **Table 1**); only one of the six was within the rVRC. The average discharge patterns of two of the four I-Dec neurons identified as phrenic premotor neurons became augmenting during C1. The three I-Dec bulbospinal neurons, all in the caudal region, changed identity with cough. Eleven I-Aug neurons were identified as motoneurons or premotor neurons. Only one of the eight I-Aug neurons found to be bulbospinal by AA, all of which were within the caudal VRC, changed to a decrementing pattern during cough. None of the I-Aug phrenic premotor ($n = 2$) or inspiratory laryngeal pre- or motoneurons ($n = 2$) exhibited a change in discharge identity. For 19 neurons, the results of AA testing and STA yielded no evidence of axonal projections to the regions tested; most of them (13 of 19) did not exhibit changed identities.

DISCHARGE PATTERNS DURING SINGLE AND REPETITIVE COUGH EPISODES

Table 1 contains detailed information about the 14 recordings and 40 neurons in the data set. Eleven single-cough and 48 multiple-cough response episodes were analyzed; two or more neurons were recorded during the cough responses in all but two episodes. Note that the instances of cough response types varied from recording to recording; most neurons were evaluated for more than one type of cough response. The majority of the response episodes contained three or fewer coughs; these are examined in greater detail in later figures and paragraphs. Fourteen response episodes were comprised of four or more cough cycles (nine 4-cough and one each of 5-, 7-, 8-, 10-, and 11-cough episodes).

When log discharge ratios were considered separately for each type of multiple-cough response episode, 16 of the 40 inspiratory neurons (40%) changed identity during at least one cycle. A greater proportion of I-Dec cells temporarily adopted an augmenting discharge pattern (12 of 23; 52%) than the reverse condition: 24% of I-Aug neurons (4 of 17) switched to a decrementing pattern during a cough cycle (**Table 1**).

The average log discharge ratios for I-Dec and I-Aug neurons during eupnea (E), cough (C), and recovery breaths (R) were plotted for cough episodes consisting of one-, two-, and three-cough cycles (**Figures 2**,**3**). **Figure 2** illustrates the log ratios for 21 I-Dec neurons recorded during a single-, double-, or triple-cough episode (left column); these data are further divided into the 14 cells that changed their discharge identity during any cycle of that cough response type (67%; middle column) and the seven that maintained their decrementing discharge pattern throughout the cough response (33%; right column). The average log ratio for all I-Dec neurons during C1 for single-, double-, and triple-cough episodes was significantly less than the ratios for the corresponding eupneic (each $p < 0.001$) and recovery periods ($p < 0.001$, $p = 0.002$, and $p = 0.005$), indicating that, on average, the difference between neuronal spike counts in the first and second halves of inspiration was reduced during C1, resulting in a discharge pattern that was less decrementing. There was no difference in the log ratios calculated for all I-Dec cells during C1 among one-, two-, and three cough episodes. The log ratio during C2 for all I-Dec cells was significantly greater than the C1 log ratio ($p = 0.001$ and $p = 0.009$), but was not different than the eupneic log ratio during double- and triple-cough episodes indicating that, on the whole, I-Dec cells returned to their eupneic discharge patterns by the second cough of the series. The log ratio during C3 was not different than that during eupnea, but it was greater than the C1 log ratio ($p = 0.003$).

Figure 3 illustrates the log ratios for 15 I-Aug neurons recorded during a response episode of fewer than four coughs. As a whole, the discharge patterns of the I-Aug neurons remained augmenting in each cycle of the cough response types shown; there was no significant difference between the log discharge ratios for any cough cycle and its corresponding eupneic period. Similar to the results for I-Dec cells, there was no difference in the log ratios calculated for all I-Aug cells during C1 among one-, two-, and three cough episodes. However, the log ratio for C1 was lower than that of C2 or C3 during triple-cough episodes ($p = 0.002$ and $p = 0.003$). In contrast to the findings for I-Dec neurons, only four of these 15 I-Aug cells exhibited a changed discharge identity during a cough response. One neuron changed its discharge identity during C1 of a single-cough episode; it also changed during all cough cycles of a triple-cough response. Another neuron from the same recording had a decrementing pattern only during C2 of a triple-cough episode. Two cells from a different recording changed their discharge identities during C2 of a double-cough episode.

C1 VS. C2 COMPARISON

The average log discharge ratios during C1 and C2 of multiple-cough responses for I-Dec neurons in the cVRC and rVRC were compared to investigate regional differences in response to cough stimuli (**Figure 4**). I-Aug neurons were not included in this analysis because our population only included three rostral neurons of this type. The average log ratio during C1 of the nine I-Dec cells in the cVRC was negative, indicating a change to an augmenting discharge pattern, and was significantly different from the ratios during eupnea ($p < 0.001$) and C2 ($p = 0.004$). The overall discharge pattern of caudal I-Dec neurons during C2 was decrementing and significantly different from eupnea ($p < 0.001$). I-Dec neurons in the rVRC ($n = 14$) maintained a decrementing discharge pattern during C1 and C2; however, the average log ratio for these cells was less during C1 compared to that during eupnea ($p = 0.002$) and C2 ($p = 0.005$). The average log ratios for C1 and C2 were significantly less in the cVRC compared to the rVRC ($p = 0.004$ and $p = 0.007$, respectively), suggesting that the I-Dec neurons that shifted to an augmenting discharge pattern

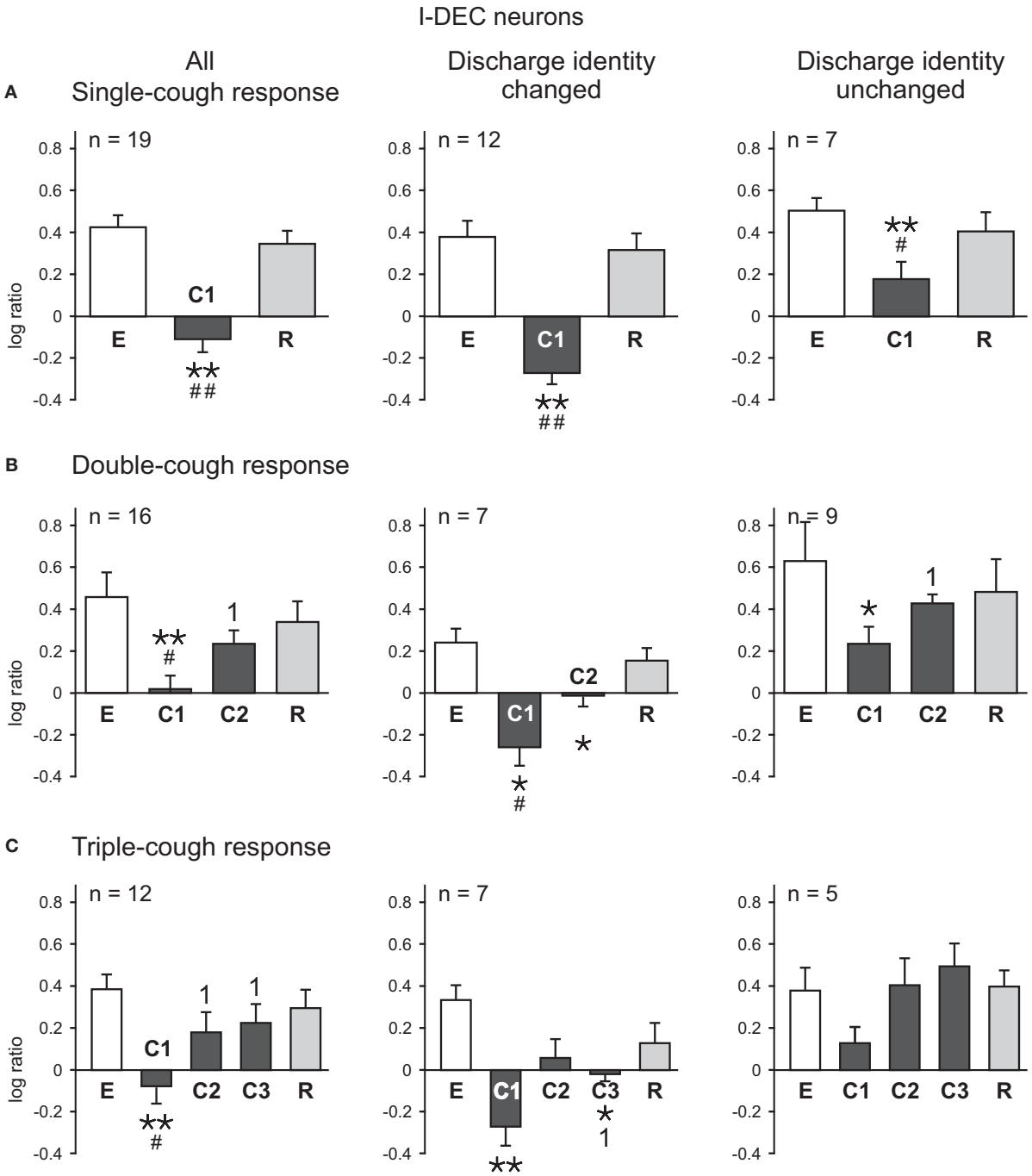

FIGURE 2 | Average log ratios of I-Dec neurons during (A) single-, (B) double-, and (C) triple-cough episodes. E represents the log ratio of the total spike counts in the five eupneic breaths immediately prior to cough onset; similarly, R depicts the log ratio of the counts in the five recovery breaths immediately following the cough episode. *, Significantly different from E; #, significantly different from R; 1, significantly different from C1. *P*-values are indicated by one ($p < 0.02$) or two ($p < 0.001$) symbols. Number of neurons (*n*) analyzed for each cough episode type is indicated on the plots. Some neurons were evaluated for more than one type of cough response. Error bars indicate the standard error of the mean.

were mostly located within the cVRC and, indeed, a significantly greater percentage of caudal I-Dec neurons changed their discharge pattern during C1 (7 of 9; 78%) than did I-Dec cells within the rVRC (three of 14; 21%) ($p < 0.014$; **Table 2**).

INSPIRATORY DRIVE

PHRENIC NERVE ACTIVITY

On average, the maximum integrated phrenic nerve amplitude increased during the first cycle of a cough episode and

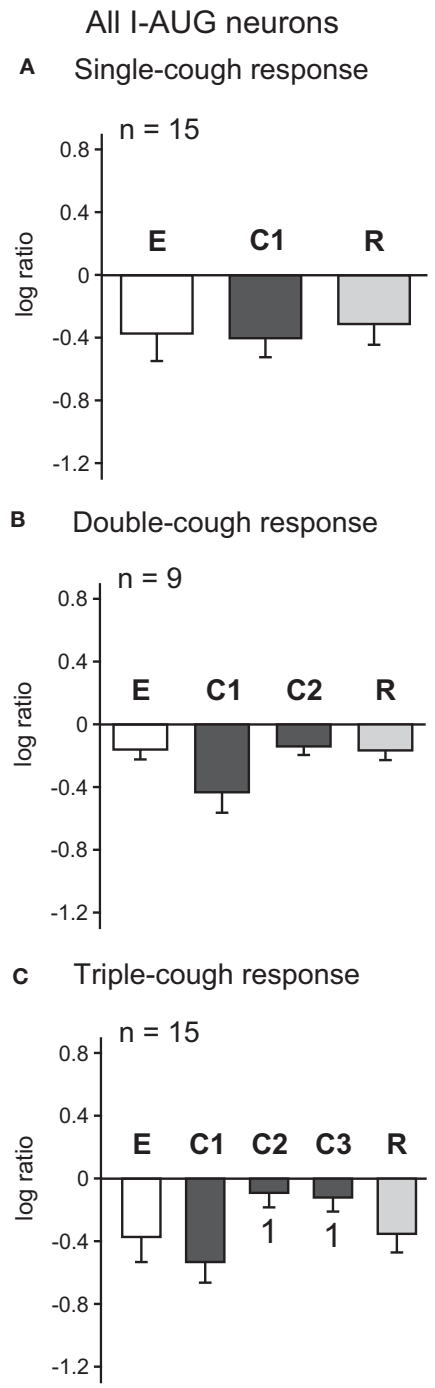

FIGURE 3 | Average log ratios of I-Aug neurons during (A) single-, (B) double-, and (C) triple-cough episodes. 1, Significantly different from C1 ($p < 0.02$). Number of neurons (n) analyzed for each cough episode type is indicated on the plots. Some neurons were evaluated for more than one type of cough response. Error bars indicate the standard error of the mean.

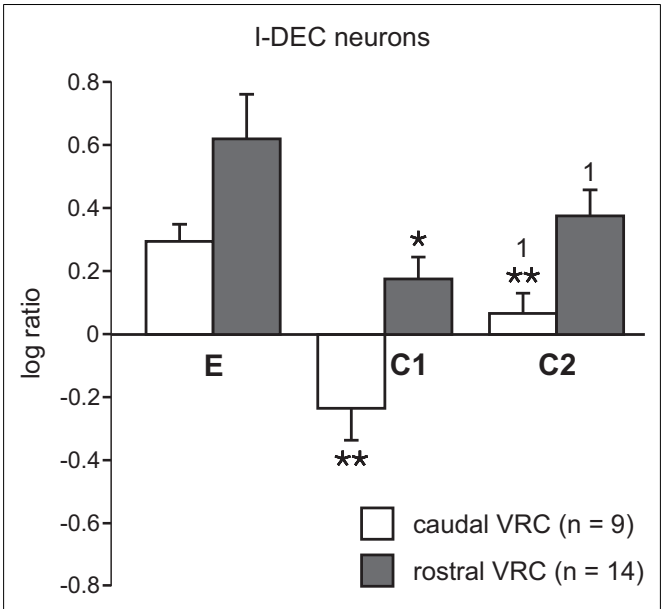

FIGURE 4 | Average log ratios of I-Dec neurons in the cVRC and rVRC. The first (C1) and second (C2) cough cycles from all repetitive cough episodes were analyzed. *, Significantly different from E; 1, significantly different from C1. *P*-values are indicated by one ($p < 0.02$) or two ($p < 0.001$) symbols. Error bars indicate the standard error of the mean.

then gradually declined during subsequent cycles (**Figure 5**). Phrenic amplitude was significantly greater during C1 ($p < 0.001$, $p < 0.001$, and $p < 0.001$, respectively) as well as during C2 ($p < 0.001$ and $p = 0.002$) of single-, double-, and triple-cough response episodes when compared to maximum amplitudes during eupnea. Furthermore, maximum phrenic amplitude during C1 was significantly greater than the amplitude during C2 for double-cough episodes ($p < 0.001$), and greater than amplitudes during C2 and C3 for triple-cough responses ($p = 0.008$ and $p = 0.012$, respectively). There was no difference in integrated phrenic amplitudes during C2 and C3 in triple-cough episodes.

Inspiratory Duration

As illustrated in **Figure 6**, cough inspiratory time (CT_I) was significantly longer during C1 cycles in averaged single-, double-, and triple-cough responses when compared with eupneic ($p < 0.001$, $p < 0.001$, and $p = 0.001$, respectively) and recovery breaths ($p < 0.001, 0.001, 0.001$). CT_I during C1 and C2 were significantly different for double- and triple-cough responses ($p < 0.001$ and 0.001), but there was no difference in CT_I between C2 and C3 in triple-cough episodes. There were also no differences in CT_I during C1 for single-, double-, and triple-cough episodes or during C2 for double- and triple-cough responses.

EVIDENCE FOR INSPIRATORY PHASE MODULATION OF TONIC EXPIRATORY NEURON INHIBITION OF INSPIRATORY DRIVE DURING MULTIPLE COUGHS

The firing rate histograms of six cells (four VRC augmenting inspiratory neurons and two tonic expiratory neurons) recorded during a double-cough response to tracheal stimulation are shown in **Figure 7A**; these cells were recorded simultaneously with 10 other neurons and integrated phrenic and lumbar nerve activities. Neurons 51, 57, and 62 were recorded from animal J and are included

Table 2 | Average discharge identities of I-Dec and I-Aug VRC neurons during the control period and the first two cough cycles in a multiple-cough response to intra-tracheal stimulation.

Discharge identity		Total VRC		cVRC		rVRC	
Control	**During cough**	**C1**	**C2**	**C1**	**C2**	**C1**	**C2**
I-Dec ($n = 23$)	Changed to I-Aug	10	6	7	4	3	2
	Unchanged	13	17	2	5	11	12
I-Aug ($n = 17$)	Changed to I-Dec	1	2	0	1	1	1
	Unchanged	16	15	14	13	2	2

in **Table 1**; I cell 66 could not be evaluated for a change in discharge identity during a cough response because it was recruited by the tracheal stimulus and so is not included in the table. The activity of each I cell increased during the cough cycles, whereas the activity of the E-Tonic neurons decreased. Cross-correlograms from pairs of represented neurons are shown in **Figure 7B**. The central peak (**Figure 7B1**) in the correlogram for the tonic E neurons (cells 49 and 55) is consistent with a shared coordinating influence. Correlograms triggered by both tonic expiratory neurons for each respective target inspiratory neuron (cells 62 and 57) had an offset trough feature indicative of putative inhibitory actions (**Figures 7B2,3**). The offset peak in the correlogram for the inspiratory neuron pair (**Figure 7B4**) is consistent with an excitatory action of cell 62 upon neuron 57. The correlation linkage map (**Figure 7D**) summarizes all pair-wise correlation features involving the four cells of **Figure 7B**. Each large "sphere" corresponds to a neuron and is color-coded to reflect respiratory modulation; arrows indicate the direction of the firing rate change during the inspiratory phase of each cough response.

Spike-triggered averages of the full-wave-rectified contralateral phrenic nerve signal were consistent with relationships represented in the linkage map. The average triggered by inspiratory neuron 57 had an offset peak (arrow, **Figure 7Ca**). The offset trough (arrow, **Figure 7Cb**) in the average triggered by tonic expiratory neuron 55 provides further evidence for functional inhibition of antecedent elements of the excitatory inspiratory neuron chain contributing to inspiratory drive.

DISCUSSION

We report that a group of I-Dec neurons in the cVRC, and to a lesser extent the rVRC, change their discharge identity from decrementing to augmenting during repetitive fictive cough. By the second cough cycle (C2), half of these I-Dec neurons returned to their eupneic decrementing firing pattern. I-Aug neurons, on the other hand, maintained their augmenting discharge identity during repetitive cough. Inspiratory phase duration was longer and phrenic burst amplitude was greater within the first cough cycle (C1) compared to eupnea. However, phase duration shortened and phrenic amplitude decreased in subsequent coughs. These results highlight a unique property of a subset of inspiratory neurons that reconfigure their discharge identity during repetitive cough.

Cough was elicited in these studies in paralyzed animals. Also known as fictive cough, the motor patterns of this behavior bear significant similarities and differences to the same behavior produced in unparalyzed animals. Abdominal motor patterns during fictive and unparalyzed cough are very similar in rise times and relative increases in magnitudes (Bolser, 1991; Bolser and Davenport, 2000; Wang et al., 2009). Inspiratory motor patterns during cough do differ somewhat, with the magnitude of inspiratory motor drive during fictive cough being less than that produced in animals that are unparalyzed (Bolser, 1991; Bolser and DeGennaro, 1994; Bolser and Davenport, 2000). The specific mechanism(s) that underlie this difference in motor drive are unknown. However, as shown in this report, the duration of the inspiratory phase of the first cough of a series is prolonged in the fictive model, just as it is in unparalyzed animals (Tatar et al., 1994; Bolser and Davenport, 2000). Our findings are very relevant to the mechanism of this inspiratory prolongation and likely apply to both paralyzed and unparalyzed animals. Furthermore, a series of investigators (Jakuš et al., 1985, 1987; Bongianni et al., 1998) have recorded the behavior of medullary respiratory neurons during cough in unparalyzed animals and their findings are very similar to observations made during fictive cough on the same populations of cells (Shannon et al., 1996, 1998, 2000).

LOG DISCHARGE RATIO

We applied a straight-forward metric of discharge pattern to the population of inspiratory neurons that we recorded. The log ratio of spike counts in the first and second halves of the inspiratory phase provided both quantitative and qualitative information regarding the discharge patterns of the neurons on a cycle-by-cycle basis. Other analyses of discharge pattern and breathing modulation (e.g., eta-squared, cycle-triggered histograms, see Cohen, 1968; Orem and Dick, 1983) are based on averaging or accumulating spike data over many breathing cycles. These metrics are most useful when applied to relatively stationary motor patterns or between prolonged changes in state/excitability of the respiratory motor system. Airway protective behaviors, such as cough, represent transient changes in motor drive to respiratory muscles that often span less than five cycles. Furthermore, phase durations can be widely variant on a cycle-by-cycle basis during cough; this can lead to "smearing" of cycle-triggered histograms, which can limit their utility when applied to this behavior.

DISCHARGE IDENTITY DURING SINGLE COUGHS

Many of the same neural elements that generate breathing also contribute to the production of cough. Shannon and coworkers (Shannon et al., 1998, 2000; Baekey et al., 2001) proposed that this network is reconfigured to produce protective airway defense

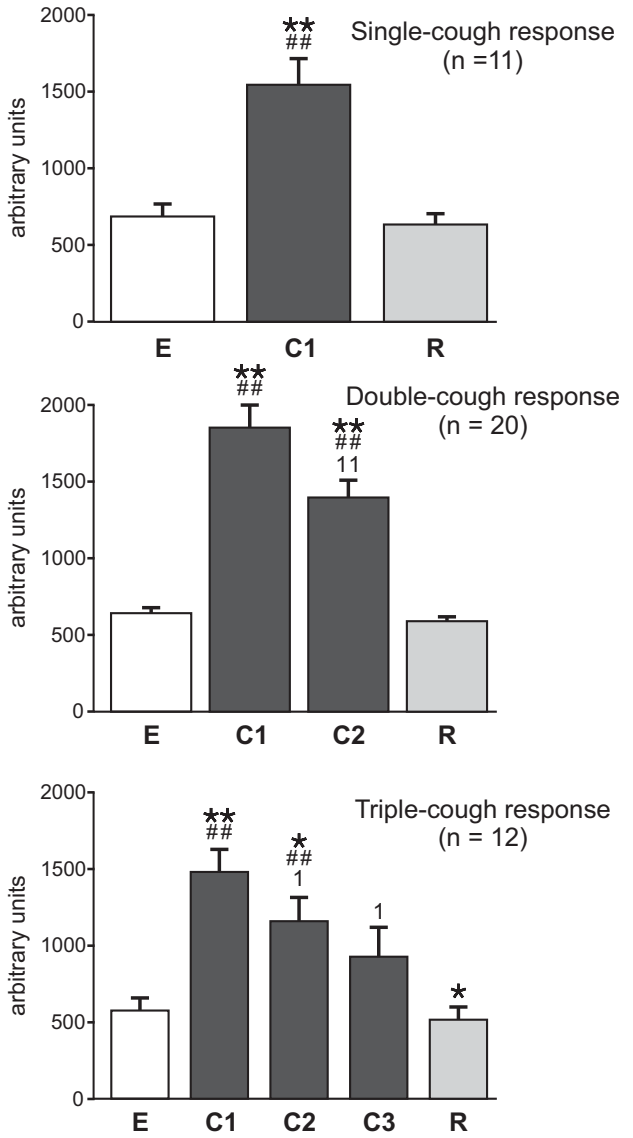

FIGURE 5 | Average phrenic burst amplitude (in arbitrary units, au) during single-, double-, and triple-cough episodes (top, middle, and bottom panels, respectively). Values for a given cough cycle (e.g., C1) were not different among these three cough response types. *Significantly different from E; #, significantly different from R; 1, significantly different from C1. *P*-values are indicated by one ($p < 0.02$) or two ($p < 0.001$) symbols. Error bars indicate the standard error of the mean.

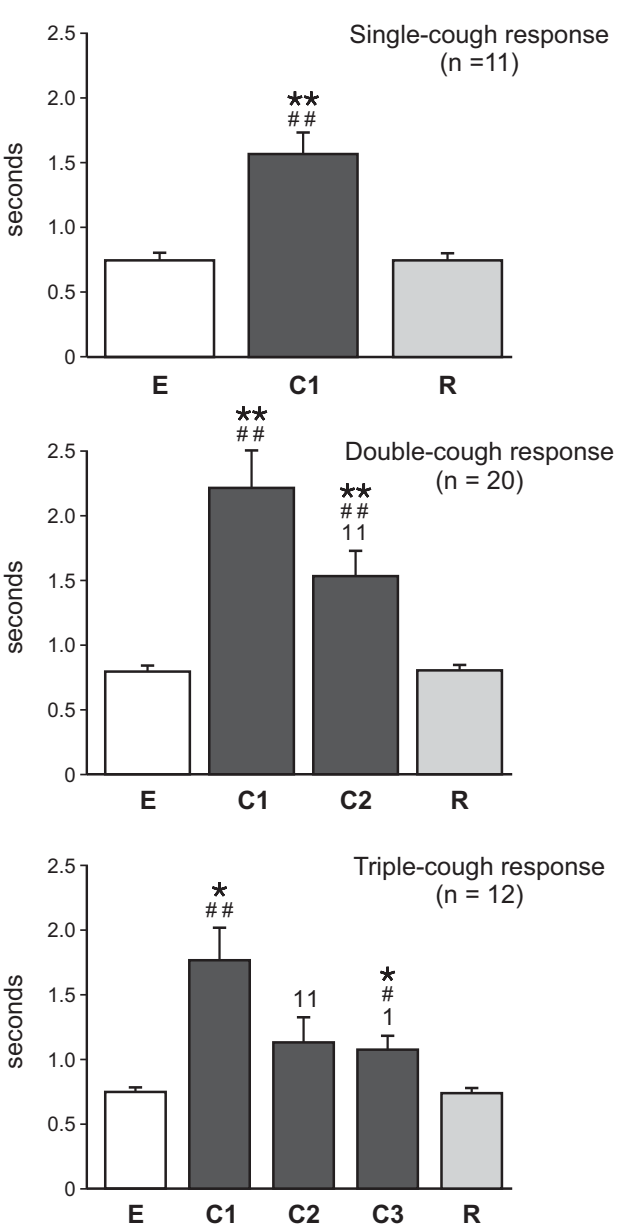

FIGURE 6 | Average inspiratory duration (s) during single-, double-, and triple-cough episodes (top, middle, and bottom panels, respectively). Values for a given cough cycle (e.g., C1) were not different among these three cough response types. *, significantly different from E; #, significantly different from R; 1, significantly different from C1. *P*-values are indicated by one ($p < 0.02$) or two ($p < 0.001$) symbols. Error bars indicate the standard error of the mean.

reflexes (such as cough, expiration reflex, sigh, gasp, sneeze, aspiration, and swallow) that have motor patterns distinctly different from breathing (Jakuš et al., 1985; Oku et al., 1994; Gestreau et al., 1996, 2000; Lieske et al., 2000; Saito et al., 2003; Baekey et al., 2004). Reconfiguration is a process by which a network of neurons is reorganized through changes in their neuronal discharge patterns and functional interactions to modify motor output (Getting and Dekin, 1985). Changes in neural discharge are typically quantified in terms of burst frequency and duration. During cough, the majority of inspiratory and expiratory neurons increase their discharge firing rate, while a smaller proportion maintain their firing rate or even decrease it (Jakuš et al., 1985, 1987; Oku et al., 1994;

Bongianni et al., 1998; Shannon et al., 1998, 2000; Gestreau et al., 2000; Baekey et al., 2001). Previous *in vivo* studies have shown that some populations of inspiratory and expiratory neurons change their discharge identity during cough (Orem and Trotter, 1993; Oku et al., 1994; Shannon et al., 1998, 2000), although published models describing reconfiguration of the respiratory neural network during cough have primarily highlighted expiratory neuron subpopulations as having labile discharge identities (Shannon et al., 1998, 2000; Bolser et al., 2006).

Reconfiguration of the central pattern generator during the inspiratory phase of cough included a switch in the discharge identity of approximately one-half of the I-Dec neurons: 43% of I-Dec neurons changed their discharge identity during C1. This result extends the observation of Shannon et al. (1998) who reported that 55% of I-Dec neurons recorded had a predominately augmenting discharge during single coughs or C1 of a multi-cough response episode. The paucity of I-Aug neurons (6%) that changed their discharge identity during C1 is in agreement with previous studies (Shannon et al., 1998, 2000).

Changes in discharge identity during cough have been reported for expiratory respiratory neurons (Oku et al., 1994; Shannon et al., 1998, 2000). Many E-Aug neurons in the rVRC and cVRC shift to a decrementing discharge pattern during single coughs or the first in a series of coughs (Shannon et al., 1998). The switch of cVRC E-Aug premotor neurons to a discharge pattern that matches the motor activity pattern in expiratory muscles may be a means to generate the muscle force and abdominal pressure required to propel air through the airways during the expulsive phase of cough (Bongianni et al., 1998; Shannon et al., 1998, 2000). Similarly, shifting I-Dec premotor and motoneurons to an augmenting pattern that mirrors the motor activity of inspiratory pump muscles (Grelot and Milano, 1991; Iscoe and Grelot, 1992; Milano et al., 1992) would allow for large increases in lung volume necessary to generate the expiratory airflow rates that will move material from the airway by increasing inspiratory muscle activation and enlarging the larynx.

Inspiratory neurons have been observed to switch their discharge identity during other airway protective behaviors. For instance, I-Dec neurons can shift to an augmenting discharge pattern during augmented breaths (Orem and Trotter, 1993). Thus, a change in discharge identity is not unique to cough and may be an important property of the mechanism by which the central pattern generator reconfigures to produce different airway protective behaviors.

The firing rate modulation of tonic expiratory neurons during cough and their functional interactions with VRC inspiratory neurons and phrenic motor neurons suggest that disinhibition contributes to the inspiratory drive of cough. These results are consistent with predictions based on recent computational models for cough motor pattern generation that include multiple circuit paths for cough receptor-mediated inspiratory drive modulation (Rybak et al., 2008; Poliacek et al., 2011; O'Connor et al., 2012). The transient switch of propriobulbar I-Dec neurons to an augmenting pattern during cough may be a component of mechanisms for enhanced suppression of tonic E neuron activity during coughs. In this context, we also note that evidence for inspiratory phase suppression of tonic E neurons by I-Dec neurons has been reported in a study on central chemoreceptor-mediated enhancement of inspiratory drive (Ott et al., 2012). A similar suppression of tonic expiratory neuron activity and the attendant inspiratory drive enhancement during cough could operate to balance the inspiratory-suppressive influence of increased blood pressure and excitation of tonic expiratory neurons caused by cough mechanics (Poliacek et al., 2011).

DISCHARGE IDENTITY DURING REPETITIVE COUGHS

To our knowledge, this is the first study to describe the discharge identity of inspiratory neurons during repetitive coughing behaviors. Approximately half of the I-Dec neurons included in this study changed to an augmenting discharge patterns during C1 and/or C2, whereas only a small portion of I-Aug neurons changed their discharge identity during C1 or C2. The neural mechanisms and synaptic or afferent effects that occur during the second half of a cough inspiratory phase to produce an augmenting pattern in some I-Dec neurons are unknown, but several possibilities can be considered.

1. *Input from recruited neurons.* Inspiratory neurons that are recruited or evoked by the cough stimulus (such as neuron 66 in **Figure 7**) may have an excitatory effect on some I-Dec neurons, transiently converting their discharge identities.
2. *Enhanced input from I-Aug neurons.* A second possible mechanism was incorporated into a model developed by O'Connor et al. (2012) to produce prolonged inhibition of tonic E neurons by I-Dec cells. This approach involves a separate population of inhibitory I-Dec neurons whose excitation by I-Aug cells is presynaptically inhibited by tonic decrementing expiratory neurons (tonic E-Dec cells). In this mechanism, enhanced activity of I-Aug and I-Dec cells during cough produces an increased inhibition of the tonic E-Dec neurons; the ensuing lessening of the presynaptic inhibition provided by the tonic E-Dec cells leads to a greater excitatory influence of the I-Aug neurons upon the I-Dec cells, possibly imparting on them an augmenting discharge pattern.
3. *Influences of cells in other brainstem areas.* The activities of raphé and pontine neurons are also affected by cough (e.g., see Jakuš et al., 1998; Baekey et al., 2003; Poliacek et al., 2004; Shannon et al., 2004) and could provide a network modulatory influence that briefly causes the discharge identity of an I-Dec neuron to assume an augmenting pattern.
4. *Input from vagal afferents – slowly adapting pulmonary stretch receptors (SARs).* Vagotomy in decerebrate cats changes the discharge identity of most pontine and raphé respiratory neurons (Dick et al., 2008; Morris et al., 2010), suggesting that alterations in vagal afferent activity can modify the discharge properties of respiratory neurons. During eupneic breathing in animals, lung inflation can terminate the inspiratory phase and enhance E-Dec activity (Hayashi et al., 1996). Coughing induces large changes in tidal volume, which would be expected to stimulate SARs. Given that I-Dec neurons are suppressed by inflation during eupnea, SARs are unlikely to mediate the alteration in discharge identity of I-Dec neurons during coughing.

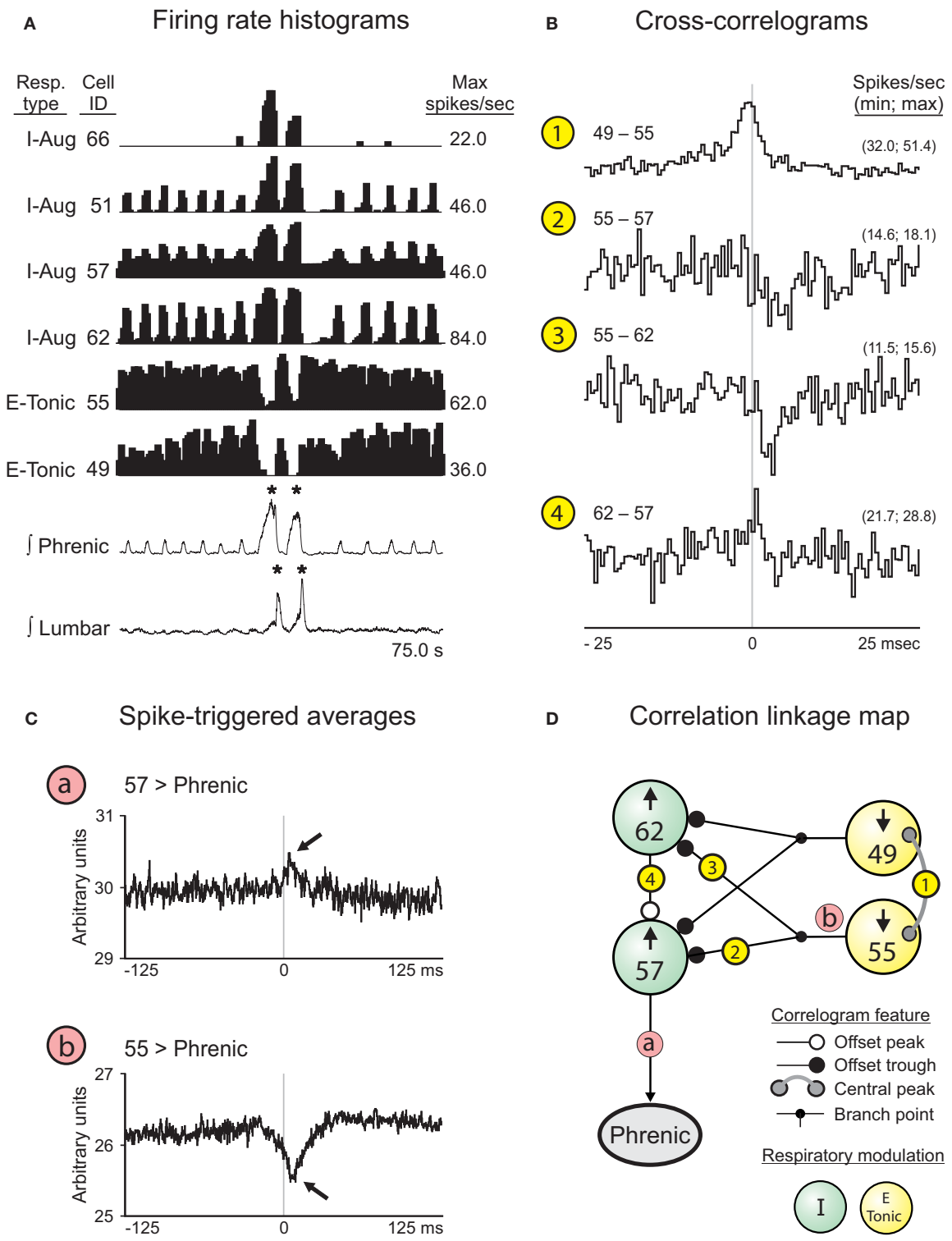

FIGURE 7 | Correlations among pairs of VRC I and E neurons responsive to cough-eliciting tracheal stimulation. (A) Firing rate histograms (binwidths = 375.0 ms) for 6 of 16 simultaneously recorded neuron spike trains during a double-cough response to tracheal stimulation. For each trace, the respiratory-modulated pattern, cell identification number, and maximum firing rate are shown. *, Amplitude of integrated phrenic (lumbar) nerve activity is ≥2 SD above the mean maximum amplitude during eupneic period. **(B)** Features in the CCHs are included in the correlation linkage map shown in **(D)**. Bin width for all CCHs = 0.5 ms. The minimum and maximum bin values, normalized to spikes per second per trigger event, are shown for each correlogram. Feature description, detectability index (equal to the ratio of the maximum amplitude of feature departure from background activity divided by the SD of the correlogram noise), half-width, and numbers of trigger neuron

(Continued)

FIGURE 7 | Continued
and target neuron spikes for each CCH are as follows: **1**: central peak, 15.0, 4.0 ms, 55,253, and 92,800; **2**: offset trough, 4.1, 1.0 ms, 92,800, and 51,671; **3**: offset trough, 5.0, 2.5 ms, 92,800, and 57,087; **4**: offset peak, 4.3, 0.5 ms, 51,671, and 57,087. **(C)** STAs of contralateral phrenic nerve activity. Bin width for both STAs = 0.5 ms. **a**: Neuron 57, peak (lag to peak = 7.5 ms). **b**: Neuron 55, dip (lag to nadir = 6.0 ms). **(D)** Correlation linkage map summarizing features found in all CCHs calculated for the group of four neurons in **(B).** Each large "sphere" represents a neuron and contains that neuron's ID code and direction of change in firing rate when tracheal stimulation elicited a cough; the cell's respiratory-modulated firing pattern is indicated by the color of the sphere (see Key). White, black, and gray circles at the ends of the lines between spheres represent central or offset peaks or troughs (see Key). Circled numbers indicate corresponding CCHs shown in **(B)**.

Peripheral chemosensory afferents are not likely to influence the activity patterns of inspiratory neurons nor modulate phase durations during a bout of cough: Hypocapnia [a consequence of repetitive coughing (unpublished observation)] blunts carotid chemoreceptor activity (Dejours, 1963) but does not inhibit cough (Suzuki et al., 1991).

Half of the 10 I-Dec cells that changed their discharge identity during the first cough of a response returned to their pre-cough I-Dec pattern during C2. This trend continued for C3 and subsequent cough cycles. The neural processes that account for the return of eupneic discharge identity before the cough episode has ended are unknown. Canning et al. (2004, 2006) have proposed the existence of specific cough receptors that are activated by stimulants similar to those that generate cough, including mechanical stimulation of the intrathoracic trachea used in the present study. We and others (Bongianni et al., 1998; Bolser and Davenport, 2000) have reported that repetitive cough behaviors occurred after mechanical stimulation of the airway was terminated. A reduction in afferent input from specific cough receptors following tracheal stimulation may account for the return of some I-Dec neurons to their eupneic discharge identity by the second cough cycle.

Another mechanism that could explain the transitory nature of changes in discharge identity during repetitive cough involves SARs and their permissive effect on cough. Blocking SAR activity with SO_2 in rabbits decreases the strength and frequency of cough induced by mechanical stimulation of the trachea (Hanácek et al., 1981). It has been proposed that the excitability of a cough gate mechanism modulated by SAR afferent feedback accounts for the permissive effect of SARs on the cough reflex (Hanácek et al., 1981; Sant'Ambrogio et al., 1984; Romaniuk et al., 1997; Bolser et al., 2006). It is unknown whether the effects of SARs on cough generation are the same on a cycle-by-cycle basis during repetitive cough. A decrease in the excitability of a threshold gating mechanism due to changes in SAR input during an episode of repetitive coughing could reduce the probability that a cough will be generated. This may be responsible for the return of some I-Dec neurons to their eupneic discharge identity.

REGIONAL DIFFERENCES IN NEURON DISCHARGE IDENTITY DURING REPETITIVE COUGHS

In the present study, a larger proportion of I-Dec neurons in the cVRC changed their discharge identity during repetitive cough compared to the rVRC. This is consistent with the results from Shannon et al. (1998) during single coughs. Regional differences in I-Dec discharge identities during cough may be an important component of the reconfiguration process. Shannon et al. (1998, 2000) proposed that early E-Aug neurons in the rVRC that switch to a decrementing discharge identity during cough provide excitatory input to cVRC bulbospinal E-Aug neurons (i.e., premotor expiratory neurons). The decrementing pattern of activity of the early and premotor E-Aug neurons matches the discharge pattern of expiratory motoneurons (Shannon et al., 1998, 2000). Furthermore, the activity duration of these neurons is limited by inhibitory input from rVRC late E-Aug neurons that do not change their discharge identity during cough. Thus, the discharge identity of E-Aug neurons and their location within the VRC may help characterize their role in the reconfiguration process during the expiratory phase of cough. An analogous relationship might exist for I-Dec neurons during the inspiratory phase of cough reported in the present study. For instance, I-Dec neurons in the cVRC may help augment phrenic discharge during cough by switching to an augmenting pattern that matches inspiratory pump muscle activity. In support of this view, we report that three of the cVRC I-Dec neurons that changed their discharge identity were bulbospinal and one was premotor to the phrenic motoneuron pool. I-Dec neurons in the rVRC that retain their discharge identity may help lengthen the inspiratory phase duration by inhibiting expiratory neurons (Shannon et al., 1998, 2000; Bolser et al., 2003). Axonal projections from I-Dec neurons with somas in the retrofacial nucleus near the rVRC to the nucleus ambiguus and reticular formation have been shown histologically with HRP labeling (Otake et al., 1990), suggesting extensive anatomical connections between the rVRC I-Dec neurons and the respiratory network.

Peripheral sensory afferent input has been shown to induce regional differences in the inspiratory neural reconfiguration process. For instance, activation of carotid chemoreceptors decreases I-Driver neural activity in the rVRC which in turn decreases inspiratory duration, but increases premotor I-Aug activity in the cVRC which augments phrenic burst amplitude (Morris et al., 1996). Other peripheral afferents such as the "cough receptors" may also demonstrate similar region-specific effects on the respiratory neural network.

CONCLUSIONS AND PERSPECTIVES

The results from this study highlight an important property of the reconfiguration process that has not been previously described for medullary inspiratory neurons during repetitive coughs as it has been for single coughs (Shannon et al., 1996, 1998). I-Dec neurons in the cVRC change their discharge identity during cough. Furthermore, as some I-Dec neurons returned to a decrementing discharge identity by the second and subsequent cough cycles, phrenic activity, and inspiratory duration also returned to its pre-cough stimulus eupneic patterns, suggesting that changes in discharge identity of I-Dec neurons within the respiratory neural network may play an important role in modifying inspiratory motor pattern during repetitive cough. Given the connectivity of I-Dec neurons and their integral role in shaping neural activity

within the respiratory network, a cough model that incorporates changing discharge identities of inspiratory neurons during sustained airway protective behaviors, such as repetitive cough, may be important to accurately predict the resulting respiratory motor patterns. A possible modification of the cough neural network proposed by Shannon et al. (1998, 2000) may include a subset of I-Dec neurons in the cVRC that send excitatory inputs to phrenic motoneurons in the form of an augmenting activity pattern either through monosynaptic or polysynaptic connections via excitatory premotor I-Aug neurons.

ACKNOWLEDGMENTS

We thank Peter Barnhill, Jan Gilliland, Rebecca McGowan, and Zhongzeng Li for excellent technical assistance. This research was supported by NIH R33 HL89104, R33 HL89071, and R01 HL103415.

REFERENCES

Baekey, D. M., Morris, K. F., Gestreau, C., Li, Z., Lindsey, B. G., and Shannon, R. (2001). Medullary respiratory neurones and control of laryngeal motoneurones during fictive eupnoea and cough in the cat. *J. Physiol. (Lond.)* 534, 565–581.

Baekey, D. M., Morris, K. F., Nuding, S. C., Segers, L. S., Lindsey, B. G., and Shannon, R. (2003). Medullary raphé neuron activity is altered during fictive cough in the decerebrate cat. *J. Appl. Physiol.* 94, 93–100.

Baekey, D. M., Morris, K. F., Nuding, S. C., Segers, L. S., Lindsey, B. G., and Shannon, R. (2004). Ventrolateral medullary respiratory network participation in the expiration reflex in the cat. *J. Appl. Physiol.* 96, 2057–2072.

Benjamini, Y., and Hochberg, Y. (1995). Controlling the false discovery rate: a practical and powerful approach to multiple testing. *J. R. Stat. Soc. Series B Stat. Methodol.* 57, 289–300.

Bolser, D. C. (1991). Fictive cough in the cat. *J. Appl. Physiol.* 71, 2325–2331.

Bolser, D. C., and Davenport, P. W. (2000). Volume-timing relationships during cough and resistive loading in the cat. *J. Appl. Physiol.* 89, 785–790.

Bolser, D. C., Davenport, P. W., Golder, F. J., Baekey, D. M., Morris, K. F., Lindsey, B. G., and Shannon, R. (2003). "Neurogenesis of cough," in *Cough: Causes, Mechanisms and Therapy*, eds H. Boushey, K. F. Chung, and J. Widdicombe (Oxford: Blackwell Publishing), 173–180.

Bolser, D. C., and DeGennaro, F. C. (1994). Effect of codeine on the inspiratory and expiratory burst pattern during fictive cough in cats. *Brain Res.* 662, 25–30.

Bolser, D. C., Poliacek, I., Jakuš, J., Fuller, D. D., and Davenport, P. W. (2006). Neurogenesis of cough, other airway defensive behaviors and breathing: a holarchical system? *Respir. Physiol. Neurobiol.* 152, 255–265.

Bongianni, F., Mutolo, D., Fontana, G. A., and Pantaleo, T. (1998). Discharge patterns of Bötzinger complex neurons during cough in the cat. *Am. J. Physiol.* 274, R1015–R1024.

Canning, B. J., Mazzone, S. B., Meeker, S. N., Mori, N., Reynolds, S. M., and Undem, B. J. (2004). Identification of the tracheal and laryngeal afferent neurones mediating cough in anaesthetized guinea-pigs. *J. Physiol. (Lond.)* 557, 543–558.

Canning, B. J., Mori, N., and Mazzone, S. B. (2006). Vagal afferent nerves regulating the cough reflex. *Respir. Physiol. Neurobiol.* 152, 223–242.

Cohen, M. I. (1968). Discharge patterns of brain-stem respiratory neurons in relation to carbon dioxide tension. *J. Neurophysiol.* 31, 142–165.

Dejours, P. (1963). Control of respiration by arterial chemoreceptors. *Ann. N. Y. Acad. Sci.* 109, 682–695.

Dick, T. E., Shannon, R., Lindsey, B. G., Nuding, S. C., Segers, L. S., Baekey, D. M., and Morris, K. F. (2008). Pontine respiratory-modulated activity before and after vagotomy in decerebrate cats. *J. Physiol. (Lond.)* 586, 4265–4282.

Gestreau, C., Grelot, L., and Bianchi, A. L. (2000). Activity of respiratory laryngeal motoneurons during fictive coughing and swallowing. *Exp. Brain Res.* 130, 27–34.

Gestreau, C., Milano, S., Bianchi, A. L., and Grelot, L. (1996). Activity of dorsal respiratory group inspiratory neurons during laryngeal-induced fictive coughing and swallowing in decerebrate cats. *Exp. Brain Res.* 108, 247–256.

Getting, P. A., and Dekin, M. S. (1985). Mechanisms of pattern generation underlying swimming in Tritonia. IV. Gating of central pattern generator. *J. Neurophysiol.* 53, 466–480.

Grelot, L., and Milano, S. (1991). Diaphragmatic and abdominal muscle activity during coughing in the decerebrate cat. *Neuroreport* 2, 165–168.

Hanácek, J., Widdicombe, J. G., and Korpás, J. (1981). Effect of SO2 inhalation on the cough reflex in rabbits. *Cesk. Fysiol.* 30, 243–245.

Hayashi, F., Coles, S. K., and McCrimmon, D. R. (1996). Respiratory neurons mediating the Breuer-Hering reflex prolongation of expiration in rat. *J. Neurosci.* 16, 6526–6536.

Iscoe, S., and Grelot, L. (1992). Regional intercostal activity during coughing and vomiting in decerebrate cats. *Can. J. Physiol. Pharmacol.* 70, 1195–1199.

Jakuš, J., Stránsky, A., Poliacek, I., Baráni, H., and Boselova, L. (1998). Effects of medullary midline lesions on cough and other airway reflexes in anaesthetized cats. *Physiol. Res.* 47, 203–213.

Jakuš, J., Tomori, Z., and Stransky, A. (1985). Activity of bulbar respiratory neurones during cough and other respiratory tract reflexes in cats. *Physiol. Bohemoslov.* 34, 127–136.

Jakuš, J., Tomori, Z., Stransky, A., and Boselova, L. (1987). Bulbar respiratory activity during defensive airways reflexes in cats. *Acta Physiol. Hung.* 70, 245–254.

Lieske, S. P., Thoby-Brisson, M., Telgkamp, P., and Ramirez, J. M. (2000). Reconfiguration of the neural network controlling multiple breathing patterns: Eupnea, sighs and gasps [see comment]. *Nat. Neurosci.* 3, 600–607.

Milano, S., Grelot, L., Bianchi, A. L., and Iscoe, S. (1992). Discharge patterns of phrenic motoneurons during fictive coughing and vomiting in decerebrate cats. *J. Appl. Physiol.* 73, 1626–1636.

Morice, A. H., Fontana, G. A., Sovijarvi, A. R., Pistolesi, M., Chung, K. F., Widdicombe, J., O'Connell, F., Geppetti, P., Gronke, L., De Jongste, J., Belvisi, M., Dicpinigaitis, P., Fischer, A., McGarvey, L., Fokkens, W. J., and Kastelik, J. (2004). The diagnosis and management of chronic cough. *Eur. Respir. J.* 24, 481–492.

Morris, K. F., Arata, A., Shannon, R., and Lindsey, B. G. (1996). Inspiratory drive and phase duration during carotid chemoreceptor stimulation in the cat: medullary neurone correlations. *J. Physiol. (Lond.)* 491, 241–259.

Morris, K. F., Nuding, S. C., Segers, L. S., Baekey, D. M., Shannon, R., Lindsey, B. G., and Dick, T. E. (2010). Respiratory and Mayer wave-related discharge patterns of raphé and pontine neurons change with vagotomy. *J. Appl. Physiol.* 109, 189–202.

O'Connor, R., Segers, L. S., Morris, K. F., Nuding, S. C., Pitts, T., Bolser, D. C., Davenport, P. W., and Lindsey, B. G. (2012). A joint computational respiratory neural network-biomechanical model for breathing and airway defensive behaviors. *Front. Physio.* 3:264. doi: 10.3389/fphys.2012.00264

Oku, Y., Tanaka, I., and Ezure, K. (1994). Activity of bulbar respiratory neurons during fictive coughing and swallowing in the decerebrate cat. *J. Physiol. (Lond.)* 480, 309–324.

Orem, J., and Dick, T. (1983). Consistency and signal strength of respiratory neuronal activity. *J. Neurophysiol.* 50, 1098–1107.

Orem, J., and Trotter, R. H. (1993). Medullary respiratory neuronal activity during augmented breaths in intact unanesthetized cats. *J. Appl. Physiol.* 74, 761–769.

Otake, K., Sasaki, H., Ezure, K., and Manabe, M. (1990). Medullary projection of nonaugmenting inspiratory neurons of the ventrolateral medulla in the cat. *J. Comp. Neurol.* 302, 485–499.

Ott, M. M., Nuding, S. C., Segers, L. S., O'Connor, R., Morris, K. F., and Lindsey, B. G. (2012). Central chemoreceptor modulation of breathing via multipath tuning in medullary ventrolateral respiratory column circuits. *J. Neurophysiol.* 107, 603–617.

Poliacek, I., Jakuš, J., Stránsky, A., Baráni, H., Halašová, E., and Tomori, Z. (2004). Cough, expiration and aspiration reflexes following kainic acid lesions to the pontine respiratory group in anaesthetized cats. *Physiol. Res.* 53, 155–170.

Poliacek, I., Morris, K. F., Lindsey, B. G., Segers, L. S., Rose, M. J., Corrie, L. W.-C., Wang, C., Pitts, T. E., Davenport, P. W., and Bolser, D. C. (2011). Blood pressure changes alter tracheobronchial cough: computational model of the respiratory-cough network and in vivo experiments in anesthetized cats. *J. Appl. Physiol.* 111, 861–873.

Romaniuk, J. R., Kowalski, K. E., and Dick, T. E. (1997). The role of pulmonary stretch receptor activation during cough in dogs. *Acta Neurobiol. Exp. (Wars)* 57, 21–29.

Rybak, I. A., O'Connor, R., Ross, A., Shevtsova, N. A., Nuding, S. C., Segers, L. S., Shannon, R., Dick, T. E., Dunin-Barkowski, W. L., Orem, J. M., Solomon, I. C., Morris, K. F., and Lindsey, B. G. (2008). Reconfiguration of the pontomedullary respiratory network: a computational modeling study with coordinated in vivo experiments. *J. Neurophysiol.* 100, 1770–1799.

Saito, Y., Ezure, K., Tanaka, I., and Osawa, M. (2003). Activity of neurons in ventrolateral respiratory groups during swallowing in decerebrate rats. *Brain Dev.* 25, 338–345.

Sant'Ambrogio, G., Sant'Ambrogio, F. B., and Davies, A. (1984). Airway receptors in cough. *Bull. Eur. Physiopathol. Respir.* 20, 43–47.

Shannon, R., Baekey, D. M., Morris, K. F., Li, Z., and Lindsey, B. G. (2000). Functional connectivity among ventrolateral medullary respiratory neurones and responses during fictive cough in the cat. *J. Physiol. (Lond.)* 525, 207–224.

Shannon, R., Baekey, D. M., Morris, K. F., and Lindsey, B. G. (1996). Brainstem respiratory networks and cough. *Pulm. Pharmacol.* 9, 343–347.

Shannon, R., Baekey, D. M., Morris, K. F., and Lindsey, B. G. (1998). Ventrolateral medullary respiratory network and a model of cough motor pattern generation. *J. Appl. Physiol.* 84, 2020–2035.

Shannon, R., Baekey, D. M., Morris, K. F., Nuding, S. C., Segers, L. S., and Lindsey, B. G. (2004). Production of reflex cough by brainstem respiratory networks. *Pulm. Pharmacol. Ther.* 17, 369–376.

Smith, J. A., Aliverti, A., Quaranta, M., McGuinness, K., Kelsall, A., Earis, J., and Calverley, P. M. (2012). Chest wall dynamics during voluntary and induced cough in healthy volunteers. *J. Physiol. (Lond.)* 590, 563–574.

Suzuki, H., Kondo, T., Yamabayashi, H., Kobayashi, I., and Ohta, Y. (1991). Influence of central respiratory activity on the cough response in anesthetized dogs. *Jpn. J. Physiol.* 41, 879–891.

Tatar, M., Sant'Ambrogio, G., and Sant'Ambrogio, F. B. (1994). Laryngeal and tracheobronchial cough in anesthetized dogs. *J. Appl. Physiol.* 76, 2672–2679.

Wang, C., Saha, S., Rose, M. J., Davenport, P. W., and Bolser, D. C. (2009). Spatiotemporal regulation of the cough motor pattern. *Cough* 5, 12.

Conflict of Interest Statement: The authors declare that the research was conducted in the absence of any commercial or financial relationships that could be construed as a potential conflict of interest.

Received: 15 March 2012; paper pending published: 23 April 2012; accepted: 03 June 2012; published online: 29 June 2012.

Citation: Segers LS, Nuding SC, Vovk A, Pitts T, Baekey DM, O'Connor R, Morris KF, Lindsey BG, Shannon R and Bolser DC (2012) Discharge identity of medullary inspiratory neurons is altered during repetitive fictive cough. Front. Physio. ***3****:223. doi: 10.3389/fphys.2012.00223*

This article was submitted to Frontiers in Computational Physiology and Medicine, a specialty of Frontiers in Physiology.

frontiers in
PHYSIOLOGY

REVIEW ARTICLE
published: 27 August 2013
doi: 10.3389/fphys.2013.00223

Developing microRNA screening as a functional genomics tool for disease research

Derek Lemons*[1,2]*, Mano R. Maurya*[1]*, Shankar Subramaniam*[1] *and Mark Mercola*[1,2]*

[1] *Department of Bioengineering, Jacobs School of Engineering, University of California, San Diego, La Jolla, CA, USA*
[2] *Muscle Development and Regeneration Program, Sanford-Burnham Medical Research Institute, La Jolla, CA, USA*

Edited by:
Raimond L. Winslow, The Johns Hopkins University, USA

Reviewed by:
Caterina Guiot, University of Torino, Italy
Jason Papin, University of Virginia, USA

****Correspondence:***
Mark Mercola, Department of Bioengineering, University of California, San Diego, 9500 Gilman Drive, MC 0412, La Jolla, CA 92093, USA
e-mail: mmercola@ucsd.edu

Originally discovered as regulators of developmental timing in *C. elegans*, microRNAs (miRNAs) have emerged as modulators of nearly every cellular process, from normal development to pathogenesis. With the advent of whole genome libraries of miRNA mimics suitable for high throughput screening, it is possible to comprehensively evaluate the function of each member of the miRNAome in cell-based assays. Since the relatively few microRNAs in the genome are thought to directly regulate a large portion of the proteome, miRNAome screening, coupled with the identification of the regulated proteins, might be a powerful new approach to gaining insight into complex biological processes.

Keywords: systems biology and network biology, microRNA target, protein-protein interaction, functional genomics, functional screens, proteomics

INTRODUCTION

Transcriptomics, proteomics and other 'omics data describing biological phenomena are amassing at an astounding rate that was unimaginable even a few years ago. In principle, researchers will be able to utilize these data to formulate and answer complex biological questions—including important questions in cardiovascular medicine. The amount of primary data is growing exponentially with the availability of disease-specific assays and powerful new technologies, such as Next-Gen Sequencing (NGS aka RNA-Seq) (Marioni et al., 2008; Wang et al., 2009), ChiP-SEQ (Johnson et al., 2007), protein microarrays (Melton, 2004; Mattoon and Schweitzer, 2009), and mass-spectroscopy-based proteomics (Hernandez et al., 2006). As of November 2012, the Gene Expression Omnibus (http://www.ncbi.nlm.nih.gov/geo/) lists 2720 datasets covering over 800,000 assays while ArrayExpress at European Bioinformatics Institute contains data from 33,868 datasets covering nearly a million assays (http://www.ebi.ac.uk/arrayexpress/). Moreover, advances in computational algorithms to identify putative connections among nodes have magnified the effect, making the sum total of 'omics information seemingly intractable. For example, the Human Protein Reference Database (http://www.hprd.org) (Keshava Prasad et al., 2009) contains information on a daunting 41,327 protein-protein interactions (PPIs), and this is probably a lower estimate. Making sense of the primary and derived information is arguably one of the largest challenges in systems biology.

One approach is to use high throughput biological screening technology to probe the nodes and networks, providing experimental validation of the computationally determined networks. Nearly five decades ago, the pharmaceutical industry refocused its efforts on screening and has since developed advanced technology, expertise, and chemical libraries, accelerating the production of new drugs that have had an enormous impact on longevity and quality of life (Kaye and Krum, 2007). A recent byproduct of this activity has been the adoption of high throughput screening approaches in academia. Although the original screening applications were target-centric, essentially designed to discover molecules that interact with a known target, the last decade has seen the development of assays designed to explore complex biological mechanisms including assays based on human induced pluripotent stem cells (hiPSCs) to model cardiovascular disease (Nsair and MacLellan, 2011; Mercola et al., 2013). Such assays are typically phenotypic, meaning that they read out morphology, behavior or physiology of cells in culture or even in whole organisms such as zebrafish or Drosophila. The advantage of phenotypic screening as a discovery tool is that it probes a plethora of biomolecules involved in a given phenotype. Phenotypic screening coupled to the identification of cellular proteins or genes targeted in the screens is termed "chemical" or "functional" genomics, depending on whether the library is a chemical or a nucleic acid, respectively, by analogy to the unbiased evaluation of the genome by classical "forward" genetic screening by mutagenesis (Stockwell, 2000).

In this review, we discuss functional genomics technologies for identifying cellular proteins and genes of interest, and application of these approaches to sift through and validate the vastness of information to gain meaningful insight into mechanisms of complex phenotypes and diseases. Key among the technologies is RNA interference (siRNA or shRNA) technology, which has proven to be a powerful method to evaluate the function of candidate genes, and even screen entire genomes to reveal pathway components that govern complex processes, including stem cell identity (Chia et al., 2010) and sensitization of tumor cells to chemotherapeutics (Whitehurst et al., 2007). By probing all genes, whole-genome RNAi strategies offers a comprehensive alternative to chemical screening to interrogate the vastness of the proteome, estimated at over 1,000,000 total human proteins, including splice variants, post-translational modifications and somatic mutations

(Jensen, 2004). This number greatly overshadows the calculated 3000–10,0000 so-called "druggable" proteins, that have topologically defined drug-binding pockets that are considered desirable, which includes enzymes, GPCRs, kinases, nuclear receptors and ion channels (Overington et al., 2006). Targeting only these classes, however, ignores many biologically interesting proteins that play important roles in disease, such as transcription factors and scaffold proteins (Stockwell, 2000; Crews, 2010).

In addition to unbiased siRNA or shRNA screens, we explore the concept that miRNA screening might be a particularly promising means of identifying critical proteins in biological control networks. miRNAs are endogenous, ∼22-nucleotide single-stranded RNAs that selectively bind and suppress multiple mRNA targets in the context of the RNA-Induced Silencing Complex (miRISC). There are only about 2000 known miRNAs in the human genome (http://www.mirbase.org), yet they are estimated to regulate 60% of the total proteome (Friedman et al., 2009). By governing translation and mRNA stability, miRNAs fine-tune nearly every normal and pathological process examined (Filipowicz et al., 2008; Bartel, 2009). In cardiovascular biology, miRNAs control early embryonic development and adult disease, exemplified by the essential roles of miR-1 and miR-133 in heart development (Zhao et al., 2007; Liu et al., 2008) and miR-21 and miR-208a in cardiac remodeling after myocardial infarction (Van Rooij et al., 2007; Thum et al., 2008) and metabolism (Grueter et al., 2012). Given their evolutionarily conserved, and arguably optimized, role in regulating proteins that occupy critical nodes in networks controlling complex biology (Shreenivasaiah et al., 2010), we postulate that screening with miRNA libraries could be used to elucidate disease-modifying mechanisms (**Figure 1**). At least conceptually, the outcome of a miRNA screen can be informative regardless of whether or not a particular miRNA is normally involved in the process being probed. On the one hand these screens may identify miRNAs that normally modulate biological phenomena, adding new dimensions to the miRNAome. On the other hand, miRNAs, when ectopically expressed, will downregulate proteins they do not normally regulate in a native biological context. Thus, miRNA screening, like chemical library screening, can reveal key regulatory proteins that elicit a given phenotype. One major roadblock is the limited ability to identify high confidence targets of miRNAs. If emerging technologies can overcome this issue, miRNA screening might become a tremendously powerful approach to elucidating systems-level control networks and identifying critical node proteins that might be ideally poised as drug targets. In this review we discuss the current technologies for functional miRNA screening and target identification, and consider the challenges that must be resolved in order to achieve the potential offered by the approach.

FUNCTIONAL GENOMICS TECHNOLOGY

Oligonucleotide libraries offer an alternative to chemical libraries for probing cardiovascular or other disease phenotypes. RNA interference (siRNA or shRNA) technology functions by introducing a double stranded small interfering (siRNA) or short hairpin (shRNA) RNA into the cell that basepairs with cognate mRNAs in the RNA-induced Silencing Complex (RISC), targeting the mRNAs for degradation.

Advances in oligonucleotide chemistry have improved siRNA technologies. For instance, modifying the second position of siRNAs with 2'-O-methyl linkage significantly reduces off-target effects that result when siRNAs act like miRNAs (i.e. target imprecisely base-paired mRNAs for downregulation by the RISC) (Jackson et al., 2006). Other chemical or sequence modifications made to the ends of the oligonucleotide strands dictate which strand of the oligonucleotide duplex become packaged into RISC, reducing off-target effects caused by the complementary strand (Schwarz et al., 2003). Furthermore, it has become common to screen pools of multiple siRNAs against a single mRNA target to increase the likelihood of eliciting a phenotypic effect (Parsons et al., 2009). Modern commercial siRNA libraries use these technologies to provide specific and potent knockdown of target genes. Examples of genome-wide siRNA screening libraries include Stealth RNAi™ and Silencer Select (Life Technologies), ON-TARGETplus and siGENOME (ThermoScientific), AccuTarget (Bioneer), and MISSION® siRNA (Sigma-Aldrich).

Compared to standard siRNAs, short hairpin RNA (shRNA) offers multiple advantages. This technology uses lessons learned from miRNA research, harnessing the cell's miRNA biogenesis machinery to process the hairpin into specific siRNA duplexes.

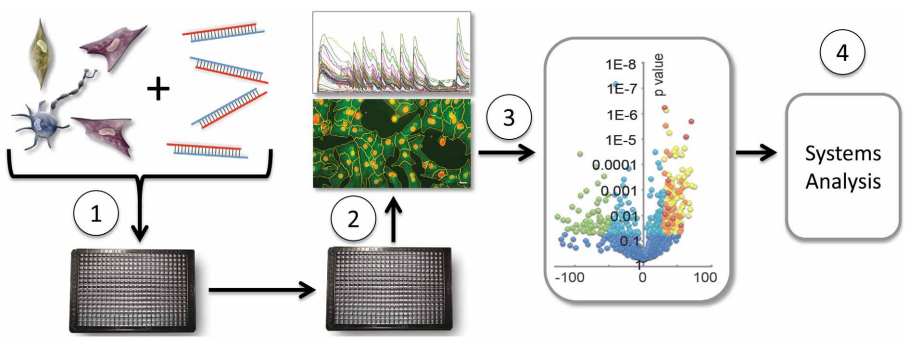

FIGURE 1 | Moderate throughput screening of miRNAs in cell-based assays. Cells are transfected with individual miRNAs from a miRNAome library in 384-well or other multiwell format (1). Following culture, either image-based (shown) or plate-reader acquisition of data, and subsequent analysis (2), profiles miRNAs by activity shown in a volcano plot (3), providing a dataset for network analysis (4) and **Figure 2**.

And, unlike many miRNAs, the shRNA sequences are typically optimized to ensure only one strand becomes packaged into RISC. shRNA is most commonly delivered to cells by transfection or infection using plasmid or viral vectors capable of providing long-lasting downregulation of target genes. The first shRNA libraries used RNA Polymerase III to transcribe the hairpin sequence (Berns et al., 2004; Moffat et al., 2006). Subsequent studies, however, showed that design based on primary miRNA transcripts (pri-miRNA) gave improved efficiency of siRNA packaging into RISC (Chang et al., 2006). Additionally, primary miRNA transcript-based shRNAs are expressed via RNA Polymerase II, allowing co-expression of fluorescent or drug-selectable transgene markers from a single promoter. Another powerful advance in shRNA technology is the use of pooled barcoded shRNAs combined with high throughput sequencing deconvolution, circumventing the need for multi-well plates, liquid handling robots, and large amounts of reagents (Sims et al., 2011). A variety of libraries are available commercially, each utilizing slightly different design strategies and delivery vectors. Examples include MISSION® (Sigma-Aldrich), BLOCK-iT™ (Life Technologies) DECIPHER (Cellecta – Free to academia), and Decode Pooled Lentiviral shRNAs (Thermo Scientific).

LOGIC OF miRNAs AS SCREENING TOOLS

miRNAs make an intriguing starting point for phenotypic screening, as they have many desirable qualities that may allow identification of pathways or networks involved in a particular process that might not be found using single gene screening methods. miRNAs co-evolved to regulate expression of the transcriptome and proteome, and therefore have selective relationships with their targets and the processes they regulate. Indeed, it is thought that entire genomes have adjusted to the pool of miRNAs in each organism by selectively removing potential target sites that, if present in transcripts, would cause undesirable downregulation that would be detrimental to the organism (Stark et al., 2005). Perhaps the most useful aspect of miRNA-genome co-evolution is that each miRNA typically targets numerous genes. Varying estimates have been suggested using computational target predictions as guidelines, but most telling is that expression profiles after miRNA overexpression or removal indicates that a large portion of the transcriptome/proteome is under the control of miRNAs, with each miRNA potentially regulating on the order of hundreds of proteins (Filipowicz et al., 2008; Selbach et al., 2008; Bartel, 2009; Friedman et al., 2009; Shirdel et al., 2011). For instance, miR-223 is estimated by proteomics to affect the expression of more than 200 genes in neutrophils alone (Baek et al., 2008). On the other hand, deletion of certain miRNAs cause no discernible developmental phenotypes (Miska et al., 2007; Alvarez-Saavedra and Horvitz, 2010), indicating that they affect only a small number of targets which are relatively specialized or that their effect on their targets is only a small percentage of the total expression level. These miRNAs, especially those that are evolutionary 'newborns' (i.e. found only in one species or genus), may function mainly to buffer expression of their targets against fluctuation due to intrinsic and extrinsic factors, and have for this reason been termed "canalizing" miRNAs (Wu et al., 2009).

From a systems biology and drug target identification perspective, the most remarkable feature of miRNAs is that they often target proteins at the nodes of important regulatory pathways (Shreenivasaiah et al., 2010; Ichimura et al., 2011). Moreover, many miRNAs, especially those conserved within vertebrates, govern multiple proteins within a single pathway (Cui et al., 2006; Ichimura et al., 2011; Sass et al., 2011; Shirdel et al., 2011). Consequently, these miRNAs function as physiological or developmental switches that fine-tune the proteome of a given cell or tissue. Specific cases include the regulation of Wnt signaling components by miR-34 (Kim et al., 2011), regulation of alternative splicing by miR-23 (Kalsotra et al., 2010), regulation of the p53 network by miR-125b (Le et al., 2011), regulation of phosphatidylinositol- 3-OH kinase (PI(3)K)–AKT signaling (Small et al., 2010), and suppression of smooth muscle specific proteins in cardiomyocytes (Liu et al., 2008). miR-21 targets PPAR alpha pathway in modulating flow-induced endothelial inflammation (Zhou et al., 2011) and miR-23b is involved in endothelial cell growth (Wang et al., 2010).

Since miRNAs govern such large-scale changes in translation, it is perhaps not surprising that they have been found to be involved in nearly every normal and pathological process examined so far (Filipowicz et al., 2008; Bartel, 2009). Given the evolutionarily strategic position of miRNAs and their ability to directly control expression of a large portion of the proteome through simultaneous targeting of multiple genes, they potentially offer an efficient means to interrogate critical processes and the potential to identify genes of interest for phenotypes which may not be affected by the single gene mutation or knockdown approaches typical of most classical genetic or even chemical biology and si/shRNA screening methods. As an example, recent whole genome miRNA screens have led to the discovery of miRNAs and target genes that allocate mesoderm and ectoderm as distinct from endoderm in the early embryo (Colas et al., 2012), modulate cardiomyocyte hypertrophy (Jentzsch et al., 2012), and regulate cell cycle re-entry of adult cardiomyocytes (Eulalio et al., 2012).

Cancer is another area where microRNA screening might reveal unanticipated therapeutic targets. For instance, recent whole-genome miRNA screen identified miR-16, miR-96, miR-182, and miR-497 as potent inhibitors of melanoma cell proliferation and viability (Poell et al., 2012), suggesting that mimics of these miRNAs optimized for use in human patients could be important therapeutic molecules. In addition to understanding the transformed state, an important aspect of cancer research where miRNA screening could be useful might be in deciphering the cellular pathways and proteins that mediate drug resistance, which could suggest combinatorial drug action, such as been recently addressed through proteomics (Erler and Linding, 2012). We expect that, in the near future, miRNA screens will discover many phenotype-modifying genes that would not and have not been identified through siRNA and chemical screens, as well as identify numerous miRNAs whose involvement in disease phenotype, progression or drug-responsiveness will provide new therapeutic targets.

Many libraries are available commercially that allow screening using miRNA mimics either in hairpin or duplex format for

the majority of known miRNAs of variety of model organisms. The oligonucleotide mimics are typically chemically modified in a manner similar to the siRNA products described above so that one strand is preferentially packaged into the RISC. Examples include Ambion® Pre-miR Precursors and miRvana™ miRNA mimics (Life Technologies), MISSION® (Sigma-Aldrich), miRIDIAN (Thermo Scientific). Unlike siRNA/shRNA screening, in which the gene affecting the phenotype is known *a priori* (although the mRNA target must be confirmed) the degeneracy of miRNA:mRNA interactions means that screening campaigns must include steps to identify the mRNA target(s) responsible for the phenotype. Below we discuss computational and biochemical methods currently used for target identification, their efficacy, and possible ways to improve the pipeline from screen dataset to target knowledge (**Figure 2**).

COMPUTATIONAL APPROACHES TO TARGET IDENTIFICATION

The development of computational tools for miRNA target prediction began in the early 2000's shortly after the discovery that miRNAs are pervasive members of animal genomes (Lagos-Quintana et al., 2001). Currently, many different tools are available, most utilizing a common set of concepts to inform their prediction algorithms, such as seed-match (complementarity between the 5′ of the miRNA—typically bases 2–8—and the bases in 3′ untranslated region (3′UTR) of an mRNA), evolutionary conservation of target sites and thermodynamic (free-energy) considerations for the interaction [**Table1**; for in depth reviews see (Alexiou et al., 2009; Xia et al., 2009; Witkos et al., 2011)].

The initial algorithms turned out to provide high sensitivity but low specificity (high rate of false-positives). One approach to solve this problem has been to prioritize targets predicted by multiple algorithms; however, taking the intersection (rather than union) leads to a corresponding loss of sensitivity (Alexiou et al., 2009). Developing advanced algorithms to take contextual cues into account would be a major advance. Some new algorithms strive to incorporate more comprehensive feature sets from experimental data and/or machine learning to try to improve the ratio of sensitivity to specificity. An improved version of TargetScan (Lewis et al., 2005), called TargetScanS, uses 6 instead of 7 nucleotide seed match followed by an A-anchor and incorporates information on the surrounding mRNA sequence to compute a context score which models the relative contributions of previously identified targeting features, including site type, site number, site location, local A+U content and 3′-supplementary pairing (Grimson et al., 2007; Garcia et al., 2011). An improved context-score called context+ score also considers target-site abundance and seed-pairing stability (Garcia et al., 2011). A multiple linear regression model was trained using 11 microarray data sets, and the context+ scores performed better than previous models. miRTarget2 is an improvement of the original miRTarget algorithm and uses a support-vector machine learning (SVM) algorithm to build prediction models based on a set of 131 features including seed conservation, other seed types, base composition, and secondary structure (Wang and El Naqa, 2008). SVMicrO is an SVM-based recent algorithm for miRNA target prediction in animals which tries to improve both sensitivity and specificity of prediction by using positive and negative target data for training the classifier (Liu et al., 2010). The algorithm increases sensitivity by only requiring a 5 basepair seed-match, and is trained using about 1000 positive miRNA-target pairs and microarray data-based 3500 negative miRNA-target pairs. The authors have shown a better true positive rate for SVMicrO as compared to many other popular algorithms on both the training data as well as a separate proteomic test data.

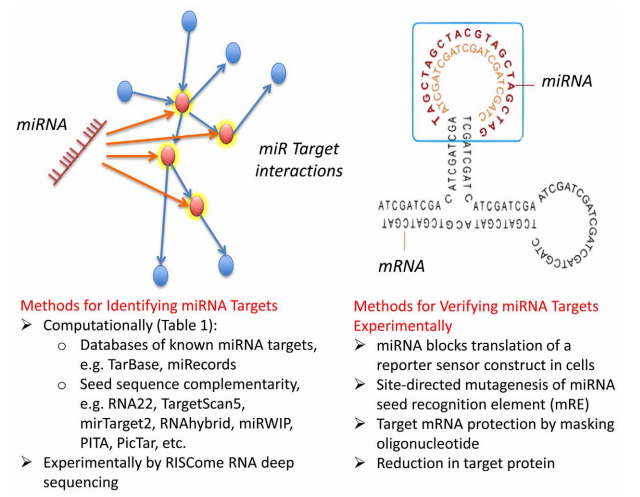

FIGURE 2 | Computational and experimental strategies to identify miRNA targets. miRNAs target multiple proteins, and in certain instances a single family of miRNAs target multiple proteins involved in a common biological process, through imprecise basepairing with recognition sequences in mRNA (see text). Commonly used computational and biochemical approaches to identify targets are summarized along with focused strategies for confirming direct interaction of a miRNA with particular mRNA targets.

BIOCHEMICAL AND PROTEOMIC APPROACHES TO TARGET IDENTIFICATION

Despite these advances, computational prediction of miRNA target sites in mammals are generally considered too error-prone to be used as the sole means of target identification, reviewed in Alexiou et al. (2009). We ascribe the problem to the fact that miRNA-mRNA pairing "rules" of most computational prediction algorithms were determined based on a small number of known targets discovered through genetic mutations and by observing changes in target regulation after abrogation of the interaction by site-directed mutation of the recognition sequence. As discussed above, contextual cues that influence site accessibility include sequences surrounding the recognition site and RNA-binding cofactors present in the cell. It is too soon to tell whether the innovations in algorithm design described in the preceding section will remedy this situation, but given that they are unlikely to model the influences of the cellular context, we expect that the problem of false positives and negatives will remain a serious issue. Thus, while many true targets have been discovered using various target prediction algorithms, they probably comprise a small percentage of the total regulatory network of the miRNA pathway.

Table 1 | Commonly used computational tools and algorithms for identification of miRNA targets.

Software/tools	Evolutionary conservation	Base-pairing/seed-match criteria	Surrounding sequence	Energy consideration	Additional filters/rules/learning using microarray data
TargetScan	Across vertebrates: human, mouse and rat	7-nt (W-C complementarity for bases 2-8 of miRNA)	Seed-match extended on both sides	Yes, *z*-score to energy of miR-target interaction	No
TargetScanS	Similar; dog and chicken as well	6-nt and A-anchor G-W wobble pair allowed	Yes	Yes	Latest version can use context information.
miRanda	*D. melanogaster*, *D. pseudoobscura* and *A. gambiae*; now extended to mouse, human and fish	7-nt and weighted seed-match		Yes	No
Diana-microT		5- to 7-nt, conditional G-W wobble pair and bulge allowed	Uses a 38-nt sliding window	Yes, uses as a filter to find miRNA3′-UTR pairs	Specialized for target mRNAs with single miRNA recognition element
PicTar	vertebrates, flies and nematodes	7-nt		Yes	Finds common targets of several miRNAs using combinations of transcription factor binding sites.
miRTarget, miRTarget2 and miRDB	Yes	7-nt		Yes, duplex stability	Uses microarray data for positive and negative targets. SVM is used in miRTarget2 to incorporate features such as other seed types, base composition, and secondary structure.
SVMicrO	Yes	5-nt to increase sensitivity	Yes	Yes	Similar to miRTaget2. Bayesian approach is also used.

Abbreviation: W-C, Watson-Crick; SVM, support-vector machine.

TRANSCRIPTOMICS AND PROTEOMICS TECHNIQUES

The first attempt at biochemically boot-strapping the identification of miRNA targets at a transcriptome scale assayed the total change in mRNA expression profile by microarray analysis caused by transfection of single miRNAs into human cells (Lim et al., 2005). In this case, transfection of either miR-1 or miR-124 shifted mRNA expression such that there was a greater resemblance to the natural profile of seen muscle or brain, the organs that normally express these miRNAs during development. Subsequent microarray studies looked at global changes in mRNA expression resulting from single miRNA overexpression, depletion, genetic mutants, and depletion of all miRNAs through mutations in the miRNA biogenesis pathway (Giraldez et al., 2006; Linsley et al., 2007). These early analyses proved that microarray profiling can provide a first approximation of the genes regulated by single or multiple miRNAs, consistent with the observation that the majority of changes in protein levels induced by miRNA regulation are attributable to changes in mRNA expression (Guo et al., 2010). However, as with microarray transcriptome analysis of transcription factor mutants, these analyses alone cannot reveal whether genes are the direct targets of the miRNAs, or are affected indirectly by factors downstream of the primary effector molecules. Although upregulated genes are unlikely to be directly affected by miRNA activity and can be excluded as direct targets, downregulated genes must be analyzed in greater detail to determine

whether or not they are targeted directly by the miRNA(s) in question.

The simple comparison of downregulated transcript sets with the computationally predicted mRNA target sets has yielded poor correlations (Alexiou et al., 2009). While sequences of downregulated mRNAs are often enriched for "seed" complementary sequences, this is not always observed. For instance, downregulated genes lacking "seed" matches may be secondarily affected by changes in direct target genes, but they can also be direct targets which harbor less common types of miRNA target sites, such as 3′ compensatory (Brennecke et al., 2005) centered sites (Shin et al., 2010), or other non-canonical binding structures (Helwak et al., 2013). Whether a transcript is a direct target of a particular miRNA may or may not be relevant to the goals of an individual screen experiment. However, if this knowledge is required, subsequent experiments will be needed to confirm a direct miRNA:mRNA interaction. Typically, confirmation is based on abolishing regulation by mutation of the miRNA recognition site within the mRNA, and an alternative is to mask the binding site with a complementary oligoribonucleotide, preventing miRNA binding and mRNA degradation (for example, see Colas et al., 2012).

Quantitative proteomics is an analogous target discovery strategy that has gained traction in recent years, as it provides a direct readout of the ultimate effect of miRNA activity (Vinther et al., 2006; Baek et al., 2008; Yang et al., 2009, 2010; Chen et al., 2011; Yan et al., 2011). This method provides an advantage over microarray analysis, since it can detect changes in expression levels of a protein even when its cognate mRNA is not downregulated at an appreciable level. Early instances include an analysis of miR-1 in HeLa cells (Vinther et al., 2006), an analysis of miR-1, 124, and 181 in HeLa cells and miR-223 in mouse knockout neutrophils (Baek et al., 2008), and subsequent studies have examined miR-21 and miR-143 (Yang et al., 2009, 2010). An example of an advanced proteomics analysis is a recent study that used Stable Isotope Labeling by Amino acids in Cell culture (SILAC) to detect differences in protein expression induced by the overexpression of miR-34a and miR-29 (Bargaje et al., 2012). Although a number of proteins related to the biological function of the miRNAs in apoptosis were found to change, the study discusses several limitations. Chief among these is that miRNAs often only reduce target protein levels by 30–60% (Hendrickson et al., 2009) meaning that commonly applied thresholds (e.g., 2-fold) are inappropriate and a more robust statistical analysis is needed. In addition, variation in protein stability might require analyses at multiple timepoints. Finally, only about 10% of the proteins detected as downregulated by Bargaje et al. for miR-34a and miR-29 were also predicted by the consensus of 5 computational algorithms (Bargaje et al., 2012), highlighting the need for evaluating potential indirect effects (in addition to validating potential targets). Finally, as for microarray analyses, many interesting targets might be missed due to low abundance. Nevertheless, even at current depths, the recent studies suggest that proteomics analysis can yield a number of targets that could feed a validation and systems analysis pipeline.

IMMUNOPRECIPITATION-BASED TARGET IDENTIFICATION TECHNIQUES

Biochemistry-based experiments have been developed to directly identify the target sequences bound by miRNAs. The first attempts of this type of assay immunoprecipitated the RISC components, and then performed microarrays or RNA sequencing to identify the captured mRNAs (Beitzinger et al., 2007; Easow et al., 2007; Zhang et al., 2007; Hendrickson et al., 2008). Such methods are promising since they should be able to identify the direct targets of mRNAs. A number of procedural modifications have improved the initial process to reduce false positive rates and increase the depth and specificity of targets discovered. These methods, referred to as Argonaute CLIP-Seq (Zisoulis et al., 2010) or Argonaute HITS-CLIP (Chi et al., 2009), utilize cross-linking prior to immunoprecipitation to firmly associate target mRNAs with miRISC. After immunoprecipitation, exposed RNA ends not covered by RISC protein are enzymatically cleaved before linkers are ligated to the bound RNA and then processed using deep sequencing. After sequencing, high tag count segments are deemed to be bonafide miRNA target sites, which are then matched computationally to individual transcripts.

Analysis of the putative recognition sites discovered by these methods indicated that not every enriched sequence has a good "seed" match to known miRNAs. This may be in part due to unknown miRNAs being present in the genome, but recent mass sequencing efforts suggest that the vast majority of miRNAs have been discovered in the major model organisms. The most likely explanation, therefore, is that the contextual cues and non-canonical pairing indeed play important roles in determining miRNA-mRNA recognition, and the data from these experiments are helping to re-define the miRNA-mRNA binding rules (Elefant et al., 2011; Wen et al., 2011).

Additional refinements to the immunoprecipitation approach have improved specificity and sensitivity. PAR-CLIP (Hafner et al., 2010) and miR-TRAP (Baigude et al., 2012) both include photoactivatable ribonucleosides in transfected miRNA mimics to allow specific cross-linking sites and higher wavelength cross-linking, which is less harmful to cells and improves RNA recovery. The PAR-CLIP method has been used to achieve single nucleotide resolution of the binding site due to the specificity of the cross-linking. Modifications to denaturing conditions and the nuclease digestion of extraneous RNA can improve data by reducing biases resulting from conditions used in previous methods (Kishore et al., 2011).

These approaches often rely on overexpression of a particular miRNA to load the RISC. The over-representation of a specific miRNA in active RISC can cause off-target interactions, possibly influenced by dosage and elevated contribution of seed sequence similarity to miRNA:mRNA association (Birmingham et al., 2006; Arvey et al., 2010). This phenomenon, however, might recapitulate the function of the overexpressed miRNA in the screen assay itself, and thus may be relevant to the identification of targets. Conversely, endogenous miRNA programmed RISC will always comprise some percentage of the total data. Both errors will introduce false positives. The miR-TRAP method seeks to avoid this issue by inclusion of a biotin tag on transfected miRNA in an effort to select only for complexes containing

specific miRNAs (Baigude et al., 2012). Perhaps most promising of new technologies, crosslinking, ligation, and sequencing of hybrids (CLASH) of RNA pulled down with AGO complexes, may provide the ability to simultaneously discover mRNAs being downregulated by RISC and the specific miRNA(s) which target them, as a miRNA sequence and a fragment of its targeted RNA sequence will be ligated together and sequenced as a single chimeric sequence (Helwak et al., 2013).

Although these immunoprecipitation-based methods can provide quantitative data about miRNA-target binding, their main drawback is that they do not quantify the extent of mRNA or protein downregulation. For this reason, a combination of proteomic/transcriptomic profiing with the direct immunoprecipitation methods might offer the best quality datasets for constructing miRNA-target interaction networks. A meta analysis of microarray data from miRNA transfection experiments compared to Argonaute CLIP-Seq data not surprisingly showed only partial overlap (Wen et al., 2011), presumably reflecting the inherent biases of each method. Such discrepancies might be predictive of direct versus indirect effects of miRNAs against target mRNAs or proteins. Furthermore, investigation of the dose-dependent effects of miRNAs against targets will likely be important for appreciating how a miRNA or anti-miRNA therapeutic will behave *in vivo*, in particular whether or not there are potentially beneficial or harmful dosage effects.

BUILDING AND VALIDATING NETWORKS

Functional screening of miRNA mimics generates a list of miRNAs that, when overexpressed, affect the desired phenotype to varying degrees. In our experience, screening about 900 miRNAs in a commercial mRNA mimic collection against a phenotypic assay results in between 30 and 200 statistically significant hits, (e.g., Colas et al., 2012), consistent with results from other complex biological assays such as (Eulalio et al., 2012; Jentzsch et al., 2012). The hits can be prioritized according to experimental goals (e.g. filtered by expression within a target tissue). Once the targets are identified through the strategies described above, they can be mapped to the human PPI network. From the human PPI, a subnetwork is obtained by retaining the edges in which one of the nodes is in the target list (**Figure 3**). This amounts to retaining all the nodes in the PPI that directly interact with at least one target gene. One can define rules about which nodes and edges from the PPI should be included. For example, one may retain only those edges in which both nodes are in the target list or those that are functionally associated. This may result in a much more sparse network.

How well do predicted networks reflect reality? A recent study Becker et al. (2012) shows that miRs are encoded in the genome as individual miRNA genes or as gene clusters and transcribed as polycistronic units. These authors estimated that about 50% of all miRNAs are co-expressed with neighboring miRNAs and, most importantly, that these clusters coordinately regulate multiple members of protein-protein interaction network clusters. Another study (Alshalalfa et al., 2012) showed that combining protein functional interaction networks with miR detection revealed several miR-regulated interaction modules that were indeed enriched in focal adhesion and prostate cancer pathways, and yet another used screen data to reveal miRNA control of p53 (Becker et al., 2012). Illustrative of such recent efforts to deduce high quality PPIs from miRNA screen datasets is the control of epithelial to mesenchymal transition by miR-200 family (Sass et al., 2011). The study first used an *in silico* approach comparing miRNA target sites from published PAR-CLIP dataset (Hafner et al., 2010) to proteomics datasets (Baek et al., 2008; Selbach et al., 2008) to conclude that miRNAs have a propensity to target proteins involved in multi-protein complexes. Furthermore, they showed that protein complexes are coordinately regulated by clusters of miRNAs, a conclusion supported by an analysis of miRNAs that regulate transcription factor response elements in cell culture (Becker et al., 2012). To probe the notion that miRNA clusters coordinately control biological processes, Sass et al. (2011) went on to show that additional members of the transcriptional complex controlling E-cadherin, in addition to previously identified members, are under coordinate control by miRNAs that reside within the miR141-200c cluster. Although these pioneering studies support the idea that combining proteomics-based target identification with a network-based strategy can be used to construct reliable miRNA:protein interaction networks, it should be emphasized that the validation has been sparse, and that large-scale approaches, such as by siRNA screening, are needed to evaluate the veracity of the regulatory networks.

SUMMARY AND PROSPECTS

Several features of miRNAs make functional, whole miRNAome screening attractive as a platform to generate systems-level descriptions of complex biological regulatory networks and help interpret the massive transcriptome datasets emerging in all areas of biology. First, the total number of miRNAs is relatively few compared to siRNA or chemical libraries; yet, because of target recognition degeneracy, the miRNAome regulates a large proportion of the proteome. Second, since miRNA recognition of mRNA transcripts is sequence based, the identification of mRNA targets poses fewer problems than associated with identification of relevant targets of small molecules from chemical screens (Rix and Superti-Furga, 2009), although methods for high throughput identification of miRNA targets remain costly and far from robust. Third, based on co-evolution of miRNAs and the networks they control, it is tempting to speculate that the nodes targeted by the miRNAs might be selective for particular biological processes, and hence comprise good points for therapeutic intervention.

Currently, screening technology combined with the availability of miRNA and si/shRNA libraries make it straightforward to design and implement a moderate throughput whole genome miRNAome or si/shRNA transcriptome screen (**Figure 1**). This includes iPSC-based disease models, which offer an unprecedented ability to interrogate disease relevant processes and reveal potential new drug targets. The bottleneck today is target identification. Ideally, proteomics datasets should provide clear and consistent results from over-expression of miRNAs. Unfortunately, there is considerable variation between datasets obtained from proteomics analysis of the same miRNA assayed by overexpression in the same cells. For instance, comparison of the proteins downregulated by miR-34a (by Bargaje et al.) revealed

only 5 proteins in common out of 3365 (Bargaje et al., 2012) and 1495 (Chen et al., 2011). Similarly, Shirdel et al. (Shirdel et al., 2011) compared the results of miR-124 overexpression and found only 10 common targets from 3 experiments, comprising only 3.7% of the smallest dataset. Similarly, the general conclusion about computational prediction resources is that none alone can perfectly identify mRNA targets, even when mRNAs are filtered by analysis (e.g. microarray type) and cell type (Baek et al., 2008; Selbach et al., 2008; Shirdel et al., 2011). Nonetheless, our experience is consistent with the conclusion of Shirdel et al. that the current methods are suitable to provide an initial prediction, and this is aided by recent resources such as mirGator and mirDIP that integrate several up-to-date miRNA target prediction databases. In practice, PPI networks are often constructed from targets from multiple prediction algorithms, see discussion in (Alexiou et al., 2009; Shirdel et al., 2011). Furthermore, we use moderate throughput siRNA screening against individual pathway components

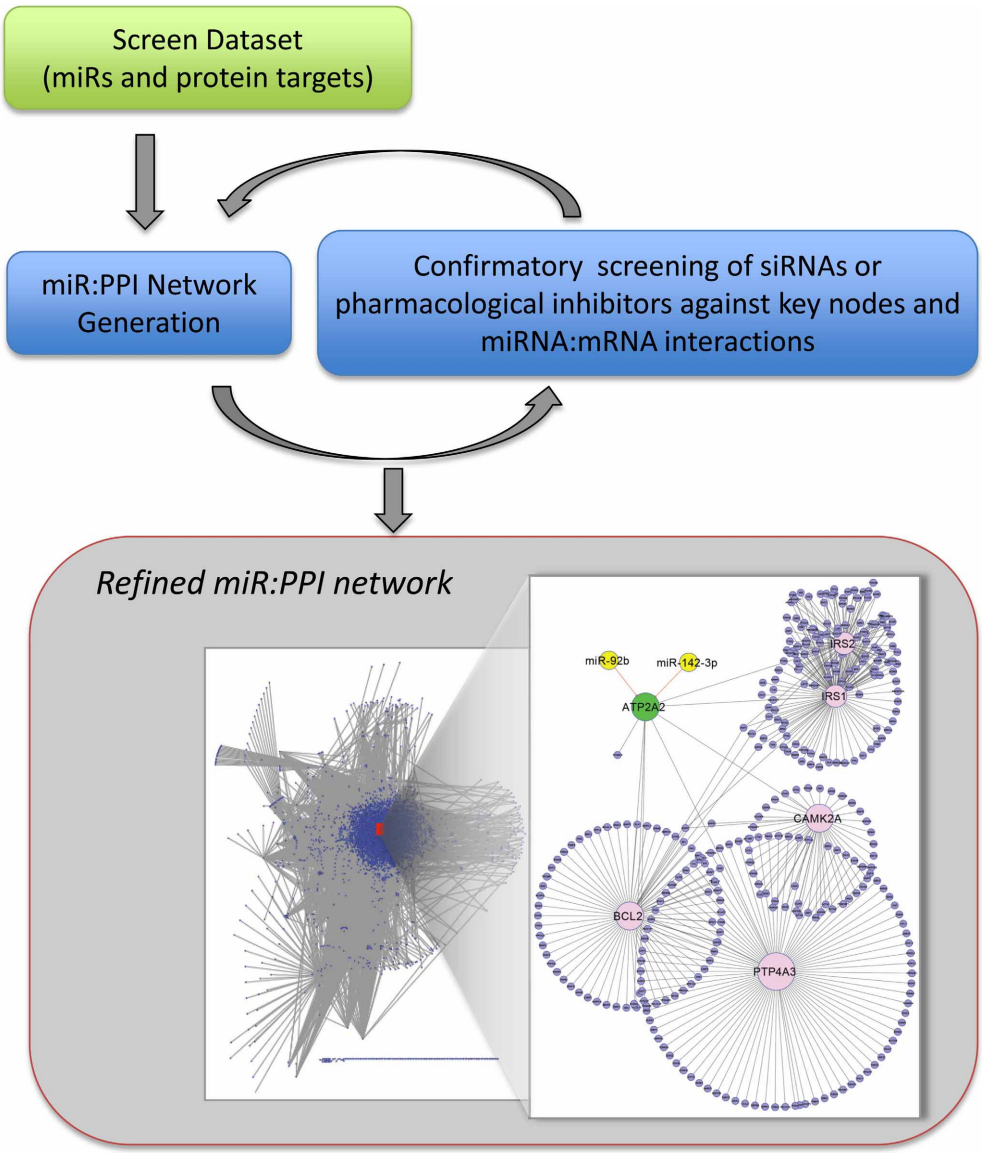

FIGURE 3 | Pipeline for iterative process of network construction and confirmatory screening of key nodes. The screen dataset (as in **Figure 1**) is filtered and used for construction of the preliminary network. We propose that it is beneficial to evaluate individual protein nodes by screening specific si/shRNAs, pharmacological inhibitors or by protein overexpression. Similarly, miR:protein interactions can be validated by monitoring protein levels and direct interaction confirmed by site-directed mutagenesis of the recognition elements in the mRNAs (see text). The confirmatory cycles lead to a refined dataset and network. Statistical significance of screen hits can be relaxed because of the confirmatory process. The interactome shown contains miRNAs (yellow) found in a screen to result in SERCA2 (ATP2A2) (green) inhibition >30%, $p < 0.05$, are evolutionarily conserved, and are upregulated in human heart failure. Inset: SERCA2 (node enlarged) centric network showing interaction with miR92b and miR-142-3b that were determined by confirmatory screening to target SERCA2 (unpublished data).

to confirm the validity of predicted PPIs (**Figure 3**) (Colas et al., 2012).

Finally, functional miRNA screening is a potentially powerful method of identifying miRNAs and PPIs that control complex biological processes. Although miRNA screening is mainly considered as a strategy to reveal miRNAs that naturally control biological processes, we propose a more expanded view, and suggest that miRNA screening also has the potential to interrogate biological networks even if the active miRNAs are not natural regulators. Like chemical and si/shRNA functional genomics screens, miRNAs screening, coupled to target identification and iterations of PPI network construction, validation and refinement, might offer an attractive pipeline to interrogate complex biology.

ACKNOWLEDGMENTS

Mark Mercola acknowledges research support from the NIH (R33HL088266 and R01HL113601), Mathers Charitable Trust, California Institute for Regenerative Medicine (RC1-000132) and the Fondation Leducq. Shankar Subramaniam acknowledges research support from the NIH (R33HL087375, U54GM69338, P01DK074868, R01HL106579, and R01HL108735). miRNA screening is supported by NIH P30AR061303 and P30CA030199.

REFERENCES

Alexiou, P., Maragkakis, M., Papadopoulos, G. L., Reczko, M., and Hatzigeorgiou, A. G. (2009). Lost in translation: an assessment and perspective for computational microRNA target identification. *Bioinformatics* 25, 3049–3055. doi: 10.1093/bioinformatics/btp565

Alshalalfa, M., Bader, G. D., Goldenberg, A., Morris, Q., and Alhajj, R. (2012). Detecting microRNAs of high influence on protein functional interaction networks: a prostate cancer case study. *BMC Syst. Biol.* 6:112. doi: 10.1186/1752-0509-6-112

Alvarez-Saavedra, E., and Horvitz, H. R. (2010). Many families of *C. elegans* microRNAs are not essential for development or viability. *Curr. Biol.* 20, 367–373. doi: 10.1016/j.cub.2009.12.051

Arvey, A., Larsson, E., Sander, C., Leslie, C. S., and Marks, D. S. (2010). Target mRNA abundance dilutes microRNA and siRNA activity. *Mol. Syst. Biol.* 6, 363. doi: 10.1038/msb.2010.24

Baek, D., Villén, J., Shin, C., Camargo, F. D., Gygi, S. P., and Bartel, D. P. (2008). The impact of microRNAs on protein output. *Nature* 455, 64–71. doi: 10.1038/nature07242

Baigude, H., Ahsanullah, Li, Z., Zhou, Y., and Rana, T. M. (2012). miR-TRAP: a benchtop chemical biology strategy to identify microRNA targets. *Angew. Chem. Int. Ed. Engl.* 51, 5880–5883. doi: 10.1002/anie.201201512

Bargaje, R., Gupta, S., Sarkeshik, A., Park, R., Xu, T., Sarkar, M., et al. (2012). Identification of novel targets for miR-29a using miRNA proteomics. *PLoS ONE* 7:e43243. doi: 10.1371/journal.pone.0043243

Bartel, D. P. (2009). MicroRNAs: target recognition and regulatory functions. *Cell* 136, 215–233. doi: 10.1016/j.cell.2009.01.002

Becker, L. E., Lu, Z., Chen, W., Xiong, W., Kong, M., and Li, Y. (2012). A systematic screen reveals MicroRNA clusters that significantly regulate four major signaling pathways. *PLoS ONE* 7:e48474. doi: 10.1371/journal.pone.0048474

Beitzinger, M., Peters, L., Zhu, J. Y., Kremmer, E., and Meister, G. (2007). Identification of human microRNA targets from isolated argonaute protein complexes. *RNA Biol.* 4, 76–84. doi: 10.4161/rna.4.2.4640

Berns, K., Hijmans, E. M., Mullenders, J., Brummelkamp, T. R., Velds, A., Heimerikx, M., et al. (2004). A large-scale RNAi screen in human cells identifies new components of the p53 pathway. *Nature* 428, 431–437. doi: 10.1038/nature02371

Birmingham, A., Anderson, E. M., Reynolds, A., Ilsley-Tyree, D., Leake, D., Fedorov, Y., et al. (2006). 3' UTR seed matches, but not overall identity, are associated with RNAi off-targets. *Nat. Methods* 3, 199–204. doi: 10.1038/nmeth854

Brennecke, J., Stark, A., Russell, R. B., and Cohen, S. M. (2005). Principles of microRNA-target recognition. *PLoS Biol.* 3:e85. doi: 10.1371/journal.pbio.0030085

Chang, K., Elledge, S. J., and Hannon, G. J. (2006). Lessons from Nature: microRNA-based shRNA libraries. *Nat. Methods* 3, 707–714. doi: 10.1038/nmeth923

Chen, Q.-R., Yu, L.-R., Tsang, P., Wei, J. S., Song, Y. K., Cheuk, A., et al. (2011). Systematic proteome analysis identifies transcription factor YY1 as a direct target of miR-34a. *J. Proteome Res.* 10, 479–487. doi: 10.1021/pr1006697

Chi, S. W., Zang, J. B., Mele, A., and Darnell, R. B. (2009). Argonaute HITS-CLIP decodes microRNA-mRNA interaction maps. *Nature* 460, 479–486.

Chia, N.-Y., Chan, Y.-S., Feng, B., Lu, X., Orlov, Y. L., Moreau, D., et al. (2010). A genome-wide RNAi screen reveals determinants of human embryonic stem cell identity. *Nature* 468, 316–320. doi: 10.1038/nature09531

Colas, A. R., McKeithan, W. L., Cunningham, T. J., Bushway, P. J., Garmire, L. X., Duester, G., et al. (2012). Whole-genome microRNA screening identifies let-7 and mir-18 as regulators of germ layer formation during early embryogenesis. *Genes Dev.* 26, 2567–2579. doi: 10.1101/gad.200758.112

Crews, C. M. (2010). Targeting the undruggable proteome: the small molecules of my dreams. *Chem. Biol.* 17, 551–555. doi: 10.1016/j.chembiol.2010.05.011

Cui, Q., Yu, Z., Purisima, E. O., and Wang, E. (2006). Principles of microRNA regulation of a human cellular signaling network. *Mol. Syst. Biol.* 2, 46. doi: 10.1038/msb4100089

Easow, G., Teleman, A. A., and Cohen, S. M. (2007). Isolation of microRNA targets by miRNP immunopurification. *RNA* 13, 1198–1204. doi: 10.1261/rna.563707

Elefant, N., Altuvia, Y., and Margalit, H. (2011). A wide repertoire of miRNA binding sites: prediction and functional implications. *Bioinformatics* 27, 3093–3101. doi: 10.1093/bioinformatics/btr534

Erler, J. T., and Linding, R. (2012). Network medicine strikes a blow against breast cancer. *Cell* 149, 731–733. doi: 10.1016/j.cell.2012.04.014

Eulalio, A., Mano, M., Ferro, M. D., Zentilin, L., Sinagra, G., Zacchigna, S., et al. (2012). Functional screening identifies miRNAs inducing cardiac regeneration. *Nature* 492, 376–381. doi: 10.1038/nature11739

Filipowicz, W., Bhattacharyya, S. N., and Sonenberg, N. (2008). Mechanisms of post-transcriptional regulation by microRNAs: are the answers in sight? *Nat. Rev. Genet.* 9, 102–114. doi: 10.1038/nrg2290

Friedman, R. C., Farh, K. K.-H., Burge, C. B., and Bartel, D. P. (2009). Most mammalian mRNAs are conserved targets of microRNAs. *Genome Res.* 19, 92–105. doi: 10.1101/gr.082701.108

Garcia, D. M., Baek, D., Shin, C., Bell, G. W., Grimson, A., and Bartel, D. P. (2011). Weak seed-pairing stability and high target-site abundance decrease the proficiency of lsy-6 and other microRNAs. *Nat. Struct. Mol. Biol.* 18, 1139–1146. doi: 10.1038/nsmb.2115

Giraldez, A. J., Mishima, Y., Rihel, J., Grocock, R. J., Van Dongen, S., Inoue, K., et al. (2006). Zebrafish MiR-430 promotes deadenylation and clearance of maternal mRNAs. *Science* 312, 75–79. doi: 10.1126/science.1122689

Grimson, A., Farh, K. K.-H., Johnston, W. K., Garrett-Engele, P., Lim, L. P., and Bartel, D. P. (2007). MicroRNA Targeting Specificity in Mammals: determinants beyond seed pairing. *Mol. Cell* 27, 91–105. doi: 10.1016/j.molcel.2007.06.017

Grueter, C. E., van Rooij, E., Johnson, B. A., DeLeon, S. M., Sutherland, L. B., Qi, X., et al. (2012). A cardiac microRNA governs systemic energy homeostasis by regulation of MED13. *Cell* 149, 671–683. doi: 10.1016/j.cell.2012.03.029

Guo, H., Ingolia, N. T., Weissman, J. S., and Bartel, D. P. (2010). Mammalian microRNAs predominantly act to decrease target mRNA levels. *Nature* 466, 835–840. doi: 10.1038/nature09267

Hafner, M., Landthaler, M., Burger, L., Khorshid, M., Hausser, J., Berninger, P., et al. (2010). Transcriptome-wide identification of RNA-binding protein and microRNA target sites by PAR-CLIP. *Cell* 141, 129–141. doi: 10.1016/j.cell.2010.03.009

Helwak, A., Kudla, G., Dudnakova, T., and Tollervey, D. (2013). Mapping the human miRNA interactome by CLASH reveals frequent noncanonical binding. *Cell* 153, 654–665. doi: 10.1016/j.cell.2013.03.043

Hendrickson, D. G., Hogan, D. J., Herschlag, D., Ferrell, J. E., and Brown, P. O. (2008). Systematic identification of mRNAs recruited to argonaute 2 by specific microRNAs and corresponding changes in transcript abundance. *PLoS ONE* 3:e2126. doi: 10.1371/journal.pone.0002126

Hendrickson, D. G., Hogan, D. J., McCullough, H. L., Myers, J. W., Herschlag, D., Ferrell, J. E., et al. (2009). Concordant regulation of translation and mRNA abundance for hundreds of targets of a human microRNA. *PLoS Biol*. 7:e1000238. doi: 10.1371/journal.pbio.1000238

Hernandez, P., Müller, M., and Appel, R. D. (2006). Automated protein identification by tandem mass spectrometry: issues and strategies. *Mass Spectrom. Rev.* 25, 235–254. doi: 10.1002/mas.20068

Ichimura, A., Ruike, Y., Terasawa, K., and Tsujimoto, G. (2011). miRNAs and regulation of cell signaling. *FEBS J.* 278, 1610–1618. doi: 10.1111/j.1742-4658.2011.08087.x

Jackson, A. L., Burchard, J., Leake, D., Reynolds, A., Schelter, J., Guo, J., et al. (2006). Position-specific chemical modification of siRNAs reduces "off-target" transcript silencing. *RNA* 12, 1197–1205. doi: 10.1261/rna.30706

Jensen, O. N. (2004). Modification-specific proteomics: characterization of post-translational modifications by mass spectrometry. *Curr. Opin. Chem. Biol.* 8, 33–41. doi: 10.1016/j.cbpa.2003.12.009

Jentzsch, C., Leierseder, S., Loyer, X., Flohrschütz, I., Sassi, Y., Hartmann, D., et al. (2012). A phenotypic screen to identify hypertrophy-modulating microRNAs in primary cardiomyocytes. *J. Mol. Cell. Cardiol.* 52, 13–20. doi: 10.1016/j.yjmcc.2011.07.010

Johnson, D. S., Mortazavi, A., Myers, R. M., and Wold, B. (2007). Genome-wide mapping of *in vivo* protein-DNA interactions. *Science* 316, 1497–1502. doi: 10.1126/science.1141319

Kalsotra, A., Wang, K., Li, P.-F., and Cooper, T. A. (2010). MicroRNAs coordinate an alternative splicing network during mouse postnatal heart development. *Genes Dev*. 24, 653–658. doi: 10.1101/gad.1894310

Kaye, D. M., and Krum, H. (2007). Drug discovery for heart failure: a new era or the end of the pipeline? *Nat. Rev. Drug Discov.* 6, 127–139. doi: 10.1038/nrd2219

Keshava Prasad, T. S., Goel, R., Kandasamy, K., Keerthikumar, S., Kumar, S., Mathivanan, S., et al. (2009). Human protein reference database–2009 update. *Nucleic Acids Res.* 37, D767–D772. doi: 10.1093/nar/gkn892

Kim, N. H., Kim, H. S., Kim, N.-G., Lee, I., Choi, H.-S., Li, X.-Y., et al. (2011). p53 and microRNA-34 are suppressors of canonical Wnt signaling. *Sci. Signal* 4, ra71. doi: 10.1126/scisignal.2001744

Kishore, S., Jaskiewicz, L., Burger, L., Hausser, J., Khorshid, M., and Zavolan, M. (2011). A quantitative analysis of CLIP methods for identifying binding sites of RNA-binding proteins. *Nat. Methods* 8, 559–564. doi: 10.1038/nmeth.1608

Lagos-Quintana, M., Rauhut, R., Lendeckel, W., and Tuschl, T. (2001). Identification of novel genes coding for small expressed RNAs. *Science* 294, 853–858. doi: 10.1126/science.1064921

Le, M. T. N., Shyh-Chang, N., Khaw, S. L., Chin, L., Teh, C., Tay, J., et al. (2011). Conserved regulation of p53 network dosage by microRNA-125b occurs through evolving miRNA-target gene pairs. *PLoS Genet*. 7:e1002242. doi: 10.1371/journal.pgen.1002242

Lewis, B. P., Burge, C. B., and Bartel, D. P. (2005). Conserved seed pairing, often flanked by adenosines, indicates that thousands of human genes are microRNA targets. *Cell* 120, 15–20. doi: 10.1016/j.cell.2004.12.035

Lim, L. P., Lau, N. C., Garrett-Engele, P., Grimson, A., Schelter, J. M., Castle, J., et al. (2005). Microarray analysis shows that some microRNAs downregulate large numbers of target mRNAs. *Nature* 433, 769–773. doi: 10.1038/nature03315

Linsley, P. S., Schelter, J., Burchard, J., Kibukawa, M., Martin, M. M., Bartz, S. R., et al. (2007). Transcripts targeted by the microRNA-16 family cooperatively regulate cell cycle progression. *Mol. Cell. Biol.* 27, 2240–2252. doi: 10.1128/MCB.02005-06

Liu, H., Yue, D., Chen, Y., Gao, S.-J., and Huang, Y. (2010). Improving performance of mammalian microRNA target prediction. *BMC Bioinformatics* 11:476. doi: 10.1186/1471-2105-11-476

Liu, N., Bezprozvannaya, S., Williams, A. H., Qi, X., Richardson, J. A., Bassel-Duby, R., et al. (2008). microRNA-133a regulates cardiomyocyte proliferation and suppresses smooth muscle gene expression in the heart. *Genes Dev*. 22, 3242–3254. doi: 10.1101/gad.1738708

Marioni, J. C., Mason, C. E., Mane, S. M., Stephens, M., and Gilad, Y. (2008). RNA-seq: an assessment of technical reproducibility and comparison with gene expression arrays. *Genome Res*. 18, 1509–1517. doi: 10.1101/gr.079558.108

Mattoon, D. R., and Schweitzer, B. (2009). Profiling protein interaction networks with functional protein microarrays. *Methods Mol. Biol*. 563, 63–74. doi: 10.1007/978-1-60761-175-2_4

Melton, L. (2004). Protein arrays: proteomics in multiplex. *Nature* 429, 101–107. doi: 10.1038/429101a

Mercola, M., Colas, A., and Willems, E. (2013). Induced pluripotent stem cells in cardiovascular drug discovery. *Circ. Res*. 112, 534–548. doi: 10.1161/CIRCRESAHA.111.250266

Miska, E. A., Alvarez-Saavedra, E., Abbott, A. L., Lau, N. C., Hellman, A. B., McGonagle, S. M., et al. (2007). Most *Caenorhabditis elegans* microRNAs are individually not essential for development or viability. *PLoS Genet*. 3:e215. doi: 10.1371/journal.pgen.0030215

Moffat, J., Grueneberg, D. A., Yang, X., Kim, S. Y., Kloepfer, A. M., Hinkle, G., et al. (2006). A lentiviral RNAi library for human and mouse genes applied to an arrayed viral high-content screen. *Cell* 124, 1283–1298. doi: 10.1016/j.cell.2006.01.040

Nsair, A., and MacLellan, W. R. (2011). Induced pluripotent stem cells for regenerative cardiovascular therapies and biomedical discovery. *Adv. Drug Deliv. Rev*. 63, 324–330. doi: 10.1016/j.addr.2011.01.013

Overington, J. P., Al-Lazikani, B., and Hopkins, A. L. (2006). How many drug targets are there? *Nat. Rev. Drug Discov.* 5, 993–996. doi: 10.1038/nrd2199

Parsons, B. D., Schindler, A., Evans, D. H., and Foley, E. (2009). A direct phenotypic comparison of siRNA pools and multiple individual duplexes in a functional assay. *PLoS ONE* 4:e8471. doi: 10.1371/journal.pone.0008471

Poell, J. B., van Haastert, R. J., de Gunst, T., Schultz, I. J., Gommans, W. M., Verheul, M., et al. (2012). A functional screen identifies specific microRNAs capable of inhibiting human melanoma cell viability. *PLoS ONE* 7:e43569. doi: 10.1371/journal.pone.0043569

Rix, U., and Superti-Furga, G. (2009). Target profiling of small molecules by chemical proteomics. *Nat. Chem. Biol*. 5, 616–624. doi: 10.1038/nchembio.216

Sass, S., Dietmann, S., Burk, U. C., Brabletz, S., Lutter, D., Kowarsch, A., et al. (2011). MicroRNAs coordinately regulate protein complexes. *BMC Syst. Biol.* 5:136. doi: 10.1186/1752-0509-5-136

Schwarz, D. S., Hutvágner, G., Du, T., Xu, Z., Aronin, N., and Zamore, P. D. (2003). Asymmetry in the assembly of the RNAi enzyme complex. *Cell* 115, 199–208. doi: 10.1016/S0092-8674(03)00759-1

Selbach, M., Schwanhäusser, B., Thierfelder, N., Fang, Z., Khanin, R., and Rajewsky, N. (2008). Widespread changes in protein synthesis induced by microRNAs. *Nature* 455, 58–63. doi: 10.1038/nature07228

Shin, C., Nam, J.-W., Farh, K. K.-H., Chiang, H. R., Shkumatava, A., and Bartel, D. P. (2010). Expanding the MicroRNA Targeting Code: functional sites with centered pairing. *Mol. Cell* 38, 789–802. doi: 10.1016/j.molcel.2010.06.005

Shirdel, E. A., Xie, W., Mak, T. W., and Jurisica, I. (2011). NAViGaTing the micronome–using multiple microRNA prediction databases to identify signalling pathway-associated microRNAs. *PLoS ONE* 6:e17429. doi: 10.1371/journal.pone.0017429

Shreenivasaiah, P., Kim, D., and Wang, E. (2010). "microRNA regulation of networks of normal and cancer cells," in *Cancer Systems Biology*, ed E. Wang (Boca Raton, FL: CRC Press), 107–123.

Sims, D., Mendes-Pereira, A., Frankum, J., Burgess, D., Cerone, M.-A., Lombardelli, C., et al. (2011). High-throughput RNA interference screening using pooled shRNA libraries and next generation sequencing. *Genome Biol.* 12, R104. doi: 10.1186/gb-2011-12-10-r104

Small, E. M., O'Rourke, J. R., Moresi, V., Sutherland, L. B., McAnally, J., Gerard, R. D., et al. (2010). Regulation of PI3-kinase/Akt signaling by muscle-enriched microRNA-486. *Proc. Natl. Acad. Sci. U.S.A.* 107, 4218–4223. doi: 10.1073/pnas.1000300107

Stark, A., Brennecke, J., Bushati, N., Russell, R. B., and Cohen, S. M. (2005). Animal MicroRNAs confer robustness to gene expression and have a significant impact on 3'UTR evolution. *Cell* 123, 1133–1146. doi: 10.1016/j.cell.2005.11.023

Stockwell, B. R. (2000). Chemical genetics: ligand-based discovery of gene function. *Nat. Rev. Genet*. 1, 116–125. doi: 10.1038/35038557

Thum, T., Gross, C., Fiedler, J., Fischer, T., Kissler, S., Bussen, M., et al. (2008). MicroRNA-21 contributes to myocardial disease by stimulating

MAP kinase signalling in fibroblasts. *Nature* 456, 980–984. doi: 10.1038/nature07511

Van Rooij, E., Sutherland, L. B., Qi, X., Richardson, J. A., Hill, J., and Olson, E. N. (2007). Control of stress-dependent cardiac growth and gene expression by a microRNA. *Science* 316, 575–579. doi: 10.1126/science.1139089

Vinther, J., Hedegaard, M. M., Gardner, P. P., Andersen, J. S., and Arctander, P. (2006). Identification of miRNA targets with stable isotope labeling by amino acids in cell culture. *Nucleic Acids Res.* 34, e107. doi: 10.1093/nar/gkl590

Wang, K.-C., Garmire, L. X., Young, A., Nguyen, P., Trinh, A., Subramaniam, S., et al. (2010). Role of microRNA-23b in flow-regulation of Rb phosphorylation and endothelial cell growth. *Proc. Natl. Acad. Sci. U.S.A.* 107, 3234–3239. doi: 10.1073/pnas.0914825107

Wang, X., and El Naqa, I. M. (2008). Prediction of both conserved and nonconserved microRNA targets in animals. *Bioinformatics* 24, 325–332. doi: 10.1093/bioinformatics/btm595

Wang, Z., Gerstein, M., and Snyder, M. (2009). RNA-Seq: a revolutionary tool for transcriptomics. *Nat. Rev. Genet*. 10, 57–63. doi: 10.1038/nrg2484

Wen, J., Parker, B. J., Jacobsen, A., and Krogh, A. (2011). MicroRNA transfection and AGO-bound CLIP-seq data sets reveal distinct determinants of miRNA action. *RNA* 17, 820–834. doi: 10.1261/rna.2387911

Whitehurst, A. W., Bodemann, B. O., Cardenas, J., Ferguson, D., Girard, L., Peyton, M., et al. (2007). Synthetic lethal screen identification of chemosensitizer loci in cancer cells. *Nature* 446, 815–819. doi: 10.1038/nature05697

Witkos, T., Koscianska, E., and Krzyzosiak, W. (2011). Practical aspects of microRNA target prediction. *Curr. Mol. Med.* 11, 93–109. doi: 10.2174/156652411794859250

Wu, C.-I., Shen, Y., and Tang, T. (2009). Evolution under canalization and the dual roles of microRNAs: a hypothesis. *Genome Res.* 19, 734–743. doi: 10.1101/gr.084640.108

Xia, W., Cao, G., and Shao, N. (2009). Progress in miRNA target prediction and identification. *Sci. China C Life Sci.* 52, 1123–1130. doi: 10.1007/s11427-009-0159-4

Yan, G.-R., Xu, S.-H., Tan, Z.-L., Liu, L., and He, Q.-Y. (2011). Global identification of miR-373-regulated genes in breast cancer by quantitative proteomics. *Proteomics* 11, 912–920. doi: 10.1002/pmic.201000539

Yang, Y., Chaerkady, R., Beer, M. A., Mendell, J. T., and Pandey, A. (2009). Identification of miR-21 targets in breast cancer cells using a quantitative proteomic approach. *Proteomics* 9, 1374–1384. doi: 10.1002/pmic.200800551

Yang, Y., Chaerkady, R., Kandasamy, K., Huang, T.-C., Selvan, L. D. N., Dwivedi, S. B., et al. (2010). Identifying targets of miR-143 using a SILAC-based proteomic approach. *Mol. Biosyst.* 6, 1873–1882. doi: 10.1039/c004401f

Zhang, L., Ding, L., Cheung, T. H., Dong, M.-Q., Chen, J., Sewell, A. K., et al. (2007). Systematic identification of *C. elegans* miRISC proteins, miRNAs, and mRNA targets by their interactions with GW182 proteins AIN-1 and AIN-2. *Mol. Cell* 28, 598–613. doi: 10.1016/j.molcel.2007.09.014

Zhao, Y., Ransom, J. F., Li, A., Vedantham, V., von Drehle, M., Muth, A. N., et al. (2007). Dysregulation of cardiogenesis, cardiac conduction, and cell cycle in mice lacking miRNA-1-2. *Cell* 129, 303–317. doi: 10.1016/j.cell.2007.03.030

Zhou, J., Wang, K.-C., Wu, W., Subramaniam, S., Shyy, J. Y.-J., Chiu, J.-J., et al. (2011). MicroRNA-21 targets peroxisome proliferators-activated receptor-alpha in an autoregulatory loop to modulate flow-induced endothelial inflammation. *Proc. Natl. Acad. Sci. U.S.A.* 108, 10355–10360. doi: 10.1073/pnas.1107052108

Zisoulis, D. G., Lovci, M. T., Wilbert, M. L., Hutt, K. R., Liang, T. Y., Pasquinelli, A. E., et al. (2010). Comprehensive discovery of endogenous Argonaute binding sites in *Caenorhabditis elegans*. *Nat. Struct. Mol. Biol.* 17, 173–179. doi: 10.1038/nsmb.1745

Conflict of Interest Statement: The authors declare that the research was conducted in the absence of any commercial or financial relationships that could be construed as a potential conflict of interest.

Received: 10 May 2013; paper pending published: 20 June 2013; accepted: 02 August 2013; published online: 27 August 2013.

Citation: Lemons D, Maurya MR, Subramaniam S and Mercola M (2013) Developing microRNA screening as a functional genomics tool for disease research. Front. Physiol. ***4****:223. doi: 10.3389/fphys.2013.00223*

This article was submitted to Computational Physiology and Medicine, a section of the journal Frontiers in Physiology.

frontiers in
PHYSIOLOGY

REVIEW ARTICLE
published: 26 August 2013
doi: 10.3389/fphys.2013.00229

Systems biology of platelet-vessel wall interactions

Scott L. Diamond*, Jeremy Purvis, Manash Chatterjee and Matthew H. Flamm

Department of Chemical and Biomolecular Engineering, Institute for Medicine and Engineering, University of Pennsylvania, Philadelphia, PA, USA

Edited by:
Raimond L. Winslow, The Johns Hopkins University, USA

Reviewed by:
Shawn Shadden, University of California, Berkeley, USA
Mark Alber, University of Notre Dame, USA

****Correspondence:***
Scott L. Diamond, Department of Chemical and Biomolecular Engineering, 1024 Vagelos Research Laboratory, University of Pennsylvania, Philadelphia, PA 19104, USA
e-mail: sld@seas.upenn.edu

Blood systems biology seeks to quantify outside-in signaling as platelets respond to numerous external stimuli, typically under flow conditions. Platelets can activate via GPVI collagen receptor and numerous G-protein coupled receptors (GPCRs) responsive to ADP, thromboxane, thrombin, and prostacyclin. A bottom-up ODE approach allowed prediction of platelet calcium and phosphoinositides following $P2Y_1$ activation with ADP, either for a population average or single cell stochastic behavior. The *homeostasis assumption* (i.e., a resting platelet stays resting until activated) was particularly useful in finding global steady states for these large metabolic networks. Alternatively, a top-down approach involving *Pairwise Agonist Scanning* (PAS) allowed large data sets of measured calcium mobilization to predict an individual's platelet responses. The data was used to train neural network (NN) models of signaling to predict patient-specific responses to combinatorial stimulation. A kinetic description of platelet signaling then allows prediction of inside-out activation of platelets as they experience the complex biochemical milieu at the site of thrombosis. Multiscale lattice kinetic Monte Carlo (LKMC) utilizes these detailed descriptions of platelet signaling under flow conditions where released soluble species are solved by finite element method and the flow field around the growing thrombus is updated using computational fluid dynamics or lattice Boltzmann method. Since hemodynamic effects are included in a multiscale approach, thrombosis can then be predicted under arterial and venous thrombotic conditions for various anatomical geometries. Such systems biology approaches accommodate the effect of anti-platelet pharmacological intervention where COX1 pathways or ADP signaling are modulated in a patient-specific manner.

Keywords: platelet, thrombosis, hemodynamic, ADP, thromboxane

INTRODUCTION

A systems biology approach for platelets seeks to predict kinetic processes during clotting or bleeding episodes. A multiscale modeling framework should facilitate the bridging of genomics/proteomics studies with platelet phenotype and vessel pathophysiology under hemodynamic conditions. Such a framework should quantify risks and severity of such episodes for a given phenotype/genotype as well as the safety and efficacy of pharmacological intervention.

PLATELET GENOMICS

Genome-wide association studies (GWAS) have found rather modest associations of SNPs (single nucleotide polymorphisms) with thrombosis or vascular disease (Wellcome Trust Case Control Consortium, 2007; Ouwehand, 2007). A GWAS focused specifically on coronary artery disease (CAD) identified 4 loci linked to CAD (Samani et al., 2007), but mechanistic understanding of these SNPs awaits exploration and may not necessarily be platelet-linked. Jones et al. (2007) measured platelet response, calcium mobilization, aggregometry, and FACS determination of response to ADP or GPVI activation with collagen-related peptide (CRP) in 506 healthy volunteers to define inter-individual variability. Importantly, SNPs in the GP6 locus were linked to about 35% of the variation in response to CRP. Variability in response to ADP was associated with polymorphisms in the platelet $P2Y_{12}$ receptor (Fontana et al., 2003). However, it currently remains difficult to use GWAS or genotyping information to predict risk for a specific patient. Greliche et al. (2013) conclude from their genome-wide SNP interaction analysis that common SNPs were unlikely to have strong interactive impact on the risk of venous thrombosis. Few if any genomic studies quantitatively predict an individual's blood function during clotting or bleeding disease scenarios under hemodynamic conditions.

PLATELET TRANSCRIPTOME AND PROTEOMICS

Platelets contain a microRNA (miR) pool and a translatable mRNA pool that declines with a platelet's age in the circulation. McRedmond et al. (2004) identified 2928 mRNA species using Affymetrix arrays. Many of the top 50 most abundant platelet mRNAs correlated with secreted or membrane proteins such as β_2-microglobulin, platelet factor 4, factor XIII, GPIb, α_{IIb}, etc. Similarly, Gnatenko et al. (2003) found 2147 mRNA species and Bugert et al. (2003) found 1526 mRNA species in purified platelets. More recent direct sequencing methods identified ~9000 mRNA species in platelets (Bray et al., 2010), more comparable in size to the transcriptome of megakaryocytes. Also, platelets contain a functional spliceosome. For example, the processing of tissue factor (TF) mRNA and translation of TF upon platelet activation was found in activated platelets (Schwertz et al., 2006), although TF activity was only detectable

in sonicated platelet membranes. The human platelet proteome has been examined and an important web-based resource is now available to explore protein-protein interactions within platelets (Boyanova et al., 2011).

Inter-individual variation in platelet reactivity, even in a normal population, has been associated with a number of factors including: female gender, fibrinogen level, ethnicity, inherited variations, and polymorphisms (Hetherington et al., 2005; Bray, 2007). Unfortunately, no single genomic or proteomic factor is a strong predictor of hyper-reactivity in typical subjects and the need for advanced functional phenotyping motivates the development of systems biology tools to quantify blood function.

CLOTTING UNDER FLOW CONDITIONS

Collagen is sufficient to capture and activate platelets under venous wall shear rates (γ_w ~100–200 s^{-1}). In the arterial circulation (γ_w ~1000–2000 s^{-1}), collagen adsorbed von Willebrand factor (vWF) facilitates platelet capture, allowing collagen induced GPVI signaling and subsequent $\alpha_2\beta_1$ and $\alpha_{2b}\beta_3$ activation. Under flow conditions, red blood cells help enrich the platelet concentration by ~3–8× in the plasma layer near the wall. At pathological high shear exposures (>5000 s^{-1}) encountered in severe stenosis, mechanical heart valves, and continuous LVAD pumps, the plasma vWF may undergo structural changes such as a transition from a globular to an extended state (Schneider et al., 2007), likely increasing the availability of A1 domains in the vWF polymer for multivalent contacting with platelet GPIb receptors. Interestingly, severe stenosis and LVAD pumps can lead to an acquired von Willebrand disease, demonstrating the importance of local hemodynamics on the systemic circulation.

GROWTH OF THE PLATELET AGGREGATE VIA AUTOCATALYTIC SIGNALING

Collagen triggers GPVI clustering, leading to rapid phosphorylation of the GPVI-associated Fc receptor by Src family tyrosine kinases. Such phosphotyrosine residues are recognized by Syk, and the binding and activation of Syk activates $PLC_{\gamma 2}$. $PLC_{\gamma 2}$ converts phosphatidylinositol (PI)-4,5-P_2 (PIP_2) to inositol 1,4,5-trisphosphate (1,4,5-IP_3 or IP_3) and diacyclglycerol (DAG). IP_3 opens Ca^{2+} channels in the platelet dense tubular system (DTS). Depletion of DTS Ca^{2+} results in STIM1 activation and binding to Orai1, leading to store operated calcium entry (SOCE). DAG/Ca^{2+} activates protein kinase C (PKC) in platelets, which in turn governs several serine/threonine phosphorylation events.

Beyond the first monolayer of platelets adherent to collagen/VWF, the addition of subsequent layers of platelets to the growing thrombus is strongly potentiated by locally released ADP and thromboxane (TXA_2) as well as locally generated thrombin.

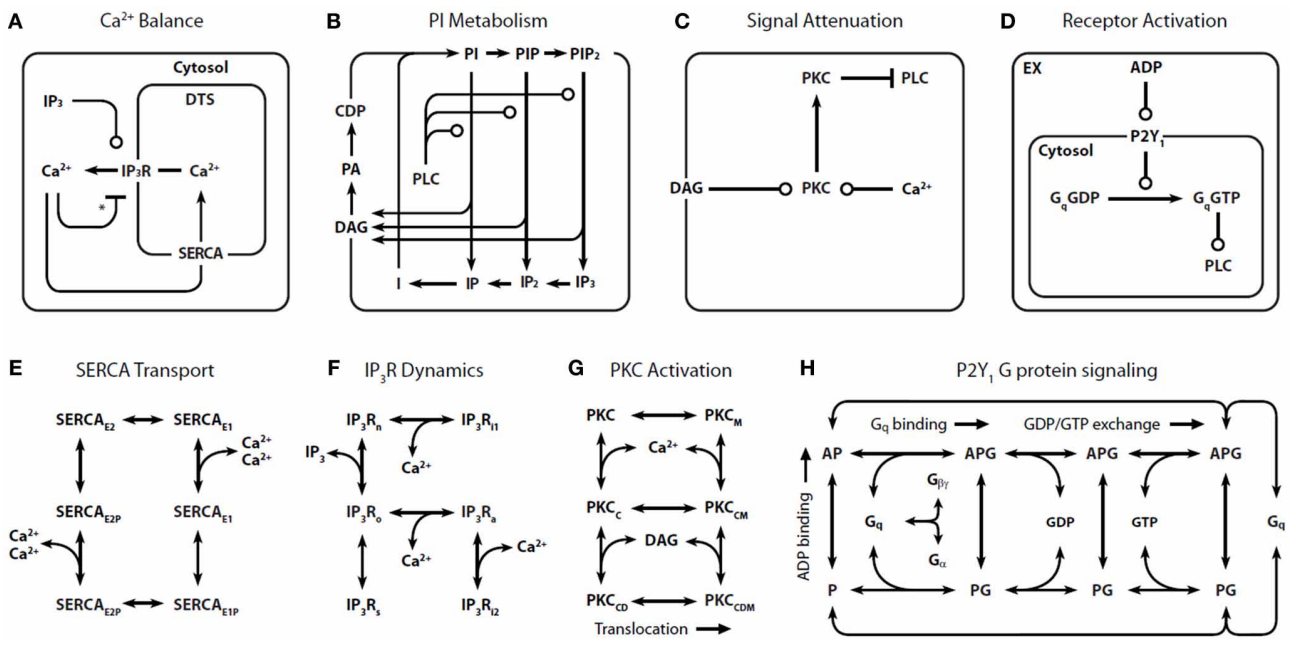

FIGURE 1 | Detailed reaction schemes for platelet signaling modules. Four interconnected models were defined: **(A)** Ca^{2+} module: cytosolic and DTS compartments are separated by the DTS membrane, which contains the IP3R and SERCA. **(B)** Phosphoinositide (PI) module: Membrane-bound PIs are cleaved by PLC-β to form diffusible inositol phosphates and DAG, which are substrates for resynthesis of PIs. **(C)** PKC module: Ca_i^{2+} and DAG activate PKC, which migrates to the plasmamembrane where it phosphorylates PLC-β. **(D)** $P2Y_1$ module: extracellular ADP binds to and activates $P2Y_1$. Active $P2Y_1$ accelerates guanine nucleotide exchange on bound Gq. The Gq·GTP binds and activates PLC-β, which increases the GTPase activity of Gq·GTP. Molecular kinetic descriptions are embedded in the signaling modules for: **(E)** SERCA catalytic cycle (Dode et al., 2002): Subscripts: E1, facing cytosol; E2, facing DTS; P, phosphorylated. **(F)** IP3R dynamics (Sneyd and Dufour, 2002): Subscripts: n, native; i1, inhibited; o, open; a, active; s, shut, i2, inhibited. **(G)** PKC activation: Active kinase is bound to Ca_i^{2+} and DAG and located at the PM. Subscripts: M, located at the PM; C, Ca^{2+}-bound; D, DAG-bound. **(H)** $P2Y_1$ activation module: Rate equations describing the interactions among ADP, P2Y1, and Gq were modeled according to the ternary complex model described in Kinzer-Ursem and Linderman (2007). Abbreviations: A, ADP; P, P2Y1; G, Gq. *Ca^{2+} both activates and inhibits IP3R.

ADP activates $P2Y_1$ and $P2Y_{12}$ while TXA_2 activates the TP receptor and thrombin cleaves PAR1 and PAR4. Activation of a GPCR causes an exchange of GTP for GDP on the α subunit of the G protein and dissociation of the α and βγ subunits. Both these units in turn interact with secondary effectors such as PLCβ and adenylate cyclase. Human platelets express at least 10 forms of Gα (including members of the Gq, Gi, G12, and Gs families) (Brass et al., 2006; Offermanns, 2006). Thrombin, ADP, and TXA_2 activate PLCβ via Gq. PLCβ generates IP_3 from membrane PIP2. Rising Ca^{2+} levels activate the Ras family member, Rap1B via Cal-DAG GEF. Rap1B activation is a precursor to $\alpha_{IIb}\beta_3$ activation and allows the platelets to form aggregates with other platelets through fibrinogen cross-bridging. Ca^{2+}-dependent signaling drives myosin light chain kinase and activation of GTP binding proteins of the Rho family (Klages et al., 1999). Rho activation in turn activates kinases like p160ROCK and 5 LIM-kinase that can phosphorylate myosin light chain kinase and cofilin to regulate actin-dependent cytoskeletal shape changes (Pandey et al., 2006).

Endothelial derived prostacyclin (PGI_2) binds the IP receptor and causes Gs mediated increase in adenyl cyclase activity. Also, NO from the endothelium and platelets can activate guanylate cyclase resulting in elevated cGMP levels that subsequently inhibit the hydrolysis of cAMP by intracellular phosphodiesterases. Taken together these mechanisms elevate intracellular cAMP levels, which strongly downregulate platelet signaling. Agonists coupled to Gi family members inhibit cAMP production in platelets, thus allowing activation to proceed unhindered (Yang

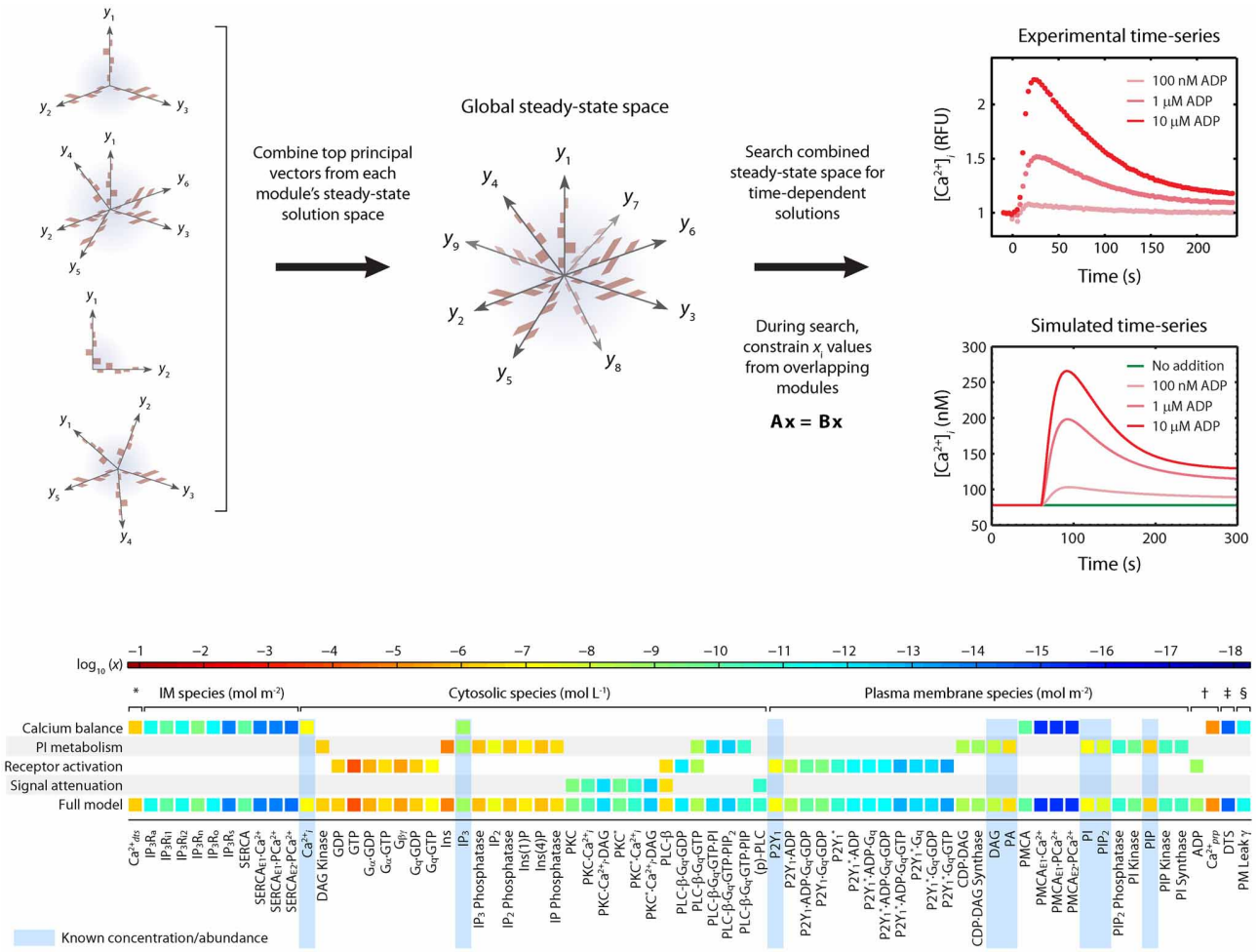

FIGURE 2 | Homeostasis requirement: Assembly of full model from steady-state modules using principle component analysis (PCA). The full model is assembled by combining PCA-reduced, steady-state solution spaces from each module into a combined steady state solution space. This global space is searched for full-length, steady-state solution vectors that satisfy both the steady state requirements of each module and the desired time-dependent properties when the steady-state is perturbed. A simple linear constraint is imposed for every pair of modules that share a common molecule c_i to ensure that steady state solutions are consistent. To assemble the platelet signaling model, a set of 16 PC vectors representing all 72 unknown variables in the model were used as search directions in a global optimization routine. The global solution space was searched for models with accurate dynamic behavior using experimental time-series data for ADP-stimulated Ca^{2+} release. Species are grouped according to compartment. Color values correspond to molar concentrations (mol/L or mol/m^2) or as indicated: *DTS species (mol L^{-1}). †Extracellular species (mol L^{-1}). ‡DTS volume (L). §PM leak conductance/area (S m^{-2}).

et al., 2002). Additionally the βγ subunits of these receptors can activate PLCβ and the γ isoform of PI3K. The effectors for PI3K include Rap1b and Akt (Woulfe et al., 2002).

ADP is stored in platelet dense granules and is released upon activation. $P2Y_1$ and $P2Y_{12}$ are the primary receptors for this agonist. $P2Y_1$ is Gq coupled and signaling through this receptor causes Ca^{2+} mobilization, shape change, and thromboxane generation. $P2Y_{12}$ is the target of the commonly used anti-platelet drug Plavix, and is a Gi2 coupled receptor that inhibits cAMP production in platelets.

Thrombin is a potent platelet agonist that causes fast mobilization of intracellular Ca^{2+}, and activation of phospholipase A_2 and subsequent thromboxane generation (Offermanns et al., 1997). Also, thrombin can trigger Rho dependent signaling pathways in platelets (Moers et al., 2003), that contribute to actin modeling and shape change. Thrombin signals through the protease-activated receptor (PAR) family of GPCRs. PAR1 and PAR4 are expressed on human platelets, while PAR3 and PAR4 are expressed on mouse platelets. Thrombin cleaves the N-terminus of these receptors, exposing a new N-terminus that serves as a tethered ligand for these receptors. Synthetic peptides are able to selectively activate these receptors and mimic the actions of thrombin (for example, SFLLRN for PAR1, and AYPGKF for PAR4). Kinetic studies have shown that the human platelet response to thrombin is biphasic and involves first signaling through PAR1 and subsequent signaling through PAR4 (Covic et al., 2000). In mouse platelets signaling occurs primarily via PAR4, and is facilitated by PAR3. In addition to the PAR receptors, GP1bα has high affinity for thrombin. Absence of GP1bα reduces responses to low doses of thrombin and diminishes PAR1 signaling, suggesting that this receptor facilitates signaling through the PARs (Dormann et al., 2000). Ca^{2+} mobilization also activates phospholipase A_2 (PLA_2), which in turn converts membrane phospholipids to arachidonic Acid. TXA_2 is produced from membrane arachidonate by the aspirin sensitive cyclooxygenase (COX-1) enzyme. TXA_2 causes Ca^{2+} mobilization, aggregation, secretion, phosphoinositide hydrolysis, and protein phosphorylation. TXA2 can diffuse across the membrane and activate nearby platelets, but its activity is limited by the molecule's short half life (∼30 s).

SYSTEMS BIOLOGY MODELS OF PLATELET-VESSEL WALL INTERACTIONS

BOTTOM-UP MODEL OF ADP ACTIVATION OF $P2Y_1$ RECEPTOR

In our representation of $P2Y_1$ activation (**Figure 1**) (Purvis et al., 2008), binding of extracellular ADP to P2Y1 leads to activation of Gq through GDP/GTP exchange reactions. Gq·GTP is a substrate for GTPase activating proteins (GAPs) such as PLC-β and RGS4, which can accelerate Gq·GTP hydrolysis over 1000-fold. Although other ADP receptors are involved in platelet Ca^{2+} signaling (e.g., $P2X_1$ and $P2Y_{12}$), the $P2Y_1$ receptor (∼150 copies/platelet) contributes 90% of the Ca^{2+} signal.

Because of the inherent complexity in a model of this size, we constructed four signaling "modules": (1) Ca^{2+} release and uptake (**Figure 1A**), (2) phosphoinositide (PI) metabolism (**Figure 1B**), (3) PKC regulation of phospholipase C-β (PLC-β) (**Figure 1C**), and (4) P2Y1 G-protein signaling (**Figure 1D**). These modules use previously validated or data-consistent kinetic networks for SERCA, IP3-Receptor, PKC translocation, and GPCR signaling (**Figures 1E–H**).

Assembling the four modules together results in a global ODE model that has 77 reactions, 132 fixed kinetic rate constants, and 70 species. Since the reaction network (**Figure 1**) and the kinetic parameters are fixed, the reaction topology of the model is also fixed. Such a model takes the general form: $d\boldsymbol{c}/dt = F(\boldsymbol{c})$ and $\boldsymbol{c}(t = 0) = \boldsymbol{c}_o$ where $\boldsymbol{c}$ is a vector of all species concentrations and $\boldsymbol{c}_o$ is a specified initial condition vector at $t = 0$.

To determine appropriate sets of $\boldsymbol{c}_o$ that are suitable for use in modeling platelets, a challenge exists that the copy number of each species in a resting platelet is not known. Imposing a *homeostasis assumption* results in powerful tool to define a set of acceptable $\boldsymbol{c}_o$ vectors. The homeostasis assumption states that a resting platelet remains resting until activated. This means that an acceptable initial condition $\boldsymbol{c}_o$ also represents a steady state for the system and will satisfy the equation $d\boldsymbol{c}/dt = 0$. Finding a global $\boldsymbol{c}_o$ involves assembling the steady state solutions of each module (**Figure 2**).

The first phase of the method involves generating a compact representation of the steady-state solutions for each module. First, conservative bounds are chosen for $\boldsymbol{c}$ based on physiological and practical considerations. Also, because molecular concentrations can span several orders of magnitude, it is most efficient to delineate this range of values on a logarithmic scale rather

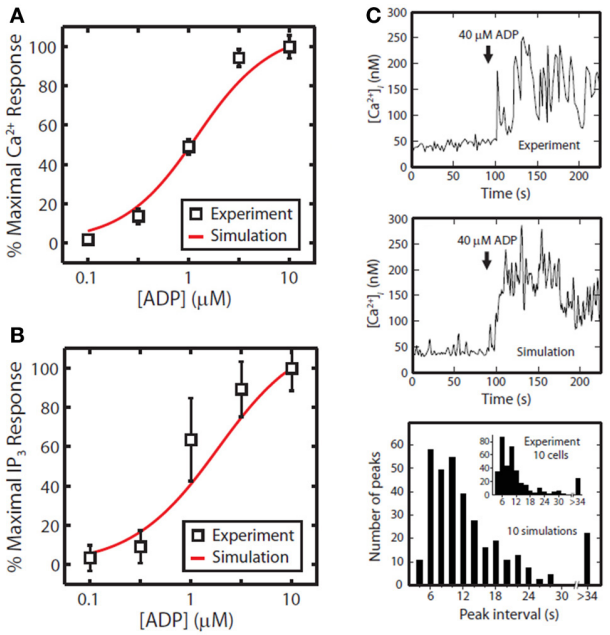

FIGURE 3 | Tests of P2Y1 signaling model. ADP dose response for the full platelet model from 100 nM to 10 μM ADP for calcium mobilization **(A)** or IP3 generation **(B)**. Stochastic simulation of a single platelet **(C)**. A single, fura-2-loaded platelet was immobilized on a fibrinogen-coated coverslip and activated with 40 μM ADP at $t = 90$ [Ca^{2+} trace from Heemskerk et al. (2001)]. After 90 s of simulated rest, the platelet model was activated by setting extracellular [ADP] to 40 μM. Simulated interval times were binned in 2 s increments for direct comparison with experiment (*inset*).

than a linear scale. Once the sampling distribution for **c** has been defined, steady-state solutions ($\boldsymbol{c}_o = \boldsymbol{c}_{ss}$) for each module are calculated using fixed kinetic parameters for each reaction in the module. For non-oscillating systems, steady-state solutions may be obtained by simulating the system until equilibrium is reached (i.e., until $d\boldsymbol{c}/dt = 0$). In the third step, a large collection of steady-state solutions for each module is subjected to principal component analysis (PCA) (Purvis et al., 2009). PCA is then used to transform these points to a new coordinate set that optimally covers the space of steady-state solutions using the fewest number of dimensions. For example, if two molecule concentrations in the steady-state space are highly correlated due to participation in the same reaction, PCA will locate a single dimension to represent each pair of points in the transformed space. Ultimately, these new dimensions will be combined across all modules to search for global solutions that lie in the steady-state space for the fully combined network. Since PCA is a linear method, a steady-state solution space that is highly nonlinear may require more principal component vectors to accurately estimate the solutions. The reduction procedure is shown for the human platelet model comprising 4 interlinked signaling modules (**Figure 2**). For this step, we generated more than 10^9 sets of initial guesses ($\boldsymbol{c}_o$) for each module, computed the initial value problem for each $\boldsymbol{c}_o$ until a steady state was reached ($d\boldsymbol{c}/dt \approx 0$), and selected only

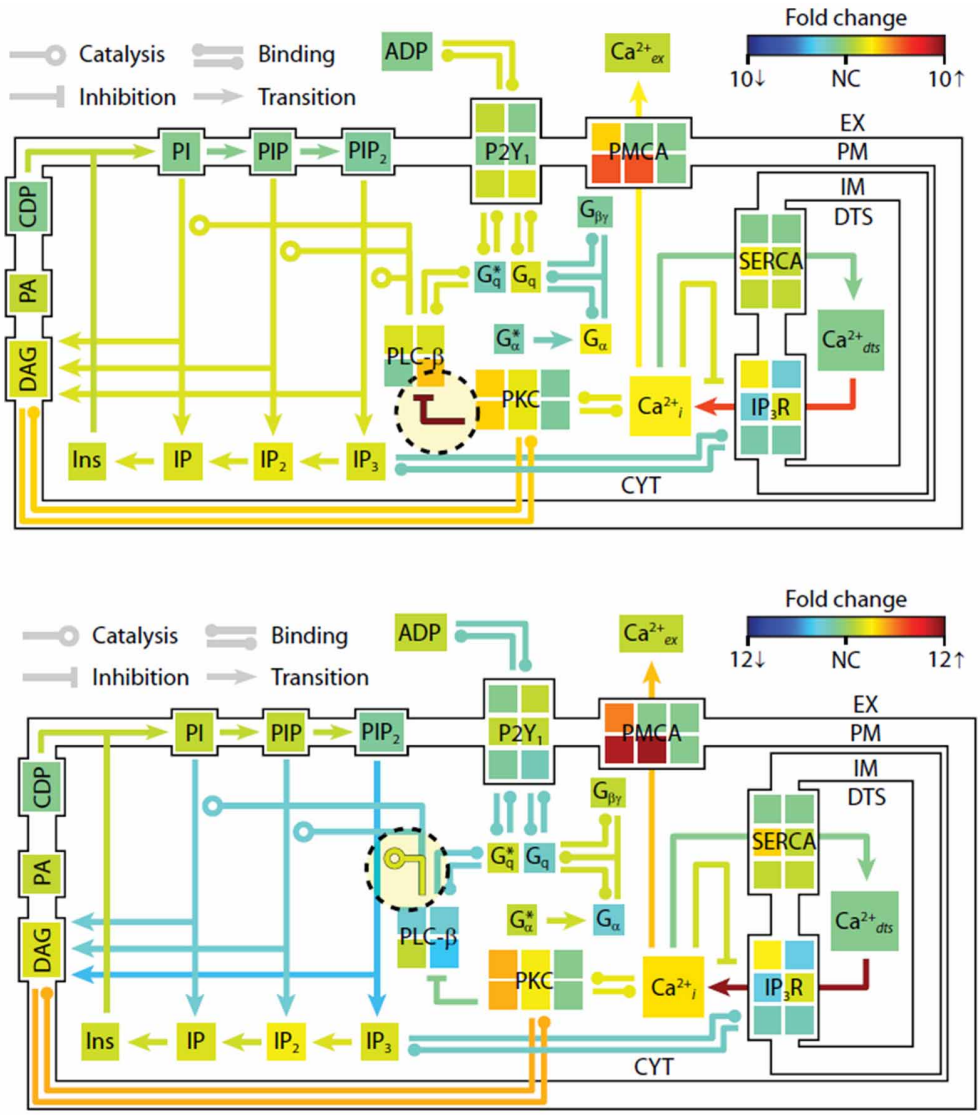

FIGURE 4 | Shifts in steady-state profiles caused by kinetic perturbations. The steady-state platelet model was perturbed by changing selected kinetic parameters (±10-fold) and simulating for 1 h. After approaching a new steady state, the model concentrations and fluxes were determined relative to their original steady-state values and colored according to fold-change. Green indicates no change (NC) relative to initial flux/concentration. Red indicates a relative increase and blue indicates a relative decrease. Note that the color scale in each panel is normalized separately to maximize distinctions in fold change. New steady states were achieved after (**top**) 10-fold decrease in PKC-mediated inhibition of PLC-β, and (**bottom**) 10-fold increase in PIP2 hydrolysis (10-fold increase in *kcat* of hydrolysis). *, active state.

those steady states ($\boldsymbol{c_{ss}}$) that were consistent with known concentrations (i.e., $[Ca^{2+}]_o$ ~100 nM). Interestingly, only a small fraction of initial guesses produce steady-state solutions that are also consistent with known concentration values. For example, it was shown that only 50,000 of 10^9 initial guesses (0.005%) in the Ca^{2+} balance module (**Figure 1A**) met both requirements and were suitable for further analysis. This observation shows that the kinetic topology of these molecular networks places very strong constraints on the range of concentrations that can exist at steady state. In biological terms, this suggests that fixed kinetic properties at the molecular level (e.g., IP3R and SERCA kinetics) can affect not only the dynamical features of a biochemical system but can also determine the abundance of chemical species and the compartmental structures that contain them. A fully assembled initial condition vector results (bottom, **Figure 2**) results in new hypotheses about allowable concentrations and ratios of concentrations (i.e., IP3/SERCA ratio is very small). The allowed $\boldsymbol{c_o} = \boldsymbol{c_{ss}}$ is consistent with the known resting levels of Ca2+, IP_3, P2Y1, DAG, PA, PI, PIP_2, and PIP (bottom, **Figure 2**) as well as the stimulated response of platelets to increasing amounts of ADP (right, **Figure 2**). With a global simulation of P2Y1 signaling, it is possible to simulate the ADP dose-response of calcium mobilization and IP3 generation in platelets as well as the mobilization of intracellular calcium in a single platelet due to stochastic fluctuations (**Figure 3**).

Since many initial condition vectors can be found to allow a resting platelet to remain resting and then respond appropriately to stimulation, investigation of these multiple steady states and associated cell responses can allow an *ad-hoc* sensitivity analysis. Some species (flexible nodes) may vary widely in the allowed initial condition vectors but have little effect on system response. In contrast, other species (rigid nodes) may be forced to take on values in a very narrow range due to the kinetic constraints of the problem.

To examine the changes in steady-state properties caused by kinetic perturbations in the P2Y1 model, we altered the rates of important regulatory reactions and observed the system response to each perturbation. Each perturbation cause a brief adjustment phase lasting ~200 s followed by a more gradual phase characterized by a new steady-state profile. After 1 h of simulated time, steady-state concentrations and reaction fluxes were quantified relative to their original steady-state levels (**Figure 4**). In a computational perturbation, the inhibition of phospholipase C-β (PLC-β) activity by PKC was reduced 10-fold. Since PKC has a negative-feedback role in suppressing the platelet-stimulating activity of PLC-β, this perturbation caused a 2-fold increase

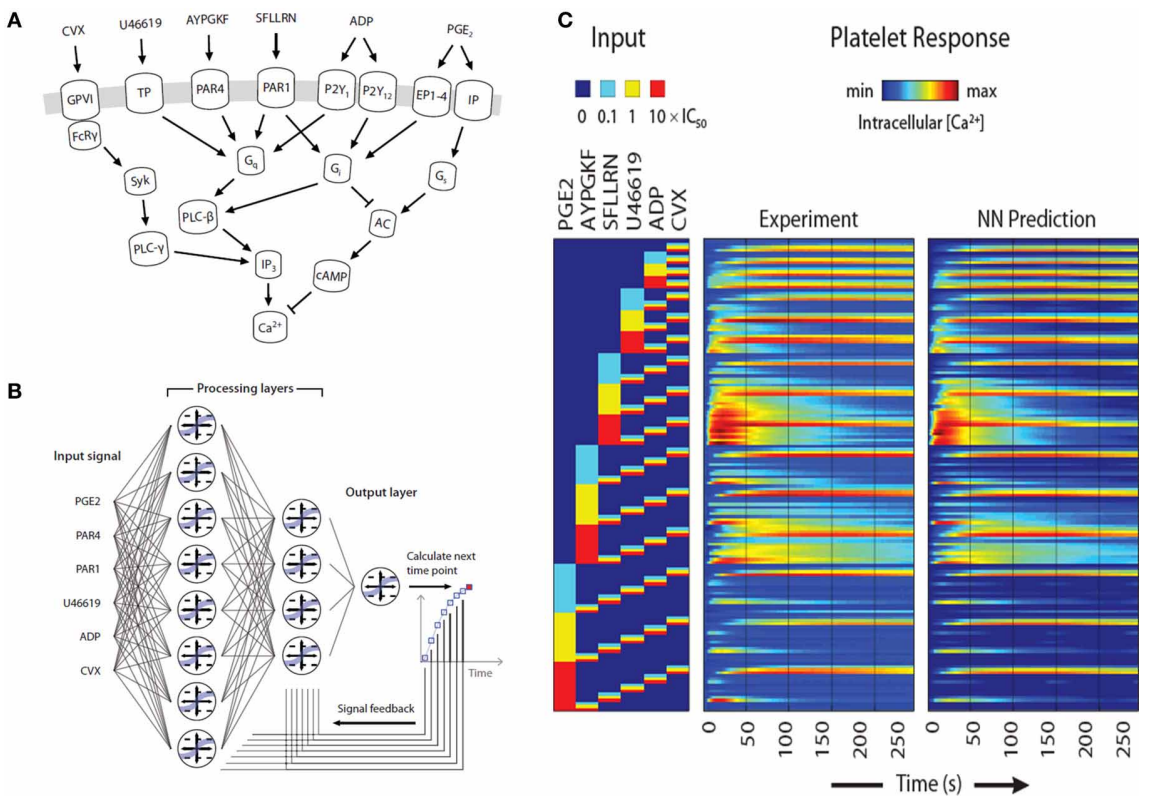

FIGURE 5 | Pairwise agonist scanning to predict global calcium response in human platelets. (A) Simplified schematic of signaling pathways examined in this study that converge on intracellular calcium release in human platelets. **(B)** Dynamic NN model used to train platelet response to combinatorial agonist activation. A sequence of input signals representing agonist concentrations is introduced to the network at each time point. Processing layers integrate input values with feedback signals to predict the next time point. **(C)** A total of 154 calcium traces were measured for single and pairwise activation using 6 different agonists ("Experiment") and used for neural network training. The NN training accurately predicted ("NN Prediction") the training data.

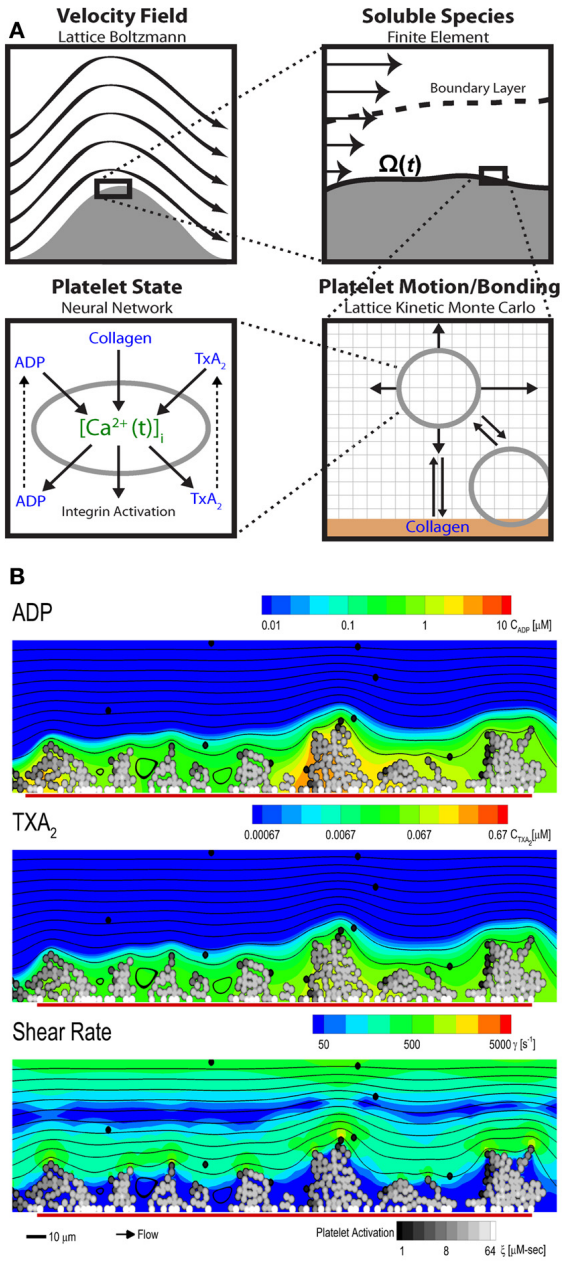

FIGURE 6 | Multiscale modeling. The multiscale model has four main components **(A)** fluid flow, transport of soluble species, motion and binding of platelets, and the activation state of each platelet. The fluid flow is perturbed by the growing clot and is determined using the lattice Boltzmann method. The released soluble agonists form a boundary layer in the flow, and this process is determined using the finite element method. Platelet motion and bonding are simulated with lattice kinetic Monte Carlo. Platelet activation state is estimated from the history of intracellular calcium concentration, which is determined by a neural network model. **(B)** Multiscale simulation of patient-specific platelet deposition under flow for a specific donor and PAS-trained neural network of calcium signaling. Platelet activation (black, unactivated; white, activated) and deposition at 500 s (inlet wall shear rate, 200 s^{-1}) showing released ADP (top) and TXA_2 (middle) and perturbation of the flow field (bottom). Flow: left to right (streamlines, black lines); surface collagen (250 μm long): red bar.

in steady-state PIP_2 hydrolysis, elevated IP_3 concentration, and accelerated Ca^{2+} release. This was a compensatory effect caused by the negative feedback loop involving Ca^{2+}-regulated activity of PKC, a resulting new hypothesis that can be probed experimentally. In another example, increasing the hydrolytic activity of PLC-β for the substrate PIP_2 by 10-fold caused an expected stimulatory effect, raising intracellular calcium and steady-state levels of cytosolic inositol phosphates (IP_3, IP_2, and IP) between 2- and 3-fold. Interestingly, reaction fluxes for phosphoinositide hydrolysis were diminished, possibly due to substrate depletion. Taken together, these examples illustrate the system-wide effects of perturbations in the kinetic rate processes. The procedure could easily be extended to examine multiple simultaneous perturbations in both reaction rates and steady-state concentrations. In future applications of this approach, genomic or proteomic information of multiple perturbations could be used to help predict platelet signaling phenotypes.

TOP-DOWN SIGNALING APPROACHES

The prior example required about 200 parameters to describe P2Y1 signaling. In contrast, *top-down* approaches in systems biology allow the construction of large data sets to predict system response without precise knowledge of intracellular pathways. During thrombosis, platelets respond simultaneously to collagen activation of GPVI and $\alpha_2\beta_1$, ADP activation of $P2Y_1$, $P2Y_{12}$, and $P2X_1$, thromboxane activation of TP, and thrombin activation of PAR1 and PAR4, while NO and PGI_2 dampen responsiveness (**Figure 5A**). We have developed a 384-well plate assay to measure platelet calcium mobilization in response to single and pairwise agonist stimulation at 0.1, 1, and $10XEC_{50}$, a method termed PAS (Chatterjee et al., 2010). We developed a six agonist probe set for activation of $P2Y_1$/$P2Y_{12}$, PAR1, PAR4, TP, IP, and GPVI pathways and measured the EC_{50} for each agonist (ADP, EC_{50} = 1.17 μM; SFLLRN, 15.2 μM; AYPGKF, 112 μM; U46619, 1.2 μM; PGE_2, 25 μM; and convulxin, 0.005 μM). To capture how the 6 molecular signals are processed by activated platelet, we trained a 2-layer neural network (NN) model (**Figure 5B**) that predicted time-course behavior of the training set of pairwise combinations of the six agonists (**Figure 5C**). We used a nonlinear autoregressive network with exogenous inputs (NARX) model to predict successive time points from all 154 Ca^{2+} release curves gathered by experiment. The NN model, which was trained on pairwise agonist stimulation with both agonists added simultaneously, was successful in predicting response to sequential addition of agonists and ternary agonist stimulation (Chatterjee et al., 2010). With 4077 NN simulations fully spanning the 6 dimensional agonist space, 45 combinations of 4, 5, and 6 agonists (predicted to range from strong synergism to strong antagonism) were selected and confirmed experimentally ($R = 0.88$), revealing a highly synergistic condition of high U46619/PGE_2 ratio, consistent with the known thrombotic risk of COX-2 therapy.

Furthermore, PAS provided 135 pairwise synergy values that allowed a unique phenotypic scoring and differentiation of individuals. We measured synergy vectors for 10 healthy donors in replicate. From clustering analysis, 7 of 10 donors self-clustered when tested twice in a 2-week period, revealing at least two major

phenotype classes. Thus, PAS offers a sensitive, patient-specific experimental and computational platform for understanding how a cell integrates many inputs. The trained NN is ideal for use in a multiscale model of clotting under flow conditions.

PLATELET INTERACTIONS WITH THE VESSEL WALL

The multiscale systems biology model accommodates platelet signaling, platelet adhesion to collagen and other activated platelets, release of soluble agonists, thrombus growth, and distortion of the prevailing flow field (**Figure 6A**). The lattice Boltzmann (LB) method is used to solve for the velocity field of the fluid. Platelets in the growing aggregate release ADP and TXA2 into the fluid, and a boundary layer is formed with the flow. The dynamics of this process are determined with a finite element method solution of the convection-diffusion-reaction equation for each of the soluble species, ADP and TXA_2. Platelets move in the fluid by convection and RBC-augmented dispersion. They also bind to the collagen surface as well as previously bound platelets. The motion and binding of platelets is simulated using the convective lattice kinetic Monte Carlo (LKMC) algorithm validated for stochastic convective-diffusive particle transport (Flamm et al., 2009, 2011, 2012). The level of integrin activation and associated adhesiveness for each platelet is related to the cumulative intracellular calcium concentration. The intracellular calcium concentration is determined using a NN trained on a specifc patient's platelet PAS phenotyping experiment. Using this multiscale approach, Multiscale simulations predicted the density of platelets adherent to the surface, platelet activation states, as well as the spatiotemporal dynamics of ADP and TXA_2 release, morphology of the growing aggregate, and the distribution of shear along the solid-fluid boundary (**Figure 6B**). Platelets stick to the collagen surface and release ADP and TXA_2 which forms a boundary layer extending up to 10 μm from the thrombus. Boundary layer concentrations of up to 10 μM ADP and 0.1 μM TXA_2 were found by simulation. TXA_2 concentrations were found to be sub-physiological (<0.0067 μM or <0.1 xEC_{50}) until a sufficient platelet mass accumulated at the surface after ∼250 s. Boundary layer ADP concentrations were within the effective dynamic range (0.1–10 μM) throughout the simulation. The strong temporal and spatial fluctuations in the concentration of ADP were predominately driven by the short release time (5 s), whereas the longer release time of TXA_2 (100 s) smoothed fluctuations. The shear rate along the solid-fluid boundary became nonuniform during the simulation (5–10-fold increase above 200 s^{-1}) due to surface roughness. At 500 s, the platelet deposit was characterized by platelet clusters 20–30 μm in length, fully consistent with microfluidic measurements of platelet cluster size on collagen at this shear rate (Colace et al., 2011). Platelet accumulation rates on collagen as detected using microfluidic chambers (Maloney et al., 2010) and were highly consistent with simulation predictions for 3 separate donors (each with a trained NN model) in the presence of TXA_2 antagonism (indomethacin or aspirin), ADP antagonism with a $P2Y_1$ inhibitor, or IP activation (with iloprost).

CONCLUSION

For multi-scale modeling of platelet-vessel wall interactions, a given modeling route at each scale has advantages and disadvantages. Top-down models (like NNs) are most easily obtained in a patient-specific manner to describe platelet function, however they typically fail to identify specific intracellular regulators. Bottom-up models (like ODE models) of platelet signaling provide molecular precision but face three challenges: (1) difficulty in parameterization, (2) difficulty in fitting to high dimensional data, and (3) incomplete knowledge. Both NN and ODE models are both relatively fast in terms of computational speed. Lattice kinetic Monte Carlo (LKMC) methods provide a balance of speed and sub-micron spatial precision, particularly for discrete cellular systems over millimeter-scale phenomenon and 100 or 1000s of cells. LKMC methods are also relatively easy to program and facilitate the passing of information with other lattice based methods (like Lattice Boltzman or finite elements). LKMC methods become exceedingly slow for molecular simulations of large ensembles when time steps become impossibly small. For solving 2D flow problems, Lattice Boltzman is relatively fast and easy to implement and has no issues of numerical stability. One of the biggest numerical challenges is solving multi-component, reaction-diffusion problems with spatial gradients. Wall-derived TF triggers coagulation and ∼10–100 PDEs must be solved to calculate thrombin and fibrin levels in a growing thrombus. Solving large PDE systems is especially computationally intensive (days or weeks) and resists parallel processing.

A central goal in blood systems biology is to elucidate the regulatory complexity of cellular signaling across a large ensemble of interacting cells responding to numerous spatiotemporal stimuli in the presence of pharmacological mediators, ideally in a patient-specific and disease-relevant context (i.e., containing hemodynamics). Developing tools to define platelet variations between patients and the relationship of platelet phenotype to prothrombotic or bleeding traits will have significant impact in stratifying patients according to risk. This multiscale approach also makes feasible patient-specific prediction of platelet deposition and drug response in more complex *in vivo* geometries such as stenosis, aneurysms, stented vessels, valves, bifurcations, or vessel rupture (for prediction of bleeding risks) or in geometries encountered in mechanical biomedical devices.

REFERENCES

Boyanova, D., Nilla, S., Birschmann, I., Dandekar, T., and Dittrich, M. (2011). PlateletWeb: a systems biologic analysis of signaling networks in human platelets. *Blood* 119, e22–e34. doi: 10.1182/blood-2011-10-387308

Brass, L. F., Stalker, T. J., Zhu, L., and Woulfe, D. S. (2006). "Signal transduction during platelet plug formation," in *Platelets, 2nd Edn.*, eds D. Alan and M. D. Michelson (Burlington, VT: Academic Press), 1376.

Bray, P. F. (2007). Platelet hyperreactivity: predictive and intrinsic properties. *Hematol. Oncol. Clin. North Am.* 21, 633–645, v-vi. doi: 10.1016/j.hoc.2007.06.002

Bray, P. F., Nagalla, S., Delgrosso, K., Ertel, A., Rigoutsos, I., and McKenzie, S. E. (2010). High throughput sequencing of the human platelet transcriptome. *Blood* 116, 481.

Bugert, P., Dugrillon, A., Gunaydin, A., Eichler, H., and Kluter, H. (2003). Messenger RNA profiling of human platelets by microarray hybridization. *Thromb. Haemost.* 90, 738–748.

Chatterjee, M. S., Purvis, J. E., Brass, L. F., and Diamond, S. L. (2010). Pairwise agonist scanning predicts cellular signaling responses to combinatorial stimuli. *Nat. Biotechnol.* 28, 727–732.

Colace, T., Falls, E., Zheng, X., and Diamond, S. L. (2011). Analysis of

morphology of platelet aggregates formed on collagen under laminar blood flow. *Ann. Biomed. Eng.* 39, 922–929. doi: 10.1007/s10439-010-0182-4

Covic, L., Gresser, A. L., and Kuliopulos, A. (2000). Biphasic kinetics of activation and signaling for PAR1 and PAR4 thrombin receptors in platelets. *Biochemistry* 39, 5458–5467.

Dode, L., Vilsen, B., Van Baelen, K., Wuytack, F., Clausen, J. D., and Andersen, J. P. (2002). Dissection of the functional differences between sarco(endo)plasmic reticulum Ca2+-ATPase (SERCA) 1 and 3 isoforms by steady-state and transient kinetic analyses. *J. Biol. Chem.* 277, 45579–45591. doi: 10.1074/jbc.M207778200

Dormann, D., Clemetson, K. J., and Kehrel, B. E. (2000). The GPIb thrombin-binding site is essential for thrombin-induced platelet procoagulant activity. *Blood* 96, 2469–2478.

Flamm, M. H., Colace, T. V., Chatterjee, M. S., Jing, H., Zhou, S., Jaeger, D., et al. (2012). Multiscale prediction of patient-specific platelet function under flow. *Blood* 120, 190–198. doi: 10.1182/blood-2011-10-388140

Flamm, M. H., Diamond, S. L., and Sinno, T. (2009). Lattice kinetic Monte Carlo simulations of convective-diffusive systems. *J. Chem. Phys.* 130, 094904. doi: 10.1063/1.3078518

Flamm, M. H., Sinno, T., and Diamond, S. L. (2011). Simulation of aggregating particles in complex flows by the lattice kinetic Monte Carlo method. *J. Chem. Phys.* 134, 034905. doi: 10.1063/1.3521395

Fontana, P., Dupont, A., Gandrille, S., Bachelot-Loza, C., Reny, J. L., Aiach, M., et al. (2003). Adenosine diphosphate-induced platelet aggregation is associated with P2Y12 gene sequence variations in healthy subjects. *Circulation* 108, 989–995. doi: 10.1161/01.CIR.0000085073.69189.88

Gnatenko, D. V., Dunn, J. J., McCorkle, S. R., Weissmann, D., Perrotta, P. L., and Bahou, W. F. (2003). Transcript profiling of human platelets using microarray and serial analysis of gene expression. *Blood* 101, 2285–2293. doi: 10.1182/blood-2002-09-2797

Greliche, N., Germain, M., Lambert, J. C., Cohen, W., Bertrand, M., Dupuis, A. M., et al. (2013). A genome-wide search for common SNP x SNP interactions on the risk of venous thrombosis. *BMC Med. Genet.* 14:36. doi: 10.1186/1471-2350-14-36

Heemskerk, J. W., Willems, G. M., Rook, M. B., and Sage, S. O. (2001). Ragged spiking of free calcium in ADP-stimulated human platelets: regulation of puff-like calcium signals *in vitro* and *ex vivo*. *J. Physiol.* 535(Pt 3), 625–635. doi: 10.1111/j.1469-7793.2001.00625.x

Hetherington, S. L., Singh, R. K., Lodwick, D., Thompson, J. R., Goodall, A. H., and Samani, N. J. (2005). Dimorphism in the P2Y1 ADP receptor gene is associated with increased platelet activation response to ADP. *Arterioscler. Thromb. Vasc. Biol.* 25, 252–257.

Jones, C. I., Garner, S. F., Angenent, W., Bernard, A., Berzuini, C., Burns, P., et al. (2007). Mapping the platelet profile for functional genomic studies and demonstration of the effect size of the GP6 locus. *J. Thromb. Haemost.* 5, 1756–1765. doi: 10.1111/j.1538-7836.2007.02632.x

Kinzer-Ursem, T. L., and Linderman, J. J. (2007). Both ligand- and cell-specific parameters control ligand agonism in a kinetic model of g protein-coupled receptor signaling. *PLoS Comput. Biol.* 3:e6. doi: 10.1371/journal.pcbi.0030006

Klages, B., Brandt, U., Simon, M. I., Schultz, G., and Offermanns, S. (1999). Activation of G12/G13 results in shape change and Rho/Rho-kinase–mediated myosin light chain phosphorylation in mouse platelets. *J. Cell Biol.* 144, 745–754. doi: 10.1083/jcb.144.4.745

Maloney, S. F., Brass, L. F., and Diamond, S. L. (2010). P2Y12 or P2Y1inhibitors reduce platelet deposition in a microfluidic model of thrombosis while apyrase lacks efficacy under flow conditions. *Integr. Biol.* 2, 183–192. doi: 10.1039/b919728a

McRedmond, J. P., Park, S. D., Reilly, D. F., Coppinger, J. A., Maguire, P. B., Shields, D. C., et al. (2004). Integration of proteomics and genomics in platelets: a profile of platelet proteins and platelet-specific genes. *Mol. Cell. Proteomics* 3, 133–144. doi: 10.1074/mcp.M300063-MCP200

Moers, A., Nieswandt, B., Massberg, S., Wettschureck, N., Gruner, S., Konrad, I., et al. (2003). G13 is an essential mediator of platelet activation in hemostasis and thrombosis. *Nat. Med.* 9, 1418–1422. doi: 10.1038/nm943

Offermanns, S. (2006). Activation of platelet function through G protein-coupled receptors. *Circ. Res.* 99, 1293–1304. doi: 10.1161/01.RES.0000251742.71301.16

Offermanns, S., Toombs, C. F., Hu, Y.-H., and Simon, M. I. (1997). Defective platelet activation in G aq-deficient mice. *Nature* 389, 183–186. doi: 10.1038/38284

Ouwehand, W. H. (2007). Platelet genomics and the risk of atherothrombosis. *J. Thromb. Haemost.* 5(Suppl. 1), 188–195. doi: 10.1111/j.1538-7836.2007.02550.x

Pandey, D., Goyal, P., Bamburg, J. R., and Siess, W. (2006). Regulation of LIM-kinase 1 and cofilin in thrombin-stimulated platelets. *Blood* 107, 575–583. doi: 10.1182/blood-2004-11-4377

Purvis, J. E., Chatterjee, M. S., Brass, L. F., and Diamond, S. L. (2008). A molecular signaling model of platelet phosphoinositide and calcium regulation during homeostasis and P2Y1 activation. *Blood* 112, 4069–4079. doi: 10.1182/blood-2008-05-157883

Purvis, J. E., Radhakrishnan, R., and Diamond, S. L. (2009). Steady-state kinetic modeling constrains cellular resting states and dynamic behavior. *PLoS Comput. Biol.* 5:e1000298. doi: 10.1371/journal.pcbi.1000298

Samani, N. J., Erdmann, J., Hall, A. S., Hengstenberg, C., Mangino, M., Mayer, B., et al. (2007). Genomewide association analysis of coronary artery disease. *N. Engl. J. Med.* 357, 443–453. doi: 10.1056/NEJMoa072366

Schneider, S. W., Nuschele, S., Wixforth, A., Gorzelanny, C., Alexander-Katz, A., Netz, R. R., et al. (2007). Shear-induced unfolding triggers adhesion of von Willebrand factor fibers. *Proc. Natl. Acad. Sci. U.S.A.* 104, 7899–7903. doi: 10.1073/pnas.0608422104

Schwertz, H., Tolley, N. D., Foulks, J. M., Denis, M. M., Risenmay, B. W., Buerke, M., et al. (2006). Signal-dependent splicing of tissue factor pre-mRNA modulates the thrombogenicity of human platelets. *J. Exp. Med.* 203, 2433–2440. doi: 10.1084/jem.20061302

Sneyd, J., and Dufour, J. F. (2002). A dynamic model of the type-2 inositol trisphosphate receptor. *Proc. Natl. Acad. Sci. U.S.A.* 99, 2398–2403. doi: 10.1073/pnas.032281999

Wellcome Trust Case Control Consortium. (2007). Genome-wide association study of 14, 000 cases of seven common diseases and 3, 000 shared controls. *Nature* 447, 661–678. doi: 10.1038/nature05911

Woulfe, D., Jiang, H., Mortensen, R., Yang, J., and Brass, L. F. (2002). Activation of Rap1B by Gi family members in platelets. *J. Biol. Chem.* 277, 23382–23390. doi: 10.1074/jbc.M202212200

Yang, J., Wu, J., Jiang, H., Mortensen, R., Austin, S., Manning, D. R., et al. (2002). Signaling through Gi family members in platelets. *J. Biol. Chem.* 277, 46035–46042. doi: 10.1074/jbc.M208519200

Conflict of Interest Statement: The authors declare that the research was conducted in the absence of any commercial or financial relationships that could be construed as a potential conflict of interest.

Received: 26 May 2013; accepted: 05 August 2013; published online: 26 August 2013.

Citation: Diamond SL, Purvis J, Chatterjee M and Flamm MH (2013) Systems biology of platelet-vessel wall interactions. Front. Physiol. ***4****:229. doi: 10.3389/fphys.2013.00229*

This article was submitted to Computational Physiology and Medicine, a section of the journal Frontiers in Physiology.

frontiers in
PHYSIOLOGY

ORIGINAL RESEARCH ARTICLE
published: 24 September 2013
doi: 10.3389/fphys.2013.00260

Modeling steady state SO_2-dependent changes in capillary ATP concentration using novel O_2 micro-delivery methods

Nour W. Ghonaim[1]*, Graham M. Fraser[2], Christopher G. Ellis[1,2], Jun Yang[1,3] and Daniel Goldman[1,2]

[1] Department of Biomedical Engineering Graduate Program, Western University, London, ON, Canada
[2] Department of Medical Biophysics, Western University, London, ON, Canada
[3] Department of Mechanical and Materials Engineering, Western University, London, ON, Canada

Edited by:
Pankaj Qasba, HHS-National Intitutes of Health-Heart Lung and Blood Institute, USA

Reviewed by:
Caterina Guiot, University of Torino, Italy
Nikolaos Tsoukias, Florida International University, USA

***Correspondence:**
Nour W. Ghonaim, Biomedical Engineering Graduate Program, Western University, 2001 Spencer Engineering Building, London, ON N6A 5B9, Canada
e-mail: nghonaim@uwo.ca

Adenosine triphosphate (ATP) is known to be released from the erythrocyte in an oxygen (O_2) dependent manner. Since ATP is a potent vasodilator, it is proposed to be a key regulator in the pathway that mediates micro-vascular response to varying tissue O_2 demand. We propose that ATP signaling mainly originates in the capillaries due to the relatively long erythrocyte transit times in the capillary and the short ATP diffusion distance to the electrically coupled endothelium. We have developed a computational model to investigate the effect of delivering or removing O_2 to limited areas at the surface of a tissue with an idealized parallel capillary array on total ATP concentration. Simulations were conducted when exposing full surface to perturbations in tissue O_2 tension (PO_2) or locally using a circular micro-outlet (~100 μm in diameter), a square micro-slit (200 × 200μm), or a rectangular micro-slit (1000 μm wide × 200 μm long). Results indicated the rectangular micro-slit has the optimal dimensions for altering hemoglobin saturations (SO_2) in sufficient number capillaries to generate effective changes in total [ATP]. This suggests a threshold for the minimum number of capillaries that need to be stimulated *in vivo* by imposed tissue hypoxia to induce a conducted micro-vascular response. SO_2 and corresponding [ATP] changes were also modeled in a terminal arteriole (9 μm in diameter) that replaces 4 surface capillaries in the idealized network geometry. Based on the results, the contribution of terminal arterioles to the net change in [ATP] in the micro-vascular network is minimal although they would participate as O_2 sources thus influencing the O_2 distribution. The modeling data presented here provide important insights into designing a novel micro-delivery device for studying micro-vascular O_2 regulation in the capillaries *in vivo*.

Keywords: adenosine triphosphate (ATP), microcirculation, capillaries, computational model, simulation, local PO_2 perturbation, O_2 regulation, micro-delivery device

INTRODUCTION

The microcirculation plays the important role of delivering and regulating the exchange of oxygen (O_2) and nutrients to surrounding live metabolic tissue. The transport processes in the microcirculation are tightly controlled and highly integrated. Since proper O_2 supply to tissue is critical for cellular function and survival, the mechanisms underlying O_2 transport and distribution have been under thorough investigation. The microvasculature has to continuously adjust erythrocyte distribution and hence O_2 supply to meet the varying demand of metabolic tissue. During exercise, erythrocyte supply rate increases delivering more O_2 carrying erythrocytes to the microvasculature. The highly regulated system implies the presence of signaling components that link tissue O_2 demand with blood flow and microvascular function.

A great amount of evidence suggests the involvement of the erythrocyte as a sensor and a key player in this regulation mechanism (Stein and Ellsworth, 1993; Ellsworth et al., 1995, 2008). Erythrocytes are the carriers of O_2, bound to hemoglobin, in the microcirculation. Erythrocytes also contain large amounts of adenosine triphosphate (ATP) (Miseta et al., 1993), a potent vasodilator, and are known to release it under hypoxic conditions (Bergfeld and Forrester, 1992; Jagger et al., 2001; González-Alonso et al., 2002). Once ATP is released, it binds to purinergic receptors (P2Y) on the vascular endothelium eliciting a vasodilatory signal which is conducted upstream in the arteriolar tree (Ellsworth et al., 2008). The resulting vaso-relaxation of smooth muscle cells (SMCs) surrounding upstream arterioles increases erythrocyte supply rate to meet the metabolic demand of the hypoxic region downstream that initiated the release of ATP from erythrocytes.

For a long time, arterioles have been investigated as a major site of microvascular signaling (Duling and Berne, 1970; Duling, 1974; Jackson, 1987). This has been assumed, mainly, due to the large longitudinal PO_2 gradients that exist at the arteriolar level. In terms of ATP mediated signaling, the presence of SMCs implies that the released ATP will act locally and instantaneously elicit a signal. However, the relatively short erythrocyte transit times in arterioles are anticipated to largely compromise the localization of this ATP signal, while the parabolic flow profile in the arteriole

means only those cells closest to the wall experience the largest change in O_2 saturation (SO_2) and hence contribute to the signal. Cells flowing in the centerline will be experiencing a lesser drop in SO_2 and any released ATP will be carried downstream (Ellis et al., 2012).

Venules may also be involved in the regulation of O_2 supply since they act as the collectors of large populations of deoxygenated ATP-releasing erythrocytes. However, the diversity in the erythrocyte SO_2 levels as they drain from various upstream capillaries indicates that venules may only contribute to the overall vaso-dilatory signal (Ellis et al., 2012). Fine-tune regulation of O_2 distribution to specific capillaries or microvascular units in the microcirculation demands the signal be highly localized. This may only be achieved at the capillary level. Erythrocytes traverse capillaries with long transit times and are in almost direct contact with the capillary endothelium. Hence, released ATP, mediated by erythrocyte deoxygenation, will be effectively transferred to purinergic receptors on the endothelium. Many studies have shown that the capillary endothelium is conductive when locally stimulated by vasodilators (Dietrich, 1989; Dietrich and Tyml, 1992a,b; Song and Tyml, 1993; Collins et al., 1998; Bagher and Segal, 2011). Therefore, we hypothesize that the capillary bed is the major site for O_2 regulation in the microcirculation (Ellis et al., 2012).

To test this hypothesis, we have been examining the microvascular response to local perturbations in tissue O_2 tension (PO_2) using a novel O_2 micro-delivery tool (Ghonaim et al., 2011). We have created an O_2 micro-delivery (and removal) system that allows for altering local tissue PO_2 and hence erythrocyte SO_2 in a few selected capillaries at the surface of the Extensor Digitorum Longus (EDL) muscle of the rat (**Figure 1**). This system replaces the gas exchange chamber originally used in our group to alter surface tissue PO_2 of the entire bottom surface of the muscle (Ghonaim et al., 2011; Ellis et al., 2012). The chamber is positioned in the platform of an inverted microscope and is connected to computer controlled gas flow meters which allows for capturing video images of the microvascular response to PO_2 perturbations while simultaneously controlling chamber PO_2 levels. Erythrocyte SO_2 values are calculated based on a dual-wavelength image capture system and video sequences are post-processed to extract functional images and hemodynamic information as previously described (Ellis et al., 1990, 1992; Japee et al., 2004, 2005a,b).

In our novel O_2 micro-delivery setup, ultrathin plastic/glass sheet patterned with an O_2 delivery micro-outlet replaces the gas permeable membrane in the original chamber (Ghonaim et al., 2011; Ellis et al., 2012). Data presented earlier (Ghonaim et al., 2011) show that circular micro-delivery outlets (100 μm in diameter) can alter SO_2 in single capillaries flowing directly over the outlet. However, in order to elicit microvascular responses, the optimal outlet dimensions should allow for a sufficient number of capillaries within a network to be stimulated to produce a large enough ATP signal. This should be accomplished while ensuring the high localization of the stimulus to affect only the desired capillaries. This requires testing with various O_2 outlet sizes and dimensions. Combining the possible technical challenges involved

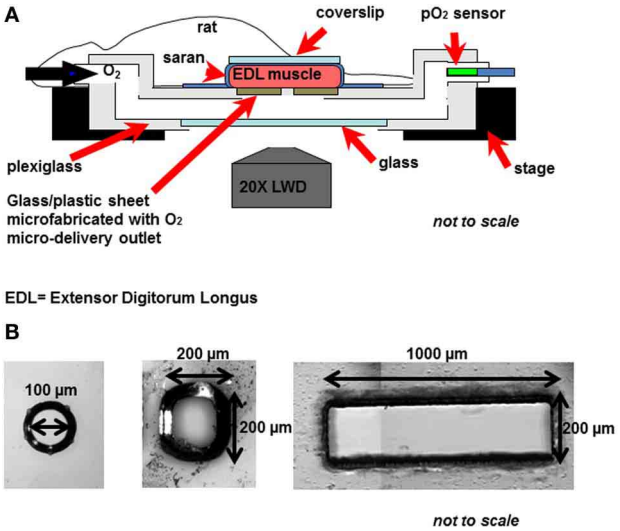

FIGURE 1 | (A) The novel O_2 micro-delivery approach. Extensor Digitorum Longus (EDL) rat muscle is surgically exposed and positioned on the viewing platform of an inverted microscope. O_2 is delivered to the surface of the muscle through a micro-outlet patterned in ultrathin glass/plastic sheet (Ghonaim et al., 2011). O_2 levels in the gas exchange chamber near the muscle surface are oscillated using computer controlled flow meters. Real-time videos of the trans-illuminated tissue are monitored and recorded using a dual-wavelength video microscopy system (Ellis et al., 1990, 1992; Japee et al., 2004, 2005a,b) **(B)** Three designs of the oxygen micro-delivery outlet are tested: circular micro-outlet (~100 μm in diameter) (Ghonaim et al., 2011), a square micro-slit (200 × 200 μm), and a rectangular micro-slit (1000 μm wide × 200 μm long).

in creating multiple designs of the O_2 micro-delivery device with the inherent complexities of the O_2 regulation system led us to develop a computational model for the system under investigation.

Recently, Goldman et al. (2012) presented a theoretical mathematical model based on previous work by Goldman and Popel (1999) and Arciero et al. (2008) to describe O_2 and ATP transport in the rat EDL microcirculation when using the original O_2 exchange chamber. In this study we employ the same approach to calculate SO_2 and ATP changes in selected capillaries flowing over an O_2 delivery outlet of specific dimensions. Three designs of the O_2 delivery micro-outlet were tested: circular outlet (100 μm in diameter), square outlet (200 × 200μm), and rectangular slit (200 μm long × 1000 μm wide). Average capillary SO_2 and ATP level at steady-state were calculated at various chamber PO_2 levels (15, 40, and 150 mmHg) relative to a zero flux boundary condition. In order to simplify the system under investigation, an idealized three dimensional (3D) parallel array capillary geometry has been used. Simulations were also run on a 3D idealized array geometry in which a terminal arteriole (9 μm in diameter) replaced 4 capillaries and was positioned 30 μm from the bottom tissue surface. These simulations allowed for investigating the potential role of the terminal arteriole in O_2 regulation. Confirming previous findings (Ghonaim et al., 2011), the results indicated that radial O_2 diffusion from an O_2 delivery micro-outlet regardless of its dimensions is limited to

~50 μm, while axial diffusion affects ~100 μm of tissue. The rectangular slit has the important property of ensuring that capillaries surrounding the network of interest are all experiencing the same PO_2 drop, which minimizes re-oxygenation and emphasizes the ATP signal. This design also produces sufficient ATP release in multiple capillaries that it should be able to consistently elicit micro-vascular responses, although this remains to be confirmed experimentally. The results presented here also predict minimal contribution of terminal arterioles to the net magnitude of ATP emerging from capillary network although they would participate as O_2 sources and hence influence the O_2 distribution. In the future, 3D capillary networks reconstructed from experimental data can be modeled which will provide more realistic data and help more closely predict changes in various parameters.

MATERIALS AND METHODS

OXYGEN TRANSPORT MODEL

In this work, O_2 transport and ATP transport were modeled in an idealized 3D capillary network consisting of an array of parallel capillaries (oriented in the y direction). The computational model of O_2 transport was based on a finite-difference model described by Goldman and Popel (1999, 2000, 2001). In the model, the reaction-diffusion equation below was used to describe time-dependent tissue PO_2 $P(x,y,z,t)$:

$$\frac{\partial P}{\partial t} = \left[1 + \frac{c_{Mb}}{\alpha}\frac{dS_{Mb}}{dP}\right]^{-1}\left\{D\nabla^2 P - \frac{1}{\alpha}M(P) + \frac{1}{\alpha}D_{Mb}c_{Mb}\nabla\cdot\left(\frac{dS_{Mb}}{dP}\nabla P\right)\right\} \quad (1)$$

where D is the tissue O_2 diffusion coefficient, α is the tissue O_2 solubility, and $M(P)$ is consumption rate of O_2 in tissue (**Table 1**). O_2 transport in tissue was facilitated by the presence of myoglobin where c_{Mb} is myoglobin concentration, D_{Mb} is the myoglobin diffusion coefficient, and $S_{Mb}(P) = P/(P + P_{50,Mb})$ is the myoglobin SO_2. Convective transport of O_2 in the microvessels at each axial location y was described using the following time-dependent mass balance equation for capillary SO_2, $S(y,t)$:

$$\frac{\partial S}{\partial t} = -\left[C + \alpha_b\frac{dP_b}{dS}\right]^{-1}\left\{-u\left[\tilde{C} + \tilde{\alpha}_b\frac{dP_b}{dS}\right]\frac{\partial S}{\partial y} - \frac{1}{\pi R}\oint j\cdot d\theta\right\} \quad (2)$$

where u is the mean blood velocity, R is the capillary radius, j is the O_2 flux at (y,θ) out of the capillary, C and $\tilde{C}$ are blood O_2-binding capacities, respectively, directly related to hematocrit:

$$C = H_T C_{Hb}$$
$$\tilde{C} = H_D C_{Hb}$$

where H_T is tube (volume-weighted) hematocrit, H_D is discharge (flow-averaged) hematocrit, and C_{Hb} is the binding capacity of hemoglobin (**Table 1**) (Goldman and Popel, 2001). P_b is the blood PO_2, and α_b and $\tilde{\alpha}_b$ are volume- and flow-weighted blood O_2 solubilities, respectively (Goldman and Popel, 2001), where,

$$\alpha_b = H_T\alpha_{cell} + (1 - H_T)\,\alpha_{pl}$$
$$\tilde{\alpha} = H_D\alpha_{cell} + (1 - H_D)\,\alpha_{pl}$$

where α_{cell} and α_{pl} are the O_2 solubilities inside the erythrocyte and in the plasma (Goldman and Popel, 2001). The O_2 flux at the capillary-tissue interface was given by:

$$j = \kappa(P_b - P_w) \quad (3)$$

where κ is the mass transfer coefficient and P_w is the tissue PO_2 at the capillary surface. κ is a function of hematocrit as it describes the effect of RBC spacing on O_2 diffusion and exchange between capillary and tissue (Eggleton et al., 2000). At the capillary surface, the boundary condition was specified as:

$$-D\alpha\frac{\partial P_w}{\partial n} = j \quad (4)$$

where n is the unit vector normal to the capillary surface and j is given by equation (3). In the model presented here, zero O_2 flux conditions (no O_2 exchange across tissue boundary) were specified at the tissue boundaries, except where PO_2 was fixed on part or all of the bottom surface to represent the effect of the O_2 exchange chamber (see below). As in the model described by Goldman and Popel (1999), Michaelis–Menten consumption kinetics, $M = M_0P/(P + P_{cr})$, and the Hill equation for the oxyhemoglobin saturation curve, $S(P) = P^n/(P^n + P_{50}^n)$, were used along with the above O_2 transport equations to calculate tissue O_2 transport.

Hemodynamic parameters (erythrocyte mean velocity, v_{rbc}, and hematocrit, H_T) were determined from *in vivo* experimental measurements in the EDL muscle of the rat. The capillary

Table 1 | Parameter values used in oxygen and ATP transport simulations.

Parameter	Value
α	3.89×10^{-5} ml O_2 ml^{-1} mmHg^{-1}
D	2.41×10^{-5} cm^2 s^{-1}
P_{cr}	0.5 mmHg
c_{Mb}	1.02×10^{-2} ml O_2 ml^{-1}
D_{Mb}	3×10^{-7} cm^2 s^{-1}
P_{50}	37 mmHg
n(Hill exponent)	2.7
$P_{50,\ Mb}$	5.3 mmHg
C_{Hb}	0.52 ml O_2 ml^{-1}
v_{rbc}	1.45×10^{-2} cm s^{-1}
H_T	0.19
H_D	0.2
C_0	1.4×10^{-9} mol s$^{-1}\cdot$cm^{-3}
C_1	0.891
k_d	2.0×10^{-4} cm s^{-1}

network consisted of 72 parallel capillaries, each of which was discretized into 50 cylindrical segments, and the tissue domain surrounding the capillaries had dimensions of 216 × 532× 500 μm and was discretized into 7,304,853 computational nodes using a grid spacing of approximately 2 μm (**Figure 2A**). Capillary entrance SO_2 (65%) and the tissue O_2 consumption rate (1.5×10^{-4} ml O_2/ml/s) were set based on previous experimental data (Fraser et al., 2012).

For simulations that included a terminal arteriole in the 3D network geometry, the arteriole (9 μm in diameter) was positioned ∼30 μm from the bottom tissue surface and replaced 4 capillaries in the original parallel array capillary geometry (**Figure 2B**). Simulations including the arteriole were run at both 65 and 80% arteriolar entrance SO_2.

ATP TRANSPORT MODEL

ATP transport in the idealized 3D capillary network was modeled as described by Goldman et al. (2012), based on the O_2 transport mathematical model described above (Goldman and Popel, 2000). Using a capillary entrance ATP concentration of zero, plasma [ATP] was calculated by using a finite-difference method to solve the following continuum partial differential equation (Goldman et al., 2012):

$$(1 - H_T)\frac{\partial}{\partial t}[\mathrm{ATP}] = -u\,(1 - H_D)\frac{\partial}{\partial y}[\mathrm{ATP}] + H_T C_0\,(1 - C_1 S) - \frac{2}{R}k_d\,[\mathrm{ATP}] \quad (5)$$

where u is the mean blood velocity at axial location y, H_D, and H_T are the discharge and tube hematocrit, respectively, and R is capillary radius. C_0 and C_1 (**Table 1**) are constants used to linearly approximate the ATP release rate as a function of SO_2, while k_d provides an approximation of ATP degradation by the endothelium as previously described (Arciero et al., 2008).

To calculate the steady-state distributions of tissue PO_2 and capillary SO_2 and [ATP], time-dependent O_2 transport and ATP transport simulations were run, using zero initial conditions for all variables, until there were minimal changes in tissue O_2 consumption and PO_2, and capillary O_2 flux, SO_2 and [ATP] between consecutive time steps.

TISSUE PO_2 BOUNDARY CONDITIONS USED TO MODEL OXYGEN EXCHANGE CHAMBER

For the idealized capillary geometry, 3D tissue PO_2 distribution and capillary [ATP] at steady state were calculated for O_2 delivery using full gas exchange chamber, circular micro-outlet (100 μm in diameter), square micro-outlet (200 × 200 μm), or a rectangular micro-slit (1000 μm wide × 200 μm long). For each chamber type, simulations were run at 3 PO_2 boundary conditions either over full surface (with full gas exchange chamber) or only at the micro-slit opening: 15, 40, and 150 mmHg. For the cases in which the PO_2 boundary condition is altered only at the microslit opening, the rest of the tissue surrounding the micro-slit is set to zero O_2 flux boundary condition. The results from all simulations were compared to a fourth control case in which full surface is set to zero O_2 flux boundary condition.

For the idealized capillary geometry that includes the terminal arteriole, O_2 diffusion was modeled for full chamber or a rectangular micro-slit (1000 μm wide × 200 μm long) at the 4 PO_2 boundary conditions discussed above. Each set of simulations was run with arteriolar entrance SO_2 of 65% or to 80%. **Table 2** lists

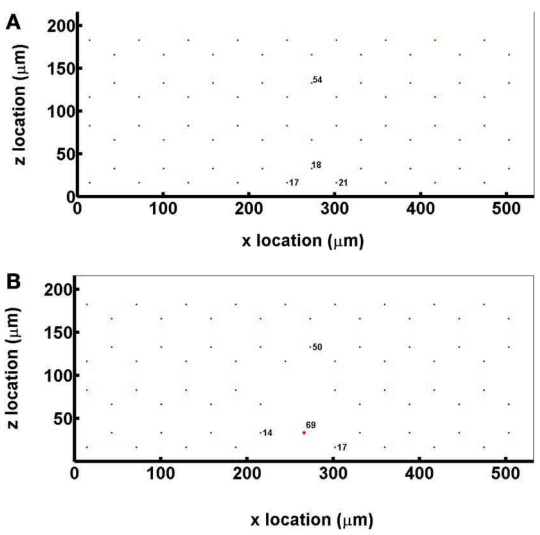

FIGURE 2 | (A) A cross sectional view of the idealized capillary parallel array geometry showing the positioning and numbering of the 72 hexagonally arranged capillaries in the modeled network. **(B)** A cross sectional view of the idealized capillary parallel array geometry with a terminal arteriole (vessel 69, 9 μm in diameter) replacing 4 capillaries within 30 μm from bottom tissue surface.

Table 2 | List of boundary conditions used in oxygen and ATP transport simulations.**

Network specifications	Chamber type tested	Corresponding figure in manuscript	PO_2 condition at chamber outlet (in each chamber type tested)
Capillary array	Full chamber	3	• Zero O_2 flux (Control)
	Circle	4	• 40 mmHg
	Square	5	• 15 mmHg
	Rectangle	6	• 150 mmHg
Capillary array with arteriole (entrance $SO_2 = 65\%$)	Full chamber	8	• Zero O_2 flux (Control)
			• 40 mmHg
	Rectangle	10	• 15 mmHg
			• 150 mmHg
Capillary array with arteriole (entrance $SO_2 = 80\%$)	Full chamber	9	• Zero O_2 flux (Control)
			• 40 mmHg
	Rectangle	11	• 15 mmHg
			• 150 mmHg

***Summary of transport simulations, chamber types, and boundary conditions.*

the summary of simulations and boundary conditions used in this study.

RESULTS

MATHEMATICAL MODELING OF SO_2-DEPENDENT ATP RELEASE IN CAPILLARY NETWORKS IN RESPONSE TO LOCALIZED TISSUE PO_2 PERTURBATIONS

In this study, the release of ATP in capillaries mediated by tissue hypoxia and the de-saturation of hemoglobin was modeled in a 3D idealized parallel capillary network. The dependence of the magnitude of total ATP release on the number of de-oxygenated capillaries was also examined. Based on our previously described experimental work (Ghonaim et al., 2011), we mathematically simulated O_2 delivery to and removal from selected capillaries on the surface of skeletal muscle tissue (rat EDL) using three designs of O_2 exchange micro-outlets used in our *in vivo* experiments (**Figure 1**). In order to compare local O_2 perturbations using the micro-outlets to global perturbations using the full gas exchange chamber (Ghonaim et al., 2011; Ellis et al., 2012), O_2 delivery to and removal from the entire bottom tissue surface was also modeled. For each set of simulations, 3D tissue PO_2 distribution profiles and corresponding 3D capillary [ATP] maps were generated. Plots of calculated SO_2 and [ATP] along the length of selected capillaries (21, 18, 17, 54) at steady state were also created. All simulations were run using software written in Fortran, and the results were analyzed and the plots were produced using MATLAB.

Full surface gas exchange chamber

In this set of simulations, the 3D PO_2 distribution in the tissue and corresponding SO_2 and [ATP] distribution along capillary length were modeled for the control scenario in which the full bottom tissue surface is exposed to PO_2 perturbations. This would experimentally simulate using the full gas exchange chamber. As shown in **Figure 3**, at 40 mmHg, steady-state tissue PO_2 and capillary [ATP] distributions are comparable to the no-flux control condition. At the venular end of the capillaries, SO_2 values ranged from ∼50% for surface capillaries (21, 18, and 17) to ∼40% for capillaries deeper than 100 μm into the tissue (capillary 54), and the corresponding capillary [ATP] values were within 15% of those at zero O_2 flux boundary condition. However, under imposed tissue hypoxia (15 mmHg), the surface capillaries dropped their SO_2 by ∼70% which corresponded to ∼40% higher steady state capillary [ATP] relative to zero flux condition (**Figure 3C**). This was clearly depicted in the corresponding vessel map (**Figure 3B**). The deeper capillary (54) was less affected with ∼30% lower hemoglobin SO_2 and ∼12% increase in ATP release relative to zero flux. Exposing the full tissue surface to relatively high chamber PO_2 (150 mmHg) had the most significant impact on [ATP] in the capillary network. At 150 mmHg, hemoglobin SO_2 in both surface and deep tissue capillaries converged to ∼100% with ∼70% decrease in steady state [ATP] relative to no-flux (**Figure 3C**). The depth of the PO_2 perturbation into the tissue when using the full gas exchange chamber was ∼100 μm as shown in the 3D PO_2 profiles (**Figure 3A**).

Circular O_2 delivery micro-outlet

To investigate the effect of limiting the number of capillaries stimulated by local tissue PO_2 perturbations, we started by modeling capillary SO_2 and [ATP] changes when using a circular O_2 micro-outlet (100 μm in diameter, see **Figure 1**). Similar to previously discussed data (Ghonaim et al., 2011), substantive changes in local tissue PO_2 due to diffusion outwards from the circular outlet is limited to less than ∼50 μm, as shown in the 3D tissue PO_2 profiles (**Figure 4A**). Also, the hypoxic and hyperoxic stimuli were highly localized to only those capillaries directly over the micro-outlet (17, 18, 21) as shown in the vessel maps (**Figure 4B**). At 40 mmHg chamber PO_2 level, calculated capillary SO_2 and [ATP] were in close agreement with the no-flux control for both surface and deep tissue capillaries with values being within ∼1 and ∼3%, respectively (**Figure 4C**). Under imposed hypoxia, the capillary SO_2 dropped as capillaries crossed the micro-outlet region reaching a minimum value ∼40 μm downstream of the outlet after which SO_2 levels increased slightly due to re-oxygenation by surrounding capillaries. At the venular end, steady state SO_2 levels in surface capillaries were 15% lower relative to zero flux while capillary 54 experienced only a 6% drop in SO_2. This corresponded to only 10% increase in [ATP] in surface capillaries while [ATP] in capillary 54 remained unchanged relative to zero flux. At 150 mmHg, the increase in capillary SO_2 level is observed directly over the micro-outlet region reaching a maximum at the outlet exit. The capillary SO_2 levels dropped sharply downstream of the outlet due to O_2 diffusion into adjacent capillaries and tissue. Surface capillary SO_2 decreased to ∼63 and deep tissue capillaries to 51% ∼200 μm downstream of the outlet. This corresponded to ∼40% decrease in [ATP] in surface capillaries and ∼20% decrease in [ATP] of deeper tissue capillaries relative to zero flux condition.

Square O_2 delivery micro-outlet

Next, we simulated the effect of increasing the area of O_2 exchange, and hence perturbing a greater number of capillaries, by simulating an O_2 delivery micro-outlet 200 × 200 μm square. Similar to the circular micro-outlet design and as previously described (Ghonaim et al., 2011), the change of local tissue PO_2 surrounding the square outlet is limited to less than ∼50 μm, as shown in the 3D tissue PO_2 profiles (**Figure 5A**). In the case of the square micro-outlet, a larger number of surface capillaries experience the PO_2 perturbations, 7 of which were directly over the micro-outlet (**Figure 5B**). Also, capillaries at both sides of those directly over the outlet seemed to be slightly affected by the PO_2 perturbations. At 40 mmHg, calculated SO_2 and capillary [ATP] distributions were similar to the no-flux control with surface capillaries having 15% higher SO_2 and 10% lower [ATP] values relative to zero flux condition (**Figure 5C**). As observed with the circular micro-outlet, re-oxygenation of stimulated capillaries following imposed hypoxia (15 mmHg) was at ∼40 μm downstream of the square micro-outlet (**Figure 5C**). At the capillary venular end, SO_2 level of surface capillaries dropped by ∼51% while capillary 54 experienced only a 15% drop in SO_2 relative to zero flux. This corresponded to ∼32% increase in [ATP] in surface capillaries

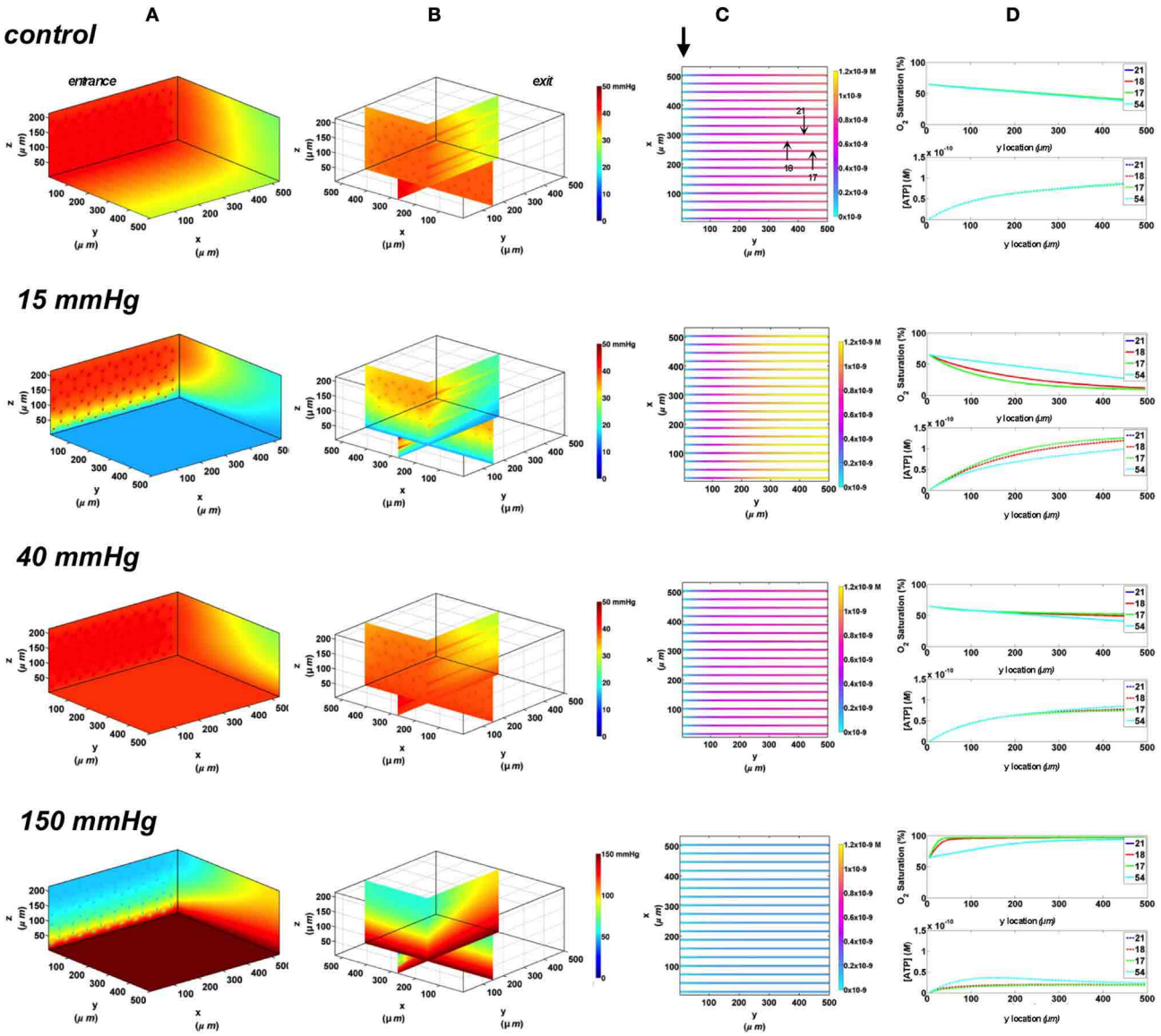

FIGURE 3 | Simulations of 3D PO_2 and capillary [ATP] distribution in a tissue with idealized parallel capillary arrangement (72 hexagonally packed capillaries). In these simulations, we are modeling O_2 delivery to bottom tissue surface using the full gas exchange chamber (Ghonaim et al., 2011; Ellis et al., 2012). Full bottom tissue surface is exposed to 15, 40, or 150 mmHg chamber PO_2 level relative to a zero flux control boundary condition **(A)** Spatial 3D tissue PO_2 distribution (mmHg) at capillary entrance perspective **(B)** a capillary exit perspective showing combined *X*–*Z* plane slice at $Y = 150\,\mu m$ and *Y*–*Z* plane slice at $X = 277\,\mu m$ **(C)** bottom perspective of a vessel map depicting distribution of [ATP] (mol/L = M) along the capillaries. Bolded arrow marks capillary entrance **(D)** Plots of SO_2 (%) and [ATP] changes along capillary length in selected capillaries (21, 18, 17, 54) marked by arrows on the vessel map. Capillaries 21 and 17 are 16 μm from tissue surface, capillary 18 is 33 μm from tissue surface, and capillary 54 is deeper in the tissue, at 133 μm, and hence it is not shown in the current perspective of the vessel map. Note change in PO_2 scale from 0 to 50 mmHg in first three cases to 0–150 mmHg when surface is exposed to 150 mmHg.

while only 7% increase in [ATP] in capillary 54 relative to zero flux. At 150 mmHg, capillary SO_2 levels increased across the micro-delivery outlet reaching maximum values at the venular end of the outlet region. Similar to the results observed with the circular micro-outlet, SO_2 values sharply dropped downstream of the square micro-outlet bringing surface capillary SO_2 to ~83% and deeper capillaries to ~70% ~200 μm downstream of the outlet. This corresponded to ~66% decrease in [ATP] in surface capillaries and ~42% decrease in [ATP] of deeper tissue capillaries.

Rectangular O_2 delivery micro-slit

The largest dimensions for an O_2 delivery micro-outlet currently being tested in our *in vivo* studies are for a rectangular micro-slit (1000 μm wide × 200 μm long). Since the 3D tissue dimensions in our computational model are less than the

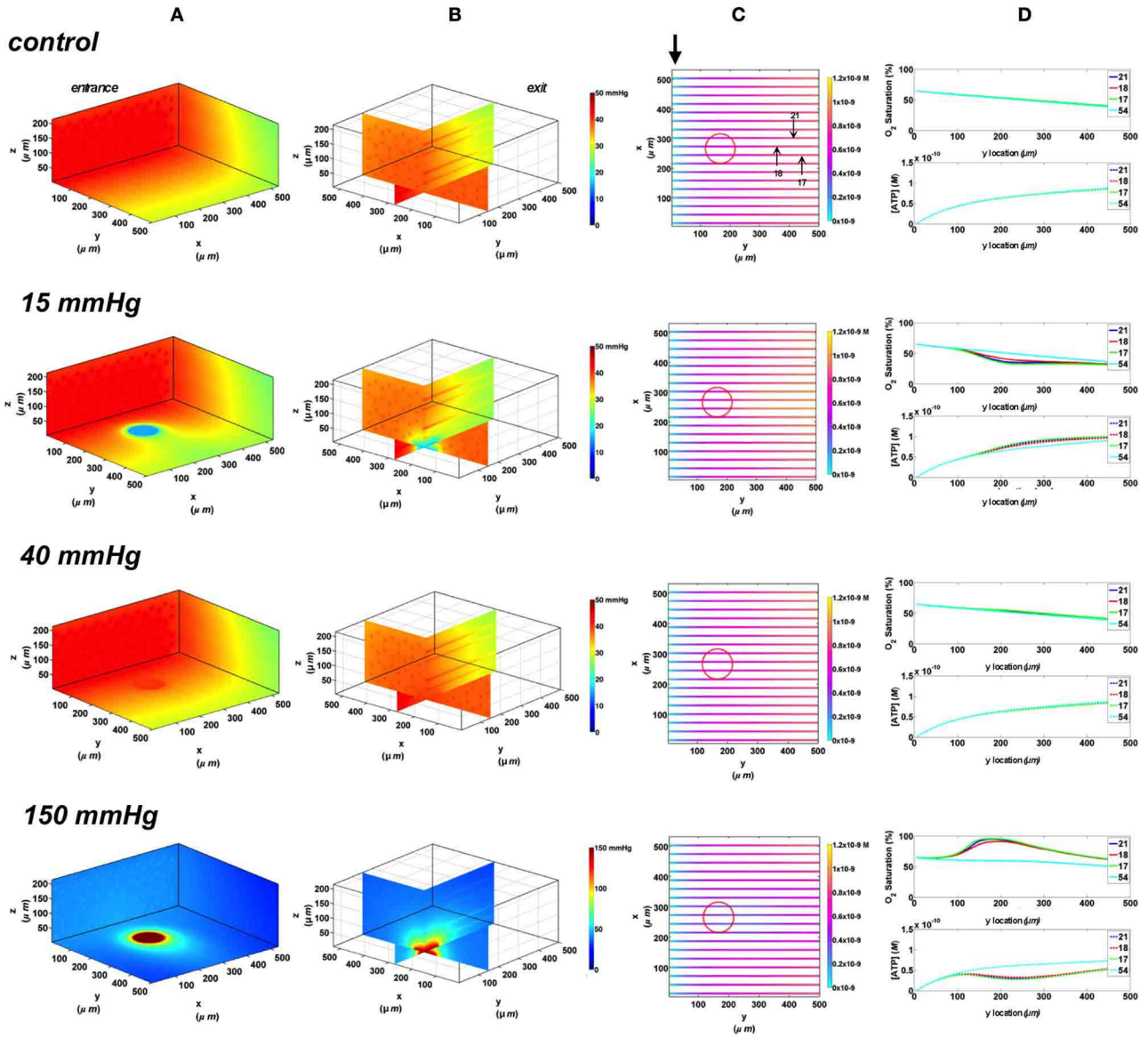

FIGURE 4 | Simulations of 3D PO_2 and capillary [ATP] distribution in a tissue with idealized parallel capillary arrangement (72 hexagonally packed capillaries). In these simulations, we are modeling O_2 delivery through a circular oxygen micro-delivery outlet (100 μm in diameter) to bottom tissue surface using novel micro-delivery approach (see **Figure 1**). Tissue surface directly on top of the micro-delivery outlet is exposed to 15, 40, or 150 mmHg chamber PO_2 level relative to a zero flux control boundary condition **(A)** Spatial 3D tissue PO_2 distribution (mmHg) at capillary entrance perspective **(B)** a capillary exit perspective showing combined *X–Z* plane slice at $Y = 150\,\mu m$ and *Y–Z* plane slice at $X = 277\,\mu m$ **(C)** bottom perspective of a vessel map depicting distribution of [ATP] (mol/L = M) along the capillaries. Bolded arrow marks capillary entrance **(D)** Plots of SO_2 (%) and [ATP] changes along capillary length in selected capillaries (21, 18, 17, 54) marked by arrows on the vessel map. Capillaries 21 and 17 are 16 μm from tissue surface, capillary 18 is 33 μm from tissue surface, and capillary 54 is deeper in the tissue, at 133 μm, and hence it is not shown in the current perspective of the vessel map.

width of the experimental micro-slit, the effect of the slit extends to both edges of the tissue allowing us to visualize the depth of the PO_2 distribution into the tissue. As shown in the 3D PO_2 plots (**Figure 6A**), the PO_2 perturbations extended ~100 μm into the tissue with local tissue PO_2 changes similar to what was observed with other outlet designs. All surface capillaries shown on the vessel map are affected by the PO_2 perturbation as the outlet covers the entire surface width (**Figure 6B**). At 40 mmHg, calculated SO_2 and capillary [ATP] distributions were similar to the no-flux control with surface capillaries having 17% higher SO_2 and 10.3% lower [ATP] values relative to zero flux O_2 boundary condition (**Figure 6C**). Under imposed hypoxia (15 mmHg), re-oxygenation of de-saturated surface capillaries was not observed within 200 μm downstream of the micro-slit. However, capillary SO_2 seemed to plateau approximately 100 μm downstream of the micro-slit. At the capillary

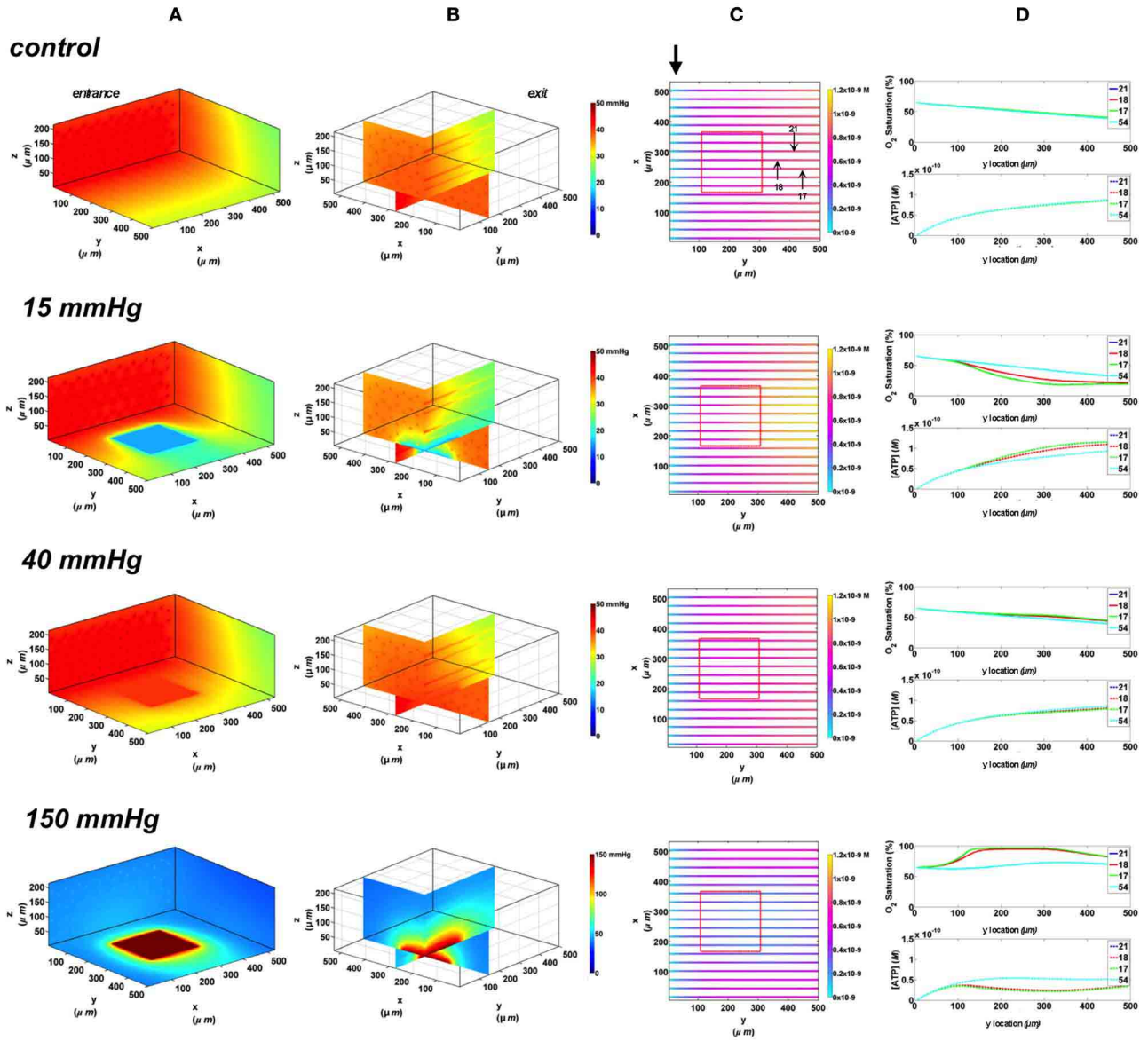

FIGURE 5 | Simulations of 3D PO_2 and capillary [ATP] distribution in a tissue with idealized parallel capillary arrangement (72 hexagonally packed capillaries). In these simulations, we are modeling O_2 delivery through a square oxygen micro-delivery outlet ($200 \times 200 \mu m$) to bottom tissue surface using our previously described novel micro-delivery approach (see **Figure 1**). Tissue surface directly on top of the micro-delivery outlet is exposed to 15, 40, or 150 mmHg chamber PO_2 level relative to a zero flux control boundary condition **(A)** Spatial 3D tissue PO_2 distribution (mmHg) at capillary entrance perspective **(B)** a capillary exit perspective showing combined *X–Z* plane slice at $Y = 150 \mu m$ and *Y–Z* plane slice at $X = 277 \mu m$ **(C)** bottom perspective of a vessel map depicting distribution of [ATP] (mol/L = M) along the capillaries. Bolded arrow marks capillary entrance **(D)** Plots of SO_2 (%) and [ATP] changes along capillary length in selected capillaries (21, 18, 17, 54) marked by arrows on the vessel map. Capillaries 21 and 17 are 16 μm from tissue surface, capillary 18 is 33 μm from tissue surface, and capillary 54 is deeper in the tissue, at 133 μm, and hence it is not shown in the current perspective of the vessel map.

venular end, SO_2 level of surface capillaries dropped by ∼56% while capillary 54 experienced a ∼20% drop in SO_2 relative to zero flux condition. This corresponded to ∼35% increase in [ATP] in surface capillaries and only 8% increase in [ATP] in capillary 54 relative to zero flux. At 150 mmHg, capillary SO_2 levels increased across the micro-delivery outlet reaching maximum values at the venular end of the outlet region. Similar to the results observed with the previously discussed micro-outlet designs, SO_2 values instantly dropped downstream of the rectangular micro-slit bringing surface capillary SO_2 to ∼90% and deep capillaries to ∼80% ∼200 μm downstream of the outlet. This corresponded to ∼69% decrease in [ATP] in surface capillaries and ∼55% decrease in [ATP] of deeper tissue capillaries.

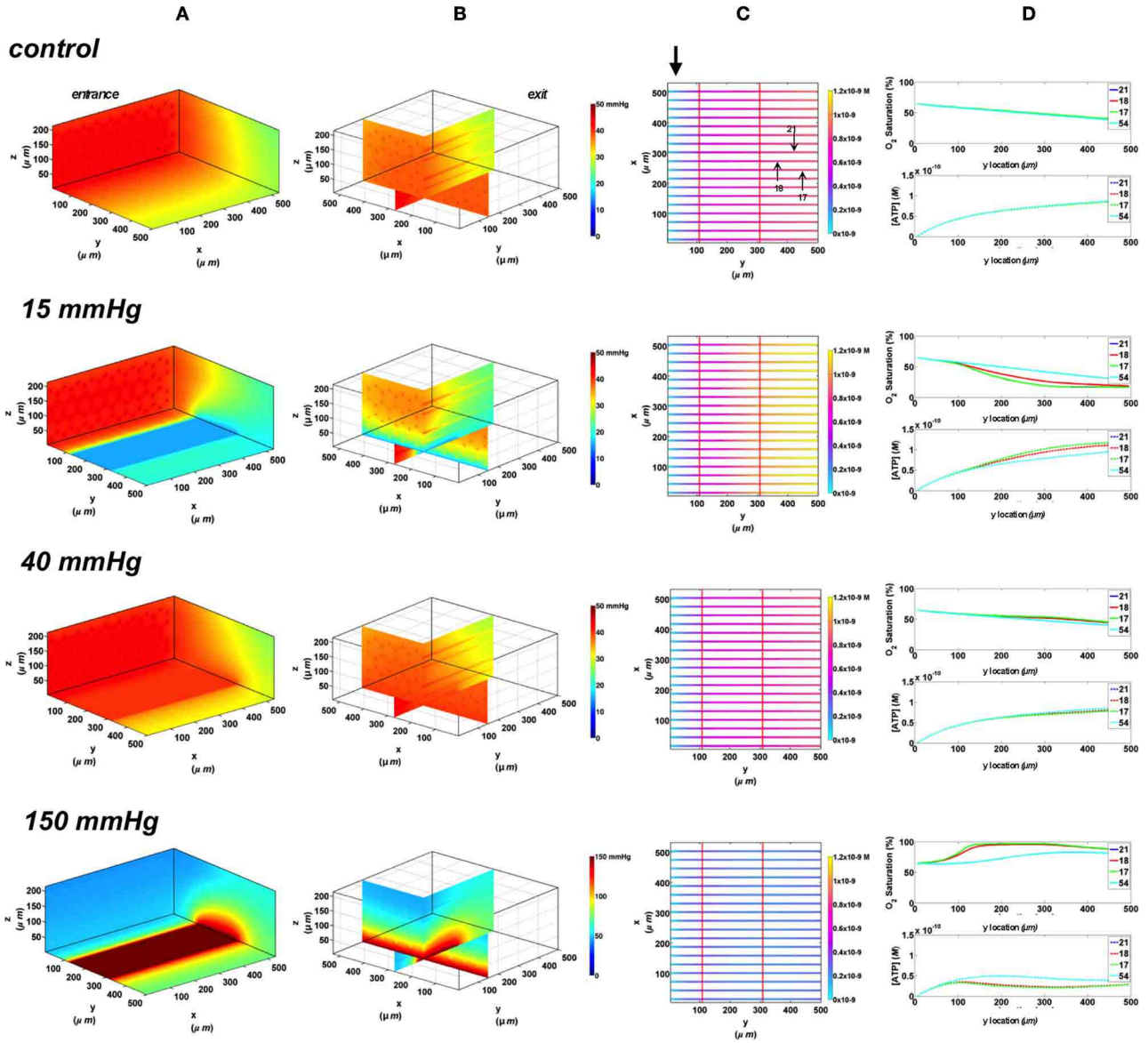

FIGURE 6 | Simulations of 3D PO_2 and capillary [ATP] distribution in a tissue with idealized parallel capillary arrangement (72 hexagonally packed capillaries). In these simulations, we are modeling O_2 delivery through a rectangular oxygen micro-delivery outlet (1000 μm wide × 200 μm long) to bottom tissue surface using our previously described novel micro-delivery approach (see **Figure 1**). Tissue surface directly on top of the micro-delivery outlet is exposed to 15, 40, or 150 mmHg chamber PO_2 level relative to a zero flux control boundary condition **(A)** Spatial 3D tissue PO_2 distribution (mmHg) at capillary entrance perspective **(B)** a capillary exit perspective showing combined *X*–*Z* plane slice at $Y = 150\,\mu m$ and *Y*–*Z* plane slice at $X = 277\,\mu m$ **(C)** bottom perspective of a vessel map depicting distribution of [ATP] (mol/L = M) along the capillaries. Bolded arrow marks capillary entrance **(D)** Plots of SO_2 (%) and [ATP] changes along capillary length in selected capillaries (21, 18, 17, 54) marked by arrows on the vessel map. Capillaries 21 and 17 are 16 μm from tissue surface, capillary 18 is 33 μm from tissue surface, and capillary 54 is deeper in the tissue, at 133 μm, and hence it is not shown in the current perspective of the vessel map.

Comparing change in relative ATP magnitude in response to varying the area of imposed tissue hypoxia

The change in the total magnitude of ATP (ATPtot) in the modeled network relative when imposing a hypoxic challenge (15 mmHg boundary condition) was calculated as percent increase above ATPtot at zero flux (**Figure 7**). Percent increase in ATP magnitude in the network was compared when exposing all of the bottom tissue surface to hypoxia (full chamber) or locally using the three micro-outlet designs discussed above. As shown in **Figure 7**, the total ATP magnitude increased with increase in micro-outlet dimensions and essentially the number of capillaries experiencing the PO_2 drop. The percent increase in ATPtot was more than doubled when locally perturbing tissue PO_2 using the rectangular micro-slit compared to the other micro-outlet

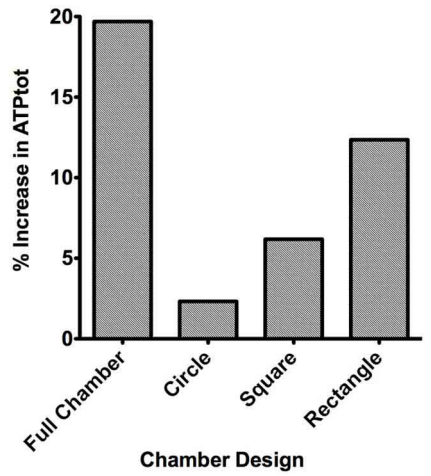

FIGURE 7 | Percent increase in the total magnitude of ATP (ATPtot) relative to zero flux control boundary condition calculated for idealized parallel capillary network with no arteriole at 15 mmHg chamber PO_2 level. Percent increase in ATP magnitude in the network were calculated when entire bottom tissue surface is exposed to the PO_2 perturbation using full gas exchange chamber or locally using a circular (100 μm in diameter), square (200 × 200 μm) or rectangular O_2 delivery micro-slit (1000 μm wide × 200 μm long).

designs. The total ATP magnitude calculated when limiting the area of tissue hypoxia using the rectangular micro-slit was only 38% lower relative to full exposed surface (**Figure 7**). The increase in the total ATP magnitude in a network exposed to local hypoxia was minimal (∼2%) when using the circular micro-outlet or and only 6% above that zero flux when using the square micro-outlet.

MATHEMATICAL MODELING OF ARTERIOLAR SO_2 AND ATP CONCENTRATION IN RESPONSE TO LOCALIZED TISSUE PO_2 PERTURBATIONS

In order to investigate the role terminal arterioles play in regulating SO_2-mediated ATP signaling in capillary networks, particularly in the EDL muscle where larger arterioles are located much deeper in the tissue, the 3D idealized capillary geometry was modified to include a terminal arteriole, 9 μm in diameter, positioned 30 μm away from bottom tissue surface. The 3D tissue PO_2 distribution as well as SO_2 and [ATP] in the arteriole (vessel 69) and in the surrounding surface (capillaries 14 and 17) and deep tissue capillaries (represented by capillary 50) were modeled. Simulations were run for the case in which the full tissue surface is exposed to PO_2 perturbations (original gas exchange chamber) and for the case of spatially limited O_2 delivery using the rectangular O_2 delivery micro-slit. Also, the effect of varying arteriolar entrance SO_2 on the overall magnitude of ATP in response to altered tissue PO_2 was examined.

Full surface gas exchange chamber at 65 and 80% arteriolar entrance SO_2

In the 3D tissue PO_2 profiles and [ATP] vessel maps generated for these simulations, the PO_2 perturbations were shown to affect the terminal arteriole to a much lesser extent than the surface capillaries (**Figures 8A,B**, **9A,B**). Also, these simulations showed the influence of the arteriole as an O_2 source on the SO_2 levels of nearby surface capillaries. For instance, the steady state SO_2 level in capillary 14, positioned right next to the arteriole, was ∼25% higher than the zero flux control condition when exposed to 40 mmHg chamber PO_2 and identical to the SO_2 level of the terminal arteriole (**Figures 8**, **9**). However, the SO_2 level of the deeper tissue capillary (50), which was located at the same depth as capillary 54, was unchanged relative to zero flux. In general, the different arteriolar entrance SO_2 has no effect on the surface or deep tissue capillaries and had minimal influence on the arteriolar SO_2 at steady state. At 15 mmHg, the SO_2 level of the terminal arteriole entering at 65% dropped by 60% relative to zero flux condition corresponding to 44% increases in [ATP]. A smaller drop in SO_2 was calculated (52% decrease) for the arteriole entering at 80% corresponding to 40% increase in [ATP]. The SO_2 level in the surrounding surface capillaries as well as deeper tissue capillaries dropped by ∼70 and 35%, respectively, corresponding to ∼45 and 16% higher steady state capillary [ATP] relative to zero flux (**Figures 8C**, **9C**). At 150 mmHg, hemoglobin SO_2 levels in surface and deep tissue capillaries as well as in the arteriole converged to ∼100% with ∼77% decrease in steady state [ATP] in the capillaries and 75% decrease in [ATP] in the arteriole relative to zero flux control (**Figures 8C**, **9C**).

Rectangular oxygen delivery micro-slit at 65 and 80% arteriolar entrance SO_2

In these simulations, the capillary array that includes the terminal arteriole is exposed to local perturbations in tissue PO_2 through the rectangular micro-slit. At 40 mmHg chamber PO_2, the calculated steady state SO_2 and [ATP] levels at the venular end of surface and deep tissue capillaries as well as in the arteriole are within 5% of those at zero flux condition and uninfluenced by the arteriolar entrance SO_2 (**Figures 10**, **11**). Under imposed hypoxia (15 mmHg), the calculated arteriolar SO_2 values at steady state were 50% higher than the case in which the full surface is exposed to the PO_2 perturbations and identical to those of deeper tissue capillaries. Hence, a minimal drop in SO_2 (38% decrease) was calculated in the arteriole relative to zero flux. These arteriolar steady state SO_2 values were uninfluenced by the different arteriolar entrance SO_2. The influence of the arteriole as an O_2 source to nearby capillaries downstream of the micro-slit can be clearly observed in the 3D PO_2 profiles at 15 mmHg (**Figures 10A**, **11A**). However, the surface capillaries (14, 17) experienced a sharper drop in SO_2 in response to the imposed hypoxia with 53% drop in SO_2 and a corresponding 39% increase in [ATP]. As observed when locally stimulating surface capillaries in the absence of the arteriole, capillaries were re-oxygenated ∼40 μm downstream of the hypoxic micro-slit region. At 150 mmHg, the steady state SO_2 levels in surface capillaries and in the arteriole converged to ∼88% while the SO_2 level of capillary 50 was slightly lower at 83% which corresponded to 65% and 57% decrease in [ATP], respectively, relative to zero flux (**Figures 10C**, **11C**).

Estimating relative arteriolar ATP magnitude in response to tissue PO_2 perturbations

In order to estimate the contribution of the terminal arteriole to ATP mediated signaling in capillary networks, the

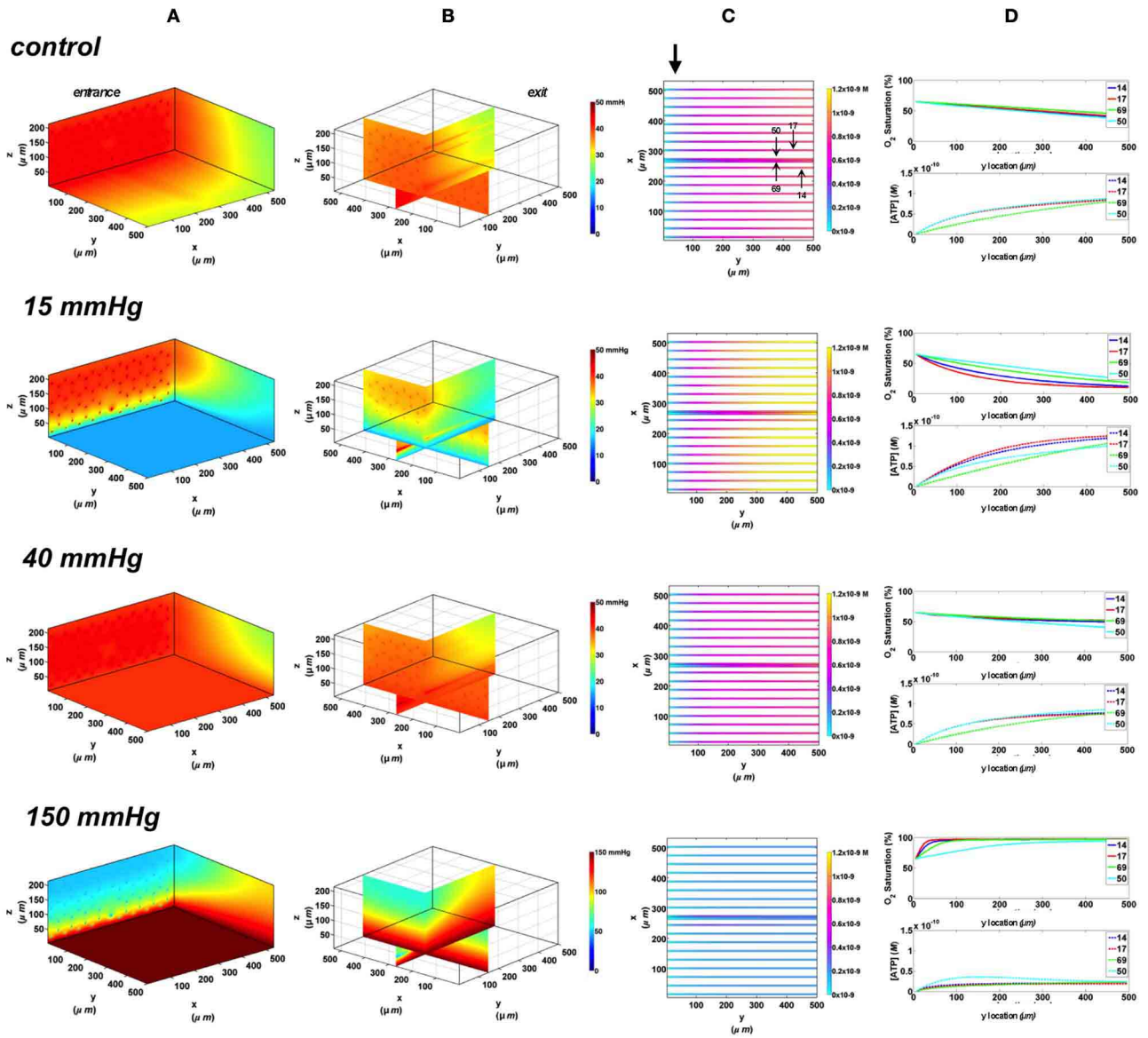

FIGURE 8 | Simulations of 3D PO_2 and capillary [ATP] distribution in a tissue with idealized parallel capillary arrangement (68 hexagonally packed capillaries), which includes a traversing terminal arteriole (vessel 69) at an entrance SO_2 of 65%. In these simulations, we are modeling O_2 delivery to bottom tissue surface using the full gas exchange chamber (Ghonaim et al., 2011; Ellis et al., 2012). Full bottom tissue surface is exposed to 15, 40, or 150 mmHg chamber PO_2 level relative to a zero flux control boundary condition **(A)** Spatial 3D tissue PO_2 distribution (mmHg) at capillary entrance perspective **(B)** a capillary exit perspective showing combined *X–Z* plane slice at $Y = 150\,\mu m$ and *Y–Z* plane slice at $X = 266\,\mu m$ **(C)** bottom perspective of a vessel map depicting distribution of [ATP] (mol/L = M) along the arteriole and surrounding capillaries. Bolded arrow marks arteriolar and capillary entrance **(D)** Plots of SO_2 (%) and [ATP] changes along vessel length in selected vessels (14, 17, 69-arteriole, 50) marked by arrows on the vessel map. Capillary 17 is 16 μm from tissue surface, the arteriole and capillary 14 are 33 μm from tissue surface, and capillary 50 is deeper in the tissue, at 133 μm, yet is shown adjacent to the arteriole in the current perspective of the vessel map.

steady state magnitude of ATP in the arteriole (ATPart) at various tissue PO_2 conditions was calculated and normalized against total ATP magnitude in the network (ATPtot) under zero flux condition (**Figure 12**). The relative arteriolar ATP magnitudes were calculated when full tissue surface is exposed to the PO_2 perturbations (full gas exchange chamber) or to local perturbations using the rectangular O_2 delivery micro-slit. As shown in **Figure 12**, the arteriolar ATP magnitude decreased with increase in chamber PO_2 level. However, the model suggested that under hypoxic conditions (15 mmHg), the terminal arteriole would contribute less than 3% of the total ATP signal originating from a capillary network. Also, although the percent decrease in ATP magnitude in the arteriole is similar to that calculated

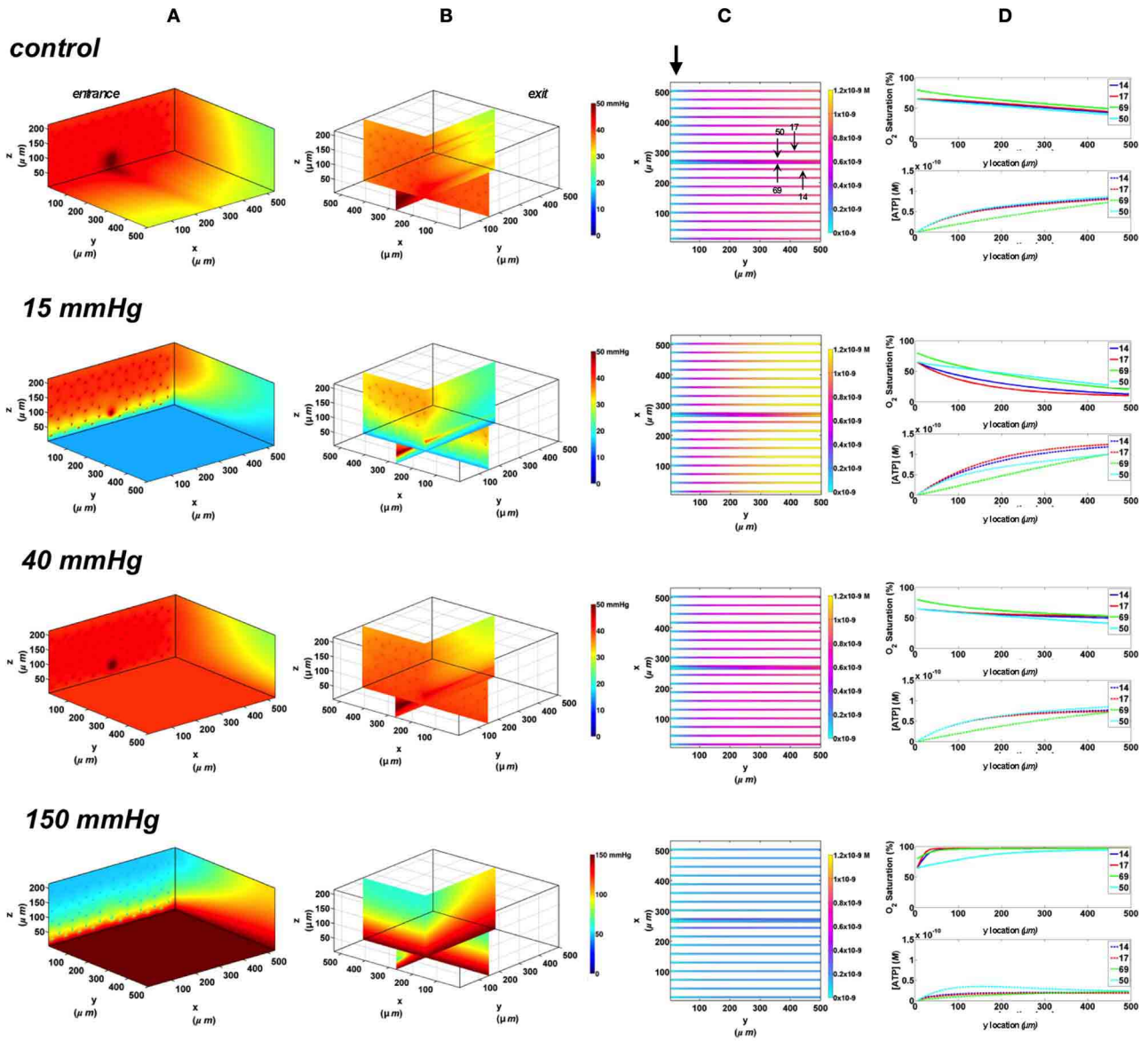

FIGURE 9 | Simulations of 3D PO_2 and capillary [ATP] distribution in a tissue with idealized parallel capillary arrangement (68 hexagonally packed capillaries), which includes a traversing terminal arteriole (vessel 69) at an entrance SO_2 of 80%. In these simulations, we are modeling O_2 delivery to bottom tissue surface using the full gas exchange chamber (Ghonaim et al., 2011; Ellis et al., 2012). Full bottom tissue surface is exposed to 15, 40, or 150 mmHg chamber PO_2 level relative to a zero flux control boundary condition **(A)** Spatial 3D tissue PO_2 distribution (mmHg) at capillary entrance perspective **(B)** a capillary exit perspective showing combined *X–Z* plane slice at $Y = 150\,\mu m$ and *Y–Z* plane slice at $X = 266\,\mu m$ **(C)** bottom perspective of a vessel map depicting distribution of [ATP] (mol/L = M) along the arteriole and surrounding capillaries. Bolded arrow marks arteriolar and capillary entrance **(D)** Plots of SO_2 (%) and [ATP] changes along vessel length in selected vessels (14, 17, 69-arteriole, 50) marked by arrows on the vessel map. Capillary 17 is 16 μm from tissue surface, the arteriole and capillary 14 are 33 μm from tissue surface, and capillary 50 is deeper in the tissue, at 133 μm, yet is shown adjacent to the arteriole in the current perspective of the vessel map.

for the total network when increasing chamber PO_2 from 15 to 150 mmHg, the absolute change in ATP magnitude (moles) in the arteriole is ∼95% less. Finally, it should be noted that [ATP] in the arteriole is ∼20% lower when limiting area of PO_2 perturbations using the rectangular micro-slit.

DISCUSSION

In the microcirculation, ATP is released from the erythrocytes in an SO_2 dependent manner. Released ATP would bind to purinergic receptors on the vascular endothelium which activates a signaling pathway leading to the opening of Ca^{2+} gated K^+ channels and the hyperpolarization of the endothelial cell

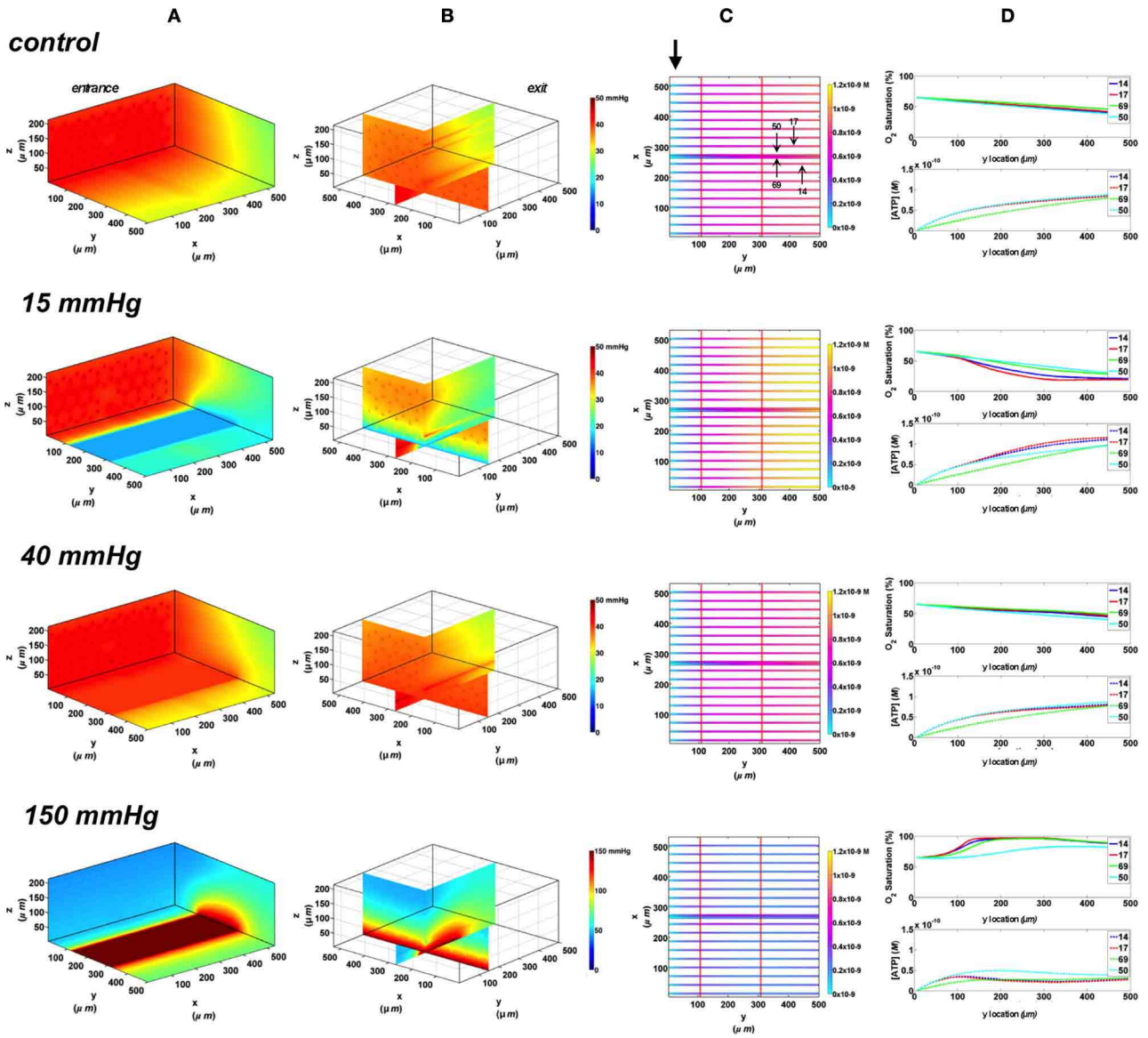

FIGURE 10 | Simulations of 3D PO_2 and capillary [ATP] distribution in a tissue with idealized parallel capillary arrangement (68 hexagonally packed capillaries), which includes a traversing terminal arteriole (vessel 69) at an entrance SO_2 of 65%. In these simulations, we are modeling O_2 delivery through a rectangular oxygen micro-delivery outlet (1000 μm wide × 200 μm long) to bottom tissue surface using our previously described novel micro-delivery approach (see **Figure 1**). Tissue surface directly on top of the micro-delivery outlet is exposed to 15, 40, or 150 mmHg chamber PO_2 level relative to a zero flux control boundary condition **(A)** Spatial 3D tissue PO_2 distribution (mmHg) at capillary entrance perspective **(B)** a capillary exit perspective showing combined *X–Z* plane slice at $Y = 150\,\mu m$ and *Y–Z* plane slice at $X = 266\,\mu m$ **(C)** bottom perspective of a vessel map depicting distribution of [ATP] (mol/L = M) along the arteriole and surrounding capillaries. Bolded arrow marks arteriolar and capillary entrance **(D)** Plots of SO_2 (%) and [ATP] changes along vessel length in selected vessels (14, 17, 69-arteriole, 50) marked by arrows on the vessel map. Capillary 17 is 16 μm from tissue surface, the arteriole and capillary 14 are 33 μm from tissue surface, and capillary 50 is deeper in the tissue, at 133 μm, yet is shown adjacent to the arteriole in the current perspective of the vessel map.

(Ellsworth et al., 2008; Tran et al., 2012). The hyperpolarization signal is then conducted upstream through gap junctions. At the arteriolar wall, the incoming hyperpolarization signal is conducted to the SMC layer through myo-endothelial gap junctions resulting in vaso-relaxation and increase in erythrocyte supply rate (Ellsworth et al., 2008; Tran et al., 2012). The magnitude of the hyperpolarization signal would depend on the number of endothelial cells activated along the capillary and on the total number of capillaries stimulated within a network under hypoxic conditions. This understanding of how erythrocyte-released ATP controls micro-vascular O_2 delivery is consistent with the modeling results presented in this paper. The net increase in total ATP magnitude in the network with increase in the area exposed to hypoxia is the summative contribution of additional stimulated

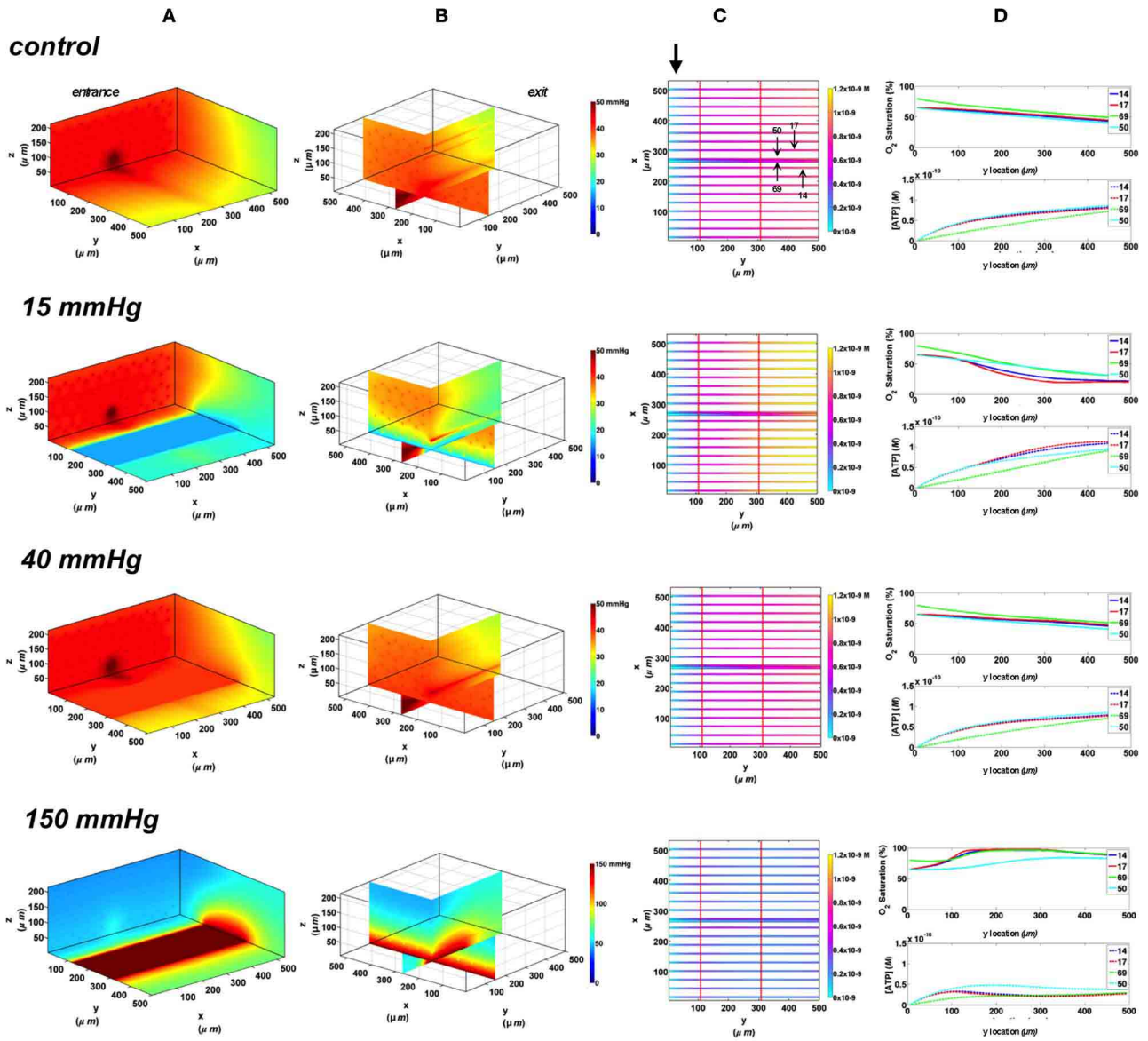

FIGURE 11 | Simulations of 3D PO_2 and capillary [ATP] distribution in a tissue with idealized parallel capillary arrangement (68 hexagonally packed capillaries), which includes a traversing terminal arteriole (vessel 69) at an entrance SO_2 of 80%. In these simulations, we are modeling O_2 delivery through a rectangular oxygen micro-delivery outlet (1000 μm wide × 200 μm long) to bottom tissue surface using our previously described novel micro-delivery approach (see **Figure 1**). Tissue surface directly on top of the micro-delivery outlet is exposed to 15, 40, or 150 mmHg chamber PO_2 level relative to a zero flux control boundary condition **(A)** Spatial 3D tissue PO_2 distribution (mmHg) at capillary entrance perspective **(B)** a capillary exit perspective showing combined *X*–*Z* plane slice at $Y = 150\,\mu m$ and *Y*–*Z* plane slice at $X = 266\,\mu m$ **(C)** bottom perspective of a vessel map depicting distribution of [ATP] (mol/L = M) along the arteriole and surrounding capillaries. Bolded arrow marks arteriolar and capillary entrance **(D)** Plots of SO_2 (%) and [ATP] changes along vessel length in selected vessels (14, 17, 69-arteriole, 50) marked by arrows on the vessel map. Capillary 17 is 16 μm from tissue surface, the arteriole and capillary 14 are 33 μm from tissue surface, and capillary 50 is deeper in the tissue, at 133 μm, yet is shown adjacent to the arteriole in the current perspective of the vessel map.

capillaries (**Figures 3–7**). Also, these results help explain our observations of no vascular response when experimentally testing the effect of O_2 delivery through a circular micro-outlet (100 μm in diameter) *in vivo* (Ghonaim et al., 2011). Although this design maybe optimal for locally altering SO_2 in single capillaries, the stimulus would probably not be sufficient to elicit a micro-vascular response. Increasing the dimensions of the micro-outlet would be necessary to stimulate a large enough number of capillaries, thus amplifying total magnitude of ATP release and signal.

Also, as our modeling data suggest, increasing the micro-outlet dimensions minimizes the effect of stimulated capillary

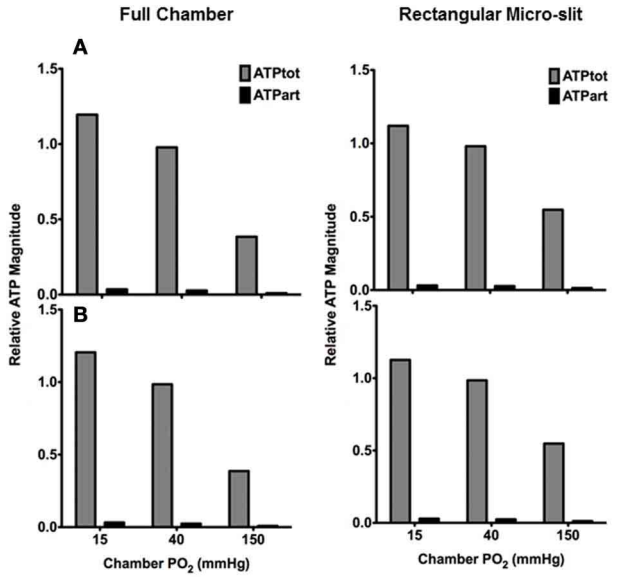

FIGURE 12 | Total ATP magnitude (moles) at steady state calculated for entire network (ATPtot from all 68 capillaries) or in the terminal arteriole only (ATPart) normalized against ATPtot calculated at no-flux condition. Relative ATP magnitudes are calculated for an idealized 3D parallel capillary array network with a terminal arteriole (9 μm in diameter) positioned 30 μm from tissue surface. Simulations were run with entire bottom tissue surface being exposed to PO_2 perturbations using full gas exchange chamber or locally using a rectangular O_2 delivery micro-slit (1000 μm wide × 200 μm long). For both conditions, relative ATP magnitudes are calculated for the case in which the terminal arteriole has an entrance SO_2 of **(A)** 65% or **(B)** 80%.

re-oxygenation downstream of the micro-outlet. This is because the capillaries of interest would be surrounded by capillaries experiencing the same drop in PO_2. This is more representative of the situation *in vivo* as the outlet physiologically simulates an arteriole crossing the capillary bed acting as an O_2 source or a venule withdrawing O_2, which would affect multiple capillaries. In terms of the signaling response, delayed re-oxygenation following hypoxic stimulation ensures the ATP signal persists longer distances downstream thus stimulating a larger number of endothelial cells. Since each endothelial cell in skeletal muscle is ∼100 μm long, using the rectangular slit is estimated to activate at least 3.5 endothelial cells in each stimulated capillary. In comparison with the square micro-outlet, which has the same length (200 μm) as the rectangular micro-slit, ∼1 more endothelial cell is activated per capillary with the latter design. It should be noted that in the modeled geometry, which lacks realistic capillary branching and has an idealized, uniform capillary density, we are examining relative changes in the total magnitude of ATP when using various outlet designs. During *in vivo* experiments, a maximum of two micro-vascular units ∼10 capillaries may be positioned along the entire width of the rectangular micro-slit, while only one or two capillaries with a branching point could be positioned over the circular micro-outlet (Ghonaim et al., 2011). Hence a 1000 μm wide × 200 μm long outlet might cover the threshold number of capillaries needed to elicit a micro-vascular response. This indicates the rectangular micro-slit would be optimal for stimulating enough capillaries by imposed hypoxia to generate high enough ATP signal.

The limited amount of change in tissue PO_2 due to diffusion (∼50 μm), as measured from the 3D tissue PO_2 profiles, beyond the edge of the micro-outlets (**Figures 4A–6A** and **4B–6B**) was consistent with our previous observations (Ghonaim et al., 2011). The simulations indicated that the PO_2 perturbations are highly localized to only those capillaries directly over the micro-outlet region. Experimentally, the results suggest that the micro-outlet should be positioned at least 50 μm downstream of the terminal feeding arteriole to ensure that micro-vascular responses are only elicited from the capillaries positioned directly over the outlet. The extent of axial O_2 diffusion in the tissue when using the rectangular micro-slit was 50% deeper than that previously modeled for the circular micro-outlet (**Figures 6B**, **10B**, **11B**) (Ghonaim et al., 2011) and similar to that of the full surface model (Ghonaim et al., 2011; Ellis et al., 2012). Due to the shape of the PO_2 profile, the maximal axial diffusion distance is estimated from the center of the outlet. The increase in the axial diffusion distance might be a compromise when using larger O_2 micro-outlets. With our current microscopic techniques we are unable to resolve vessels deeper than 60 μm.

Since in our experiments, we examine micro-vascular signaling from selected capillaries, it was critical that we assess the possible contribution of arterioles beyond our ability to focus. Since arterioles have relatively higher erythrocyte velocities than in the capillaries, they are anticipated to experience a much lesser change in SO_2 in response to PO_2 perturbations. This was supported by our simulation data (**Figures 8–11**). The main effect of a nearby terminal arteriole on a capillary within 50 μm is that it would act as an O_2 source. As shown in our modeling data (**Figures 8D–11D**), higher measured SO_2 in a capillary relative to other capillaries with comparable flow rates in the same preparation might imply the presence of a nearby arteriole. Since arterioles in the EDL muscle preparation are deeper in the tissue, their contribution to the total magnitude of ATP in a locally stimulated capillary network is probably negligible. The contribution of a terminal arteriole positioned directly over the micro-slit ∼30 μm from bottom surface was calculated to be less than 3% of the total magnitude of the ATP (**Figure 12**). Hence, when locally stimulating capillaries, even in the presence of an underlying arteriole, the observed micro-vascular responses mediated by intra-luminal ATP would be primarily due to ATP released in the stimulated capillaries.

In conclusion, we have modeled SO_2-dependant changes in [ATP] at steady state in 3D idealized parallel capillary networks in response to local PO_2 perturbations. As the number of affected capillaries increases, the total magnitude ATP in the network increases. The results indicated that O_2 delivery or removal to overlaying tissue through a rectangular micro-slit (1000 μm wide × 200 μm long) would be optimal relative to other micro-outlet designs of smaller dimensions or a full surface classical exchange type chamber. Using the rectangular micro-slit it is anticipated

that a sufficient number of capillaries will be stimulated to produce a large enough magnitude of ATP to elicit micro-vascular responses. This would be accomplished while maintaining the stimulus localized to the selected capillaries. The results also indicated that terminal arterioles have minimal influence on the total magnitude of ATP in the network under hypoxic condition. Hence, when locally stimulating the capillary bed, the majority of the signal elicited by ATP release would originate in the capillaries. The computational model presented provides valuable insights into how to study the ATP release mechanism and signaling in capillary networks *in vivo*. The modeling data help guide us in the design of an optimal tool for studying SO_2-dependent ATP release in capillaries *in vivo*. In the future, we aim to model time-dependent ATP release to local PO_2 perturbations in a realistic capillary network geometry reconstructed from experimental data. Combining our *in vivo* experimental observations with computational modeling of the dynamics of SO_2-dependent ATP release will help provide a more comprehensive understanding of O_2 mediated blood flow regulation in micro-vascular networks.

ACKNOWLEDGMENTS

This work was supported via the NSERC Alexander Graham Bell Canada Graduate Scholarship (CGSD) and the Western Graduate Research Scholarship (WGRS) to Ghonaim. This research was also supported by grant funding from NIH (HL089125) to Ellis and Goldman and from the Canadian Institutes of Health Research (MOP 102504) to Ellis and Goldman. Jun Yang is grateful for financial support from Natural Sciences and Engineering Research Council of Canada (NSERC).

REFERENCES

Arciero, J. C., Carlson, B. E., and Secomb, T. W. (2008). Theoretical model of metabolic blood flow regulation: roles of ATP release by red blood cells and conducted responses. *Am. J. Physiol. Heart Circ. Physiol.* 295, H1562–H1571. doi: 10.1152/ajpheart.00261.2008

Bagher, P., and Segal, S. S. (2011). Regulation of blood flow in the microcirculation: role of conducted vasodilation. *Acta. Physiol. (Oxf.)* 202, 271–284. doi: 10.1111/j.1748-1716.2010.02244.x

Bergfeld, G. R., and Forrester, T. (1992). Release of ATP from human erythrocytes in response to a brief period of hypoxia and hypercapnia. *Cardiovasc. Res.* 26, 40–47. doi: 10.1093/cvr/26.1.40

Collins, D. M., McCullough, W. T., and Ellsworth, M. L. (1998). Conducted vascular responses:communication across the capillary bed. *Microvasc. Res.* 56, 43–53. doi: 10.1006/mvre.1998.2076

Dietrich, H. H. (1989). Effect of locally applied epinephrine and norepinephrine on blood flow and diameter in capillaries of rat mesentery. *Microvasc. Res.* 38, 125–135. doi: 10.1016/0026-2862(89)90021-6

Dietrich, H. H., and Tyml, K. (1992a). Microvascular flow response to localized application of norepinephrine on capillaries in rat and frog skeletal muscle. *Microvasc. Res.* 43, 73–86. doi: 10.1016/0026-2862(92)90007-C

Dietrich, H. H., and Tyml, K. (1992b). Capillary as a communicating medium in the microvasculature. *Microvasc. Res.* 43, 87–99. doi: 10.1016/0026-2862(92)90008-D

Duling, B. R. (1974). Oxygen sensitivity of vascular smooth muscle.11. *In vivo* studies. *Am. J. Physiol.* 227, 42–49.

Duling, B. R., and Berne, R. M. (1970). Longitudinal gradients in periarteriolar oxygen tension: a possible mechanism for the participation of oxygen in local regulation of blood flow. *Circ. Res.* 27, 669–678. doi: 10.1161/01.RES.27.5.669

Eggleton, C. D., Vadapalli, A., Roy, T. K., and Popel, A. S. (2000). Calculations of intracapillary oxygen tension distributions in muscle. *Math. Biosci.* 167, 123–143. doi: 10.1016/S0025-5564(00)00038-9

Ellis, C. G., Ellsworth, M. L., and Pittman, R. N. (1990). Determination of red blood cell oxygenation *in vivo* by dual video densitometric image analysis. *Am. J. Physiol.* 258, H1216–H1223.

Ellis, C. G., Ellsworth, M. L., Pittman, R. N., and Burgess, W. L. (1992). Application of image analysis for evaluation of red blood cell dynamics in capillaries. *Microvasc. Res.* 44, 214–225. doi: 10.1016/0026-2862(92)90081-Y

Ellis, C. G., Milkovich, S. L., and Goldman, D. (2012). What is the efficiency of ATP signaling from erythrocytes to regulate distribution of O_2 supply within the microvasculature? *Microcirculation* 5, 440–450. doi: 10.1111/j.1549-8719.2012.00196.x

Ellsworth, M. L., Ellis, C. G., Goldman, D., Stephenson, A. H., Dietrich, H. H., and Sprague, R. S. (2008). Erythrocytes: oxygen sensors and modulators of vascular tone. *Physiology* 24, 107–116. doi: 10.1152/physiol.00038.2008

Ellsworth, M. L., Forrester, T., Ellis, C. G., and Dietrich, H. H. (1995). The erythrocyte as a regulator of vascular tone. *Am. J. Physiol.* 269, H2155–H2161.

Fraser, G. M., Goldman, D., and Ellis, C. G. (2012). Microvascular flow modeling using *in vivo* hemodynamic measurements in reconstructed 3D capillary networks. *Microcirculation* 19, 510–520. doi: 10.1111/j.1549-8719.2012.00178.x

Ghonaim, N. W., Lau, L. W., Goldman, D., Ellis, C. G., and Yang, J. (2011). A micro-delivery approach for studying microvascular responses to localized oxygen delivery. *Microcirculation* 18, 646–654. doi: 10.1111/j.1549-8719.2011.00132.x

Goldman, D., Fraser, G. M., Ellis, C. G., Sprague, R. S., Ellsworth, M. L., and Stephenson, A. (2012). Toward a multiscale description of microvascular flow regulation: O_2 dependent release of ATP from human erythrocytes and the distribution of ATP in capillary networks. *Front. Physiol.* 3:246. doi: 10.3389/fphys.2012.00246

Goldman, D., and Popel, A. S. (1999). Computational modeling of oxygen transport from complex capillary networks. Relation to the microcirculation physiome. *Adv. Exp. Med. Biol.* 471, 555–563. doi: 10.1007/978-1-4615-4717-4_65

Goldman, D., and Popel, A. S. (2000). A computational study of the effect of capillary network anastomoses and tortuosity on oxygen transport. *J. Theor. Biol.* 206, 181–194. doi: 10.1006/jtbi.2000.2113

Goldman, D., and Popel, A. S. (2001). A computational study of the effect of vasomotion on oxygen transport from capillary networks. *J. Theor. Biol.* 209, 189–199. doi: 10.1006/jtbi.2000.2254

González-Alonso, J., Olsen, D. B., and Saltin, B. (2002). Erythrocyte and the regulation of human skeletal muscle blood flow and oxygen delivery: role of circulating ATP. *Circ. Res.* 91, 1046–1055. doi: 10.1161/01.RES.0000044939.73286.E2

Jackson, W. F. (1987). Arteriolar oxygen reactivity: where is the sensor? *Am. J. Physiol.* 253, H1120–H1126.

Jagger, J. E., Bateman, R. M., Ellsworth, M. L., and Ellis, C. G. (2001). Role of erythrocyte in regulating local O2 delivery mediated by hemoglobin oxygenation. *Am. J. Physiol. Heart. Circ. Physiol.* 280, H2833–H2839.

Japee, S. A., Ellis, C. G., and Pittman, R. N. (2004). Flow visualization tools for image analysis of capillary networks. *Microcirculation* 11, 39–54. doi: 10.1080/10739680490266171

Japee, S. A., Pittman, R. N., and Ellis, C. G. (2005a). Automated method for tracking individual red blood cells within capillaries to compute velocity and oxygen saturation. *Microcirculation* 12, 507–515. doi: 10.1080/10739680591003341

Japee, S. A., Pittman, R. N., and Ellis, C. G. (2005b). A new video image analysis system to study red blood cell dynamics and oxygenation in capillary networks. *Microcirculation* 12, 489–506. doi: 10.1080/10739680591003332

Miseta, A., Bogner, P., Berenyi, E., Kellermayer, M., Galambos, C., Wheatley, D., et al. (1993). Relationship between cellular ATP, potassium, sodium and magnesium concentrations in mammalian

and avian erythrocytes. *Biochim. Biophys. Acta* 1175, 133–139. doi: 10.1016/0167-4889(93)90015-H

Song, H., and Tyml, K. (1993). Evidence for sensing and integration of biological signals by the capillary network. *Am. J. Physiol.* 265, H1235–H1242.

Stein, J. C., and Ellsworth, M. L. (1993). Capillary oxygen transport during severe hypoxia: role of hemoglobin oxygen affinity. *J. Appl. Physiol.* 75, 1601–1607.

Tran, C. H. T., Taylor, M. S., Plane, F., Nagaraja, S., Tsoukias, N. M., Solodushko, V., et al. (2012). Endothelial Ca^{2+} wavelets and the induction of myoendothelial feedback. *Am. J. Physiol. Cell. Physiol.* 302, C1226–C1242. doi: 10.1152/ajpcell.00418.2011

Conflict of Interest Statement: The authors declare that the research was conducted in the absence of any commercial or financial relationships that could be construed as a potential conflict of interest.

Received: 18 June 2013; paper pending published: 12 July 2013; accepted: 03 September 2013; published online: 24 September 2013.

*Citation: Ghonaim NW, Fraser GM, Ellis CG, Yang J and Goldman D (2013) Modeling steady state SO_2-dependent changes in capillary ATP concentration using novel O_2 micro-delivery methods. Front. Physiol. **4**:260. doi: 10.3389/fphys.2013.00260*

This article was submitted to Computational Physiology and Medicine, a section of the journal Frontiers in Physiology.

frontiers in
PHYSIOLOGY

PERSPECTIVE ARTICLE
published: 15 November 2013
doi: 10.3389/fphys.2013.00299

NHLBI support of systems biology

Pankaj Qasba[1]* and Jennie Larkin[2]

[1] Blood Diseases Branch, Division of Blood Diseases and Resources, HHS, National Institutes of Health, National Heart, Lung, and Blood Institute, Bethesda, MD, USA
[2] Advanced Technologies and Surgery Branch, Division of Cardiovascular Sciences, National Institutes of Health, National Heart, Lung, and Blood Institute, Bethesda, MD, USA

Edited by:
Raimond L. Winslow, Johns Hopkins University, USA

Reviewed by:
Sonia C. Cortassa, Johns Hopkins University, USA
Jeffrey J. Saucerman, University of Virginia, USA

***Correspondence:**
Pankaj Qasba, Blood Diseases Branch, Division of Blood Diseases and Resources, HHS, National Institutes of Health, National Heart, Lung, and Blood Institute, Bethesda, MD 20892-7950, USA
e-mail: pq5h@nih.gov

The National Heart, Lung, and Blood Institute (NHLBI) has recognized the importance of the systems biology approach for understanding normal physiology and perturbations associated with heart, lung, blood, and sleep diseases and disorders. In 2006, NHLBI announced the Exploratory Program in Systems Biology program, followed in 2010 by the NHLBI Systems Biology Collaborations program. The goal of these programs is to support collaborative teams of investigators in using experimental and computational strategies to integrate the component parts of biological networks and pathways into computational models that are based firmly on and validated using experimental data. These validated models are then applied to gain insights into the mechanisms of altered system function in disease, to generate novel hypotheses regarding these mechanisms that can be tested experimentally, and to then use the results of experiments to refine the models. This perspective reviews the history of dedicated systems biology programs at NHLBI and reviews some promising directions for future research in this area.

Keywords: NHLBI, NIH, funding opportunity, systems biology research, portfolio analysis

Systems biology aims to help us understand and predict the behavior of complex systems through a combination of experimental and computational approaches with each approach informing the other. Although high-throughput omic technologies may help inform a systems approach, such approaches alone do not constitute a systems biology research program. Similarly, while systems biology research requires computational modeling, neither does simply doing modeling encompass a systems biology program. Indeed, systems biology research requires both computational and experimental (often high-throughput) approaches in research program that complement and inform each other. Experiments measure the system and its key properties and responses, while computational models integrate the information and generate new testable hypotheses. This combination of experimental and computational approaches have been helping to improve the understanding of complex systems in heart, lung, and blood research for decades, and is particularly useful in understanding and even predicting the emergent properties of these systems, whose responses and characteristics may be greater than the sum of their parts. A critical early exemplar of the usefulness and impact of such approaches is Denis Noble's computational modeling of the cardiac action potential (Noble, 1962), which demonstrated that cardiac action potential results from interactions between multiple ion channels. His model helped form the basis of an active and growing cardiac simulation research community that continues to improve upon the models to refine their predictive ability and usefulness (Trayanova et al., 2012). These and other exemplars demonstrate the promise that the systems biology approach may hold to better understand complex systems, their dysfunction in disease, and support development of new therapies.

SYNOPSIS OF NHLBI ACTIVITIES TO DATE

Over the past 8 years, the National Heart, Lung, and Blood Institute (NHLBI) has invested in targeted programs to foster such integrated experimental and computational approaches in promising areas throughout the heart, lung, blood, and sleep research portfolio. Guided by input from a working group in 2004, "A Systems Biology Approach to Regulatory Networks in Heart, Lung, Blood and Sleep Research" that was chaired by Drs. Leroy Hood and Joseph Nadeau, NHLBI targeted its investment in systems biology to support research collaborations between computational and experimental researchers focused on specific research challenges.

The Request for Application (RFA) "NHLBI Exploratory Program in Systems Biology (R33)," HL06-004 and HL07-005, was designed to foster these multi-disciplinary collaborations that required integration of different types of expertise (predictive computational models, informatics, and experimental systems). To emphasize the importance of the balance and integration of these different approaches to the overall project, this program supported independent, linked R33 awards to the different collaborating investigators in the project. This multiple linked award approach was necessary as this program pre-dated the National Institutes of Health Multiple Principle Investigator policy (http://grants.nih.gov/grants/guide/notice-files/NOT-OD-07-017.html).

These linked R33 awards independently supported both the computational and experimental investigators while requiring them to work closely together to produce a single coherent, integrated project. The R33 mechanism was used to emphasize the high risk, innovative science this program intended to support. These R33 awards were not renewable, and successful projects

were expected to be competitive for subsequent investigator-initiated research proposals. To allow research communities in different stages of readiness to respond, the RFA was designed with multiple receipt dates and funded projects starting in 2006, 2007, and 2008. In the past, others have provided excellent reviews of the systems biology (Chuang et al., 2010; MacIlwain, 2011; Hood and Tian, 2012), here we provide an overview of the NHLBI support and development of the systems biology field as it applies to heart, lung, and blood research.

The "NHLBI Exploratory Program in Systems Biology" program was successful in developing this field across NHLBI research areas. Although NHLBI originally set aside $24.3 million to support nine awards, a total of twelve projects were funded for the RFA, given the number of high-quality applications. Some examples of the diversity of research supported through this program included "Blood Systems Biology," "Systems Biology of Sudden Cardiac Death," to the "Neurogenesis of Cough." Modeling approaches in these projects ranged from physics-based models, to agent-based models, to analysis of signaling networks. As this program encouraged multi-scale modeling, many of the proposals included multiple modeling approaches to address challenges at the different scales within the system. Following this successful RFAs -program, NHLBI continues to support this area by transitioning this program from RFA with a set-aside budget to an ongoing Program Announcement (PA), "NHLBI Systems Biology Collaborations (R01)"- PAR09-214. This PA was released in 2009 and had two receipt dates per year but retained a special emphasis panel for review. Between these targeted funding opportunities (RFA-HL-06-004, RFA-HL-07-005, and PAR09-214), NHLBI has committed $45.6 M between 2006 and 2012 to support systems biology research. NHLBI continues to support this PA through the renewal PAR12-138 that is active till 2015.

The purpose of this program was to build a community of researchers interested in developing, applying, and sharing systems biology approaches to the wide variety of research challenges represented across NHLBI research. This has been successful through both the original RFA program and through the various other programs supported from NHLBI. The success of this has also been shown through the large and vibrant group of HLBS researchers funded through the Interagency Modeling and Analysis Group's Multi-Scale Modeling program (IMAG/MSM). Indeed, the NHLBI systems biology program and the MSM programs have held joint meetings for the last 3 years, because of the shared research interests between the programs. These interactive meetings allow cross-cutting discussions across diverse research areas that help keep researchers informed about innovative new computational approaches of potential interest to their own research area.

An analysis of research funding of systems biology research using the NIH Reporter system (http://projectreporter.nih.gov/reporter.cfm) showed a marked growth in NHLBI systems biology research over the last 8 years (2006–2012). NHLBI support of research in this area through targeted announcements was assessed by searching the NIH Reporter database for grants funded through targeted funding opportunities RFA-HL-06-004, RFA-HL-07-005, or PAR-09-214. We determined number of awards, total costs, and number of publications in each year for each award. To determine the overall investment in the systems biology field, the same measures were taken for a search of grants that included the term "systems biology" in the title, abstract, or specific aims. This general search included only R21, R13, R33, and R01-equivalent grant mechanisms, excluding Program Projects (P01) and cooperative agreements. This analysis showed that the targeted funding announcements were responsible for the vast majority of systems biology projects supported by NHLBI from 2006 to 2009 (See **Figure 1**). However, starting in 2009, funding from these targeted announcements leveled off to about $5 M–$7 M per year, while the overall systems biology portfolio increased dramatically starting in 2009. Analysis of the output of the three targeted programs through publications shows an expected lag, with publications increasing from 2006 to 2009 then remaining steady, as it takes several years for the fruits of research to result in publications.

A visualization of the key terms from the grants identified from the overall "systems biology" analysis from NIH Reporter identifies overall themes across the portfolio (See **Figure 2**). The most common terms were "mathematical model," "gene expression," "candidate gene," "stem cells," and "heart failure." This analysis shows the diversity of scientific areas across the NHLBI portfolio using the systems biology approach: from heart failure, airway, and epithelial cell biology, to blood cell and stem cell regulation and infection. Approaches such as gene expression cut across disease areas, from pulmonary fibrosis, blood cells, to cardiovascular disease. This visualization gives a snapshot of the current NHLBI systems biology portfolio and highlights areas of strength and its diversity.

GOING FORWARD

Going forward we hope to see continued growth of systems biology approaches to diverse research challenges, where they are useful and appropriate, as the integration of computational and biological/experimental methodologies can provide greater insight to complex biology. One area of particular interest is the potential of systems biology to help guide and accelerate translational research. For instance, an integrated systems level approach may prove useful in accelerating targeted drug development and reduced off-target drug effects (Sorger and Allerheiligen, 2011). Systems approaches may also help quantify behavioral influences on disease propensity. Such integration across physiological, genetic, and behavioral models is identified as a challenge in the current Interagency Multi-Scale Modeling Initiative, "Predictive Multiscale Models for Biomedical, Biological, Behavioral, Environmental and Clinical Research (Interagency U01)" (http://grants.nih.gov/grants/guide/pa-files/PAR-11-203.html).

Another developing area of interest is personalized precision medicine that promises individualized modeling to refine and target treatments to each person. While earlier examples of personalized medicine were seen in the field of pharmacogenomics (Jiayi et al., 2009), precision medicine includes a variety of different research areas, explicitly including mathematical modeling. For example in the cardiovascular arena, personalized models of the cardiovascular system are being developed that incorporate image-based information about the heart or major vessels

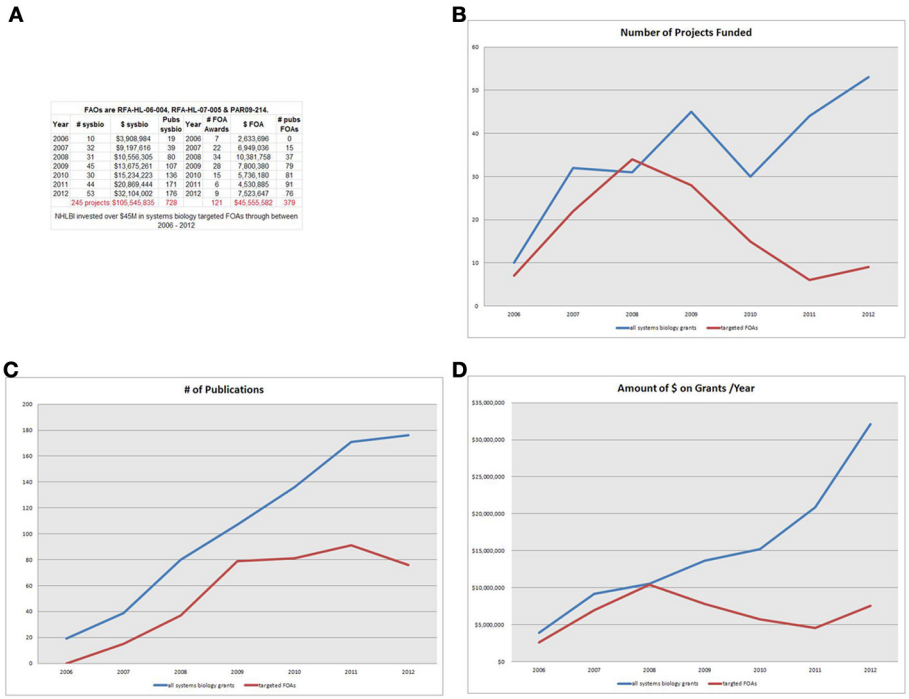

FIGURE 1 | (A) NHLBI investment-Legend-NHLBI invested over $45 M in systems biology targeted FOAs through between 2006 and 2012. **(B)** # of projects-Legend-For the first three years, the targeted systems biology FOAs make up most of the awards in the NHLBI portfolio. But as RFA funding ends, the number of awards self-identifying as systems biology projects increases (2011 and beyond). **(C)** # of publications-Legend-Publications from the targeted FOAs gain impact in 1–3 year lag following funding, continuing to increase through 2011, although funding peaked for targeted FAOs in 2008. **(D)** Amount of $ on grants/year-Legend- Through 2008, virtually all funding goes to the RFA awards. However other (non-FOA) systems biology grants accelerate rapidly from 2009 to 2012.

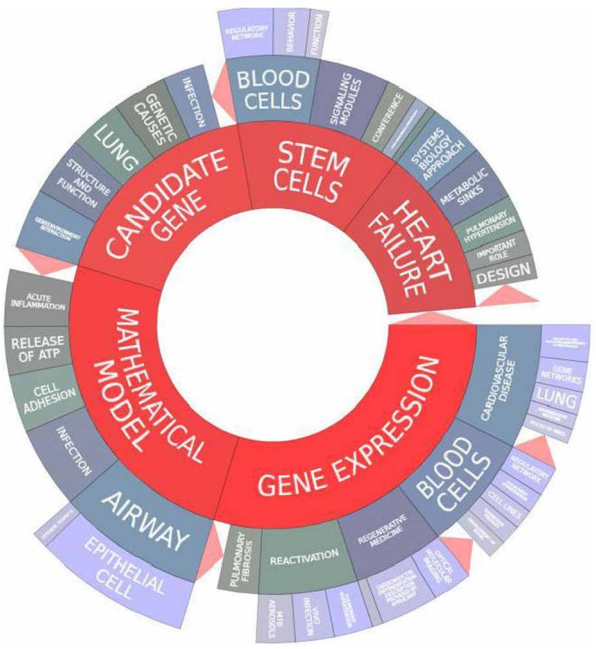

FIGURE 2 | NIH Reporter visualization of themes across the NHLBI systems biology portfolio (2006–2012).

from individual patients to generate predictive models tailored to that individual. Examples range from patient-specific models of cardiovascular mechanics (Krishnamurthy et al., 2013), to pre-surgical patient-specific aneurism models that help surgeons plan the surgery for each patient (Xiao et al., 2013), to application of individualized mathematical predictive models of blood flow in coronary arteries (Pijls and Sels, 2012), which has become a gold standard for invasive assessment of physiologic stenosis and an indispensable tool for decision making in coronary revascularization. Additionally, evidence that systems biology approaches have the potential to improve translation is the FDA approval of infusion pumps based on comprehensive models for diabetes. Models accurately recreated the precise and dynamic glucose-regulating function of a healthy pancreas (Kovatchev et al., 2009; Zhang et al., 2010).

Another area of interest is network-based approaches that seek to provide new insights into health and disease, by understanding complex interactions at the scale of individuals, tissues, or cells and the impact of disease state or therapeutics on disturbing these networks. One example is the Common Fund Library of Integrated Network based Cellular Signals (LINCS, http://www.lincsproject.org/) managed jointly by NHLBI and the National Human Genome Institute (NHGRI). LINCS aims to create a network-based understanding of biology by cataloging changes in gene expression and other cellular processes that occur when

cells are exposed to a variety of perturbing agents and by using computational tools to integrate this diverse information into a comprehensive view of normal and disease states that can be applied for the development of new biomarkers and therapeutics. Another NHLBI program designed to utilize evolving knowledge of cellular and molecular networks to define common mechanism-associated traits across organ systems is Cross Organ Mechanism-Associated Phenotypes for Genetic Analyses of Heart, Lung, Blood, and Sleep Diseases (MAPGen, http://mapgenprogram.com/). The program identifies and characterizes common pathobiologic traits and/or mechanisms that cross organ systems and diseases with the ultimate goal of redefining heart, lung, blood, and sleep disorders based on newfound knowledge of the underlying molecular and/or cellular pathobiology. More recently, research in the MapGen program is making important strides to highlight our understanding of cellular networks and their relation to human diseasome, which may help foster network medicine (Barabasi et al., 2011; Chan and Loscalzo, 2012). Given the functional interdependencies between the molecular components in a human cell, a disease is rarely a consequence of an abnormality in a single gene but reflects the perturbations of the complex intracellular network (Loscalzo and Barabasi, 2011). The hope is that network medicine will provide a platform to methodically dissect molecular complexity of a particular disease. This may allow both identification of common molecular underpinnings of differing phenotypes, as well as identification of divergent molecular mechanisms that may underlie clinically similar phenotypes. Such molecular phenotypes will allow more precise diagnosis and more targeted therapies and treatments.

Similarly, another tool -genomic DNA footprinting- enables mapping of millions of *in vivo* binding sites for hundreds of transcription factors simultaneously in primary human cells (Lazarovici et al., 2013). The tools target a key bottleneck limiting construction of comprehensive regulatory networks for human cells typically requiring one-by-one or few-by-few discovery of connections between transcriptional regulators. The resulting maps enable the construction of accurate, comprehensive transcriptional regulatory networks that can, identify key regulatory factors for biological processes, help map networks associated with specific disease states and pinpoint specific regulatory factors that play a pathogenic role in disease (Maurano et al., 2012).

Finally, these emerging areas show the promise that systems biology approaches hold to help address key biomedical research challenges. The NHLBI programs have proven effective in fostering the development and application of these approaches across a wide range of areas, and we look forward to the day when researchers readily/keenly accept such quantitative approaches as part of a robust research strategy, just as DNA sequencing or RNA expression has become a common activity in biomedical research and not the sole domain of a few experts.

The views expressed by PQ and JL in this commentary are personal and do not necessarily represent those of the US Government.

REFERENCES

Barabasi, A. L., Gulbahce, N., and Loscalzo, J. (2011). Network medicine: a network-based approach to human disease. *Nat. Rev. Genet.* 12, 56–68. doi: 10.1038/nrg2918

Chan, S. Y., and Loscalzo, J. (2012). The emerging paradigm of network medicine in the study of human disease. *Circ. Res.* 111, 359–374. doi: 10.1161/CIRCRESAHA.111.258541

Chuang, H., Hofree, M., and Ideker, T. (2010). A decade of systems biology. *Annu. Rev. Cell Dev. Biol.* 26, 721–744. doi: 10.1146/annurev-cellbio-100109-104122

Hood, L., and Tian, Q. (2012). Systems approaches to biology and disease enable translational systems medicine. *Genomics Proteomics Bioinformatics* 10, 181–185. doi: 10.1016/j.gpb.2012.08.004

Jiayi, L., Shan, W., Joseph, B., and Brian, M. (2009). Warfarin pharmacogenomics. *Pharm. Ther.* 34, 422–427.

Kovatchev, B. P., Breton, M., Man, C. D., and Cobelli, C. (2009). *In silico* preclinical trials: a proof of concept in closed-loop control of type 1 diabetes. *J. Diabetes Sci. Technol.* 3, 44–55.

Krishnamurthy, A., Villongco, C. T., Chuang, J., Frank, L. R., Nigam, V., Belezzuoli, E. et al. (2013). Patient-specific models of cardiac biomechanics. *J. Comput. Phys.* 244, 4–21. doi: 10.1016/j.jcp.2012.09.015

Lazarovici, A., et al. (2013). Probing DNA shape and methylation state on a genomic scale with DNase I. *Proc. Natl. Acad. Sci. U.S.A.* 110, 6376–6381. doi: 10.1073/pnas.1216822110

Loscalzo, J., and Barabasi, A. L. (2011). Systems biology and the future of medicine. *Wiley Interdiscip. Rev. Syst. Biol. Med.* 3, 619–627. doi: 10.1002/wsbm.144

MacIlwain, C. (2011). Systems biology: evolving into the mainstream. *Cell* 144, 839–841. doi: 10.1016/j.cell.2011.02.044

Maurano, M. T., Humbert, R., Rynes, E., Thurman, R. E., Haugen, E., Wang, H., et al. (2012). Systematic localization of common disease-associated variation in regulatory DNA. *Science* 337, 1190–1195. doi: 10.1126/science.1222794

Noble, D. (1962). A modification of the Hodgkin-Huxley equations applicable to Purkinje fibre action and pacemaker potentials. *J. Physiol.* 160, 317–352.

Pijls, N. H. J., and Sels, J-W. E. M. (2012). Functional measurement of coronary stenosis. *J. Am. Coll. Cardiol.* 59, 1045–1057. doi: 10.1016/j.jacc.2011.09.077

Sorger, P. K., and Allerheiligen, S. R. B. (2011). "Quantitative and systems pharmacology in the post-genomic era: New approaches to discovering drugs and understanding therapeutic mechanisms," in *An NIH White Paper by the QSP Workshop Group*, (Bethesda: NIH).

Trayanova, N. A., O'Hara, T., Bayer, J. D., Boyle, P. M., McDowell, K. S., Constantino, J., et al. (2012). Computational cardiology: how computer simulations could be used to develop new therapies and advance existing ones. *Europace* 14, v82–v89. doi: 10.1093/europace/eus277

Xiao, N., Humphrey, J. D., and Figueroa, C. A. (2013). Multi-scale computational model of three- dimensional hemodynamics within a deformable full-body arterial network. *J. Comput. Phys.* 244, 22–40. doi: 10.1016/j.jcp.2012.09.016

Zhang, Y., Jones, P. L., and Jetley, R. (2010). A hazard analysis for a generic insulin infusion pump. *J. Diabetes Sci. Technol.* 4, 263–283.

Conflict of Interest Statement: The authors declare that the research was conducted in the absence of any commercial or financial relationships that could be construed as a potential conflict of interest.

Received: 31 July 2013; paper pending published: 25 August 2013; accepted: 29 September 2013; published online: 15 November 2013.

*Citation: Qasba P and Larkin J (2013) NHLBI support of systems biology. Front. Physiol. **4**:299. doi: 10.3389/fphys.2013.00299*

This article was submitted to Computational Physiology and Medicine, a section of the journal Frontiers in Physiology.